ANCHAM

ANALYTICAL CHEMISTRY

NOVEMBER 15, 1995

Postionization Depth Profiling 4033

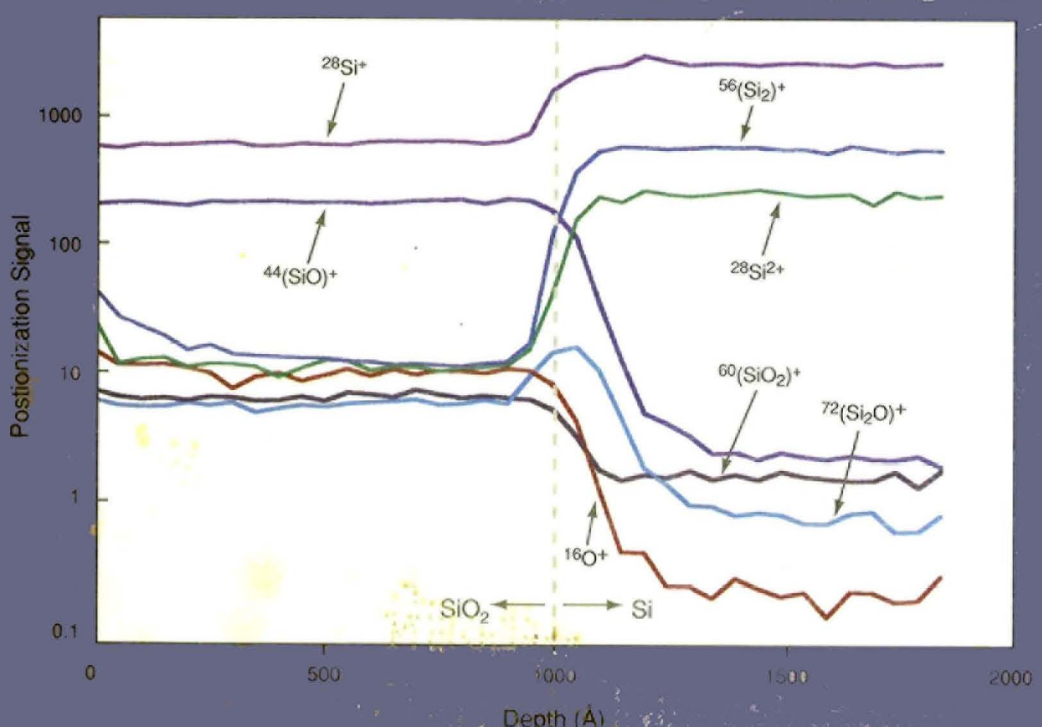

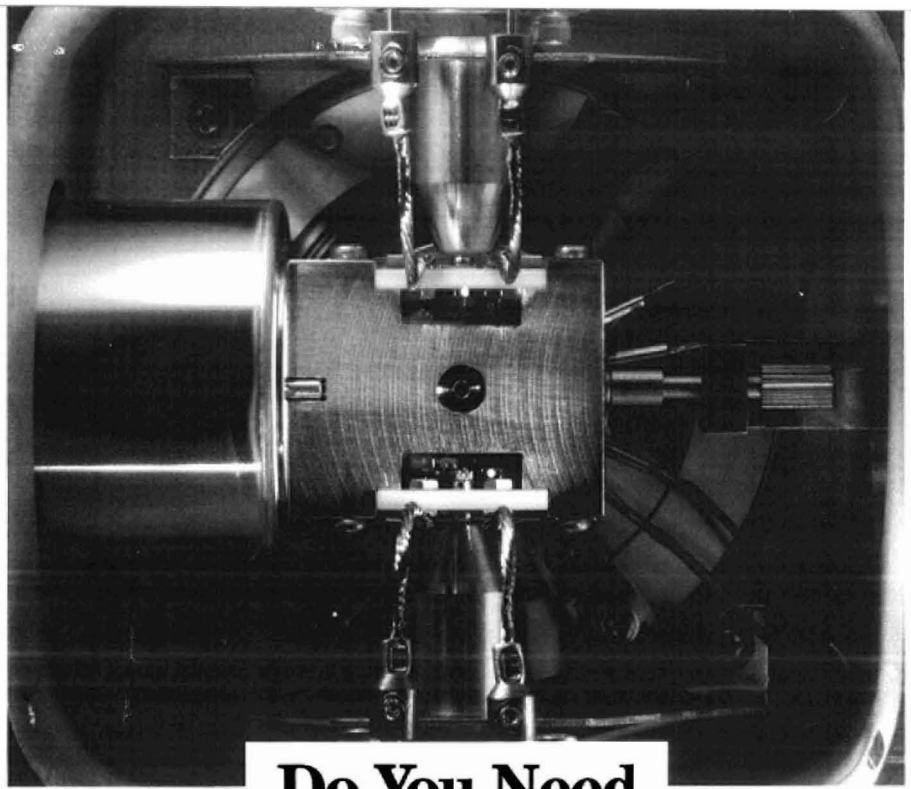

Do You Need A Comprehensive GC/MS Solution?

The Shimadzu GC/MS QP-5000. The new generation. Compact and complete.

Regardless of whether you work in water, air, or soil analysis, or whether you are looking for environmental analysis, additives in food, or forensics drug abuse, our new GC/MS QP-5000 is sure to exceed your expectations. Its mass spectrometer, covering the range 10 amu to 700 amu, is coupled to the proven performance of the GC-17A gas chromatograph, including AFC for setting carrier related flows and pressures. Our new GC/MS QP-5000 has been designed for the most stringent analytical methodology as well as routine analytical laboratory work. Its compactness and range of features are truly impressive. The overall width of the GC and MS is just 72.5 cm (28.5"). All system operations are controlled by Microsoft® Windows™-based software. The GC/MS QP-5000 is a highly sensitive bench-top GC/MS with computer-simulation-optimized ion optics and fully automated vacuum control. Available options include a jet-separator interface, a high capacity turbomolecular pump, chemical-ionization, and a direct inlet system for low volatiles. Call your nearest Shimadzu Representative today for more details on the GC/MS QP-5000. You can count on a prompt response from us.

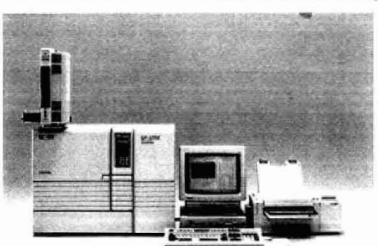

Microsoft® Windows™ is a registered trademark of Microsoft Corporation, Redmond, WA, USA.

SHIMADZU CORPORATION,
International Marketing Division
3, Kanda-Nishikicho 1-chome, Chiyoda-ku, Tokyo 101, Japan
Phone: 81(3)3219-5641 Fax.: 81(3)3219-5710

SHIMADZU SCIENTIFIC INSTRUMENTS, INC.
7102 Riverwood Drive, Columbia, Maryland 21046, U.S.A.
Phone: 1(410)381-1227 Fax.:1(410)381-1222

SHIMADZU EUROPA GmbH
Phone: 49(203)7687-0 Fax.: 49(203)766625 Germany.

SHIMADZU (ASIA PACIFIC) PTE LTD.
Phone: 65-778 6280 Fax.: 65-779 2935 Singapore.

SHIMADZU OCEANIA PTY. LTD.
Phone: 61(2)684-4200 Fax.: 61(2)684-4055 Australia.

*For more information, please contact us.

SHIMADZU

Solutions for Science
since 1875

ANALYTICAL CHEMISTRY

VOLUME 67, NUMBER 22

Analytical Chemistry (ISSN 0003-2700) is published semi-monthly by the American Chemical Society, 1155 16th St., NW, Washington, DC 20036. Second-class postage paid at Washington, DC, and at additional mailing offices. Postmaster: Send address changes to Member & Subscriber Services, P.O. Box 3337, Columbus, OH 43210 Canadian GST Reg. No. 127571347

1995 subscription rates include air delivery outside the U.S., Canada, and Mexico. Canadian subscriptions are subject to 7% GST.

	Members	Nonmembers (personal)	Nonmembers (institutional)
U.S.	$ 40	$ 85	$ 570
Canada and Mexico	77	122	607
Europe	123	168	653
Other countries	148	193	678

Members may share/donate their personal subscriptions with/to libraries and the like but only after 5 years from publication.

Nonmember rates in Japan: Rates above do not apply to nonmember subscribers in Japan, who must enter subscription orders with Maruzen Company Ltd., 3–10, Nihonbashi 2-chome, Chuo-ku, Tokyo 103, Japan. Tel: (03) 272-7211.

For multi-year and other rates, call toll free 800-227-5558 in the U.S. and Canada; in the Washington, DC, metropolitan area and outside the U.S., call 202-872-4363; fax 202-872-4615.

Single issues, current year, $24.00 except review issue, $50.00, and LabGuide, $50.00; **back issues and volumes and microform editions** available by single volume or back issue collection. For information or to order, call the number listed for subscription orders; or write the Microform & Back Issues Office at the Washington address.

Subscription orders by phone may be charged to VISA, MasterCard, or American Express. Call toll free 800-333-9511 in the continental U.S.; in the Washington, DC, metropolitan area and outside the continental U.S., call 202-872-8065. Mail orders for new and renewal subscriptions should be sent with payment to American Chemical Society, Department L-0011, Columbus, OH 43268-0011.

Changes of address must include both old and new addresses with ZIP code and a recent mailing label. Send all address changes to the ACS Columbus address. Please allow 6 weeks for change to become effective. **Claims for missing issues** will not be allowed if loss was due to failure of notice of change of address to be received in the time specified; if claim is dated (a) North America—more than 90 days beyond issue date, (b) all other foreign—more than 180 days beyond issue date. Hard copy claims are handled at the ACS Columbus address.

Instructions for authors of AC Research and guidelines for the Instrumentation, Report, Analytical Approach, and A/C Interface features are published in the Jan. 1 issue, p. 229, or can be obtained from our e-mail reflector "acinfo@acs.org" using the keyword phrases "ac research" or "ac apguide," respectively. Please consult these instructions prior to submitting a manuscript for consideration for publication.

Manuscripts for publication in AC Research (4 copies of text and illustrative material) should be submitted to the Editor at the University of North Carolina address. Please include a signed copyright status form; a copy of this document appears on p. 235 of the Jan. 1 issue. Manuscripts for publication in the A-page section should be submitted to the Washington editorial staff.

Supporting information is noted in the table of contents with a ■. It is available as photocopy ($12.00 for up to 3 pages and $1.50 per page for additional pages, plus $2.00 for foreign postage) or as 24× microfiche ($12.00, plus $1.00 for foreign postage). Canadian residents should add 7% GST. See supporting information notice at the end of journal article for number of pages. Orders must give complete title of article, names of authors, journal, issue date, and page numbers. Prepayment is required and prices are subject to change. In 1995, electronic supporting information is available to current journal subscribers via the Internet using either gopher or World Wide Web protocols. Most often, the material is available as PDF files, which may be viewed using Adobe's Acrobat Reader, a program that is freely available on the Internet. However, some articles may include computer programs, PostScript files, word-processing files, experimental data in a standard format (e.g., crystallographic parameters in CIF format), etc. In order to download the supplementary material files, users will need to enter their journal subscriber number, which can be found on the mailing label. Detailed instructions for using this service can be found on the Internet. With gopher, connect to pubs.acs.org, go to the "ACS Publications" selection, then to the "Supporting Information" selection. Read the README file in this directory for detailed instructions. When using a WWW client (e.g., Mosaic, Netscape), connect to the URL "http://pubs.acs.org/" and select the "Supporting Info. for Journals" link. For further information on electronic access, send electronic mail to gopher@acsinfo.acs.org, or phone (202) 872-4434. For information on microforms, contact Microforms & Back Issues at the ACS Washington address or phone (202) 872-4554. Supporting information, except structure factors, also appears in the microfiche edition.

Journals Department, American Chemical Society, 2540 Olentangy River Road, P.O. Box 3330, Columbus, OH 43210 (614-447-3600, Ext. 3171; TELEX 6842086; Fax 614-447-3745)

Member & Subscriber Services: American Chemical Society, P.O. Box 3337, Columbus, OH 43210 (614-447-3776; 800-333-9511)

Advertising Management: Centcom, Ltd., 1599 Post Rd. East, P.O. Box 231, Westport, CT 06881 (203-256-8211; fax 203-256-8175)

ANCHAM 67(22) 4033–4220 (1995)
ISSN 0003-2700

ANALYTICAL CHEMISTRY®

NOVEMBER 15, 1995
Volume 67, Number 22

ACCELERATED ARTICLES

ARTICLES

TECHNICAL NOTES

■ Supporting information for this paper is available separately (consult a current masthead page for ordering information). Supporting information is available to subscribers electronically via the Internet at http://pubs.acs.org (WWW) and pubs.acs.org (Gopher). All supporting information except for structure factor tables will also appear following the paper in the microfilm edition of the journal.

* In papers with more than one author, the asterisk indicates the name of the author to whom inquiries about the paper should be addressed.

Accelerated Articles

Anal. Chem. 1995, *67*, 4033–4039

Detection of Sputtered Neutrals by Ultrahigh-Intensity Postionization in the Near-Infrared

Michael L. Wise,* A. Bruce Emerson, and Stephen W. Downey*

AT&T Bell Laboratories, 600 Mountain Avenue, Murray Hill, New Jersey 07974

Characterization of sputtered semiconductor materials by ultrahigh-intensity postionization has been performed utilizing a high repetition rate, regeneratively amplified, ultrafast Ti–sapphire laser coupled with a modified magnetic-sector SIMS instrument. The laser produces 120-fs pulses with focused intensities well in excess of 10^{14} W/cm^2 at 800 nm and 1 kHz. Studies of common matrices such as GaAs, InP, InGaAsP, and SiO_2 indicate that both singly and multiply charged ions as well as molecular ions can be detected with high efficiency in both surface analysis and depth-profiling sputtering modes. Relative sensitivity factors for the different elements are determined and related to the photoionization mechanism and to the other factors that can affect the detection efficiency. Future directions for such a technique are discussed.

The depth profiling of dopant concentrations across ultrathin device structures is critical to microelectronic device design and fabrication. Secondary ion mass spectrometry (SIMS) remains a common and extremely important technique for the characterization of semiconductor devices. However, SIMS suffers from strong matrix effects which can complicate the characterization of elemental concentrations at and near the interfaces of two materials. For this reason, complementary analytical techniques referred to as sputtered neutral mass spectrometry (SNMS) have been developed. In SNMS, usually a laser or an electron beam is used to ionize the neutral species in the gas phase above the sample after ion beam sputtering. At the cost of additional complexity when compared to SIMS, these "postionization" techniques can accomplish surface analysis and depth profiling with high sensitivity and relative freedom from matrix effects.

Laser postionization comes in two varieties. In sputter-initiated resonance ionization mass spectrometry, a tunable laser is used to selectively ionize one species via multiphoton ionization through one or more resonant electronic levels.[1] This technique can often achieve 100% ionization of the resonant species within the irradiated volume[2] but does not ionize nonresonant species with high efficiency. The absence of interferences can therefore produce detection limits below the ppb level.[3] Alternatively, sputtered or desorbed atoms from surfaces can be ionized nonresonantly by utilizing lasers capable of producing very high intensities.[4] Until recently, both approaches used nanosecond-pulsed lasers, the difference being that resonance ionization used millijoule energies and megawatt intensities while nonresonant ionization uses hundreds of millijoules and gigawatt intensities. Neither approach is suited for detecting all sputtered species with uniform high efficiency under one set of laser parameters in a large sample volume. The application of ultrahigh-intensity laser pulses (>10^{14} W/cm^2) to nonresonant postionization[5] increases the probability that many species, regardless of ionization potential, will be ionized with equal efficiency within the given volume. Ideally, such a technique would allow all sputtered species to be simultaneously quantified with a uniform sensitivity that is independent of the electronic structures of the species or variations in the matrix. This may, in turn, permit the quantification of elemental concentrations in complex multicomponent structures with little or no reliance on standards. Such work has already been investigated using picosecond laser pulses at the fundamental and harmonic wavelengths of the Nd–YAG laser.[6]

(1) Kimock, F. M.; Baxter, J. P.; Winograd, N. *Chem. Phys. Lett.* **1982**, *88*, 581–584.
(2) Downey, S. W.; Emerson, A. B. *Anal. Chem.* **1991**, *63*, 916–918.
(3) Arlinghaus, H. F.; Sparr, M. T.; Thonnard, N. *J. Vac. Sci. Technol. A* **1990**, *8*, 2318–2322.
(4) Becker, C. H.; Gillen, K. T. *Anal. Chem.* **1984**, *56*, 1671–1674.
(5) Dyer, M. J.; Jusinski, L. E.; Helm, H.; Becker, C. H. *Appl. Surf. Sci* **1991**, *52*, 151–157.
(6) Becker, C. H.; Hovis, J. S. *J. Vac. Sci. Technol. A* **1994**, *12*, 2352–2356.

0003-2700/95/0367-4033$9.00/0

This paper will evaluate nonresonant, ultrahigh-intensity post-ionization utilizing a high repetition rate, regeneratively amplified ultrafast Ti–sapphire laser capable of producing focused intensities in excess of 10^{14} W/cm^2 at 800 nm. A survey of a number of different materials indicates that both singly and multiply charged ions as well as molecular ions can be detected with high efficiency in both surface analysis and depth-profiling sputtering modes. Using these data, relative sensitivity factors for different elements are determined and related to the photoionization mechanism and to the other factors that can affect detection efficiency. In addition, future directions for such a technique are explored.

EXPERIMENTAL SECTION

(1) Laser. The laser system for producing high-intensity, femtosecond pulses is comprised of four lasers: a pump laser and oscillator, a second pump laser, and an amplifier. The system is supplied by Clark–MXR (Model CPA-1000) and fits on one 4 ft × 8 ft optical table. A continuous Ar ion laser (Coherent Innova 90) operating on all lines pumps a Ti-doped sapphire rod in the passively self-mode locked (Model NJA4) oscillator. The repetition rate of the pulses in the NJA4 is set by the cavity length and is 92 MHz. The output of the oscillator is typically 400 mW at 800 nm. The pulse width out of the oscillator is less than 100 fs.

The output pulses from the NJA4 contain less than 10 nJ/pulse and must be amplified for high-intensity applications. Prior to amplification, the pulses must be stretched temporally in order to efficiently extract energy from the gain medium in the regenerative amplifier without incurring optical damage. The pulses are increased to ~300 ps by a (Model PS-1000) pulse stretcher/isolator. This is achieved dispersively by eight passes off a grating which changes the optical path length of the different wavelengths ($\Delta\lambda \approx 10$ nm) comprising the short pulses.

The regenerative Ti–sapphire amplifier (Model TRA-1000) is pumped by an intracavity frequency-doubled, Q-switched Nd–YAG laser (ORC-1000). Between 7 and 11 W of ~1 kHz pulsed 532-nm light is used to pump the amplifier. The ORC is triggered by a submultiple of the pulse train out of a photodiode monitoring the output of the NJA oscillator. In this way, the ORC and the Pockels cell controlling the lasing and cavity dumping of the TRA-1000 can be synchronized to arriving stretched pulses from the PS-1000. When a selected pulse is confined to the amplifier cavity by the Pockels cell, it makes ~10 trips through the gain medium before being dumped out by the cell. The output power is ~1.5 W.

The stretched, amplified pulses are routed through the PS-1000 to the pulse compressor (Model PC-1000), where four passes on another grating are used to shorten the pulse width back to nearly their width coming out of the NJA. The efficiency of the compressor is ~60–70%, producing an output power of ~1 W.

The pulses emanating from the laser system were temporally characterized by a home-made autocorrelator. In the autocorrelator, the laser beam is first equally split into two parts on a beam splitter, one part moving toward a stationary hollow retroreflector and the other toward a moving hollow retroreflector. The moving retroreflector is mounted on a translatable stage driven by a piezoelectric screw-drive actuator. The two beams are then sent back to the beam splitter where they are displaced horizontally from one another. From the beam splitter, the two beams travel to a turning mirror, through a lens, and finally into a β-barium borate (BBO) frequency-doubling crystal where they are recombined. The 400-nm light from the doubling crystal is first filtered to remove the 800-nm fundamental and then detected by a photodiode. A boxcar averager and computer interface integrates the signal and sends it to a Macintosh computer.

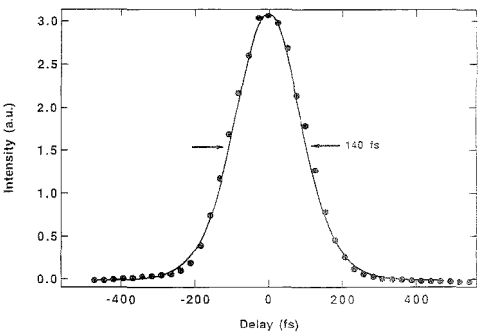

Figure 1. Autocorrelation spectrum of the laser pulse. The fit to the curve represents the autocorrelation peak shape expected if the individual laser pulses have time-dependent intensity $I(t) = \mathrm{sech}^2(t)$.

Changing the distance between the beam splitter and the moving hollow retroreflector changes the beam path of one of the split pulses and allows one of the pulses to be scanned over the other in time. The detected signal from the doubling crystal is then proportional to the degree of overlap of the recombined pulses. Figure 1 shows the 400-nm light intensity generated in the doubling crystal as a function of delay time. The delay time was computed by taking twice the distance that the moving hollow retroreflector was translated and dividing by the speed of light. The fit to the curve represents the autocorrelation peak shape expected if the individual laser pulses have time-dependent intensity $I(t) = \mathrm{sech}^2(t)$.[7] Deconvolution of the autocorrelation trace indicates a fwhm laser pulse width of 140 fs. All the experiments shown here were conducted with pulse widths measured between 110 and 150 fs. It is noted that the autocorrelation spectra were collected after the laser had been attenuated by two thin (1.1 mm) glass neutral density filters identical to those used in the ion signal vs laser intensity experiments presented in the Results section. The chromatic dispersion in these optics would cause the autocorrelation spectra to indicate only a slightly longer pulse length than those actually produced by the laser system.

(2) Sputtering, Ionization, and Detection. The instrument is a modified UHV magnetic-sector secondary ion mass spectrometer. Sputtering Xe ions are produced in a duoplasmatron ion source and mass filtered with a Wien filter. Primary ion energies are set at 4 keV relative to the sample, resulting in an angle of incidence of ~60° relative to the sample normal. The beam has a spot size of ~100-μm (fwhm) diameter. Beam current is measured by monitoring the current at the sample with a picoammeter while the primary beam strikes the steel sample holder. Secondary electron emission is suppressed during the measurement. For surface analysis, the primary ion beam is pulsed so as to preserve the sample. Each sputtering pulse (1 kHz) is 600 ns long. To perform a depth profile, the primary ion beam is cycled between continuous, rastered sputtering to create the crater and pulsed sputtering, during which the ion signals

(7) Diels, J. M.; Fontaine, J. J.; McMichael, I. C.; Simoni, F. *Appl. Opt.* 1985, *24*, 1270–1282.

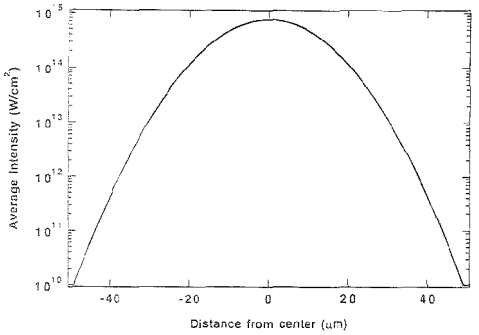

Figure 2. Time-averaged laser intensity at the focus of the 35-cm focal length lens as a function of distance from the center of the focus. Calculations are based on a pulse energy of 700 μJ and a pulse length of 140 fs.

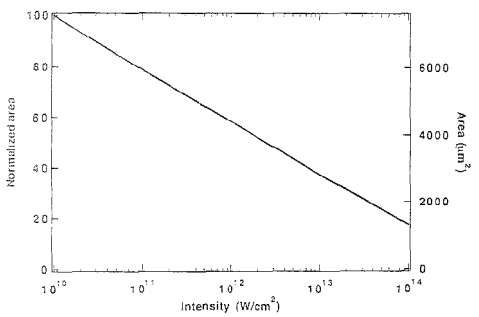

Figure 3. Cross-sectional areas at the focus of the laser beam with different average intensities. Calculations are based on a pulse energy of 700 μJ and a pulse length of 140 fs.

are measured. The pulsed sputtering ion detection occurs in the center of the crater to avoid side-wall effects.

The laser beam fires ~3 μs after the start of the sputter pulse. The laser is allowed into the chamber through a CaF_2 vacuum window and is focused ~100 μm in front of the sample surface by a 35-cm focal length planoconvex lens external to the chamber. The focused laser beam diameter can be calculated using the equation for the focusing of a collimated Gaussian beam given by

$$2\omega_0 = (4\lambda/\pi)(F/D) \qquad (1)$$

where $2\omega_0$ is the waist diameter, λ is the wavelength, F is the focal length of the lens, and D is the diameter of the beam before entering the lens (8.6 mm). Based on eq 1, a focused beam diameter of 41 μm is estimated. Figure 2 shows the time-averaged laser intensity as a function of distance from the center of the focus for a typical laser pulse with an energy of 700 μJ and a pulse width of 140 fs. Actual peak intensities are 3.67 times larger than the averaged intensities represented here.[8] Additionally, Figure 3 shows the cross-sectional area of the beam at the different intensities.

The sample holder is biased 6.2 kV greater than the grounded ion extraction plate, which is located ~4 mm from the sample.

(8) Gibson, G.; Luk, T. S.; Rhodes, C. K. *Phys. Rev. A* **1990**, *41*, 5049–5052.

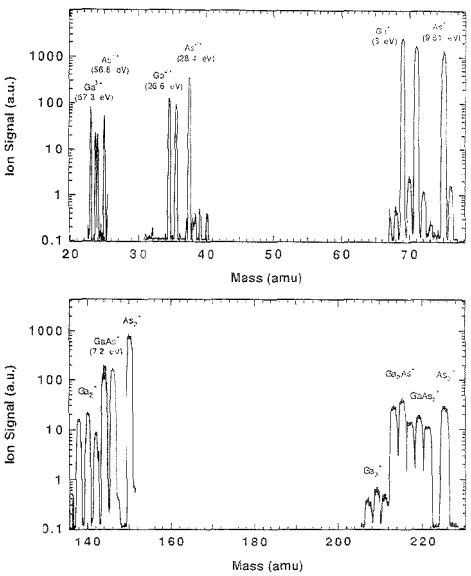

Figure 4. Postionization mass spectrum of Xe^+-sputtered GaAs. The average intensity of the focused laser beam was 4 × 10^{14} W/cm². The total energy required for ionization of some of the species is shown in parentheses. Some background $^{23}Na^+$ appears to add to the $^{69}Ga^{3+}$ peak at m/e = 23. Also present are ions resulting from residual gas species.

After extraction, the photoions created in the laser pulse are energy and mass analyzed before striking a Daly[9] detector. Perpendicular to the axis of the laser beam, the focused laser spot is significantly smaller than the instrumental acceptance volume defined by limiting apertures in the instrument and the primary ion beam spot size (~100 μm). Correspondingly, the laser defines the detected ionization volume in this dimension. Along the axis of the beam, the detected ion volume is defined by the ion beam spot size coupled with limiting apertures on the instrument such as a ~1-mm-diameter hole in the extractor. The laser beam has a depth of field of ~3 mm and, as a result, does not expand significantly within the ion detection region. The Daly detector is calibrated from 1 to 5 kV and is variable during a mass spectrum or depth profile in order to create a larger dynamic range for the instrument. The output of the detector is sampled by a boxcar integrator and sent to a computer via an analog to digital (A/D) interface card.

RESULTS

A number of samples were analyzed under static sputtering conditions to characterize the detection of different species using ultrahigh-intensity postionization. Figures 4 and 5 show mass spectra collected for GaAs and InP, respectively. In each case, the spectra were taken over the mass ranges necessary to resolve all the possible singly charged atoms, dimers, and trimers, as well as all the detectable multiply charged atoms. As an additional check, both surfaces were also measured at least once using

(9) Daly, N. R. *Rev. Sci. Instrum.* **1960**, *31*, 264.

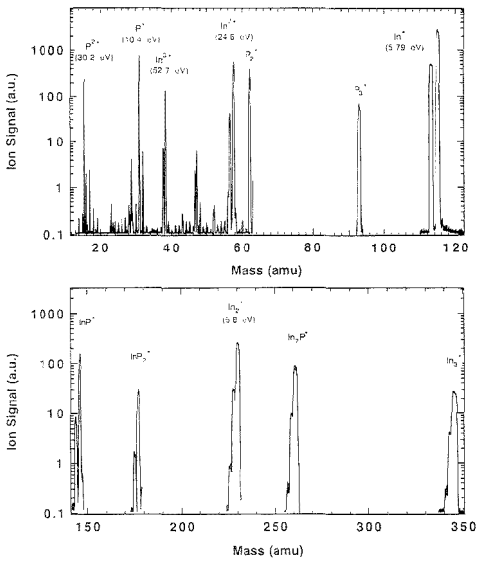

Figure 5. Postionization mass spectrum of Xe^+-sputtered InP. The average intensity of the focused laser beam was 4 × 10^{14} W/cm^2. The total energy required for ionization of some of the species is shown in parentheses. $^{115}In^+$ is disproportionately small compared to $^{113}In^+$ and appears to have saturated the detector. All the calculations for atomic In are based on the $^{113}In^+$ signal. Also present are ions resulting from residual gas species.

Table 1. Distribution of Detected Ions from Xe^+-Sputtered GaAs and InP Obtained with an Average Laser Intensity of 4 × 10^{14} W/cm^2

element	atoms/ molecules	atomic ratio +1/+2/+3	IP (eV) 1st	2nd	3rd
GaAs					
Ga	87/13	100/5/1	6	20.57	30.7
As	43/57	100/25/3	9.81	18.63	28.34
InP					
In	92/8	100/4/1	5.785	18.86	28.02
P	44/56	100/31/–	10.484	19.72	30.156

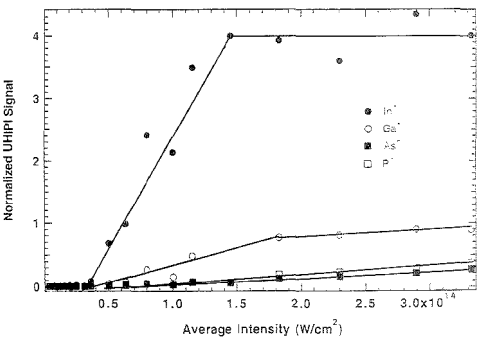

Figure 6. Dependence of atomic postionization signals on average laser intensity from Xe^+-sputtered $In_{0.4}Ga_{0.1}As_{0.2}P_{0.3}$. The signals have been scaled to reflect all isotopes. The ratio of In^+ and Ga^+ signals at high intensities is equal to the ratio of In and Ga in the sample.

continuous sputtering instead of pulsed sputtering. No difference in the results was observed, eliminating the possibility of elemental segregation at the surface between sputtering pulses.

Singly, doubly, and triply charged ions of the primary matrix elements are easily resolved in the mass spectra, demonstrating the ability to create ions even with high ionization potentials (IPs). In addition, all the possible singly charged dimers and trimers are detected to some degree with the correct isotopic ratios expected on the basis of the natural abundances of the constituents. This suggests that Xe^+ sputtering at large incident angles (~60°) produces significant quantities of sputtered clusters while the laser beam only causes moderate fragmentation during the ionization process. No multiply charged dimers such as $GaAs^{2+}$ were detected to any great degree. However, these species are mostly isobaric with the singly charged species and their hydrides, making detection difficult. Table 1 shows the relative fractions of each matrix element detected in atomic and molecular forms as well as the ratios of the relative charge states of the detected atomic species. These ratios were obtained by simply summing all the signals from the atoms and molecules that contained a given element while correcting for the stoichiometry of the molecules. For those elements with low first IPs, In and Ga, the vast majority of each detected element is found in the form of the singly charged atom. In contrast, those elements with relatively high first IPs, As and P, are detected in roughly equal amounts as atoms and as molecules.

As demonstrated by the number of species in the mass spectra, the postionization technique provides the opportunity to measure all the elements within a matrix simultaneously because of the nonselective nature of the ionization process. However, in order to quantify the elements in a given matrix without the use of standards, it is critical that 100% of the species within a well-defined volume be ionized (saturation). If these conditions are met, the ion yield from all the detected atoms and molecules can simply be summed to give a representation of the elemental concentration of the matrix being studied. The relative sensitivity factors (RSFs) obtained from the technique were determined by summing all the species measured in the GaAs and InP mass spectra. When all the species containing Ga are summed and compared to all the species containing As, one finds that the total detected Ga:As ratio is 1:1.3. Likewise, the same calculation for In and P indicates a total In:P ratio of 1:5.7. The GaAs results nearly reflect the 1:1 stoichiometry in GaAs, but the InP results yield a rather poor representation of the InP stoichiometry, suggesting that all the relevant sputtered species are not being detected with a uniform efficiency.

An effective technique to determine whether the ionization of a given species is saturated is to measure ion yield vs laser intensity. Where saturation occurs, the ion yield should increase very slightly with laser intensity, reflecting only the slow expansion of the ionization volume.[6] With this in mind, the ion yield from a sample composed of 40% In, 10% Ga, 20% As, and 30% P was measured while the laser pulse intensity was varied by use of neutral density filters. Sample composition was confirmed by Rutherford back-scattering (RBS). Figure 6 shows the signals for In^+, Ga^+, As^+, and P^+ as a function of average intensity at the focus of the laser beam. At low laser intensities, the ion signal is seen to be constant and may be assumed to reflect only a background secondary ion contribution to the ion signal, not a laser-induced signal. However, above ~3 × 10^{13} W/cm^2, the ion

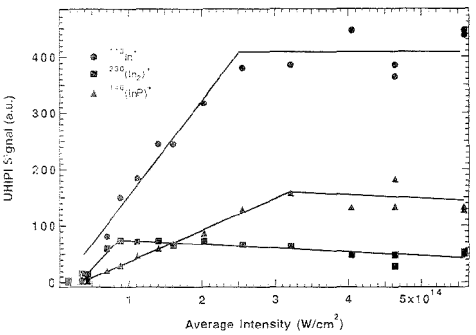

Figure 7. Dependence of sputtered molecule postionization signals on average laser intensity for $In_{0.4}Ga_{0.1}As_{0.2}P_{0.3}$. Some signals decrease with increasing intensity due to fragmentation of molecules.

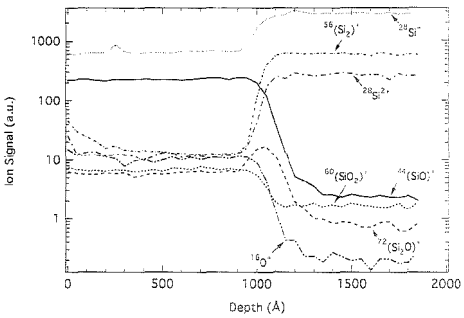

Figure 8. Depth profile of a sample composed of 1000-Å SiO_2 on bulk Si. The average intensity of the laser beam was 5×10^{14} W/cm².

yield for In and Ga rises rapidly with intensity before abruptly leveling off at an average intensity of $\sim 1.5 \times 10^{14}$ W/cm². Here the ionization process appears to be saturated, and the ratio of the absolute signals for In^+ and Ga^+ is nearly exactly equal to the ratio of the elemental concentrations of In and Ga in the sample. The higher IP species, As and P, also display a rapidly rising ion yield with intensity, but the increase is slower than that of the lower IP species. It is difficult to discern whether As and P actually reach a saturation condition. Under the conditions used in these experiments, the As^+ and P^+ signals fall short of the values expected if their relative signals were to be proportional to the concentrations of As and P in the matrix.

It is not surprising that the In^+ and Ga^+ signals would appear proportional to the actual concentrations of In and Ga in the sample. Of all the dimers and trimers sputtered from the quaternary sample, all the molecules containing In and Ga are also saturated at the higher laser intensities but comprise only a minor fraction of the total detected In and Ga. As a result, the corresponding singly charged ions provide a good representation of the actual elemental concentrations. The low amount of detected In- and Ga-containing molecules is surprising, because sputtered group III clusters are known to be quite stable, especially with Xe bombardment.[10] This suggests that these molecules are fragmented by the laser. In contrast, As and P are tied up to a considerable extent in stable, high ionization potential sputtered molecules. Consequently, As^+ and P^+ alone cannot give a good representation of the elemental concentrations. Almost as much As and P is found in As_2^+ and P_2^+ as is found in As^+ and P^+. These molecules not only detract from the atomic signals, they may not be ionized completely to saturation either.

Competing with molecule formation during sputtering is the molecular fragmentation during the ionization process. Figure 7 displays the ion yield from In^+, InP^+, and In_2^+ as a function of average laser intensity. It is recognized that there are some differences in the In^+ profile in this figure and the last figure which can be attributed to minor day-to-day differences in laser parameters. The InP^+ and In_2^+ signals appears to saturate at $\sim 3 \times 10^{14}$ and $\sim 1 \times 10^{14}$ W/cm², respectively, after which there appears to be a slight decrease in the ion yield with laser intensity. Correspondingly, the In^+ signal is flat or increases slightly when saturated. This upward trend in a saturated singly charged atom is perhaps more discernible in the saturated Ga^+ data shown in Figure 6. A general decrease of the molecular signal along with a corresponding increase in the atomic signal as laser intensity increases can clearly be ascribed to fragmentation during the laser ionization process. The extent of the fragmentation for any of the detected clusters is unknown. If the goal of complete fragmentation is desired, average intensities in excess of 10^{15} W/cm² and/or alternative sputtering conditions may be required.

Depth-profiling experiments allow further characterization of the postionization technique at 800 nm. Figure 8 displays a depth profile of a sample composed of 1000-Å SiO_2 thermally grown on a Si substrate. Seven different masses were monitored during the experiment. As expected, oxygen-containing species decrease and exclusively silicon-containing species increase in the transition from the SiO_2 to the bulk Si. This of course reflects the lack of oxygen and the greater density of Si in the bulk material. More significant, however, is the fact that the molecular species detected in the depth profile provide information about the actual bonding patterns in the respective matrices. For instance, the Si_2^+ signal accounts for only 2% of the Si signal in the SiO_2 while accounting for 22% in the Si bulk, mirroring the lack of Si−Si bonding in the SiO_2 and the abundance of Si−Si bonding in the Si. Interestingly, a hump in the Si_2O^+ can be detected at the interface. The sputtered SiO_2/Si interface is composed of a nonstoichiometric and rapidly changing mixture of oxygen and silicon which is reflected in the enhancement of this cluster.

Moreover, Figure 8 also contains some indications of molecular fragmentation. Because the ionization process is independent of the sputtering, any single sputtered species should be ionized and detected identically whether it comes from SiO_2 or bulk Si. Therefore, if both Si^+ and Si^{2+} were created exclusively from the same precursor species, such as sputtered Si atoms, they would both be expected to change by the same amount in going from one matrix to the other. In fact, Si^{2+} increases by a factor of 24 when going from SiO_2 to bulk Si while Si^+ increases only by a factor of 4.4. For this reason, it must be assumed that either or both Si^+ and Si^{2+} is created from sputtered precursor species other than just sputtered atoms. One possible explanation would have SiO clusters from the oxide fragment to make additional Si^+ while having Si_2 from the bulk Si preferentially fragment to make Si^{2+}.

Promisingly, the depth profile results predict the relative silicon densities in SiO_2 and bulk Si within a factor of 2. It is important to note that SiO_2 and Si sputter at nearly identical rates, thus

(10) Downey, S. W.; Emerson, A. B.; Kopf, R. F. *Nucl. Instrum. Methods Phys. Res.* 1992, *B62*, 456–462.

making comparison between the two matrices easier. The density of Si (atoms/cm^3) in bulk Si is 2.3 times higher than in thermally grown SiO_2. If all the Si-containing species in the SiO_2 and Si depth profile are summed, one finds that ~4.6 times more Si is detected in the Si bulk than in the oxide. By comparison, the secondary ion yield for Si is more than 2 orders of magnitude greater from SiO_2 than Si when Xe^+ sputtered.[11] Most likely, incomplete detection of the sputtered SiO_x species detracts somewhat from the total Si signal in the SiO_2. Nonetheless many other explanations are possible. The relative sensitivity factor for silicon in the two matrices is affected by the partitioning of each element into atoms and molecules during the sputtering coupled with differing ionization efficiencies for these species. In the next section, it will be shown that ionization efficiency depends strongly upon ionization potential; the first IPs for Si, SiO, and O are 8.15, 11.5 and 13.6 eV, respectively. Note how severe this dependence may be, as the detected O^- is less than 1% of the SiO^- and Si^+.

DISCUSSION

The results presented in this paper are encouraging. If all the relevant sputtered species are measured, the technique appears to be able to determine the relative elemental compositions of a number of matrices with reasonable accuracy and without the use of standards. While many factors can affect ion yield, these effects appear to cause only small changes to the resultant elemental RSFs. Nonetheless, as is evident by the poor O^+ detection from SiO_2, improvements in the implementation of the technique are necessary for critical applications such as characterization of completely unknown materials.

Clearly, one major factor that affects the RSFs is ionization efficiency. Obtaining saturation ionization within a well-defined volume for an array of different species is complicated by the fact that, during a single laser pulse, the irradiated region of the sputtered neutrals is exposed to a large intensity gradient in both space and time. Photoionization under these conditions can be separated into two regimes. Ionization at relatively low intensities where the photon energy is much smaller than the ionization potential can be described by a multiphoton ionization (MPI) model.[8,12–16] MPI is strongly dependent on the electronic structure of the species being ionized. Alternatively, under the conditions of longer wavelength and high intensity, the ionization process can transition from a multiphoton ionization (MPI) mechanism to a tunneling ionization (TI) mechanism.[8,12,13,17–20] TI is described classically as the tunneling of an electron out of its bound potential well due to the reduction of the ionization barrier by an external electric field.

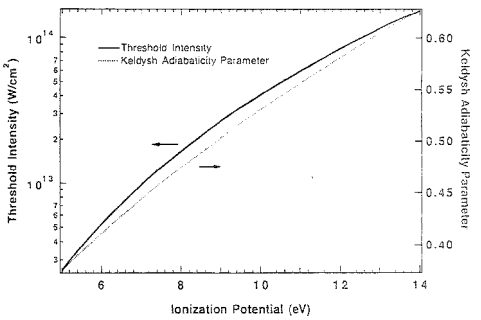

Figure 9. Calculated threshold intensity for tunneling ionization and the Keldysh adiabaticity parameter as a function of ionization potential. The KAP is calculated for an intensity of 3 × 10^{14} W/cm^2.

The conditions under which tunneling ionization occurs have been described by a number of models. One simple model assumes that the onset of TI will occur at the point at which the potential barrier to ionization is suppressed due to an external electric field by an amount equal to the ionization potential of the atom or molecule. In one dimension, the threshold intensity for TI, I_{th}, is defined as[8,13,17,18]

$$I_{th} = cE_{ion}^4/128\pi e^6Z^2 \qquad (2)$$

where c is the speed of light, E_{ion} is the ionization potential, e is the charge on an electron, and Z is the charge state of the ion. This prediction has been shown to be in good agreement with studies on rare-gas atoms.[8,17,18] Figure 9 displays the calculated threshold intensities as a function of IP based on eq 2. I_{th} ranges from 4 × 10^{12} to 1 × 10^{14} W/cm^2 for the species measured in these experiments. The intensities in a substantial part of the beam are well above the lower threshold intensities (Figures 2 and 3), predicting ionization by TI in the high-intensity regions of the laser beam. Importantly, the threshold intensity only describes the onset of the TI mechanism. It does not describe the extent of ionization which is dependent on an ionization rate and the pulse length. Nevertheless, on the basis of the measurements of ion signal vs laser intensity for a number of species, it was found empirically that it required ~10 times the I_{th} to achieve saturation of the ionization process under the conditions used in these experiments. This partially explains the low detection sensitivity for the high-IP species such as SiO and O.

The transition from MPI to TI can also be described by the Keldysh adiabaticity parameter (KAP), γ, which relates the average kinetic energy of an electron in a laser field (ponderomotive potential) to the ionization potential of the atom or ion.[13,17,18,20] γ is defined by

$$\gamma = \sqrt{E_{ion}/(e^2E^2/2m_e\omega^2)} \qquad (3)$$

where E is the electric field and ω is the frequency of the laser. The frequency term, ω, is related to the condition that the tunneling must occur faster than the wave period of the laser light. TI is predicted when $\gamma < 1$ while MPI is predicted when $\gamma > 1$. The calculated KAPs as a function of IP at an intensity of 3 × 10^{14} W/cm^2 are also shown in Figure 9. For all the measured elements, γ lies between 0.40 and 0.65. As a result, tunneling ionization is also predicted by the Keldysh theory.

(11) Downey, S. W.; Emerson, A. B. *Surf. Interface Anal.* **1992**, *20*, 53–59.
(12) Codling, K.; Frasinski, L. J. *J. Phys. B: At. Mol. Opt. Phys.* **1993**, *26*, 783–809.
(13) Freeman, R. R.; Bucksbaum, P. H. *J. Phys. B* **1991**, *24*, 325–347.
(14) Kaesdorf, S.; Hartmann, M.; Schröder, H.; Kompa, K. L. *Int. J. Mass Spectrom. Ion Processes* **1992**, *116*, 219–247.
(15) L'Huillier, A.; Lompre, L. A.; Mainfray, G.; Manus, C. *J. Phys. B* **1983**, *16*, 1363–1381.
(16) Perry, M. D.; Szoke, A.; Landen, O. L.; Campbell, E. M. *Phys. Rev. Lett.* **1988**, *60*, 1270–1273.
(17) Mevel, E.; Breger, P.; Trainham, R.; Petite, G.; Agostini, P.; Migus, A.; Chambaret, J.; Antonetti, A. *Phys. Rev. Lett.* **1993**, *70*, 406–409.
(18) Augst, S.; Strickland, D.; Meyerhofer, D. D.; Chin, S. L.; Eberly, J. H. *Phys. Rev. Lett.* **1989**, *63*, 2212–2215.
(19) Ammosov, M. V.; Golovinsky, P. A.; Kiyan, I. Y.; Krainov, V. P.; Ristic, V. M. *J. Opt. Soc. Am. B* **1992**, *9*, 1225–1230.
(20) Keldysh, L. V. *Sov. Phys. JETP* **1965**, *20*, 1307–1314.

Conceivably, ionization at the focus of the laser beam also occurs to some degree by a MPI mechanism. MPI may be relatively efficient for low-IP species, accounting for a substantial portion of the detected signal. In and Ga display low-lying electronic levels which are close to resonant for two- or three-photon transitions (1 photon = 12 500 cm^{-1}). These low-lying electronic states may also be strongly ac Stark shifted to become more closely resonant. Naturally, ionization by both MPI and TI simultaneously will be enhanced relative to ionization by TI alone as a result of a greater effective ionization volume since MPI can occur in the "wings" of the Gaussian laser beam. In fact, according to Figure 3, those species able to be ionized at laser intensities $I > 10^{12}$ W/cm^2 would have an effective ionization volume 3 times larger than those species requiring $I > 10^{14}$ W/cm^2.

The sensitivity of laser ionization utilizing high intensity and long wavelengths to differences in ionization potential is further supported by the work of others. Becker and Hovis ionized sputtered neutrals from semiconductor materials with all four harmonics of a Nd–YAG laser capable of producing 35-ps pulses with focused intensities near 10^{14} W/cm^2.[6] Interestingly, the ionization at 1064 nm, the wavelength predicted to move the photoionization most greatly into the tunneling regime, produced the greatest IP dependence of any of the other wavelengths. This wavelength also produced relatively small amounts of multiply charged species. In contrast, the experiments conducted at 532 nm produced the most uniform ionization efficiencies and the largest numbers of multiply charged ions. According to the theory, 532-nm light would be expected to ionize to a greater extent by the MPI mechanism.

Other factors contributing to the ion yield for a given species are the velocity and angular distribution of the sputtered neutrals. These factors are important because detection of sputtered species by pulsed lasers constitutes a density detector in that the species do not move significantly through the laser beam volume on the time scale of the laser pulse. As a result, those species that move relatively slowly (higher mass) are detected with higher efficiency since they have a greater density in the irradiated volume. The density difference between two masses should be $(m_1/m_2)^{1/2}$, assuming that the two species are sputtered with identical angular distributions and energies. This correction has been applied to some of the experimental results with mixed results in terms of improving or worsening the measured RSFs with respect to the known bulk concentrations. In fact, the validity of such a simple correction is questionable. Very likely, all the atoms and molecules are sputtered with differing amounts of kinetic energy and differing angular distributions. Experimental conditions that can affect this ratio are the width of the sputtering ion beam pulse and the distance of the laser from the sample surface. If the sputtering pulse is relatively long and the beam–sample separation is relatively small, then the mass correction is valid except for large differences in mass. An accurate correction would require further investigation into these dynamics.

Based on the factors presented here that can affect the elemental RSFs, three possible alterations to the technique are apparent. Increasing laser intensity by changing focusing conditions and/or laser parameters may be extremely effective at increasing the quantitative capabilities of this system. This is reinforced by the fact that a laser intensity $I \approx 10I_{th}$ is required to saturate a given species. Additionally, the formation of clusters during sputtering could be reduced by enhancing sample atomization. Higher ion energies, or lighter ions, such as Ar and Kr, used at more near-normal angles may be effective. In this way, the complications of detecting many species in each matrix as well as the effects of molecular fragmentation and varying energy/angular distributions may be reduced. As mentioned earlier, even higher laser intensities (>10^{13} W/cm^2) may further dissociate clusters. Finally, the wavelength of the laser may be changed by doubling or tripling. The choice of wavelength of light used for ionization appears to be extremely important even with ultraintense laser intensities.[6] In fact, while tunneling ionization may dominate at long wavelengths, the use of shorter wavelengths to try to bolster the MPI mechanism may improve atomization and detection efficiency. All three of these changes are currently being explored in the laboratory.

CONCLUSIONS

Nonresonant, ultrahigh-intensity postionization utilizing a 100-fs pulsed laser at 800 nm has been characterized. Average intensities at the focus of the beam are estimated to be greater than 10^{14} W/cm^2. Multiply charged atoms as well as singly charged molecules are detected. In addition, evidence indicating molecular fragmentation during the ionization process is observed.

Tunneling ionization and multiphoton ionization are predicted to occur concurrently in the laser ionization region. The ionization process displays a strong dependence on laser intensity and ionization potential. Saturation of the ionization can be achieved for those species with relatively low ionization potentials. By summing all the sputtered species together, a reasonably accurate representation of relative elemental concentrations for one matrix or between two matrices can be obtained in a number of cases. Use of a higher laser intensity, a different wavelength of light, or different sputtering conditions may improve the sensitivity of the technique.

The use of high repetition rate, ultrashort pulse lasers for postionization is best suited for time-of-flight mass spectrometry because of the overall ionization efficiency and potential high data acquisition rate. Moreover, high spatial resolution (submicrometer) focused ion beams, used for the analysis of ultrasmall samples, like semiconductor devices and their defects, also have high pulse repetition capability but possess low average current and secondary ion yield. Improving the useful yield is imperative for samples that contain 10^6–10^7 atoms (<100 nm^3) because sputtering will destroy the sample, and all ions need to be recorded to characterize the sample.

ACKNOWLEDGMENT

We thank Len Feldman and Bonnie Weir for the RBS analysis that determined the elemental concentrations in the InGaAsP sample.

NOTE ADDED IN PROOF

A publication related to this work recently became available: Brummel, C. L.; Willey, K. F.; Vickerman, J. C.; Winograd, N. *Int. J. Mass Spectrom. Ion Processes* **1995**, *143*, 257.

Received for review June 19, 1995. Accepted September 20, 1995.[⊗]

AC950620W

[⊗] Abstract published in *Advance ACS Abstracts*, November 1, 1995.

Articles

Anal. Chem. **1995,** *67,* 4040–4043

pH-Defining Equilibrium between Water and Supercritical CO_2. Influence on SFE of Organics and Metal Chelates

Karen L. Toews, Robert M. Shroll, and C. M. Wai*

Department of Chemistry, University of Idaho, Moscow, Idaho 83844

Neil G. Smart†

Company Research Laboratory, British Nuclear Fuels plc, Springfields Works, Salwick, Preston PR4 OXJ, U.K.

A direct measurement of the pH of water in contact with supercritical CO_2 was made by observing the spectra of a pH indicator with a UV–vis spectrophotometer. The pH was analyzed under pressures of 70–200 atm and temperatures of 25–70 °C. The measured pH varied from 2.80 to 2.95, and relative standard deviations of <1.5% were achieved. The effects of pH on the efficiency of supercritical fluid extraction of metals and ionizable organic species in water-containing systems are discussed.

Supercritical fluid extraction (SFE) has become an attractive alternative to conventional solvent extraction for the recovery of organic compounds and metal chelates from solid and aqueous samples.[1,2] Carbon dioxide is the gas of choice for SFE because of its moderate critical constants, inertness, low cost, and availability in pure form. In many environmental applications, water is often present in an SFE system, either as a part of the original sample or added deliberately. The presence of water has been shown to facilitate the extraction of metal ions from solid materials using the in situ chelation technique in supercritical CO_2.[2,3] The role of water in the SFE of organics and metals is not well understood. Water in contact with carbon dioxide becomes acidic due to the formation and dissociation of carbonic acid:

$$CO_2 + H_2O \rightleftharpoons H_2CO_3 \rightleftharpoons H^+ + HCO_3^-$$

Determining the pH of water in contact with supercritical CO_2 is essential to understanding SFE of both metal ions and ionizable organic species. For SFE of metal ions, complexing agents are used to neutralize the metal charge and to transport the metals into the CO_2 phase. The degree of dissociation of the complexing agents is dependent on the pH of the solution. If the complexing agents are not ionized at the solution pH, complexation and transportation of metal ions into the nonpolar supercritical CO_2 will be inefficient. The pH of the solution may also influence the metal species present. Some metal species are extracted efficiently at a given pH, while other species may be extracted to a lesser degree or not at all. Similarly, the extraction efficiency of ionizable organics is affected by the solution pH. An acidic medium may cause organic species to become charged, decreasing their solubility in CO_2 and altering the degree of matrix association. When extracting metals or ionizable organics from a solid matrix, hydrogen ions in the small amount of water present in the sample may interact with the matrix, making the ions more accessible to ligand attack and extraction. Knowledge of the pH of the system is useful in both predicting favorable extraction conditions and interpreting experimental results.

pH can be approximated by using Henry's law to calculate the solubility of CO_2 in water and then using the pK_a of carbonic acid to determine the degree of dissociation. Henry's law requires ideal gas behavior and a dilute solution. Under supercritical conditions, these assumptions are not necessarily valid. Prior to this study, no direct measurements have been made of the pH of water in contact with supercritical CO_2. pH determinations have been approached from a theoretical standpoint, using Henry's law to predict solubility.[3] Landmark CO_2 solubility studies were published by Weibe and Gaddy in the 1940s, while the subject has been studied more recently by King et al.[4–6] Additionally, studies have been published reporting K_a values for carbonic acid at different temperatures and pressures.[7–9] These measurements allow the calculation of pH, though the summation of errors and approximations from these works is substantial. A more suitable approach is the determination of pH via direct measurement. In this study, the pH of water in contact with CO_2 is measured by observing the UV–vis spectrum of a pH indicator. The pH is

† On secondment at the Department of Chemistry, University of Idaho.

(1) Hawthorne, S. B. *Anal. Chem.* **1990,** *62,* 633A.
(2) Lin, Y.; Smart, N. G.; Wai, C. M. *Trends Anal. Chem.* **1995,** *14,* 123.
(3) Wang, S.; Elshani, S.; Wai, C. M. *Anal. Chem.* **1995,** *67,* 919.
(4) Weibe, R.; Gaddy, V. L. *J. Am. Chem. Soc.* **1940,** *62,* 815.
(5) Weibe, R. *Chem. Rev.* **1941,** *29,* 475.
(6) King, M. B.; Mubarak, A.; Kim, J. D.; Bott, T. R. *J. Supercrit. Fluids* **1992,** *5,* 296.
(7) Ellis, A. J. *J. Chem. Soc.* **1959,** 3689.
(8) Harned, H.; Davis, R. J. *J. Am. Chem. Soc.* **1943,** *65,* 2030.
(9) Read, A. J. *J. Solution Chem.* **1975,** *4,* 53.

0003-2700/95/0367-4040$9.00/0

measured at various temperatures and pressures both above and below the critical point.

EXPERIMENTAL SECTION

Equipment. A Varian (Sunnyvale, CA) Cary 2200 spectrometer was used to measure the UV–vis spectrum. Scans were recorded from 340 to 650 nm at 10 nm/s in a high-pressure view cell.[10] The cell body was made of stainless steel and had a volume of 14.9 mL. The quartz cell windows had a diameter of 1.27 cm and were sealed using Teflon V rings under compression. The cell path length was 7.6 cm. Cell temperature was controlled using a Blue M (Blue Island, IL) MagniWhirl full visibility water bath, and the temperature of the cell was monitored with a thermocouple and a Fluke (Everett, WA) controller. The CO_2 was delivered by an Isco (Lincoln, NE) 260D syringe pump and controller. The cell was thermally insulated from the UV–vis spectrometer. A VWR Scientific (West Chester, PA) pH meter with a Cole Parmer (Chicago, IL) polymer electrode was used to standardize the buffer solutions.

Chemicals. SFC/SFE grade CO_2 obtained from Air Products (Allentown, PA) was used. N_2 was obtained from Oxarc (Spokane, WA). All solutions were prepared with deionized water. Bromophenol blue (Eastman Kodak, Rochester, NY) was used as the indicator and was dissolved in deionized water to yield a 0.04% (w/v) solution. Buffers for calibration were prepared from stock citric acid and sodium hydroxide solutions. A 0.2 N stock solution of citric acid (ACS specifications, Mallinckrodt Chemical Works, St. Loius, MO) and a 0.2 N stock sodium hydroxide (ACS specifications, Fisher Scientific, Fairlawn, NJ) solution were prepared. These two stock solutions were mixed in varying volumes to produce six buffers in the pH range 2.6–3.6. Primary pH standards used were pH 2.0 glycine (VWR Scientific) and pH 4.0 potassium hydrogen phthalate (EM Scientific, Gibbstown, NJ).

Procedure. The experimental system was calibrated using the following method. Six citric acid buffer solutions ranging from pH 2.6 to 3.6 were spiked with bromophenol blue and calibrated against the pH meter. Citric acid buffer solutions were used due to the inherent temperature insensitivity of these systems (between 25 and 91 °C, pH change of 0.01 pH unit).[11] The citric acid buffers (10 mL) were individually placed in the UV–vis cell and heated to the desired temperatures, followed by spectral determination. The cell was pressurized with 175 atm of N_2 gas and the procedure repeated. An additional spectrum of acidified water (pH 3) containing indicator was determined as above, both in the absence and in the presence of N_2 gas.

The effect of CO_2 on the pH of water containing a small amount (1.54×10^{-3}%) of indicator was determined as follows. Ten milliliters of the water–indicator solution was placed in the high-pressure cell and preheated to the desired temperature. The cell was pressurized with CO_2, sealed, and allowed to equilibrate for between 30 and 60 min in a thermostatic system. The UV–vis spectra were then obtained. For each measurement, fresh solution was used and the above procedure repeated. A minimum of two determinations were carried out at each condition studied. A standard linear regression was performed on calibration data, and discrimination intervals were calculated for each pH data point. The errors increased with increasing temperature and ranged from 0.4 to 1.4% relative standard deviation at the 95% confidence level.

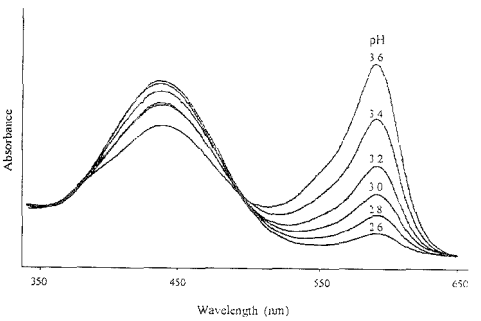

Figure 1. Absorption spectra of bromophenol blue (1.54×10^{-3}%) in citric acid buffers over the wavelength range 340–650 nm.

Using Henry's law, a pH value of 3.1 is predicted for an aqueous solution at 50 °C in contact with 150 atm CO_2. Bromophenol blue is reported to undergo a color transformation over the pH range 3.0–4.6.[12] Using a simplified indicator model, bromophenol blue, which is a weak acid, would be expected to exist as a neutral molecule at a lower pH and as an ionized species at higher pH. The acidic form of the indicator has an electronic transition at 430 nm, while the basic form has an electronic transition at 590 nm. The spectra of the buffer–indicator solutions were recorded over the pH range 2.6–3.6 (see Figure 1). With increasing pH, the absorbance at 590 nm increases, while the absorbance at 430 nm decreases.

Theory. To compensate for the imprecision of cell alignment, absorbance ratios were used to determine pH. The absorbances (A_i) of the solutions at wavelengths of 430 and 590 nm can be expressed as

$$A_{430} = C_{430}\epsilon_{430}L \tag{1}$$

$$A_{590} = C_{590}\epsilon_{590}L \tag{2}$$

where C_i is concentration, ϵ_i is the molar absorptivity, and L is the path length. Since the cell path length is constant, eqs 1 and 2 may be equated as follows:

$$A_{430}/C_{430}\epsilon_{430} = A_{590}/C_{590}\epsilon_{590} \tag{3}$$

Rearranging gives

$$A_{430}/A_{590} = C_{430}/\epsilon_{430}/C_{590}\epsilon_{590}$$

Since $\epsilon_{430}/\epsilon_{590}$ is constant, and the ratio of neutral to ionized indicator (C_{430}/C_{590}) is proportional to the hydrogen ion concentration, eq 4 may be rewritten as

$$A_{430}/A_{590} \propto C_{430}/C_{590} \propto [H^+] \tag{5}$$

(10) Laintz, K. E.; Wai, C. M.; Yonker, C. R.; Smith, R. D. *Anal. Chem.* **1992**, *64*, 2875.

(11) Britton, H. T. S. *Hydrogen Ions*; D. Van Norstrand Co.: Princeton, NJ, 1956; Vol. 1, p 355.

(12) Clark, W. M. *Determination of Hydrogen Ions*; The Williams & Wilkins Co.: Baltimore, MA, 1928; p 65.

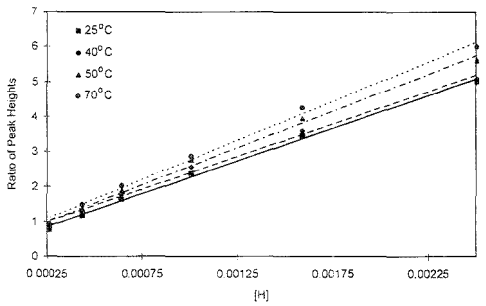

Figure 2. Calibration curves obtained from the ratio of A_{430}/A_{590} versus hydrogen ion concentration for citric acid buffers having pH between 2.6 and 3.6, containing bromophenol blue at temperatures of 25, 40, 50, and 70 °C.

Thus, the pH of water in contact with CO_2 can be determined by comparison with a calibration curve plotting A_{430}/A_{590} versus $[H^+]$.

RESULTS AND DISCUSSION

From the six citric acid calibration buffers, the A_{430}/A_{590} values were plotted against hydrogen ion concentration (see Figure 2). Values were recorded at 25, 40, 50, and 70 °C at atmospheric pressure, and linear plots were obtained. The effect of pressure on the calibration plots was determined by repeating the above procedure under 175 atm of N_2 at 50 °C. No effect was observed within the confidence limits of the calibration.

Additionally, the effect of pressure on a weakly acidic but unbuffered solution of bromophenol blue was assessed. The spectra taken while the cell was pressurized with 175 atm of N_2 were compared with a spectrum of the same solution at atmospheric pressure. The two spectra were the same within experimental error. This confirms that pressure changes have little or no effect on the ratio of neutral to ionized species present at a given pH.

Equilibrium pH of Water in Contact with CO_2. The time required for equilibrium to be reached between CO_2 (supercritical and subcritical) and water was studied. A water indicator solution was heated to 50 °C and pressurized with 200 atm of CO_2 (supercritical CO_2). The cell was allowed to equilibrate for varying time intervals before the spectra were recorded. A similar experiment was conducted at 23 °C (subcritical). For supercritical CO_2, a constant peak ratio was achieved in 30 min, while in the subcritical case, 60 min was required. The difference is thought to be due to the lower diffusion coefficient of CO_2 in H_2O at the lower temperature.

Equilibrium pH measurements of the CO_2/H_2O system were carried out over the temperature range 25–70 °C and pressure range 70–200 atm. The pH values varied from 2.80 to 2.95 (see Table 1 and Figure 3). According to Table 1, the pH of water in equilibrium with supercritical CO_2 shows little variation with temperature and pressure in the ranges specified by our experiments. It is known that the solubility of gaseous CO_2 in water is proportional to the partial pressure of the gas based on Henry's law. In the liquid region, the solubility of CO_2 in water is rather independent of pressure because the partial molar volume of liquid CO_2 varies little with pressure. The solubility behavior of supercritical CO_2 in water appears to resemble that of liquid CO_2, and consequently, the pH of water at equilibrium is nearly constant

Table 1. pH of Water in Equilibrium with CO_2 at Different Temperatures and Pressures[a]

	temperature (°C)			
pressure (atm)	25	40	50	70
70	2.83 ± 0.02	2.84 ± 0.02	2.90 ± 0.02	2.95 ± 0.02
80	2.82 ± 0.02	2.84 ± 0.02	2.88 ± 0.02	2.93 ± 0.04
100	2.83 ± 0.02	2.83 ± 0.02	2.88 ± 0.02	2.89 ± 0.03
150	2.82 ± 0.02	2.80 ± 0.01	2.85 ± 0.02	2.86 ± 0.03
200	2.80 ± 0.01	2.80 ± 0.01	2.85 ± 0.02	2.84 ± 0.03

[a] Error values represent standard deviations at the 95% confidence level.

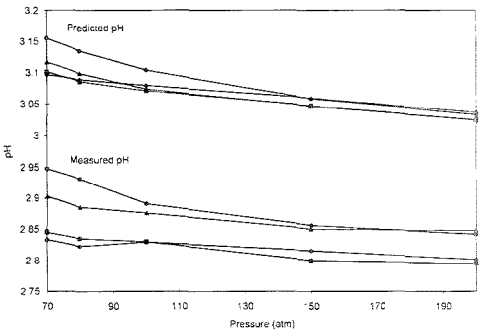

Figure 3. Variation of pH of water in equilibrium with supercritical CO_2 at temperatures of (◆) 25, (■) 40, (▲) 50, and (●) 70 °C and pressures of 70, 80, 100, 150, and 200 atm.

in the temperature and pressure ranges of most SFE experiments. Figure 3 shows that pH decreases by <0.1 unit when the pressure of supercritical CO_2 increases from 70 atm to 200 atm in the temperature range of 40–70 °C. Increasing temperature tends to lower the solubility of CO_2 in water and hence would raise the pH. The increase in pH is about 0.1 unit from 40 to 70 °C at 70 atm and <0.1 unit from 80 to 200 atm CO_2 pressure. The standard deviations of our pH measurements at the 95% confidence limit are in the range of 0.01–0.03 units.

The pH values calculated from literature solubility data and equilibrium constants are also given in Figure 3.[4-7] A comparison of our measured pH values and the calculated pH values reveals that the relative trends with temperature and pressure are similar, but the absolute values are different by 0.2–0.3 pH unit. The discrepancies are probably caused by the different CO_2 concentrations and ionic strengths used in obtaining the experimental pK_a values. Additionally, some pK_a measurements involve substantial errors. For instance, Ellis cites errors up to 20% in conductivity measurements used in the determination of pK_a values.[7]

Relevance of Results to SFE. The results obtained in this study provide an accurate measurement of the pH value likely to be encountered in SFE from matrices containing water. This will provide a means for predicting which systems will be amenable to SFE. In extraction of ionizable organic species from aqueous matrices, compounds will be most efficiently removed if they are in a neutral form at pH 3. Examples of ionizable organic species which are neutral at pH 3 are numerous. Recent literature shows

(13) Hedrick, J. L.; Taylor, L. T. *J. High Resolut. Chromatogr.* 1990, *13*, 312.
(14) Tang, P. H.; Ho, J. S. *J. High Resolut. Chromatogr.* 1994, *17*, 509.

that phenols, aromatic amines, sulfonylurea herbicides, chlorotriazines, organophosphorous pesticides, and phenylurea pesticides can all be extracted with high efficiency.[13-21] Examples of compound classes which will be difficult to extract in the presence of water are nitrogen-containing bases (which protonate under acidic conditions), and highly acidic species, like carboxylic acids. Extractions of aqueous systems containing nitrogenous bases have recently been investigated.[22] At pH < 3, six of the bases investigated were expected to be protonated. These charged species have low solubilities in supercritical CO_2 and consequently should be difficult to extract. Five of the six bases were unable to be extracted with neat CO_2. The presence of large lipophilic groups partially compensates for the poor solubility of charged species in CO_2.

Many strategies have been developed to prevent ionization of basic or acidic compounds. The most common approach has been to exclude water by means of a two-step extraction approach. The first step involves passing the sample solution through a solid phase extraction disk, which retains the compounds of interest but allows the water to pass. The compounds are then eluted from the disk using SFE. This approach has been used in the extraction of sulfonylureas, acid herbicides, aromatic amides, phenols, and organochlorine pesticides, to name a few.[13,16,17,23] Another approach used in the extraction of amines from water involved the addition of a strong base modifier to the extraction cell.[13,22] The strong base effectively saturated the solution with hydroxide ions, allowing the more weakly basic amines to deprotonate and be extracted as free bases. Utilizing N_2O rather than CO_2 as the supercritical fluid prohibits the formation of an acid in aqueous solution and eliminates the possibility of carbamate formation in amine extractions.[16] Extraction of acid herbicides, phenols, and fatty acids has been accomplished by derivitizing acidic functional groups and extracting the less polar reaction products.[21] Finally, water has been excluded from aqueous pesticide samples by freeze-drying the samples prior to extraction.[19]

Metal extraction by in situ chelation is also pH dependent. Since charged metal ions are not soluble in supercritical CO_2, ligands are used to complex the metal and provide charge neutralization. In order for metal complexation to occur, the ligand must ionize to some degree. Since many extractions are done in the presence of excess ligand, and complexation kinetics and thermodynamics are favorable, the degree of ionization need not be large. Favorable extractions have been achieved with ligands like β-diketones and ionizable crown ethers whose pK_a values are in the range of 4–6. In addition to having low to moderate pK_a values, ligands must also be stable at pH 3. The commonly used sodium dialkyldithiocarbamate decomposes to CS_2 and NHR_2 below pH 4.[25] Not only is the form of the ligand affected by pH, but the identity of the metal species depends on solution pH as well. The degree of hydrolysis a metal undergoes is a function of pH: at high pH, many species form insoluble hydroxides and precipitate from solution. For this reason, metal ions at low pH values are generally more extractable than those at high pH values. Vast quantities of solvent extraction data exist for various metal and ligands systems.[26] This provides a useful database for predicting metal extractability and ligand efficiency for SFE from water-containing matrices. Ligands which form stable neutral complexes with metal ions at pH 3 should be useful in SFE as well, provided they show reasonable solubility in supercritical CO_2.

Finally, matrix effects are highly pH dependent. The ubiquitous silica matrix at pH 3 will have free silanol groups present. These groups could potentially provide ions (metals or ionizable organic species) with competitive binding sties, reducing the tendency of the ions to be extracted into CO_2. Several research groups have reported the influence of the matrix on extraction efficiency.[2,4,15,17,18,21] If extraction from a given matrix is not favorable at pH 3, the matrix may be modified by blocking reactive groups with an excess of counterions.[14] Independent studies by Wai et al. and Steinheimer et al. have shown that the presence of water may be beneficial.[2,3,21] The hydrogen ions are thought to help liberate ions from solid matrices, perhaps by an ion exchange mechanism.

CONCLUSIONS

A method for the accurate determination of the pH of water in contact with CO_2 has been demonstrated. Conditions relevant to those often used for SFE have been studied. Over the temperature range 25–70 °C and pressure range 70–200 atm, the pH of water ranged between 2.80 and 2.95. pH increases with increasing temperature and decreases with increasing pressure. The results of this study allow extraction efficiencies to be predicted for both metal species and ionizable organics. Solvent extraction data at pH 3 provide useful guidelines in predicting metal extraction efficiencies. Evaluating the neutrality and stability of ionizable organic species at pH 3 provides an estimation of extractability from water containing samples.

ACKNOWLEDGMENT

This work was supported by British Nuclear Fuel plc and by NSF–Idaho EPSCoR Program under NSF Cooperative Agreement OSR-9350539.

Received for review June 14, 1995. Accepted August 25, 1995.[⊗]

AC950585T

(15) Oostdyk, T. S.; Grob, R. L.; Snyder, J. L.; McNally, M. E. *Anal. Chem.* **1993**, *65*, 596.
(16) Ashraf-Khorassani, M.; Taylor, L. T. *Anal. Chem.* **1990**, *62*, 1177.
(17) Howard, A. L.; Taylor, L. T. *J. High Resolut. Chromatogr.* **1993**, *16*, 39.
(18) Howard, A. L.; Taylor, L. T. *J. Chromatogr. Sci.* **1992**, *30*, 374.
(19) Alzaga, R.; Durand, G.; Barcelo, D.; Bayona, J. M. *Chromatographia* **1994**, *38* (7/8), 502.
(20) Cross, R. F.; Ezzell, J. L.; Richter, B. E. *J. Chromatogr. Sci.* **1993**, *31*, 162.
(21) Steinheimer, T. R.; Pfeiffer, R. L.; Scoggin, K. D. *Anal. Chem.* **1994**, *66*, 645.
(22) Hedrick, J. L.; Taylor, L. T. *J. High Resolut. Chromatogr.* **1992**, *15*, 151.
(23) Liu, M. H.; Kapila, S.; Nam, K. S.; Elseewi, A. A. *J. Chromatogr.* **1993**, *639*, 151.
(24) Hawthorne, S. B.; Miller, D. J.; Nivens, D. E.; White, D. C. *Anal. Chem.* **1992**, *64*, 405.
(25) Wai, C. M. In *Preconcentration Techniques*; Alfassi, Z. B., Wai, C. M., Eds.; CRC Press: Boca Raton, FL, 1961; Chapter 4.
(26) De, A. K.; Khopkar, S. M.; Chalmers, R. A. *Solvent Extraction of Metals*, Chalmers, R. A., Ed., Van Nostrand Reinhold Co.: London, 1970.

[⊗] Abstract published in *Advance ACS Abstracts,* October 1, 1995.

Anal. Chem. **1995**, *67*, 4044–4052

Vacuum Distillation Coupled with Gas Chromatography/Mass Spectrometry for the Analysis of Environmental Samples

Michael H. Hiatt

National Exposure Research Laboratory, Characterization Research Division, U.S. Environmental Protection Agency, P.O. Box 93478, Las Vegas, Nevada 89193-3478

A procedure is presented that uses a vacuum distillation/gas chromatography/mass spectrometry system for analysis of problematic matrices of volatile organic compounds. The procedure compensates for matrix effects and provides both analytical results and confidence intervals from a single sample analysis. Surrogate compounds are used to measure matrix effects relating to boiling point and relative volatility and to provide the information necessary to accurately determine analyte concentration. Relative volatility values (α) are experimentally determined for 114 organic compounds and are shown to be comparable to gas–water partition coefficients. These compounds include those with boiling points up to 245 °C and gas–water partition coefficients less than 15 000. Multiple samples are tested, and the accuracy of determinations is shown to be within 5% for water, soil, and oil matrices. Method detection limits are below 1 ppb for most analytes studied.

One of the major objectives of the analytical chemistry research program at the EPA's Characterization Research Division (National Exposure Research Laboratory) in Las Vegas is to broaden the array of pollutants that can be determined with conventional analytical instrumentation. The U.S. Environmental Protection Agency (EPA) has developed a vacuum distillation method for determining the concentration of volatile organic compounds (VOCs) in environmental samples[1] and identified the relationships controlling analyte recovery and the potential of surrogate-based matrix corrections.[2] The purpose of the present study was to incorporate a surrogate-based matrix correction in a general vacuum distillation/gas chromatography/mass spectrometry (VD/GC/MS) method to be used for routine environmental analyses. At the same time, the list of applicable analytes has been better defined and documented.

Suitable compounds would reflect the effects of a matrix on analyte recovery as functions of boiling point (β-effects) and relative volatility (α-effects). Through the analyses of multiple samples, the ability of the specified surrogates to predict matrix effects is demonstrated. The surrogate prediction routine is simple and provides accurate determination of analyte concentrations in aqueous and mixed-phase samples. The quality assurance needed to document a VD/GC/MS analysis is performed by simply reviewing the surrogate performance in the sample. This replaces the need for costly matrix spikes or standard addition analyses.

A vacuum distillation procedure for determining the relative volatility of analytes as a constant (α_K-values) is presented. The α_K-values for 114 compounds are experimentally determined and shown to be comparable to their gas–liquid partition coefficients (K). The α_K-values determined in this study are an improvement over previously reported[2] α-values (normalized), as the analyst can use published K values to identify potential analytes and estimate their behavior. The boiling point and K value of an analyte govern its performance and determine whether it is suitable for VD/GC/MS analyses. Suitable analytes include compounds with boiling points up to 245 °C and partition coefficients up to 15 000; note that this range includes compounds not normally considered as VOCs (e.g., nitrosamines, aniline, and pyridine). Through multiple analyses of various matrices, the accuracy that can be expected for determining an analyte is reported. Method detection limits for VOCs are in the low ppb range for water, soil, and oil matrices.

EXPERIMENTAL SECTION

Vacuum Distillation Apparatus. The vacuum distiller has been previously described.[1,2] In the current study, a Nupro toggle valve (0.172-in. orifice) was used as the sample chamber valve. A vacuum gauge was installed between the cryoloop and the vacuum pump to monitor the integrity of the apparatus under vacuum. The vacuum was considered acceptable at a pressure of 0.5 Torr or less.

The condenser column was normally held at 5 °C during vacuum distillations and at 40 °C between distillations. Water was used to replace isopropyl alcohol as the temperature-controlling fluid in the condenser.

GC/MS Apparatus. A Hewlett-Packard mass spectrometer (Model 5972) and gas chromatograph (HP5890 Series II with Model MJSC metal jet separator) with a 60-m × 0.53-mm-i.d., 3.0-μm film thickness VOCOL capillary column (Supelco, Bellefonte, PA) was used for the determination of analytes from the vacuum distillation apparatus. Gas chromatograph operating conditions were 3 min at 10 °C, 50 °C/min ramp to 40 °C; 5 °C/min ramp to 120 °C; 20 °C/min ramp to 220 °C; and isothermal at 220 °C for 3.4 min, resulting in a total run time of 28 min. The jet separator was held at 210 °C and the transfer line at 280 °C. The mass spectrometer was operated at 3.1-s scans of 38–270 amu. The injector was interfaced to the vacuum distillation apparatus by connecting the carrier inlet gas line to the cryoloop valve and back

(1) Hiatt, M. H.; Youngman, D. R.; Donnelly, J. R. *Anal. Chem.* **1994**, *66*, 905–908.
(2) Hiatt, M. H.; Farr C. M. *Anal. Chem.* **1995**, *67*, 426–433.

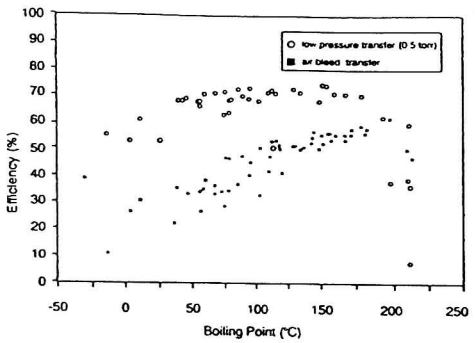

Figure 1. Cryoloop trapping efficiencies.

to the injector. The injector inlet temperature was 240 °C, and the inlet pressure was 10 psi.

Sample Preparation. Aqueous samples were prepared directly in the 100-mL round bottom flask used in the vacuum distillation of the sample. Modified samples were prepared by weighing the amount of matrix modifier (i.e., glycerin, salt), adding water, and then adding the analytes of interest. The 2% soap samples were prepared by adding 0.1 mL of soap concentrate (Micro Concentrated Cleaning Solution, International Products Corp., Burlington, NJ) to the water sample. Samples were spiked with a 10-μL methanol solution containing analytes at the concentrations listed in Table 1.

Two spike techniques were used to study the matrices not soluble in water. The first technique was to simply spike into a slurry of the sample and 5 mL of water, this is referred to as a *water spike*. The second technique, an attempt to maximize matrix contact, is referred to as a *vacuum spike*. The introduction of analytes to a soil sample contained in a vacuum has been reported to be a more difficult spike to recover and is potentially a more accurate spiking technique compared with the water spike.[3] The vacuum spike in this study entailed several steps, the first of which involved weighing the soil in the sample flask and injecting the spike with a syringe onto the material. The flask was then attached to the vacuum distillation apparatus, and the soil plus spike was cryogenically cooled by immersing the flask in a liquid nitrogen bath (−196 °C). When the flask and sample were thoroughly cooled, the apparatus vacuum pump was used to lower the flask pressure to 0.5 Torr. After the air had been removed (3−5 min) and the sample chamber valve closed to isolate the sample, the flask was warmed to 30 °C. After a 1-h equilibration period, the mixture was again cooled cryogenically and removed from the apparatus, 5 mL of water was added, and the sample was reconnected to the apparatus.

Three different soils of varying water and organic contents were used in this study. Soils 1 and 2 were garden soils that were 37 and 15% water and 21 and 16% organic matter, respectively. Soil 3 was a desert soil containing 3% water and 1% organic matter. Cod liver oil (Squibb Cod Liver Oil Mint Flavored, E. R. Squibb & Sons, Inc., Princeton, NJ) was used as the oil matrix. This material was selected as the oil matrix due to its low content of the analytes to be determined. This matrix was assumed to mimic both waste oils and the lipid content of biological samples in its effects on the analyte recovery.

Vacuum Distillation Procedure. Prior to a vacuum distillation, the condenser column was cooled to 5 °C. The sample contained in the 100-mL flask (normally at room temperature) was evacuated for 10 min, the water vapors were collected on the condenser column, and the distillate to be analyzed was collected in the cryoloop immersed in liquid nitrogen (−196 °C). The sample chamber valve was closed at the completion of the vacuum distillation and the cryoloop valve switched to allow the GC carrier gas to sweep the cryoloop. The cryoloop's liquid nitrogen bath was removed and replaced with a hot water bath (70−90 °C) to volatilize the distillate. The transfer of the distillate to the GC is completed after 2.5 min. After the sample was vacuum distilled, the condenser column was heated to 40 °C while being evacuated with the vacuum pump for 10 min; this removed the condensed water and potential contaminants. All measurements of analytes were performed by the GC/MS analysis of the transfered vapor.

RESULTS AND DISCUSSION

The α- and β-effects were demonstrated using GC/MS analyses of a methanol solution containing the vacuum distillates.[2] In this study, the vacuum distillates were analyzed as vapor transfer between the vacuum distiller and the GC/MS. Interfacing the GC/MS and vacuum distiller simplifies analysis but adds another potential source of analyte loss that was evaluated. The next phase of this study was to determine the α-values for the analytes and to select surrogates for measuring the α- and β-effects. The final phase of this study was the analyses of a variety of matrices to test the GC/MS/VD method.

The transfer of vapors from the cryoloop to the GC was investigated for its effect on analyte recoveries. Cryoloop trapping efficiencies were investigated by comparing injections of analytes directly into the GC/MS with the injection of analytes into the vacuum stream just before the cryoloop. Figure 1 shows the cryoloop trapping efficiencies for injections of analytes at a low pressure (0.5 Torr) and at a greater pressure (created by allowing air to be drawn into the cryoloop simultaneous with the injection on the cryoloop). The injection with air simulates the pressure within the cryoloop at the initiation of a vacuum distillation (sample flask is at atmospheric pressure), and the low-pressure injection simulates the cryoloop internal pressure later in a vacuum distillation cycle when the air has been evacuated.

The plot of analyte recoveries versus boiling point (Figure 1) shows that trapping efficiencies vary closely in relation to an analyte's boiling point. The most volatile analytes are trapped least effectively for both injection pressures. The analyte efficiencies improve with increasing boiling point up to 220 °C. Analytes with boiling points above 220 °C also demonstrate lower efficiencies and most likely reflect a less efficient transfer from the cryoloop to the GC. The trapping efficiency drops when air is bled into the cryoloop. This indicates that efficiency drops with increasing pressure (mass transfer), and, therefore, during a vacuum distillation, the efficiency of the cryotrap will increase as air is evacuated

(3) McDaniel, J. A. *The Effect of Water Added to Soils on the Analysis of Volatile Organic Compounds*; Book of Abstracts; Pittsburgh Conference: New Orleans, LA, 1992; Abstract 711.
(4) U.S. Environmental Protection Agency. *Handbook of RCRA Ground-Water Monitoring Constituents: Chemical & Physical Properties*; Office of Solid Waste: Washington, DC, 1992.
(5) Li, J.; Dallas, A. J.; Eikens, D. I.; Carr, P. W.; Bergmann, D. L.; Hait, M. J.; Eckert, C. A. *Anal. Chem.* **1993**, *65*, 3212−3218.
(6) Vitenberg, A. G. *J. Chromatogr.* **1991**, *556*, 1−24.
(7) Snyder, J. R.; Dawson, S. A. *J. Geophys. Res.* **1985**, *90*, 3797−3805.

Table 1. Relative Volatility Values (α_K)

compound	surr[a]	bp[b,4] (°C)	concn[c] (ppb)	K[d]	α_K-value av[e]	α_K-value dev[f]
		Volatile Gases				
dichlorodifluoromethane		−30	80		0.07	0.02
trichlorofluoromethane		24	80		0.20	0.02
vinyl chloride		−13	80		0.48	0.06
chloroethane		12	80		1.01	0.02
chloromethane		−24	80		1.37	0.07
bromomethane		4	80		1.82	0.12
		Volatiles				
1,1-dichloroethene		37	40		0.63	0.07
carbon tetrachloride		76	40		0.64	0.02
hexafluorobenzene	α	82	25		0.86	0.06
1,1-dichloropropene		104	40		0.88	0.03
1,1,1-trichloroethane		74	40	1.41[5]	1.31	0.04
allyl chloride		45	100		1.34	0.45
2,2-dichloropropane		69	40		1.37	0.18
tetrachloroethene		121	40	1.55[5]	1.43	0.03
pentafluorobenzene	α	85	9		1.51	0.04
iodomethane		42	100		2.29	0.43
trans-1,2-dichloroethene		48	40		2.3	0.46
trichloroethene		87	40		2.34	0.09
isopropylbenzene		152	40	2.20[5]	2.75	0.05
fluorobenzene	α	85	9		3.5	0.21
benzene		80	40	4.36[5]	3.55	0.27
ethylbenzene		136	40	3.28[5]	3.6	0.12
1,4-difluorobenzene	α	88	9		3.83	0.07
toluene		111	40	3.93[5]	3.88	0.12
m,p-xylenes		138	40		3.91	0.11
benzene-d_6	c	79	26	4.4	3.92	0.27
1,1-dichloroethane		57	40		4.12	0.08
toluene-d_8	β	111	25		4.28	0.09
n-propylbenzene		159	40	2.49[5]	2.43	0.04
cis-1,2-dichloroethene		60	40		5.34	0.07
o-xylene		144	40	5.11[5]	5.54	0.09
o-xylene-d_{10}	α	143	25	5.1	6.14	0.2
chlorobenzene-d_5	α + β	131	25		6.27	0.17
chloroform		62	40	5.85[5]	6.39	0.09
styrene		145	40		6.87	0.36
chlorobenzene		132	40		6.07	0.24
bromobenzene		156	40		7.89	0.73
bromobenzene-d_5	β	155	25		7.93	0.59
4-bromo-1-fluorobenzene	c	152	25		8.05	0.7
methylene chloride		40	40	9.33[5]	10.1	1.6
methylene chloride-d_2	c	40	24		11.1	1.9
1,2-dichloropropane		96	40		10.9	0.2
1,2-dichloropropane-d_6	c	95	21		11	0.1
1,1,1,2-tetrachloroethane		130	40		11.6	0.6
bromodichloromethane		90	40		12.3	0.6
trans-1,3-dichloropropene		112	40		14.1	0.7
bromochloromethane		68	40		15.4	0.4
1,2-dichloroethane		84	40	20.23[5]	18.7	0.9
dibromochloromethane		120	40		19.2	1.4
cis-1,3-dichloropropene		104	40		19.6	1.4
1,2-dichloroethane-d_4	α	84	25	20	20	
bromoform		150	40		23.4	2.4
dibromomethane		97	40		23.9	1.7
1,3-dichloropropane		120	40		24.9	1.9
1,2-dibromoethane-d_4	α	131	26		26	1.7
1,1,2-trichloroethane		114	40		26.2	2.4
1,1,2-trichloroethane-d_3	c	112	20		26.6	0.7
1,2-dibromoethane		132	40		26.7	2
1,1,2,2-tetrachloroethane		146	40		30.3	2.8
cis-1,4-dichloro-2-butene		152	100		33.3	8.1
1,2,3-trichloropropane		157	40		33.6	2.9
trans-1,4-dichloro-2-butene		156	100		33.8	7.4
		Neutral Semivolatiles				
n-butylbenzene		183	40	1.65[5]	1.88	0.08
sec-butylbenzene		173	40		1.91	0.04
hexachlorobutadiene		215	40		2.08	0.06
p-isopropyltoluene		183	40	2.25[5]	2.5	0.07
tert-butylbenzene		169	40		2.72	0.05
decafluorobiphenyl	β	206	25		3.03	0.06
1,3,5-trimethylbenzene		165	40	3.52[5]	3.75	0.18
2-chlorotoluene		159	40		4.04	0.17
1,2,4-trimethylbenzene		169	40		4.5	0.4

Table 1 (Continued)

compound	surr[a]	bp[b,4] (°C)	concn[c] (ppb)	K[d]	α_K-value av[e]	α_K-value dev[f]
			Neutral Semivolatiles			
4-chlorotoluene		162	40		4.78	0.43
1,3-dichlorobenzene		173	40		5.72	0.73
1,4-dichlorobenzene		174	40		6.14	0.84
1,2,4-trichlorobenzene		214	40		7.73	1.22
1,2-dichlorobenzene		180	40		7.86	1.19
1,2,4-trichlorobenzene-d_3	β	213	25		7.88	1.19
1,2-dichlorobenzene-d_4	β	181	24		8.03	1.23
1,2,3-trichlorobenzene		218	40		11.3	1.6
pentachloroethane		162	100		13.2	3.3
naphthalene		218	40		16.7	2.2
naphthalene-d_8	c	217	25		18	3.7
1,2-dibromo-3-chloropropane		196	40		38.9	4.9
			Soluble Volatiles			
diethyl ether	35		80		34.9	5.7
ethyl methacrylate		117	100		48.4	2.8
methyl methacrylate		101	100		71.4	4.1
methacrylonitrile		90	100		102.9	2.4
acrolein		53	200	180[6]	116.8	1
4-methyl-2-pentanone		117	100		119.9	8.4
2-hexanone		128	100		131.1	2.1
ethyl acetate-2-^{13}C	α	77	250	150[6]	150	
acrylonitrile		78	100		161	32
acetophenone-d_5	c	202	100		161	20
isobutanol		108	100		175	156
tetrahydrofuran		66	n/a		456	67
acetonitrile		82	100	1200[7]	545	103
acetone		56	100	580[6]	600	32
acetone-d_6	α	57	490	600[6]	600	
2-butanone		80	100	380[6]	770	110
propionitrile		97	100		1420	320
1,4-dioxane-d_8	α	101	240	5800	5800	
1,4-dioxane		101	100	5750[6]	6200	700
			Basic Semivolatiles			
N-nitrosodimethylamine		154	500		129	37.3
N-nitrosomethylethylamine		165	500		1900	800
N-nitrosodi-*n*-propylamine		206	500		2400	2000
N-nitrosodiethylamine		177	500		4900	2200
aniline		184	500		13700	2300
o-toluidine		200	500		15200	2100
			Marginal			
1-methylnaphthalene-d_{10}	β	241	100		67	
2-methylnaphthalene		245	500		67	17
2-picoline		129	100		6800	5200
pyridine		116	100		13100	600
pyridine-d_5	α	115	100	15000	15000	
N-nitrosodibutylamine		240	500		21000	5000

[a] Surrogate type: α, α-surrogate; β, β-surrogate; and c, check surrogate. [b] Boiling point of analyte. [c] Concentration of analyte solutions used to determine α-values. [d] Partition coefficient of analyte between headspace and water at 20 °C. [e] Three to four replicates. [f] Standard deviation, 1σ.

from the sample flask. The loss of analyte occuring at the cryoloop is not easily distinguished from losses due to analyte condensation, and therefore these cryoloop losses are included as a component of β-effects.

The boiling point–condensation relationship previously described[2] is minimized in this study as both the samples and standard solutions are vacuum distilled (previous study did not vacuum distill standard solutions) using the same vacuum distillation conditions. Because analyte condensation on the condenser, cryoloop trapping efficiencies, and the cryoloop-to-GC transfer are essentially the same for samples and standards, there is a normalization of the β-effects. The β-surrogates (surrogates to measure boiling point effects) are now used to rectify any variation of boiling point effects between the analyses of standard solutions and the analyses of samples (including the cryoloop-to-GC transfer).

The effects produced by varying the condenser column operating temperature were evaluated by comparing analyte responses obtained from direct GC injection of analytes with those from the vacuum distillation of analytes using different condenser temperatures. Figure 2 presents the relationship of analyte recovery to condenser temperature using the surrogates naphthalene-d_8 and ethyl acetate-2-^{13}C as representative analytes. The recoveries of both analytes are maximized when the condenser column is between −6 and 10 °C. As these compounds have greatly different boiling points, the β-effects (at the condenser) appear to be at a minimum when the condenser column temperature is between −6 and 10 °C. The minimizing of the β-effect

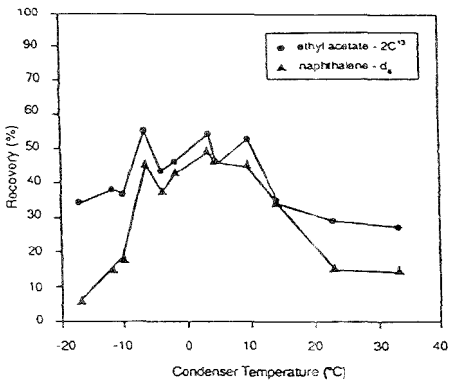

Figure 2. Analyte recovery versus condenser column temperature.

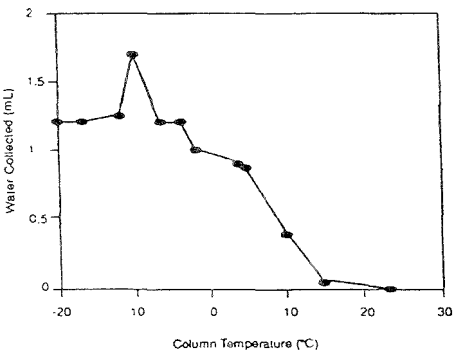

Figure 3. Water collected on condenser column versus condenser column temperature.

enhances the response of the higher boiling analytes and simplifies the correction of such effects.

The amount of water being collected on the condenser column was also a consideration. Preparation of the condenser column between distillations is made simpler if the amount of condensed water is minimized. Water collected as a function of condenser column temperature (Figure 3) shows that the amount of water collected decreases as the condenser column temperature is increased. A condenser operating temperature between −6 and 10 °C minimizes analyte condensation, and one between 5 and 10 °C minimizes water collected. The operating temperature of 5 °C was used in this study to allow for some temperature fluctuations with minimal impact on analyte recoveries.

Determination of Relative Volatility Values. The recovery of an analyte in the absence of observable β-effects depends on its relative volatility. Using the same operating conditions to perform each distillation within a set (a series of 10-min vacuum distillations required to completely evaporate a 5-mL sample) makes the influence of β-effects (within experimental variation) consistent. With the response of analytes comparable between distillations in a set, the rate of removing analytes by distillation (α-effects) can be measured. Therefore, the recovery of an analyte corresponding to its relative volatility is calculated to be its response in the initial vacuum distillation divided by the sum of responses for the set.

A cylindrical flask (15-mm i.d., 8-cm length) replaced the standard 100-mL round bottom flask for this part of the study. The cylindrical flask produced a constant sample surface (2.7 cm^2) in the flask and a more reproducible distillation rate of water (<0.5 mL of water per 10 min at 20 °C). The use of a 100-mL round bottom flask to contain the water sample would have resulted in a rapidly changing surface area (decreasing as water is vaporized) that would have to be addressed when comparing the vacuum distillations within a set. The cylindrical flask also had the advantage of slowing the vacuum distillation of analytes (greatest impact on the least volatile analytes) and exaggerating the losses related to α-effects. While the cylinder would not be as desireable as the round bottom flask for routine analyses, using the cylinder made the distinction between analytes (related to α-effects) easier to observe and measure.

The cryoloop efficiency varies with pressure, and, to make distillation conditions the same within a set, it was necessary to remove air from the flask containing the sample prior to the first vacuum distillation. The evacuation of air was accomplished by cryogenically freezing the spiked sample in liquid nitrogen and then evacuating the flask for 3–5 min. The sample was then warmed to 20 °C, and the first vacuum distillation was performed.

The first vacuum distillation of each set was performed while the sample was immersed in a 20 °C water bath. The sample temperatures used after the initial vacuum distillation were varied (20–45 °C using a water bath) to exaggerate the range of recoveries corresponding to a degree of relative volatility (α-values). When fewer vacuum distillations (higher sample temperatures) were required to evaporate the 5-mL sample, the recovery differences between the lower α-valued analytes were emphasized. More vacuum distillations (lower sample temperatures) emphasized the differences between the higher α-values.

It was also observed that the relative volatilities of several of the more soluble analytes (i.e., pyridine and the nitrosamines) would vary as a function of the initial vacuum distillation time. The relative volatilities of these analytes would increase as the vacuum distillation times were increased, which seems to indicate that some analytes exhibit a retention time gap in the condenser or the formation of an azeotrope with the water collected in the condenser column. For this study, the relationship of recovery to relative volatility for these analytes was determined using initial vacuum distillation times between 2 and 5 min.

The recoveries of selected surrogates (benzene-d_6, *o*-xylene-d_{10}, 1,2-dichloroethane-d_4, ethyl acetate-2-^{13}C, acetone-d_6, dioxane-d_8, and pyridine-d_5) were then used to plot the α-value versus recovery relationship. The values of their partition coefficients (25 °C) were assigned as their respective α-values so that interpolated α-values (α_K-values) would correspond to partition coefficients. The α_K-values for 114 analytes were experimentally determined and are listed in Table 1. The assignment of the α_K-value for pyridine-d_5 was an estimation.

It was observed that when the sample boiled vigorously, a large amount of water collected on the condenser, the recoveries of the less volatile analytes were greatly improved, and the recoveries of the more volatile analytes were diminished. This made the recovery versus α_K-value relationship less distinct and interpolation of values less precise. Therefore, a set was not used to determine α_K-values if the initial distillation boiled (the only distillation in a set prone to boil vigorously).

Table 2. Matrix Surrogates and Their Respective Ranges

range		surrogate pairs	
type	values	first	second
α_K-values	0.07–3.0	hexafluorobenzene	fluorobenzene
		hexafluorobenzene	1,4-difluorobenzene
		pentafluorobenzene	fluorobenzene
		pentafluorobenzene	1,4-difluorobenzene
	3.0–6.3	fluorobenzene	*o*-xylene-d_{10}
		fluorobenzene	chlorobenzene-d_5
		1,4-difluorobenzene	*o*-xylene-d_{10}
		1,4-difluorobenzene	chlorobenzene-d_5
	6.3–20	*o*-xylene-d_{10}	1,2-dichloroethane-d_4
		o-xylene-d_{10}	1,2-dibromoethane-d_4
		chlorobenzene-d_5	1,2-dichloroethane-d_4
		chlorobenzene-d_5	1,2-dibromoethane-d_4
	20–150	1,2-dichloroethane-d_4	ethyl acetate-2-^{13}C
		1,2-dichloroethane-d_4	acetone-d_6
		1,2-dibromoethane-d_4	ethyl acetate-2-^{13}C
		1,2-dibromoethane-d_4	acetone-d_6
	150–15000	ethyl acetate-2-^{13}C	1,4-dioxane-d_8
		ethyl acetate-2-^{13}C	pyridine-d_5
		acetone-d_5	1,4-dioxane-d_8
		acetone-d_6	pyridine-d_5
bp (°C)	80–111	toluene-d_8	80 °C[a]
		chlorobenzene-d_5	80 °C
	111–131	toluene-d_8	chlorobenzene-d_5
		toluene-d_8	bromobenzene-d_5
		chlorobenzene-d_5	80 °C
	131–155	toluene-d_8	bromobenzene-d_5
		chlorobenzene-d_5	bromobenzene-d_5
		chlorobenzene-d_5	1,2-dichlorobenzene-d_4
	155–181	chlorobenzene-d_5	1,2-dichlorobenzene-d_4
		bromobenzene-d_5	1,2-dichlorobenzene-d_4
		bromobenzene-d_5	decafluorobiphenyl
	181–206	bromobenzene-d_5	decafluorobiphenyl
		1,2-dichlorobenzene-d_4	decafluorobiphenyl
		1,2-dichlorobenzene-d_4	1,2,4-trichlorobenzene-d_3
	206–220	1,2-dichlorobenzene-d_4	1,2,4-trichlorobenzene-d_3
		decafluorobiphenyl	1,2,4-trichlorobenzene-d_3
		decafluorobiphenyl	1-methylnaphthalene-d_{10}
	220–250	decafluorobiphenyl	1-methylnaphthalene-d_{10}
		decafluorobiphenyl	1-methylnaphthalene-d_{10}

[a] The effects relating to an analyte with a boiling point at or less than 80 °C are assumed to be negligible.

A listing of published partition coefficients values in Table 1 shows that the α_K-values are a good estimator of analyte partition coefficients. The exception would be for those analytes with α_K-values greater than 5800, where the estimate of the partition coefficient (and α_K-value) for pyridine-d_5 could introduce error.

Selection of Surrogates. The recovery of an analyte is related to its α-value and its boiling point, and these relationships can be quantified using surrogates.[2] Table 1 identifies the surrogates used in this study. The α-surrogates represent ranges of α_K-values, and their recoveries are used to describe the α_K-value versus recovery relationship. β-Surrogates represent ranges of boiling points, and their recoveries are used to describe the analyte recovery versus boiling point relationship. Those surrogates identified as check surrogates in Table 1 were spiked into all samples to check analyses and calculations.

The analytes and α-surrogates are grouped in five divisions by their α_K-values (Table 2). Each of these groups has four surrogates to describe how the analytes of the group behave. The α-surrogates are selected so that there are two pairs of surrogates with similar α_K-values bracketing a group of analytes. The replicate calculations that can be made then provide the analyst with a means to assess confidence in the measurements. The surrogate pairings shown in Table 2 identify the combinations of surrogates used to calculate α-effects.

The boiling point groupings and their respective surrogate pairings used in β-effect calculations are also presented in Table 2. The β-surrogates represent seven increments of boiling recovery relationship. Surrogates are not used to address the recovery–boiling point relationship for the boiling points below 80 °C. The compounds with boiling points below 40 °C generally are not concentration stable (losses due to evaporation) in a surrogate spiking solution and do not withstand routine handling. While there is a drop in cryotrap trapping efficiencies for those analytes with boiling points below 80 °C, a greater effort to profile the lowest boiling analytes is of limited value considering the cost of frequent replacement of a surrogate solution and the potential vaporization of the most volatile analytes prior to analysis. The effects of not having a pair of lower boiling surrogates is seen in the poorer quality analyses reported for the lowest boiling analytes.

The vacuum distillation of an actual sample can yield different values for analytes compared with the values obtained by vacuum distillation of the same amount of analytes in a standard solution. In this study, the comparison is called *relative recovery*. The component of relative recovery of an analyte that is related to its α_K-value is referred to as α-effect or R_α. The relative recovery related solely to its boiling point (vapor pressure) is referred to as β-effect or R_β and includes those relative losses that occur at the cryoloop and the condenser column. The relative recoveries of the α- and β-surrogate compounds predict how other analytes behave in the same sample matrix relative to the analyses of a standard solution (in distilled water). Once the relative recovery of analytes from a matrix is established, the responses of analytes in a standard solution are used to determine analyte concentrations.

The evaluation of α- and β-effects was undertaken with two approaches. The first approach was to initially measure the α-effects by using those surrogates with boiling points less than 150 °C. After the α-effects were predicted, the β-effects were calculated as the difference between the relative recoveries predicted using α-values and their measured recoveries. This approach worked well for aqueous samples, as the β-effects were observed to be minimal adjustments to relative recoveries. This first approach was not adequate for soils, where the β-effect could be significant for analytes that have boiling points below 130 °C (likely due to the partitioning between the solid phase and the vapor phase). There were too few unaffected surrogates to describe the α-effects when soils were analyzed. Therefore, as a second approach, the β-effects were determined prior to the α-effects. This second approach, however, still required an initial estimate of the α-effects on the β-surrogates before the β-effects could be calculated. This second approach was used for generating the data reported in this study.

The initial approximation of α-effect on the β-surrogates is accomplished by using the α-surrogates fluorobenzene and 1,2-dichloroethane-d_4 (boiling points of 85 and 84 °C, respectively) to approximate α-effects on the β-surrogates with the assumption that β-effects are minimal at 85 °C. The equation

$$\ln(R_\alpha) = a\alpha_K + c \qquad (1)$$

where R_α is the surrogate's relative recovery corresponding to its α_K-value, a and c are constants, and α_K is the relative volatility

Table 3. Percent Accuracy of Surrogate Predictions for Various Matrices and Method Detection Limits in Parts per Billion[a]

	water[b]				soil[c]				oil[d]			
analyte subset	$\bar{A}_T$[e]	$\bar{A}_{dev}$[f]	$\bar{\alpha}_T$[g]	MDL[h]	$\bar{A}_T$	$\bar{A}_{dev}$	$\bar{\alpha}_T$	MDL	$\bar{A}_T$	$\bar{A}_{dev}$	$\bar{\alpha}_T$	MDL
volatile gases	111 ± 18	5–35	1	0.5–5.2	97 ± 6	18–28	8	0.6–5	99 ± 14	8–31	36	7–66
volatiles	100 ± 2	0–10	1	0.1–1.0	98 ± 5	0–20	3	0.1–0.7	97 ± 10	2–70	35	0.1–14
soluble volatiles	95 ± 11	1–70	17	0.4–40	113 + 78	2–300	9	1–6	108 ± 15	3–150	34	4–35
neutral semivolatiles	102 ± 17	1–40	2	0.2–0.7	98 ± 8	2–13	7	0.2–1.2	81 ± 23	18–60	42	1–30
basic semivolatiles	132 ± 5	9–37	40	22–33	115 ± 9	7–19	19	11–27	81 ± 32	4–150	17	300–500
marginal analytes	87 ± 27	8–24	87	3–36	120 ± 69	5–61	31	1–100	61 ± 48	3–24	146	36

[a] Method detection limits are equal to 3 times the average standard deviation (1σ) of three sets of seven replicate analyses performed on three nonconsecutive days. [b] 5-mL water samples. [c] 5-g soil samples (vacuum spike, soil 3). [d] 1-g oil samples (vacuum spike, cod liver oil). [e] The group average ($\pm 1\sigma$) of all analytes contained in the analyte group. Accuracy of each analyte was determined using 3–4 replicates. [f] The range of individual analyte standard deviations (1 sigma) of the replicate analyses by analyte group. [g] The group average variation between predictions of the surrogate pairs for the replicate analyses. [h] The range of analyte MDLs within the analyte group.

of the surrogate, describes the α-effect versus recovery relationship.[2] The relative recoveries of the β-surrogates toluene-d_8, chlorobenzene-d_5, bromobenzene-d_5, and 1,2-dichlorobenzene-d_4 are adjusted for their α-effects (R_β = measured recovery/R_α). The resulting relative recovery represents the component of the relative recovery related to β-effects. Similarly, the α-surrogates 1,2-dichloroethane-d_4 and 1,4-dioxane-d_8 are used to solve eq 1 and to interpolate R_β for the β-surrogate 1-methylnaphthalene-d_{10}.

Using the β-surrogate R_β values, the R_β–boiling point relationship is described using the equation

$$R_\beta = a(\mathrm{bp} - \mathrm{bp}_0) + b \qquad (2)$$

where R_β is the relative recovery corresponding to the boiling point, a and b are constants, bp is the analyte's boiling point, and bp_0 is the lowest boiling point of the β-surrogate used in the solution.[2] The impact of a single β-surrogate relative recovery measurement error is minimized by calculating three solutions to eq 2 for each analyte. The β-surrogate pairs used to solve eq 2 for groups of analytes by boiling point are identified in Table 2. The average and standard deviation of three R_β values (only two solutions for the 80–111 °C and 220–250 °C ranges) generate the predicted analyte relative recovery, $\bar{R}_\beta \pm r_\alpha$, corresponding to β-effects. The resultant $\bar{R}_\beta$ for each α-surrogate is used to correct their measured relative responses (R_α = measured recovery/$\bar{R}_\beta$) to isolate the relative recoveries related to α-effects.

The α-surrogate corrections are performed by grouping analytes with similar α_K-values. The α-effects exhibited by those compounds at the limits of a group are the best data to describe the α-effects for those analytes within these groups, and therefore pairs of α-surrogates are selected to represent the extremes of each group's range of α_K-values (i.e., surrogates hexafluorobenzene and fluorobenzene represent the lower and upper ends of the grouping of α-values between 0.07 and 3).

One lower value α-surrogate and one higher value α-surrogate are selected to calculate the relationship of relative recovery to α_K-values within the group. Using the four possible combinations of surrogates to solve eq 1, each analyte will have four α-effect measurements. The predicted relative recovery relating to α-effects for an analyte is $\bar{R}_\alpha \pm r_\alpha$. The predicted relative recovery that includes α- and β-effects is

$$\bar{R}_T = \bar{R}_\alpha \bar{R}_\beta \qquad (3)$$

where $\bar{R}_\beta$ is the average bias using eq 2 for the combinations of β-surrogates in the analytes boiling point grouping.

The associated variance term for eq 3 is

$$r_T^2 = r_\alpha^2 + r_\beta^2 \qquad (4)$$

Accuracy and standard deviation associated with the surrogate corrections are calculated as

$$A_T \pm \alpha_T = (\bar{R}_T \pm r_T)/(\text{measured recovery}) \qquad (5)$$

where the measured recovery is the response of the analyte from a sample analysis compared with the analyte response in the vacuum-distilled standard of the same concentration. Performing replicate vacuum distillations, the average and standard deviation of resulting determinations of A_T are identified as $\bar{A}_T \pm \bar{A}_{dev}$, and the average α_T is $\bar{\alpha}_T$.

Water Sample Analyses. The list of analytes used in this study is long, and therefore some grouping of data was necessary for presentation. Analytes are categorized as the following subsets: volatile gases (boiling points ≤30 °C), volatiles (boiling points >30 °C and <160 °C), soluble volatiles (α_K > 34), semivolatiles (boiling point >150 °C), and basic semivolatiles. The *marginal analyte* subset was created for those analytes at the limits of the method. Table 1 identifies the analytes in each grouping. Analytical results ($\bar{A}_T \pm \bar{A}_{dev}$, and $\bar{\alpha}_T$) are provided as either the average or the range of the results for each of the analytes contained in a group. The individual analyte data are available as supporting information.

Analyses of distilled water and distilled water modified to simulate more extreme aqueous matrices were conducted to evaluate the accuracy of the VD/GC/MS method with the specified surrogate corrections. The $\bar{A}_T \pm \bar{A}_{dev}$ and the $\bar{\alpha}_T$ values for the vacuum distillation of various water samples are presented in Table 3. The surrogates accurately profile analyte performance in water matrices, and determinations are continually accurate to within 5% of the spiked values. For those analytes not normally considered as volatile (e.g., nitrosamines), the system is less accurate. The method detection limits (MDLs) were determined using the Resource Conservation and Recovery Act (RCRA) guidelines[8] (see footnote in Table 3). The mass spectrometer

(8) U.S. Environmental Protection Agency. *Test Methods for Evaluating Solid Waste, SW-846*; Office of Solid Waste: Washington, DC, 1992.

response for most analytes indicated that lower MDLs could easily be obtained should they be required in the future.

Distilled water proves to be an ideal matrix, as the $\bar{A}_T$ values for the individual analytes are consistently within 5% of the spiked value for distilled, water and the precision errors ($\bar{A}_{dev}$) and $\bar{\alpha}_T$ are typically <5%. The addition of salt increases the relative recovery of most analytes, especially those analytes with greater α-values. The salting effects are as expected, but the important finding is that the α-surrogates correctly compensate for the increases in relative recoveries, as $\bar{A}_T$ is consistently within 5% of the spiked concentrations. The addition of glycerin depresses the analyte response relative to their α_K-values, but again $\bar{A}_T$ is within 5% of the spiked values for most of the analytes. Such high content of soluble organic compounds is certainly an unusual sample, but the accuracy of such analyses demonstrates the reliability of the surrogate corrections.

The addition of soap produces one of the most difficult aqueous matrices for VOC determinations as the foaming produces an irregular interface between vapor and liquid. Foaming with bubbles expanding to more than than 25 mL was persistent throughout the vacuum distillations. However, the quality of the analyte determinations was still very similar to that obtained with distilled water. Nitrosamines, as a group, had recoveries lower than those predicted, but their behavior was not dissimilar from that observed with distilled water.

The higher boiling analytes are susceptible to cross-contamination. It was reported that the vapors of analytes being distilled that have boiling points >220 °C were >90% condensed on the condenser.[2] The removal of analytes between analyses was effective for most analytes (>99%) with the exception of the highest boiling analytes, primarily *N*-nitrosodibutylamine and 2-methylnaphthalene, where >2% could remain. While the percentage of analyte available for carryover is not normally significant, 2% remaining on the condenser may be a greater amount of analyte than that condensed in the cryoloop and therefore a relatively significant source of contamination. The condenser temperatures used to eliminate carryover are an apparatus limitation and evidently are not sufficient to completely remove the highest boiling analytes. Heating the condenser column to higher temperatures would be expected to minimize carryover and generally improve the performance for *N*-nitrosodibutylamine and 2-methylnaphthalene.

A 20% methanol solution was previously shown to have minimal impact on the vacuum distillation of analytes when the cryoloop condensate was being analyzed by aqueous injection.[2] With the configuration used in this study, however, >20 μL of methanol interfered with the measurement of many analytes. It appears that the interferences are a result of poorer chromatography of some analytes (higher α-values) and an attenuated mass spectrometer response to analytes that coelute with methanol. Lower recovery of higher boiling analytes is also observed and likely is related to less efficient transfer of those analytes from the cryoloop to the GC. The net effects on analytes is primarily a depressed recovery of those compounds with higher α_K-values or higher boiling points or those that elute with methanol. The presence of 50 μL of methanol in a sample affects the chromatography of most analytes. The impact of methanol on chromatography is critical, and therefore the methanol content of prepared samples is limited to 10 μL.

Even small amounts of methanol would periodically affect (attenuated mass spectrometer response) those analytes that coelute with methanol. Diethyl ether consistently coelutes with methanol, and on occasion $\bar{A}_T$ is biased high for this analyte. Trichlorofluoromethane and acrolein are affected to a lesser degree. Changing the chromatography conditions could improve these analyte accuracies. Adding isotopes of the analytes (especially for ether) to the surrogate mix would detect the occurrence of the effect and provide a means for correcting the attenuated responses (i.e., isotopic dilution).

Larger sample sizes can be used with minimal impact on the accuracy of analyte determinations. Analyses of 25-mL samples yield relative recoveries very similar to those for 5-mL samples. While A_T for the higher α_K-value analytes begins to exceed 10% deviation from the spiked concentrations, including the confidence window generated by $\pm a_T$ would generate a window larger than A_T that includes the true analyte concentration. Only the nitrosamines indicated a bias in accuracy that could not be compensated by the a_T. There was also some variation in the mass spectrometer response to the lowest boiling analytes. The presence of naturally occurring gases in the samples (carbon dioxide) was apparently causing mass spectrometer pressure fluctuations.

Sample bath temperatures of 10 and 30 °C were used to investigate the sensitivity of vacuum distillation to ambient temperatures. The low end of this temperature range reduced the relative recoveries >50%. The higher end increased the analyte responses relative to the increasing α_K-value. The surrogate corrections remain accurate with few exceptions. The $\bar{A}_T$ values for nitrosamine concentrations generally exceed the true concentrations by >10%, and the windows generated using $\bar{\alpha}_T$ are too small to compensate. When the nitrosamines are of particular concern, the sample analyses should be more constrained in temperature and sample size variations. The response for the poorer performing analytes can be improved with the addition of salt, but this normally should not be required.

Soil Sample Analyses. The evaluation of soil matrices requires some assurance that there is matrix interaction. Rather than performing soil sorption−time studies, two different spiking techniques were used (the water spike, and the more rigorous vacuum spike). It was found that the accuracy of the analyses was equivalent for the two techniques. While the recoveries of analyte were lower with the vacuum spike, the surrogates were similarly affected and were accurate in predicting analyte recoveries. This indicates that while the α- and β-effects may differ by degree of matrix interaction, the matrix effects are still accurately described using the α- and β-surrogates.

In the same manner as the water analyses, the $\bar{A}_T$, $\bar{A}_{tr-v}$, and $\bar{\alpha}_T$ values for the soil analyses are presented as subset results (individual analyte data available as supporting information). The soil results are presented in Table 3 (vacuum spike soil 3) and are similar to results from water analyses. The MDLs reported in Table 3 are also very similar to those reported for water (<1 ppb for most analytes). The detector response to analytes indicated that lower MDLs could easily be obtained, but the levels being reported already exceed most needs. Analyses of soils 1 and 2 provided a greater variation in analyte accuracy that indicates that the organic content of a soil will greatly influence analyte behavior. Soil 1 was a heavily mulched garden soil and was 21% organic matter and 37% water. Soil 2 was another garden

soil that contained less organic matter (16% organic matter and 15% water). The analyses of the higher organic content soils demonstrated good accuracy for most analytes.

The list of analytes for the soil analyses is abbreviated due to apparent degradation of some analytes. Acrolein apparently degrades very rapidly and is poorly recovered from soil. Ethyl acetate-2-^{13}C and ethyl methacrylate were similarly affected but could be recovered from soil 3 when they were added using the water spike technique. These analytes were not considered as viable analytes in the soil samples studied. Therefore, the surrogate, ethyl acetate-2-^{13}C, is not recommended as an α-surrogate for soils but rather as a check surrogate to identify when such degradation occurs. The surrogate, 1,4-dioxane-d_8, is substituted for ethyl acetate-2-^{13}C in the 20−150 α_K-value grouping, and the surrogate, 1,2-dibromoethane-d_4, is a substitute for ethyl acetate-C^{13} in the 150−15000 α_K-value grouping.

The relative recoveries of acrylonitrile, methacrylonitrile, and propionitrile were at times unexpectedly low. This occurred only when the analytes were vacuum-spiked into soil 1 or 2. It appears that these analytes degrade in a soil matrix and may not be viable analytes for soil analyses.

Acetonitrile is not accurately measured due to recurring spectral interference. The manual integration of acetonitrile is required, and a different temperature program would likely improve this analyte's performance. An MDL of 100 ppb is reported for 2-picoline, although the MDL was actually calculated to be 5 ppb. The higher MDL is listed to minimize the frequency of manual integrations (poorly defined chromatographic peak) that would be required at the lower value.

Oil Sample Analyses. Analyses of cod liver oil proved sensitive for most analytes despite a decrease in the relative recovery of most analytes. The organic content also produced spectral interferences that made some determinations difficult and the determination of several analytes impossible. The relative recoveries for the analytes are very similar for both water spike and vacuum spike techniques, suggesting the oil matrices are not as difficult as soil to spike. Both spike techniques produce $\bar{A}_T$, $\bar{A}_{dev}$, and $\bar{\alpha}_T$ results that are accurate and quite similar. Table 3 presents the $\bar{A}_T$, $\bar{A}_{dev}$, and $\bar{\alpha}_T$ values as group results (vacuum spike of cod liver oil).

The analytes, *N*-nitrosodibutylamine and 2-methylnaphthalene, were poorly recovered from the oil matrix and had relative recoveries below 1%. The $\bar{A}_T$ values for these analytes indicate that the determination of analytes with boiling points greater than 240 °C in oil should not be considered quantitative. Warming the sample to improve recoveries would not be desirable because much of the matrix would also be vaporized and would likely become system contamination.

The MDLs for analytes in an oil matrix are listed in Table 3. The limits are much improved compared with earlier work,[1] reflecting the ability of the surrogates to correct for matrix effects and produce more precise results. A 0.2-g oil sample seems well suited for waste oil analyses; and the MDLs for the smaller sample sizes meet current criteria, and the smaller sample minimizes matrix spectral interference. Of course, such interferences would vary by sample.

The analyses of the various matrices and the use of specific compounds as surrogates have identified some additional matrix effects that should be monitored. The use of ethyl acetate-2-^{13}C has evolved from an α-surrogate for water analyses to a check surrogate to detect potential degradation of analytes for soil analyses. The variation of accuracy predictions of the nitrosamines shows that an additional surrogate might be beneficial if it contains an amine or a nitroso functional group.

The check surrogates methylene chloride-d_2, benzene-d_5, 1,1,2-trichloroethane-d_3, and bromofluorobenzene are effective in monitoring the behavior of the majority of analytes. The surrogate 1,2-dichloropropane-d_6 has spectral interferences from the higher hydrocarbon-containing sample matrices. The frequency of manual integrations that were necessary makes this compound undesirable for routine use. The surrogate 1,1,2-trichloroethane-d_3 was also affected but to a lesser degree.

Analytes that have either boiling points or relative volatilities at the limits of the method should be scrutinized closely. The check surrogates acetophenone-d_5 (boiling point 202 °C and α_K-value 161) and naphthalene-d_8 (boiling point 217 °C and α_K-value 18) are very useful in identifying how the matrices are affecting the higher boiling analytes (to 220 °C) and those with higher relative volatility (α-value to 200).

While all the analytes studied perform very well in an ideal matrix such as distilled water, a high content of organic matter can greatly impact the accuracy of analyte determinations. The analyst, however, is warned when such effects occur (in addition to the performance of check surrogates) upon reviewing a_T (or r_T) values for the analytes, as they will normally exceed 50% when accuracy of a determination is outside a 70−130% window for the analyte.

CONCLUSION

This work demonstrates the accuracy and sensitivity of VD/GC/MS and surrogate-based matrix corrections. The list of analytes is not limited to VOCs but can be expanded to include compounds that have partition coefficients up to 15 000 and boiling points up to 245 °C. The prediction of matrix effects on analyte recoveries with confidence intervals provides the analyst and data users with a powerful tool to interpret data and eliminates the need for additional analyses, such as matrix spikes, to estimate such effects. The accuracy of VD/GC/MS allows the analyses of standard solutions (distilled water) to be used for the determination of analytes in different matrices as well as sample sizes without compromising the usefulness of the data.

ACKNOWLEDGMENT

The EPA, through its Office of Research and Development (ORD), funded and performed the research described here. This paper has been subjected to the agency's peer review and has been approved as an EPA publication. Mention of trade names or commercial products does not constitute endorsement or recommendation for use. The U.S. Government has the right to retain a nonexclusive, royalty-free license in and to any copyright covering this article.

SUPPORTING INFORMATION AVAILABLE

Four tables containing individual analyte data for the matrices analyzed, including the $\bar{A}_T$, $\bar{A}_{dev}$, and $\bar{\alpha}_T$ values for each analyte from the analyses of water, water/glycerin, water/salt, and water/soap matrices, the MDLs for each analyte in water, soil, oil, and waste oil matrices, the $\bar{A}_T$, $\bar{A}_{dev}$, and $\bar{\alpha}_T$ values for each analyte from the analyses of soils 1−3 using both vacuum and water spikes, and the $\bar{A}_T$, $\bar{A}_{dev}$, and $\bar{\alpha}_T$ values for each analyte from the analyses of cod liver oil (14 pages). Ordering information is given on any current masthead page.

Received for review June 19, 1995. Accepted September 5, 1995.[⊗]

AC9506140

[⊗] Abstract published in *Advance ACS Abstracts,* October 15, 1995.

Anal. Chem. 1995, *67*, 4053–4056

Structural Study of Electrolysis-Induced Degradation of the Growth Hormone Releasing Peptide His-D-Trp-Ala-Trp-D-Phe-Lys-NH_2

Hung-Yuan Cheng,* Louisa L. Davis, Michael J. Huddleston, and Steven A. Carr

Physical and Structural Chemistry Department, SmithKline Beecham Pharmaceuticals, King of Prussia, Pennsylvania 19406

Growth hormone releasing peptide (GHRP, sequence His-D-Trp-Ala-Trp-D-Phe-Lys-NH_2) is a synthetic hexapeptide under consideration for transdermal iontophoretic drug delivery. Cyclic voltammetry, controlled-potential electrolysis, HPLC/UV analysis, LC/MS/MS analysis, and EPR spin-trapping studies indicate that the electrolysis-induced oxidative degradation of GHRP is likely to be mediated by electrogenerated oxygen radicals from the electrolysis of water. Within 2 h and up to 2.5 V versus an Ag/AgCl reference electrode, the peptide backbone remains largely intact. The chemical modifications are selectively on imidazole (histidine) and indole (tryptophan). Strategies for alleviating the electrolysis-induced degradation of GHRP are proposed.

Transdermal iontophoresis is a drug delivery scheme in which the transport of ionic drugs through skin is facilitated by the application of low-level electric current. This technique has attracted much attention in the field of peptide and protein drug delivery because of the prospect for noninvasive systemic deliveries of charged macromolecules and the advantage of bypassing both the gastrointestinal enzyme degradation and the first-pass hepatic metabolism.[1,2] In addition, the electronic control aspect of the technique offers a wide range of opportunities for engineering novel controlled-release devices.[3] We have recently developed a prototype iontophoretic device for the transdermal delivery of growth hormone releasing peptide (GHRP).[4] GHRP is a synthetic hexapeptide that has been shown to stimulate the release of growth hormone (GH) in humans via intravenous administration.[5,6]

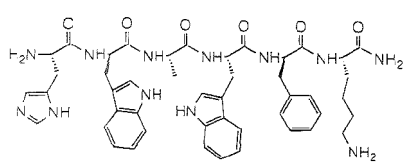

For a pharmaceutical formulation, the stability of the drug substance under various physical and chemical conditions must be evaluated. In iontophoretic drug delivery, the drug substance comes in direct contact with the electrode during the passage of electric current. In essence, the drug patch compartment acts as an electrochemical cell in which the voltage at the working (delivery) electrode fluctuates with variations in current density, overall impedance, concentration gradient, and other factors. For GHRP, which is positively charged (at pH < 9) and delivered from the anodic compartment, this means possible oxidative degradation of the peptide at an applied voltage exceeding the solvent breakdown threshold. We report here the results of a structural study of electrolysis-induced degradation of GHRP in pH 5 acetate buffer both near and beyond the oxidative solvent decomposition potentials using a platinum working electrode. Cyclic voltammetry, bulk electrolysis, HPLC analysis, on-line LC/MS/MS, and spin-trapping electron paramagnetic resonance (EPR) techniques are used to investigate the electrochemical reactions and to characterize the products. The objective here is to gain a better understanding of the electrochemical process in order to rationally optimize the electrical control parameters for iontophoretic delivery of GHRP.

EXPERIMENTAL SECTION

Electrochemistry. A three-electrode potentiostat system was used for the electrochemical experiments. A platinum disk electrode was used for cyclic voltammetry, and a large area (20 cm^2) platinum gauze electrode was used for bulk electrolysis. All applied potentials are measured versus an Ag/AgCl reference electrode. Cyclic voltammetry was carried out using a BAS-100 electrochemical analyzer (Bioanalytical Systems, West Lafayette, IN), and bulk electrolysis was carried out using a PAR 173 Potentiostat (Princeton Applied Research, Princeton, NJ). The electrolyte solution contained 0.15 M NaCl and 0.01 M sodium acetate adjusted to pH 5 with acetic acid.

HPLC Analysis. A Beckman ultrasphere ODS 5 μm, 4.6 mm × 25 cm column was used for monitoring the disappearance of the GHRP and the formation of products upon electrolysis. The mobile phase was composed of 23 g of $NH_4H_2PO_4$ and 11.2 mL of H_3PO_4 in 150 mL water adjusted to pH 3.0 with $N(C_2H_5)_3$, then 400 mL of CH_3CN and enough water to make up 2 L. The UV detection was set at 220 nm and flow rate at 1 mL/min.

LC/ESMS and LC/ESMS/MS Analyses. Chromatographic separations were carried out using a Beckman System Gold (San

(1) Parasrampuria, D.; Parasrampuria, J. *J. Clin. Pharm. Ther.* **1991**, *16*, 7–17.
(2) Cullander, C.; Guy, R.H.; *Adv. Drug Delivery Rev.* **1992**, *8*, 291–329.
(3) Chien, Y. W. Systemic delivery of peptide-based pharmaceuticals by transdermal periodic iontotherapeutic system. In *Dermal and Transdermal Drug Delivery*; Gurny, R., Teubner, A., Eds.; Wissenschaftliche Verlagsgesellschaft mbH: Stuttgart, 1993; pp 129–152.
(4) Ellens, H.; Lai, Z.; Marcello, J.; Davis, C.; Cheng, H.-Y.; Oh, C. K.; Okabe, K. Transdermal iontophoretic delivery of GHRP in rats. *Int J. Pharm.*, submitted
(5) Ilson, B. E.; Jorkasky, D. K.; Curnow, R. T.; Stote, R. M. *J. Clin. Endocrinol. Metab.* **1989**, *69*, 212–214.
(6) DeBell, W. K.; Fezzoli S. S.; Thorner, M. O. *J. Clin. Endocrinol. Metab.* **1991**, *72*, 1312–1316.

0003-2700/95/0367-4053$9.00/0

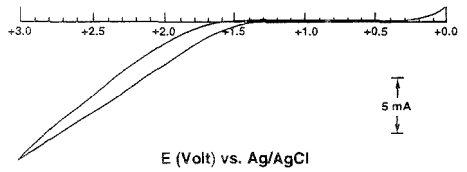

Figure 1. Cyclic voltammogram of 5 mM GHRP in pH 5.0 acetate buffer with 0.15 M NaCl using a platinum working electrode.

Ramon, CA) equipped with a programmable solvent module and variable wavelength detector. Three nanomoles of the original sample was injected onto a 2.1 mm × 25 cm C_{18} column at a flow rate of 200 μL/min. The gradient was programmed to start at 20% B (B = 90% CH_3CN, 10% H_2O, 0.1% TFA; A = 0.1% TFA) and increase linearly to 50% B in 10 min, and then it was held at 50% B for 20 min. The column effluent was split approximately 25:1, with the minor portion going to the mass spectrometer and the remainder going to the UV detector.

Electrospray (ES) mass spectra were recorded as previously described[7,8] on a Perkin-Elmer Sciex API-III triple quadrupole mass spectrometer (Thornhill, Canada) fitted with an articulated, pneumatically assisted nebulization probe and an atmospheric pressure ionization source. The ion-spray needle voltage was operated at 4.5 kV, with the orifice at 80 V. Online LC/ESMS/MS data were acquired automatically using the RAD program in the Sciex software. The mass spectrometer, in product ion mode, was scanned repetitively from m/z 50 to 950 in 1.0 m/z steps at a rate of 5.8 s/scan. All precursor ions chosen for MS/MS were the $(M + 2H)^{2+}$ for each component of interest. Collision gas was a mixture of argon/nitrogen (85:15), with a collision gas thickness (CGT) of 7×10^{14} molecules/cm^2 (obtained using a value of ~700 for the CGT setting on the API-III). The potential difference between Q0 and Q2 was ~60 V, and this potential, when multiplied by the charge state of the precursor ion, is approximately equal to the collision energy.

EPR Spin-Trapping. A Bruker ER-100 electron paramagnetic resonance spectrometer and an in situ EPR electrochemical cell were used to verify the formation of hydroxyl radicals during electrolysis. The procedure for in situ generation of free radicals has been described previously.[9] The electrolyte solution contained the same acetate buffer plus a 10 mM concentration of the spin-trapping agent 5,5-dimethylpyrroline *N*-oxide (DMPO). The EPR spectra were recorded 5 min after a potential step to 1.5 V.

Chemicals. The GHRP (SK&F 110679) and the all-Phe analog SKF 105544 were obtained from SmithKline Beecham Pharmaceuticals. The spin-trapping agent 5,5-dimethylpyrroline *N*-oxide was obtained from Aldrich. The amino acid chemical kit was purchased from Sigma.

RESULTS AND DISCUSSION

Cyclic voltammetry of 5 mM GHRP in pH 5 acetate/NaCl solution indicates very little electrochemical activity before the onset of the oxidative solvent background around 1.2–1.3 V, as shown in Figure 1. Among the 20 naturally occurring amino acids, a generally broad wave was observed for cysteine (0.65 V), methionine (0.91 V), tryptophan (0.93 V), and tyrosine (1.00 V) in the same system. GHRP contains two tryptophan residues, yet no corresponding voltammetric wave was observed. Perhaps the embedded tryptophans were less accessible for electrode oxidation. It is not uncommon that the heterogeneous charge transfer to proteins and peptides is kinetically hindered.[10] We cannot determine the contribution from direct oxidation of the peptide at >1.2 V because of the large magnitude of the solvent background.

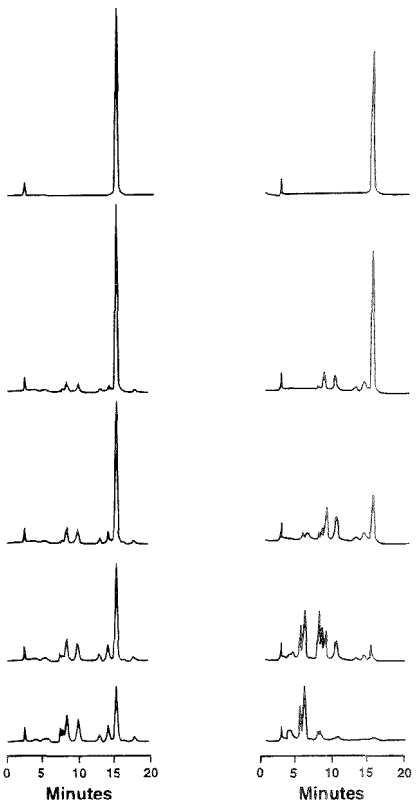

Figure 2. HPLC analyses of the electrolysis-induced degradation products of GHRP. The applied potential are 1.5 and 2.5 V for the left and right columns, respectively. The elapsed times after the initiation of electrolysis, from top to bottom, are 0, 30, 60, 90, and 120 min.

Controlled-potential electrolyses of GHRP were carried out at 1.0, 1.5, 2.0, and 2.5 V, separately. The disappearance of GHRP and the formation of products were monitored by HPLC with the UV detection set at 220 nm. There was no change in the peptide concentration for hours after the initiation of electrolysis at 1.0 V. However, at higher applied potentials, both time-dependent and potential-dependent degradation of the peptide was observed. Figure 2 shows the time-elapsed chromatographic sequences at the applied potentials of 1.5 and 2.5 V. The chromatograms reveal a clear pattern of product formation. The product distribution

(7) Huddleston, M. J.; Bean, M. F.; Carr, S. A. *Anal. Chem.* **1993**, *65*, 877–884.
(8) Carr, S. A.; Huddleston, M. J.; Bean, M. F. *Protein Sci.* **1993**, *2*, 183–196.
(9) Cheng, H.-Y.; Davis, L. L.; Bender, P. E.; Gleason, J. *J. Electrochem. Soc.* **1989**, *136*, 3679–3683.
(10) Armstrong, F. A.; Hill H. A. O.; Walton, N. J. *Acc. Chem. Res.* **1988**, *21*, 407–413.

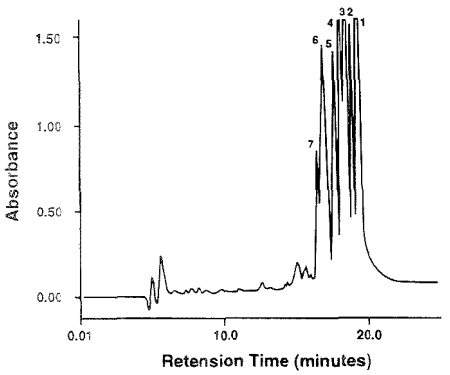

Figure 3. UV chromatogram for the corresponding LC/MS/MS analysis. The numbers identify the products listed in Table 1.

shifted toward shorter retention time at the higher applied potential and/or longer electrolysis times. Almost all degradation products have a shorter retention time than that for GHRP, implying that the products are more polar than the parent compound or are smaller fragments.

There was some concern that pH change might contribute to the degradation of the peptide. The solution pH dropped from pH 5.0 to 4.0 after 3 h of vigorous electrolysis at 2.5 V. We have determined by HPLC that GHRP is stable for hours in pH 2–5 aqueous solutions without any trace of degradation in the absence of an applied potential.

A reverse-phase HPLC procedure was adapted for the LC/MS/MS analysis of the products (see the Experimental Section). Following electrolysis of GHRP at 1.5 V for 1 h, HPLC separation of the ensuing mixture produced nearly identical chromatographic traces by UV or electrospray MS detection. The corresponding chromatogram for UV detection is shown in Figure 3. The major chromatographic peaks for MS/MS analysis are labeled 1–7 in reverse order of retention, with peak 1 being the unreacted peptide. The results of LC/MS/MS analysis are summarized in Table 1.

The MS/MS data provide important insights into the electrodegradation process. The peptide backbone of GHRP essentially remained intact, as significant fragmentation of the peptide did not occur even at the applied potential of 2.5 V. The chemical modifications were mainly on His^1, Trp^2, and Trp^4 which contain either an indole or an imidazole group, which is known to be susceptible to oxidative degradation. Phe is more resistant to electrooxidation, since MS/MS analysis indicated no chemical modifications on Phe. To verify this, additional electrolysis experiments were carried out on an experimental compound SKF 105544 (H-Phe-D-Phe-Ala-Phe-D-Phe-Lys-NH_2), which has all Phes instead of Trps and His. After 1 h of controlled-potential electrolysis at 1.5 V, HPLC analysis/UV detection showed that >90% of the starting material remained, with only a minor HPLC peak (about 5%) appearing at a longer retention time than that of the parent compound. This confirmed that Phe is, indeed, more resistant to electrolysis-induced oxidation.

It is difficult to judge the extent to which direct electrooxidation of the peptide has occurred because of the overwhelming electrolytic reaction from the breakdown of solvent. We did not find in the literature similar electrochemical studies on peptides

Table 1. MS/MS Analysis of Electrolysis Products of GHRP

peak[a]	M_r	
1	872.5 (parent)	product scan of m/z 437 $(M + 2H)^{2+}$
2	870.6 (parent − H_2)	product scan of m/z 436 $(M + 2H)^{2+}$ indicates His^1 or Trp^2 with (− H_2)
3	888.4 (parent + O)	product scan of m/z 445 $(M + 2H)^{2+}$ indicates Trp^2 with a (+ O)
4	888.4 (parent + O)	product scan of m/z 445 $(M + 2H)^{2+}$ indicates Trp^4 with a (+ O)
5	886.4 (parent − H_2 + O)[b]	product scan of m/z 444 $(M + 2H)^{2+}$ indicates Trp^4 with a (+ O) and either His^1 or Trp^2 with (− H_2)
6 and 7	904.6 (parent + O_2)	product scan of m/z 453 $(M + 2H)^{2+}$ indicates both Trp^2 and Trp^4 with a (+ O)

[a] Peak numbering refers to Figure 3. [b] $M_r(1)$. Possible $M_r(2)$ = 887.4 (C-terminal deamidation).

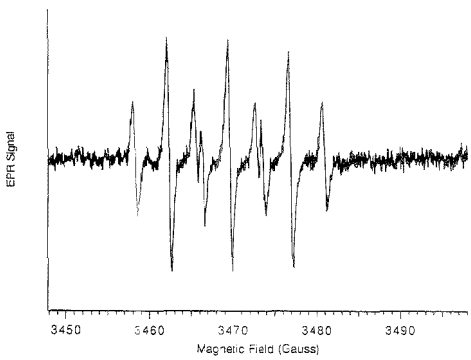

Figure 4. EPR spectrum resulting from spin-trapping of the radicals formed during electrolysis of the buffer/peptide solution. Conditions: E = 1.2 V for 5 min; microwave frequency, 9.74 GHz; modulation, 100 KHz; peak-to-peak modulation, 2 G, receiver gain, 10^6.

to provide us with a useful comparison. However, some structural clues might be found in studies of oxygen radical-mediated degradation of proteins.[11,12] A plausible explanation for such a product distribution pattern as revealed by the MS/MS data is that of a hydroxyl radical-mediated oxidative pathway. Hydroxyl radicals have been shown to form at a platinum anode during the electrolysis of water.[13] If hydroxyl radicals were, indeed, generated in our system during electrolysis, they would attack indole (Trp) or imidazole (His) in the peptide structure to form mono- (+ O) or disubstituted (+ O_2) hydroxylated products. This might be followed by the loss of H_2O to form the dehydrogenated (− H_2) products. Dehydrogenation might also occur via direct hydrogen abstraction by $OH^{\bullet}$, followed by the loss of an additional hydrogen to form a double bond. The (− H_2 + O) products might be the combination of a hydroxylation and a dehydrogenation on two different residues or the result of further $2e^-/2H^+$ electrooxidation of a hydroxylated product.

(11) Stadtman, E. R. *Science* **1992**, *257*, 1220–1224 and references cited therein.
(12) Davis, K. J. A.; Delsignore, M. E.; Lin, S. W. *J. Biol. Chem.* **1987**, *262*, 9902–9907.
(13) Kasai, P. H., Mcleod, D., Jr. *J. Phys. Chem.* **1978**, *82*, 619–621.

Finally, in situ electrogeneration and trapping of radical species in the EPR cavity was carried out using an electrolytic EPR flat cell fitted with a platinum gauze working electrode. In the presence of a 10 mM concentration of the spin-trapping agent DMPO, electrolysis of the peptide/acetate buffer solution at 1.2 V resulted in the characteristic EPR signal shown in Figure 4. The hyperfine splitting pattern is that of a 1:2:1 triplet (A_H = 4.0 G) on top of a 1:1:1 triplet (A_N = 7.3 G). The spectrum is identical to that reported for 5,5 dimethyl-2-pyrrolidone-1-oxyl (DMPOX).[14] One possible mechanism to account for the electrogeneration of DMPOX from the spin-trapping agent DMPO would involve the addition of the hydroxyl radical (from electrolysis of water) to DMPO, followed by $2e^-/2H^+$ oxidation of the intermediate to form the more stable DMPOX.

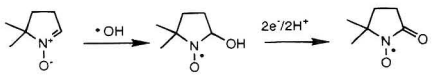

DMPO DMPOX

The spin-trapping result provides additional data to support the hypothesis that oxygen-derived radicals could be involved in the electrolysis-induced degradation of GHRP.

CONCLUSION

The electrolysis-induced degradation of GHRP is likely to be mediated by oxygen radical species which are formed at the water decomposition potential. Although substitutions or modifications of the more oxidation-prone amino acid residues could result in a more stable peptide for iontophoretic drug delivery, the modifications would alter completely its pharmacological profile. Two alternative strategies to minimize the electrolysis-induced oxidative degradation may be envisioned. One would be separate the drug substance from the electrode by some kind of physical barrier, such as a conductive, water-permeable membrane. A second strategy would be to scavenge the oxygen radicals by including an excess amount of pharmaceutical antioxidants in the formulation. Both strategies have been implemented and are under evaluation.

ACKNOWLEDGMENT

We thank Drs. Glynn Wilson and Michael Moore for helpful discussions.

Received for review June 16, 1995. Accepted August 24, 1995.[⊗]

AC950607B

(14) Rosen, G. M., Rauckman, E. J. *Mol. Pharmacol.* **1980**, *17*, 233–238.

[⊗] Abstract published in *Advance ACS Abstracts,* October 1, 1995.

Anal. Chem. 1995, *67*, 4057–4064

Rotating Microdisk Voltammetry

Xiaoping Gao and Henry S. White*

Department of Chemistry, University of Utah, Salt Lake City, Utah 84112

The influence of the supporting electrolyte concentration on the steady-state voltammetric behavior of a 12.5-μm-radius rotating Pt disk electrode (angular velocity, ω = 0–378 rad/s) has been investigated for several electrochemical reactions in acetonitrile solutions. The results demonstrate that the voltammetric response is a strong function of the ratio of the supporting electrolyte and redox concentrations (C_{elec}/C_{redox}) as well as the charge of the reactant (z). For the oxidation or reduction of monovalent and divalent species (e.g., [(trimethylammonio)methyl]-ferrocene (z = +1) and methylviologen (z = +2)), the observed voltammetric limiting currents are found to increase linearly with $\omega^{1/2}$, independent of C_{elec}/C_{redox}. Voltammetric currents corresponding to the oxidation or reduction of neutral reactants (e.g., ferrocene and nitrobenzene (z = 0)) show a more complex dependence on C_{elec}/C_{redox}. In solutions containing an appreciable quantity of supporting electrolyte, $C_{elec}/C_{redox} > 0.1$, mass transport limited currents are found to increase linearly with $\omega^{1/2}$. However, for $C_{elec}/C_{redox} < 0.1$, the voltammetric currents *decrease* with increasing ω. The unusual behavior observed for neutral species in low ionic strength solution is interpreted in terms of the rate of migration of charge-balancing electrolyte ions to the electrode surface, relative to the rate of removal of the same ions by forced convection. In low ionic strength solutions, electrolyte ions are removed by forced convection more rapidly than they are replenished by migration, resulting in a decrease in the electrical driving force for electron transfer.

One of several advantages of using microelectrodes in electrochemical investigations is the ability to perform quantitative measurements in low ionic strength solutions.[1,2] For instance, a steady-state, sigmoidal-shaped voltammetric curve can be readily obtained at a stationary 10-μm-radius Pt microdisk electrode in solutions in which the concentration of the supporting electrolyte is significantly lower than the concentration of redox-active species, i.e., $C_{elec}/C_{redox} \ll 1$. This experimental capability essentially eliminates the requisite use of solutions containing a large excess concentration of an inert supporting electrolyte and has provided new opportunities for fundamental investigations and applications of electrochemistry in low ionic strength solutions.[3]

The ability to perform voltammetric measurements in low ionic strength solutions using microelectrodes is a result of the transient fluxes of supporting electrolyte ions in response to the electric field created by electrogeneration of charged products. For example, consider the oxidation of 1 mM ferrocene (Fc) in an unstirred acetonitrile solution containing a small quantity (~10 μM) of tetrabutylammonium hexafluorophosphate ($TBA^+PF_6^-$) (conditions that correspond to $C_{elec}/C_{redox} \ll 1$). As initially described by Amatore et al.[1] and Oldham,[2] oxidation of Fc to the cation Fc^+ (ferrocenium) results in a depletion layer surrounding the microelectrode, in which the electrical charge associated with Fc^+ is balanced by a local increase and decrease in the concentrations of the electrolyte anion PF_6^- and cation TBA^+, respectively. For Fc oxidation, charge compensation primarily occurs by migration of PF_6^- from the bulk solution to the electrode, resulting in the concentration of PF_6^- within the depletion layer being significantly larger than that in the bulk of the solution. A consequence of this increase in ionic concentration is that the conductivity of the depletion layer is significantly higher relative to the bulk solution value, allowing voltammetric measurements to be made under conditions that are normally considered to be prohibitively resistive.

Although the near-surface electrolyte conductivity is greatly increased relative to the bulk conductivity, a significant ohmic potential loss occurs across the depletion layer during voltammetric experiment using microelectrodes. This potential loss can be expressed as the difference in the electrostatic potential between the bulk of the solution (ϕ^S) and the plane of electron transfer (ϕ^{PET}, where the PET corresponds roughly to the closest approach of the redox molecules to the surface[4]). Based on simple thermodynamic arguments, the quantity ($\phi^{PET} - \phi^S$) can be readily related to the applied electrode potential (E) and the equilibrium surface concentrations of the electrochemical reactant and product. Thus, for the general redox reaction, $O + e \rightleftharpoons R$,

$$(E - E^\circ) - (\phi^{PET} - \phi^S) = (RT/nF) \ln(C_O/C_R) \quad (1)$$

where C_O and C_R represent the concentrations of O and R at the PET. Equation 1 is simply the Nernst equation written to take into account the effect of the electrostatic potential at the PET on the chemical potentials of O and R. It has been theoretically[2] and experimentally[3c] demonstrated that ($\phi^{PET} - \phi^S$) increases at a rate of RT/nF (~59/n mV at room temperature) per decade decrease in C_{elec}/C_{redox}. For the steady-state voltammetric oxidation of Fc, the effect is manifested in a shift in the voltammetric half-wave potential ($E_{1/2}$) to more positive potentials in lower ionic strength solutions. In the total absence of a supporting electrolyte (including ionic impurities), the theoretical description of this

(1) Amatore, C.; Fosset, B.; Bartelt, J.; Deakin, M. R.; Wightman, M. R. *J. Electroanal. Chem.* **1988**, *256*, 255.
(2) Oldham, K. B. *Electroanal. Chem.* **1988**, *250*, 1.
(3) There is a large number of examples in the literature of electochemical measurements made in low ionic strength solutions using microelectrodes. Recent articles that provide listings of this literature include the following: (a) Ciszkowska, M.; Osteryoung, J. G. *Anal. Chem.* **1995**, *67*, 1125. (b) Kounaves, S. P.; Deng, W. *Anal. Chem.* **1993**, *65*, 375. (c) Pendley, B. D.; Abruna, H. D.; Norton, J. D.; Benson, W. E.; White, H. S. *Anal. Chem.* **1991**, *63*, 2766.
(4) Norton, J. D.; White, H. S.; Feldberg, S. W. *J. Phys. Chem.* **1990**, *94*, 6772.

0003-2700/95/0367-4057$9.00/0

problem indicates that the electrostatic potential drop within the depletion layer is sufficiently large to prevent the faradaic reaction from occurring at a significant rate. Thus, all electrochemical studies employing microelectrodes appear to require a finite concentration of supporting electrolyte.[5]

In this report, we describe steady-state voltammetric experiments in low ionic strength solutions using a *rotating* microdisk electrode (RMDE). As in experiments using a conventional-size rotating disk electrode (RDE), rotation of a microelectrode results in an increase in the convective diffusional flux of the electroactive component to the electrode surface. Although a rigorous theoretical description of diffusional–convective transport to a RMDE does not currently exist, the hydrodynamic velocity profiles for a rotating disk are independent of the electrode size (assuming the electrode is shrouded in a larger insulating plane), suggesting that voltammetric limiting currents, i_{lim}, for a RMDE will have a similar dependence on rotation rate as that predicted for a RDE. Indeed, Mallouk et al.[6] have previously investigated the response of a 12.5-μm-radius Pt RMDE in aqueous solutions containing 1 M KCl as supporting electrolyte. These authors reported that i_{lim} for $Fe(CN)_6^{4-}$ oxidation increased linearly with the square root of the angular velocity of the electrode, $\omega^{1/2}$, for large values of ω. An analogous linear relationship between i_{lim} and $\omega^{1/2}$ is predicted by the well-known Levich equation for a conventional-size RDE.[7]

In addition to increasing the convective–diffusional flux of the reactant to the electrode surface, fluid flow induced by rotation of the electrode also increases the rate at which product ions are removed from the surface. Thus, for a RMDE employed in low ionic strength solutions, it may be anticipated that the structure of the depletion layer that comprises the product, reactant, and charge-compensating electrolyte ions will be significantly altered relative to the depletion layer structure in an unstirred solution. The situation is schematically depicted in Figure 1, in which the oxidation of a neutral reactant (e.g., Fc) in a low ionic strength solution ($C_{elec}/C_{redox} \ll 1$) is considered again. As described above, in the absence of electrode rotation, the electrochemical generation of a charged product (Fc^+) causes the migration of charge-compensating anions (PF_6^-) toward the electrode surface, resulting in an increase in the concentration of ions (Fc^+ and PF_6^-) within the depletion layer. Fluid convection induced by rotation of the electrode (shown by arrows in Figure 1a) will tend to transport these ions away from the surface. Evidently, the steady-state concentration of the ions within the depletion layer will depend on the rate of migration of PF_6^- to the surface, relative to the rate of convective transport of PF_6^- away from the surface.

At sufficiently high rotation rates, the convective transport of electrogenerated and charge-compensating ions away from the electrode surface is anticipated to occur at a much larger rate than migration of PF_6^- from the bulk solution to the electrode. Consequently, the concentration of PF_6^- in the depletion layer is

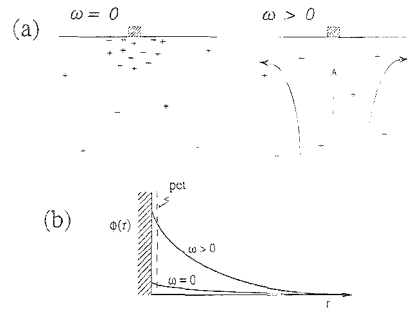

Figure 1. Schematic diagram of (a) the ion and (b) the potential distributions at a stationary ($\omega = 0$) and rotating ($\omega > 0$) microdisk electrode. ϕ^{PET} is the electrostatic potential (vs bulk solution) at the plane of electron transfer.

expected to decrease, asymptotically approaching the bulk solution PF_6^- concentration as the rotation rate is increased. However, as described above, the accumulation of charge-compensating ions within the depletion layer is necessary in order to observe a voltammetric response in low ionic strength solutions. Thus, the decrease in ion concentration resulting from electrode rotation will cause a decrease in the depletion layer conductivity, thereby increasing the potential drop ($\phi^{PET} - \phi^{S}$) across the depletion layer, Figure 1b. This physical scenario raises the interesting question of whether it is possible for an electrochemical reaction to occur at a RMDE in very low ionic strength solutions.

In the current work, we have examined the influence of rotation rate on the voltammetric response of a 12.5-μm-radius Pt RMDE for several electrochemical reactions. Our results indicate that fluid convection causes an increase in the potential drop ($\phi^{PET} - \phi^{S}$) in low ionic strength solutions, resulting, for some reactions, in a dramatic decrease in the voltammetric current as the rotation rate is increased. The voltammetric response of the RMDE, however, is strongly dependent on the electric charge of the reactant (z) as well as the ratio C_{elec}/C_{redox}. The results suggest that the use of microelectrode voltammetry in analytical applications involving flowing systems (e.g., detectors in chromatography[8]) or as models of chemistry occurring on dispersed semiconductor or metal particles[9] may be complicated by the complex dependence of the reaction driving force on fluid convection.

EXPERIMENTAL SECTION

Chemicals. Ferrocene (Fc) was sublimed twice under vacuum. [(Trimethylammonio)methyl]ferrocene ($TMAFc^+$) hexafluorophosphate and methylviologen (MV^{2+}) hexafluorophosphate were prepared by metathesis of the corresponding halide salt (TMAFcI and $MVCl_2$) with ammonium hexafluorophosphate. Acetonitrile (CH_3CN, HPLC grade) was used as received. Tetrabutylammonium hexafluorophosphate ($TBAPF_6$) was recrystallized from ethanol. Nitrobenzene (NB) was stored over molecular sieves.

Rotating Microdisk and Electrochemical Apparatus. The Pt microdisk electrode was constructed by sealing a 12.5-μm-radius

(5) Theoretical analysis (refs 2 and 3c) indicates that the half-wave potential, $E_{1/2}$, for the oxidation of neutral species shifts ~59 mV per 10-fold decrease in C_{elec}/C_{redox} (assuming a symmetrical 1:1 electrolyte). Thus, for $C_{elec}/C_{redox} = 0$, $E_{1/2}$ is infinitely large. However, ionic impurities in the solvent will limit $E_{1/2}$ to finite values. For instance, in the absence of an electrolyte, and using carefully purified solvent, $E_{1/2}$ for Fc oxidation in CH_3CN is shifted positive by 209 mV from $E^{o'}(Fc/Fc^+)$. This shift corresponds to an ionic impurity concentration of 80 nM (ref 3c).

(6) Mallouk, T. J.; Cammarata, V.; Crayston, J. A.; Wrighton, M. S. *J. Phys. Chem.* **1986**, *90*, 2150.

(7) Levich, V. *Physicochemical Hydrodynamics*; Prentice-Hall: Englewood Cliffs, NJ, 1962.

(8) (a) Sloss, E.; Ewing, A. G. *Anal. Chem.* **1993**, *65*, 577. (b) O'Shea, T.; Lunte, S. M. *Anal. Chem.* **1993**, *65*, 247. (c) Lu, W.; Cassidy, R. M. *Anal. Chem.* **1993**, *65*, 1649.

(9) (a) McMurray, H. N. *J. Phys. Chem.* **1994**, *98*, 9861. (b) Fleischmann, M.; Ghoroghchian, J.; Rolison, D.; Pons, S. *J. Phys. Chem.* **1986**, *90*, 6392. (c) Rolison, D. *Chem. Rev.* **1990**, *90*, 867.

Pt wire in an 8-mm-diameter glass tube. The position of the disk relative to the axis of rotation in RMDE experiments is critical in determining the fluid velocity profiles effecting mass-transfer rates. In these experiments, we have attempted to center the disk at the center of the glass tube (corresponding approximately to the axis of rotation). Analysis of the voltammetric response (vide infra) suggests that the disk is located ~250 μm from the rotation axis. The electrode was polished using 0.02-μm Al_2O_3, rinsed with water, and sonicated in water for 4 min to remove polishing debris. The radius of the microelectrode was measured to be r_0 = 14.9 μm, as computed on the basis of the voltammetric limiting current for Fc oxidation in acetonitrile and the literature value for the diffusion coefficient of Fc (2.4×10^{-5} cm^2/s).[10]

A commercial rotating disk apparatus (Fine Instrument Co., Model No. PIR) was used to rotate the microelectrode at angular velocities between 0 and 378 rad/s. A standard three-electrode cell (~30 mL) containing a Ag/AgO_x reference electrode and a Pt wire counter electrode was employed throughout. Voltammograms were recorded using a BAS CV 27 potentiostat. The current was low-pass filtered to reduce noise originating at the electrical contact made to the shaft of the rotating electrode. All voltammetric data were recorded at a scan rate of 10 mV/s.

RESULTS AND DISCUSSION

To our knowledge, no exact theoretical treatment exists that describes convective–diffusive transport to a RMDE. In principle, a description of the RMDE response can be obtained from the simultaneous solution of the differential equations governing momentum and mass transport to a rotating microdisk. Smyrl and Newman considered a similar problem involving radial diffusion at the edges of a conventional-size RDE.[11] They obtained a relationship describing the dependence of the voltammetric current on rotation rate for situations in which the depletion layer thickness is considerably smaller than the electrode dimension. In this limit, radial diffusion at the edge of the RDE accounts for a small percentage (~1%) of the total flux. However, as will be shown below, radial diffusion represents a significant fraction of the total flux to a microdisk, even at relatively large rotation rates.

The electrochemical responses of a stationary microdisk (area $\approx 2 \times 10^{-6}$ cm^2) and a rotating disk of conventional size (area $\approx$ 0.5 cm^2) have relatively simple and well-known descriptions. It is useful to consider these two cases in some detail in order to gain insight into the magnitude of the effects that fluid convection might have on the behavior of a RMDE.

In the presence of an excess concentration of a supporting electrolyte ($C_{elec}/C_{redox} \gg 1$), molecular diffusion of the reactant from the bulk solution to the surface of a stationary microdisk electrode produces a true steady-state limiting current density (i_{lim}/A) that can be expressed as[12]

$$i_{lim}/A = 4nFDC^*/\pi r_0 \qquad (2)$$

where A is the electrode area, D is the diffusion coefficient, C^* is the concentration of the reactant in the bulk of the solution, and r_0 is the electrode radius. For a microdisk electrode, the diffusional flux converges toward the surface in a quasi-radial fashion. Equation 2 demonstrates clearly that the current density at a stationary microdisk increases as the electrode size is decreased.

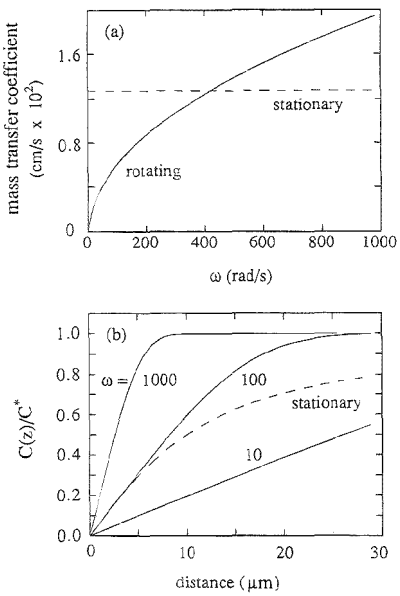

Figure 2. (a) Mass transfer coefficients for stationary and rotating disk electrodes. (b) Dimensionless reactant concentration profiles for stationary and rotating disks. The mass transfer coefficient and concentration profile for the stationary disk are independent of ω and are computed assuming a 10-μm-radius disk. The concentration profile for the stationary disk is computed along the direction normal to the electrode surface directly above the center of the disk, eq 5.

The analogous expression for a large rotating disk electrode is given by the Levich equation,

$$i_{lim}/A = 0.620nFD^{2/3}\,\omega^{1/2}\nu^{-1/6}C^* \qquad (3)$$

where ω is the angular velocity (rad/s) and ν is the kinematic viscosity. Equation 3 is derived on the assumption of an infinitely large planar electrode, without interference from radial diffusion at the electrode edges. Equation 3 indicates that the current density is independent of the electrode size.

The dependencies of i_{lim}/A on electrode size (eq 2) and angular velocity (eq 3) for stationary and rotating disks, respectively, suggest that the magnitude of current enhancement resulting from rotation of a microdisk will depend strongly on r_0 as well as on ω. For instance, i_{lim}/A resulting from radial diffusion (eq 2) will dominate the total flux to a microdisk if r_0 is sufficiently small. In this situation, rotation of a microelectrode is not expected to have a significant effect on the current. Conversely, for a sufficiently large value of r_0, radial diffusion (eq 2) will be negligibly small, and the convective–diffusive flux described by eq 3 will dominate the response of the electrode, resulting in a linear dependence of current on $\omega^{1/2}$.

Mass-transfer coefficients (m) for a 10-μm-radius stationary disk and a RDE are plotted in Figure 2a. The magnitude of ω at which

(10) Kuwana, T.; Bublitz, D. E.; Hoh, D. E. *J. Am. Chem. Soc.* **1960**, *82*, 5811.
(11) Smyrl, W. H.; Newman, J. *J. Electrochem. Soc.* **1971**, *118*, 1079.
(12) Saito, Y. *Rev. Polarogr.* **1968**, *15*, 177.

comparable fluxes are predicted to result from radial diffusion (at a stationary disk) and linear convection–diffusion (at a rotated disk) can be estimated from this plot. Values of m are determined from the usual definition,[13]

$$i_{lim}/A = nFmC^* \quad (4)$$

yielding $m_{stationary} = 4D/\pi r_0$ and $m_{RDE} = 0.620D^{2/3}\omega^{1/2}\nu^{-1/6}$ (by inspection of eqs 2–4). The results plotted in Figure 2a suggest that i_{lim} at a stationary 10-μm-radius electrode is equivalent to that of a RDE (of equivalent size) rotated at $\omega = 400$ rad/s. Furthermore, since the convective–diffusive flux increases very rapidly with increasing ω, m_{RDE} is comparable to $m_{stationary}$ for all angular velocities within the normal working range employed in RDE experiments (10–1000 rad/s).

The effect of rotation on the concentration profiles of the redox species and electrolyte ions at a microelectrode will be considered in more detail in a later section. Here, we briefly examine the approximate thicknesses of the depletion layer at stationary and rotating microdisks. Figure 2b shows normalized reactant concentration profiles, $C(z)/C^*$, normal to the electrode surface for a stationary 10-μm radius and for a RDE at different values of ω. For the RDE, the concentration profile within the depletion layer is uniform across the electrode surface. For a stationary disk, the convergent flux of reactant dictates that the reactant concentration increases as one moves in a radial direction away from the center of the disk into the solution. Thus, for the purpose of comparing the depletion layer thicknesses, the profile of $C(z)/C^*$ for the stationary disk is computed normal to the surface at the center of the electrode. $C(z)/C^*$ for the stationary microdisk is given by[12]

$$\frac{C(z)}{C^*} = 1 - \tan^{-1}\frac{2^{1/2}r_0}{[(z^2 - r_0^2) + ((z^2 - r_0^2)^2 + 4z^2r_0^2)^{1/2}]^{1/2}} \quad (5)$$

and the corresponding equation for a RDE is[13]

$$\frac{C(z)}{C^*} = \frac{(3B)^{-1/3}}{0.8934}\int_0^z \exp\left(\frac{-z^3}{3B}\right) dz \quad (6)$$

where $B = D\nu^{1/2}/0.51\omega^{3/2}$. Inspection of Figure 2b shows that the thickness of the depletion layer surrounding a microdisk is expected to be a relatively strong function of ω. However, the depletion layer thicknesses for the stationary 10-μm-radius electrode and a RDE are comparable for all reasonable values of ω. The similar magnitudes of the depletion layer thicknesses suggest that rotation will have a significant effect on the concentration profiles of the various species that constitute the depletion layer. For $\omega \gg 100$ rad/s, convection will reduce the thickness of the depletion layer to a value significantly smaller that predicted for a stationary disk. In this limit, the concentration profiles are approximated by the theoretical description of convective–diffusional transport to a conventional size RDE. On the other hand, at low rotation rates, e.g., $\omega \ll 100$ rad/s, the depletion layer for the RDE is predicted to be much larger than that of the stationary microdisk, as shown in Figure 2b. In this limit, the concentration profiles are approximated by the theoretical description of diffusional transport to a stationary disk. At intermediate rotation rates, convective–diffusional transport and radial molecular diffusion will make approximately equal contributions to the transport of the reactant.

The qualitative description presented above allows several predictions to be made about the behavior of a RMDE. First, rotation of a 10-μm-radius electrode over a reasonable range of ω should result in a significant enhancement of i_{lim}. This is verified by the experimental data presented below. Second, from the definition of the mass transport coefficient for a stationary disk ($m_{stationary} = 4D/\pi r_0$), it is clear that the effect of rotation will be less influential as the electrode radius decreases. For instance, for $r_0 = 0.1$ μm, $m_{stationary} = 1.3$ cm/s, which is ~100 times larger than m_{RDE} for all reasonable values of ω (see Figure 2a). For such a small electrode, rotation should have an insignificant effect on the voltammetric currents.

We note that the above discussion is limited to situations where the microdisk is centered directly on the axis of rotation. As will be discussed below, m_{RDE} can be significantly larger when the electrode is not centered exactly at the rotation axis, since the fluid velocity tangential to the surface of a rotating disk is dependent on the radial position (vide infra). The above discussion is also limited to situations where an excess amount of an electrolyte is present in the bulk of the solution ($C_{elec}/C_{redox} \gg 1$), such that migration of ions is negligibly small compared to diffusive and convective transport. As shown below, a rather dramatic decrease in i_{lim} is observed at a RMDE for some electrochemical reactions when this condition is not fulfilled.

In a related problem, Tait et al. have investigated the effect of fluid convection on i_{lim} at microdisks inside a narrow channel.[14] Finite difference simulations were used to compute the convective–diffusive flux assuming a parabolic flow distribution within the channel. These studies were limited to solutions containing an excess concentration of supporting electrolyte ($C_{elec}/C_{redox} \gg 1$).

RMDE Voltammetry of Charged Redox-Active Molecules. The voltammetric response of the 12.5-μm-radius Pt RMDE was initially examined as a function of the supporting electrolyte concentration in CH_3CN solutions containing either 1 mM $TMAFc^+$ or MV^{2+} as the redox-active species. As shown in Figure 3, sigmoidal-shaped voltammograms were obtained both in the presence and in the absence of a supporting electrolyte (10 mM $TBAPF_6$) for angular velocities, ω, between 0 and 378 rad/s. We observed that rotation of the microelectrode significantly enhances the mass transport limiting currents corresponding to the $1 - e^-$ oxidation of $TMAFc^+$ and the $1 - e^-$ reduction of MV^{2+}, in agreement with the behavior of the RMDE reported by Mallouk et al.[6] However, the absolute value of the voltammetric current (at constant ω) is dependent on the concentration of the supporting electrolyte. For instance, the limiting current measured for MV^{2+} reduction is ~25% larger in the absence of a supporting electrolyte than in solutions containing 10 mM $TBAPF_6$ (Figure 3b). To account for this difference, we recall the analysis by Amatore et al.[1] of coupled migrational and diffusional fluxes to a stationary microelectrode. In the presence of an excess support-

(13) Bard, A. J.; Faulkner, L. R. *Electrochemical Methods*; Wiley: New York, 1980.

(14) Tait, R. J.; Bury, P. C.; Finnin, B. C.; Reed, B. L.; Bond, A. M.: *Electroanal. Chem.* **1993**, *356*, 25.

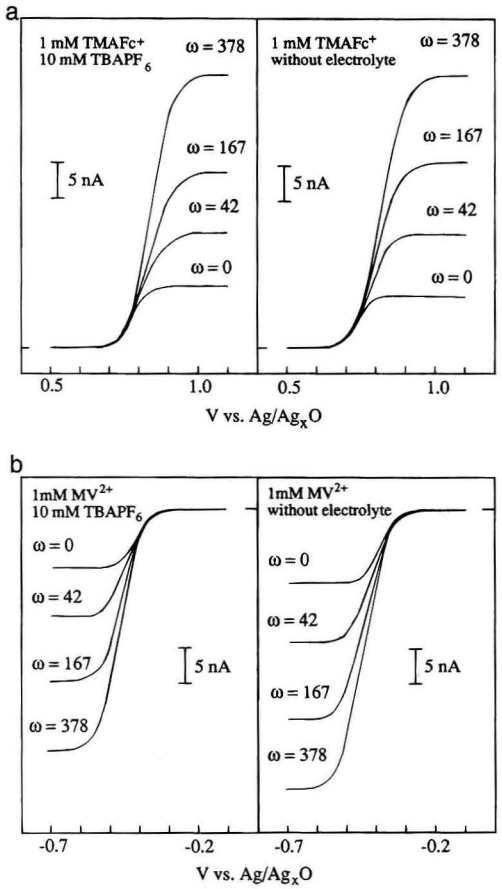

Figure 3. Voltammetric response of a Pt RMDE (radius ≈ 14.9 μm) for (a) the 1 − e⁻ oxidation of 1 mM $TMAFc^+$ and (b) the 1 − e⁻ reduction of 1 mM MV^{2+} in CH_3CN. Voltammetric curves were obtained in the presence and in the absence of supporting electrolyte (10 mM $TBAPF_6$), as indicated in the figures. Scan rate, 10 mV/s.

ing electrolyte ($C_{elec}/C_{redox} \gg 1$), the electric field in the solution is negligibly small, and the steady-state voltammetric current is expected to be controlled solely by diffusion of the reactant to the surface. For this condition, the current at a stationary electrode is given by eq 2, which, for convenience, can be written as

$$i_{lim}^{xs} = 4nFDr_oC^* \quad (7)$$

In solutions in which the concentration of supporting electrolyte is less than that of the redox species ($C_{elec}/C_{redox} \ll 1$), significant electric fields exist within the depletion layer, and transport of the charged species MV^{2+} and $TMAFc^+$ to the electrode surface is controlled by both diffusion and migration. For a spherical microelectrode, Amatore et al. have shown that for such situations, i_{lim} is given by[1]

$$i_{lim}/i_{lim}^{xs} = 1 \pm z\{1 + \beta[\ln(1 - \beta^{-1})]\} \quad (8)$$

where $\beta = (1 + |z|)(1 - z/n)$. In eq 8, n is positive for reductions and negative for oxidations. The sign (±) is taken as positive when $n < z$ and negative when $n > z$.

For MV^{2+} reduction, $z = 2$ and $n = 1$, yielding a theoretical $i_{lim}/i_{lim}^{xs} = 1.27$. The corresponding experimental value is 1.25 (computed from the ratio of the limiting currents for $\omega = 0$, Figure 3b). Similarly, $z = 1$ and $n = -1$ for $TMAFc^+$ oxidation, yielding $i_{lim}/i_{lim}^{xs} = 0.85$. The corresponding experimental value is 0.85. It is apparent that eq 8 yields excellent predictions of the influence of migration at a stationary microdisk. Unfortunately, no analogous analytical expression exists that allows computation of the current at a RMDE in the absence of an electrolyte (conditions where the flux results from combined convection, diffusion, and migration). Experimentally, we find that the ratio of limiting currents (i_{lim}/i_{lim}^{xs}) for MV^{2+} reduction remains nearly constant over the range of ω accessible in this study (decreasing slightly from 1.25 at $\omega = 0$ to 1.22 at $\omega = 378$ rad/s), although there is no apparent a priori reason for this ratio to remain constant. On the other hand, i_{lim}/i_{lim}^{xs} for $TMAFc^+$ oxidation increases from 0.85 at $\omega = 0$ to 1.04 at $\omega = 378$ rad/s.

Figure 4 shows plots of i_{lim} on the square root of the angular velocity ($\omega^{1/2}$) for MV^{2+} reduction, in the presence and in the absence of 10 mM $TBAPF_6$. The nonlinear dependence of i_{lim} on $\omega^{1/2}$ at low ω is essentially identical to that reported by Mallouk et al.[6] for $Fe(CN)_6^{4-}$ oxidation in a 1 M KCl solution using a 12.5-μm-radius Pt RMDE. At $\omega^{1/2} > 5$ $(rad/s)^{1/2}$, the limiting current increases linearly with $\omega^{1/2}$, indicating that convective diffusion is the predominant mode of transport of the reactant to the surface. However, extrapolation of this linear region to $\omega = 0$ yields a nonzero intercept, demonstrating that radial diffusion also contributes significantly to the flux over the investigated range of ω. The fact that the extrapolated intercept is smaller than the measured value of i_{lim} at $\omega = 0$ suggests that the contribution of the radial diffusion is smaller when the electrode is rotating.

The slope of the linear region of the plot of i_{lim} vs $\omega^{1/2}$ (1.54 $nA/(rad/s)^{1/2}$) is ~2.7 times larger than that predicted by the Levich equation. We believe that this is due to the microdisk being positioned slightly off the center axis of rotation (Figure 5). For such a geometry, Chin and Litt[15] and Mohr and Newman[16] have demonstrated (ignoring the contribution of radial diffusion) that the current at a RDE will be given by

$$i_{lim}/A = 0.64nFD^{2/3}\omega^{1/2}\nu^{-1/6}C^*\epsilon^{1/3} \quad (9)$$

where ϵ (the so-called eccentricity factor) is defined as the ratio of the distance between the axis of rotation and the center of the disk (R) relative to the radius of the microdisk (r_o): $\epsilon = R/r_o$. Equation 9, which is applicable in the limit $R \gg r_o$, indicates that the voltammetric current increases as the cube root of the displacement of the electrode from the axis of rotation. Physically, this results from the dependence of the tangential fluid velocity on the radial distance r from the center of the electrode. For a rotating disk, both the angular (v_ϕ) and radial (v_r) fluid velocities are proportional to the position r. Thus, the rate at which the

(15) Chin, D.-T.; Litt, M. *J. Electrochem. Soc.* **1973**, *120*, 1338.
(16) Mohr, C. M.; Newman, J. *J. Electrochem. Soc.* **1975**, *122*, 928.

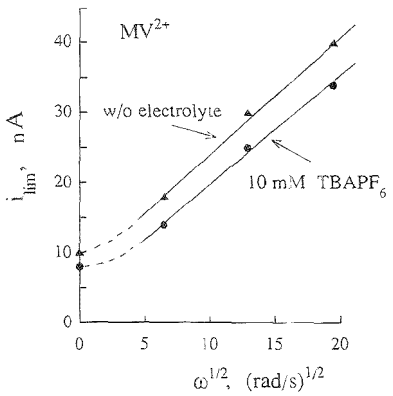

Figure 4. Dependence of limiting current, i_{lim}, on angular velocity for the reduction of MV^{2+} in the absence and in the presence of a supporting electrolyte.

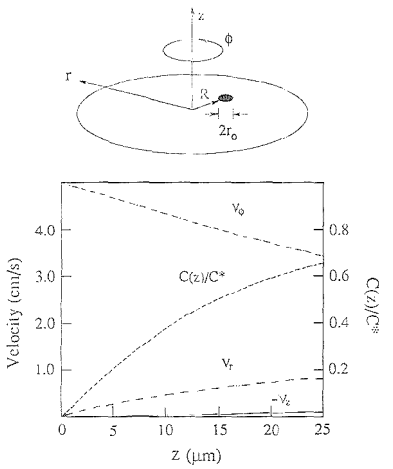

Figure 5. (Top) Schematic diagram of a rotating microdisk offset from the axis of rotation by a distance R. (Bottom) Velocity profiles normal to the surface of an offset RMDE (R = 250 μm). $C(z)/C^*$ is the dimensionless concentration reactant profile for a 14.9-μm-radius stationary disk, computed assuming that transport occurs only by molecular diffusion, eq 5.

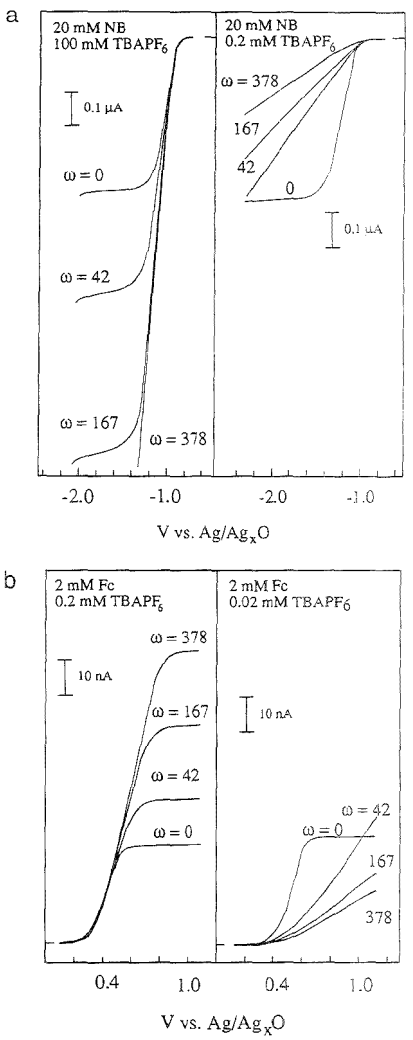

Figure 6. Voltammetric response of a Pt RMDE (radius ≈ 14.9 μm) for (a) the 1 − e⁻ reduction of 20 mM NB and (b) the 1 − e⁻ oxidation of 2 mM Fc in CH_3CN as a function of the supporting electrolyte ($TBAPF_6$) concentration (indicated on the figure). Scan rate, 10 mV/s.

reactant is transported to the electrode surface (by tangential convective flow) will increase if the electrode is located off of the rotation axis (i.e., $R \neq 0$).

From the data in Figure 4, and using $D = 1.35 \times 10^{-5}$ cm²/s for MV^{2+}, we compute $\epsilon = 20.4$, corresponding to $R \approx 300$ μm. Similar values R were determined from voltammetric measurements using different redox systems; for instance, for Fc oxidation, R was measured to be 210 μm. Given the cubic dependence of R on measured values of i_{lim}, the agreement between these values appears quite reasonable.

RMDE Voltammetry of Neutral Redox-Active Molecules. In the preceding section, we have shown that the voltammetric behavior of a RMDE in solutions containing charged redox species (z = +1 or +2) is adequately described (albeit qualitatively) by extension of existing theories of mass transport at stationary and rotating disks. We now consider the oxidation and reduction of neutral (z = 0) reactants at a RMDE. Figure 6 shows the voltammetric responses of the RMDE corresponding to the 1 − e⁻ reduction of nitrobenzene (NB) and the 1 − e⁻ oxidation of Fc. We observe that, in the presence of an appreciable quantity of electrolyte, the voltammetric behavior for these two redox systems is qualitatively similar to that previously discussed for MV^{2+} and $TMAFc^+$. For instance, Figure 6a shows that i_{lim} for the reduction of 20 mM NB increases with increasing rotation rate in CH_3CN solutions containing 100 mM $TBAPF_6$. A similar behavior is observed for oxidation of 2 mM Fc in the presence of 0.2 mM $TBAPF_6$. In each case, a plot of i_{lim} vs $\omega^{1/2}$ exhibits linear

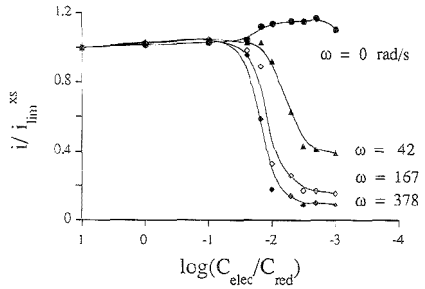

Figure 7. Plot of normalized steady-state current i/i_{lim}^{xs} as a function of $\log(C_{elec}/C_{redox})$ for the oxidation of 2 mM ferrocene in acetonitrile. i_{lim}^{xs} is the limiting current measured at $\log(C_{elec}/C_{redox}) = 1$ for each rotation rate, ω. The four data sets correspond to ω = 0, 42, 167, and 378 rad/s. The supporting electrolyte is $TBAPF_6$.

behavior at high angular velocities. The slope of the linear region of the i_{lim} vs $\omega^{1/2}$ curves yields ϵ and R values that are in reasonable agreement with the corresponding values determined for the MV^{2+} system.

When the ratio C_{elec}/C_{redox} is decreased below a critical value, the voltammetric current at the RMDE is observed to decrease with increasing rotation rate. Figure 6b, for instance, shows that a 10-fold decrease in the electrolyte concentration (from 0.2 to 0.02 mM $TBAPF_6$) results in a dramatic change in the voltammetric response for Fc oxidation. The $i-V$ curves no longer have a sigmoidal shape but are drawn out, suggestive of either a kinetic or an ohmic potential limitation that is dependent upon both the angular velocity and C_{elec}/C_{redox}.

The results of a number of voltammetric experiments for Fc oxidation are summarized in Figure 7 as plots of i/i_{lim}^{xs} vs C_{elec}/C_{redox} for different angular velocities. Here, i is the voltammetric current measured at 1.05 V vs Ag_2O (Note: i is used rather than i_{lim}, since a true limiting current is not obtained at small C_{elec}/C_{redox}.). In these experiments, the concentration of Fc was held constant at 2 mM, and the concentration of $TBAPF_6$ was varied from 2 μM to 20 mM. i_{lim}^{xs} was taken as the value of the limiting current at $C_{elec}/C_{redox} = 10$ for computing i/i_{lim}^{xs} at each specific rotation rate.

The data in Figure 7 clearly demonstrate that there is a precipitous decrease in current for all non-zero values of ω when $C_{elec}/C_{redox} < 0.1$. Voltammetric data were also obtained for the reduction of NB in CH_3CN solution, in which C_{elec}/C_{redox} was held constant at 0.01, and the concentration of NB was varied from 20 mM to 1 M. The dependence of i/i_{lim}^{xs} on ω for these data (not shown) was essentially identical to that shown in Figure 7 and, more importantly, was found to be independent of the absolute concentration of NB. Based on these data sets, we conclude that the unusual decrease in voltammetric currents is only a function of C_{elec}/C_{redox} and ω, and is not a function of the absolute concentrations of either C_{elec} or C_{redox}.

Figure 7 also shows that there is a small increase (~10%) in the limiting current at a stationary disk ($\omega = 0$) as the electrolyte concentration is decreased. This nonideal behavior is probably due to a slight decrease in the solution viscosity as the ionic strength is lowered.

In considering the above behavior, we note that the heterogeneous rate constants for the oxidation of Fc and the reduction of NB in CH_3CN are sufficiently large that the effects of slow electron transfer should be negligible in slow-scan RMDE experiments. Thus, according to the arguments presented in the introduction, the decrease in voltammmetric currents upon rotation of the electrode must result from an increase in the potential drop between the microdisk surface and the bulk solution ($\phi^{EC'} - \phi^{S}$). This dependence results from the charge-compensating ions being convected away from the rotating electrode surface. From Figure 7, it is apparent that even relatively low rotation rates result in rapid convective transport of charge-compensating ions away from the electrode surface.

The effect of electrode rotation is examined in more detail by considering the individual components of the fluid velocity (v_ϕ, v_r, and v_z, where the cylindrical coordinate system is defined in Figure 5). The magnitudes of these velocities are computed from the following approximate expressions derived by Levich:[7]

$$v_\phi \approx r\omega[1 + b\xi + (^1/_3)a\xi^3]$$

$$v_r \approx r\omega[a\xi - (^1/_2)\xi^2 - (^1/_3)b\xi^3] \qquad (10)$$

$$v_z \approx (\omega\nu)^{1/2}[-a\xi + (^1/_3)\xi^3]$$

where ξ is defined as $z(\omega/\nu)^{1/2}$, and the constants a and b are equal to 0.510 and −0.616, respectively. Figure 5b shows v_ϕ, v_r, and v_z computed using the following parameters (corresponding to the experimental parameters of the current work): ω = 200 rad/s, ν = 0.00452 cm^2/s, and r ($\equiv R$) ~ 250 μm. In examining these curves, a key point is to recall is that the fluid flow affects the driving force for electron transfer via the disruption of the depletion layer structure; fluid flow beyond the depletion layer region should have very little influence on depletion layer structure. Thus, in order to define an appropriate length scale for considering the effects of convection, the dimensionless concentration profile for a neutral reactant at a stationary microdisk is also plotted in Figure 5b (using the experimentally determined value of r_0 = 14.9 μm and eq 5).

Inspection of the plots of v_ϕ, v_r, and v_z suggests that the significant velocity components are those associated with flow tangential to the electrode surface (i.e., v_r and v_ϕ). This follows from v_z being negligibly small within the depletion layer (i.e., for z < 25 μm) in comparison to either v_r or v_ϕ. Thus, the fluid velocity at any point within the depletion layer can be approximated by $v = (v_r^2 + v_\phi^2)^{1/2}$. The net relative fluid velocity, v_{net}, which is defined here as the difference between the fluid velocity at some distance z from the electrode surface and the velocity of the electrode, is the critical parameter in determining the rate at which ions are removed from the depletion layer. This parameter is given by $v_{net} = (v_r^2 + (v_\phi - \omega R)^2)^{1/2}$. For z = 10 μm, we compute $v_{net} \approx$ 0.9 cm/s. Thus, assuming that the potential drop in the depletion layer is altered whenever charge-balancing ions are moved ~1 radius from the electrode surface, the time scale on which rotation alters the depletion layer structure can be estimated as $|r_0/v_{net}|$. For r_0 = 14.9 μm, t_{expt} is equal to ~2 ms. For larger values of z, the corresponding time scale to alter the depletion layer decreases; however, as noted above, any effect of convection on the concentration profiles at distances far from the surface is expected to have an inconsequential effect on the potential and ion distributions near the surface. On the other hand, v_{net} decreases rapidly at very small values of z (< 1 μm).

Thus, although our choice of $z = 10\ \mu m$ in computing t_{expt} is rather arbitrary, any value of z within the depletion layer that is not too small or too large will yield a comparable value of t_{expt}.

When the time required for migration of electrolyte ions from the bulk of the solution to the electrode is longer than t_{expt}, the ion profiles that define the depletion layer structure (which is necessary to perform voltammetry in low ionic strength solutions) can no longer be established. Consequently, the solution resistivity and $(\phi^{PET} - \phi^{S})$ become sufficiently large that the reaction will not be driven at the normal convection–diffusion-controlled rate.

Recent computer simulations[17] of the chronoamperometric response of microspherical electrodes indicate the time required for the potential and ion distribution to be established following a potential step is on the order of $\sim 10^{-1}$ s for the oxidation of a neutral redox species at a 10-μm-radius electrode when $C_{elec}/C_{redox} = 10^{-2}$. The corresponding value for the oxidation of a charged reactant ($z = +1$) is 10^{-5} s. Since the value of t_{expt} computed for the RMDE (2 ms) is intermediate between these cases, it follows that a highly conductive depletion layer can be established at a RMDE in low ionic strength solutions for the reduction (or oxidation) of a charged species, but not for a neutral species.

CONCLUSION

The voltammetric response of a Pt RMDE is dependent on the charge of the electroactive reactant and the ratio C_{elec}/C_{redox}. For charged species, $z \neq 0$, the observed dependence of i_{lim} on ω and C_{elec}/C_{redox} appears to be interpretable in terms of existing mathematical treatments of fluid convection and ion migration, albeit only in a qualitative fashion. A rigorous description of the behavior of a rotating microelectrode that takes into account the comparable magnitude of radial diffusion and convective diffusion, as well as the eccentricity factor, is not yet established.

RDME voltammetric currents corresponding to the oxidation or reduction of a neutral redox species have a much more complex dependence on C_{elec}/C_{redox}. In low ionic strength solutions, the voltammetric currents have been shown to decrease with increasing ω whenever $C_{elec}/C_{redox} \ll 0.01$. This behavior results from electrolyte ions being removed from the depletion layer by forced convection more rapidly than they are replenished by migration. We have qualitatively shown that this competition of transport paths results in an increase in the solution resistance and, thus, a decrease in the driving force for electron transfer.

The complex nature of RMDE behavior on the parameters z, C_{elec}/C_{redox}, ϵ, and ω can be expected to apply to other electrochemical systems involving forced convection. For instance, there has been recent interest in the use of microelectrodes as on-line detectors in chromatography, since the use of a microelectrode eliminates the need of a large excess concentration of supporting electrolyte.[8] Such an application may involve flow of the carrier fluid past a small microelectrode, which, as shown here for a RMDE, can alter the potential distribution near the electrode surface. The degree to which the potential distribution is altered will be determined largely by the analyte charge (z), thus making it difficult to obtain a useful relationship between the detector signal and analyte concentration. The present results are also relevant to the use of microelectrodes as models for electrochemical reactions that occur on small metal particles dispersed in a solution (by rapid stirring or gas sparging).[9] In these situations, it seems altogether reasonable that increased convection may have a significant and adverse effect on reaction rates, in clear opposition to conventional wisdom.

ACKNOWLEDGMENT

The assistance of Keith Stevenson in preliminary RMDE experiments is greatly appreciated. H.S.W. also acknowledges stimulating discussions with Prof. William H. Smyrl (University of Minnesota) on the subject of radial diffusion at rotating disks. This work was supported by the Office of Naval Research.

Received for review May 1, 1995. Accepted August 2, 1995.[⊗]

AC9504124

(17) Smith, C. P.; White, H. S., 1994, unpublished results.

[⊗] Abstract published in *Advance ACS Abstracts*, September 15, 1995.

Anal. Chem. 1995, *67*, 4065–4070

Trace Measurements of RNA by Potentiometric Stripping Analysis at Carbon Paste Electrodes

Joseph Wang,* Xiaohua Cai, Jianyan Wang, and Colleen Jonsson

Department of Chemistry and Biochemistry, New Mexico State University, Las Cruces, New Mexico 88003

Emil Paleček

Institute of Biophysics, Academy of Sciences of the Czech Republic, 612 65 Brno, Czech Republic

Remarkably low levels of ribonucleic acid (RNA) can be measured by coupling its adsorptive accumulation onto carbon paste electrodes with constant current potentiometric stripping analysis (PSA). The computerized PSA operation effectively addresses the high background response inherent to carbon surfaces, while the anodic pretreatment of the electrode greatly enhances the preconcentration efficiency. The detection limit for tRNA (10 pg, 4×10^{-16} mol) is substantially lower than that reported recently (Palaček, E.; Fojta, M. *Anal. Chem.* 1994, *66*, 1566) for analogous voltammetric measurements at mercury surfaces. Variables influencing the accumulation and stripping processes of RNA are explored and optimized. Results are reported for measurements of RNA in the presence of excess dsDNA, for PSA of synthetic polyribonucleotides, for hybridization of complementary strands of synthetic polyribonucleotides, for enzymatic hydrolysis of RNA, and for flow injection operation. Such solid electrode experiments obviate the need for mercury electrodes or a deoxygenation step and open the door for modern RNA detectors and probes.

Ribonucleic acid (RNA) is a biopolymeric constituent of the cell, which can be translated into protein sequences (in the case of mRNA), function as structural molecules (in the case of tRNA and rRNA), or serve as a biocatalyst during gene expression. Consequently, there is considerable interest in determining low levels of different kinds of RNA and in measuring RNA in the presence of DNA. Absorption (UV) spectroscopy is commonly used for measuring RNA and DNA in nucleic acid samples.[1] Yet, the optical procedure cannot differentiate between RNA and DNA, and its detection limit is ~0.1 mg/L. Separation techniques, such as liquid chromatography,[2] gel electrophoresis,[3] and capillary zone electrophresis,[4] are more often used for measuring RNA and RNA fragments.

Relatively few studies have been devoted to electroanalysis of RNA, as compared to numerous ones dealing with DNA.[5–8] These include polarographic,[9] cyclic voltammetric,[10] capacitance,[11] and adsorptive stripping[12] measurements. These schemes have commonly relied on the cathodic redox and interfacial processes of RNA at mercury drop electrodes. Solid electrode experiments, which may open the door to modern RNA probes and detectors, have not been intensively explored due to large background current contributions at these surfaces.

This article describes an effective solid electrode protocol, based on potentiometric stripping analysis (PSA), for measuring low levels of RNA. PSA, originally developed for monitoring trace metals,[13,14] couples the effective preconcentration step (inherent to stripping analysis) with monitoring of the potential of the working electrode (as a function of time) during the stripping step. The time required for stripping the accumulated analyte is thus proportional to its solution concentration. While this relatively new stripping technique has been widely used for trace metal analysis,[15] it has not been applied for the quantitation or study of nucleic acids. In the following, we will illustrate that the effective accumulation of tRNA onto carbon paste electrodes can be followed by passage of a constant (anodic) current to yield a well-defined PSA peak over a nearly flat baseline. Picogram quantities of RNA can thus be conveniently detected without the need for a mercury surface or an oxygen removal step. Such coupling of solid-state sensors, simplified operation, picogram detection limits, and microliter volumes is shown below to offer new opportunities for nucleic acids measurements and research.

EXPERIMENTAL SECTION

Apparatus. The TraceLab potentiometric stripping unit (PSU20, Radiometer, Denmark), was used in connection with an IBM PS/2 55SX computer. In accordance with the TraceLab protocol, the potentials were sampled at a frequency of 30 kHz, the derivative signal (dt/dE) was plotted against the potential, and the peak area (following baseline fitting) served as the analytical signal. Voltammetric experiments were performed with a BAS-100A electrochemical analyzer. Most experiments were carried out in a BAS VC-2 cell, containing a 1.0 mL solution. The carbon paste working electrode, Ag/AgCl reference electrode (Model RE-

(1) Holden, M.; Pirie, N. *Biochim. Biophys. Acta* **1955**, *16*, 317.
(2) Preston, M. R. *J. Chromatogr.* **1983**, *275*, 178.
(3) Chan, K.; Koutny, L.; Yeung E. S. *Anal. Chem.* **1991**, *63*, 746.
(4) Huang, X.; Shear, J.; Zare, R. *Anal. Chem.* **1990**, *62*, 2049.
(5) Palecek, E. *Bioelectrochem. Bioenerg.* **1986**, *15*, 275.
(6) Palecek, E. *Bioelectrochem. Bioenerg.* **1988**, *170*, 421.
(7) Palecek, E. In *Topics in Bioelectrochemistry and Bioenergetics*; Millazo, G., Ed.; Wiley: Chichester, 1983; Vol. 5, p 65.
(8) Brett, C. M. A.; Brett, A. M.; Serrano, S. *J. Electroanal. Chem.* **1994**, *366*, 225.
(9) Reynaud, J. *Bioelectrochem. Bioenerg.* **1976**, *3*, 561.
(10) Fojta, M.; Teijeiro, C.; Palecek, E. *Bioelectrochem. Bioenerg.* **1994**, *34*, 69.
(11) Paleček, E.; Doskocil, J. *Anal. Biochem.* **1974**, *60*, 518.
(12) Paleček, E.; Fojta, M. *Anal. Chem.* **1994**, *66*, 1566.
(13) Jagner, D. *Anal. Chim.* **1979**, *51*, 342.
(14) Jagner, D. *Trends Anal. Chem.* **1983**, *2* (3), 53.
(15) Wang, J. *Analytical Electrochemistry*; VCH Publishers: New York, 1994.

0003-2700/95/0367-4065$9.00/0

1. BAS), and platinum wire auxiliary electrode joined the cell through holes in its Teflon cover. The carbon paste [made of 70/30 w/w graphite powder (Acheson 38, Fisher)/mineral oil (Sigma; free of DNase, RNase or protease)] was housed in a Teflon body to give a 3.5-mm-diameter disk surface. Electrical contact to its inner side was made with a stainless-steel screw. Small (microliter) volume experiments were performed with a two-electrode system, involving a 0.6-mm-diameter carbon paste electrode (housed in a micropipet tip) and a Ag/AgCl wire (placed/coiled on the working electrode tip body). A copper wire served as a contact to the microcarbon paste electrode. The flow injection system consisted of a carrier reservoir, a micropump (BAS Model 1001), an injection valve (Rainin Model 5041) with a 20-μL sample loop, interconnecting Teflon tubing, and a thin-layer carbon paste detector (BAS Model TL-A). All glassware, containers, and the cell (with the exception of the electrodes) were sterilized by autoclaving for 30 min. The electrodes were thoroughly rinsed with sterilized water prior to use.

The UV absorption of the RNA was measured with a diode array spectrophotometer (Model 8452A, Hewlett Packard). Temperature control (during the RNase experiment) was achieved with a digital temperature controller (Model 9101, Fisher).

Reagents. The following chemicals were obtained from Sigma and were used as received: transfer RNA (tRNA, from bakers' yeast, lyophilized powder; Catalog No. R8759), double-stranded calf thymus DNA (dsDNA, activated and lyophilized; Catalog No. D4522), polyguanylic acid (poly(G), potassium salt; Catalog No. P4404), polyuridylic acid (poly(U), potassium salt; Catalog No. P9528), polycytidylic acid (poly(C), potassium salt; Catalog No. P4903), polyadenylic acid (poly(A), potassium salt; Catalog No. P9403), ribonuclease (RNase, EC 3.1.27.5, Type X-A, from bovine pancreas), and diethyl pyrocarbonate (DEPC). The RNase stock solution was prepared with 10 mM Tris buffer, pH 7.[16] Total RNA from human lung tissue was prepared using RNAsol (precipitated and suspended in DEPC-treated water). All aqueous media used for preparing the RNA solutions were treated with 0.1% w/w DEPC for 12 h at 37 °C and were then autoclaved for 30 min,[16] while all other solutions were prepared with sterile doubly distilled water. A 1000 mg/L RNA solution was diluted before use, as needed for the specific experiment. The RNA and DNA concentrations were verified by UV measurements at 260 nm. A 0.2 M acetate buffer solution (pH 5.0) served as supporting electrolyte.

Procedure. The smoothed carbon paste surface was pretreated prior to each measurement by applying a potential of +1.7 V for 60 s, using the electrolyte solution. The accumulation of RNA proceeded from a stirred solution for different times (depending on its level), using a potential of +0.5 V. After completion of the accumulation, the potentiostat was disconnected, and the preconcentrated RNA was oxidized by applying a constant oxidizing current (usually 4 μA). Stripping voltammetric experiments were carried out using a similar accumulation step, followed by a 5-s rest period, and a positive-going square-wave potential scan. For small-volume experiments, the combined working/reference electrode assembly was immersed in a drop (5–100 μL) of the RNA solution on a parafilm. The solution was vibrated to facilitate the accumulation (by using a stirrer to vibrate the plastic support). Details of the flow injection operation are given below. All accumulation and stripping steps were carried out at room temperature (23 ± 0.5 °C).

(16) Maniatis, E.; Sambrook, J. *Molecular Cloning: A Laboratory Manual*; Cold Springs Harbor Laboratory: New York, 1982; p 190.

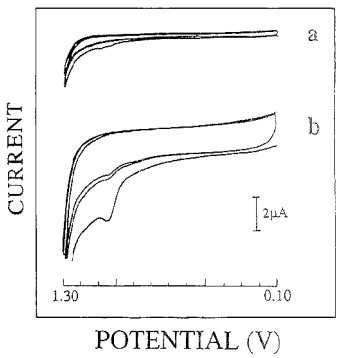

Figure 1. Repetitive cyclic voltammograms for 2 mg/L tRNA at the untreated (a) and pretreated (b) carbon paste electrodes, after a 2-min stirring at +0.1 V. Scan rate, 100 mV/s; electrolyte, acetate buffer (pH 5.0; 0.2 M, 1.0 mL). Pretreatment (b) for 60 s at −1.7 V.

RESULTS AND DISCUSSION

The anodic pretreatment of carbon paste greatly enhances the adsorptive accumulation of RNA. Figure 1 displays repetitive cyclic voltammograms for 2 mg/L tRNA at the untreated (a) and pretreated (b) carbon paste electrodes after 2 mins stirring at +0.1 V. A very small anodic peak (E_p = +1.02 V) is observed at the untreated surface. In contrast, this peak increases substantially (>15-fold) after the electrode is activated. No peaks are observed in the cathodic branch. Subsequent scans exhibit substantially smaller peaks, corresponding to the response of the solution-phase RNA (and hence indicating rapid desorption of the product). Similar small peaks were observed at the treated electrodes without prior accumulation (not shown). Notice also the substantially larger background current contribution and envelope following the surface activation. According to Adams and coworkers,[17] the electrochemical pretreatment produces a more hydrophilic surface state and a concomitant removal of organic layers. Such a change in the surface state appears to facilitate the interfacial accumulation of RNA. The similar oxidation peak potentials (before and after the treatment) indicate that the treated surface has no electrocatalytic activity.

Of the nucleic acid bases, only guanine and adenine can be oxidized at carbon electrodes.[18,19] Our experimental data, and those of others,[18] suggest that the cyclic voltammetric anodic peak of RNA corresponds to the oxidation of the guanine residue. For example, similar cyclic voltammetric profiles were observed for analogous experiments using the synthetic ribonucleotide poly (G), which contains only guanine residues (not shown). In addition, guanine and adenine displayed defined oxidation peaks at +0.9 and +1.2 V, respectively. The oxidation of these monomeric bases commonly occurs at potentials ~0.2 V lower that those of the bases bound in the polynucleotide.[18] In view of the large solvent decomposition current, it is more difficult to evaluate the signal of the bound adenine residue [at the solution pH (5) examined].

(17) Rice, M.; Galus, Z.; Adams, R. N. *J. Electroanal. Chem.* **1983**, *143*, 89.
(18) Brabec, V.; Koudelka, J. *Bioelectrochem. Bioenerg.* **1980**, *7*, 793.
(19) Kafil, J.; Cheng, H. Y.; Last, T. *Anal. Chem.* **1986**, *58*, 285.

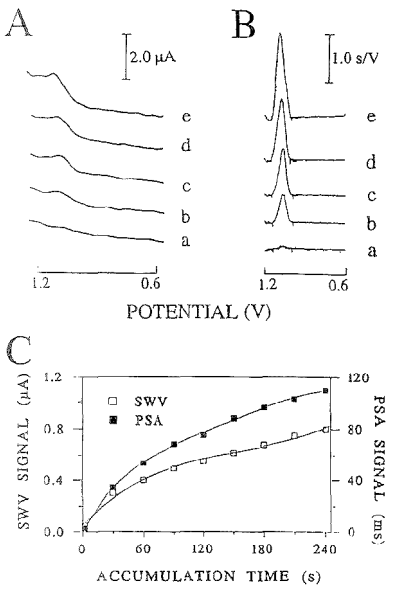

Figure 2. Square-wave voltammetric (A) and PSA (B) peaks for 1 mg/L tRNA following different accumulation times: 2 (a), 30 (b), 60 (c), 120 (d), and 240 (e) s. Preconcentration potential, 0.5 V; stripping current (B), 8 μA; amplitude and frequency (A), 10 mV and 40 Hz, respectively; stirring rate (during accumulation), 400 rpm. Electrolyte and pretreatment, as in Figure 1. (C) displays the resulting time-dependent plots.

The adsorption of RNA onto the treated carbon paste electrodes can be used as an effective preconcentration step prior to the measurement of the surface species. In this way, highly sensitive measurements of RNA can be achieved by means of adsorptive stripping analysis. Figure 2 displays the voltammetric (A) and potentiometric (B) stripping responses for 1 mg/L tRNA for increasing accumulation periods [ranging from 2 (a) to 240 (e) s]. The square-wave voltammetric response, while increasing with the preconcentration time, is poorly defined and superimposed on a rising background current. In contrast, a sharper and well-defined response, coupled with a nearly flat background, is observed in the PSA operation. Convenient measurements are thus feasible following very short accumulation periods. Yet, the longer the time, the more RNA is adsorbed, and the larger the peak area is observed. As indicated also from the resulting peak area versus accumulation time plot, the peak rises rapidly at first and then more slowly. For a 60-s accumulation (curve c), the response is about 15 times that attained with a 2-s accumulation (curve a). Overall, the data of Figure 2 clearly demonstrate the advantage of the potentiometric stripping mode over its voltammetric counterpart for trace measurements of RNA. As will be illustrated later, such sensitivity advantage becomes even more pronounced for monitoring lower (ultratrace) levels of RNA. The stripping step, coupled with the subsequent conditioning one, result in a complete desorption of the accumulated RNA. Hence, a single carbon paste surface can be used repetitively without affecting the precision (see data below).

Various procedure parameters, such as the accumulation potential or stripping current, have a profound effect upon the

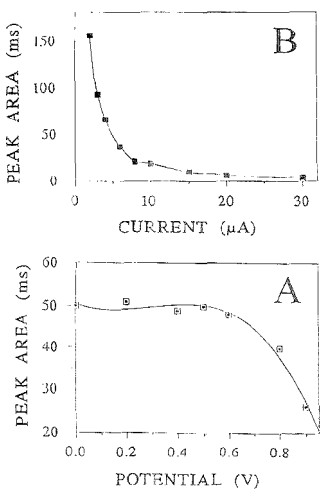

Figure 3. Effect of accumulation potential (A) and stripping current (B) on the PSA response for 1 mg/L tRNA. Accumulation for 30 s; stripping current, 4 μA. Other conditions as in Figure 2B.

PSA response for RNA (Figure 3). For example, while the peak area is only slightly affected by increasing the accumulation potential between 0.0 and 0.6 V, it decreases rapidly at higher potentials, approaching the peak potential (A). The RNA response decreases sharply upon raising the stripping current between 2 and 10 μA, and then decays more slowly (B). Such larger time signals for small stripping currents reflect the reduced oxidation rates. A large background noise accompanied the peaks for stripping currents smaller than 4 μA. A potential of +0.5 V and a current of 4 μA were thus selected for most subsequent quantitative work. The solution pH can affect the peak area and potential. For example, the response increased rapidly upon increasing the pH from 4 to 5, and decreased gradually above 5.3, e.g., to 60% and 40% of its maximum value at pH 7.4 and 9, respectively. The peak potential decreased linearly, from +1.07 to +0.82 V, upon raising the pH from 4 to 9 (not shown; Britton–Robinson buffer solutions; 5 mg/L tRNA and 30-s accumulation). An acetate buffer solution (pH 5.0) was used in all subsequent work, as it yielded the most favorable background response (compared to sodium chloride or phosphate buffer solutions). Carbon pastes containing 70% w/w graphite yielded the most favorable signal-to-background characteristics. With lower graphite contents, it was difficult to resolve the RNA response from the background one, while higher ones (>70% w/w) were not suitable for the paste binding. We also assessed the effect of the pretreatment time and potential and found that 60 s at +1.7 V yields the most favorable conditions (not shown). Similar signals were observed by carrying out the pretreatment in the presence and absence of the target RNA. Such in situ pretreatment capability (in the presence of the analyte) greatly benefits the practical utility of the sensor.

The bioanalytical utility is based on the correlation between the stripping response and the RNA concentration. A series of five concentration increments, from 0.5 to 2.5 mg/L tRNA, was used to evaluate the linearity. Figure 4A displays potentiograms for this series following a 30-s accumulation. The well-defined

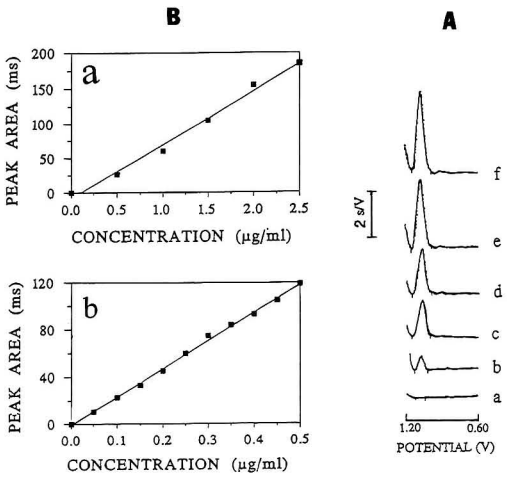

Figure 4. (A) Potentiograms obtained for solutions of increasing tRNA concentrations from 0.5 to 2.5 mg/L tRNA (b–f), along with that for the blank solution (a). Also shown (B) are the resulting calibration (a) and another plot over the range 50–500 μg/L (b). Accumulation for 0.5 (a) and 2 (b) min; stripping current, 4 μA; other conditions as in Figure 2B.

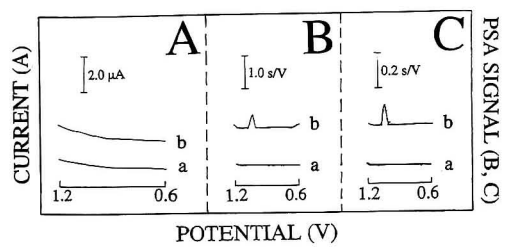

Figure 5. Voltammetric (A) and potentiometric (B, C) stripping response curves for 10 μg/L (trace b in panels A, B) and 5 μg/L (trace b in panel C) tRNA, along with the corresponding background response (traces a). Preconcentration for 5 (A, B) and 10 (C) min; stripping current, 3 (B) and 0.3 (C) μA; solution volume, 1 mL (A, B) and 5 μL (C). Other conditions as in Figure 2.

peaks allow convenient quantitation of these concentrations. The resulting calibration plot, shown in Figure 4B, graph a, is highly linear (correlation coefficient, 0.991). A longer (2-min) accumulation period was used in connection with smaller concentration increments over the 50–500 μg/L range. As shown in Figure 4B, graph b, this experiment also yielded a linear calibration plot (correlation coefficient, 0.998).

The coupling of the efficient adsorptive accumulation and a microprocessor-controlled potentiometric stripping results in extremely low detection limits. Figure 5 (parts A and B, trace b) displays the voltammetric and potentiometric stripping responses for a 10 μg/L tRNA solution following a 5-min accumulation. No response is observed for the square-wave voltammetric stripping operation. In contrast, a well-defined peak is obtained in the PSA experiment. The limit of detection—calculated from 3 times the noise (of Figure 5B, trace b)—was found to be 3 μg/L, or 3 ng in the 1-mL solution used. The corresponding value for the square-wave voltammetric operation is about 150 μg/L, i.e., 50 times higher (not shown). Substantially lower PSA mass detection limits can be achieved by decreasing the volume requirement. Such a decrease (to the microliter domain) is also important, in view of the volumes employed in analogous electrophoretic measurements of RNA. Figure 5C displays the PSA response for 5 μg/L tRNA in a 5-μL droplet. The sample was vibrated to facilitate the preconcentration. A sharp peak (over a flat baseline) is observed following a 10-min accumulation. A detection limit of around 2 μg/L can be estimated on the basis of the signal-to-noise characteristics of these data. This means that 10 pg of tRNA (i.e., $\sim 4 \times 10^{-16}$ mol based on an average molecular weight of 2.6×10^4) can be detected in the 5-μL solution used. Such a remarkably low detection limit compares favorably with that (100 pg) reported recently for analogous stripping voltammetric measurements at a hanging mercury drop electrode.[12] A substantially higher detection limit, 1 mg/L, was estimated for analogous PSA measurements of total RNA which consists primarily of rRNA (10-min accumulation; not shown). Apparently, the preconcentration efficiency is higher for smaller-size RNAs.

Repetitive measurements using 5-μL volumes require a new sample drop for each accumulation/stripping cycle (due to partial evaporation of the sample), yet such repetitive runs yielded reproducible results. Larger drops (100 μL) allow repetitive runs in the same solution. For example, a series of 10 repetitive measurements of 0.1 mg/L tRNA (in a 100-μL sample) resulted in a mean peak area of 7.8 ms and a relative standard deviation (RSD) of 8.0% (2-min accumulation and 0.3-μA stripping current; not shown). Better precision (RSD of 3.1%) was obtained for 10 repetitive measurements of 1 mg/L tRNA in a stirred 1-mL solution (1-min accumulation).

Low molecular weight interferences that may be present in RNA samples can be eliminated by transferring the electrode (with the accumulated nucleic acid) to a blank electrolyte medium.[12] Such an adsorptive/transfer stripping protocol has been traditionally performed manually, by rinsing the electrode (after the accumulation) and dipping it in the blank solution.[12] Our data indicate that the RNA-modified carbon paste electrode gives similar signals in the sample and blank solutions. We also developed a more elegant and simplified protocol for adsorptive/transfer stripping experiments based on the medium-exchange character of flow injection systems.[20] In flow injection analysis (FIA), the preconcentration period can be started as the sample plug arrives in the detector and terminates after its passage through. The actual potentiometric measurement of the accumulated RNA can thus be performed after the arrival of the carrier blank solution. Figure 6 (traces b–d) displays the flow injection PSA response for repetitive injections of 20-μL samples containing 5 mg/L (i.e., 100 ng) tRNA. Well-defined and reproducible peaks are observed, along with a favorable background response (potentiogram a). A flow rate of 125 μL/min and an accumulation time of 150 s were employed to ensure an effective accumulation while performing the stripping in the presence of the carrier solution (based on the dispersion profile/residence time of the sample plug). Such a FIA/PSA operation thus results in an injection rate of about 20 samples/h and a reproducible delivery of microliter RNA samples to the carbon paste detector. Compared to earlier batch operations, the FIA/PSA protocol should also facilitate the automation of RNA assays, as desired

(20) Wang, J.; Freiha, B. *Anal. Chem.* **1983**, *55*, 1285.

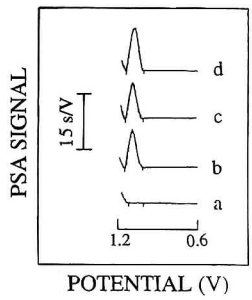

Figure 6. Flow injection PSA response for 20 μL samples containing 0 (a) and 5 (b–d) mg/L tRNA. Flow rate, 125 μL/min; stripping current, 0.8 μA; carrier solution, acetate buffer (0.2 M, pH 5); accumulation time, 150 s.

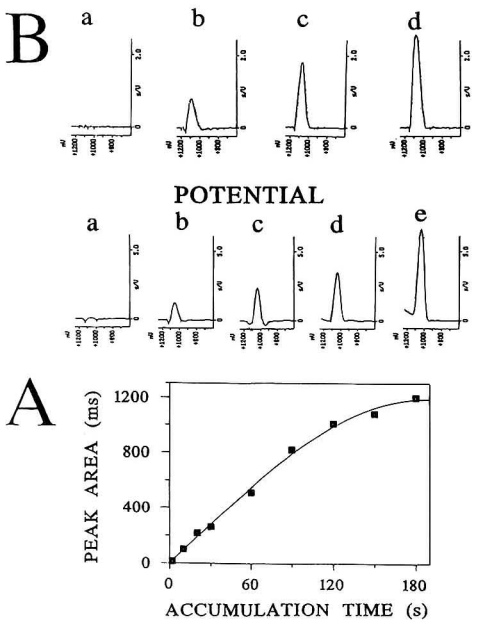

Figure 7. Adsorptive PSA of polyguanylic acid. (A) Potentiograms for 3 mg/L poly(G) following different accumulation times: 2 (a), 10 (b), 20 (c), 30 (d), and 60 (e) s. (B) Response for increasing levels of poly(G): 0 (a), 1 (b), 2 (c), and 3 (d) mg/L with 30-s accumulation. Stripping current, 4μA. Other conditions as in Figure 2B.

for routine bioanalytical work. Batch PSA-transfer experiments may be more useful for fundamental studies aimed at elucidating structural transitions of RNA or its interactions with various agents.

Measurements of low RNA levels in the presence of DNA is a challenging and important task.[10,12] In view of the high sensitivity of the present procedure toward tRNA (as compared to analogous measurements of dsDNA), the latter has a very small effect upon the RNA response of interest. This was examined in measurements of 1mg/L tRNA in the presence of increasing levels of dsDNA (over the 0.5–20 mg/L range). Only 9%, 13%, 17%, and 20% increases in the RNA signal were observed in the presence of 2-, 3-, 10-, and 20-fold excess, respectively, of dsDNA (not shown).

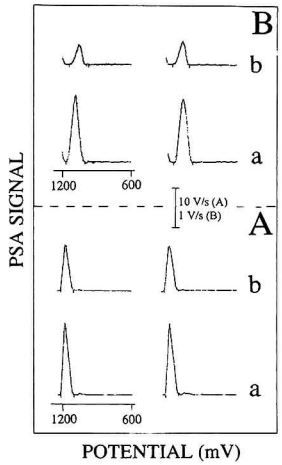

Figure 8. Adsorptive/transfer PSA hybridization experiment. Traces a: Response of poly(A)- and poly(G)-modified electrodes in the blank electrolyte (panels A and B, respectively). Traces b: As in traces a but after transfering the modified electrodes to electrolyte solutions containing 20 mg/L poly(U) or 2 mg/L poly(C) (panels A and B, respectively). Conditions: accumulation for 1 min using electrolyte solutions containing 10 mg/L poly(A) or 1 mg/L poly(G) (A and B, respectively). Stripping started after 10 s-stirring at +0.5 V, using currents of 12 (A) and 8 (B) μA; electrolytes, (A) 0.1 M Britton–Robinson buffer, pH 7; (B) acetate buffer, pH 5.

The presence of RNase in the sample matrix does not interfere in the measurement of RNA. This allows use of the PSA procedure for monitoring the progress of enzymatic hydrolysis reactions. For example, the time dependence of such reactions was investigated by analyzing the tRNA/RNase mixture at different times intervals (1 mg/L tRNA, 0.5 mg/L RNase, 37 °C; not shown). The PSA peak increased rapidly (up to 45% of its original value) within the first 10 min and then started to level off (for samples taken over the entire 60 min experiment). A similar profile, but with a 110% signal enhancement, was observed using a 1.0 mg/L RNase solution. Analogous cyclic voltammetric/hydrolysis experiments at the mercury electrode yielded a similar temporal profile, but with a decrease (rather than increase) of the RNA response.[10] This difference may be due to different conditions of the RNA hydrolysis that result in different chain lengths of the RNA cleavage products.

Figure 7 displays the PSA response for the synthetic polyribonucleotide poly(G). As expected from its high guanine content, poly(G) yields a well-defined PSA peak (at a potential similar to that of RNA) . This peak increases rapidly upon increasing the accumulation time (A) or the poly(G) concentration (B). Convenient quantitation of low milligrams per liter levels of the synthetic polyribonucleotide can thus be accomplished following a 30-s accumulation. As expected, no response was observed for analogous measurements of poly(U) or poly(C). Similar measurements of poly(A) yielded no response at pH 5 (due to the large background) but a defined peak at pH 7 (associated with the lowered oxidation potential).

Batch adsorptive/transfer PSA experiments are particularly attractive for following hybridization reactions between complementary strands of polyribonucleotides. For example, in Figure

8 traces a are potentiograms obtained after transfering the poly(A)- and poly(G)-modified electrodes to the background electrolyte solution (panels A and B, respectively). Well-defined and stable peaks are observed for the polyribonucleotide-modifed electrodes in the blank solution. Substantially smaller (65% and 35%) and yet stable peaks are observed at these electrodes upon repeating the experiment in the presence of the complementary strand [poly(U) or poly(C)] in the exchange solution (traces b, panels A and B, respectively). The decrease of the signal in the presence of the complementary strand was proportional to its concentration in the exchange solution, as was indicated for different levels of this strand (not shown). Such dependence holds great promise for the design of sequence-selective sensors.

In conclusion, we have demonstrated that PSA can be used for measuring ultratrace levels of RNA following its adsorptive accumulation onto carbon paste electrodes. Such PSA operation effectively addresses the large background contribution inherent to carbon electrodes. The new adsorptive PSA procedure offers substantial lowering of the detection limit, not only compared to analogous voltammetric measurements but also in comparison to stripping voltammetry at mercury electrodes. Such application of solid electrodes, and the elimination of the deoxygenation step, may open the door to new RNA probes and detectors. For example, the RNA-modified carbon paste electrode can be used for investigating structural transitions and interactions of RNA. Pretreated carbon paste or fiber electrodes may be useful for amperometric detection for liquid chromatography or capillary zone electrophoresis. The new FIA operation may also facilitate the assay and study of nucleic acids. Similar results for single- or double-stranded DNA will be reported elsewhere in the near future. The new coupling of solid-state sensors, picogram detection limits, microliter volumes, and simplified operation should expand the role of electroanalysis in nucleic acids research.

ACKNOWLEDGMENT

The technical assistance of L. Partin, M. Balakrishnan, and L. Chen is greatly appreciated.

Received for review May 30, 1995. Accepted July 25, 1995.[*]

AC950520Q

[*] Abstract published in *Advance ACS Abstracts*, October 15, 1995.

Anal. Chem. 1995, *67*, 4071–4076

Characterization of a Ferrocene-Containing Polyacrylamide-Based Redox Gel for Biosensor Use

Hai-zhi Bu, Susan R. Mikkelsen,* and Ann M. English*

Department of Chemistry and Biochemistry, Concordia University, 1455 de Maisonneuve Boulevard West, Montreal, Quebec, Canada H3G 1M8

A novel neutral ferrocene-containing polyacrylamide-based redox gel was prepared from the copolymerization of vinylferrocene (VF) with acrylamide and *N,N'*-methylenebisacrylamide in a one-step procedure. Hydroxypropyl-β-cyclodextrin (HPCD) was used to convert water-insoluble VF into the water-soluble VF-HPCD inclusion complex, allowing the copolymerization to be performed in aqueous solution. A new ternary catalyst, consisting of flavin mononucleotide, H_2O_2, and *N,N,N',N'*-tetramethylethylenediamine, was developed for initiating the polymerization. A redox gel electrode, fabricated by covering the redox gel on the surface of a carbon paste electrode with a dialysis membrane, exhibits quasi-reversible electrochemical characteristics. The electrocatalytic properties of a glucose biosensor prepared by entrapping glucose oxidase in the redox gel were investigated. The simplicity and reproducibility of its preparation make this new redox gel a good candidate for biosensor applications.

Among enzyme-based biosensors,[1-3] reagentless amperometric enzyme electrodes have received much attention in recent years.[4-5] In the preparation of reagentless amperometric enzyme electrodes, the redox mediators are immobilized so that leakage of the redox species from the enzyme electrode is averted. Various methods for co-immobilization of enzymes and redox mediators have been utilized by different research groups.

Heller's group has reported biosensor applications of cross-linked redox gels[7] containing glucose oxidase (GOx) based on poly(vinylpyridine) (PVP) with complexed $(bpy)_2OsCl$ (bpy = 2,2'-bipyridine). Free pyridine groups were quaternized with either the bromoacetic or the bromopropionic acid ester of *N*-hydroxysuccinimide to promote cross-linking with lysines on the enzyme surface. However, competition between the desired aminolysis of the *N*-hydroxysuccinimide groups and their spontaneous hydrolysis brought about unsatisfactory variation from film to film. Subsequently they developed an improved redox polymer [PVP containing complexed $(bpy)_2OsCl$ and partially quaternized with bromoethylamine] for the immobilization of oxidoreductases. The electrochemical characteristics of this redox polymer in the absence of protein[8] and the steady-state electrochemical response of GOx immobilized in the polymer[9] were examined. Heller's group has recently reported two new osmium-based three-dimensional redox hydrogel enzyme electrodes. These were formed by cross-linking poly(1-vinylimidazole) complexed with $Os(bpy)_2Cl$[10] or $Os(4,4'$-dimethyl-$bpy)_2Cl$[11] and poly(ethylene glycol) diglycidyl ether in the presence of GOx or lactate oxidase. The glucose sensor has since been developed for subcutaneous in vivo glucose monitoring.[12]

Okamoto's group has designed highly flexible ferrocene-containing siloxane polymers. These facilitate electron transfer from the reduced flavin cofactor of several oxidases, and several highly stable amperometric biosensors based on these polymeric systems have been constructed.[13-18] Calvo and co-workers reported the direct electrical communication between a new ferrocene-containing acrylamide–acrylic acid copolymer and GOx or horseradish peroxidase.[19] A kinetic model, based on fast electron diffusion from the electrode to the ferrocenium redox centers and subsequent enzyme oxidation in the hydrogel film, was validated with experimental results. A new polycationic redox hydrogel, obtained by derivatization of poly(allylamine) with ferrocene carboxaldehyde and cross-linking of the resulting soluble redox polymer with GOx via epichlorohydrin, was also reported by Calvo and co-workers.[20] Foulds and Lowe reported the syntheses of N-substituted pyrrole monomers containing redox-active side chains.[21] The monomers were anodically polymerized to form redox-active films, and GOx was entrapped in ferrocene-containing polypyrrole films to construct a reagentless glucose electrode. GOx biosensors based on entrapment within

(1) Byfield, M. P.; Abuknesha, R. A. *Biosens. Bioelectron.* **1994**, *9*, 373.
(2) Sethi, R. S. *Biosens. Bioelectron.* **1994**, *9*, 243.
(3) Turner, A. P. F. *Curr. Opin. Biotechnol.* **1994**, *5*, 49.
(4) Davies, M. L.; Tighe, B. J. *Sel. Electrode Rev.* **1991**, *13*, 159.
(5) Heller, A.; Maidan, R.; Wang, D. L. *Sens. Actuators B* **1993**, *13*, 180.
(6) Usmani, A. M., Akmal, N., Eds. *Diagnostic Biosensor Polymers*; Maple Press: York, PA, 1994.
(7) Gregg, B. A.; Heller, A. *Anal. Chem.* **1990**, *62*, 258.
(8) Gregg, B. A.; Heller, A. *J. Phys. Chem.* **1991**, *95*, 5970.
(9) Gregg, B. A.; Heller, A. *J. Phys. Chem.* **1991**, *95*, 5976.
(10) Ohara, T. J.; Rajagopalan, R.; Heller, A. *Anal. Chem.* **1993**, *65*, 3512.
(11) Ohara, T. J.; Rajagopalan, R.; Heller, A. *Anal. Chem.* **1994**, *66*, 2451.
(12) Csoregi, E.; Schmidtke, D. W.; Heller, A. *Anal. Chem.* **1995**, *67*, 1240.
(13) Hale, P. D.; Inagaki, T.; Karan, H. I.; Okamoto, Y.; Skotheim, T. A. *J. Am. Chem. Soc.* **1989**, *111*, 3482.
(14) Inagaki, T.; Lee, H. S.; Skotheim, T. A.; Okamoto, Y. *J. Chem. Soc., Chem. Commun.* **1989**, 1181.
(15) Gorton, L.; Karan, H. I.; Hale, P. D.; Inagaki, T.; Okamoto, Y.; Skotheim, T. A. *Anal. Chim. Acta* **1990**, *228*, 23.
(16) Hale, P. D.; Boguslavsky, L. I.; Inagaki, T.; Karan, H. I.; Lee, H. S.; Skotheim, T. A.; Okamoto, Y. *Anal. Chem.* **1991**, *63*, 677.
(17) Lee, H. S.; Liu, L. F.; Hale, P. D.; Okamoto, Y. *Heterocycl. Chem.* **1992**, *3*, 303.
(18) Hale, P. D.; Lee, H. S.; Okamoto, Y. *Anal. Lett.* **1993**, *26*, 1.
(19) Calvo, E. J.; Danilowicz, C.; Diaz, L. *J. Chem. Soc., Faraday Trans.* **1993**, *89*, 377.
(20) Calvo, E. J.; Danilowicz, C.; Diaz, L. *J. Electroanal. Chem.* **1994**, *369*, 279.
(21) Foulds, N. C.; Lowe, C. R. *Anal. Chem.* **1988**, *60*, 2473.

0003-2700/95/0367-4071$9.00/0

other redox polymers were also reported. These include ferrocene-substituted polylysines,[22] poly(mercapto-*p*-benzoquinone),[23] and polyferrocenes.[24]

Vinylferrocene (VF), a reasonably effective mediator for GOx,[25] can undergo free radical polymerization to yield poly(vinylferrocene) (PVF) with a molecular weight range from 920 to 26 300.[26] The electrochemical behavior of PVF and ferrocene is quite similar, but field effects in the macromolecular environment influence the microscopic potential for oxidation of adjacent ferrocene residues in the polymer.[26] PVF-modified electrodes were also used to fabricate glucose biosensors,[27,28] and Irie and Tanaka reported a redox copolymer formed of *N*-isopropylacrylamide copolymerized with VF [poly(NIPAA/VF)].[29] Oyama and co-workers carried out the electrochemical characterization of a poly(NIPAA/VF) film using quartz crystal oscillators[30] and subsequently used the thermoshrinking property of this polymer to fabricate GOx electrodes.[31]

Cyclodextrins form inclusion complexes with various hydrophobic molecules[32,33] and have been widely used in analytical chemistry[34] and electrochemistry.[35] Recently, the water-soluble inclusion complex of 1,1′-dimethylferrocene with (2-hydroxypropyl)-*β*-cyclodextrin (HPCD) has been used in bioelectrocatalysis[36] and a glucose biosensor[37] by Luong and co-workers. In the present study, VF–HPCD inclusion complexes were copolymerized with acrylamide (AA) and *N,N′*-methylenebisacrylamide (BIS). Polyacrylamide is the most commonly used support matrix in enzyme immobilization[38] and gel electrophoresis[39] because of its good chemical and mechanical stability and its inertness to microbial degradation. Moreover, polyacrylamide and its derivatives have been exploited as immobilization matrices for enzyme electrodes.[40–47] This paper reports the preparation and properties of a novel redox gel which was formed in aqueous solution in a one-step procedure on VF, AA, and BIS copolymerization and designated PVAB. A new catalyst system, consisting of flavin mononucleotide, H_2O_2, and *N,N,N′,N′*-tetramethylethylenediamine (FMN–H_2O_2–TEMED), was developed for the polymerization. The electrochemical characterization of the redox gel is reported, and the catalytic properties of GOx entrapped in the gel are presented.

EXPERIMENTAL SECTION

Materials. Acrylamide (AA), *N,N′*-methylenebisacrylamide (BIS), vinylferrocene (VF), hydroxypropyl-*β*-cyclodextrin (HPCD, average MW 1500), *N,N,N′,N′*-tetramethylethylenediamine (TEMED), H_2O_2, α-D-glucose, and 3-(2-pyridyl)-5,6-bis(4-benzenesulfonic acid)-1,2,4-triazine (ferrozine) were purchased from Aldrich. Flavin mononucleotide (FMN), trichloroacetic acid (TCA), and mineral oil (light white oil, $d = 0.84$ g/mL) were received from Sigma. Mono- and dibasic sodium phosphate were from Fisher, ethylferrocene (EF) was from Strem, and carbon powder (99.9995% purity) was from Johnson Matthey. Glucose oxidase (GOx) from *Aspergillus niger* (EC 1.1.3.4) was obtained from Boehringer Mannheim (Grade II, 238 units/mg). All chemicals were used as received, and solutions were prepared using nanopure water (Barnstead). Other suppliers were as follows: dialysis membrane (6000–8000 MW cutoff), Spectrum Medical Industries; electrode body (4 mm diameter, 2 mm deep) and Ag/AgCl reference electrode, BAS, (West Lafayette, IN); and platinum wire, Fisher.

Preparation of the PVAB Redox Gel. A stock solution of 50 mM HPCD was prepared by adding the powder to 0.1 M sodium phosphate buffer, pH 7.0 (PB), and stirring at room temperature. Solid VF was added to the HPCD stock solution, which was stirred in a sealed container for 2 h and stored at 4 °C. A VF–HPCD molar ratio of 1:5 was used in all polymerization solutions. Stock solutions of 400 mg/mL (5.63 M) monomer and 25 mg/mL (0.16 M) cross-linking reagent were prepared by dissolving AA and BIS in PB. Both solutions were filtered through 0.45-μm disk filters and stored at 4 °C. Aliquots of the stock solutions (AA, 0.68 mmol; BIS, 0.05 mmol) were mixed with VF (0.20–2.00 μmol), and to catalyze the photopolymerization, FMN (30 nmol), H_2O_2 (1.76 μmol), and TEMED (3.30 μmol) were added, and then the final volume was adjusted to 1.0 mL. Since oxygen inhibits polymerization, the reagent mixture was deoxygenated by flowing water-saturated N_2 over its surface for 10 min, the container was sealed tightly, and the mixture was irradiated with a 9-W UV lamp (Ultra-Violet Products Inc.) until a semirigid gel block was observed (~30–260 min), at which time polymerization was considered complete.

Quantitation of Ferrocene Iron in the PVAB Gel. Iron released from the ferrocene species in the PVAB by 5% TCA was analyzed spectrophotometrically on a diode array spectrophotometer (Hewlett-Packard Model 8451A) using ferrozine as a colorimetric reagent.[48] The PVAB gel (1 mL) was subjected to exhaustive washing with PB, dispersed into particles by passage through an 18-gauge syringe needle, and added to 0.3 M TCA with 55 mM phosphate in a final volume of 60 mL. Standard solutions containing 4.49–22.45 μM ethylferrocene (EF) were prepared by mixing 3.2–16.0-mL aliquots of a 84.2 μM EF stock solution with 1 mL of a gel formed from the copolymerization of AA and BIS in the absence of VF (i.e., a blank PAB gel) and dispersed into particles as above, and the EF-containing gel suspensions were added to the TCA solution. A reagent blank contained the same components with the exception of EF, and

(22) Iijima, S.; Mizutani, F.; Yabuki, S.; Tanaka, Y.; Asai, M.; Katsura, T.; Hosaka, S.; Ibonai, M. *Anal. Chim. Acta* **1993**, *281*, 483.
(23) Arai, G.; Masuda, M.; Yasumori, I. *Chem. Lett.* **1992**, 1791.
(24) Hendry, S. P.; Cardosi, M. F.; Turner, A. P. F. *Anal. Chim. Acta* **1993**, *281*, 453.
(25) Cass, A. E. G.; Davis, G.; Francis, G. D.; Hill, H. A. O.; Aston, W. J.; Higgins, I. J.; Plotkin, E. V.; Scott, L. D. L.; Turner, A. P. F. *Anal. Chem.* **1984**, *56*, 667.
(26) Smith, T. W.; Kuder, J. E.; Wychick, D. *J. Polym. Sci.* **1976**, *14*, 2433.
(27) Chen, C. J.; Liu, C. C.; Savinell, R. F. *J. Electroanal. Chem.* **1993**, *348*, 317.
(28) Nguyen, A. L.; Luong, J. H. T. *Appl. Biochem. Biotechnol.* **1993**, *43*, 117.
(29) Irie, M.; Tanaka, T. *Polym. Prepr., Jpn.* **1991**, *40*, 461.
(30) Oyama, N.; Tatsuma, T.; Takahashi, K. *J. Phys. Chem.* **1993**, *97*, 10504.
(31) Tatsuma, T.; Saito, K.; Oyama, N. *Anal. Chem.* **1994**, *66*, 1002.
(32) Cramer, F.; Saenger, W.; Spatz, H. C. *J. Am. Chem. Soc.* **1967**, *89*, 14.
(33) Saenger, W. *Angew. Chem., Int. Ed. Engl.* **1980**, *19*, 344.
(34) Li, S.; Purdy, W. C. *Chem. Rev.* **1992**, *92*, 1457.
(35) Bersier, P. M.; Bersier, J.; Klingert, B. *Electroanalysis* **1991**, *3*, 443.
(36) Brown, R. S.; Luong, J. H. T. *Electroanalysis* **1994**, *6*, 391.
(37) Groom, C. A.; Luong, J. H. T. *Biosensors Bioelectronics* **1994**, *9*, 305.
(38) O'Driscoll, K. F. In *Methods in Enzymology, Immobilized Enzymes and Cells*; Mosbach, K., Ed.; Academic Press: New York, 1976; Vol. 44, pp 169–183.
(39) Hames, B. D. In *Gel Electrophoresis of Proteins, A Practical Approach*, 2nd ed.; Hames, B. D., Rickwood, D., Eds.; IRL Press: Oxford, 1990; pp 1–147.
(40) Hicks, G. P.; Updike, S. J. *Anal. Chem.* **1966**, *38*, 726.
(41) Guilbault, G. G.; Montalvo, J. G., Jr. *Anal. Lett.* **1969**, *2*, 283.
(42) Montalvo, J. G., Jr.; Guilbault, G. G. *Anal. Chem.* **1969**, *41*, 1897.
(43) Guilbault, G. G.; Montalvo, J. G., Jr. *J. Am. Chem. Soc.* **1970**, *92*, 2533.
(44) Tor, R.; Freeman, A. *Anal. Chem.* **1986**, *58*, 1042.
(45) Stein, K.; Schwedt, G. *Anal. Chim. Acta* **1993**, *272*, 73.
(46) Lange, M. A.; Chambers, J. Q. *Anal. Chim. Acta* **1985**, *175*, 89.
(47) Willner, I.; Riklin, A.; Lapidot, N. *J. Am. Chem. Soc.* **1990**, *112*, 6438.
(48) Badia, A.; Thai, N. H. H.; English, A. M.; Mikkelsen, S. R.; Patterson, R. T. *Anal. Chim. Acta* **1992**, *262*, 87.

the blank, samples, and standards were heated in a water bath at 90–95 °C for 15 min, cooled to room temperature, centrifuged to remove the gel particles, and analyzed for iron as previously described.[48]

Working Electrode Preparation. Carbon paste was prepared by thoroughly mixing carbon powder with mineral oil in a 2:1 ratio (w/w) in a mortar. A carbon paste electrode (CPE,[49] surface area 0.13 cm^2) was manufactured by pressing a portion of the resulting paste into the well of an electrode body and manually smoothing the electrode surface on clean paper. A redox gel electrode (RGE) was fabricated by placing a small piece (~2 × 2 × 1 mm) of PVAB gel on the sensing surface of a CPE. The gel layer was covered and flattened to a thickness of ~0.1–0.2 mm with a dialysis membrane, which was anchored with a rubber O-ring. The resulting RGE was exhaustively washed with PB and subjected to cyclic voltammetry in PB from 0.0 to 0.6 V (vs Ag/AgCl) at 10 mV/s until a steady-state profile was reached, typically after 3–5 cycles. RGEs that had reached steady-state signals were used for the cyclic voltammograms reported here, unless otherwise noted.

Cyclic Voltammetry. A BAS-100A electrochemical analyzer was used for cyclic voltammetry. A standard three-electrode cell configuration was adopted with an Ag/AgCl reference electrode, a platinum counter electrode, and a CPE, RGE, or GOx-containing redox gel electrode (GOx-RGE). Approximately 1.5 mL of PB in the cell was bubbled with water-saturated N_2 for 10 min to remove oxygen, and the electrochemical measurements were carried out under a continuous N_2 purge at room temperature (22–24 °C). Unless otherwise stated, voltammograms were recorded from 0.0 to 0.6 V (vs Ag/AgCl) at a scan rate of 0.01 V/s.

RESULTS AND DISCUSSION

Catalysis of Radical Polymerization. Ammonium persulfate–TEMED,[44] ammonium persulfate–riboflavin,[42] riboflavin–TEMED,[50] and ammonium persulfate–3-(dimethylamino)propionitrile (DMAPN)[51] are commonly used catalyst systems for the polymerization of mixtures of AA and BIS. However, none of these catalysts worked effectively when VF was added to the polymerization mixture. Thus, several other systems were tested, including H_2O_2–FMN, H_2O_2–TEMED, FMN–TEMED, and FMN–H_2O_2–TEMED. Only FMN–H_2O_2–TEMED was found to be an efficient polymerization catalyst, and optimal concentrations were 30 μM FMN, 1.76 mM H_2O_2, and 3.30 mM TEMED.

With the FMN–H_2O_2–TEMED system, the polymerization of AA with BIS was complete in 10 min. In the presence of 0.20–2.00 mM VF, however, the polymerization times had to be extended to ~30–260 min. Moreover, it was observed that the polymerization proceeded very slowly over ~80% of the reaction, but once a distinct gel matrix began to form, the polymerization process was complete in 15 min or less, no matter how much VF was added. These results suggest that VF participates in the copolymerization as a retarder,[52] suppressing the polymerization of AA and BIS. Although VF acts as a retarder, it was found that 80–94% of VF in solution is incorporated into high-molecular-weight polymers that cannot diffuse out of the gel.

Iron analysis was used to determine the immobilized VF concentration ($[VF]_{imm}$), where $[VF]_{imm}$ includes only those VF species that cannot diffuse out of the gel matrix. EF was used as a ferrocene standard to construct a calibration curve because of its structural similarity to the copolymerized VF moiety. EF was demetalated by 5% TCA,[48] and linear regression of absorbance at 564 nm (corrected for the reagent blank) vs EF concentration (μM) for standard solutions containing 4.49–22.45 μM EF yielded $A_{564} = 0.005 + 0.027[EF]$ ($R = 0.9997$). A set of redox gels were prepared using different VF concentrations in the polymerization solutions ($[VF]_{sol}$), rinsed exhaustively with PB to remove any free Fe-containing species, and analyzed for iron as described above. Ignoring any possible volume changes on polymerization, the percent yield of VF immobilized in the gel can be determined as follows:

$$\% \text{ yield} = [VF]_{imm}/[VF]_{sol} \times 100 \quad (1)$$

The yield was constant at ~94% for $[VF]_{sol}$ between 0.20 and 0.80 mM, but at higher $[VF]_{sol}$, the yield decreased, reaching a value of ~80% at 2.00 mM.

In the polymerization of AA with BIS, TEMED is usually added as an accelerator of polymerization. Since the free base form of TEMED is reactive, polymerization may be delayed or even prevented at low pH.[39] Using the new FMN–H_2O_2–TEMED catalyst system, it was found that between pH 5 and 14, the polymerization time ranged from 30 to 40 min when 0.40 mM VF was present in the polymerization mixture; below pH 3.8, the polymerization rate slowed down sharply, and polymerization appeared to be completely inhibited below pH 3. Nevertheless, a working pH range of 5–14 for the FMN–H_2O_2–TEMED catalyst will allow its use under most conditions involving the immobilization of biomolecules.

Electrochemical Characterization of the PVAB Redox Gel. Since the PVAB copolymer is a new redox gel, full characterization of its electrochemical properties was carried out. To establish that VF copolymerized with AA and BIS, a gel was prepared from a solution containing 1.2 mM VF, 0.68 M AA, and 0.05 M BIS, which was polymerized using the catalyst system FMN–H_2O_2–TEMED. A RGE was fabricated using the unwashed redox gel, and over a 1-h period, 30 cyclic voltammograms were recorded from 0.0 to 0.6 V (vs Ag/AgCl) at a scan rate of 0.01 V/s immediately after the RGE was immersed in N_2-saturated PB in the cell. Both the anodic (E_{pa}) and cathodic (E_{pc}) peak potentials shifted in the cathodic direction with successive scans; E_{pa} shifted from 340 to 255 mV (vs Ag/AgCl) and E_{pc} from 190 to 155 mV (vs Ag/AgCl). After 20 cyclic voltammograms, E_{pa} and E_{pc} remained essentially constant. The anodic peak current (i_{pa}) decreased slightly to a steady-state value (~1.3 μA), whereas the cathodic peak current (i_{pc}) remained almost constant over the entire 1-h period when i_{pa} approached i_{pc}. The electrochemical stability of the RGE subjected to 30 cyclic voltammograms was excellent, indicating that the remaining VF-derived electroactive species cannot diffuse from the gel.

In a second experiment, a blank PAB gel was used to fabricate a blank gel electrode (BGE). The BGE was immersed in 1.20 mM VF, and the VF-saturated BGE was transferred to a cell

(49) Dryhurst, G.; McAllister, D. L. In *Laboratory Techniques in Electroanalytical Chemistry*; Kissinger, P. T., Heineman, W. R., Eds.; Marcel Dekker: New York, 1984; pp 294–301.

(50) Bharucha, A. D.; Ven Murthy, M. R. In *Methods in Enzymology, Recombinant DNA*; Wu, R., Ed.; Academic Press: San Diego, 1992; Vol. 216, pp 168–179.

(51) Oliver, B. N.; Egekere, J. O.; Murray, R. W. *J. Am. Chem. Soc.* **1988**, *110*, 2321.

(52) Odian, G. *Principles of Polymerization*, 2nd ed.; John Wiley and Sons: New York, 1981; pp 242–251.

Table 1. Dependence of Electrochemical Properties of VF and EF Species on Different Chemical Environments

system[b,c]	electrochemical properties[a] $E_{1/2}$ (mV vs Ag/AgCl)	ΔE_p (mV)	i_{pa}/i_{pc}
CPE/0.20 mM VF-HPCD	339	100	1.62
CPE/0.20 mM EF-HPCD	283	116	5.95
BGE/0.20 mM VF-HPCD	316	58	1.65
BGE/0.20 mM EF-HPCD	263	48	1.66
RGE (steady state)[d]	198	90	0.90
RGE (unwashed)[e]	265	150	1.29

[a] Cyclic voltammetry was performed from 0.00 to 0.60 V (vs Ag/AgCl) at a scan rate of 0.01 V/s. [b] All measurements were carried out in 0.1 M phosphate buffer, pH 7.0. [c] Abbreviations used: CPE, carbon paste electrode; BGE, blank gel electrode; RGE, redox gel elecrode; VF, vinylferrocene; EF, ethylferrocene; and HPCD, hydroxypropyl-β-cyclodextrin. [d] Extensively washed RGE that had been subjected to cyclic voltammetry until a steady-state profile was reached. [e] A RGE that was fabricated from an unwashed PVAB redox gel. The data given are from the first cyclic voltammogram obtained with the electrode.

containing N_2-saturated PB and immediately subjected to 30 cyclic voltammograms. The observed shifts in both E_{pa} and E_{pc} were small ($\leq$10 mV), but i_{pa} and i_{pc} decayed sharply with time and approached zero. These results indicate that the free electroactive species can readily diffuse in and out of the blank PAB gel; thus, VF must be covalently bound to the gel matrix during polymerization since the peak currents did not approach zero in the first experiment.

To verify that VF copolymerized with AA and BIS, a third experiment was performed in which EF was substituted for VF, and all other procedures were the same as in the first experiment. The results of cyclic voltammetry of the EF-containing gel electrode indicate that over 20 cyclic voltammograms, both E_{pa} and E_{pc} shifted only slightly, while i_{pa} and i_{pc} decreased abruptly and approached zero. Hence, EF was not retained in the gel when EF–HPCD was present in the polymerization mixture. The presence of a vinyl substituent (–CH=CH_2) in VF and an ethyl substituent (–CH_2CH_3) in EF indicates that trapping of VF in the gel matrix must result from the copolymerization of VF via its vinyl group with AA and BIS.

Electrochemical Properties of VF in Different Environments. Table 1 lists the half-wave potential [$E_{1/2} = (E_{pa} + E_{pc})/2$], peak separation ($\Delta E_p = E_{pa} - E_{pc}$), and ratios of anodic to cathodic peak currents (i_{pa}/i_{pc}) for VF and EF in different chemical environments. The half-wave potential of EF is more negative than that of VF in the same environment, consistent with the stronger electron-donating character of the ethyl group. Covering the CPE surface with the PAB gel matrix (BGE systems in Table 1) caused distinct negative shifts in $E_{1/2}$ and sharp reductions in ΔE_p for both VF–HPCD and EF–HPCD. The ratio i_{pa}/i_{pc} for EF–HPCD decreased ~4-fold to the value observed for VF–HPCD, suggesting that adsorption of neutral EF on the electrode surface is less extensive when the gel is present. The PAB gel environment thus improves the electrochemical reversibility of VF–HPCD and EF–HPCD compared to that observed at the bare CPE. Furthermore, the $E_{1/2}$ (263 mV vs Ag/AgCl) of EF–HPCD at the BGE is close to the first-cycle $E_{1/2}$ (265 mV vs Ag/AgCl) of an unwashed RGE (Table 1), revealing that copolymerized VF is initially present in the gel as an inclusion complex, since EF–HPCD and copolymerized VF–HPCD should possess similar $E_{1/2}$ values. Thus, the $E_{1/2}$ of the unwashed RGE gradually decreases from a value similar to that of EF–HPCD and stabilizes at the $E_{1/2}$ value for immobilized, uncomplexed VF (198 mV vs Ag/AgCl). The parameters given in Table 1 show that the RGE possesses quasi-reversible electrochemical characteristics.

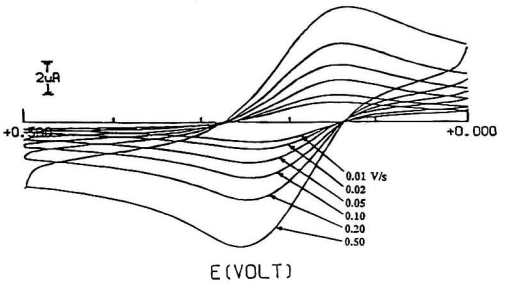

Figure 1. Steady-state cyclic voltammograms of a RGE containing 1.09 mM immobilized VF in N_2-saturated PB at different scan rates.

Characterization of Charge Transfer. Typical steady-state cyclic voltammograms at different potential scan rates using a RGE containing 1.09 mM immobilized VF are shown in Figure 1. Faster scan rates result in greater peak separations, and the peak currents (i_p) depend linearly on the square root of scan rate ($\nu^{1/2}$). Assuming that electron transfer to and from the redox centers is under diffusion control, cyclic voltammetry[53] allows the determination of the product $D_{ct}^{1/2}C^*$, where D_{ct} is the diffusion coefficient for the diffusion-like transport of charge through the gel film and C^* is the concentration of redox centers in the film; thus, D_{ct} may be calculated when C^* is known. From the slopes of plots of i_p against $\nu^{1/2}$, values of $D_{ct}^{1/2}C^*$ at different $[VF]_{imm}$ were estimated to be $10^{-(10\pm1)}$ mol cm^{-2} $s^{-1/2}$, comparable to the value (10^{-9} mol cm^{-2} $s^{-1/2}$) obtained for an acrylamide–acrylic acid ferrocene copolymer which contained a longer arm between the ferrocenyl group and the polymer backbone.[19] At $[VF]_{imm}$ values of 1.6×10^{-6} and 9.3×10^{-7} mol/cm^3, D_{ct} was calculated to be 2.6×10^{-7} and 6.3×10^{-8} cm^2/s, respectively. The observed dependence of D_{ct} on C^* is in accordance with results obtained for other fixed-site redox polymers.[54]

A set of redox gels containing different $[VF]_{imm}$ (0.19–1.61 mM) were prepared, and RGEs were fabricated from these gels. Figure 2 shows that the steady-state anodic peak current increased with increasing $[VF]_{imm}$. The significant upward curvature indicates positive deviation of the peak currents from a linear dependence on $[VF]_{imm}$, which is consistent with the fact that the diffusion coefficients increase with increased redox site concentrations,[54] as observed above.

Using a constant molar ratio of AA to BIS (13.6:1) and a constant $[VF]_{sol}$ (1.0 mM), a set of redox gels with different AA concentrations were prepared by altering the AA concentration in the polymerization mixture ($[AA]_{sol}$). The volume change from polymerization solution to gel was insignificant, and the results obtained for iron analysis of these gels indicated that $[AA]_{sol}$ has no measurable effect on $[VF]_{imm}$. The effect of $[AA]_{sol}$ on the anodic peak current (i_{pa}) was negligible between 0.45 and 0.70

(53) Murray, R. W. In *Electroanalytical Chemistry*; Bard, A. J., Ed.; Marcel Dekker: New York, 1984; Vol. 13, pp 191–368.
(54) Inzelt, G. In *Electroanalytical Chemistry*; Bard, A. J., Ed.; Marcel Dekker: New York, 1994; Vol. 18, pp 138–157.

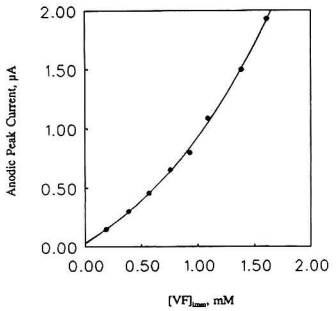

Figure 2. Steady-state anodic peak current of a RGE vs concentration of VF immobilized in the redox gel ([VF]$_{imm}$). Cyclic voltammetry was performed in N_2-saturated PB from 0.0 to 0.5 V vs Ag/AgCl at 0.01 V/s.

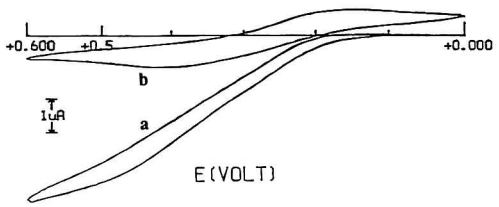

Figure 3. Cyclic voltammograms of a GOx-containing redox gel electrode (GOx-RGE) containing 0.91 mM immobilized VF and 1.0 mg/mL entrapped GOx in N_2-saturated PB. (a) No glucose. (b) 50 mM glucose. Cyclic voltammetry was performed at 5 mV/s.

M, but above 0.7 M, i_{pa} decreased with increasing $[AA]_{sol}$. A possible interpretation is that by increasing $[AA]_{sol}$, and hence the rigidity of the final gel matrix, the charge diffusion coefficient, D_{ct}, is reduced.

The change in i_{pa} and i_{pc} vs pH for a RGE containing 0.93 mM immobilized VF was also examined. The peak currents were relatively insensitive to pH over the range 2–10, but they decrease sharply above pH 10. This may be due to nucleophilic attack of OH^- on the ferrocenium ion, which would result in loss of ferrocene residues in the gel layer.[55] The useful pH range for the RGE is 4–10.

Use of the PVAB Gel in a Glucose Biosensor. A redox gel containing entrapped GOx was prepared from a polymerization mixture containing 1.0 mg/mL GOx and 1.0 mM VF. A GOx-RGE was fabricated using the gel and extensively washed with PB. In the presence of glucose (50 mM) in N_2-saturated PB, a steady-state electrocatalytic oxidation wave (Figure 3a) was obtained due to oxidation of glucose by the GOx-RGE:

$$2Fc \xrightarrow{\text{electrode}} 2Fc^+ + 2e^- \quad (2)$$

$$\text{GOx-FAD} + \text{glucose} \rightarrow \text{GOx-FADH}_2 + \text{gluconolactone} \quad (3)$$

$$\text{GOx-FADH}_2 + 2Fc^+ \rightarrow \text{GOx-FAD} + 2Fc + 2H^+ \quad (4)$$

where GOx-FAD and GOx-FADH$_2$ represent the oxidized and reduced forms, respectively, of the flavin adenine dinucleotide

(55) Prins, R.; Korswagen, A. R.; Kortbeek, A. G. T. G. *J. Organomet. Chem.* **1972**, *39*, 335.

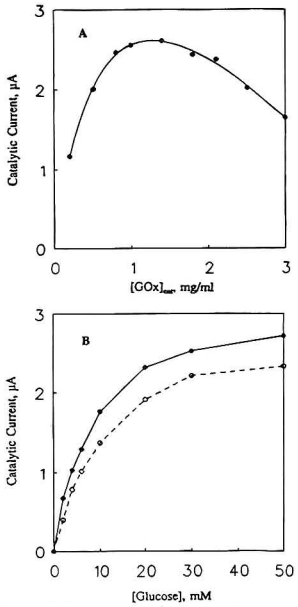

Figure 4. (A) Catalytic current vs concentration of entrapped GOx ($[GOx]_{ent}$). The GOx-RGE (electrode surface area 0.13 cm^2) was prepared using a redox gel containing 0.91 mM immobilized VF, and measurements were taken in N_2-saturated PB containing 50 mM glucose at 0.4 V vs Ag/AgCl. (B) Catalytic current vs glucose concentration. Measurements were taken with a GOx-RGE containing 1.0 mg/mL entrapped GOx and 0.91 mM immobilized VF in PB under N_2 (●) and air (○) at 0.4 V vs Ag/AgCl.

bound to the active site of GOx, and Fc represents a ferrocene residue. GOx-FADH$_2$ is reoxidized by immobilized ferricenium cations (Fc^+) in the gel with a corresponding release of two protons. No reduction wave is seen on the reverse potential scan, indicating that all the ferricenium centers are reduced by GOx-FADH$_2$ (eq 4) in the presence of excess glucose. Figure 3b shows that the GOx-RGE exhibits irreversible electrochemical characteristics ($\Delta E_p \approx 265$ mV), which suggests that GOx entrapped in the gel matrix hinders electron self-exchange between neighboring redox centers and/or electron transfer between the redox sites and the surface of the CPE.

To examine the effects of GOx loading, a series of PVAB gels were prepared from solutions containing a fixed concentration (1.0 mM) of VF ($[VF]_{imm} = 0.91$ mM) and varying GOx concentrations from 0.2 to 3.0 mg/mL. Steady-state catalytic currents (i_{ss}) of the GOx-RGEs were examined at 0.4 V (vs Ag/AgCl) in N_2-saturated PB with 50 mM glucose. Assuming all the GOx was entrapped in the gels, Figure 4A reveals that i_{ss} initially increased sharply with increasing concentration of entrapped enzyme ($[GOx]_{ent}$) but then showed a gradual decline. In the rising part of the curve, i_{ss} must be limited by GOx activity in the gel, but the decrease in i_{ss} at higher $[GOx]_{ent}$ suggests that the current becomes limited by charge transfer and that GOx has an insulating effect on the redox gel. Similar behavior was reported by Ohara et al.[11] on varying GOx concentrations in their gels containing complexed Os(4,4′-dimethyl-bpy)$_2$Cl.

Steady-state response curves, shown in Figure 4B, were obtained at a GOx-RGE containing 1.0 mg/mL entrapped GOx

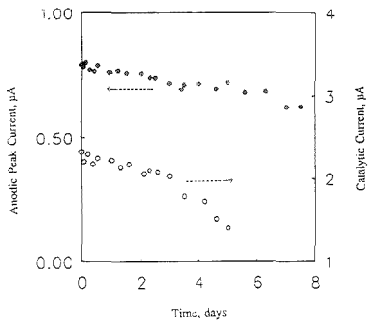

Figure 5. Stability vs time of a RGE containing 0.93 mM immobilized VF (●) and a GOx-RGE containing 0.91 mM immobilized VF and 1.0 mg/mL entrapped GOx (○). Data points represent anodic peak currents of the RGE measured in N_2-saturated PB from 0.0 to 0.5 V vs Ag/AgCl at 0.01 V/s and catalytic currents of the GOx-RGE measured in N_2-saturated PB with 50 mM glucose at 0.4 V vs Ag/AgCl.

and 0.91 mM immobilized VF over a 0–50 mM glucose concentration range. The GOx-RGE shows typical Michaelis–Menten behavior toward glucose, and the reduced i_{ss} observed in air-saturated PB results from competition between the Fc^+ centers and O_2 for the reduced form of GOx. Conversion of i_{ss} to current density gives a value of ~13.5 $\mu A/cm^2$ for the GOx-RGE in 10 mM glucose in N_2-saturated PB (Figure 4B), which is surprisingly high considering the extremely low VF loading of the PVAB gel (~0.3% of the dry weight of PVAB). Glucose biosensors, constructed from polymerized ferrocenes [PVF[27,28] and poly(ferrocenylenemethylene)[24]], exhibited catalytic current densities in 10 mM glucose (~24–38 $\mu A/cm^2$) that are only 2–3-fold higher than those observed here. It should be noted that the voltammetric method used in this work yields catalytic currents that represent total active enzyme since, with excess glucose present, all GOx in the gel is in the reduced form at the beginning of the anodic scan. This is not the case with amperometric measurements at fixed potential, where GOx would be in the oxidized form throughout the gel, and the rate of glucose arrival would be measured.

The long-term stabilities of a RGE ($[VF]_{imm}$ = 0.93 mM) and a GOx-RGE ($[VF]_{imm}$ = 0.91 mM, [GOx] = 1.0 mg/mL), which were stored in PB at 4 °C under nonsterile conditions when not in use, are shown in Figure 5. The sensors were used only to record the data points shown in Figure 5. The data in this figure indicate that the observed currents decrease slowly over 1 week for the RGE, but more rapidly over 3 days for the GOx-RGE. When not fabricated into RGEs, the PVAB gels exhibit excellent long-term storage stability in sealed vials at 4 °C under nonsterile conditions. For example, a RGE fabricated from a 2-month-old gel had over 85% of the signal of a RGE fabricated from a freshly prepared gel. A similar comparison for GOx-RGEs revealed that PVAB gels with entrapped GOx can be stored for up to 1 month with <15% loss in signal.

The reproducibilities of the RGE and GOx-RGE fabrication methods were also tested using gels identical to those used in Figure 5. The mean ± SD of the anodic peak currents obtained at 10 RGEs was 808 ± 24 nA (from 0.0 to 0.5 V vs Ag/AgCl at 10 mV/s) with a coefficient of variation (CV) of 3.1%. The mean ± SD of the catalytic currents from 10 GOx-RGEs was 2.30 ± 0.15 μA (50 mM glucose at 0.4 V vs Ag/AgCl) with a CV of 6.4%. Moreover, it took only ~1 min to fabricate the RGEs or GOx-RGEs once the gels were prepared. Considering the excellent storage stability of the gels and the good stability of the modified electrodes, along with their excellent reproducibilities, this new redox gel should find applications in the construction of reagentless amperometric biosensors.

CONCLUSIONS

The novel redox gel prepared by the combination of one of the most commonly used classes of redox mediators, the ferrocenes, and the most widely used gel matrix in bioanalysis, cross-linked polyacrylamide, offers several advantages over other redox polymers[4–6] used in biosensor construction. These advantages are the following: (1) simple and rapid gel preparation by a one-step procedure; (2) since the polymerization reaction is performed in neutral aqueous solution, loss of activity during enzyme entrapment should be negligible; (3) polyacrylamide-based gels contain up to ~94% water by weight, which is a more suitable environment for enzymes than the commonly used chemically deposited high-density polymer films or carbon pastes; (4) preparation and performance of the RGE and GOx-RGE are very reproducible; (5) although the percent by weight of ferrocene residues in the copolymer is extremely low (~0.3%) compared to other ferrocene-containing polymers,[24,27,28] the catalytic current densities for the GOx-RGEs are high, indicating that the immobilized mediators in the gel are highly efficient; and (6) in the presence of glucose, the response of the GOx-RGE to dissolved oxygen is comparable to or less than those reported by others.[7–19] It is anticipated that the new redox gel system discussed here can be modified for the practical measurement of glucose and used to entrap other enzymes to fabricate the corresponding biosensors without appreciable difficulty.

ACKNOWLEDGMENT

The authors are grateful to the Natural Sciences and Engineering Research Council of Canada (NSERC) for financial support, and Dr. Fernando Battaglini for helpful discussions.

Received for review May 24, 1995. Accepted August 24, 1995.[⊗]

AC950505L

[⊗] Abstract published in *Advance ACS Abstracts,* October 1, 1995.

Anal. Chem. 1995, *67*, 4077–4085

Interaction between Dihydroxy Bile Salts and Divalent Heavy Metal Ions Studied by Polarography

G. Feroci, A. Fini, and G. Fazio

Istituto di Scienze Chimiche, Università di Bologna, Bologna, Italy

P. Zuman*

Department of Chemistry, Clarkson University, Potsdam, New York 13699-5810

The interaction between anions of dihydroxy bile acids (BS^-) (chenodeoxycholate, ursodeoxycholate, hyodeoxycholate, and deoxycholate) and divalent metal ions (Cu^{2+}, Cd^{2+}, Pb^{2+}, and Zn^{2+}) was followed by polarography. For solutions containing 0.1 mM metal(II) ions (M^{2+}), invariability of the half-wave potentials and limiting currents at [BS^-] below about 1 mM indicates the absence of interactions of M^{2+} with monomeric BS^-. At [BS^-] between about 1 and 7 mM, the shifts of the half-wave potentials indicate formation of soluble complexes. Simultaneously, the decrease of limiting current indicates formation of slightly soluble compounds of M^{2+} with small aggregates of bile salts. Between about 7 and 10 mM BS^-, the solutions are saturated with the compounds of M^{2+} with small aggregates of BS^-. The current of M^{2+} is a function of solubility of this product. At concentrations above about 10 mM BS^-, increase of current indicates formation of large ("micelle-like") aggregates bearing free COO^- groups, responsible for the increase in solubility. Exact concentrations corresponding to the limits of individual ranges depend on the natures of both BS^- and M^{2+}. Overall equilibrium constants for the reaction of M^{2+} with small aggregates of BS^-, obtained from $i/i_d = f[BS^-]$ plots and the solubility of these compounds, indicate dependence on the nature of the metal ion. The stabilities of the complexes increases and their solubilities decrease in the sequence $Cu^{2+} > Cd^{2+} > Zn^{2+} > Pb^{2+}$, characteristic for interactions of M^{2+} with carboxylate ions. Structure of the bile salt also affects the solubility of complexes formed, but the sequence or reactivity is different for each individual metal ion. The position and stereochemistry of individual hydroxy groups probably affects the stacking of bile anions in the small aggregates, yielding slightly soluble complexes. The formation of larger aggregates occurs at concentrations of BS^- comparable with reported values of critical micelle concentration.

Bile contains—in addition to alkali and alkaline earth metal ions—ions of iron, manganese, copper, molybdenum, and zinc at levels ranging from 5 to 20 μg per gram of the solid content.[1] These levels can be even higher in lithiasic biles, as indicated by the amounts of these metals found in pigment or cholesterol gallstones.[2] Bodily fluids contain high concentrations of anions, such as hydrogen carbonate, dihydrogen phosphate, anions of fatty acids, and others, which readily form slightly soluble salts with Ca^{2+} and heavy metal ions. Precipitation of such compounds of limited solubility results in formation of deposits denoted as calculi. Alternatively, they can act as seeds for nucleation and crystallization of other substances.

It has been postulated that bile salts (BS^-) or their aggregates (often denoted as micelles) interact with calcium ions, lower the activity of free Ca^{2+} aquo ions,[3] and inhibit the precipitation of slightly soluble calcium salts of biliary anions, such as bilirubinates, lecithins, and anions of fatty acids.[4] Similar interactions can be assumed to occur between bile salt and heavy metal ions, but the experimental evidence for such reactions has been rather limited. Thus, for Fe^{2+} ions, it has been postulated,[5,6] on the basis of dialysis studies, that binding of Fe^{2+} by taurocholate was stronger than that by its aggregates.

To demonstrate that bile salts can act as metal ion buffers, preventing precipitation of heavy metal salts with other anions, the reactions of cholate[7-9] and glycocholate[8] with metal(II) ions were studied. Polarography was the method of choice since it offers information concerning the equilibria between BS^- and M^{2+} ions. In solutions, where the reduction of M^{2+} remains reversible, the shifts of half-wave potentials offer information about the presence of rapidly established equilibria between free M^{2+} aquo ions and their labile complexes. Moreover, changes in the limiting current of M^{2+} yield information on relatively slowly established heterogeneous equilibria between M^{2+} and their slightly soluble compounds. It is an advantage of polarography that measurements can be carried out directly in the reaction mixture, in the presence of colloidal and solid particles. Under such conditions, the use of spectrophotometry, HPLC, or ion-selective electrodes is more limited. In the case of potentiometric measurements, adsorption of colloidal and solid particles can affect the data obtained with a membrane electrode. To minimize the effects of

(1) Fini, A.; Roda, A. in *Acidi Biliari: Ricerca e Applicazioni Terapeutiche*; Roda, A., Pellicciari, R., Eds.; Momento Medico: Bologna, Italy, 1991; p 88ff.

(2) Hervey, R. C.; Taylor D.; Petrunka, C. N.; Murray, A. D.; Strasberg, S. M. *Hepatology* **1985**, *5*, 129–132.

(3) Moore, E. W.; Celic, L.; Ostrow, J. D. *Gastroenterology* **1982**, *83*, 1079–1089.

(4) Ostrow, J. D.; Celic, L.; Moore, E. W. *Gastroenterology*, **1984**, *86*, A1335.

(5) Sanyal, A. J.; Hirsch, J. I.; Moore E. W. *J. Lab. Clin.* **1990**, *116*, 76–86.

(6) Sanyal, A. J.; Hirsch, J. I.; Moore, E. W. *Gastroenterology* **1991**, *100*, A792.

(7) Feroci, G.; Fini, A.; Zuman, P. *Bioelectrochem. Bioenerg.* **1992**, *29*, 91–102.

(8) Feroci, G.; Fazio, G.; Fini, A.; Zuman, P. *J. Pharm. Sci.* **1995**, *84*, 119–125.

(9) Feroci, G.; Fini, A.; Fazio, G.; Zuman, P. *J. Colloid Interface Sci.* **1994**, *166*, 180–190.

0003-2700/95/0367-4077$9.00/0

adsorption, dc polarography is preferred over differential pulse polarography.

Studies on trihydroxy bile salts indicated that monomeric bile salts practically do not interact with Cu^{2+}, Cd^{2-}, Zn^{2+}, and Pb^{2+} (refs 7–9), nor with Fe^{2+} (ref 10). Taurocholate[7–10] does not react either in the monomeric form or in aggregates. Unconjugated bile salts, as well as glycocholate bearing a carboxylate group, react with all M^{2+} ions studied at "premicellar" concentrations of BS^-. Observed reactions are attributed to an interaction of M^{2+} with small aggregates of BS^-. These reactions yield both soluble and slightly soluble species. At concentration of BS^- above the critical micelle concentration (cmc), formation of larger aggregates takes place, which show much higher solubility due to an excess of free COO^- groups. Turbidimetric results paralleled polarographic results. Diametrically opposite conclusions of our studies,[7–10] as compared to those reached by Moore's group[5,6] in their studies on the reaction of Fe^{2+}, are probably due to their use of dialysis, which is not suitable for study of equilibria between metal ions and labile complexes. In the course of dialysis, such equilibria are perturbed.

In this study, reactions of Cu^{2+}, Cd^{2-}, Zn^{2+}, and Pb^{2+} are reported. Cu^{2+} and Zn^{2+} are present in biological systems, whereas Cd^{2+} and Pb^{2+} are xenobiotic, toxic species. It was of interest to show how bile salts might be involved in a detoxification of these ions. The reduction of Cu^{2+}, Cd^{2+}, and Pb^{2+} at the dropping mercury electrode in the absence of BS^- is reversible, while that of Zn^{2+} is irreversible. Reactions of these ions with the following dihydroxy bile acids were studied, which differ in the position and orientation of the hydroxy groups in the steroid moiety: chenodeoxycholate(I) (CDC), ursodeoxycholate(II) (UDC), deoxycholate(III) (DC), and hyodeoxycholate(IV) (HDC).

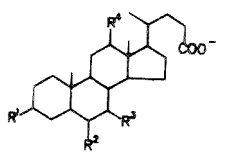

	R^1	R^2	R^3	R^4
I	αOH	H	αOH	H
II	αOH	H	βOH	H
III	αOH	H	H	αOH
IV	αOH	αOH	H	H

EXPERIMENTAL SECTION

Apparatus. Polarographic current–voltage curves were recorded using an Amel Mark 472 polarograph using an electrolytic cell with a saturated calomel electrode. The dropping mercury electrode used had the following characteristics: $m = 1.9$ mg s^{-1} at $h = 50$ cm, $t_1 = 4.2$ s, controlled drop time $t = 2.0$ s.

The cyclic voltammetry (CV) curves (Figure 1) were obtained with a hanging mercury drop electrode ($A = 3$ mm^2) using the Model 433-A trace analyzer (Amel Instruments, Milano, Italy).

Chemicals and Solutions. Sodium salts of chenodeoxycholic and deoxycholic as well as hyodeoxycholic acids were obtained from Sigma (St. Louis, MO); ursodeoxycholic acid was a gift from Alfa-Wasserman (Bologna, Italy). All compounds were used as delivered. Copper(II), lead(II), cadmium(II), and zinc(II) nitrates were analytical grade from Carlo Erba (Milano, Italy).

Stock solutions of bile salts were prepared freshly, usually less than 24 h before the experiment, using oxygen-free distilled water, either by dissolution of a sodium salt or by dissolution of an appropriate quantity of the acid in sodium hydroxide solution to maintain a small fraction of the acid in the free form, in order to control the final pH of the solution. The final pH of all solutions, after being filtered through a 0.45 μm Millipore disk, was 7.80.

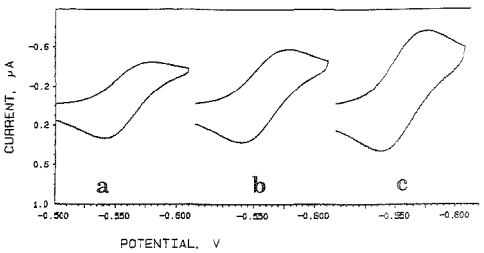

Figure 1. Cyclic voltammograms for the system: 1×10^{-4} M Cd^{2+}, 1×10^{-3} M deoxycholate, and 0.15 M $NaNO_3$ at 25 °C: (a) 50, (b) 100, (c) 200 mV/s; slowly dropping DME, natural $t_1 = 14.2$ s, delay 5 s.

Procedures. Solutions containing 1×10^{-4}–1×10^{-1} M bile salt and 1.10^{-4} M divalent metal ion, in which the ionic strength was adjusted by addition of sodium nitrate to $\mu = 0.15$, were equilibrated by shaking for 24 h. These solutions were then deoxygenated with a stream of nitrogen, and polarographic current–voltage were curves recorded. For evaluation of the free metal ion concentration, the ratio of the limiting current (i) in the presence of bile salt to the limiting current governed by diffusion (i_d), recorded in the absence of bile salt, was used. Unbuffered solutions were investigated in this study to avoid introduction of additional ligands; pH values of these solutions were adjusted (when necessary) to 7.8. At this pH, all the acids are in their ionized forms, and the metal(II) ions do not precipitate as hydroxides. This follows for solutions of Cd^{2+} and Zn^{2+} from reported[11] pH limits at which precipitation of hydroxide in unbuffered solution occurs (pH 7.9 for Cd^{2+} and 7.8 for Zn^{2+} at 1×1.0^{-4} M M^{2+}). For Cu^{2+} (pH 6.5) and Pb^{2+} (pH 7.2), the onset of precipitation is evidently shifted to higher pH in the presence of bile salts acting as surfactant. This has been proved by identical wave heights of Cu^{2+} and Pb^{2+} ions in the presence of 0.1 mM bile salts at pH 7.8 and in solutions at pH 3 in the absence of bile salts. Reversibility of the reduction process has been confirmed by CV (Figure 1).

The reported values of half-wave potentials, measured relative to that of Tl^+ ions as internal standard, are accurate to 0.005 V and are reported vs SCE. The limiting currents were measured with an accuracy of 5%. The values of overall equilibrium constants K_i and K_j are reproducible to 0.2 pK units (from triplicate sets of experiments). The estimates of concentrations corresponding to the edges of individual concentration ranges have an uncertainty of 0.2 pBS (where pBS = −log $[BS^-]$).

RESULTS

Polarographic limiting currents of reductions of metal(II) ions in the presence of bile salts (BS^-) are proportional to the concentration of free M^{2+} aquo ions. Denoting the current at a given $[BS^-]$ as i and the diffusion current in the absence of BS^- (or at $[BS^-] < 0.1$ mM) as i_d, the ratio i/i_d can be plotted as a

(10) Fini, A.; Feroci, G.; Fazio, G.; Zuman, P. *Eur. J. Pharm. Sci.*, submitted for publication.

(11) Kolthoff, I. M., Elving, P. J., Eds. *Treatise on Analytical Chemistry*, 2nd ed.; J. Wiley: New York, 1983; Part I, Vol. 3, pp 384 and 385.

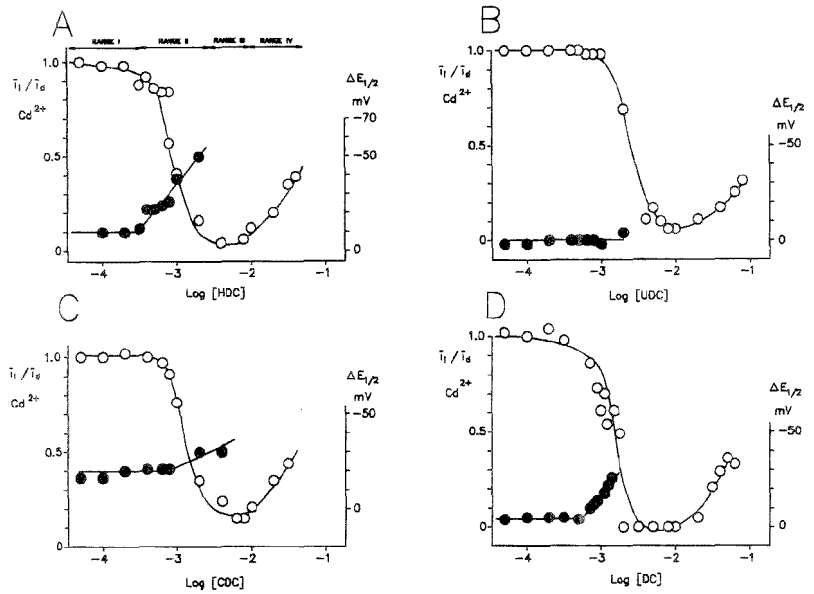

Figure 2. Dependence of the relative limiting current (i/i_d) (○, left-hand scale) and half-wave potential changes ($E_{1/2}$) (●, right-hand scale) in solution of 1×10^{-4} M Cd^{2+} and 0.15 M $NaNO_3$ on the concentration of the bile salt: (A) for hyodeoxycholate, (B) for ursodeoxycholate, (C) for chenodeoxycholate, and (D) for deoxycholate at 25 °C.

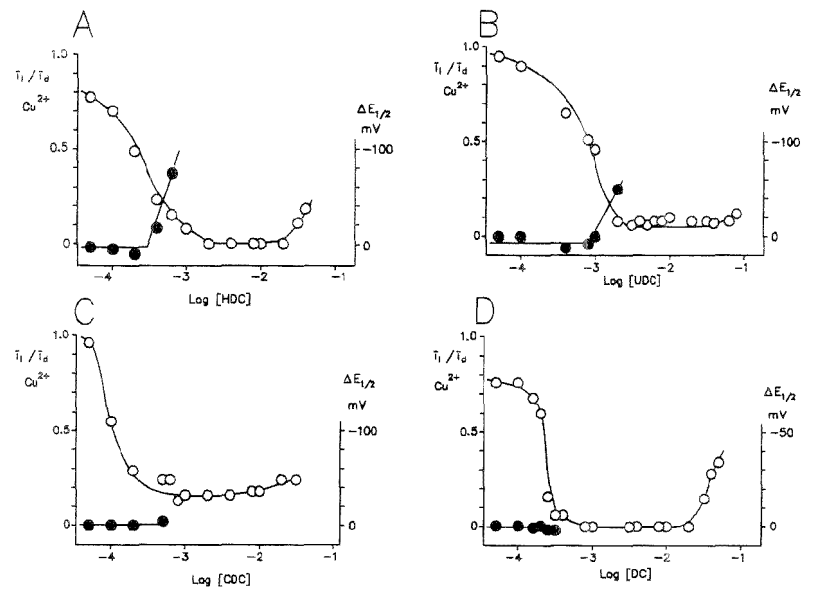

Figure 3. Dependence of the relative limiting current (i/i_d) (○, left-hand scale) and half-wave potential changes ($E_{1/2}$) (●, right-hand scale) in solution of 1×10^{-4} M Cu^{2+} and 0.15 M $NaNO_3$ on the concentration of the bile salt: (A) for hyodeoxycholate, (B) for ursodeoxycholate, (C) for chenodeoxycholate, and (D) for deoxycholate at 25 °C.

function of log [BS^-] (Figures 2–5). On these plots, it is possible to distinguish up to four ranges (Figure 2A). For some combinations of bile salts and M^{2+}, all four ranges I–IV can be observed. In other combinations, range I or III can be rather narrow, and in some, range IV cannot be reached within the accessible range of [BS^-] (Figure 4D).

In Figures 2–4, only the half-wave potentials of waves corresponding to electrolysis resulting in a rapidly established equi-

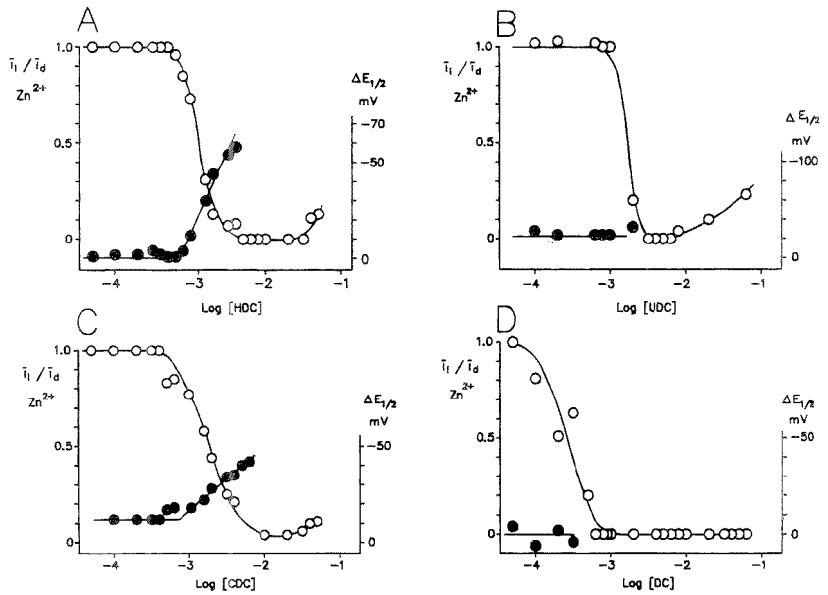

Figure 4. Dependence of the relative limiting current (i/i_d) (○, left-hand scale) and half-wave potential changes ($E_{1/2}$) (●, right-hand scale) in solution of 1×10^{-4} M Zn^{2+} and 0.15 M $NaNO_3$ on the concentration of the bile salt: (A) for hyodeoxycholate, (B) for ursodeoxycholate, (C) for chenodeoxycholate, and (D) for deoxycholate at 25 °C.

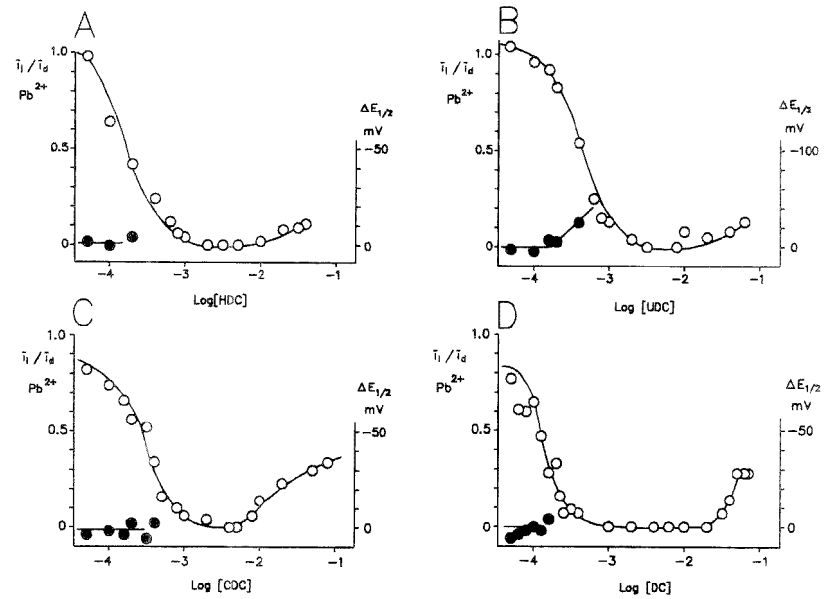

Figure 5. Dependence of the relative limiting current (i/i_d) (○, left-hand scale) and half-wave potential changes ($E_{1/2}$) (●, right-hand scale) in solution of 1×10^{-4} M Pb^{2+} and 0.15 M $NaNO_3$ on the concentration of the bile salt: (A) for hyodeoxycholate, (B) for ursodeoxycholate, (C) for chenodeoxycholate, and (D) for deoxycholate at 25 °C.

librium between the oxidized and reduced forms of the metal (called "reversible") are given for Cu^{2+}, Cd^{2+}, and Pb^{2+}. Only for such reversible systems is it possible to obtain information about thermodynamic quantities from variations of half-wave potentials. The values of half-wave potentials at higher [BS^-], where the reduction is irreversible, were not included. Such

values have no simple physical meaning. Since the reduction of Zn^{2+} ions is only quasireversible, half-wave potentials in Figure 5 indicate only trends in the ease of reduction. Information obtained from limiting currents is independent of the rate of the electrode process. The limiting current changes offer information about chemical reactions occurring in the studied solutions independent of the electrode process being reversible or irreversible.

The changes of limiting currents and half-wave potentials in individual ranges can be described as follows:

Range I. The limiting current does not change with increasing concentration of the bile salt, and the half-wave potential of the reduction of the metal ion remains unchanged.

Range II. A decrease of the limiting current with increasing concentration of the bile salt is observed. Simultaneously, in the majority of cases, a shift of the half-wave potential to more negative values with increasing concentration of the bile salt occurs. In this range, solutions become turbid, indicating formation of slightly soluble compounds, formed by the interaction of bile salts and metal ions, which are in equilibrium with soluble species.

Range III. Limiting currents attain the smallest value and remain independent of concentration of the bile salt. The intensity of the current in this range is directly proportional to the solubility of the compound formed by the interaction of the bile salt and the metal(II) ion. In some instances, where the solubility is very low, the intensity of the current in this range of concentration of the bile salt limits to zero. In this range, the reduction of the metal ion becomes irreversible, probably due to a surface coverage of the electrode by slightly soluble species; hence, the half-wave potentials measured do not have a simple physical meaning. In this range, solutions also remain turbid.

Range IV. The limiting currents of metal(II) ions increase with increasing concentration of the bile salt. Simultaneously, the turbidity of the solution decreases, and in some instances the solution becomes translucent. The half-wave potentials are shifted to more negative values with increasing concentration of the bile salt, but the reduction remains irreversible, preventing simple correlation between these shifts and the complex formation.

Based on experimental results, the interactions of metal(II) ions with studied dihydroxy bile salts can be described by the following equations:

$$M^{2+}(\text{solution}) + 2e \rightleftharpoons M(0)(Hg) \quad (1)$$

$$n BS^-(\text{solution}) \rightleftharpoons (BS)_n^{n-}(\text{solution}) \quad \text{fast} \quad (2)$$

$$(BS)_n^{n-}(\text{solution}) + M^{2+}(\text{solution}) \rightleftharpoons M(BS)_n^{(n-2)-}(\text{solution}) \quad \text{fast} \quad (3)$$

$$p BS^-(\text{solution}) \rightleftharpoons (BS)_p^{p-}(\text{solution}) \quad \text{fast} \quad (4)$$

$$(BS)_p^{p-}(\text{solution}) + M^{2+}(\text{solution}) \rightleftharpoons M(BS)_p^{(p-2)-}(\text{solution}) \quad \text{fast} \quad (5)$$

$$M(BS)_p^{(p-2)-}(\text{solution}) + (p-2)Na^+(\text{solution}) \rightleftharpoons M(BS)_pNa_{(p-2)}(\text{solid}) \quad \text{slow} \quad (6)$$

$$M(BS)_pNa_{(p-2)}(\text{solid}) + r BS^-(\text{solution}) + r Na^+(\text{solution}) \rightleftharpoons M(BS)_{(p+r)}Na_{(p+r-2)}(\text{solid}) \quad (7)$$

$$M(BS)_{(p+r)}Na_{(p+r-2)}(\text{solid}) \rightleftharpoons M(BS)_{(p+r)}^{(p+r-2)-}(\text{solution}) + (p+r-2)Na^+(\text{solution}) \quad (8)$$

$$(BS)_p^{p-}(\text{solution}) + r BS^-(\text{solution}) \rightleftharpoons (BS)_{(p+r)}^{(p+r)-}(\text{solution}) \quad (9)$$

$$(BS)_{(p+r)}^{(p+r)-}(\text{solution}) + M^{2+}(\text{solution}) \rightleftharpoons M(BS)_{(p+r)}^{(p+r-2)-}(\text{solution}) \quad (10)$$

In range I, the equilibrium 3 is shifted to the left, most probably because the equilibrium 2 is also shifted to the left. Hence, the reduction of metal ions M^{2+} following reaction 1 is not affected by the presence of the bile salt, and consequently, the half-wave potential and the limiting current are both independent of $[BS^-]$.

In range II, equilibria 2–5 are shifted to the right. As equilibria 2 and 3 are rapidly established, the half-wave potential of reduction of reaction 1 is shifted to more negative potentials with increasing concentration of the bile salt. As long as the reduction occurs reversibly, the shift of the half-wave potential ($E_{1/2}$) follows eq 11:

$$E_{1/2} = (E_{1/2})_{aq} + \frac{0.059}{2} \log \frac{K_i}{K_i + [BS^-]^n} \quad (11)$$

where $(E_{1/2})_{aq}$ is the potential of the reduction of M^{2+} in the absence of the bile salt and K_i is the equilibrium constant corresponding to reaction 3, defined as

$$K_i = [Me^{2-}][(BS)_n^{n-}]/[M(BS^-)_n^{(n-2)}]$$

At $[BS^-] \gg K_i$, eq 11 simplifies to

$$E_{1/2} = \text{const} - 0.029n \log [BS^-] \quad (12)$$

Thus, the plot of $E_{1/2} = f(\log [BS^-])$ consists of two linear segments with an intersection at $-\log [BS^-] = pK_i$.

In range III, equilibrium 6 is partly shifted to the right. Because the equilibrium between $M(BS)_pNa_{(p-2)}$ in the precipitate and the oligomer $(BS)_p^{p-}$ in the solution is established slowly relative to the time window of the measurement (typically 3 s), the decrease in current in this range is a measure of the concentration of the free M^{2+} aquo ions in these solutions.

For a slowly established heterogeneous equilibrium, it is possible to derive for the current i (relative to the current i_d observed in the absence of the bile salt or the current measured in range I) expression 13,

$$i/i_d = K_j/(K_j + [BS^-]^p) \quad (13)$$

where

$$K_j = [Me^{2+}][(BS)_p^{p-}][M(BS)_p^{(p-2)-}]$$

Therefore, the plot of i/i_d as a function of $\log [BS^-]$ has a dissociation curve with an inflexion point at $-\log [BS^-] = pK_j$.

The steepness of this dissociation curve depends on the number of participating bile salt anions, p.

Available experimental data indicate that in some cases $pK_i = pK_j$ and $n = p$. In such cases, the complex which is predominant in the solution is also the least soluble one. In other instances, $pK_i \neq pK_j$ and $n \neq p$, indicating that a complex other than the least soluble one predominates in the solution.

In range III, all equilibria 2–6 are shifted to the right. Under these conditions, concentrations of M^{2+}, $M(BS)_n^{(n-2)-}$, and $M(BS)_p^{(p-2)-}$ are all low. The concentration of the free metal ion M^{2-}, and hence the limiting current of M^{2+}, are governed by the solubility product, $K_{sp} = [M^{2+}][BS^-]^p$. The transport to the electrode involves both free ions M^{2+} and soluble complex anions, $M(BS)_n^{(n-2)-}$ and $M(BS)_p^{(p-2)-}$. For n and p in the expected range between 1 and 4, the differences in the diffusion coefficients do not affect substantially the ratio i/i_d, partly because the ratio of diffusion coefficients is a small value, and partly because the relationship involves the diffusion coefficients in a square root.

In range IV, a solubilization of the precipitate takes place. This can be achieved, in principle, in two ways: (a) Anions of the bile salt can add to the slightly soluble compound $M(BS)_pNa_{(p-2)}$ in reaction 7. This is followed by a shift of equilibrium 8 to the right. (b) Alternatively, a larger aggregate $(BS)_{(p+r)}^{(p+r)-}$ is formed in the solution in reaction 9, which can form a larger complex species in reaction 10. As the species $M(BS)_{(p+r)}^{(p+r-2)}$ has a more negative charge due to a larger number of free carboxylic groups not bound bound to the metal than $M(BS)_p^{(p-2)-}$, the larger species is more soluble. Dissolved complex $M(BS)_{(p+r)}^{(p-r-2)-}$ is in a rapidly established equilibrium—reversed reaction 10—with the reducible ions M^{2+}.

Changes in the polarographic limiting current are paralleled by changes in the turbidity of the reaction mixture. In range I, solutions remain translucent. Turbidity increases in range II, reaches its maximum in range III, and decreases in range IV, where at sufficiently high concentration of BS^-, solutions become translucent.

Investigated systems can be characterized by several quantities:

(a) The value of log $[BS^-]$ at which the two linear segments of the $E_{1/2} = f(\log [BS^-])$ plots intersect (if accessible). This value corresponds according to eq 11 to the value of pK_i.

(b) The slope of the $E_{1/2} = f(\log [BS^-])$ plot ($dE_{1/2}/dpBS = 0.029n$). At $pBS > pK_i$, this offers information about the number of BS^- bound to a M^{2+} ion, provided that the electrode process is reversible and effects of adsorption can be neglected.

(c) The value of pBS at which the dependence of i/i_d on log $[BS^-]$ shows an inflection point of the dissociation curve. At this pBS, $i/i_d = 0.5$, and the value of $-\log [BS^-] = pK_j$.

(d) The slope of a tangent to the plot of $i/i_d = f(\log [BS^-])$ at the inflection point. This offers information about the number (p) of bile salt anions bound to the metal ion in the slightly soluble compound $M(BS)_pNa_{(p-2)}$.

All the data in a–d can be obtained in range II.

(e) The limiting current in range III, which is proportional to the concentration of the free metal M^{2+}. This enables determination of the solubility of $M(BS)_pNa_{(p-2)}$ and solubility product K_{sp} (if the value of p is known).

Apart from these quantitative data, two semiquantitative types can be obtained:

(f) The concentration of bile salt at which the first decrease in limiting current is observed. This can be considered as the lower edge of range II. This value offers semiquantitative information about equilibria 4–6.

(g) The concentration of bile salt where, at concentration higher than that corresponding to range III, the current of reduction of M^{2+} shows the first increase. This concentration can be considered as the lower edge of range IV and offers semiquantitative information about equilibria 7 and 8 or 9 and 10, respectively.

Values of pK_i obtained from shifts of half-wave potentials and offering information about reactions 2 and 3 are, in most instances, practically equal to values of pK_j obtained from the decrease in limiting currents, corresponding to reactions 4–6. As discussed in more detail below, that means that at $n = p$, the same complex predominates in the bulk of the solution and in the precipitate, and the sequence of reactions corresponding to processes in ranges II and III simplifies to reactions 1, and 4–6.

The shapes of the $i/i_d = f(\log [BS^-])$ plots indicate that, in some instances, a single complex with a given p predominates, while in others several complexes are present simultaneously. In a complex system like the one involved, which might be further complicated by mixed complexes involving hydroxo ligands, qualitative agreement of experimental data with the predicted shape of $i/i_d = f(\log [BS^-])$ plots is the best that can be expected.

Similarly, eqs 7–10 qualitatively describe the increase in current in range IV and are in accordance with conversion of a slightly soluble species into a well soluble species. No information is available to decide whether formation of larger, soluble aggregates results from additions of BS^- anions to the precipitate following reactions 7 and 8 or whether formation of larger aggregates (reaction 9), observed in the absence of bile salts, is followed by their reaction with M^{2+} ions (reaction 10). The proposed interpretation is supported by formation of soluble large aggregates in solutions containing only Na^+ ions.[12]

Data available for dihydroxy bile acid anions are summarized in Table 1.

DISCUSSION

Comparison of Figures 2–5 and data for individual systems (Table 1) indicates that, for all systems, principally four situations occur. At sufficiently low concentration of the bile salt, where monomers predominate, there is little interaction between the metal ion and the bile acid anions. In range II, roughly between 0.1 and 10 mM bile salt, both soluble complexes and slightly soluble species are formed. It is assumed that, in this range, small aggregates (dimers to tetramers, premicellar species) are formed which interact with divalent metal ions. For these aggregates, where the two carboxylate groups are located close to each other, the interaction with metal ion results in a slightly soluble precipitate. In the majority of cases studied, the values of pK_j obtained from the decrease in current (Table 1) and characterizing the slowly established equilibrium between metal ions in the solution and metal ions bound in a precipitate are similar to the values of pK_i obtained from shifts of half-wave potentials, reflecting the rapidly established equilibrium between aquo ions of metals and labile complexes. This indicates that the soluble labile complexes which predominate in the solution have practically the

(12) Reference 1, pp 52–54.

Table 1. Quantities Characterizing Interactions of Bile Acids Anions with Metal(II) Ions[a]

	range II concn,[b] mM	pK_j[c]	pK_i[d]	slope,[e] mV	solubility,[f] mM	range IV concn,[g] mM
			Compounds with Cu^{2+}			
HDC	~0.05	3.5	3.5		~0.02	20
CDC	~0.05	3.9	3.4		0.18	10
UDC	0.1	3.0	3.0		0.08	70
DC	0.1	3.6	<3.5		0.01	20
			Compounds with Cd^{2+}			
HDC	0.3	3.1	3.5	60	0.03	10
CDC	0.5	2.9	3.1	20	0.05	10
UDC	1.0	2.6	2.9		0.06	10
DC	0.3	2.8	3.3	45	<0.01	10
			Compounds with Pb^{2+}			
HDC	~0.05	3.7	3.8		<0.01	5
CDC	~0.05	3.5	3.5		<0.01	5
UDC	~0.05	3.3	3.8	80?	<0.01	7
DC	~0.05	3.9	3.8		<0.01	20
			Compounds with Zn^{2+}			
HDC	0.4	3.0	2.2	85	<0.01	30
CDC	0.4	2.8	3.1	35	0.03	20
UDC	0.9	2.8	2.8		<0.01	6
DC	~0.05	3.6	<3.4		<0.01	60

[a] Bile salts: HDC, hyodeoxycholate (3α,6α-di-hydroxy); CDC, chenodeoxycholate (3α,7α-dihydroxy); UDC, ursodeoxycholate (3α,7β-dihydroxy); DC, deoxycholate (3α,12α-dihydroxy). [b] Upper concentration limit in range II. [c] $pK_j = -\log [BS^-]$, where $i/i_d = 0.5$. [d] $pK_j = -\log [BS^-]$, corresponding to the intersection of the two linear segments of the $E_{1/2} = f(\log [BS])$ plot. [e] $dE_{1/2}/d \log [BS]$. [f] From limiting current of M^{2+} in range III. [g] Lowest concentration limit of range IV.

Table 2. Comparison of Stability Constant of Reaction of Acetate Ions and Anions of Some Dicarboxylic Acids with Metal(II) Ions with pK_j Values Obtained for Dihydroxy Bile Acid Anions

	Reactions of Acetate Ions[a]			
	$-\log K_1$[b]	$-\log \beta_2$[c]	$-\log \beta_3$[d]	$-\log \beta_4$[e]
Zn^{2+}	0.9	1.2	1.6	1.4
Cd^{2+}	1.0	1.5	1.8	1.7
Cu^{2+}	1.7	2.6	2.6	2.5
Pb^{2+}	2.1	3.3	4.9	

	Reaction of Anions of Dicarboxylic Acids (pK_1[b])			
	Su[f]	Ma[g]	Ox[h]	Cyc[i]
Zn^{2+}	2.3	3.0	3.5	2.3
Cd^{2+}	1.4	2.1	2.7	
Cu^{2+}		5.0	4.5	4.4
Pb^{2+}	2.4	2.6	7.0	

	Reaction of Dihydroxy Bile Acid Anions (pK_j[j])			
	HDC[k]	CDC[l]	UDC[m]	DC[n]
Zn^{2+}	2.2	3.1	2.8	3.6
Cd^{2+}	3.3	3.1	2.9	2.8
Cu^{2+}	3.5	3.9	3.0	3.6
Pb^{2+}	3.7	3.5	3.3	3.9

[a] Mean values, ref 13. [b] $K_1 = [M(Ac)^+]/[M^{2+}][Ac^-]$. [c] $\beta_2 = [M(Ac)_2]/[M^{2+}][Ac^-]^2$. [d] $\beta_3 = [M(Ac)_3^-]/[M^{2+}][Ac^-]^3$. [e] $\beta_4 = [M(Ac)_4^{2-}]/[M^{2+}][Ac^-]_4$. [f] Succinic acid, $HOOC(CH_2)_2COOH$. [g] Malonic acid, $HOOCCH_2COOH$. [h] Oxalic acid, $(HOOC)_2$. [i] Cyclohexane-1,2-dicarboxylic acid. [j] $pK_j = -\log [BS^-]$, where $i/i_d = 0.5$. [k] Hyodeoxycholate. [l] Chenodeoxycholate. [m] Ursodeoxycholate. [n] Deoxycholate.

same composition as the species which are in equilibrium with solid particles of the precipitate.

The data in range II, obtained from measurements of current (pK_j), are more reliable than those obtained from the shifts of half-wave potentials (pK_i), which can be affected by adsorption phenomena. The values of pK_j are therefore used in the comparison with values of stability constants for complex formation of M^{2+} ions with acetates and anions for some dicarboxylic acids[13] (Table 2). The negative logarithms of stability constants for reactions with one, two, three, or four acetate ions with M^{2+} all increase in the same sequence, $Zn^{2+} < Cd^{2+} < Cu^{2+} < Pb^{2+}$, indicating increasing stability of the Me−O bonds. For HDC and UDC, the values of pK_j (which are significantly larger than those for acetate) increase in the same sequence. Principally the same sequence is observed also for CDC and DC with two exceptions: for CDC the value for interaction with Cu^{2+} and for DC the value for reaction with Zn^{2+} are both larger than expected only on the basis of the affinity to form the Me−O bond. Some additional factors seem to play a role, the nature of which has not been identified.

For dicarboxylic acid anions (Table 2), the reactivity of Zn^{2+} ions is in all instances larger than that of Cd^{2+}, contrary to the sequence observed for acetates, HDC, CDC, and UDC. For succinic and malonic acids, the reactivity of Pb^{2+} is smaller than expected on comparison with acetate ions. It should be considered that in chelate complexes, additional factors can play a role. One of them is ring strain, the other a mutual interaction of the two carboxylate groups, transmitted either by induction effects through the methylene groups or by resonance effects operating in oxalate ions. Studied dicarboxylic acids are thus not the most suitable models for comparison with reactions of bile salts. A better model would be anions of cyclohexane-1,2-dicarboxylic acids, but data for their complex formation with metal(II) ions are currently not available for all ions studied. It can be concluded that the affinity of COO^- groups for individual Me^{2+} ions plays the most important role for their reactions with both acetates and bile salts in solutions.

Effects of structure on solubility are more difficult to interpret. Changes in solubility depend mainly on variations of interactions both in the solid and liquid phase. In the solid phase, variations in lattice energies and possibly even the type of lattice involved will depend on stacking of sterol complexes. In solutions, the factors affecting the solvent−solute interactions will include solvation of bile salt anions, their oligomers, metal ions, and resulting soluble complexes. Such interactions will be affected by the aggregation of both bile salts and complexes of M^{2+} ions, with aggregates bearing two COO^- groups close to each other being of particular importance.

The effect of the structure of anions of bile salts on the solubility of their complexes with M^{2+} can be interpreted predominantly in terms of the size and structure of small aggregates of BS^-. There is little reliable information available concerning the number of anion units in these small aggregates (usually considered to be dimers to tetramers) and on forces binding them together. Such forces can be a manifestation either of hydrogen bonding between hydroxy groups of adjacent molecules or of interaction between hydrophobic portions of individual steroid molecules.

(13) Perrin, D. *Stability Constant of Metal−Ion Complexes, Part B, Organic Ligands*; Pergamon Press: Oxford, 1979.

Table 3. Comparison of Hydrophobic Parameters with the Solubility of Products of Reactions of Metal(II) Ions with Bile Salts

bile salts	hydrophobic parameters: log P'_{HA}[a]	log P'_{HA^-}[a]	HI_{HA}[b]	HI_{A^-}[b]	solubility, mM: H^+[c]	Cu^{2+}	Cd^{2+}	Zn^{2+}	Pb^{2+}
HDC	3.08	2.28			0.015	0.02	0.03	<0.01	<0.01
CDC	3.28	2.25	1.37	0.59	0.027	0.18	0.05	0.03	<0.01
UDC	3.00	2.20	0.49	−0.31	0.009	0.08	0.06	<0.01	<0.01
DC	3.50	2.65	1.46	0.72	0.028	<0.01	<0.01	<0.01	0.01

[a] Data from ref 12. P'_{HA} is the intrinsic partition coefficent of the acid: P'_{A^-} is the intrinsic partition coefficient of the anion for the 1-octanol−water mixture. [b] Data from ref 13. HI_{HA} is the hydrophobicity index of the acid; HI_{A^-} is the hydrophobicity index of the anion obtained from HPLC data. [c] Data from ref 14. Solubility of bile acid in water at pH 3.0.

Were the hydrogen bonding the predominant effect, the aggregation and thus the complex formation would be strongly dependent on the number of hydroxy groups in the steroid molecule and their stereochemistry. Our experiments indicate relatively small differences between the solubilities of metal(II) complexes with the dihydroxy bile salts studied in this work and those of the trihydroxy bile salt complexes reported earlier.[7-9] Predominant roles of hydrogen bonding would also be reflected in a principal difference between complexes of CDC and UDC, which differ in stereoisomerism of the hydroxy groups in position 7. Data observed for reaction of Cd^{2+} and Pb^{2+} indicate similar solubility of complexes with CDC and UDC, and the differences observed for the reactions of Cu^{2+} and Zn^{2+} are relatively small. It can be concluded that hydroxy bonding is not the predominant factor affecting solubilities of complexes of BS^- with M^{2+}.

To evaluate the role of the hydrophobicity of the bile salts on the solubilities of the products of their reactions with M^{2+} ions, comparison with the hydrophobic indexes[14,15] is used. These indexes (Table 3) increase in the sequence UDC < HDC < CDC < DC. In accord with this sequence, products of reactions of M^{2+} with DC are the least soluble among investigated compounds (Table 3). On the other hand, for the remaining three bile salts, there seems to be no correlation between hydrophobicity indexes[14,15] of individual acids and the solubilities of their compounds with M^{2+}. The solubility of the undissociated bile acids[16] increases with increasing hydrophobicity index (Table 3). But there is no simple correlation between the hydrophobicity of the bile salt and the solubilities of its compounds with divalent metal ions.

The predominant factor governing the solubility of $M(BS)_pNa_{(p-2)}$ is the nature of the metal(II) ion. The solubility decreases in the sequence $Cd^{2+} > Cu^{2+} > Zn^{2+} > Pb^{2+}$, similarly as observed for corresponding oxalates (Table 4)[17]. For UDC and CDC, the solubility of compounds with Cd^{2+} is smaller than expected. This sequence is different from that of the affinity of the metal(II) to form a Me−O bond, which governs the stability of complexes of bile salts in the solution.

To interpret better the dependence of solubility on the nature of the metal(II) involved, it would first be necessary to ascertain

Table 4. Comparison of the Solubility of Metal(II) Oxalate with the Solubilities of the Products of Reaction of Metal(II) Ions with Bile Acid Anions (Solubilities in Millimolar Concentration)

M^{2+}	oxalate[a]	HDC[b]	CDC[c]	UDC[d]	DC[e]
Cd^{2+}	0.20	0.03	0.05	0.06	<0.01
Cu^{2+}	0.17	0.02	0.18	0.08	<0.01
Zn^{2+}	0.05	<0.01	0.03	0.01	<0.01
Pb^{2+}	0.05	<0.01	<0.01	<0.01	<0.01

[a] Data from ref 15. [b] Hyodeoxycholate. [c] Chenodeoxycholate. [d] Ursodeoxycholate. [e] Deoxycholate.

Table 5. Comparison of the Concentrations at Which the Precipitates of the Metal(II) Compounds with Small Aggregates of Bile Salts Begin To Dissolve with Reported Values of cmc

bile salts	cmc[a]: H_2O	0.15 M NaCl	concn at the beginning of range IV[b]: Cu^{2+}	Cd^{2+}	Zn^{2+}	Pb^{2+}
HDC[c]	14	6	20	10	30	5
CDC[d]	9	4	10	10	20	5
UDC[e]	19	7	70	10	6	7
DC[f]	10	3	10	10	>60	20

[a] Data from ref 16. [b] The lowest concentration at which an increase in limiting current of M2+ was observed. [c] Hyodeoxycholate. [d] Chenodeoxycholate. [e] Ursodeoxycholate. [f] Deoxycholate.

that the composition of precipitate $M(BS)_pNa_{(p-2)}$ is the same for all bile salts studied. Attempts are therefore currently being made to determine the content of metal in the precipitates formed. This approach is, nevertheless, complicated by the colloidal character of the resulting products. To achieve the formation of a precipitate, the reaction of M^{2+} with BS^- must be carried out in the presence of an excess of BS^-. Under such conditions, some of the BS^- ions present in excess are adsorbed on the precipitate of $M(BS)_pNa_{(p-2)}$. Consequently, analyzed products will not have stoichiometric composition. The determination of the content of the metal in the precipitate hence does not offer information about the number of ligands, p.

Finally, the conditions accompanying the dissolving of the precipitate at sufficiently high concentrations of bile salt will be discussed (Table 5). The concentration at which the increase in current is first observed is considered to be the lower limit of range IV. This concentration is of the same order of magnitude as the reported[18] values of the cmc. These cmc values probably represent a concentration at which larger aggregates $(BS)_n^{n-}$ (consisting of ~5−10 units) are formed. Differences between the limit of range IV and cmc values can be attributed to differences in solubilities of $(BS)_n^{n-}$ and $M(BS)_pNa_{(p-2)}$. These, in turn, are affected by the differences in the interaction of both anions with the solvent and by the variations in strength of the interaction in the solid state. Any comparison can be further complicated by differences in the predominant number of bound ligands $(p - r)$ for individual metal ions.

To summarize, small aggregates (dimers, trimers, or tetramers) of bile salts react with M^{2+} ions and form complexes which are slightly soluble. The solubilities of these compounds depend primarily on the nature of the metal(II) and its affinity for

(14) Roda, A.; Minutello, A.; Angellotti, M. A.; Fini, A. *J. Lipid Res.* **1990**, *31*, 1433−1442.
(15) Neuman, D. M. *J. Lipid Res.* **1989**, *30*, 719−730.
(16) Fini, A.; Roda, A.; Fugazza, R.; Grigolo, B. *J. Solution Chem.* **1985**, *14*, 595−603.
(17) *Handbook of Chemistry and Physics*, 67th ed.; CRC Press: Boca Raton, FL, 1986.
(18) Roda, A.; Hofmann, A. F.; Mysels, K. J. *J. Biol. Chem.* **1983**, *258*, 6362−6370.

carboxylate groups. The decrease of solubility in the sequence $Cd^{2+} > Cu^{2+} > Zn^{2+} > Pb^{2+}$ parallels that observed for corresponding oxalates. To a lesser degree, the solubility of formed species depends on the nature of the bile salt, the deoxycholates forming the least soluble species. The observed differences are attributed primarily to differences of stacking of bile salt molecules in small aggregates. No simple relationship to the hydrophobicity of the bile salt and the solubility of $M(BS)_pNa^{(z-2)}$ has been found. The concentration of bile salt at which larger, more soluble aggregates are formed was found to be in a range similar to that in which cmc values have been reported. The nature of the metal ion included in the aggregate affects structure and possibly composition of soluble aggregates.

ACKNOWLEDGMENT

This work was supported by Murst Funds.

Received for review May 23, 1994. Accepted July 25, 1995.[⊗]

AC940519B

[⊗] Abstract published in *Advance ACS Abstracts*, September 1, 1995.

Anal. Chem. **1995**, *67*, 4086–4090

Voltammetric Studies of Carbon Disk Electrodes with Submicrometer-Sized Structural Diameters

Danny K. Y. Wong* and Lisa Y. F. Xu

School of Chemistry, Macquarie University, Sydney, New South Wales 2109, Australia

A procedure for the fabrication of carbon disk electrodes with tip diameters approaching 100 nm is described. In this procedure, quartz capillaries are initially pulled down to a small tip by a horizontal micropipet puller. A high gas pressure (900 kPa) is then applied to force methane gas through the pulled capillary while it is being pyrolyzed. A prolonged pyrolysis duration (4 min) is employed to form a carbon deposit at the tip of the capillary in order to construct a carbon disk electrode. Electrical contact is then made between the carbon deposit and a nichrome wire via a small pool of mercury inside the capillary. Hence, unlike the construction procedures for many other microelectrodes, there is no epoxy sealing, cutting, or beveling of electrodes needed in the fabrication procedure for ultrasmall carbon disk electrodes. The fabricated electrodes are then characterized by cyclic voltammetry in a dopamine solution, showing a well-defined sigmoidal response for the oxidation of dopamine with minimal background charging current. The absence of epoxy resin at the tip of carbon disk electrodes also permits electroanalysis in nonaqueous media.

Microelectrodes are often used in many voltammetric studies owing to several advantageous features over conventionally sized electrodes.[1-5] Some of these features include reduced ohmic drop, enhanced mass transport, and discrimination against charging currents.

A number of microelectrodes of different geometries have now been reported in the literature.[3] These include microdisk and arrays of microdisks, microband, microcylinder, and ultrathin ring electrodes. Also, disk-shaped electrodes with radii as small as 10 Å to 20 μm have been constructed.[6] While many of these electrodes have very small areas, in general, they have considerably large total structural diameters, making them not suitable for use in such microenvironments as the extracellular region in the brain[7-12] and the cytoplasm of single cells,[13-18] where many neurotransmitters can be easily detected anodically. This prompted a number of research groups to construct electrodes with very small structural diameters. For example, Kelly and Wightman[19] beveled the surface of carbon fiber electrodes to a sharp tip (~10 μm) which showed enhanced faradaic currents. Kim et al.[20] reported an elegant procedure for constructing carbon ring electrodes with tip diameters approaching 1 μm by pyrolysis of methane inside pulled quartz capillaries. Similarly, Saraceno et al.[21] described a methodology involving a low-temperature pyrolysis of ethylene on nickel to fabricate carbon disk electrodes with ~1.8 μm tip diameters. More recently, Strein and Ewing[22] reported the construction of electrodes with an overall physical dimension as small as 400 nm by flame-etching carbon fibers to small tip diameters which were then insulated with a phenol–allylphenol copolymer. To date, only carbon fiber electrodes and ultrasmall carbon ring electrodes are often employed in extracellular voltammetry[7-12] and intracellular voltametry.[13-18] This is presumably due to the simple construction procedure and the higher fabrication success rate of these two types of electrodes. Also, these sharp electrodes facilitate smooth penetration into the specimen and minimize tissue damage along the track made by the electrode. In addition, Garguilo and Michael[23] pointed out the suitability of small modified electrodes, for example, by immobilizing enzymes and redox mediators in a cross-linkable polymer on the electrodes, to be used as an in vivo probe since leaching of the enzymes and redox mediators into the surroundings was minimal. These workers fabricated choline microsensors from carbon fibers (7 or 10 μm diameter and lengths of 200–400

(1) Wightman, R. M. *Anal.Chem.* **1981**, *53*, 1125A–1134A.
(2) Wightman, R. M. *Science* **1988**, *240*, 415–420.
(3) Wightman, R. M.; Wipf, D. O. In *Electroanalytical Chemistry*; Bard, A. J., Ed.; Dekker: New York, 1989; Vol. 15, pp 267–353.
(4) *Electroanalysis* **1990**, *2*, 175–262.
(5) Bond, A. M.; Oldham K. B.; Zoski C. *Anal. Chim. Acta* **1989**, *216*, 177–230.
(6) Penner, R. M.; Heben, M. J.; Longin, T. L.; Lewis, N. S. *Science* **1990**, *250*, 1118–1121.
(7) Baur, J. E.; Kristensen, E. W.; May, L. J.; Wiedemann, D. J.; Wightman, R. M. *Anal. Chem.* **1988**, *60*, 1268–1272.
(8) Wiedemann, D. J.; Kawagoe, K. T.; Kennedy, R. T.; Ciolkowski, E. L.; Wightman, R. M. *Anal. Chem.* **1991**, *63*, 2965–2970.
(9) Schroeder, T. J.; Jankowski, J. A.; Kawagoe, K. T.; Wightman, R. M.; Lefrou, C.; Amatore, C. *Anal. Chem.* **1992**, *64*, 3077–3083.
(10) Pihel, K.; Schroeder, T. J.; Wightman, R. M. *Anal. Chem.* **1994**, *66*, 4532–4537.
(11) Leszczyszyn, D. J.; Jankowski, J. A.; Viveros, O. H.; Diliberto, E. J., Jr.; Near, J. A.; Wightman, R. M. *J. Biol. Chem.* **1990**, *265*, 14736–14737.
(12) Wightman, R. M.; Jankowski, J. A.; Kennedy, R. T.; Kawagoe, K. T.; Schroeder, T. J.; Leszczyszyn, D. J.; Near, J. A.; Diliberto, E. J., Jr.; Viveros, O. H. *Proc. Natl. Acad. Sci. U.S.A.* **1991**, *88*, 10754–10758.
(13) Chen, T. K.; Luo, G.; Ewing, A. G. *Anal. Chem.* **1994**, *66*, 3031–3035.
(14) Meulemans, A.; Poulain, B.; Baux, G.; Tauc, L.; Henzel, D. *Anal. Chem.* **1986**, *58*, 2088–2091.
(15) Meulemans, A.; Poulain, B.; Baux, G.; Tauc, L. *Brain Res.* **1987**, *414*, 158–162.
(16) Lau, Y. Y.; Chien, J. B.; Wong, D. K. Y.; Ewing, A. G. *Electroanalysis* **1991**, *3*, 87–95.
(17) Lau, Y. Y.; Wong, D. K. Y.; Ewing, A. G. *Microchem. J.* **1993**, *47*, 308–316.
(18) Chien, J. B.; Saraceno, R. A.; Ewing, A. G. *Redox Chemistry and Interfacial Behavior of Biological Molecules*; ECS Symposium Series; Plenum Press: New York, 1988; pp 417–424.
(19) Kelly, R. S.; Wightman, R. M. *Anal. Chim. Acta* **1986**, *187*, 79–87.
(20) Kim, Y.-T.; Scarnulis, D. M.; Ewing, A. G. *Anal. Chem.* **1986**, *58*, 1782–1786.
(21) Saraceno, R. A.; Engstrom, C. E.; Rose, M.; Ewing, A. G. *Anal. Chem.* **1989**, *61*, 560–565.
(22) Strein, T. G.; Ewing, A. G. *Anal. Chem.* **1992**, *64*, 1368–1373.
(23) Garguilo, M. G.; Huynh, N.; Proctor, A.; Michael, A. C. *Anal. Chem.* **1993**, *65*, 523–528.

0003-2700/95/0367-4086$9.00/0

μm) to detect choline in extracellular fluid of brain tissues. Apart from carbon electrodes, ultrasmall platinum and gold electrodes can be conveniently constructed by depositing platinum[24] and gold[25] onto carbon ring electrodes. Also, Bond et al.[26] recently constructed copper microdisk electrodes from borosilicate-coated copper microwires (7 μm diameter copper wire insulated in a 5 mm outer diameter borosilicate glass tube), extending the range of microelectrode surfaces available.

In general, it is highly desirable to extend the techniques hitherto developed in intracellular voltammetry to systems involving mammalian neurons (~20 μm diameter). However, this is not easily accomplished, primarily due to the still relatively large structural dimensions of electrodes to date. By positioning beveled carbon electrodes adjacent to single bovine chromaffin cells in culture, Wightman and co-workers[11,12] detected a large increase in current spikes arising from apparent secretion of discrete packets of easily oxidized molecules from the cells. The results were shown to be consistent with direct chemical measurement of single exocytotic events. More recently, Chen et al.[13] amperometrically monitored the catecholamine exocytosis from single monoaminergic pheochromocytoma cells of rats using beveled carbon fiber electrodes placed very close to the cells. Thus, these investigations have shown the possibility of direct electrochemical observation of quantal release from mammalian cells. These investigations also show that there is a real need to devise a simple and convenient technique to construct yet smaller electrodes in order to probe such small biological environments.

In our attempt to fabricate ultrasmall electrodes, we initially adopted the procedure reported by Kim et al.[20] for constructing carbon ring electrodes. Briefly, the procedure involves first pulling quartz capillaries in a methane–oxygen flame down to a 1–5 μm tip. Pyrolysis of methane is then carried out on the inside wall of the pulled quartz capillaries. This procedure requires the use of quartz capillaries because the softening point of quartz is at temperatures above that for initial pyrolysis of methane. The tip of the capillary is then filled with epoxy, followed by a cut with a scapel to expose a thin carbon ring. Electrical contact to the carbon deposit is accomplished with mercury and a stainless steel wire. In our work, we discovered that quartz capillaries can be easily pulled to very small tips (<1 μm) using a horizontal pipet puller. As a result, these tips can be filled with carbon by a prolonged pyrolysis time, forming an ultrasmall carbon disk electrode. In addition, the carbon seems to form a relatively nonporous structure at the tip and it adheres onto the wall of the capillary. Hence, there is no epoxy sealing or cutting of electrodes involved in constructing the carbon disk electrodes. It is thus a relatively simple procedure to construct electrodes with submicrometer-sized structural diameters. This paper describes the optimum conditions required in the fabrication of ultrasmall carbon disk electrodes and voltammetric results obtained in the characterization experiments of these electrodes.

EXPERIMENTAL SECTION

Reagents. Dopamine (Sigma Chemicals), cobaltocenium hexafluorophosphate, and tetraethylammonium tetrafluoroborate (Aldrich Chemical Co.) were used without further purification. A pH 7.4 citrate–phosphate buffer solution was prepared with Milli-Q water (Milli-Q Reagent Water System) daily. Dopamine solution (1.0×10^{-4} M) was prepared in pH 7.4 citrate–phosphate buffer. Cobaltocenium cation solution (5.0×10^{-5} M) was prepared by dissolution of cobaltocenium hexafluorophosphate in two solvents, acetonitrile and dichloromethane, respectively, in 0.10 M Et_4NClO_4 as supporting electrolyte. These solutions were stirred for 2 h to dissolve the colbatocenium hexafluorophosphate. All solutions were purged with nitrogen for 20 min prior to voltammetry. After deaeration, a blanket of nitrogen was kept over the solutions.

Apparatus. Ultrasmall electrodes were fabricated by pulling quartz capillaries (0.5 mm i.d., 1.1 mm o.d., Sutter Instrument Co.) using a Model P-2000 Puller (Sutter Instruments Co.). Voltammetric measurements were carried out with an ElectroLab System (Bionexus Pty Ltd., Wollongong, Australia). The electrochemical cell consisted of a 15 mL glass vial with three holes in a plastic cap to accommodate a three-electrode system. A Ag/AgCl (saturated KCl solution) electrode was used as a reference electrode and a platinum wire as the auxiliary electrode. All experiments were performed in a Faraday cage. Wave slopes of all cyclic voltammograms were calculated from a plot of $\log[(I_{lim} - I)/I]$ (where I denotes current and I_{lim} the limiting current on the voltammogram) vs potential, with the half-wave potential ($E_{1/2}$) being the intercept on the potential axis.

Fabrication of Ultrasmall Carbon Disk Electrodes. Ultrasmall carbon ring electrodes were fabricated as described previously.[20] Ultrasmall carbon disk electrodes were constructed by the following procedure: quartz capillaries were initially pulled with a Model P-2000 puller. This puller uses a carbon dioxide laser as a heat source and thus provides sufficient heat to melt the quartz capillaries. Following the same procedure for constructing carbon ring electrodes,[20] methane gas was passed through the capillary at a pressure of ~900 kPa while being thermally pyrolyzed for 4 min using a Bunsen burner. This was then sufficient to form a carbon deposit at the tip of the capillary. Electrical contact to the carbon deposit was accomplished with mercury and a nichrome wire. A schematic diagram of the ultrasmall carbon disk electrode is shown in Figure 1.

Safety Considerations. Fabrication of ultrasmall carbon disk electrodes involves the application of methane gas at a high pressure (900 kPa) through fine tips of quartz capillaries. Extreme care must be taken to avoid outburst of methane gas to naked flames during pyrolysis. Graphite ferrules were used in this work to ensure a secure and tight fit of quartz capillaries to a stainless steel tubing connected to a methane gas cylinder.

RESULTS AND DISCUSSION

Effects of Pyrolysis Conditions. In the fabrication of ultrasmall electrodes, quartz capillaries were initially pulled to a very small tip, typically in the range of 100–1000 nm. As a result of the small dimension, a relatively high pressure was applied to ensure a continuous flow of methane gas through the capillary during pyrolysis. In a study involving the determination of bubble pressure to estimate the outer diameter of soda glass micropipets, Mittman et al.[27] reported that a pressure of at least 200 kPa was necessary to obtain a fine stream of bubbles emerging from a 500 nm tip immersed in methanol solution. In our experiments,

(24) Chen, T. K.; Lau, Y. Y.; Wong, D. K. Y.; Ewing, A. G. *Anal. Chem.* **1992**, *64*, 1264–1268.
(25) Lau, Y. Y.; Wong, D. K. Y.; Ewing, A. G. *Electroanalysis* **1992**, *4*, 865–869.
(26) Bond, A. M.; Brainina, Kh. Z.; Koppenol, M. *Electroanalysis* **1994**, *6*, 275–284.
(27) Mittman, S.; Flaming, D. G.; Copenhagen, D. R.; Belgum, J. H. *J. Neurosci. Methods* **1987**, *22*, 161–166.

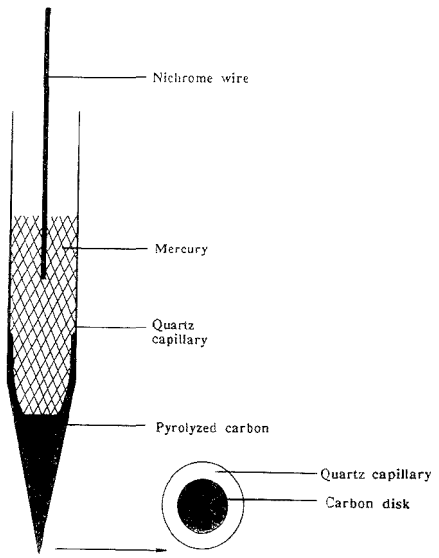

Figure 1. Schematic of an ultrasmall carbon disk electrode.

we have examined the appearance of the tips obtained after performing pyrolysis with a gas pressure ranging from 500 to 1000 kPa through the pulled quartz capillaries. After applying pressures less than 850 kPa, visual examination under an optical microscope revealed that the carbon deposit formed did not reach all the way to the tip but ceased a short distance from the tip inside capillaries of diameters in the 100–1000 nm range. Cutting or beveling the capillaries would have aided in exposing the carbon surface. However, this would have inevitably enlarged the tip diameters and we thus have not proceeded further with these electrodes. On the other hand, when a pressure higher than 950 kPa was applied, the tips of the electrodes were always found to be damaged and not useful for further experiments. From these results, an optimum pressure of 900 kPa was applied in all subsequent experiments and a well-defined voltammogram was obtained in the characterization experiments (vide infra).

In another experiment, we investigated the duration of pyrolysis required to promote the formation of a compact carbon deposit inside quartz capillaries of diameters between 100 and 1000 nm. A range of pyrolysis time from 2 to 7 min was employed. With a duration shorter than 3 min, the characterization experiment involving cyclic voltammetry of dopamine (vide infra) at the fabricated electrodes yielded a nonsigmoidal response with a large background charging current. This seems to indicate that insufficient carbon deposit and/or a rather porous structure was formed at the tip of electrodes. However, when a duration longer than 5 min was applied, the tips of the fabricated electrodes were again found to be damaged. Hence, in this work, a pyrolysis time of 4 min seems to be an optimum duration in the fabrication of ultrasmall carbon disk electrodes. Despite a wide range of tip diameters from 100–1000 nm, electrodes fabricated by employing a pressure of 900 kPa and pyrolysis duration of 4 min were found to produce well-defined cyclic voltammograms in the characterization experiments as described below.

We also examined the tip dimension of carbon disk electrodes and the morphology of the carbon deposit formed at the tip using scanning electron microscopy. Figure 2a shows a photograph of the often short and sharp tips of carbon disk electrodes obtained, a feature similar to that of ultrasmall carbon ring electrodes. Such a feature is particularly attractive for in vivo experiments as this permits minimal tissue damage upon implantation and also very careful selection of the region of tissue where measurements can be performed. The micrographs of the two electrodes in Figure 2a were then magnified, as shown in Figure 2b. From Figure 2b, the tip diameters of the two electrodes were estimated to be approximately 300–400 (left) and 500 nm (right), respectively. Owing to the small size of the tip of electrodes, it has been difficult to obtain micrographs of the carbon surface at the tip of electrodes with sufficiently clear contrast between the carbon and the glass insulator. Nonetheless, the carbon deposit seems to have formed in distinct small globules within the capillary during pyrolysis. In general, these small globules appear to be evenly distributed in the deposit and adhere to the inside wall of the quartz capillary with no observable cracks.

Electrochemical Behavior. (a) In Dopamine Solution. All ultrasmall carbon disk electrodes fabricated were initially tested by cyclic voltammetry in 1.0×10^{-4} M dopamine in pH 7.4 citrate–phosphate buffer solution. Note that the tips of carbon disk electrodes are sufficiently small that they can be filled with a carbon deposit. Figure 3 shows the voltammograms obtained at the carbon disk electrodes displayed in Figure 2b. As expected, a sigmoidal response corresponding to the oxidation of dopamine with minimal background charging current was obtained at these electrodes. These results seem to indicate that the carbon deposit is a relatively nonporous structure which adheres sufficiently onto the inside wall of quartz capillaries. This feature then obviates the necessity of sealing the tips with epoxy and cutting of electrodes, in contrast to that often required in the procedure for constructing many microelectrodes. By adopting a hemispherical diffusion model around an ultrasmall disk electrode, the limiting current, I_{lim}, is given by the expression[28]

$$I_{lim} = 2\pi rnFDC$$

where r is the radius of electrode, D is the diffusion coefficient (6×10^{-6} cm^2 s^{-1} for dopamine[22]), and C is the bulk concentration of the electrolyzed species. All other symbols have their usual electrochemical meaning. By substituting the values of limiting currents in Figure 3 into this equation, the diameters of the two electrodes were calculated to be 320 (left) and 740 nm (right), respectively. These results are thus of a magnitude similar to those estimated from the micrographs shown in Figure 2b.

In examining the analytical performance of ultrasmall carbon disk electrodes, we have carried out cyclic voltammetry and square wave voltammetry of dopamine at a 1 μm carbon disk electrode, as shown in Figure 4. In these experiments, the concentration of dopamine was increased by a standard addition method. From the corresponding calibration plots, a detection limit (based on twice the level of background noise) was then determined to be $\sim 5.8 \times 10^{-7}$ (by cyclic voltammetry) and 7.6×10^{-8} M (by square wave voltammetry), with correlation coefficients of 0.996 and 0.991,

(28) Fleischmann, M.; Pons, S.; Rolison, D. R.; Schmidt, P. P *Ultramicroelectrodes*; Datatech Systems: Morganton, NC, 1987; Chapter 3.

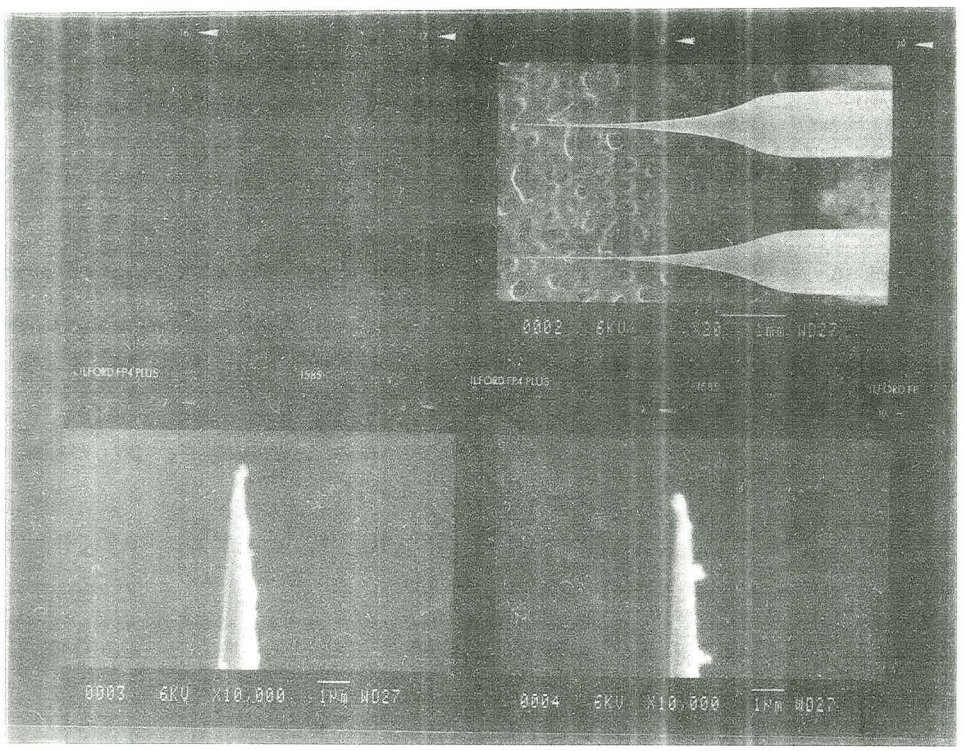

Figure 2. (a, top) A photograph of two ultrasmall carbon disk electrodes. (b, bottom) Scanning electron micrographs of the tips of carbon disk electrodes shown in (a).

respectively. These results are comparable to that (1×10^{-6} M) obtained from cyclic voltammetry at a 2.9 μm carbon ring electrode.[20]

The reversibility of the dopamine oxidation reaction at the pyrolyzed carbon surface has been assessed using the wave slope and half-wave potential of voltammogram. The wave slope and half-wave potential (vs SCE) were calculated to be 63.5 ± 5.5 mV/decade and 131 ± 11.0 mV ($N = 12$), respectively, showing a kinetically reversible reaction at the carbon disk electrodes. These data are consistent with previously reported[22] values of 75 mV/decade and 163 mV (vs SSCE), respectively, obtained at flame-etched carbon fiber electrodes. In addition, we have compared the lifetime of carbon disk electrodes and carbon ring electrodes by performing cyclic voltammetry at these electrodes daily in fresh dopamine solutions. We observed that the limiting currents obtained at carbon disk electrodes deteriorated by 10% over a period of 5 days, while that at carbon ring electrodes was reduced by 80% over the same period of time. The absence of epoxy resin, and hence no deterioration of epoxy resin, in carbon disk electrodes could possibly have extended the lifetime of electrodes.

(b) In Cobaltocenium Cation Solution. The electrochemical behavior of microelectrodes in an aqueous solution is often employed in most characterization experiments to provide an indication of the integrity of the fabricated electrodes. Bond et al.[26] recently pointed out the importance of a high-quality seal in microelectrodes in order to achieve ideal performance and noted that the use of epoxy-sealed microelectrodes might be restricted

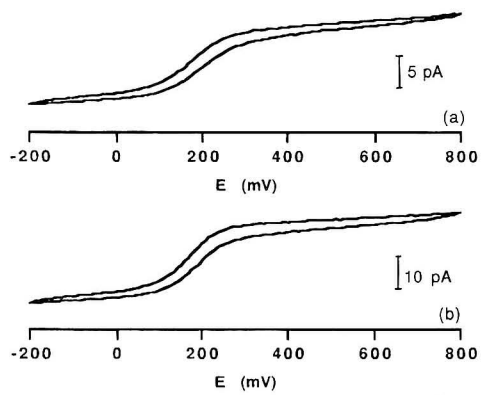

Figure 3. Cyclic voltammograms of 1.0×10^{-4} M dopamine at the carbon disk electrodes shown in Figure 2b in pH 7.4 citrate–phosphate buffer solution. Scan rate, 100 mV s^{-1}.

to aqueous media. This prompted us to examine the performance of ultrasmall carbon disk electrodes in nonaqueous solutions since there is no epoxy incorporated in the body of ultrasmall carbon disk electrodes. Also, results described above (Figure 3) seem to indicate a good seal between the carbon deposit and the inside wall of the quartz capillaries. Figure 5 shows a cyclic voltammogram obtained for the one-electron reduction of cobaltocenium cation ($[Co^{III}(\eta^5\text{-}C_5H_5)_2]^+ + e^- \rightleftharpoons [Co^{II}(\eta^5\text{-}C_5H_5)_2]$) in Et_4NClO_4,

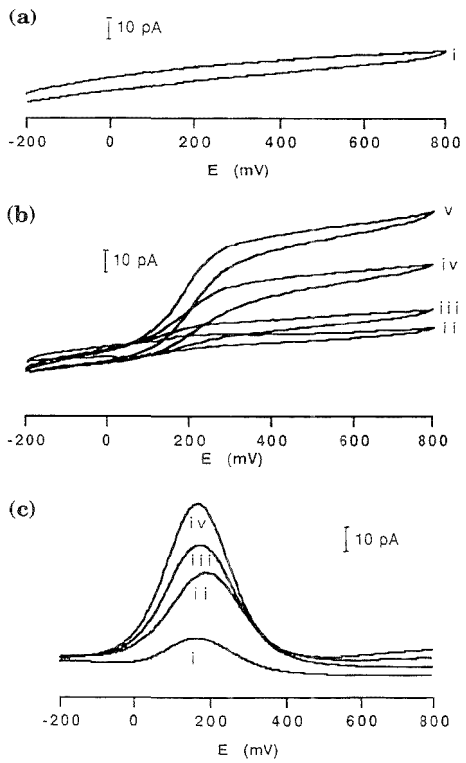

Figure 4. (a, b) Cyclic voltammograms and (c) square wave voltammograms of dopamine at a 1 μm carbon disk electrode in pH 7.4 citrate–phosphate buffer solution. Successive increase in dopamine solution was performed by a standard addition method. In (a) and (b), the scan rate is 100 mV s^{-1}. Concentration of dopamine in (a) and (b): (i) 0, (ii) 1.0×10^{-6}, (iii) 1.0×10^{-5}, (iv) 5.0×10^{-5} and (v) 1.0×10^{-4} M. In (c), the frequency of pulse is 25 Hz, and pulse amplitude is 25 mV. Concentration of dopamine in (c): (i) 5.0×10^{-7}, (ii) 1.0×10^{-6}, (iii) 1.0×10^{-5}, and (iv) 5.0×10^{-5} M.

in which (a) CH_3CN (dielectric constant 37.5[29]) and (b) CH_2Cl_2 (dielectric constant 7.3[29]) were used as the solvents, respectively. Note that a sigmoidal wave was obtained for the reduction of cobaltocenium cation in Et_4NClO_4 in both solvents, although CH_2Cl_2 is a relatively more resistive solvent. No significant deterioration in the current signal was observed even after completing 20 cycles of voltammetric scans. The wave slope and half-wave potential were calculated to be 102 ± 10.0 mV/decade and -111.9 ± 0.40 mV ($N = 5$) in CH_3CN and 219 ± 55 mV/decade and -110.6 ± 7.0 mV ($N = 5$) in CH_2Cl_2. These are compared to 70 mV/decade and -135 mV (vs an internal ferrocenium ion/ferrocene reference electrode) in CH_3CN, and 62 mV/decade and -135.6 mV (vs an internal ferrocenium ion/ferrocene reference electrode) in CH_2Cl_2 obtained at a conventional sized glassy carbon electrode.[30] Hence, the reduction of cobaltocenium cation seems to be less reversible on the ultrasmall carbon disk electrode.

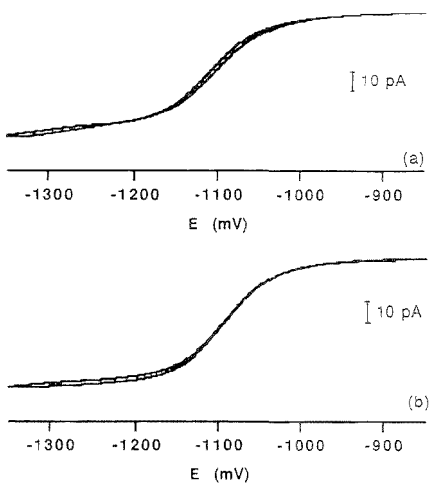

Figure 5. Cyclic voltammograms obtained at a 1 μm carbon disk electrode for the reduction of $(\eta^5\text{-}C_5H_5)_2CoPF_6$ in 0.1 M Et_4NClO_4 in (a) acetonitrile and (b) CH_2Cl_2. Scan rate, 50 mV s^{-1}.

Apart from a small overall physical dimension required for an electrode to be used in vivo, it is equally important that the fabrication procedure is simple and convenient to perform with a relatively high success rate. In the fabrication of ultrasmall carbon disk electrodes, all quartz capillaries are pulled by a horizontal micropipet puller which can nearly reproducibly (~80%) manufacture capillaries of a desired tip diameter. The other major step involves pyrolysis of methane which can also be carried out without any special skills. Hence, after experimenting with more than 500 electrodes fabricated, we have been able to reach a success rate of ~85% for construction of carbon disk electrodes with total structural diameters between 500 and 1000 nm. On the other hand, the success rate for constructing electrodes with structural diameters between 100 and 500 nm is slightly lower at ~70%. However, this still represents a significant improvement compared to a success rate of 10% in fabricating electrodes with 400 nm tip diameters.[22]

ACKNOWLEDGMENT

The authors thank Ms. Coral Gilkeson at the School of Biological Sciences, Macquarie University, for help in obtaining the SEMs of ultrasmall electrodes. Also, L.Y.F.X. acknowledges Mr. Warren Kett in setting up the high methane gas pressure system. While pursuing this study, L.Y.F.X. was supported by an Overseas Postgraduate Research Award.

Received for review May 30, 1995. Accepted August 29, 1995.[⊗]

AC9505211

(29) Fry, A. J.; Britton, W. E. In *Laboratory Techniques in Electroanalytical Chemistry*; Kissinger, P. T., Heineman, W. R., Eds.; Dekker: New York, 1984; p 369.

(30) Stojanovic, R. S.; Bond, A. M. *Anal. Chem.* **1993**, *65*, 56–64.

[⊗] Abstract published in *Advance ACS Abstracts*, October 1, 1995.

Anal. Chem. **1995**, *67*, 4091–4095

Optimization of NMR and HPLC Conditions for LC-NMR

Lee Griffiths

Pharmaceutical Department, ZENECA Pharmaceuticals, Hurdsfield Industrial Estate, Macclesfield, Cheshire SK10 2NA, U.K.

The NMR sensitivity was recognized as the major issue in the optimization of the coupled HPLC-NMR experiment. Each of the relevant interactions between HPLC parameters and NMR parameters has been examined in detail such that workers should be able to design a strategy to optimize their own experiments.

The coupling of NMR and HPLC is not a new concept: a physical link has existed for several years.[1-7] Indirect links, i.e., sequential preparative HPLC and then NMR, have existed even longer and are probably still used more widely than LC-NMR.

One-off requirements are probably more easily satisfied by sequential preparative LC and NMR, where the time taken to remove protonated solvent and transfer it to an NMR tube is small compared to the time taken to change the NMR probe.

Where many NMR problems require preseparation by LC, LC-NMR coupling becomes expedient, and the decision whether to do preparative LC and then NMR or coupled LC-NMR (apart from the availability of a probe) depends on the amount of material involved. Typical 4.6-mm LC column loadings are of the order of 10 μg, very much at the lower limit of detection of NMR, especially where a minor component (<10%) is concerned. Minor components are probably still better detected by sequential preparative LC and NMR, but only where the eluant is readily removed.

While there has been an outpouring of publications in the area over the last year or two, the comparative insensitivity of NMR remains a crucial factor in planning LC-NMR experiments. This work investigates the factors contributing to the detection limit in LC-NMR so that LC-NMR experiments can be optimized more readily.

EXPERIMENTAL SECTION

HPLC experiments were performed on a Hewlett Packard 1050 quaternary pump, injection system, and UV detector. The column was a Hichrom 25-cm × 4.6-mm-i.d. Hypersil 5-μm ODS, and the dimethyl phthalate was as supplied by Aldrich. The solvent system was 70% acetonitrile and 30% D_2O. UV detection was at 254 nm.

The NMR spectra were obtained at 400.14 MHz on a Bruker AMX400 using a 4-mm LC probe. Solvent suppression was via presaturation, the carrier (01) set at the acetonitrile frequency and the decoupler (02) set at the residual water frequency.

Stopped-flow detection was facilitated with a Spark Holland "Must" column switcher, with integral timer. This unit was, however, initiated manually at the UV peak maximum.

RESULTS AND DISCUSSION

LC-NMR can essentially be run in two modes: stopped-flow and on-flow. In the former case, the LC pump is stopped or the solvent diverted, so that the desired chromatographic peak sits motionless in the probe, allowing extended NMR acquisition. The presence of a peak is usually detected by a UV detector between the column and the NMR probe, with some time allowance made for transfer between the UV detector and the NMR probe.

With on-flow NMR detection, NMR acquisition is started with the start of the chromatography and arbitrarily broken into a series of time slices, the spectrum for each being stored in a serial file. In this situation, extending acquisition leads to a trade-off between decreased LC resolution and increased NMR sensitivity. The data are usually processed as a "pseudo-2D plot", with the normal NMR spectrum along the f2 axis and chromatographic elution time along the f1 axis. Not only is on-flow NMR detection limited in sensitivity, but gradient elution also causes problems with changes in susceptibility and drift of signals relative to the lock, whence the position of presaturation[8] for each time slice needs to be established in a separate run, doubling the time taken. The major advantage of on-flow NMR detection is the lack of need for independent detection of chromatographic peaks; this allows for the detection of, for example, nonchromophores. On-flow detection suffers the same sensitivity problems as stopped-flow, but with some additional constraints. It therefore makes sense to consider stopped-flow sensitivity first.

The first parameter to consider is the size of the NMR probe cell. Bruker, for instance, supplies a variety of sizes, quoting the outside tube dimension in millimeters. The solvent pressure is assumed to have dropped to atmospheric after the column and UV cell, so the NMR cell is constructed from glass of normal NMR tube wall thickness, whence i.d. = o.d. − 1.0 mm. Since the length of the coil is 17 mm in our probe, the nominal size of the cell is therefore 120 μL for our 4-mm cell.

In principle, the coil could detect outside of the volume it encompasses. To test this hypothesis, the Z1 shim was turned to maximum, generating a field gradient along the NMR cell equivalent to 28.9 Hz/mm or 0.07 G/cm [calibrated with a sample of known length in a 5-mm QNP (combined ^{1}H, ^{19}F, ^{31}P, ^{13}C) probe]. A normal pulse and collect spectrum then yields an image of the sensitivity vs distance along the cell, assuming the field

(1) Dorn, H. C. *Anal. Chem.* **1984**, *56*, 747A–748A.
(2) Laude, D. A.; Wilkins, C. L. *Trends Anal. Chem.* **1986**, *5*, 230–235.
(3) Albert, K.; Bayer, E. *Trends Anal. Chem.* **1988**, *7*, 288–293.
(4) Bayer, E.; Albert, K.; Nieder, M.; Grom, E.; Keller, T. *J. Chromatogr.* **1979**, *186*, 497–507.
(5) Bayer, E.; Albert, K.; Nieder, M.; Grom, E.; Rindlisbacher, M. *Anal. Chem.* **1982**, *54*, 1747–1750.
(6) Albert, K.; Nieder, M.; Bayer, E.; Spraul, M. *J. Chromatogr.* **1985**, *346* 17–24.
(7) Albert, K.; Kunst, M.; Bayer, E.; Spraul, M.; Bermel, W. *J. Chromatogr.* **1989**, *436*, 355–363.
(8) Bax, A. *J. Magn. Reson.* **1985**, *65*, 142–145.

0003-2700/95/0367-4091$9.00/0

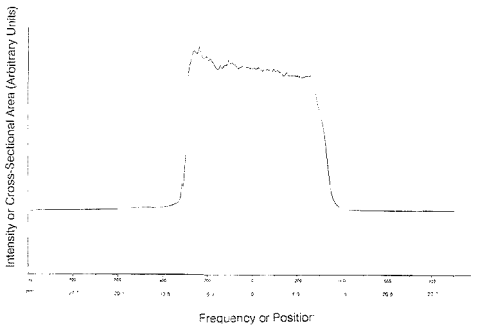

Figure 1. One-dimensional image of NMR flow cell.

gradient is linear. The resulting image is given in Figure 1. The points at which the plot drops sharply are 520 Hz (18 mm) apart, agreeing very well with the coil dimensions. However, it is clear that there is, indeed, signal detected outside the coil, which by manual integration gives 15% of the total area. The volume detected, therefore, increases from 120 to 140 μL. For the purpose of any of the mathematical models contained in this work, this volume is approximated to a cyclinder of 140 μL, considerably simplifying the treatment but introducing negligible error; 140 μL is of the same order as the volume sampled in a 5-mm high-resolution probe, but because the coil is glued directly to the cell, the sensitivity is higher. Because of the difficulty of making up and maintaining an unsealed standard sensitivity solution, the sensitivity of LC probes is not measured directly.

Until the market for LC-NMR probes becomes more competitive, this parameter will be an issue, but for the time being, the choice is simply about what size of cell to use. The coil itself distorts the field, so larger diameter cells yield better line shapes, which compensate for the slightly lower Q. Sensitivity can, therefore, be treated as roughly proportional to the cell volume.

A 5-mm cell will have a volume of 210 μL, yielding a sensitivity five-thirds times that of the 4-mm cell. The obvious question is, therefore, why not have a large cell? The answer is clearly the degradation of chromatographic resolution. A typical UV cell is 14 μL, and a microcell is 1 μL. By comparison, the NMR cell is enormous and may be considered to be extremely disruptive to the resolution.

There are several factors to consider, however. First, the design of the cell very much affects the mixing characteristics, and the broadening will not necessarily simply be proportional to size. Second, mixing within the cell can be augmented at the outlet of the cell, and simply placing a UV detector after the NMR cell to monitor line broadening within the cell could lead to erroneously high results. Last, coeluting components can be separated spectroscopically with NMR, so the chromatographic resolution is not a primary concern. If the width of an NMR spectrum is regarded as equivalent to the total retention time in a chromatogram, then a 600-MHz proton spectrum (ignoring couplings) with lines 1 Hz in width possesses $5.545 \times [(10\ \text{ppm} \times 600)/1]^2 = 2 \times 10^8$ theoretical plates,[9] while a carbon spectrum yields $5.545 \times [(220\ \text{ppm} \times 150)/1]^2 = 6 \times 10^9$ theoretical plates. In most instances, it is therefore the *sensitivity* of the cell that matters, not the chromatographic resolution per se.

(9) (a) Giddings, J. C. *Unified Separation Science*; John Wiley & Sons: New York, 1991; p 101. (b) Reference 9a, p 94.

At 1 mL/min, a 5-s-wide peak is exceptional, and one 30 s wide is far more representative: 30 s corresponds to 500 μL, so a 140-μL cell would only be detecting ~0.3 of the available peak. This is a very high price to pay for chromatographic resolution, and since the square of the resultant chromatographic peak width is the sum of the squares of all the contributions,[5] a 140-μL cell would have to be designed very badly to broaden a 500-μL peak unduly. The size of the NMR cell, therefore, needs to be considered in conjunction with the volume of the chromatographic peak.

To examine this in more detail, the sensitivity obtained for various width chromatographic peaks was modeled on the assumption that the chromatographic peak shape is Gaussian; i.e., the area of a slice through a Gaussian peak was calculated at varying positions across the peak, where the slice width is cell volume/flow rate. This is clearly a simplification, but it does represent an "ideal" peak shape, and it illustrates the time dependence of sensitivity. Furthermore, it has to be assumed that the flow through the cell is perfectly laminar, with no mixing.

Figure 2 shows the calculated sensitivity as a function of the stopped-flow delay time at various chromatographic peak widths. The flow rate is 1 mL/min, and the cell size is 140 μL. Curves are presented for chromatograph peak widths at half-height of 2, 3, 5, 10, 20, and 30 s. At 1 mL/min, assuming no turbulence, a solvent front would pass through a 140-μL cell in 8.4 s (the cell width, say). The first obvious observation for Figure 2 is that down to a chromatographic peak width of about 4 s (0.5 of cell width), provided the stopped-flow is done optimally, increased sensitivity results from decreased chromatographic peak width. When the chromatographic peak width exceeds the cell width (expressed in the same units), the sensitivity is approximately inversely proportional to chromatographic peak width. A peak width of 3 s (0.4 of the cell width) corresponds to the onset of maximum intensity, and below this there is no advantage in sensitivity, apart from a flattening of the curve, which removes the stopped-flow delay dependence. In contrast, there is decreased dependence on stopped-flow delay at very large chromatographic peak widths.

Since typical chromatographic peak widths are of the order of $\geq$30 s, the optimal sensitivity would result from a cell of 30/0.4 = 75 s long at 1 mL/min, 1250 μL, or 10-mm diameter. Rather than increase the diameter of the NMR cell (an expensive proposition), some optimization of the chromatography could result in decreased chromatographic peak widths. For late-eluting peaks, for instance, the use of gradient elution is an obvious option.

The third observation is that even the idealized NMR cell, because it is of finite volume, broadens the chromatographic peak. For the 140-μL cell at 1 mL/min, this amounts to approximately an extra 2 s when the chromatographic peak width is greater than the cell width, and considerably more when the peak width is less than the cell width. For most practical purposes, this is not significant, but of course, no cell will have perfectly laminar flow, and the question therefore remains, does the NMR cell broaden more than would be calculated from its volume above? This can, of course, be tested with an on-flow experiment, comparing the observed chromatographic peak width in the f1 direction with the theoretical. In practice, the time resolution of such an experiment is too low to obtain a meaningful result.

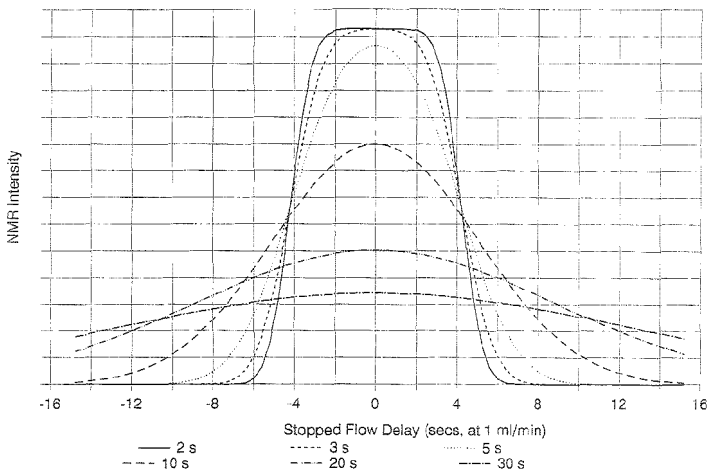

Figure 2. Signal to noise vs stopped-flow delay. Dependence on LC peak width (4-mm probe).

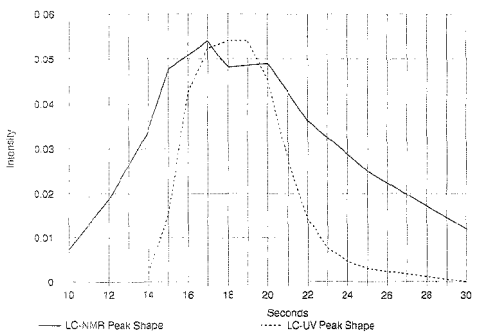

Figure 3. Chromatographic peak shapes. Comparison of Bruker NMR (4 mm) and Hewlett Packard UV (14 μL).

Instead, the stopped-flow experiment with variation of transfer time delay, the very one modeled, is more likely to yield a satisfactory result. Figure 3 shows the NMR chromatographic peak shape determined by stopped-flow/variation of transfer delay time and the UV on-line chromatographic peak shape for comparison.

By adding an extra detection cell, interposing a short connection and then the long NMR transfer tube and taking cognizance of the UV chromatographic peak and NMR chromatographic peak widths of 5.6 and 11.2 s at 1 mL/min, respectively, the various contributions to line width were characterized as

$$LW_{NMR} = \sqrt{LW_I^2 + UV + TR + NMR} \qquad (1)$$

where LW_I is the width of the peak as it exits the column, UV is the broadening by the UV cell (Hewlett Packard 1050, 14 μL), a constant equal to 8.0, TR is the broadening by the transfer tube, a constant equal to 6.5, and NMR is the broadening by the NMR cell, a constant equal to 79. While narrow chromatographic peaks would be significantly affected, normal width peaks would not be affected unduly (e.g., a chromatographic peak 30 s wide entering the UV cell would only be 31.5 s wide in the NMR cell).

The great spectroscopic separation potential of NMR makes it pertinent to reexamine the optimization of the preceding chromatography. Since chromatographic resolution is neither significantly compromised by the NMR nor is it necessarily required, flow rate and sample loading can be adjusted away from the optimal chromatographic method.

For stopped-flow, the adjustment of solvent flow rate has little implication with respect to sensitivity, apart from increased flow rate resulting in less time spent on the chromatography and perhaps slight narrowing of peaks. In a lot of instances, the viscosity of the solvent and the porosity of the column packing will impose a limit on how fast the solvent can be pumped, anyway. There are serious implications of flow rate in on-flow detection, however, and this will be considered later.

Sample loading is, however, extremely relevant to the sensitivity of stopped-flow detection. It is a well-known phenomenon of chromatography that increased peak width results from increased column loading. If the width increases less than linearly with a slope of 1.0 with respect to sample loading, however, increased NMR sensitivity will result.

Turning now to the special considerations of on-flow LC-NMR. The two conflicting requirements are the maximization of signal-to-noise via repetitive scans against the concomitant decreased chromatographic resolution.

The problem breaks down into two: how fast can I pulse, and for how long can I pulse? So far as the former is concerned, apart from the acquisition time, the two parameters to consider are the length of the presaturation pulse (which can be relatively long) and the degree to which flow removes saturation from rapid pulsing.

The number of points acquired can clearly be reduced in an effort to increase the repetition rate, with concomitant reduction in digital resolution. To obtain reasonable signal to noise and chromatographic resolution, spectral digital resolution will have

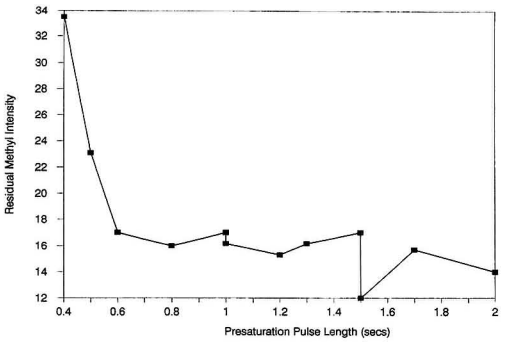

Figure 4. Effect of presentation pulse length (acetonitrile/water).

to be compromised to some degree at least. The additional benefits are smaller data tables and decreased noise (it is, after all, a de facto apodization). Provided the compromises are accepted in this respect, the limit to pulsing rate will then be the time taken to presaturate solvent signals. Clearly, the level of presaturation required will depend on the proximity of the solvent resonances relative to the resonances of interest, but what are the benefits of increased presaturation time?

Figure 4 shows the level of the residual CH_3 signal of CH_3CN relative to the ^{13}C satellite signals of CH_3CN vs the presaturation time in 70% CH_3CN/30% D_2O. In this case, there is little to be gained by prolonging the presaturation pulse beyond 0.7 s. Fortunately, this value is sufficiently low that the effect of flow on saturation must be negligible. Were it much larger, it would be difficult to differentiate complete saturation and saturation leveling off because of the introduction of unsaturated sample into the cell.

Flow will, however, affect the degree to which the sample is polarized if the magnetic field and the extent to which pulsed sample flowing out of the cell moderate saturation (as opposed to presaturation).

In our LC-NMR setup, the time delay between maximum UV absorption and maximum NMR intensity is 17 s at 1 mL/min or 283 μL. Half the volume of the UV cell is 7 μL, half the volume of the NMR cell is 70 μL, and 182 cm of 0.01 i.d.-in.-transfer tubing has a volume of 92 μL, so 114 μL of dead-volume remains. This 114 μL comprises the majority of the conical inlet to the cell and a section of tubing bridging this and the capillary inlet tube. A 114 μL dead-volume within the probe means that the sample will be at or very close to the magnetic field within the radio frequency coil for 6.8 s at 1 mL/min, plenty of time for polarization to occur. This simplifies the normally complex flow situation into one where only the removal of pulsed material from the cell, obviating saturation, need to be considered.

After a $90°_x$ pulse, magnetization relaxes along the z direction in the rotating frame according to

$$M_t(z) = M_0(1 - e^{-t/T_1}) \tag{2}$$

where M_0 is the magnetization at $t = 0$, M_t is the magnetization at time t and T_1 is the spin–lattice relaxation time. After the second pulse, the previous M_t becomes the new M_0, and so on. After the first pulse, however, relaxation occurs relative to the y axis according to

$$M_t(y) = M_0 e^{-t/T_2} \tag{3}$$

where T_2 is the spin–spin relaxation time. Any residual y component immediately prior to the second pulse contributes to the z component after the second pulse. Most treatments of saturation in flowing systems[10] assume that $T_2 \ll T_1$ whence this contribution vanishes. In solution, however, provided that an extremely high field is not employed, nor are macromolecules studied, it is more likely that $T_2 \simeq T_1$, and the treatment becomes analytically more complex. It is, however, relatively simple to solve numerically, and this was done in this work.

The number of pulses experienced by the slice of solution, ignoring turbulence and laminar flow effects, is

$$\mathrm{NP} = \frac{\text{flow rate}}{\text{cell volume} \times \mathrm{PD}} \tag{4}$$

where PD is the time between pulses. By combining eqs 2 and 3 and performing a linear interpolation for results on either side of NP given by eq 4, the effect of pulse rate on (a) quantification and (b) signal to noise was studied.

In a nonflowing system, when the time between pulses is three times the longest T_1, the system is 95% relaxed, enough for all but the most rigorous quantitative applications. For $T_1 = T_2 = 1$ s, this would be a pulse every 3 s. For our model, flowing at 1 mL/min, the sample would be 95% relaxed at 2.6 s between pulses. If the flow rate was increased to 2 mL/min, this figure would drop to 2.2 s.

Rapid pulsing often used in on-flow LC-NMR does not, therefore, compromise quantification as much as might be expected. It should be borne in mind, however, that resonances close to the solvent peaks will be attenuated by the same presaturation employed to remove the solvent peaks. Furthermore, since the solvent residuals are subject to different phase errors than the solute spectrum, baseline distortions will further compromise quantification in the region of the solvent peaks. Of more interest is the optimal pulsing for the maximum signal to noise. In this case, the above model is convoluted with the square root of the number of pulses. For 90° pulses, $T_1 = T_2 = 1$ s, and a flow rate of 1 mL/min, the optimal signal-to-noise occurs at a pulse spacing of 1.6 s. If T_1 was shorter, this figure would decrease, and if the flow rate were to increase, this figure would also decrease.

In principle, even greater signal to noise is accessible by using a smaller flip angle and a shorter pulse delay,[11] the exact position of the optimum depending on T_1 and T_2. It will be found, however, that the presaturation pulse length and the acquisition time will together impose a minimum recycle time close to the optimum pulse spacing quoted above. If very short presaturation pulses or very small data sets are usable, or the relaxation times are $\gg 1$ s, consideration should be given to the use of flip angles less than 90°.

Having defined the optimal pulse spacing, the question arises of how long to make each time slice in the pseudo-2D run. Setting aside the issue of chromatographic resolution, the longer acquisition occurs, the higher the signal (S) to noise (N), provided there is enough of the chromatographic peak present

(10) Jones, D. W.; Child, T. F. *Adv. Magn. Reson.* **1976**, *8*, 123.
(11) Ernst, R. R.; Anderson, W. A. *Rev. Sci Instrum.* **1966**, *37*, 93–102.

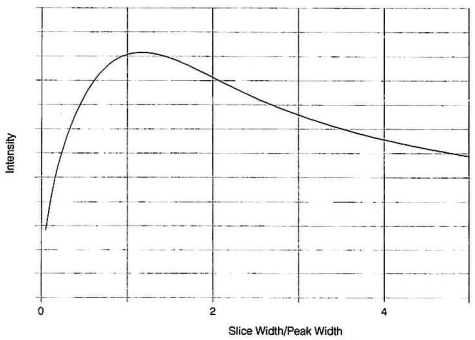

Figure 5. Signal to noise vs time slice width in LC-NMR peak (optimal start of time slice).

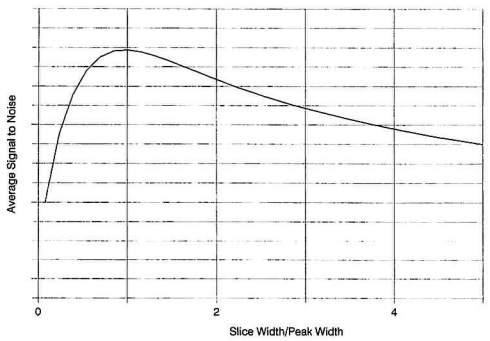

Figure 6. Signal to noise vs time slice width with random positioning (optimal to least optimal) in LC-NMR peak.

in the NMR cell, i.e.,

$$S/N = \frac{1}{\text{noise} \times \sqrt{m-n}} \sum^{i=n,m} P_i \qquad (5)$$

where noise refers to the point-to-point noise, n and m are the time slice limits (in number of pulses), and P_i is the chromatographic line shape function. Once again, for the purposes of this work, P_i is assumed to be Gaussian. Figure 5 gives the calculated signal-to-noise (in arbitrary units) vs the time slice width as a ratio of the chromatographic peak width at half-height. The position of the optimum is 1.1 times the chromatographic peak width. The calculation implicit in Figure 5, however, assumes optimal positioning of each time slice, i.e., symmetry about the center of the chromatographic peak. In practice, the onset of the time slice will be randomized relative to the chromatographic peak position. The least optimal start (or finish) of a time slice is at the peak maximum, away from the maximum there will be another time slice that straddles the peak maximum, and this slice will in turn possess higher signal. The signal to noise was therefore calculated at a variety of starting positions between the optimal start (half a time slice width before the peak maximum), and the least optimal start (the peak maximum) and the signal-to-noise values were averaged. The time slice thickness was then incremented, the calculation repeated, and so on. Figure 6 gives the signal-to-noise as a function of time slice width for averaged time slice position. The maximum is now at 0.98 times the width of the chromatographic at half-height. In both optimized start and randomized start positions of time slices, the optimum signal to noise is close to 1.0 times the chromatographic peak width at half-height.

In both cases, the slope of the plot is higher on the narrower slice width side, so there is more to lose by making the time slices too narrow than the reverse. For an isocratic run with line widths increasing with increased elution time, it is better to match the time slice width to the earlier-eluting peaks than the broader, later-eluting ones, with the additional advantage that chromatographic resolution is not compromised.

If time permits, slower flow rates should be experimented with. To a first approximation, peak height will be invariant with flow rate, and NMR sensitivity will be proportional to (peak width)$^{1/2}$ or 1/(flow rate)$^{1/2}$. In practice, diffusion will further broaden the chromatographic peaks, and the peak height will decrease. When the peak height starts to drop faster than (peak width)$^{1/2}$ increases, the optimum NMR sensitivity has been passed.

CONCLUSIONS

In the optimization of LC-NMR experiments, the NMR sensitivity is the main concern. While narrow chromatographic peaks contribute to NMR sensitivity, the separation of chromatographic peaks is not a prime concern, since NMR adds a second dimension of peak separation.

If possible, the chromatographic peak width should be adjusted so that it is less than or equal to the NMR cell width. In a stopped-flow situation, this will be for the chromatographic peak of interest. In an on-flow experiment, the situation is more complex. Optimize the width of the later-running peaks similarly for maximum sensitivity (there is nothing to lose by making earlier peaks too narrow), then optimize the time slice width. There is more to lose by using too narrow a slice, so tend to optimize the slice width on earlier-running peaks. Increasing the column loading will often increase NMR sensitivity, but chromatographic peaks will eventually broaden faster than loading and chromatographic peaks will tail. Higher loading can be tolerated if the peak of interest is before a partially coeluting peak, rather than after. The 4.6-mm-diameter column loadings in LC-NMR are typically 100 μg.

This process of optimization can pose organizational problems where the NMR expert lacks chromatographic skill or the chromatographer feels reluctant to reoptimize his or her system to a different set of criteria.

ACKNOWLEDGMENT

Thanks are due to Klaus Albert and Ulrich Braumann of the University of Tubingen, Manfred Spraul and Martin Hoffman of Bruker Spectrospin, and David Catlow and Ian Greenway of ZENECA for their helpful discussions.

Received for review May 25, 1995. Accepted August 24, 1995.[⊗]

AC950508Y

[⊗] Abstract published in *Advance ACS Abstracts,* October 1, 1995.

Anal. Chem. **1995**, *67*, 4096–4100

Determination of Octane Numbers and Reid Vapor Pressure of Commercial Petroleum Fuels Using FT-Raman Spectroscopy and Partial Least-Squares Regression Analysis

John B. Cooper,*,† Kent L. Wise,† James Groves,† and William T. Welch‡

Department of Chemistry and Biochemistry, Old Dominion University, Norfolk, Virginia 23529, and Research and Development Department, Ashland Petroleum Company, Ashland, Kentucky 41114

A Fourier transform Raman spectrometer was used to collect the Raman spectra of 208 commercial petroleum fuels. The individual motor and research octane numbers (MON and RON, respectively) were determined experimentally using the industry standard ASTM knock engine method. Partial least-squares regression analysis was used to build regression models which correlate the Raman spectra of 175 of the fuels with the experimentally determined values for MON, RON, and pump octane number (the average of MON and RON) of the fuels. Each of the models was validated using leave-one-out validation. The standard errors of validation are 0.415, 0.535, and 0.410 octane units for MON, RON, and pump octane number, respectively. By comparing the standard error of validation to the standard deviation for the experimentally determined octane numbers, it is evident that the accuracy of the Raman determined values is limited by the accuracy of the training set used in creating the models. The Raman regression models were used to predict the octane numbers for the fuels which were not used to build the models. The results compare favorably with the leave-one-out validation. Also, it is demonstrated that the experimentally determined Reid vapor pressures are highly correlated with the Raman spectra of the fuel samples and can be predicted with a standard error of 0.568 psi.

The Clean Air Act of 1989 has mandated radical changes in the petroleum refining industry. Based on seasonal and geographical considerations, commercial gasoline blends must meet stringent environmental requirements while at the same time providing automotive compatibility and efficiency.[1] Conventional methods of determining these characteristics of a fuel are time consuming and expensive. Examples include determining total aromatics and olefins via gas chromatography, determining octane numbers via ASTM knock engine methods, and determining vapor pressure via the Grabner method.

As early as 1950, Raman spectroscopy was proposed as a method to determine aromatics and olefins in hydrocarbon mixtures.[2,3] However, until recently, extensive use of Raman spectroscopy in the characterization of hydrocarbons has not been practical. One early limitation to Raman analysis was the absence of a high-intensity and stable excitation source. This problem has been overcome with the advent of lasers. Another limitation was the presence of fluorescence in hydrocarbon fuels when excited by visible lasers. The development of Fourier transform Raman spectrometers, however, now allows Raman spectra to be collected using near-IR lasers (e.g., the Nd:YAG laser emitting at 1064 nm) which eliminate or severely reduce fluorescence in petroleum fuels.

Recently, Raman spectroscopy has been demonstrated as a viable quantitative technique in the analysis of analytes which are present in liquid mixtures as minor components.[4] Chung, Clarke and others have demonstrated that Raman spectroscopy can be used in the qualitative analysis of aviation fuel for the determination of general hydrocarbon makeup, aromatic components, and additives.[5,6] Williams and co-workers have shown that FT-Raman spectroscopy in combination with chemometrics can be used to determine gas oil cetane number and cetane index.[7] In addition, Seasholtz et al. have demonstrated quantitative analysis of the percentage of each fuel in fuel mixtures containing three unleaded gasolines.[8] Despite these investigations, Raman spectroscopy is still not significantly utilized in the industrial analysis of petroleum fuels.

In contrast, near-IR absorbance/reflectance spectroscopy has gained wide acceptance in the industrial analysis of octane number and total aromatic as well as individual aromatic species concentrations in petroleum fuels during the blending process.[9,10] Multivariate analysis of near-IR spectra currently provides real-time feedback for on-line process control of blending operations (as well as other processes) at the Ashland Petroleum refineries in Cattletsberg, KY, Canton, OH, and St. Paul, MN. Despite the success of near-IR spectroscopy in the petroleum industry, it also

† Old Dominion University.
‡ Ashland Petroleum Co.

(1) Rhodes, A. K. *Oil Gas J.* **1994**, 17 Jan, 16–25.
(2) Dubenbostel, B. F. U.S. Patent 2,527,121, 24 Oct, 1950.
(3) Heigl, J. J.; Black, J. F.; Dudenbostel, B. F. U.S. Patent 2,527,122, 24 Oct, 1950.
(4) Shope, R.; Vickers, T. J.; Mann, C. K. *Appl. Spectrosc.* **1988**, *42*, 468–473.
(5) Chung, W. M.; Wang, Q.; Sezerman, U.; Clarke, R. H. *Appl. Spectrosc.* **1991**, *45*, 1527–1532.
(6) Clarke, R. H.; Chung, W. M.; Wang, Q.; DeJesus, S.; Sezerman, U. *J. Raman Spectrosc.* **1991**, *22*, 79–82.
(7) Williams, K. P. J.; Aries, R. E.; Cutler, D. J.; Lidiard, D. P. *Anal. Chem.* **1990**, *62*, 2553–2556.
(8) Seasholtz, M. B.; Archibald, D. D.; Lorber, A.; Kowalski, B. R. *Appl. Spectrosc.* **1989**, *43*, 1067–1072.
(9) Maggard, S. M. PCT Int. Appl. WO 91 15,762, 17 Oct, 1991; U.S. Pat. Appl. 506,391, 09 Apr, 1990.
(10) Maggard, S. M.; Welch, W. T. PCT Int. Appl. WO 92 10,738, 25 Jun, 1992; U.S. Pat. Appl. 626,132, 11 Dec, 1990.

0003-2700/95/0367-4096$9.00/0

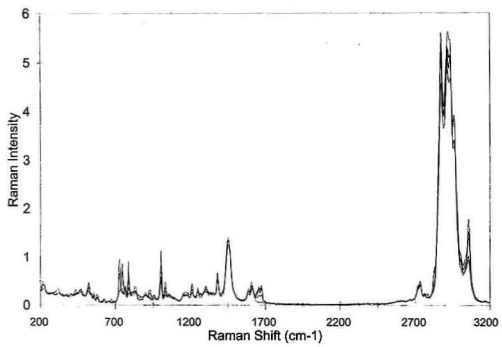

Figure 1. Five overlaid FT-Raman spectra of commercial petroleum fuels. These spectra are representative of the majority of the 208 petroleum fuels.

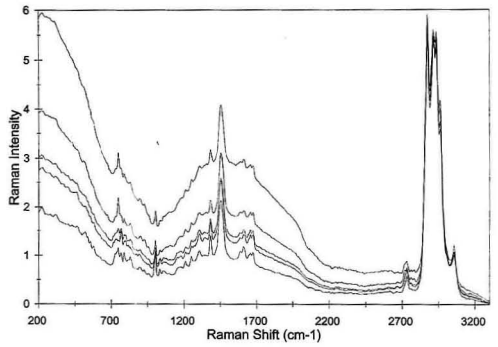

Figure 2. FT-Raman spectra of the five fluorescent commercial petroleum fuels. Of the 208 fuels, these are the only five which fluoresce when excited with 1064 nm radiation.

has certain limitations. For example, the overtone absorbances which constitute a near-IR spectrum are typically broad and ill-resolved. This results in a decrease in the "chemical information" contained in the spectral data. In the case of blends containing *o*-, *m*-, and *p*-xylene isomers, near-IR spectroscopy is incapable of quantifying individual isomer concentrations. We have recently shown, however, that fiber-optic Raman spectroscopy with partial least-squares analysis is capable of quantifying individual xylene isomer concentrations (with standard errors of <0.5 vol %) in hydrocarbon blends containing significant concentrations of all three isomers.[11] This advantage over near-IR spectroscopy is due to the abundant yet sharp and well-resolved spectral peaks in the Raman spectra.

In this article, we describe the use FT-Raman spectroscopy and partial least-squares (PLS) regression analysis to accurately determine the research octane number (RON), the motor octane number (MON), the pump octane number (pump), and the Reid vapor pressure (RVP) of 208 commerical petroleum fuel blends produced by the Ashland Petroleum Co.

EXPERIMENTAL SECTION

The Ashland Petroleum Co. (Ashland, KY) supplied 208 commercial fuel blends from its Cattletsberg refinery. The fuels were sealed in 6 dram glass vials with Teflon-lined caps. Headspace in the vials was kept to a minimum. The samples were shipped overnight, and upon arrival at Old Dominion University, they were immediately placed in an explosion-proof freezer maintained at −18 °C. Prior to shipment, the samples were stored by Ashland at −40 °C for several months. During this time, the motor and research octane numbers were experimentally determined using current ASTM knock engine methods (ASTM method D2699 for determination of RON and ASTM method D2700 for determination of MON). In addition, the Reid vapor pressure was determined for 201 of the 208 samples. The RVP bomb was equilibrated at 38 °C, and the vapor pressure was measured and corrected for barometric pressure via the Grabner method.

Each octane number was determined at three different knock engine laboratories (Ashland knock engine labs in St. Paul, Canton, and Cattletsberg). The average standard deviation for all of the samples was ~0.4 octane unit.

The Raman spectra of the 208 samples were acquired using a Nicolet 950 FT-Raman spectrometer. A 180° collection geometry was used. Prior to spectral acquisition, a sample was removed from the freezer, warmed until no condensation appeared on the container, and placed in the sample holder. The Nd:Yag laser (1064 nm) was focused through the glass to the center of the container. The laser power incident on the glass container wall ranged from a high value of 380 mW to a low value of 356 mW. Although it is possible to maintain laser power at the sample at a constant value, the slight variations better approximate the fluctuations which might be expected in a "real-world" application. Each spectrum consisted of 200 scans, collected over 110 s at 8 cm^{-1} resolution with Happ-Genzel apodization being used in the transformation. All spectra were mean-centered and variance scaled and subsequently processed using Quant-IR PLS software (Nicolet).

RESULTS

Figure 1 shows the FT-Raman spectra for five of the 208 petroleum fuels. These samples are representative of the majority of samples received. For octane analysis, the petroleum fuels were divided into two groups. One group (the training set) consisted of 188 petroleum fuels, and the other group (the test set) consisted of 20 fuels. The subdivision into two groups was random and was performed prior to any PLS analysis. The Raman spectra for each of the samples in the training set were taken and were used to construct PLS regression models correlating the Raman spectra with the octane numbers for each sample. In these models, two Raman spectral regions were used: 2510−3278 and 196−1851 cm^{-1}. From these regression models, it is evident that the model-predicted octane values for five samples consistently show large deviations from their experimentally determined values. The Raman spectra for these samples are shown in Figure 2. These spectra differ dramatically from those of the remaining samples. The difference is due to a weak fluorescent background which decreases to zero in the CH stretching region of the spectra. These samples were removed from the training set, and new regression models were constructed. Leverage plots for the resulting models were used to eliminate eight additional spectra from the training set, bringing the total number of standards to

(11) Cooper, J. B.; Flecher, P. E.; Vess, T. M.; Welch, W. T. *Appl. Spectrosc.* **1995**, *49*, 586−592.

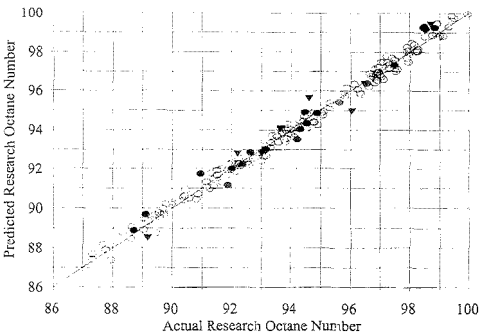

Figure 3. Predicted versus actual plot for research octane number: ○ (total of 175), samples which were included in the training set; ● (total of 20), samples in the test set; and ▼ (total of 8), highly leveraged samples which were removed from the training set prior to constructing the PLS regression model.

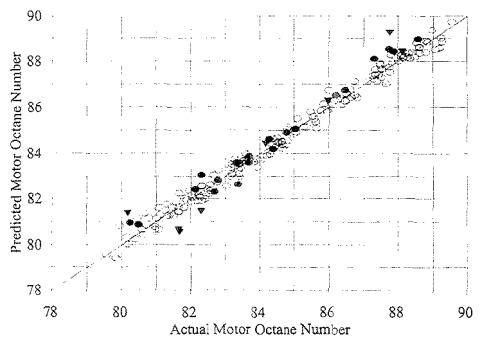

Figure 4. Predicted versus actual plot for motor octane number: ○ (total of 175), samples which were included in the training set; ● (total of 20), samples in the test set; and ▼ (total of 8), highly leveraged samples which were removed from the training set prior to constructing the PLS regression model.

175 for RON, MON, and pump models. The predicted versus actual octane plots for RON, MON, and pump are given in Figures 3–5, respectively. These plots include the predicted values for the eight most leveraged samples which were removed from the training set. Table 1 includes the number of factors included in each of the models as well as the standard error of validation using the leave-one-out validation method.

For the fluorescent samples, the background under the CH stretching region is linear. Hence, a separate regression model was constructed using only the 2510–3278 cm^{-1} region. This regression model did not contain the fluorescent samples in the training set either. Once this model was constructed, the model was used to predict the octane numbers for the fluorescent samples. These values are given in Table 2, along with values for models constructed using the entire spectral region (196–3278 cm^{-1}) and the spectral regions used in the octane models (2510–3278 and 196–1851 cm^{-1}).

In addition to leave-one-out validation for the regression models, the models were also used to predict the octane numbers of the test set. These results are plotted in Figures 3–5 (the test set values are plotted as ●).

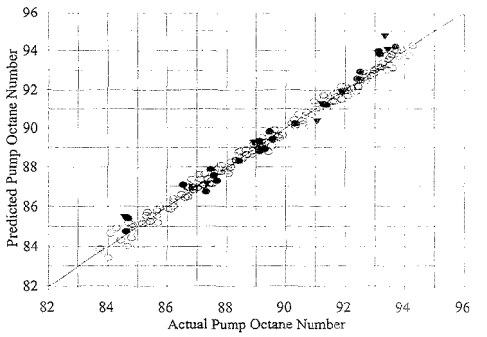

Figure 5. Predicted versus actual plot for pump octane number: ○ (total of 175), samples which were included in the training set; ● (total of 20), samples in the test set; and ▼ (total of 8), highly leveraged samples which were removed from the training set prior to constructing the PLS regression model.

Table 1. Standard Errors of Validation for Partial Least-Squares Regression Models

determined property[a]	low value	high value	no. of factors	no. of standards	SEV
MON	75.563	89.550	8	175	0.415
RON	87.325	99.950	10	175	0.535
pump	83.738	94.288	9	175	0.410
RVP (psi)	7.070	14.735	8	175	0.568

[a] Spectral regions used in models: 196–1851 and 2510–3278 cm^{-1}.

The above-described procedure was also used to construct models which correlate the RVP with the Raman spectra. Of the 208 samples, only 201 had experimentally determined RVPs associated with them. The training set consisted of 175 samples (the five fluorescent samples and one highly leveraged sample being removed from the 201 samples), and the remaining 20 samples were used as the test set and were identical to the test set used for the octane determinations. The predicted versus actual values for the resulting model constructed from the 175 standards are plotted in Figure 6, where the test set values are plotted as ●.

DISCUSSION

In the analyzed petroleum blends, there are in excess of 300 individual chemical species of varying concentrations, all of which affect the octane numbers of the samples. Despite the complexities of the samples, the resulting Raman correlation models predict the octane numbers remarkably well. This is evident both in the standard errors of validation for the models determined with leave-one-out validation and by the prediction of the test set. In both cases, the standard error is comparable to the standard deviation for the experimentally determined values (0.4 octane unit). This suggests that in this work, the ability of Raman spectroscopy to predict the octane numbers of commercially available fuels is limited primarily by the accuracy of the training set. It is reasonable to expect that if the accuracy of the octane values in the training set is improved, the standard errors for the models will be reduced even further.

Of the 208 petroleum fuels supplied by Ashland Petroleum, only five exhibit any fluorescence when excited with 1064 nm

Table 2. Predicted Values for Five Fluorescent Petroleum Samples Using Various Spectral Regions

sample no.	actual	entire spectrum[a]	2 spectral regions[b]	CH region[c]
		RON Model Predicted Values		
175	94.66	141.43	103.51	95.29
176	88.61	110.50	93.19	89.06
177	94.80	127.14	101.10	95.20
179	93.97	107.34	96.76	94.78
209	94.57	115.74	95.94	92.94
		MON Model Predicted Values		
175	85.02	116.89	87.15	85.31
176	80.45	93.71	80.67	80.10
177	85.16	105.44	86.63	85.78
179	83.63	93.07	84.39	83.98
209	83.13	97.70	83.16	82.76
		Pump Model Predicted Values		
175	89.82	117.99	103.74	89.88
176	84.53	96.87	90.32	84.71
177	89.98	109.09	99.06	90.63
179	88.80	97.24	92.71	89.38
209	88.85	101.03	93.57	87.88
		RVP (psi) Model Predicted Values		
175	10.80	31.97	42.64	9.44
176	10.40	18.78	23.79	9.40
177	11.32	23.69	30.12	10.44
176	11.68	18.93	21.87	11.82
209	10.07	21.37	27.03	12.29

[a] 196–3278 cm^{-1}. [b] 196–1851 and 2510–3278 cm^{-1}. [c] 2510–3278 cm^{-1}.

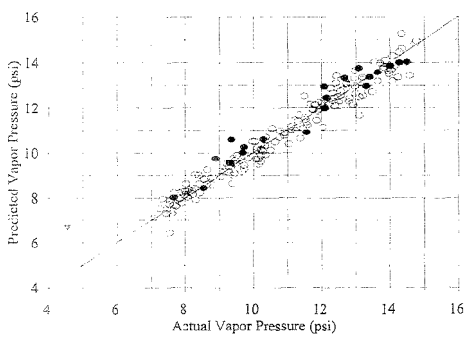

Figure 6. Predicted versus actual plot for Reid vapor pressure: ○ (total of 175), samples which were included in the training set; ● (total of 20), samples in the test set; and ▼, a highly leveraged sample which was removed from the training set prior to constructing the PLS regression model.

radiation. This is attributable to the long wavelength of the laser. We have also obtained the Raman spectra of 100 of these fuels using a dispersive Raman instrument with excitation at 852 nm and have found that 10% of these samples exhibit significant fluorescence. Since longer wavelength excitation is not presently practical for a dispersive system, the use of a Fourier-transform instrument is preferred when collecting Raman spectra of highly colored petroleum fuels. Even in the case of the five fluorescent samples (using the FT-Raman), the fluorescence is weak and decays to the baseline in the CH stretching region of the spectrum. As shown in Table 2, a model constructed using the entire spectral region (fingerprint and CH stretching regions) results in large prediction errors for these samples. If the region between the fingerprint and CH stretching regions is eliminated from the model, the error improves but is still relatively high. By using only the baseline-corrected CH stretching region, however, the models become highly accurate in predicting the octane numbers. In the construction of all of the PLS regression models, the spectra were mean-centered and variance-scaled prior to processing. For the present and previous work in our laboratories, this has resulted in more accurate and robust models than those obtained if other or no preprocessing of the data was performed. We believe that the primary reason for this improvement is the existence of slight intensity changes due to variations in the laser power during the collection of the Raman spectra of the training set. Although it is possible to rigorously control the laser output in the laboratory environment and therefore yield more accurate models, the models will not be as robust unless the spectra of the samples to be predicted are subjected to the same rigorous control of the laser intensity. This is not likely to be the case for many industrial applications.

Accepting that some degree of laser intensity variation is inevitable in an industrial application, it is still possible to improve the performance of the system via calibration. As an extreme example, we have acquired the Raman spectra of one of the fuel samples using laser powers of both 250 and 450 mW. These spectra represent extremes in laser power variations. In addition, the spectrum of toluene was acquired under the same conditions as the spectra in the training set (380 mW) as well as at 250 and 450 mW. The intensity of the strongest toluene peak in the CH stretching region (the calibration peaks) was used to construct a calibration ratio for the extreme spectra by dividing the calibration peak intensity acquired under training set conditions by the calibration peak intensity acquired under one of the extreme laser power conditions. This ratio was then multiplied by each of the intensities in the extreme spectrum of the petroleum sample to give a normalized spectrum. In both cases (250 and 450 mW), the models predict the octane numbers as well as if the spectrum had been acquired under similar laser power conditions. Without the calibration step, the extreme spectra result in predicted octane numbers with high errors.

CONCLUSIONS

FT-Raman spectroscopy in combination with partial least-squares regression analysis can be used to construct highly correlated models relating a petroleum fuel's Raman spectrum to its motor octane number, its research octane number, its pump octane number, and its Reid vapor pressure. Using leave-one-out validation, the standard errors for MON, RON, and pump are 0.415, 0.535, and 0.410 octane units, respectively. For the RVP model, the standard error of validation is 0.568 psi. Using a blind test set of 20 petroleum fuels, the regression models predict MON, RON, and pump with average absolute errors of 0.389, 0.383, and 0.365 octane units, respectively. Using the same blind test set, the RVP model yields an average absolute error of 0.425 psi.

For the experimentally determined RON and MON values, the average standard deviation is 0.4 octane unit. This suggests that the regression models are limited primarily by the accuracy of the training sets. This is comparable to the accuracy reported for near-IR absorbance/reflectance methods currently being used by the petroleum refinery industry.[9,10] Although near-IR spectroscopy appears to be capable of similar quantitative results in octane measurement, near-IR analysis requires that petroleum samples be classified prior to PLS regression analysis. For example, Ashland Petroleum Co. currently separates fuels into

either oxygenated or nonoxygenated fuels. Subsequently, the fuels are separated into high and low octane fuels. Finally, PLS regression analysis models are used to predict the octane numbers of fuels within each category.

In the present study, no preclassification of fuels was performed. Of the 208 fuels utilized in the study, 79 of the samples were oxygenated with methyl *tert*-butyl ether (MTBE). Hence, Raman spectroscopy has the demonstrated ability to quantitate octane numbers and vapor pressure across a diverse range of fuel compositions with *a single multivariate model* for each property being quantified. This capability has not been demonstrated with near-IR spectroscopy.

In addition, Raman spectroscopy has the demonstrated advantage of also being able to quantitatively determine chemical species in hydrocarbon blends where near-IR analysis fails.[11] Hence, Raman spectrscopy may prove to be a more viable method of fast and efficient quality control in the industrial setting. With the use of fiber-optic probes, Raman spectroscopy could eventually be used for an on-line process control similar to existing near-IR systems.

ACKNOWLEDGMENT

We gratefully acknowledge the financial support of this work by the Ashland Petroleum Co., the Virginia Center for Innovative Technology, and the National Science Foundation.

Received for review May 15, 1995. Accepted August 28, 1995.[⊗]

AC9504631

[⊗] Abstract published in *Advance ACS Abstracts,* October 1, 1995.

Anal. Chem. 1995, *67*, 4101–4111

Chromogenic and Fluorogenic Crown Ether Compounds for the Selective Extraction and Determination of Hg(II)

Bikas Vaidya, Jerzy Zak,† Glenn J. Bastiaans, and Marc D. Porter*

Microanalytical Instrumentation Center, Ames Laboratory USDOE, and Department of Chemistry, Iowa State University, Ames, Iowa 50011

Johnny L. Hallman, Nabeel A. R. Nabulsi, Marty D. Utterback, Bozena Strzelbicka, and Richard A. Bartsch*

Department of Chemistry and Biochemistry, Texas Tech University, Lubbock, Texas 79409

Two novel crown ether compounds, *N,N'*-bis(2-hydroxy-5-nitrobenzyl)-4,13-diazadibenzo-18-crown-6 (CCE) and *N,N'*-bis(7-hydroxy-4-methylcoumarin-8-methylene)-4,13-diazadibenzo-18-crown-6 (FCE), have been synthesized as potential reagents for the selective extraction and determination of heavy metal ions. Characterizations of the acid–base reactivity and the heavy metal ion extraction capabilities are reported. Both CCE and FCE undergo four-step ionization processes with associated tautomeric transformations and form stable complexes with divalent metal cations that can be extracted into 1,2-dichloroethane. Extraction constants for Ba(II), Ca(II), Cd(II), Cu(II), Hg(II), Pb(II), and Sr(II) have been determined for both reagents. For CCE, the extraction order is Hg(II) ≫ Pb(II) > Cu(II) > Cd(II) > Ca(II) > Sr(II) > Ba(II), whereas the order for FCE is Hg(II) ≫ Cu(II) > Pb(II) > Cd(II) > Ca(II) > Sr(II) > Ba(II). The selectivity of CCE for Hg(II) over the next-best-extracted cation, Pb(II), is $\sim 2 \times 10^7$ and that of FCE for Hg(II) over next-best-extracted cation, Cu(II), is $\sim 5 \times 10^6$. Potential applications to chemical analysis, based on the unprecedented selectivity of both reagents for Hg(II), are briefly examined.

Since their discovery,[1] a wide variety of crown ethers have been created[2,3] for applications in solvent extraction[4–9] and isotope separation,[10] as components in ion-selective electrodes,[11–14] and for many other purposes.[15] Lipophilic crown ethers constitute an interesting subgroup of these compounds, largely because of their ability to extract selectively metal ions from an aqueous solution into an organic medium. One particularly attractive strategy couples the selective binding of metal ions by such compounds and the ability of the resulting complex to form an ion pair with a chromogenic or fluorogenic dye.[16–22] The resulting neutrally charged, ion-paired complex is then partitioned into an organic phase and detected optically.

The success of these efforts has led to the construction of crown ethers with pendant proton-ionizable chromophoric or fluorophoric groups, i.e., side arms. The incorporation of such side arms eliminates the ion pairing step, which facilitates applications in chemical analysis processes (see Scheme 1). Several forms of this type of crown ether have been synthesized and evaluated for the selective determination of alkali, alkaline earth, and heavy metal ions.[23–40] The diprotonic chromogenic and fluorogenic crown ethers **1**[23,26,27,31,37] and **2**,[24,27] respectively, developed by Takagi and co-workers, have proven particularly effective as selective extraction agents for divalent metal cations.

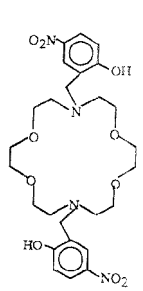

1

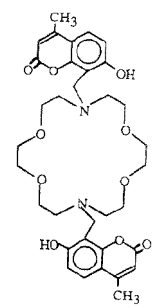

2

† Permanent address: Department of Chemistry, The Silesian Technical University, 44-100 Gliwice, Poland.

(1) Pedersen, C. J. *J. Am. Chem. Soc.* **1967**, *89*, 7017–7036.
(2) Bradshaw, J. S. In *Synthetic Multidentate Macrocyclic Compounds*; Izatt, R. M., Christensen, J. J., Eds.; Academic Press: New York, 1978; pp 53–109.
(3) Gokel, G. W.; Korzeniowski, S. H. *Reactivity and Structure Concepts in Organic Chemistry*; Springer-Verlag: New York, 1982; Vol. 13.
(4) Frensdorff, H. K. *J. Am. Chem. Soc.* **1971**, *93*, 4684–4688.
(5) Pannell, K. H.; Rambrick, D. C.; Lewandos, G. S. *J. Organomet. Chem.* **1975**, *99*, C21–C23.
(6) Danesi, P. R.; Meider-Gorican, H.; Chiarizia, R.; Scibona, G. *J. Inorg. Nucl. Chem.* **1975**, *37*, 1479–1483.
(7) Danesi, P. R.; Chiarizia, R.; Saltelli, A. *J. Inorg. Nucl. Chem.* **1978**, *40*, 1119–1125.
(8) Sadakane, A.; Iwachido, T.; Toei, K. *Bull. Chem. Soc. Jpn.* **1975**, *48*, 60–63.
(9) Bartsch, R. A.; Czech, B. P.; Kang, S. I.; Stewart, L. E.; Walkowiak, W.; Charwicz, W. A.; Heo, G. S.; Son, B. *J. Am. Chem. Soc.* **1985**, *107*, 4997–4998.
(10) Katalnikov, S. G.; Mysheltsov, I. A. *Tr. Inst.-Mosk. Khim.-Tekhnol. Inst. im. D. I. Mendeleeva* **1989**, *156*, 3–24.
(11) Ryba, O.; Petranek, J. *Talanta* **1976**, *23*, 158–159.
(12) Rechnitz, G. A.; Eyal, E. *Anal. Chem.* **1972**, *44*, 370–372.
(13) Patranek, J.; Ryba, O. *Anal. Chim. Acta* **1974**, *72*, 375–380.

0003-2700/95/0367-4101$9.00/0

Scheme 1

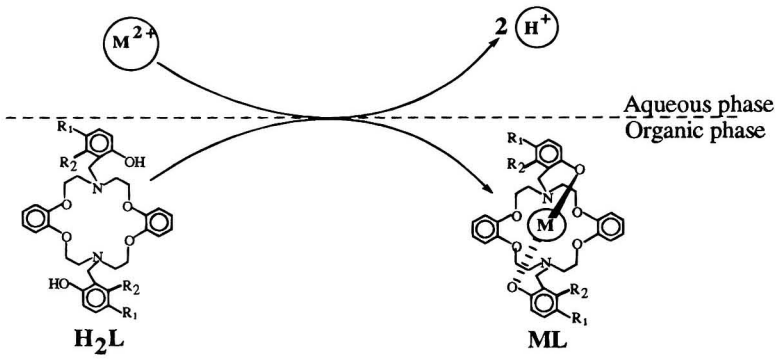

However, both **1** and **2** exhibit only marginal selectivity for Hg(II), a species of critical environmental importance.[23,24]

As part of our collective interests in this area, we initiated a joint effort to design, construct, and characterize crown ether compounds with improved selectivity for binding heavy metal cations. To this end, we have synthesized dibenzo analogs of **1** and **2**, denoted as CCE and FCE, respectively. In comparison to

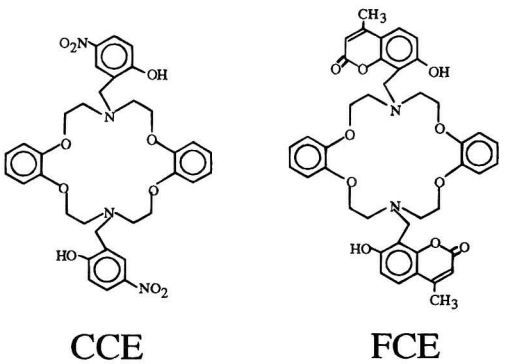

1 and **2**, the presence of the benzo groups in both CCE and FCE should increase the rigidity of the crown ether ring, reduce the basicity of the ring oxygens, and increase overall lipophilicity. We have found that the introduction of the benzo groups produces ligands with an unprecedented selectivity for Hg(II). The following sections describe these findings along with the synthesis, ionization behavior, and divalent metal ion binding capabilities of these novel chromogenic and fluorogenic ionophores.

EXPERIMENTAL SECTION

Reagents and Instrumentation. Reagent-grade inorganic and organic chemicals were obtained from commercial suppliers and used without purification. THF was distilled from benzophenone ketyl, and DMF was stored over 4 Å molecular sieves for at least 1 week. All aqueous solutions were prepared with distilled water that was subsequently deionized using a Millipore Milli-Q water system. Buffer solutions were prepared from solutions of chloroacetic acid (for pH 2–4), 4-morpholineethanesulfonic acid (for pH 4–8), or boric acid (for pH >8) by adding tetramethylammonium hydroxide, lithium hydroxide, or sodium hydroxide solution until the desired pH was obtained.

Infrared (IR) spectra were acquired with a Perkin Elmer Model 1600 FT-IR. ^{1}H NMR spectra were recorded with a Bruker AF-200 spectrophotometer, with chemical shifts reported downfield

(14) Mascini, M.; Pallozzi, F. *Anal. Chim. Acta* **1974**, *73*, 375–382.
(15) Hiroka, M. *Crown Compounds: Their Characteristics and Applications*; Elsevier: Amsterdam, 1982; Vol. 12, pp 151–213.
(16) Sanz-Medel, A.; Gomis, D. B.; Alvarez, J. R. G. *Talanta* **1981**, *28*, 425–430.
(17) Sanz-Medel, A.; Gomis, D. B.; Fuente, E.; Jimeno, S. A. *Talanta* **1984**, *31*, 515–519.
(18) Nazarenko, A. Y.; Pyatnitskii, I. V.; Stolyarchuk, T. A. *Zh. Anal. Khim.* **1981**, *36*, 1719–1721.
(19) Sumiyoshi, H.; Nakahara, K.; Ueno, K. *Talanta* **1977**, *24*, 763–765.
(20) Pyatnitskii, I. V.; Nazarenko, A. Y. *Russ. J. Inorg. Chem.* **1980**, *25*, 592–594.
(21) Abrodo, P. A.; Gomis, D. B.; Sanz-Medel, A. *Microchem. J.* **1984**, *30*, 58–70.
(22) Jawaid, M.; Ingman, F. *Talanta* **1978**, *25*, 91–95.
(23) Nishida, H.; Tazaki, M.; Takagi, M.; Ueno, K. *Mikrochim. Acta* **1981**, *1*, 281–287.
(24) Nishida, H.; Katayama, Y.; Katsuki, H.; Nakamura, H.; Takagi, M.; Ueno, K. *Chem. Lett.* **1982**, 1853–1854.
(25) Nakamura, H.; Nishida, H.; Takagi, M.; Ueno, K. *Anal. Chim. Acta* **1982**, *139*, 219–227.
(26) Shiga, M.; Nishida, H.; Nakamura, H.; Takagi, M.; Ueno, K. *Bunseki Kagaku* **1983**, *32*, E293–E300.
(27) Takagi, M.; Ueno, K. *Top. Curr. Chem.* **1984**, *121*, 39–65.
(28) Katayama, Y.; Nita, K.; Ueda, M.; Nakamura, H.; Takagi, M. *Anal. Chim. Acta* **1985**, *173*, 193–209.
(29) Sasaki, K.; Pacey, G. *Anal. Chim. Acta* **1985**, *174*, 141–149.
(30) Kimura, K.; Tanaka, M.; Kitazawa, S.; Shono, T. *Chem. Lett.* **1985**, 1239–1240.
(31) Sakai, Y.; Kawano, N.; Nakamura, H.; Takagi, M. *Talanta* **1986**, *33*, 407–410.
(32) Katayama, Y.; Fukuda, R.; Takagi, M. *Anal. Chim. Acta* **1986**, *185*, 295–306.
(33) Takagi, M.; Nakamura, H. *J. Coord. Chem.* **1986**, *15*, 53–82.
(34) Kimura, K.; Tanaka, M.; Shono, T. *Bull. Chem. Soc. Jpn.* **1987**, *60*, 3068–3070.
(35) Katayama, Y.; Fukuda, R.; Iwasaki, T.; Nita, K.; Takagi, M. *Anal. Chim. Acta* **1988**, *204*, 113–125.
(36) Czech, B. P.; Babb, D. A.; Czech, A.; Bartsch, R. A. *J. Heterocycl. Chem.* **1989**, *26*, 199–203.
(37) Takagi, M. In *Cation Binding by Macrocycles*; Inoue, Y., Gokel, G. W., Eds.; Dekker: New York, 1990; pp 465–495.
(38) Brown, P. R.; Bartsch, R. A. In *Topics in Inclusion Science*; Osa, T., Atwood, J. L., Eds.; Kluwer Academic Publishers: Dordrecht, 1991; Vol. 2, pp 1–57.
(39) Wilcox, K.; Pacey, G. E. *Talanta* **1991**, *38*, 1315–1324.
(40) Blair, T. L.; Desai, J.; Bachas, L. G. *Anal. Lett.* **1992**, *25*, 1823–1834.

from TMS. Determinations of pH were performed with an Orion Research digital ionalyzer (Model 501) and an Orion combination glass pH electrode (Model 91-04). The pH electrode was calibrated with a set of standard aqueous buffer solutions (Fisher); all values of pH independent of solution composition are reported with respect to this calibration. Absorbance measurements were conducted with a computer-controlled Hewlett Packard diode array spectrophotometer (HP8452A) at a spectral resolution of 2 nm and integration time of 2 s. Fluorescence measurements were performed with a 1 cm quartz cell and a SPEX double monochromator spectrofluorimeter (Fluorolog 2-F112AI) equipped with a 450 W xenon lamp; a spectral band pass of 1 nm and a scan rate of 1 nm/s were used. All the mathematical and graphical simulations were performed using a spreadsheet program (Kaleidagraph).

Ditosylate of *N*-Tosyldiethanolamine (3). *N*-Tosyldiethanolamine[41] (92.5 g, 0.357 mol) was dissolved in 600 mL of pyridine. The solution was stirred at −10 °C in an ice−salt bath, and tosyl chloride (136.1 g, 0.722 mol) was added at such a rate that the temperature was maintained below −8 °C. The reaction mixture was stirred for 1 h, refrigerated overnight, and poured into 500 mL of a slurry of ice and 6 N HCl. CH_2Cl_2 (200 mL) was added, and the layers were separated. The organic layer was washed with 6 N HCl (3 × 50 mL) and water (2 × 50 mL) and evaporated in vacuo. The resultant golden oil was triturated with MeOH (~50 mL) and solidified after 0.5 h. Recrystallization from MeOH gave 153.8 g (76%) of a white solid with mp 96−98 °C (lit.[42] mp 78−79 °C). ^{1}H NMR ($CDCl_3$): δ 2.33 (s, 9 H), 3.22−3.51 (t, 4 H), 3.97−4.28 (t, 4 H), 7.15−7.90 (m, 12 H).

***N*-Tosylbis-[2-(2-hydroxyphenoxy)ethyl]amine (4).** To a stirred, −5 °C solution of catechol (16.80 g, 0.153 mol) and 2 drops of concentrated HCl in Et_2O (30 mL) was added 6.43 g (0.0765 mol) of dihydropyran; the solution was then stirred for 1 h at this temperature. The acid catalyst was destroyed by addition of 5% aqueous $NaHCO_3$, the Et_2O was evaporated in vacuo, and the aqueous layer was extracted with CH_2Cl_2 (75 mL). The organic solution was washed with 5% aq $NaHCO_3$ (2 × 50 mL) and water (2 × 50 mL), dried over $MgSO_4$, and evaporated in vacuo to give 10.31 g of a yellow oil. ^{1}H NMR analysis revealed that the oil was 50% in the mono-THP-protected catechol, with the remainder being the di-THP-protected catechol.

The impure mono-THP-protected catechol was dissolved in DMF (200 mL) under nitrogen, and *t*-BuOK (4.48 g, 40 mmol) was added. The solution was stirred at 80 °C for a 6 h period while a solution of the ditosylate of *N*-tosyldiethanolamine (9.80 g, 17.3 mmol) in DMF (50 mL) was added dropwise. The solution was then stirred at 80 °C for an additional 5 days, and the solvent was removed in vacuo. The residue was dissolved in CH_2Cl_2 (200 mL), washed with water (3 × 50 mL), and dried over $MgSO_4$. The solvent was evaporated in vacuo, and the residue was dissolved in 200 mL of 1:1 MeOH−CH_2Cl_2 (v/v). After addition of concentrated HCl (12 drops), the solution was stirred overnight at room temperature. The resulting precipitate was filtered and recrystallized from 1:1 toluene−EtOAc (v/v) to give 5.85 g (69%) of **4** as off-white needles with mp 171−173 °C. ^{1}H NMR (acetone-d_6): δ 2.32 (s, 3 H), 3.50−3.74 (t, 4 H), 4.00−4.29 (t, 4 H), 6.75 (s, 8 H), 7.12 (s, 2 H), 7.12−7.80 (q, 4 H). IR (KBr): 3438 (OH), 1271, 1149 (SO_2) cm^{-1}. Anal. Calcd for $C_{23}H_{25}NO_6S$: C, 62.29; H, 5.68. Found: C, 62.43; H, 5.75.

Dimesylate of *N*-Tosyldiethanolamine (5). According to the procedure of Crossland and Servis,[43] *N*-tosyldiethanolamine[41] (5.18 g, 20 mmol), Et_3N (4.64 g, 46 mmol), and mesyl chloride (5.04 g, 44 mmol) were reacted in 35 mL of CH_2Cl_2 at −5 °C. After workup, the solid was recrystallized from EtOH (200 mL) to give 6.06 g (73%) of **4** as a white solid, mp 62−64 °C. ^{1}H NMR ($CDCl_3$): δ 2.45 (s, 3 H), 3.07 (s, 6 H), 3.50 (t, 4 H), 4.41 (s, 4 H), 7.36 (d, 2 H). IR (deposit from CH_2Cl_2 on a NaCl plate): 1339, 1155 (SO_2), 1124 (C−O) cm^{-1}. Anal. Calcd for $C_{13}H_{21}NO_8S_3$: C, 37.57; H, 5.10. Found: C, 37.67; H, 5.10.

***N*,*N*′-Ditosyl-4,13-diazadibenzo-18-crown-6 (6).** Bisphenol **4** (4.00 g, 9.0 mmol) was dissolved in 500 mL of MeCN, and powdered Cs_2CO_3 (9.00 g, 23 mmol) was added. The mixture was stirred at reflux for 5 h, followed by the addition of a solution of dimesylate **5** (3.38 g, 8.14 mmol) in 45 mL of MeCN during a 2.2 h period. The mixture was refluxed for 3 days and filtered. The filter cake was rinsed with CH_2Cl_2. The filtrate and rinsing were combined and evaporated in vacuo. The residue was chromatographed on silica gel with CH_2Cl_2 as eluent to provide 3.01 g (55%) of **6** as a white solid with mp 225−227 °C (lit.[44] 215−216 °C). ^{1}H NMR ($CDCl_3$−DMSO-d_6 ~10:1): δ 2.41 (s, 6 H), 3.73 (t, 8 H), 4.12 (t, 8 H), 4.12 (t, 2 H), 6.70−7.00 (m, 8 H), 7.28 (d, 2 H).

4,13-Diazadibenzo-18-crown-6 (7). To a mixture of cyclic ditosylamide **6** (4.10 g, 6.13 mmol) and Na_2HPO_4 (1.85 g) in 410 mL of 5:1 dioxane−methanol (v/v) was added 60 g of freshly prepared, pulverized 6% Na(Hg) amalgam.[45] The mixture was stirred at 80 °C for 2 days and filtered. The solvent was removed in vacuo, and the residue was dissolved in CH_2Cl_2. The solution was washed with water until the aqueous layer was neutral, dried over $MgSO_4$, and evaporated in vacuo to give 2.10 g (95%) of **7** as white needles with mp 181−183 °C (lit.[44] 175−177 °C). ^{1}H NMR ($CDCl_3$): δ 2.42 (br s, 2 H), 3.13 (t, 8 H), 4.12 (t, 8 H), 6.85 (s, 8 H).

***N*,*N*′-Bis(2-hydroxy-5-nitrobenzyl)-4,13-diazadibenzo-18-crown-6 (CCE).** A solution of **7** (1.00 g, 2.79 mmol) and Et_3N (1.20 g, 11.9 mmol) in 40 mL of THF was cooled to 0 °C and a solution of 2-hydroxy-5-nitrobenzyl bromide (1.28 g, 6.13 mmol) in 20 mL of THF was added over a 20 min period. The mixture was stirred at 0 °C for 8 h, refluxed for 4 h, and filtered. The filter cake was washed with cold THF and cold deionized water (3 × 20 mL) and dried with a C_6H_6 azeotrope in a Dean−Stark trap. The C_6H_6 was evaporated in vacuo to provide 1.67 g (93%) of CCE as a light yellow solid with mp 225−227 °C dec. ^{1}H NMR (DMSO-d_6): δ 3.17 (t, 8 H), 3.91 (s, 4 H), 4.12 (t, 8 H), 6.70−7.00 (m, 10 H), 8.00 (d, 2 H, J_o = 8.96 Hz, J_m = 2.90 Hz), 8.18 (d, 2 H, J = 2.88 Hz). IR (KBr): 3498 (OH), 1336 (NO_2), 1253, 1218, 1124 (C−O) cm^{-1}. Anal. Calcd for $C_{32}H_{36}N_4O_{10}$: C, 61.81; H, 5.49. Found: C, 61.87; H, 5.46.

***N*,*N*′-Bis(7-hydroxy-4-methylcoumarin-8-methylene)-4,13-diazadibenzo-18-crown-6 (FCE).** To 0.60 g (1.67 mmol) of **7** dissolved in 53 mL of 15:1 THF−DMF (v/v) with gentle warming was added 7-hydroxy-4-methylcoumarin (0.66 g, 3.74 mmol) dissolved in 3 mL of THF, followed by 0.41 g (5.0 mmol) of formalin. The mixture was stirred for 8 days at room

(41) Graf, E.; Lehn, J. M. *Helv. Chim. Acta* **1981**, *64*, 1051−1065.
(42) Pettit, G. R.; Chamberland, M. R.; Green, B. *Can. J. Chem.* **1967**, *45*, 1555−1560.
(43) Crossland, R. K.; Servis, K. L. *J. Org. Chem.* **1970**, *35*, 3198−3196.
(44) Högberg, S. A. G.; Cram, D. J. *J. Org. Chem.* **1975**, *40*, 151−152.
(45) Feiser, L. F.; Feiser, M. *Reagents for Organic Synthesis*; Wiley: New York, 1970; Vol. 1, pp 1030−1033.

Scheme 2[a]

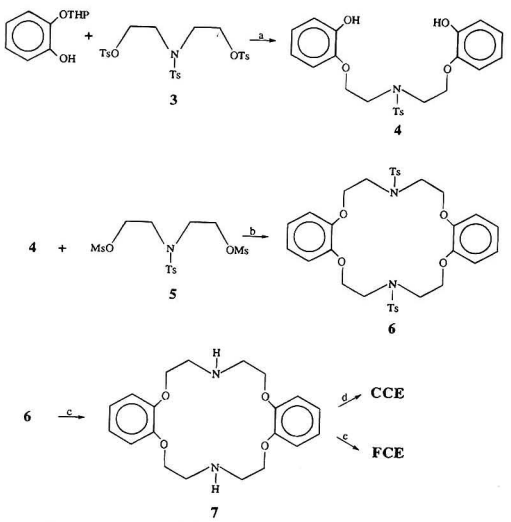

[a] (a) *t*-BuOK, DMF. (b) Cs_2CO_3, MeCN. (c) Na(Hg), Na_2HPO_4, MeOH. (d) 2-Hydroxy-4-nitrobenzyl bromide, Et_3N, THF. (e) 7-Hydroxy-4-methylcoumarin, formalin, THF–DMF.

temperature, and the solvent was removed in vacuo with heating up to 70 °C. The residue was suspended in 150 mL of C_6H_6 and refluxed in a Dean–Stark trap for 2 days. The dried mixture was filtered, and the filter cake was rinsed with C_6H_6. The filter cake was place in a small extraction thimble and extracted with $CHCl_3$ in a hot vapor extraction apparatus for 5 days. The $CHCl_3$ solution was filtered, and the filter cake was rinsed with 3 mL of cold $CHCl_3$ to afford 0.66 g (54%) of FCE as a white solid which had very poor solubility in common organic solvents. IR (deposit from a $CDCl_3$ solution on a NaCl plate): 1706 (C=O), 1208, 1128 (C–O) cm^{-1}. Anal. Calcd for $C_{42}H_{42}N_2O_{10}$: C, 68.65; H, 5.76. Found: C, 68.49; H, 5.50. Based on its poor solubility, the white solid was suspended in 20 mL of $CHCl_3$, and 2.0 g of freshly ground K_2CO_3 was added. The mixture was stirred overnight and filtered. The resulting yellow solution was evaporated in vacuo to give a bright yellow solid with mp 225 °C dec. ^1H NMR ($CDCl_3$): δ 2.36 (s, 6 H), 2.95 (br s, 8 H), 3.80–4.30 (m, 12 H) 5.96 (s, 2 H), 6.60–6.85 (m, 8 H), 6.94 (d, 2 H, J_o = 8.74), 7.29 (d, 2 H, J_o = 8.74). Anal. Calcd for $C_{42}H_{41}N_2O_{10}K{\cdot}0.5H_2O$: C, 64.52; H, 5.41. Found: C, 64.65; H, 5.20.

Acid Dissociation Constants. Acid dissociation constants were determined by analysis of spectral data for CCE and FCE in buffers prepared in 7:3 MeOH–water (v/v) with hydrochloric acid, formic acid, 4-morpholinepropanesulfonic acid, or boric acid and tetramethylammonium hydroxide. The ionic strength was adjusted to 0.10 M with tetramethylammonium bromide. Spectra were measured after dilution of a 50 μL sample of a 50 μM CCE or FCE solution to 5.00 mL with buffer.

Extraction Procedure. Metal ion extractions were performed by mixing 5.00 mL of a 1.0 mM metal nitrate solution with 5.00 mL of a 25 μM crown ether solution in 1,2-dichloroethane. The large excess of metal ions was used to facilitate the determination of the extraction constant by ensuring a negligible change in the aqueous phase metal ion concentration after extraction. The resulting mixture was shaken for 30 min. After the mixture was left to stand for 12 h to allow the two phases to separate, the organic phase concentrations of the free and complexed forms of CCE or FCE were determined spectroscopically. Buffer solutions were used to control the pH of the aqueous solutions.

RESULTS AND DISCUSSION

Synthesis of CCE and FCE. The routes for the synthesis of CCE and FCE are shown in Scheme 2. Although the preparation of the key intermediate 4,13-diazadibenzo-18-crown-6 (**7**) was first communicated by Högberg and Cram[44] in 1974, only a very low yield was reported. Using the sequence shown in Scheme 2, **7** was obtained in a much higher yield in only three steps. Intermediate **7** was then converted to CCE and FCE by one-step adaptations of reactions utilized by Takagi and co-workers for the preparation of **1**[28] and **2**.[24] The final coupling of the fluorophore unit in FCE was more difficult to achieve than the chromophore coupling to give CCE. FCE had very poor solubility in common organic solvents and was transformed into a more soluble potassium monophenoxide form by reaction with K_2CO_3.

General Reactivity Considerations and Formulation for the Determination of Acid Dissociation Constants for CCE and FCE. Diazacrown ethers with two proton-ionizable chromogenic and fluorogenic side arms behave as polybasic acids.[26,27,33] As such, the stepwise acid–base equilibrium for CCE and FCE can be written as

$$H_4L^{2+} = H_3L^+ + H^+ \quad (1)$$

$$H_3L^+ = H_2L + H^+ \quad (2)$$

$$H_2L = HL^- H^+ \quad (3)$$

$$HL^- = L^{2-} + H^+ \quad (4)$$

Thus, the neutral form (H_2L) of CCE or FCE can be successively protonated to form mono- (H_3L^+) and dicationic (H_4L^{2+}) cationic forms or successively deprotonated to produce mono- (HL^-) and dianionic (L^{2-}) forms. The corresponding acid dissociation constants (K_{ai}) for eqs 1–4 can be formulated in terms of concentrations (assuming activity coefficients of unity), as exemplified by eq 5.

$$K_{a1} = [H_3L^+][H^+]/[H_4L^{2+}] \quad (5)$$

At a more detailed structural level, however, zwitterion formation is possible, which would lead to a more complex multicomponent equilibrium. Zwitterion formation can occur if the phenolic groups of the side arms are stronger acids than the amine group of the crown ether ring.[46] Zwitterion formation is also influenced by solvent, whereby polar solvents promote the formation of zwitterions, and nonpolar solvents favor the nonionic forms.[26] In addition, the presence of the two amine–phenol group pairs in CCE and FCE can lead to a variety of tautomeric species. Scheme 3 summarizes each of the above possibilities. Thus, the deprotonation of H_4L^{2+} to L^{2-} can pass through a host of alternate intermediates, the distribution of which is dependent on several

(46) Albert, A.; Serjeant, E. P. *The Determination of Ionization Constants: A Laboratory Manual*, 3rd ed.; Chapman and Hall: New York, 1984; pp 126–134.

Scheme 3[a]

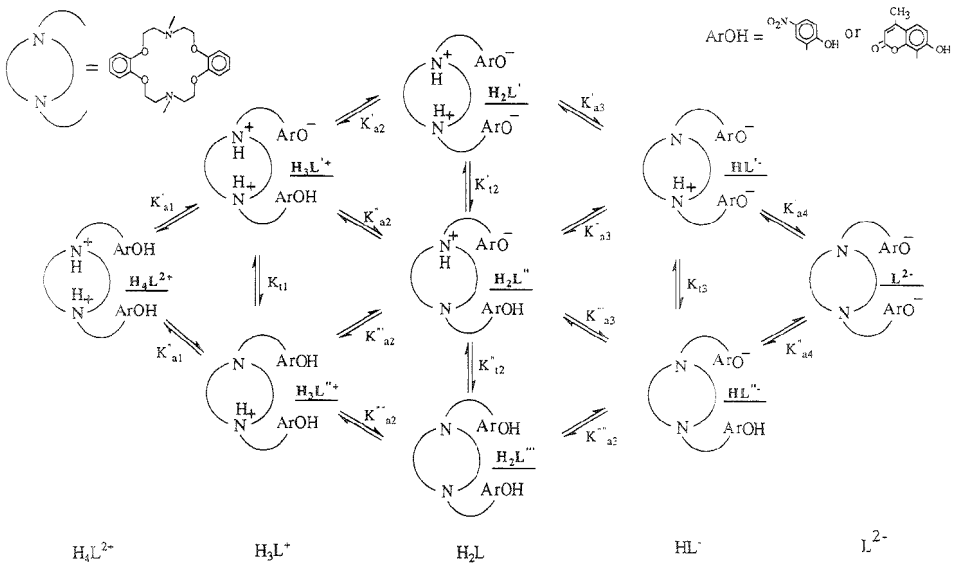

[a] Protons omitted for clarity.

factors, including the cation, ionic strength, and polarity of the solvent. Fully protonated CCE or FCE can then transform from H_4L^{2+} to H_3L^+ through the loss of a proton from either the ammonium or the phenolic functionalities, yielding the respective tautomeric forms $H_3L'^+$ and $H_3L''^+$. Similarly, the loss of a proton from H_3L^+ could give rise to three different forms of H_2L, i.e., H_2L', H_2L'', and H_2L'''. The loss of a third proton results in the formation of HL^-, which can exist as, HL'^- or HL''^-, and finally, the deprotonation of HL^- yields L^{2-}. In each of these cases, the tautomeric equilibrium can be expressed with the designations given in Scheme 3 as

$$K_{t1} = [H_3L'^+]/[H_3L''^+] \quad (6)$$

$$K_{t2}' = [H_2L']/[H_2L''] \quad (7)$$

$$K_{t2}'' = [H_2L'']/[H_2L'''] \quad (8)$$

$$K_{t3} = [HL'^-]/[HL''^-] \quad (9)$$

As a consequence of the tautomeric equilibria, the acid dissociation constants as exemplified by eq 5 are the sum of the acid dissociation constants for each of the possible protonic states.[46] For example, K_{a1} is the sum of K_{a1}' and K_{a1}'', where K_{a1}' and K_{a1}'' represent the dissociation of H_4L^{2+} to $H_3L'^+$ and $H_3L''^+$, respectively. Furthermore, each of the tautomeric equilibria can be related to the appropriate dissociation constants following Scheme 3 and as shown by eq 10 for K_{t1}.

$$K_{t1} = K_{a1}'/K_{a1}'' \quad (10)$$

To complete the development of the multistep equilibrium for CCE and FCE, the analytical concentration of the crown ether (C_t) can be defined as the sum of the concentrations of all of their possible protonic states and is expressed by

$$C_t = [H_4L^{2+}] + [H_3L^+] + [H_2L] + [HL^-] + [L^{2-}] \quad (11)$$

Combining the formulization for the acid–base equilibria for reactions 1–4 with that in eq 11, the concentration of each protonic form of the crown ether as a function of hydrogen ion concentration can be written as represented in eq 12 for H_4L^{2+},

$$[H_4L^{2+}] = C_t[H^+]^4/G \quad (12)$$

where

$$G = [H^+]^4 + [H^+]^3K_{a1} + [H^+]^2K_{a1}K_{a2} + [H^+]K_{a1}K_{a2}K_{a3} + K_{a1}K_{a2}K_{a3}K_{a4}$$

Finally, following the additivity law, the absorbance (A_λ) of a solution of CCE or FCE at a given wavelength (λ) can be written as

$$A_\lambda = \{[H_4L^{2+}]\epsilon_{\lambda,H_4L^{2+}} + [H_3L^+]\epsilon_{\lambda,H_3L} + [H_2L^+]\epsilon_{\lambda,H_2L} + [HL^-]\epsilon_{\lambda,HL} + [L^{2-}]\epsilon_{\lambda,L^{2-}}\}l \quad (13)$$

where $\epsilon_{\lambda,i}$ is the molar absorptivity for each of the forms of CCE or FCE at λ and l is the optical path length in a transmission measurement. These formulations will be used in a subsequent section to characterize the equilibria for CCE and FCE.

Optical Properties of CCE and FCE as a Function of Solution pH and Acid Dissociation Constants. (a) Optical

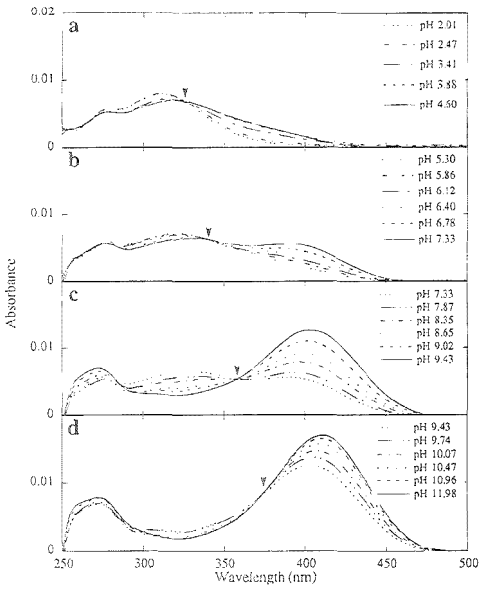

Figure 1. Absorbance spectra of CCE in 7:3 MeOH–water (v/v) as a function of pH: (a) pH 2.01–4.60, (b) 5.30–7.33, (c) 7.33–9.43, and (d) 9.43–11.98. The arrows point to the isosbestic points.

Properties. Figure 1 details the absorption spectra of CCE between 250 and 500 nm as a function of pH. A 7:3 MeOH–water (v/v) solution was used for solubility purposes. At pH 2 and below (Figure 1a), CCE has an absorption maximum at 312 nm. Increases in pH (Figure 1) result in the appearance of a new feature at much longer wavelengths that undergoes a continuous evolution in neutral and alkaline solutions. At pH 12 and above, the absorbance maximum is at 410 nm. Over this pH range, four isosbestic points are observed: 326 nm at pH 2–5 (Figure 1a), 340 nm at pH range of 5–7 (Figure 1b), 358 nm at pH 7–9 (Figure 1c), and 374 nm at pH 9–12 (Figure 1d). The existence of the four isosbestic points is consistent with the stepwise deprotonation process shown in Scheme 3. In addition, as described below, the continual evolution of the spectrum reflects the existence of a tautomeric equilibrium at each step in the dissociation process.

Considerations of the acid–base chemistry and the related optical properties of the parent chromophore of CCE (i.e., *p*-nitrophenol) provide insight into the structural changes that accompany the spectral changes shown in Figure 1. Based on the pH-dependent spectral data for structural analogs of the chromophoric side arms of CCE (i.e., *p*-nitrophenol and 2-hydroxy-5-nitrobenzyl alcohol[23,47]), the changes in the spectra at high pH (Figure 1c,d) primarily reflect the acid–base chemistry of the side arms. The acid–base chemistry of the amine functionalities is therefore dominant at low pH. However, the tautomeric transformation of a small amount of the chromophoric side arm gives rise to a small spectral change in the low pH region.

Absorption spectra for FCE were also examined as a function of pH under the same experimental conditions used for Figure 1.

(47) Koshland, D. E., Jr.; Karkhanis, Y. D.; Latham, H. G. *J. Am. Chem. Soc.* **1964**, *86*, 1448-1450.

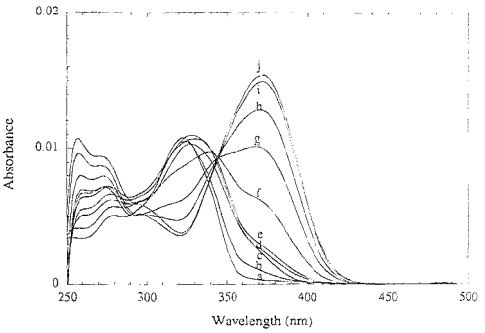

Figure 2. Absorbance spectra of FCE in 7:3 MeOH–water (v/v) as a function of pH: (a) pH 1.9, (b) 4.0, (c) 6.2, (d) 7.2, (e) 8.2, (f) 9.4, (g) 9.9, (h) 10.3, (i) 11.2, and (j) 12.0.

A portion of the results is shown in Figure 2. Though the spectra lack well-defined isosbestic points (an observation not at present understood), the overall behavior of FCE is similar to that of CCE, with absorbance maxima at slightly longer wavelengths at low pH and slightly shorter wavelengths at high pH. The pH range for the transformations occurs at slightly higher values (~3–12.5). Further, a comparison of the spectra of FCE between pH 8 and 11 (see Figure 2) with those of the parent chromophore (7-hydroxy-4-methylcoumarin) reveals that the changes in the high pH range arise primarily from the dissociation of the phenolic protons. Therefore, as with CCE, the changes in the spectra at low pH are attributed to the acid–base chemistry of the amine functionalities and the corresponding tautomeric equilibria.

(b) Determination of Acid Dissociation Constants. Based on the above observations, CCE and FCE are present predominantly in their H_4L^{2+} forms at pH 2. Thus, the molar absorptivity ($\epsilon_{\lambda i}$) for H_4L^{2+} can be readily calculated. The same analysis can be applied to the data at the upper pH limit, where CCE and FCE exist almost exclusively in their L^{2-} forms. Additionally, since the absorbance for CCE at 358 nm remains constant in the pH ranges 4–5 and 7–10, and the absorbance for FCE at 344 nm remains constant in the pH range 5–6 and above pH ~8, the values of pK_{a1} and pK_{a2} can be determined. The value of pK_{a1} is found from the absorbance data below pH 5. The value of pK_{a2} can be determined from the absorbance data between pH 5 and 7 using the method described by Albert and Serjeant,[48]

$$pK_a = pH + \log \frac{A_I - A}{A - A_{HI}} \qquad (14)$$

where A, the absorbance at the analytical wavelength (358 nm for CCE and 344 nm for FCE), is the sum of the absorbances of the deprotonated species (A_I) and its conjugated acid (A_{HI}).

The remaining two pK_a values can be determined by a mathematical simulation of the equilibria using the absorption maxima for the protonated and deprotonated forms of the chromophores. This was accomplished by estimating values for $\epsilon_{\lambda,H_2L^-}$, ϵ_{λ,H_3L}, ϵ_{λ,HL^-}, pK_{a3}, and pK_{a4} and then calculating absorbances using eq 13 at all three wavelengths for the absorbance spectra shown in Figures 1 and 2. Typically, the first estimates

(48) Reference 46, pp 70–73.

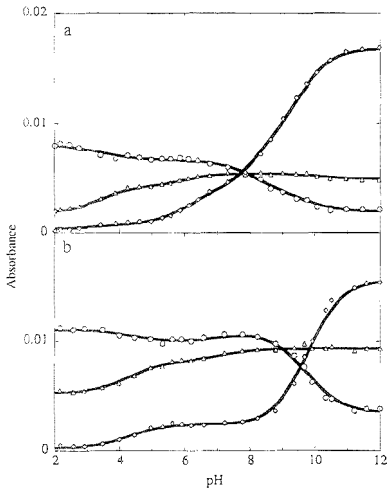

Figure 3. Measured absorbances (a) for CCE in 7:3 MeOH–water (v/v) at 312 (○), 358 (△), and 410 nm (◇) and (b) for **FCE** in 7:3 MeOH–water (v/v) at 322 (○), 344 (△), and 372 nm (◇) in the pH range of 2–12. Symbols represent experimental data, and solid lines represent the simulated data. The uncertainty of the absorbance data is about the size of the symbols.

Table 1. Molar Absorptivities ($\epsilon \times 10^{-3}$, L mol^{-1} cm^{-1}) of CCE and FCE at Selected Wavelengths in 7:3 Methanol–Water (v/v)

	CCE		
species	312 nm	358 nm	400 nm
H_4L^{2+}	19.2	4.4	1.0
H_3L^{+}	16.2	10.0	1.8
H_2L	15.6	13.0	9.0
HL^{-}	9.0	13.0	22.2
L^{2-}	4.6	11.8	40.2

	FCE		
species	322 nm	344 nm	370 nm
H_4L^{2+}	25.7	12.3	0.6
H_3L^{+}	23.4	19.0	5.6
H_2L	25.1	21.7	18.5
HL^{-}	17.5	21.7	5.6
L^{2-}	8.2	21.7	36.2

for $\epsilon_{\lambda,H_3L^+}$, ϵ_{λ,H_2L}, and ϵ_{λ,HL^-} were chosen to be between the values for H_2L^{2+} and L^{2-}. The two pK_a values and molar absorptivities were changed iteratively (increments of 0.05 and 100 M^{-1} cm^{-1} for the pK_a values and molar absorptivities, respectively) until the average relative deviation between the simulated and experimental absorbance data at each of the three wavelengths was <5%. The simulated and measured absorbances at the three wavelengths are compared in Figure 3a for CCE and Figure 3b for FCE. The simulated data are shown by the solid lines. The agreement between the simulated and the experimental data at all three wavelengths confirms the effectiveness of the simulation. The absorption coefficients for the different ionized forms of CCE and FCE in 7:3 MeOH–water (v/v) are listed in Table 1. The pK_a values are listed in Table 2, which also includes the results of a study of ionic strength effects (see below) and comparison with the pK_a values for **1**, **2**, and related functional analogs.

In agreement with the earlier interpretation of the optical data, the pK_a values for *p*-nitrophenol given in Table 2 support the general assignment of the processes at high pH to the transformation of the phenolic functional groups of CCE. However, the difference in the pK_a values for each of the steps indicates that a subsequent dissociative step initiates before completion of the ongoing step. These transformations, when coupled with the existence of tautomeric equilibria, hinder an overall structural description for each of the steps in the dissociation process. Nevertheless, each dissociative step can proceed through a variety of possible pathways, with the viability of each pathway dependent on the polarity and ionic strength of the solution. The existence of multiple pathways in the dissociation of CCE is evident from the spectral data shown in Figure 1a, which reflects the conversion of H_4L^{2+} to H_3L^{+}. This series of spectra exhibit an increase in the absorbance at the absorbance maximum (410 nm) for the L^{2-} form of CCE that corresponds to ~10% conversion of the chromophoric side arms. This low level of conversion is inconsistent with a transformation that occurs solely through either of the two pathways in Scheme 3. Thus, the loss of the first proton from CCE yields both $H_3L''^{+}$ (~90%) and $H_3L'^{+}$ (~10%) as products.[49] These data also reveal that K_{a1}'' is greater than K_{a1}' by almost an order of magnitude and that K_{11} is ~9.

(c) Effects of Ionic Strength and Identity of Cation. The effects of the ionic strength of the solution and of the identity of the cation on the acid–base chemistry of CCE and FCE have also been investigated. An assessment of the former provides insight into the possible pathways for the dissociation of the two species. A study of the latter probes the importance of cation uptake into the crown ether cavity on reactivity. The results of these experiments, which used $(CH_3)_4N^+$, Li^+, and Na^+ as cations and focused primarily on CCE, are summarized in Table 2.

The ionic strength dependences of the acid–base chemistry were examined using two different cations: $(CH_3)_4N^+$ and Li^+. In both cases, the pK_a values in the first, second, and fourth dissociative steps exhibited an increase as the ionic strength of the methanolic solution increased, whereas the value for pK_{a3} remained essentially constant. The trends in the pK_{a1}, pK_{a2}, and pK_{a4} values can be qualitatively attributed to the relative stabilization of each of the possible species in each of the dissociative steps from microscopic charge considerations.[50] Thus, in agreement with the analysis of the optical data shown in Figure 1a, the transformation of H_4L^{2+} to H_3L^{+} leads primarily to $H_3L''^{+}$ (as opposed to $H_3L'^{+}$) as the more stable product. That is, the increase in the pK_{a1} with the increase in the ionic strength, as observed for CCE in Table 2, argues that the higher ionic strength favors the protonated form (H_4L^{2+}) more than the deprotonated form (H_3L^{+}). Since $H_3L'^{+}$ has larger relative charge separation than H_4L^{2+}, $H_3L''^{+}$ should be the major species formed.

The second dissociative step, $H_3L^{+} \rightarrow H_2L$, can be analyzed in a similar but more qualitative manner. From the ionic strength dependences, there are two possible dominant pathways: $H_3L'^{+} \rightarrow H_2L''$ and $H_3L''^{+} \rightarrow H_2L'''$. Both pathways are expected to exhibit an increase in pK_a values with increasing ionic strength. The spectroscopic data reveal that ~30% of the chromogenic side

(49) We also attempted to investigate the structural details of these transformations using infrared Fourier-transform spectroscopy. Unfortunately, the low solubility of both CCE and FCE precluded detection of any N–H vibrational modes, features which would have aided our assessment.

(50) Finston, H. L.; Rychtman, A. C. *A New View of Current Acid–Base Theories*; Wiley: New York, 1982.

Table 2. Acid Dissociation Constants for CCE, FCE, and Related Compounds in Solutions of Varied Ionic Strength and Cation Content

compd	solvent	ionic strength (M)	cation	pK_{a1}	pK_{a2}	pK_{a3}	pK_{a4}
CCE	70% MeOH	0.01–0.035	$(CH_3)_4N^+$	3.42	6.00	8.15	9.65
CCE	70% MeOH	0.1	$(CH_3)_4N^+$	3.90	6.30	8.20	10.10
CCE	70% MeOH	0.1	Na^-	3.50	6.00	8.00	8.90
CCE	70% MeOH	0.01–0.1	Li+	3.60	6.20	8.15	9.75
CCE	70% MeOH	0.5–0.7	Li^+	3.95	6.48	8.10	10.15
1[a]	10% dioxane	0.1	$(CH_3)_4N^+$	4.03	5.52	9.80	
p-nitrophenol[b]	water			7.15			
p-nitrophenol[c]	70% MeOH	0.1	$(CH_3)_4N^+$	8.03			
FCE	70% MeOH	0.01–0.035	$(CH_3)_4N^+$	4.30	7.21	9.35	10.05
FCE	70% MeOH	0.1	Na^+	4.80	6.40	8.30	10.00
FCE	70% MeOH	0.01–0.1	Li^+	4.40	7.00	9.65	10.40
2[d]	10% dioxane			4.28	7.23	10.38	
7-hydroxy-4-methylcoumarin[e]	water			7.84			
7-hydroxy-4-methyl coumarin[c]	70% MeOH	0.1	Na^-	8.80			

[a] Reference 26. [b] Reference 46, p 145. [c] Vaidya, B.; Porter, M., unpublished results. [d] Reference 33. [e] Moriya, T. *Bull. Chem. Soc. Jpn.* 1983, *56*, 6–14.

arms have been affected by the transformation at the completion of the second dissociation step. Therefore, a large fraction (~70%) of H_2L must be present as H_2L'''. These data, together with the shift of tautomeric equilibria toward species with a lower charge as ionic strength decreases, indicate that H_2L''' and H_2L'' are present to a greater extent than H_2L'. These conclusions are consistent with the pathways predicted by the ionic strength dependences, although small contributions from the other two pathways are also possible.

The development of a description of the pathways for the third dissociative step is also hampered by the complexities affecting the above treatments. Based on the large relative amounts of H_2L''' and H_2L'' prior to dissociation and the virtual absence of an ionic strength dependence of the pK_a values, it is likely that all three of the possible conversions are of importance. The collective result of these conversions yields roughly equal amounts of HL'^- and HL''^-, with HL''^- present at a marginally (a few percent) larger amount over HL'^-.

Lastly, the ionic strength dependences for the conversion of HL^- to L^{2-} indicate that the favored pathway is the conversion of HL'^- to L^{2-}. This finding suggests that the tautomeric conversion of HL''^- to HL'^- plays an obvious role in the process by the resupply of HL'^- upon conversion to L^{2-}.

The cation dependences reveal that the acid strengths of the ionizable protons in each of the steps are affected by Na^+, but not notably so by Li^+ and $(CH_3)_4N^-$. Comparisons of the sizes of each of these species to the cavity diameters of CCE and FCE reveal that Li^+ has an ionic diameter (1.80 Å[51]) smaller than that required for strong interactions within the cavity and that steric effects block the movement of $(CH_3)_4N^+$ (ionic diameter 4.30 Å[51]) into the cavity. On the other hand, the uptake of Na^+ (ionic diameter 2.32 Å[51]) is driven, in part, by a more favorable size match-up with the cavity of the parent crown ether, 18-crown-6 (diameter 2.68–2.86 Å[52]). This added driving force results in the uptake of Na^+ by CCE, which induces an effective decrease in the pK_a value. Thus, the pK_a data obtained using Li^+ and $(CH_3)_4N^+$ more accurately reflect the intrinsic reactivity of each of the dissociative steps. We believe that similar arguments apply to an acid–base reactivity description of FCE.

In closing this section, we note that only three acid–base transitions have been reported for **1**, and **2**, and structurally related compounds.[26,27,33] It is not yet clear whether these differences reflect the inherent reactivity of the compounds or the properties of the solvent system (e.g., the 7:3 MeOH–water solvent system used herein and the 1:9 dioxane–water solvent system utilized in the studies of **1**[26] and **2**[33]).

Scheme 4

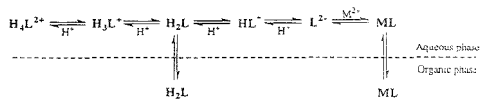

Metal Ion Extraction. (a) Equilibrium Formulation. Capabilities of CCE and FCE for extraction of divalent metal cations into 1,2-dichloroethane were tested. As a starting point, the overall equilibrium for the extraction of a metal ion by a proton-ionizable crown ether is considered. A generalized description of the overall process is shown in Scheme 4, which depicts the transfer of the neutral extractant from the organic phase to the aqueous phase, the multistep ionization and metal ion complexation in the aqueous phase, and the movement of the neutral complex (ML) into the organic phase. The equilibrium between H_2L in an organic phase and a divalent metal cation, M^{2+}, in aqueous phase can then be described as

$$[H_2L]_o + [M^{2+}]_{aq} = [ML]_o + 2[H^-]_{aq} \qquad (15)$$

where $[H_2L]_o$ and $[ML]_o$ are the equilibrium concentrations of H_2L and ML in the organic phase and $[M^{2+}]_{aq}$ and $[H^-]_{aq}$ are the equilibrium concentrations of M^{2+} and H^+ in the aqueous phase, respectively. The extraction constant for this equilibrium, K_{ex}, is written as

$$K_{ex} = \frac{[ML]_o[H^+]_{aq}^2}{[H_2L]_o[M^{2+}]_{aq}} \qquad (16)$$

(51) Huheey, J. E. *Inorganic Chemistry*; Harper & Row: New York, 1983; pp 73–78.

(52) Lamb, J. D.; Izatt, R. M.; Christensen, J. J. In *Progress in Macrocyclic Chemistry*; Izatt, R. M., Christensen, J. J., Eds.; Wiley: New York, 1981; Vol. 2, pp 41-90.

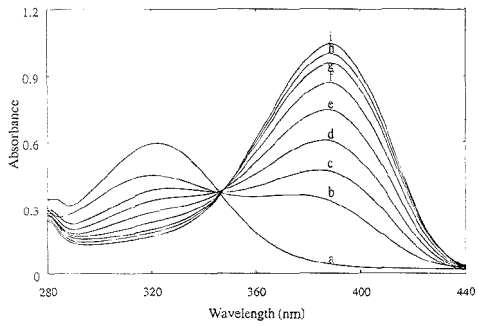

Figure 4. Absorbance spectra for 25 μM CCE solutions in 1,2-dichloroethane before (a) and after extraction of Hg(II) from an aqueous 1.0 mM Hg(II) solution at pH 2.0 (b), 2.2 (c), 2.5 (d), 2.7 (e), 3.0 (f), 3.2 (g), 3.4 (h), and 3.9 (i).

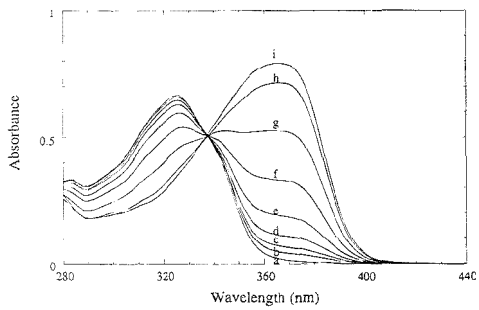

Figure 5. Absorbance spectra for 25 μM FCE solutions in 1,2-dichloroethane before (a) and after extraction of Cd(II) from aqueous 1 mM Cd(II) solution at pH 5.8 (b), 6.0 (c), 6.3 (d), 6.5 (e), 6.8 (f), 7.0 (g), 7.3 (h), and 7.6 (i).

This equation can be recast to give

$$\log K_{ex} = \log q - 2\mathrm{pH} - \log [M^{2+}]_{aq} \qquad (17)$$

where $q = [ML]_o/[H_2L]_o$.

(b) Metal Ion Extraction. Figures 4–6 summarize the extraction data of CCE and FCE for Ba(II), Ca(II), Cd(II), Cu(II), Hg(II), Pb(II), and Sr(II). Figure 4 shows the absorption spectra of CCE in 1,2-dichloroethane before (spectrum a) and after extraction of Hg(II) (spectra b–i) as a function of the pH of the aqueous solution. The pH was varied incrementally between 2 and 4. Formation of the complex results in a bathochromic shift in the spectrum and an increase in molar absorptivity as compared to the spectrum of uncomplexed CCE. Increasing the pH of the aqueous solution enhances formation of the complex, which reaches a maximum at pH ~4. The absorbance maximum of the complex is 388 nm and has an ϵ of 4.1×10^4 L mol^{-1} cm^{-1}. An isosbestic point at 348 nm confirms the existence of only two forms of CCE in the organic phase, as well as the negligible loss of CCE to the aqueous phase during the extraction process.

The complexes formed by CCE and FCE with the other metal ions exhibit similar spectral characteristics but have different pH dependences. For example, Figure 5 presents the pH-dependent absorption spectra of FCE in 1,2-dichloroethane before and after

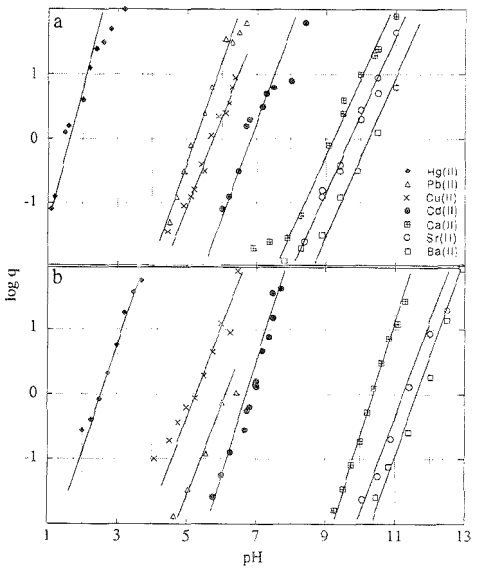

Figure 6. Selectivity of CCE (a) and FCE (b) shown by log([ML]$_o$/[H$_2$L]) vs pH plots, where M(II) is Hg(II), Pb(II), Cu(II), Cd(II), Ca(II), Sr(II), and Ba(II).

the extraction of Cd(II). Changes in the spectra are similar to those noted in Figure 4. In the case of Cd(II), however, the uptake by FCE as well as by CCE (see below) occurs at higher pH values, which translates to lower values for K_{ex}.

Figure 6 summarizes the pH dependences of the metal complexation for CCE and FCE. For each of the cations, the plots of log q exhibit a linear dependence on pH, with a nominal slope of 2. This dependence confirms the general applicability of eq 15 in describing the extraction process. The changes in the spectral properties of the chelates upon complexation, which are similar to those observed for the dissociation of the phenolic protons of H_2L to L^{2-} in Figures 1 and 2, are consistent with this conclusion.

The pH dependences of log q shown in Figure 6 can be used to calculate the values of K_{ex} for each of the metal ions with CCE and FCE. These data are presented in Table 3, together with reported values for **1**[31] and **2**.[35] CCE and FCE display similar but not identical binding preferences. For CCE, the order is Hg(II) ≫ Pb(II) > Cu(II) > Cd(II) > Ca(II) > Sr(II) > Ba(II). The order for FCE is Hg(II) ≫ Cu(II) > Pb(II) > Cd(II) > Ca(II) > Sr(II) > Ba(II). The selectivity of CCE for Hg(II) over the next-best-extracted cation, Pb(II), is 2×10^7, and that for FCE for Hg(II) over the next-best-extracted cation, Cu(II) is 5×10^6. Both values reflect unprecedented selectivities for Hg(II). Comparisons to the K_{ex} values for **1** and **2** further reveal that both CCE and FCE have significantly greater binding strengths for Hg(II), suggesting an opportunity for these novel crown ethers in chemical analysis (see below).

Insights into the complexation properties of CCE and FCE toward Hg(II) can be developed by comparison with those of **1** and **2**. With the important exception of Hg(II), the orders of preference toward metal ion binding for CCE and **1** are the same.

Table 3. Extraction Constants and Selectivity Factors of CCE, FCE, 1, and 2 for Ba(II), Ca(II), Cd(II), Cu(II), Hg(II), Pb(II), and Sr(II)

metal ion	$-\log K_{ex}$				selectivity factor[a]		
	CCE	1[b]	FCE	2[c]	CCE	FCE	1
Hg(II)	0.28	5.8	2.20	*d*	1	1	1
Pb(II)	7.58	5.4	8.92	*d*	2.0×10^7	5.2×10^6	0.4
Cu(II)	8.52	5.6	7.94	*d*	1.7×10^8	8.7×10^5	0.6
Cd(II)	10.50	8.4	10.80	*d*	1.6×10^{10}	4.0×10^8	4.0×10^2
Ca(II)	15.30	12.5	16.70	14.7	6.8×10^{15}	3.2×10^{14}	5.0×10^6
Sr(II)	16.40	13.5	19.10	16.1	1.3×10^{16}	7.9×10^{16}	5.0×10^7
Ba(II)	17.70	15.1	20.70	17.1	2.7×10^{17}	3.2×10^{18}	2×10^{10}

[a] Selectivity factor = K_{ex}(Hg)/K_{ex}(M(II). [b] Reference 31. [c] Reference 35. [d] Data not available.

However, the binding by CCE of cations other than Hg(II) is notably weaker than that of **1**. The same conclusion, based on a more limited comparison of divalent metal ion species, is applicable for FCE relative to **2**. These differences in binding reflect a complex mixture of chemical and structural effects[37] which include the relative sizes of the crown ether ring and the cation, the size and spatial orientation of the side arms, and the relative hardness/softness of the interactions of the active groups in the cavity. We attribute the generally lower K_{ex} values of CCE and FCE relative to **1** and **2**, respectively, to the increased rigidities of the cavities of CCE and FCE that result from the incorporation of the two benzo groups into the ring. This stiffening represents a barrier to the adaptation of a structural arrangement favorable for interaction of CCE and FCE with metal ions. On the other hand, the reduction of electron density at the four alkyl aryl ether oxygens due to delocalization by resonance into the benzo group substituents of CCE and FCE provides for softer ring oxygen binding sites that enhance the extraction of the soft metal Hg(II). Together, these effects result in the *remarkable selectivity* of CCE and FCE toward Hg(II).

The differences in the K_{ex} values of CCE and FCE can also be ascribed to steric effects that are coupled with chemical affinity issues. With the exception of Cu(II), the K_{ex} values of CCE for all of the metal ions examined are larger than those of FCE. The differences for each metal ion reflect contributions from the steric hindrance imposed by the more bulky side arms and the weaker acidity of the phenol functional groups of the side arms of FCE. We attribute the favored uptake of Cu(II) by FCE (as opposed to Pb(II)) to the smaller size of Cu(II), which reduces the steric barrier for complexation.

Potential Applications. The extraction data suggest the potential application of CCE and FCE as reagents for the selective detection of Hg(II) ion. With CCE, such an application would be developed using absorbance-based measurements, whereas FCE offers the possibility of fluorescence detection. In the latter case, we envisioned the selective extraction of the Hg(II)−FCE species, which has its absorbance maximum shifted to longer wavelength by ~60 nm from that of unbound FCE. Such a strategy could then take advantage of the enhanced detection capabilities of fluorescence as opposed to the absorbance-based technique. Unfortunately, as is usually the case,[53,54] we have found that the fluorescence of FCE is quenched by the uptake of Hg(II), as well as by Pb(II) and Cu(II). In contrast, the fluorescence is not quenched by the complexation of Cd(II), Ca(II), Sr(II), and Ba(II). Based on these observations, it is likely that the quenching of fluorescence by Hg(II), Pb(II), and Cu(II) results from the heavy atom effect via spin−orbital coupling.[54] Although FCE could still be used in a determination of Hg(II) by absorbance measurements, it was more difficult to synthesize than CCE. However, FCE could be used in determination of Cd(II) and the alkaline earth cations by fluorescence in the presence of Hg(II), Pb(II), and Cu(II) since the complexes of the latter do not fluoresce. Figure 7 shows excitation and emission spectra of FCE solution in 1,2-dichloroethane before and after extraction of Cd(II), from aqueous solutions at different pH values. The limit of detection of Cd(II), calculated using standard solutions buffered at pH 8.0 at a signal-to-noise ratio of 3, is 6 ppb.

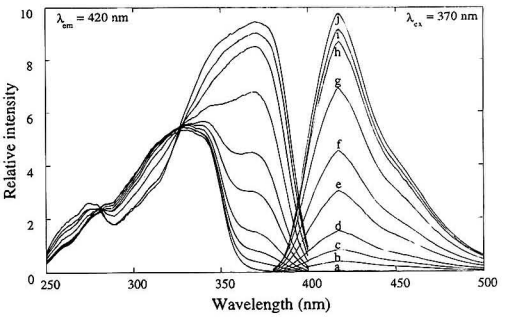

Figure 7. Excitation and emission spectra for 25 μM solutions of FCE before (a) and after extraction of Cd(II) from aqueous solutions at pH 5.6 (b), 5.8 (c), 6.0 (d), 6.3 (e), 6.5 (f), 6.8 (g), 7.0 (h), 7.3 (i), and 7.6 (j). Both the excitation and emission spectra of FCE equilibrated with aqueous solution buffered in the pH range of 5−8 were identical.

Studies of the use of CCE for the selective extraction of Hg(II) into an organic phase like 1,2-dichloroethane revealed a linear calibration curve between 0.2 and 5.0 ppm Hg(II). These tests were conducted using a 25 μM CCE solution to extract Hg(II) from a solution buffered at pH 5.0. Estimated detection limits are ~0.2 ppm at a signal-to-noise ratio of 3. Under this condition, even millimolar Ca(II), Sr(II), and Ba(II) did not exhibit a detectable interference at the detection limit. However, as expected from Figure 6b, the presence of 100 μM Cd(II) and Pb(II) led to an increase in absorbance by ~20% for a 0.2 ppm Hg(II) solution. These contributions, however, can be reduced by performing the extraction at a lower pH of the aqueous sample. In addition to other metal ions, some anions are potential interferants for the determination of Hg(II) with CCE. Chloride ion at 100 μM resulted in a decrease in absorbance of ~30% in the determination of 0.2 ppm (1 μM) Hg(II).

CONCLUSIONS

This joint effort has demonstrated that the novel crown ether compounds, CCE and FCE, exhibit a remarkable selectivity in the binding of Hg(II) over a host of other divalent metal cations [i.e., Pb(II), Cu(II), Cd(II), Ca(II), Sr(II), and Ba(II)]. These improved selectivities are attributed to the reduced basicity of the ring oxygen and enhanced rigidity of the crown ether ring through the incorporation of benzo groups in the ring structure. Efforts are presently underway to harness this selectivity for the develop-

(53) Becker, R. S.; Allison, J. B. *J. Phys. Chem* **1963**, *67*, 2662−2669.
(54) McGlynn, S. P.; Azumi, T.; Kinoshita, M. In *Molecular Spectroscopy of the Triplet State*; Prentice-Hall: Englewood Cliffs, NJ, 1969; pp 261−283.

ment of new methods for Hg(II) analysis based on conventional solvent extraction principles. Possible extensions to chemical sensor applications are also under consideration.

ACKNOWLEDGMENT

Research conducted at Iowa State University was supported by the Office of Basic Energy Research—Chemical Sciences Division of the U.S. Department of Energy—Ames Laboratory, Center for Advanced Technology Development, and by the Microanalytical Instrumentation Center of ISU. Research conducted at Texas Tech University was supported by the Division of Chemical Sciences of the Office of Basic Energy Sciences of the U.S. Department of Energy (Grant DE-FG03-94ER14416 and earlier grants). R.A.B. expresses his appreciation to Professor Makoto Takagi of Kyushu University for sharing the experimental details for the synthesis of **2**. The Ames Laboratory is operated for the U.S. Department of Energy by ISU under Contract No. W-7405-eng-82.

Received for review June 19, 1995. Accepted August 30, 1995.[⊗]

AC950619X

[⊗] Abstract published in *Advance ACS Abstracts*, October 1, 1995.

Anal. Chem. **1995,** *67,* 4112–4117

Phosphorescent Complexes of Porphyrin Ketones: Optical Properties and Application to Oxygen Sensing

Dmitri B. Papkovsky*

Department of Biosensors, Research Center of Molecular Diagnostics, Simpheropolskii Boulevard 8, 113149 Moscow, Russia

Gelii V. Ponomarev

Research Institute of Biomedical Chemistry, Pogodinskaya Street 10/2, 119021 Moscow, Russia

Wolfgang Trettnak and Paul O'Leary

Joanneum Research, Institute for Chemical and Optical Sensors, Steyrergasse 17, 8010 Graz, Austria

A new class of dyes, platinum(II) and palladium(II) complexes of the porphyrin ketones (or "oxochlorins"), exhibiting strong phosphorescence at room temperature is described. Several representative compounds were prepared and studied by spectral luminescence methods in solution. Compared to the related porphyrin and chlorin complexes, the new dyes display high photochemical stability, long wave spectral characteristics, and good compatibility with semiconductor optoelectronics (e.g., excitation by light-emitting diodes). These properties make the new dyes promising for a number of relevant applications, such as quenched phosphorescence sensing and phosphorescence probing (e.g., in binding assays). Analytical application of the porphyrin ketone complexes to phosphorescence lifetime-based sensing of molecular oxygen is described. Platinum(II) octaethylporphine ketone was dissolved in a polystyrene layer to give an oxygen-sensitive film. Oxygen measurements were performed with a prototype fiber-optic instrument based on solid-state components, such as light-emitting diodes and photodiodes. The instrument measured phosphorescence lifetime via changes in phase shift. The phosphorescence lifetime was determined to change from about 61.4 μs at zero oxygen to 16.3 μs in air (210 hPa of oxygen) at 22 °C. The analytically useful range of the sensor was 0–210 hPa of oxygen partial pressure, with a detection limit of 1.5 hPa. The precision of the device was 1.0 hPa at 210 hPa of oxygen and 0.5 hPa at zero oxygen.

Platinum(II) and palladium(II) complexes of porphyrins are known to exhibit strong phosphorescence at room temperatures,[1–4] with quantum yields of >10%. Compared to most other types of phosphorescent organic dyes, porphyrin complexes have long wave spectral characteristics of phosphorescence and significantly shorter lifetimes. These features make them attractive for some special applications, such as phosphorescent labeling of biomolecules for ultrasensitive measurements (e.g., time-resolved luminescence immunoassays[5]) and measurement of phosphorescence quenching by molecular oxygen[6–8] and some other species.[9,10]

Most of the phosphorescent porphyrin dyes presently available exhibit certain disadvantages, such as a low photochemical stability and insufficient compatibility with light sources such as light-emitting diodes (LEDs), one of the prerequisites for the development of cheap and simple analytical instrumentation. A further red-shifting of excitation and emission wavelength is also desirable for better discrimination between the measured signal and background deriving from sample luminescence or light scattering.

One possible way to design a phosphorescent porphyrin probe is to utilize peripheral substituent effects in the porphyrin compounds.[11] For example, it was observed that the introduction of fluorinated substituents may significantly improve the photostability of the porphyrins. In particular, platinum(II) and palladium(II) complexes of *meso*-tetra(pentafluorophenyl)porphine showed a high photostability compared to other porphyrin complexes, although phosphorescence quantum yields and life-

(1) Eastwood, D.; Gouterman, M. *J. Mol. Spectrosc.* **1970,** *35,* 359–375.
(2) Tsvirko, M. P.; Solov'ev, K. N.; Gradushko, A. T.; Dvornikov, S. S. *Opt. Spectrosc. (USSR)* **1975,** *38,* 705–714.
(3) Gouterman, M. In *The Porphyrins*; Dolphin, D., Ed.; Academic Press: New York, 1978; Vol. III, Chapter 1.
(4) Gurinovich, G. P.; Sevchenko, A. N.; Solov'ev, K. N. *Spectroscopy of chlorophyll and related compounds*; Science and Technology Publishing House: Minsk, 1968 (in Russian).
(5) Savitsky, A. P.; Papkovsky, D. B.; Ponomarev, G. V.; Berezin, I. V. *Dokl. Akad. Nauk SSSR* **1989,** *304,* 1005–1009.
(6) Rumsey, W. L.; Vanderkooi, J. M.; Wilson, D. F. *Science* **1988,** *241,* 1649–1651.
(7) Kavandi, J.; Callis, J.; Gouterman, M.; Khalil, G.; Wright, D.; Green, E.; Burns, D.; McLachlan, B. *Rev. Sci. Instrum.* **1990,** *61,* 3340–3347.
(8) Papkovsky, D. B.; Olah, J.; Troyanovsky, I. V.; Sadovsky, N. A.; Rumyantseva, V. D.; Mironov, A. F.; Yaropolov, A. I.; Savitsky, A. P. *Biosens. Bioelectron.* **1992,** *7,* 199–206.
(9) Beswick, R. B.; Pitt, C. W. *Chem. Phys. Lett.* **1988,** *143,* 589–592.
(10) Papkovsky, D. B.; Ponomarev, G. V.; Chernov, S. F.; Ovchinnikov, A. N.; Kurochkin, I. N. *Sens. Actuators B* **1994,** *22,* 57–61.
(11) Atwater, B. W. *J. Fluoresc.* **1992,** *2,* 237–246.

0003-2700/95/0367-4112$9.00/0

times were lower by ~1 order of magnitude.[11,12]

An alternative way is to modify the tetrapyrrole macrocycle. The heart of the porphyrin structure is an 18 π-electron aromatic system, which determines basic optical properties and electronic spectra. Hydrogenation of one or more of the *exo*-pyrrole bonds in the macrocycle (like that occurring in related structures of chlorins, bacteriochlorins, and dihydrochlorins) results in substantial red-shifting of both absorbance and emission spectra.[3] Palladium(II) and platinum(II) complexes of chlorins, bacteriochlorins, etc. are also known to show phosphorescence,[13] but they are less stable than corresponding porphyrin complexes. It is even difficult to synthesize platinum(II) complexes of the "reduced porphyrins", since metalation at elevated temperatures is accompanied by the decomposition of such compounds. For these reasons, the applicability of reduced porphyrins (for example, to the measurement of oxygen) is rather limited.

In the present paper, new porphyrin-like dyes, the platinum(II) and palladium(II) complexes of porphyrin ketones (or "oxochlorins"), are described. These new dyes show improved photochemical and chemical stability and long wave spectral characteristics. Representative compounds were synthesized and investigated with respect to their main optical properties: absorption spectra, extinction coefficients, emission spectra, phosphorescence quantum yields, and phosphorescence lifetimes. Application of these dyes to oxygen sensing is demonstrated with platinum(II) octaethylporphine ketone dissolved in an oxygen-permeable polymer layer. All oxygen measurements were performed with a home-made fiber-optic instrument based on the measurement of phosphorescence lifetime.

MATERIALS AND METHODS

Dyes. The free bases of octaethylporphine ketone (OEPK) and coproporphyrin-I-ketone tetraethyl ester (CPK-TEE) were synthesized at the Institute of Biophysics (Moscow, Russia) from the corresponding porphyrins according to a method published by Chang and Sotiriou.[14] Platinum(II) and palladium(II) porphyrin ketone complexes were prepared in a similar manner from the free bases with $PtCl_2$ and $PdCl_2$ (Aldrich, Milwaukee, WI), respectively. The metalation of the porphyrin ketones was accomplished by heating them with $PtCl_2$ in benzonitrile or with $PdCl_2$ in dimethylformamide under reflux. The complexes were purified by column chromatography on Silica gel 40 (Merck, Darmstadt, Germany), followed by recrystallization.

Oxygen-Sensitive Membranes. PtOEPK/polystyrene film coatings with a dye concentration of 2% (w/w) were prepared in similarly to the way described for the platinum(II) porphyrins.[8] An amount of 10 mg of the dye was dissolved in 10 mL of a solution of 5% polystyrene (MW 230 000; Aldrich) in toluene. Typically, 150 μL of this paint was spread onto 20 cm^2 of a polyester transparency plotter film (A4-format sheets, 0.1 mm thickness; Hewlett-Packard, Palo Alto, CA) and left for evaporation of the solvent. Foils coated with a 5–10 μM thick dye/polystyrene film were obtained by this method. Slides (20 × 10 mm^2) or disks (10 mm in diameter) were cut from the foils and used for luminescence measurements and oxygen sensing experiments.

Absorbance and Luminescence Measurements. Absorbance spectra and molar extinction coefficients for the dyes were measured in 10 × 10 mm^2 quartz cells on a Hewlett Packard 8452A diode array spectrophotometer having a spectral resolution of 2 nm. Excitation and emission spectra were measured on a Perkin Elmer LS-50 luminescence spectrometer (Perkin Elmer Corp., Norwalk, CT) equipped with a Hamamatsu R928 red-sensitive photomultiplier tube (Hamamatsu Photonics K. K., Hamamatsu City, Japan). The spectra were corrected for the instrument response. Luminescence emission yield determinations were made with platinum tetraphenylporphyrin (TPP) as a standard.[11] Phosphorescence decay time measurements were made using an intrinsic short-decay phosphorescence option of the LS-50 spectrometer. The latter realizes the time domain approach by measuring the phosphorescence intensity at different delay times. Delay time step of 0.01 ms (minimal time resolution of the instrument), gating time of 0.5 ms, and integration time of 1 s for each point were typically used. Enzfitter software package (Elsevier-Biosoft, Cambridge, U.K.) was used for acquisition of the phosphorescence decay data and calculation of the lifetime values.

A phosphate/sulfite buffer solution of pH 7.0 containing 5% Triton X-100 (Fluka, Buchs, Switzerland) was used for phosphorescence measurements at room temperature (20–25 °C). This micellar solution was ~0.05 M in KH_2PO_4 and 0.04 M in Na_2SO_3 and provided facile and continuous chemical deoxygenation with sulfite[15] and solubilization of the monomeric dye molecules. As a result, elimination of typical interferences, such as quenching by oxygen and water or self-quenching, was achieved. All luminescence studies with long-lived triplet state molecules (room temperature phosphorescence spectra, quantum yield determinations, and decay time measurements) could be easily performed without special precautions in contact with ambient air.

Oxygen Measurements. Oxygen sensing experiments were performed with a fiber-optic oxygen probe in combination with a home-made instrument. The principal scheme and construction of the instrument were described in detail earlier.[16] The instrument had a yellow light-emitting diode (LED, emission maximum, 586 nm; light output, 2500 mcd; Toshiba Corp., Tokyo, Japan) as a light source whose intensity was modulated at a frequency of 3683 Hz. The photodetector was an S2386-44K silicone photodiode from Hamamatsu Photonics K. K. A 591 nm interference filter (15 mm diameter, 5 mm thickness; DiaM, Moscow, Russia) and an RG9 glass filter (10 × 10 mm^2, 2 mm thickness; Schott, Mainz, Germany) were used for effective separation of excitation and phosphorescence light. The analog electronic scheme provided amplification, low-frequency filtering and acquisition of the phosphorescence signal, and measurement of the phase shift. The instrument allowed continuous real-time monitoring of the phosphorescence intensity and phase shift, which were both dependent on the oxygen concentration. The instrument response was variable from 5 to 50 s.

The fiber-optic oxygen probe consisted of a bifurcated 3 mm glass fiber bundle with light-protective coating. The oxygen-sensitive membranes (disks 10 mm in diameter) were fixed at the common end of the bundle, with the sensitive coating facing the sample by means of a metal ferrule. The two other arms were

(12) Khalil, G.-E.; Gouterman, M. P. U.S. Patent 4,810,655, 1989.
(13) Gradushko, A. T.; Solov'ev, K. N.; Turkova, A. E.; Tsvirko, M. P. *Biofizika (USSR)* **1975**, *26*, 602–608.
(14) Chang, C. K.; Sotiriou, C. *J. Heterocycl. Chem.* **1985**, *2*, 1739–1741.
(15) Garcia, M. E. D.; Sanz-Medel, A. *Anal. Chem.* **1986**, *58*, 1436–1440.
(16) Papkovsky, D. B.; Ponomarev, G. V.; Ogurtsov, V. I.; Dvornikov, A. A. *Proc. SPIE, Biochem. Biomed. Sens. (1993)* **1994**, *2085*, 54–60.

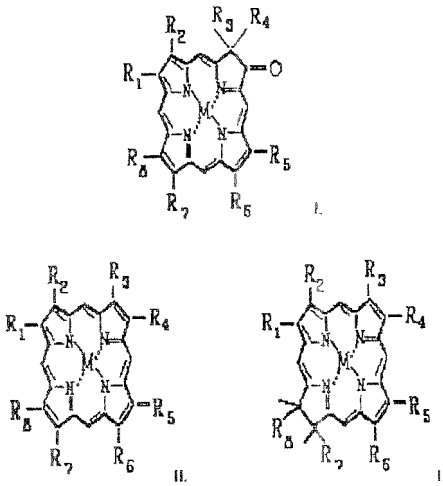

Figure 1. General chemical structures of the metal complexes (M = Pt(II) or Pd(II)) of porphyrin ketones (**I**), porphyrins (**II**), and chlorins (**III**).

connected to the light source and photodetector of the instrument.

Oxygen standards were prepared by precise mixing of pure nitrogen (99.9%) and air (20.95% O_2) in a 5 L balloon. For calibration, the fiber-optic probe with the oxygen sensor membrane was placed in a 15 mL glass tube, which was purged with a stream of standard gas mixture. Both oxygen probe and gas mixtures were typically thermostated at 22 °C.

RESULTS AND DISCUSSION

Dyes. The metal complexes of the porphyrin ketones (or oxochlorins) belong to a new class of phosphorescent dyes. A comparison of their chemical structures with the structures of the metal complexes of porphyrins and chlorins is shown in Figure 1. Representative compounds, such as lipophilic platinum(II) and palladium(II) octaethylporphine ketone (PtOEPK and PdOEPK; R_1–R_8 = $-CH_2CH_3$), were synthesized and isolated in a pure form with a minimum dye content of 99%. Other dyes investigated were platinum(II) coproporphyrin-I-ketone tetraethyl ester PtCPK-TEE) and the water-soluble platinum(II) and palladium(II) coproporphyrin-I-ketone free acid complexes (PtCPK-FA and PdCPK-FA, respectively; R_1, R_3, R_5, R_7 = $-CH_3$; R_2, R_4, R_6, R_8 = $-CH_2CH_2$-COOH). These porphyrin ketones were obtained by treatment of the corresponding porphyrins with a strong oxidizing agent (OsO_4) and appeared to be resistant to further oxidation. Due to their stability, metalation at elevated temperatures could be performed quite easily, and platinum(II) and palladium(II) complexes were obtained with high yields. The metal complexes also displayed high stability to chemical transformations, in particular to photooxidation and to degradation during long-term storage in the dark. No spectral changes were observed during 2 years of storage of crystalline dye samples in the dark and at ambient temperature.

Some other platinum(II) and palladium(II) porphyrin ketones could be prepared in a similar way. However, the chemical synthesis is limited by the starting compounds. Porphyrins which have peripheral substituents which are not stable to strong oxidation, should be avoided. Porphyrins which are not substituted symmetrically give numerous porphyrin ketone isomers which are not easy to separate.

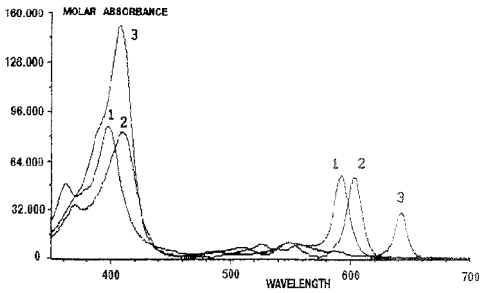

Figure 2. Absorption spectra of PtOEPK (1), PdOEPK (2), and OEPK (free base, 3) in chloroform. The *y*-axis corresponds to molar absorption values, in mM^{-1} cm^{-1}.

The electronic structure and absorption and emission spectra (see Figures 1 and 2) of the porphyrin ketones and their metal complexes showed greater similarity to chlorins than to porphyrins. In contrast to chlorins and other reduced porphyrins, which are light-unstable, the porphyrin ketones displayed a higher photochemical stability than porphyrins.

Absorption Spectra. A typical metalloporphyrin spectrum comprises the following bands (nomenclature given by Platt):[3] two *Q* bands, which can be seen between 500 and 600 nm (the lower-energy band is the electronic origin *Q*(0,0) of the lowest-energy excited singlet state), *B* bands (the very intense band *B*(0,0) (Soret band) is the origin of the second excited state and appears between 380 and 420 nm), and *N*, *L*, and *M* bands (below 350 nm). In the case of the free bases, the visible absorption spectrum changes due to a splitting of the two *Q* bands into four bands. Dramatic changes were observed in the spectra of reduced porphyrins (e.g., chlorins) and their metal complexes. Here, a strong far-red band appears in the absorption spectrum.[3]

The absorption spectra of PtOEPK, PdOEPK, and OEPK (free base) are shown in Figure 2. One can see the characteristic *B* band(s) in the near-ultraviolet (Soret) region and several visible bands, with the most intense being the long wave *Q*(0,0) band. The *B*(0,0) band of porphyrin ketone complexes displays pronounced splitting and decrease of intensity compared to the corresponding free base OEPK. The *Q*(0,0) band of the metal complexes is rather intense and sharp. Spectra of palladium(II) complexes appeared to be about 10 nm red-shifted compared with corresponding platinum(II) complexes. The main absorption characteristics are summarized in Table 1.

Solubilization in the aqueous surfactant solution (5% Triton X-100) led to slight blue-shifting and sharpening of the absorbance bands. For the polar, water-soluble PdCPK-FA, substantial broadening of the bands was also observed both in methanol and in surfactant solution. Addition of pyridine to the solutions of PtOEPK or PdOEPK in chloroform caused only trace changes in absorbance. For this reason, extra liganding ability is expected to be weak, in accordance with results for other platinum(II) or palladium(II) porphyrins.[3]

The absorbance data actually seem to be very similar to those of chlorins.[3,12] In comparison to the corresponding porphyrin complexes, the *Q*(0,0) band of the metalloporphyrin ketones

Table 1. Absorbance Data for the Porphyrin Ketone Free Bases and Their Platinum(II) and Palladium(II) Complexes

compound	solvent	$B(0,0)$ (nm) maximum	$B(0,0)$ (nm) half-width	extinctn coeff (cm^{-1} M^{-1})	$Q(0,0)$ (nm) maximum	$Q(0,0)$ (nm) halfwidth	extinctn coeff (cm^{-1} M^{-1})
PtOEPK	$CHCl_3$	398	31	86 200	592	14	55 100
	MSS[a]	396	28		589	13	
	polystyrene	398	31		592	14	
PtCPK-TEE	$CHCl_3$	397	36	82 700	592	17	45 700
	MSS[a]	397	35		589	15	
PtCPK-FA	CH_3OH	394	38		588	18	
	MSS[a]	397	40		591	18	
PdOEPK	$CHCl_3$	410	34	82 600	603	15	53 500
	MSS[a]	408	34		600	12	
	polystyrene	410	34		602	14	
PdCPK-FA	CH_3OH	406	42		599	19	
	MSS[a]	410	40		602	19	
OEPK	$CHCl_3$	408	32	151 000	642	12	30 400
CPK-FA	CH_3OH	400	40		640	12	

[a] Micellar sulfite solution.

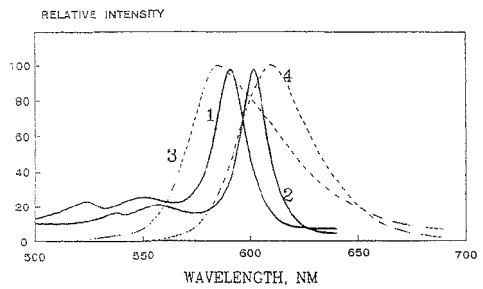

Figure 3. LED compatibility of the metalloporphyrin ketones. Comparison of the visible absorption spectra of PtOEPK (1) and PdOEPK (2), and the emission spectra of yellow (3) and orange (4) LEDs.

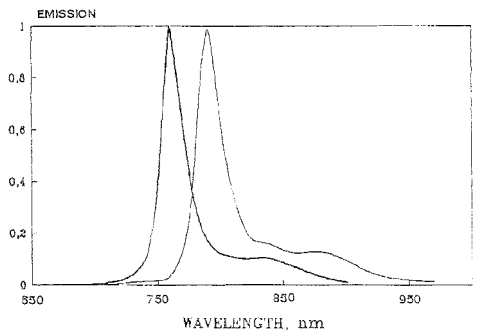

Figure 4. Corrected emission spectra of PtOEPK (1) and PdOEPK (2) in buffered micellar sulfite solution at 22 °C.

appeared to be red-shifted for ~55 nm. In addition, the intensity of the $B(0,0)$ band and the $B(0,0)/Q(0,0)$ ratio were substantially suppressed. Similarity with the chlorophyll (i.e., magnesium(II) chlorin) spectra can be mentioned.[3,17]

Absorbance characteristics of the new dyes and the oxygen membranes prepared with them showed a very good compatibility with LEDs as light sources. Overlapping of the absorbance spectra of the dyes and the emission spectra of two custom LEDs is presented in Figure 3. One can see that yellow LEDs are effective for excitation of PtOEPK, whereas orange LEDs are suitable for PdOEPK excitation.

Emission Characteristics. In deoxygenated media, the platinum(II) and palladium(II) porphyrin ketone complexes showed distinct emission in the very near-infrared region, which was attributed to room temperature phosphorescence (Figure 4). Fluorescence deriving from the ketone complexes could not be detected. If existing at all, its quantum efficiency must be 3–4 orders of magnitude lower than that of the phosphorescence. The phosphorescence excitation spectra were very close to the corresponding absorbance spectra. The main characteristics of the phosphorescence of the porphyrin ketone complexes are summarized in Table 2.

The S – T energy values (difference between lowest-energy excited singlet state and triplet state) calculated for the porphyrin ketone complexes were 3700–3800 cm^{-1} for platinum(II) complexes and 3900–4000 cm^{-1} for palladium(II) complexes. This is somewhat larger than for most of the porphyrin-like compounds.[17]

Table 2. Emission Data for the Porphyrin Ketone Complexes at 22 °C

compound	solvent	$T(0,0)$ (nm) maximum	$T(0,0)$ (nm) half-width	quantum yield	lifetime (μs)
PtOEPK	MSS[a]	758	20	0.12	60.0
	polystyrene	759	19.5		61.4[b]
PtCPK-TEE	MSS[a]	760	31	0.11	49.7
PtCPK-FA	MSS[a]	762	35	0.08	31.4
PdOEPK	MSS[a]	789	22	0.01	455
	polystyrene	790	21		480[b]
PdCPK-FA	MSS[a]	793	35	0.008	237

[a] Micellar sulfite solution. [b] Under nitrogen.

The phosphorescence efficiency (quantum yields) of the porphyrin ketone complexes was measured in micellar sulfite solution (Table 2). For the platinum(II) complexes, the quantum yields exceeded 10%, which is considered to be very high. Similar high quantum yields were observed for platinum(II) porphyrins.[1-4,11] Phosphorescence quantum yields of palladium(II) porphyrin ketones were found to be an order of magnitude lower (Table 2).

The emission spectra for the metalloporphyrin ketones were red-shifted for more than 100 nm when compared to the corre-

(17) Solov'ev, K. N.; Gladkov, L. L.; Starukhin, A. S.; Shkirman, S. F. *Spectroscopy of porphyrins: vibronic states*; Nauka i Technika: Minsk, 1985 (in Russian).

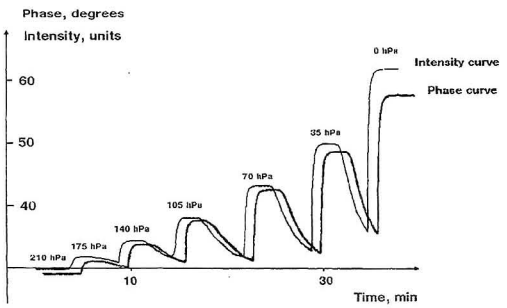

Figure 5. Oxygen measurement with a fiber-optic oxygen measurement device equipped with a PtOEPK/polystyrene oxygen-sensitive membrane. The changes in phosphorescence intensity and in phosphorescence phase shift (deg) during subsequent purging of the oxygen membrane with standard oxygen/nitrogen mixtures at 22 °C can be seen. The oxygen partial pressures are also given.

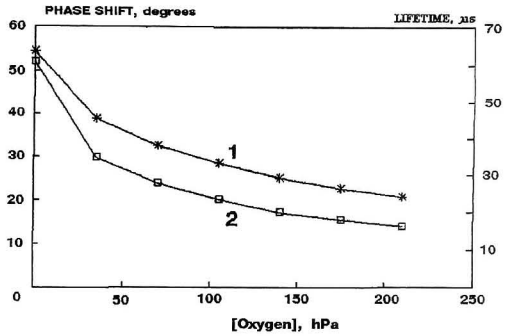

Figure 6. Calibration curve for phosphorescence lifetime-based sensing of oxygen with a PtOEPK/polystyrene oxygen-sensitive membrane at 22 °C. (1) Measured phosphorescence phase shift and (2) calculated phosphorescence lifetime.

sponding porphyrin complexes. The phosphorescence lifetimes of PtOEPK and PdOEPK appeared to be 1.5–2 times shorter. This is in agreement with theoretical and empirical considerations known for the porphyrin compounds.[3]

Like for the porphyrins, phosphorescence of the porphyrin ketone complexes is only slightly dependent upon temperature. Thus, within the studied range from +7 to +77 °C, the nonquenched lifetimes of PtOEPK and PdOEPK in polystyrene changed from 63 to 55 μs and from 502 to 410 μs, respectively. This corresponds to a temperature coefficient of ~0.2–0.3% per °C. Quantum yields also decrease similarly with temperature.

Oxygen-Sensitive Membranes. PtOEPK showed a very good solubility in polystyrene, higher than that for the corresponding platinum(II) octaethylporphine. The standard oxygen-sensitive membranes consisted of a dye/polystyrene layer which contained 2% (w/w) of PtOEPK and had a thickness of ~10 μm. The dye/polystyrene layer was applied onto a rigid and transparent polyester support. Such membranes showed an absorbance of ~1 AU at 591 nm and a strong phosphorescence with a lifetime of 61.4 μs in nitrogen and at 22 °C (single-exponential decay fitting). This is close to the value measured for PtOEPK in micellar sulfite solution (Table 2) and can be considered as the unquenched lifetime of the monomeric dye. Both phosphorescence intensity and lifetime were subject to efficient quenching by molecular oxygen in a gaseous or liquid sample matrix. Membranes with dye concentrations up to 10% (w/w) could be prepared. However, self-quenching of the dye was observed at dye concentration of 5% (w/w).

A comparative experiment was performed on photodegradation of Pt octaethylporphine polystyrene and PtOEPK/polystyrene oxygen membranes under intense and continuous illumination (polychromatic UV light, 18 h in air, 22 °C). The known coating recovered only 10% of initial dye quantified by absorbance measurements. Under the same conditions, the new oxygen probe recovered 88% of the dye. So, photostability of PtOEPK is about 10 times better than that of Pt porphyrin.

Oxygen Measurements. Oxygen sensing properties of the PtOEPK/polystyrene membranes were studied with a fiber-optic probe and a prototype instrument which allowed the simultaneous measurement of the phosphorescence intensity and the phase shift which results from the changes in phosphorescence lifetime. PtOEPK/polystyrene film coatings were suitable for quantitation of oxygen partial pressure within the range 0–210 hPa. A typical response of the oxygen measurement device to different oxygen partial pressures in the gas phase is shown in Figure 5. There, plateau regions correspond to constant oxygen pressures (shown on figure), and in between, the next gas mixture was prepared (3–6 min signal was decreased because of air diffusion) and then purged through the sensor active element. The precision of the phase measurement was 0.2° at 210 hPa of O_2 and 0.05° at 0 hPa of O_2, with a detection limit of 1.5 hPa of O_2 (3 times the standard deviation). The response time for the complete signal change (t_{100}) was determined to be below 5 s for the oxygen-sensitive membrane itself and ~60 s for the whole system. The sensor response was fully reversible, no hysteresis was seen.

Phosphorescence lifetime values were calculated from the phase shift according to the simple theoretical equation[18]

$$\tau = tg(f)/2\pi\nu \qquad (1)$$

τ is the phosphorescence lifetime, f is the phase shift, and ν is the excitation light source working frequency (i.e., 3683 Hz). The lifetime, which was determined directly with the luminescence spectrometer, was 61.4 μs in nitrogen and at 22 °C (Table 2). The calculated theoretical phase shift for this lifetime is 54.6°, and the instrument was calibrated by setting the phase shift under nitrogen and at 22 °C to this value. The phase shift changed from 54.6° at zero hPa of O_2 to 21.0° in air (210 hPa of O_2). This corresponded to a lifetime of 16.3 μs, which is in agreement with the directly determined lifetime of 17.1 μs. A calibration graph of the oxygen sensor showing phase shift and calculated lifetime vs oxygen partial pressure is presented in Figure 6. Calibration for oxygen also showed good linearity in Stern–Volmer plots (τ_0/τ vs O_2). This proves a high homogeneity of the phosphorescent dye molecules in the polystyrene matrix and a simple mechanism of dynamic quenching by oxygen.

The PtOEPK/polystyrene oxygen membranes displayed excellent storage and operational stability. No changes in spectral and quenching characteristics were observed during a period of 2 years of storage of the membranes in the dark at ambient temperature. Only minor photodegradation of the oxygen probe

(18) Lakowicz, J. R. *Principles of fluorescence spectroscopy*; Plenum Press: New York, 1983.

(below 10%) was observed during 3 weeks of continuous operation of the sensor, which did not affect oxygen measurement or calibration in the phase shift (or lifetime) mode.

CONCLUSIONS

A new class of dyes comprising platinum(II) and palladium(II) complexes of porphyrin ketones (or oxochlorins) was introduced. The dyes show strong phosphorescence at room temperture, comparable to the phosphorescence of the corresponding porphyrin complexes. The emission wavelengths are more similar to the emission of chlorins. The dyes have a photochemical and chemical stability superior to those of related chlorin and porphyrin complexes. Through varying the chemical structure (by changing the functional groups), different physicochemical properties (e.g., lipophilicity or water solubility) and phosphorescence characteristics (quantum yields, lifetime values, emission and absorption maxima) can be obtained.

Application of PtOEPK to oxygen measurement by means of a fiber-optic device based on phosphorescence lifetime measurement proved to be successful. Compared to other phosphorescent metalloporphyrins, the new dyes overcame two major drawbacks, namely, weak LED compatibility and poor photostability. Other optical approaches to oxygen sensing known to date, in which fluorescent ruthenium probes[19] and phase measurements[20] were used, also seem less advantageous due to complex luminescence decay of the probe and complex calibration for oxygen and/or high-cost instrumentation. So, the new solution (which included dye chemistry, oxygen probe optimization, and instrumental design) makes the new sensor competitive and promising for practical applications.

Moreover, oxygen-sensitive membranes consisting of PdOEPK and polystyrene could be prepared in a similar way. Due to the much longer phosphorescence lifetimes of PdOEPK (480 μs in nitrogen and at 22 °C; Table 2), these coatings have a correspondingly higher sensitivity to oxygen. In fact, they appeared to be useful for the measurement of oxygen at partial pressures below 20 hPa. The phosphorescence quantum efficiency for PdOEPK is much lower than that for PtOEPK, which may result in lower phosphorescence intensity signals and higher signal-to-noise ratios.

The spectral region of 700–900 nm is attractive for luminescence studies with complex biological samples and living tissues, where good light permeability, a reduction of the sample background signal (caused by, e.g., light scattering and sample fluorescence), and stable signals are desired. The new dyes also seem promising for such relevant analytical systems and applications. In particular, binding assays and sensitive time-resolved phosphorescence measurements could be realized with rather simple and cheap instrumentation and chemistry.

ACKNOWLEDGMENT

The research described in this paper was made possible in part by Grant No. JDC100 from the International Science Foundation and Russian Government.

Received for review May 10, 1995. Accepted August 24, 1995.[®]

AC950454S

(19) Bacon, B. R.; Demas, J. N. *Anal. Chem.* **1987**, *59*, 2780–2785.
(20) Thompson, R. B.; Lakowicz, J. R. *Anal. Chem.* **1993**, *65*, 853–856.

[®] Abstract published in *Advance ACS Abstracts*, October 1, 1995.

Anal. Chem. **1995,** *67,* 4118–4126

Glucose and Acetylcholine Sensing Multilayer Enzyme Electrodes of Controlled Enzyme Layer Thickness

Azalia Riklin and Itamar Willner*

Institute of Chemistry, The Hebrew University of Jerusalem, Jerusalem 91904, Israel

Multilayer enzyme networks assembled by a stepwise synthesis onto Au electrodes provide the basis for glucose, choline, and acetylcholine amperometric biosensors. Glucose oxidase is assembled as a multilayer array on smooth and rough Au electrodes. Electrical communication of the GOx layers with the electrode is established by the presence of ferrocenecarboxylic acid as diffusional electron mediator or by covalent linkage of [(ferrocenylmethyl)amino]caproic acid to the enzyme components. The resulting enzyme electrodes are applied as amperometric biosensors for glucose. The sensitivity of the resulting enzyme electrode is controlled by the number of enzyme layers assembled onto the electrode and by the roughness factor of the electrode surface. A multilayer enzyme array of choline oxidase (ChO) immobilized onto a rough Au electrode provides an amperometric biosensor for the amperometric detection of choline in the presence of 2,6-dichloroindophenol (DIP) as diffusional electron mediator. Stepwise organization of a multilayer biocatalytic array consisting of four layers of ChO and three layers of acetylcholine esterase (AChE) provides a bifunctional enzyme electrode for the amperometric detection of acetylcholine. In this system, choline generated by AChE hydrolysis of acetylcholine is amperometrically detected by the ChO layers in the presence of DIP acting as diffusional electron mediator. Here we report on novel means to enhance the sensitivity of multilayer enzyme electrodes by the application of rough Au electrodes as the surface for assembling the enzyme network.

The development of amperometric biosensor devices is gaining as an area of interest in biosensor technology.[1,2] A series of amperometric biosensors employ the electrochemical detection of H_2O_2 resulting from the biocatalyzed oxidation of the analyte substrate.[3-7] For example, glucose,[3,4] bilirubin,[5] and choline[6] biosensors were assembled via the application of the respective oxidative biocatalysts and the amperometric detection of hydrogen peroxide. However, the relatively high operating potentials required to detect hydrogen peroxide limit these systems due to the competitive oxidation of other oxidizable constituents in the analyzed samples. A further methodology to design amperometric biosensors involved the electrochemically stimulated biocatalyzed oxidation or reduction of the respective enzyme substrate. Direct electrical communication between the electrode surfaces and the active sites of redox proteins is usually prohibited by the insulating protein matrix.[8] This difficulty was resolved through the application of diffusional electron transfer mediators that electrically communicate the protein redox site and electrode interfaces. For example, amperometric glucose, bilirubin, and glutathione biosensors were developed using ferrocene[9] or quinone[10] derivatives, ferricyanide,[11] organic conducting salts,[12] phenoxazine compounds,[13] and *N,N'*-bipyridinium salts[14] as electron transfer mediators.

An approach to rigidify the assemblies exhibiting electron shuttling between the enzyme redox site and the transducing electrode interfaces involved the immobilization of the enzymes in redox polymers onto electrodes.[15,16] For example, immobilization of glucose oxidase in conducting polymers containing ferrocene as electron mediator or in redox polymers that include Os(III) polypyridine electron transfer units[16b] and immobilization of nitrate reductase in conducting polymers with *N,N'*-bipyridinium units[15a,17] resulted in amperometric biosensors for glucose and nitrate, respectively. A further approach to establish electrical communication between the redox protein and the electrode surface included the chemical modification of proteins by electron mediators to form "electrically wired" enzymes.[18] The effectiveness of electrical communication between the redox site and the

(1) *Biosensor, Principles and Applications*; Blum, L. J., Coulet, P. R., Eds.; Marcel Dekker, Inc.: New York, 1991.
(2) (a) *Biosensors, A Practical Approach*; Cass, A. E. G., Ed.; Oxford University Press: New York, 1990. (b) *Biosensor Technology. Fundamentals and Applications*; Buck, R. P., Hatfield, W. E., Umana, M., Bowden, E. F., Eds.; Marcel Dekker, Inc.: New York, 1990.
(3) (a) Free, M.; Free, H. *Anal. Chem.* **1984**, *56*, 6648. (b) Reach, G.; Wilson, G. S. *Anal. Chem.* **1992**, *64*, 381A.
(4) (a) Koudelka, M.; Rohner-Jeanrenaud, F.; Terrattaz, J.; Bobioni-Harsch, E.; de Rooij, N. F.; Jeanrenaud, B. *Biosen. Bioelectron.* **1991**, *6*, 31. (b) Wang, J.; Liu, J.; Chen, L.; Lu, F. *Anal. Chem.* **1994**, *66*, 3600.
(5) Wang, J.; Ozsoz, M. *Electroanalysis* **1990**, *2*, 647.
(6) (a) Kano, K.; Morikage, K.; Uno, B.; Esaka, Y.; Goto, M. *Anal. Chim. Acta* **1994**, *299*, 69. (b) Mascini, M.; Moscone, M. *Anal. Chim. Acta* **1986**, *179*, 439.
(7) (a) McNeil, C. J.; Spoors, J. A.; Cooper, J. M.; Alberti, K. G. M. M.; Mullen, W. H. *Anal. Chim. Acta* **1990**, *237*, 99. (b) Scheller, F. W.; Pfeiffer, D.; Hintsche, K.; Dramfeld, I.; Nentwig, J. *Biomed. Biochim. Acta* **1989**, *48*, 891.
(8) Heller, A. *Acc. Chem. Res.* **1990**, *23*, 128.
(9) Green, M.; Hilditch, P. *Anal. Proc.* **1991**, *28*, 374.
(10) Hu, J.; Turner, A. P. *Anal. Lett.* **1991**, *24*, 15.
(11) Lewis, B. D. *Clin. Chem.* **1992**, *38*, 2093.
(12) Gunashingham, H.; Tan, C. *Analyst* **1990**, *115*, 35.
(13) Kulys, J.; Hansen, H.; Buch-Rasmussen, T.; Wang, J.; Ozsoz, M. *Anal. Chim. Acta* **1994**, *228*, 193.
(14) Katz, E.; Riklin, A.; Willner, I. *J. Electroanal. Chem.* **1993**, *354*, 129.
(15) (a) Willner, I.; Katz, E.; Lapidot, N.; Bäuerle, P. *Bioelectrochem. Bioenerg.* **1992**, *29*, 29. (b) Gregg, B.; Heller, A. *Anal. Chem.* **1990**, *62*, 258.
(16) (a) Pishko, M.; Katakis, I.; Lindquist, S.; Ye, L.; Gregg, B.; Heller, A. *Angew. Chem., Int. Ed. Engl.* **1990**, *29*, 82. (b) Degani, Y.; Heller, A. *J. Am. Chem. Soc.* **1989**, *111*, 2357.
(17) Cosnier, S.; Innocent, Ch.; Jouanneau, Y. *Anal. Chem.* **1994**, *66*, 3198.
(18) Heller, A. *J. Phys. Chem.* **1992**, *96*, 3579.

0003-2700/95/0367-4118$9.00/0

transducer is controlled by the tether length linking the electron mediator to the protein.[19] Amperometric biosensors for glucose,[20,21] amino acids,[20] and glutathione[19] were developed by this method using ferrocene or *N,N'*-bipyridinium derivatives as electron transfer mediators.

Monolayer-modified electrodes were applied as interfaces for electrocatalyzed oxidation of biomaterials[22] and controlled electron transfer to proteins.[23] Recently, we demonstrated that redox enzymes can be organized as covalently linked protein monolayers onto electrodes by attachment to a functionalized base self-assembled thiol monolayer associated with Au electrode surfaces.[24] Electrical communication between the redox center of the protein and the electrode surface was attained by the application of diffusional electron mediators or covalent attachment of electron relay units linked to the protein through long and flexible bridging chains.[19] The sensitivities of these monolayer electrodes and the resulting amperometric signals are low due to limited amounts of enzyme attached as a monolayer to the electrode surfaces. In a preliminary study,[21] we reported on a method to enhance the sensitivity of such electrodes by the stepwise construction of a multilayer network of redox enzymes on a base self-assembled monolayer (SAM) of thiolate attached to Au electrodes. This approach has been applied successfully to develop a glucose biosensor[21] and later a bilirubin amperometric biosensor.[24b]

Here we report on the application of multilayer enzyme electrodes as amperometric sensing interfaces for glucose, choline, and acetylcholine. Specifically, we describe the detailed methods to organize multilayer enzyme electrodes and demonstrate the advantages associated with the use of rough Au surfaces as base substrate for the organization of multilayer enzyme electrodes. We also report on a method to organize multilayer enzyme electrodes consisting of two enzymes and discuss the application of bifunctional enzyme electrodes as amperometric biosensors. In this approach, one of the enzymes is a redox protein, whereas the second enzyme is non-redox-active. The analyte substrate is transformed by the non-redox-active biocatalyst to a product that is electrochemically sensed by the redox enzyme. This method is exemplified by the development of an acetylcholine sensing electrode using a multilayer electrode composed of choline oxidase and acetylcholine esterase.

EXPERIMENTAL SECTION

Electrochemical measurements were performed with a BAS CV-27 potentiostat linked to a BAS *x–y* recorder. Absorption spectra were recorded on a Kontron (Uvikon-860) spectrophotometer. Radioactivity measurements were performed with a Beckman LS 2800 liquid scintillation counter.

Tritiated iodoacetic acid (Du Pont), 4,4'-diisothiocyanato-*trans*-stilbene-2,2'-disulfonic acid disodium salt, (DIDS, Fluka), 2,6-dichloroindophenol (DIP, Aldrich), *N*-hydroxysuccinimide (NHS), 1-ethyl-3-[3-(dimethylamino)propyl]carbodiimide (EDC), ferrocenecarboxylic acid (Fc-COOH), glucose oxidase (GOx, EC 1.1.3.4), choline oxidase (ChO, EC 1.1.3.17), and acetylcholine esterase (AChE, EC 3.1.1.8) (Sigma) were purchased and used without further purification. [(Ferrocenylmethyl)amino]caproic acid (**1**) was prepared as described previously.[24b]

The electrochemical cell consisted of a three-electrode system where the chemically modified Au electrode acted as working electrode, a glassy carbon was the auxiliary electrode, isolated by a frit from the working volume, and a Ag/AgCl electrode, connected to the working volume by a Lugin capillary, was used as reference electrode. The cell was thermostated during the electrochemical measurements.

Au foils (~0.2 or 0.4 cm^2) were used as surfaces for modification. Rough Au electrodes were prepared by amalgamization as reported.[25] The gold surfaces were purified by boiling in a concentrated KOH solution for 2 h, followed by rinsing with distilled water and storage in concentrated H_2SO_4. Prior to modification, the purified electrodes were immersed in concentrated HNO_3 for 15 min and rinsed extensively with distilled water. The roughness factors of the Au foils and the rough Au electrodes were determined by recording[25] the cyclic voltammograms of the base electrodes in 0.5 M H_2SO_4. The roughness factors corresponded to ~1.2 and 30 for the Au foils and the rough amalgamated Au surfaces, respectively.

GOx-Modified Multilayer Au Electrodes. The clean gold foil or rough Au surface was immersed in a 2×10^{-2} M cystamine aqueous solution for 2 h. The monolayer-modified electrodes were then rinsed twice with water and introduced into a cold (0 °C), 0.1 M potassium phosphate buffer solution, pH = 7.3, that contained 2×10^{-2} M DIDS for 10 min. The resulting electrodes were rinsed twice with a cold phosphate buffer solution and then soaked in a GOx solution (3 mg·mL^{-1}) for 30 min at room temperature. The monolayer enzyme electrode was rinsed with a phosphate buffer solution, and the two-step procedure using the reaction with DIDS and GOx was repeated to assemble the desired number of enzyme layers on the electrodes. In the appropriate systems, further modification of the multilayer GOx electrodes by the ferrocene electron mediator was performed. The GOx multilayer electrodes were immersed in 1.5 mL of 0.1 M HEPES buffer solution, pH = 7.4, that contained 90 mg of urea, 8 mg of **1**, 12 mg of EDC, and 5 mg of NHS for 12 h at 4 °C. The resulting electrodes were washed with the HEPES buffer solution and stored dry in the refrigerator (4 °C).

Preparation of ChO and AChE Multilayer Electrode. The clean, rough Au electrodes were immersed in a 2×10^{-2} M cystamine aqueous solution for 2 h. The monolayer-modified electrodes were rinsed with water and introduced into a cold (0 °C), 0.1 M potassium phosphate buffer solution, pH = 7.3, that contained 2×10^{-2} M DIDS for 10 min. The resulting electrodes were rinsed with the aqueous buffer solution and introduced for 30 min into a potassium phosphate buffer solution, pH = 7.3, that contained 2 mg·mL^{-1} ChO and 1×10^{-4} M choline. The resulting electrodes were rinsed with the buffer solution. The two-step procedure using the reaction with DIDS and the enzyme solution was used to assemble the desired number of layers onto the electrodes. In the appropriate experiments, the ChO multilayer electrode was further used to immobilize AChE layers. After treatment of the ChO multilayer electrodes with DIDS, as

(19) (a) Willner, I.; Katz, E.; Riklin, A.; Kasher, R. *J. Am. Chem. Soc.* **1992**, *114*, 10965. (b) Willner, I.; Lapidot, N.; Riklin, A.; Kasher, R.; Zahavy, E.; Katz, E. *J. Am. Chem. Soc.* **1994**, *116*, 1428.

(20) Degani, Y.; Heller, A. *J. Am. Chem. Soc.* **1988**, *110*, 2615.

(21) Willner, I.; Riklin, A.; Shoham, B.; Rivenson, D.; Katz, E. *Adv. Mater.* **1993**, *5*, 912.

(22) Schlereth, D. D.; Katz, E.; Schmidt, H.-L. *Electroanalysis* **1995**, *7*, 46.

(23) Creager, S. E.; Olsen, K. G. *Anal. Chim. Acta* **1995**, *307*, 277.

(24) (a) Willner, I.; Riklin, A. *Anal. Chem.*, **1994**, *66*, 1535. (b) Shoham, B.; Migron, Y.; Riklin, A.; Willner, I.; Tartakovsky, B. *Biosens. Bioelectron.* **1994**, *10*, 341.

(25) Katz, E.; Schlereth, D. D.; Schmidt, H.-L. *J. Electroanal. Chem.* **1994**, *367*, 59.

described above, the electrodes were introduced into a 0.1 M phosphate buffer solution, pH = 7.3, that included 0.2 mg·mL^{-1} AChE and 1 × 10^{-4} M choline. The two-step procedure involving the reaction with DIDS and AChE was repeated to assemble the appropriate number of AChE layers onto the electrode.

Preparation of Tritiated GOx. An excess of [^{3}H]iodoacetic acid was added to a 2 mL potassium phosphate buffer solution, pH = 7.5, that included 6 mg of GOx. The mixture was stirred at room temperature for 4 h. The resulting solution was chromatographed over Sephadex G-25, and the collected fractions were assayed for their protein content by Lowry's method.[26] The appropriate fractions of high protein content were then analyzed by liquid scintillation. The counts of 1 mg of protein corresponded to 39 200 counts/min. The labeled GOx was used to modify the Au electrodes as described above. The counts of the resulting electrodes were recorded. It was assumed that roughly 50% of the emission was absorbed by the electrode surface. Hence, the experimental counts were multiplied to estimate the enzyme density.

Electrochemical Analysis of Glucose by GOx Multilayer Electrodes. The electrolyte solution consisted of 2.2 mL of 0.1 M potassium phosphate buffer, pH = 7.3. The working electrode was a multilayer GOx–Au electrode or a ferrocene-modified GOx–Au electrode. In the systems where the GOx multilayer electrode was used, 2.9 × 10^{-4} M ferrocenecarboxylic acid was introduced into the electrolyte solution as diffusional electron mediator. Samples of glucose to generate the appropriate concentration were introduced into the cell, and amperometric responses were recorded by cyclic voltammetry. All electrochemical measurements were performed at 35 ± 0.5 °C.

Electrochemical Analysis of Choline and of Acetylcholine by ChO and Cho/AChE Multilayer Electrodes. The electrolyte solution was composed of 0.1 M potassium phosphate buffer pH = 7.8, and 1 × 10^{-4} M DIP. The ChO or ChO/AChE multilayer Au electrodes were applied as working electrodes. Samples of choline or acetylcholine, at the appropriate concentrations, were introduced into the cell, and the amperometric responses were followed by cyclic voltammetry. All experiments were performed at 35 ± 0.5 °C.

RESULTS AND DISCUSSION

A GOx was immobilized on Au electrodes according to Scheme 1. A Au electrode (geometrical surface area, 0.2 cm^2; roughness factor, 1.2) was modified by 2,2′-dithiobis[ethanamine] (cystamine). Previous studies[27] indicated that the disulfide cystamine dissociates on Au surfaces, and the SAM of the thiolate is formed on the surface. The surface density of the monolayer was determined by reacting the monolayer with 2,3-dichloro-1,4-naphthoquinone, followed by electrochemical analysis of the charge associated with the two-electron reduction of the quinone units.[28] The surface density of the redox units attached to the monolayer corresponds to 5.2 × 10^{-11} mol·cm^{-2}, and this value can be considered as a lower limit to the surface density of the aminothiolate monolayer. The monolayer was reacted with the bifunctional reagent DIDS, followed by reacting the free isothiocyanate group with the enzyme GOx to generate the respective thiourea links. Layers of GOx were then attached to the primary base layer of the enzyme by a two-step procedure that included the modification of the enzyme layer with DIDS, followed by reaction of the resulting layer with the enzyme. The number of enzyme layers constructed within the network is then controlled by the sequence of steps involved in the modification procedure. The construction of the multilayer electrode is supported by an experiment employing ^{3}H-labeled GOx to organize the multilayer assembly.[21] An almost linear increase in the radioactive counts is observed upon construction of the layers. This suggests that the enzyme content in each of the deposited layers is almost identical to that of the primary enzyme layer (for further support of the network assembly, vide infra). From the number of radioactive counts associated with the base enzyme layer, we estimate the surface density of the enzyme to be (7.5 ± 1.5) × 10^{-12} mol·cm^{-2} in a monolayer configuration. It should be emphasized that we do not imply that each of the enzyme units is linked by a single bridging component to a secondary enzyme site to form an ordered multilayer assembly. The reaction of DIDS with the primary enzyme layer can yield modification of the enzyme by several linking units. As a result, several enzyme units could be attached to one enzyme component in the primary monolayer. The labeling experiments imply, however, that the density of GOx in any layer is almost unaltered during the chemical assembly of the network. Thus, we believe that the resulting GOx network associated with the electrode represents a cross-linked structure in which the density of the protein is preserved in each layer. Furthermore, we note that reaction of DIDS with the primary cystamine monolayer or the enzyme base layer yields a free isothiocyanate group for further modification, and intralayer bifunctional reaction with DIDS is eliminated. The high DIDS bulk concentration employed, and the rigid *trans*-configuration of the bifunctional reagent, presumably favor the single-site modification of the monolayer.

The resulting multilayer enzyme electrode, which includes a tailored number of layers, was then modified with **1** acting as electron mediator for GOx. The ferrocene units reveal a quasi-reversible redox wave (Figure 1, inset), where the anodic (or cathodic) currents increase as the number of layers in the network increases. By assuming that all ferrocene units linked to the protein units electrically communicate with the electrode, the charge associated with the oxidation (or reduction) of the ferrocene units represents the overall content of the electron mediator in the assembly. The coulometric analysis of the cyclic voltammograms as a function of the number of layers is shown in Figure 1. A linear increase in the content of ferrocene units is observed, suggesting that the average loading of each layer by the electron mediator is similar. Knowing the density of the enzyme in each layer of the network and the total content of ferrocene units per layer, we estimate the average loading of each GOx unit by ferrocene to be 8. It should be noted that the ferrocene electron mediator **1** includes an eight-atom bridging chain. This relatively long, flexible chain was selected to facilitate electron transfer communication between the enzyme redox site and the electrode.[19]

Figure 2 shows the amperometric responses of GOx monolayer electrodes modified by the ferrocene electron mediator consisting of one, four, and eight layers associated with the electrode in the presence of 2 × 10^{-2} M glucose. An electrobiocatalytic anodic current is observed for the electrodes that include four and eight

(26) Lowry, O. H.; Rosenbrough, P. J.; Farr, A. L.; Randall, R. J. *J. Biol. Chem.* **1951**, *193*, 265.
(27) Taniguchi, I.; Iseki, M.; Yamaguchi, H.; Yasukouchi, J. *J. Electroanal. Chem.* **1985**, *186*, 299.
(28) Katz, E.; Slov'ev, A. A. *J. Electroanal. Chem.* **1990**, *291*, 171.

Scheme 1. Organization of Multilayer GOx Network on Au Electrode and Its Modification by the Ferrocene Electron Transfer Mediator

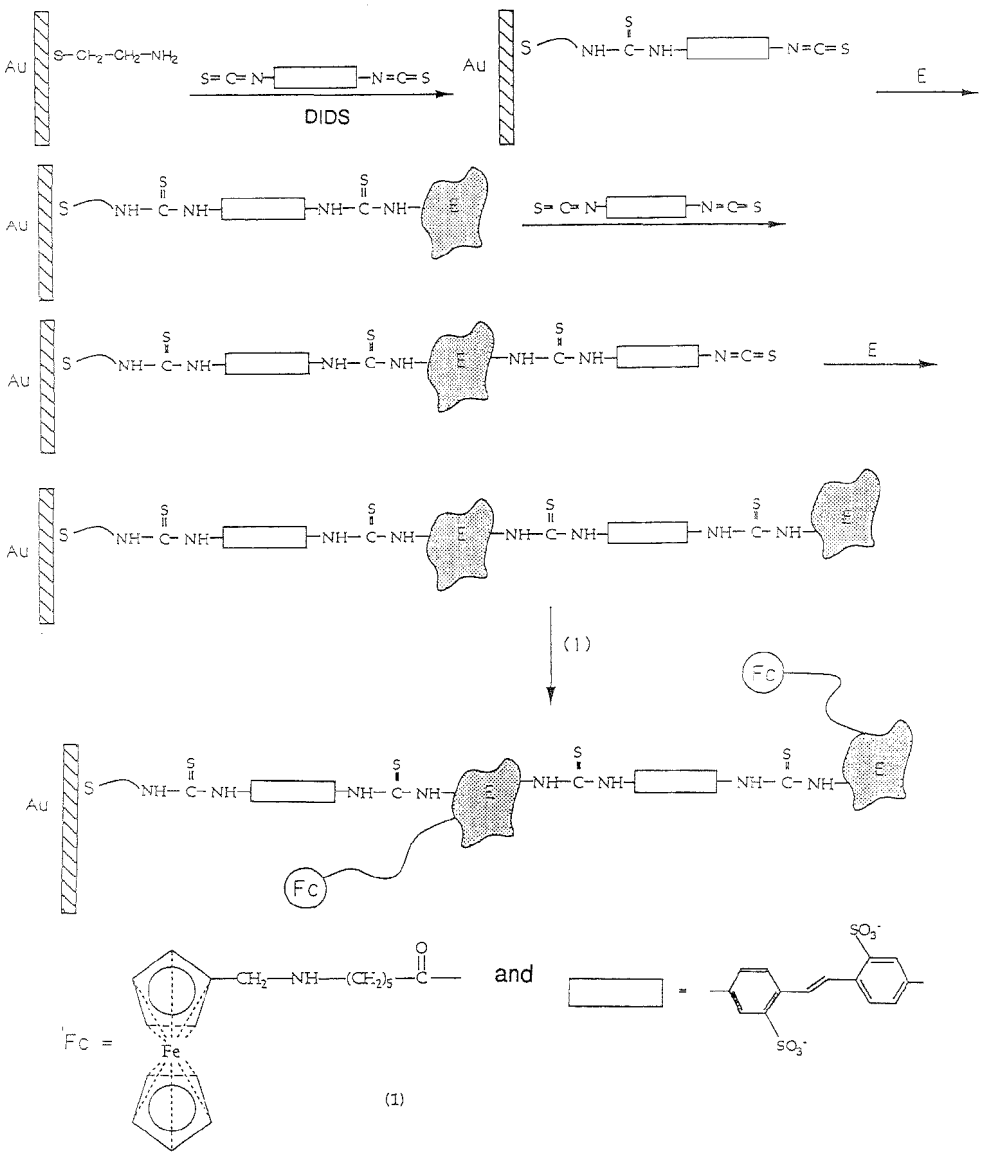

GOx layers, whereas a single monolayer does not yield a detectable anodic current. Also, the catalytic anodic current is substantially higher with the eight-layer enzyme electrode. Control experiments reveal that in the absence of tethered ferrocene units or glucose, or upon deactivation of the enzyme electrode (by heating to 90 °C for 3 min), no electrocatalytic anodic currents are detected in the electrochemical cell. This suggests that the electron relay units tethered to GOx facilitate electron transfer communication between the protein redox site and the electrode interface, as schematically presented in Scheme 2. Electrochemical oxidation of the ferrocene units mediates the oxidation of the redox-active flavin cofactor of GOx,[29] and biocatalyzed oxidation of glucose generates the catalytic anodic current. The results demonstrate an important feature of multilayer enzyme electrodes.

(29) Wilson, R.; Turner, A. P. F. *Biosens. Bioelectron.* **1992**, *7*, 165.

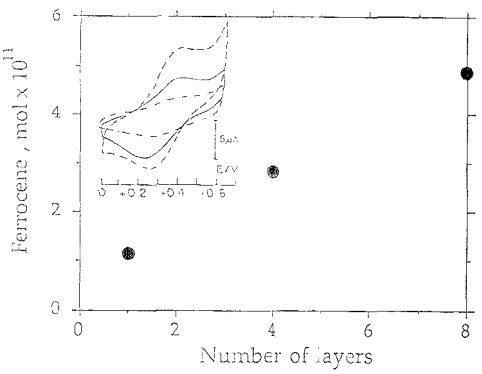

Figure 1. Coulometric analysis of ferrocene content on GOx multilayer as a function of the number of layers. (Inset) Cyclic voltammograms of ferrocene units: (·—·) one layer, (—) four layers, (- - -) eight layers. Electrode area, 0.2 cm^2; electrolyte solution, phosphate buffer, 0.1 M, pH = 7.3; scan rate of cyclic voltammograms, 200 $mV \cdot s^{-1}$.

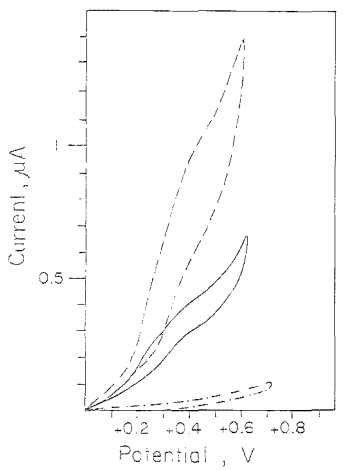

Figure 2. Cyclic voltammograms of ferrocene-modified GOx multilayer electrodes in the presence of 0.02 M glucose: (·—·) one layer, (—) four layers. (- - -) eight layers. All experiments were performed with a Au foil, 0.2 cm^2, in 0.1 M phosphate buffer, pH = 7.3, 35 ± 0.5 °C, under Ar; scan rate, 2 $mV \cdot s^{-1}$.

whereby the sensitivity of the electrode is tuned by the number of layers associated with the network. We see that by increasing the number of layers, the electrobiocatalyzed anodic current is enhanced. With the four-layer GOx network electrode, we have examined the anodic currents developed in the electrochemical cell as a function of glucose concentration (Figure 3a). The amperometric responses increase as the glucose concentration is elevated, and the current reaches a saturation value at high glucose concentrations. Significant differences in the generated amperometric signals are observed up to a glucose concentration corresponding to 15 mM. This range is adequate for monitoring normal and deviating glucose levels in blood. The saturated constant amperometric responses at high glucose concentrations suggest that the active sites of the enzyme units are saturated at

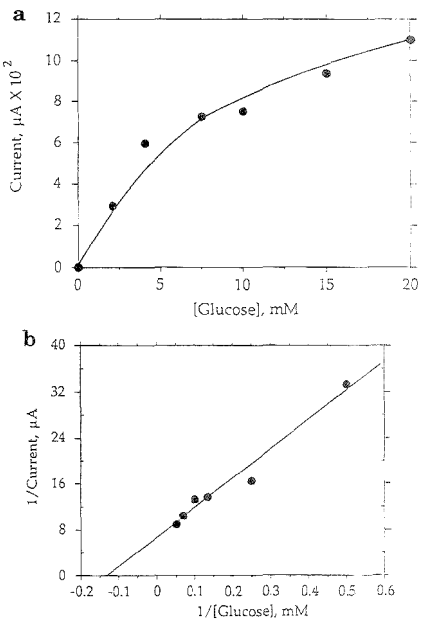

Figure 3. (a) Calibration curve of electrocatalytic anodic current developed by a four-layer ferrocene-modified GOx electrode as a function of glucose concentrations. Results are recorded by maintaining the enzyme electrode, surface area 0.2 cm^2, at a fixed potential (E = +0.4 V vs Ag/AgCl) and sequential injection of glucose into the electrochemical cell. Electrolyte consists of phosphate buffer, 0.1 M, pH = 7.3. Amperometric responses were recorded at 35 ± 0.5 °C under Ar. (b) Kinetic analysis of the electrocatalytic anodic currents at different glucose concentrations according to the Michaelis–Menten model.

Scheme 2. Electrical Communication of the GOx-Assembled Multilayer and the Electrode Surface Using Redox-Tethered Units Covalently Linked to the Protein

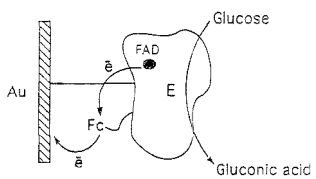

these glucose levels. Assuming that effective electrical communication between the ferrocene units and the electrode exists and, similarly, that efficient electrical interaction between the electron mediator and GOx redox site takes place, then the rate of electrocatalyzed oxidation of glucose is controlled by the biocatalyzed transformation at the enzyme redox center. That is, the electrocatalytic anodic current is proportional to the rate of the biocatalyzed oxidation of glucose. This allows Michaelis–Menten analysis of the electrobiocatalyzed oxidation of glucose according to eq 1, where I represents the observed anodic current

$$I = I_{max}[S]/(K_m + [S]) \quad (1)$$

at any glucose concentration,[30] I_{max} is the saturation value of the

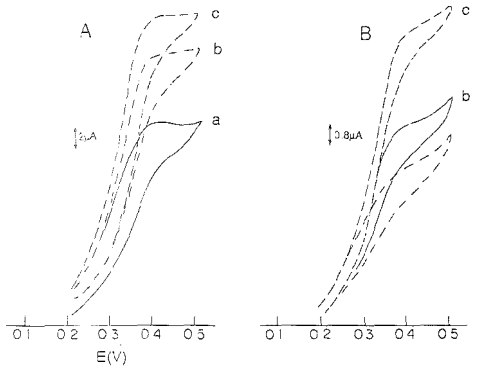

Figure 4. Cyclic voltammograms of a four-layer GOx electrode in the presence of 2.9×10^{-4} M ferrocenecarboxylic acid as diffusional electron mediator and glucose: (a) 0, (b) 6.8×10^{-3}, (c) 36×10^{-3} M. (A) In the presence of a rough Au electrode (geometrical area, 0.4 cm^2; roughness factor, 30). (B) In the presence of a smooth Au electrode (geometrical area, 0.4 cm^2; roughness factor, 1.2). All experiments were recorded in phosphate buffer, 0.1 M, pH = 7.3, 35 ± 0.5 °C, under Ar; scan rate, 2 $mV \cdot s^{-1}$.

anodic current, and K_m is the apparent Michaelis–Menten constant. Rearrangement of eq 1 yields eq 2, which enables the analysis of the enzyme kinetics. Figure 3b shows the Line-

$$1/I = K_m/I_{max}[S] + 1/I_{max} \quad (2)$$

weaver–Burk plot of the experimental results depicted in Figure 3a, according to eq 2. A linear plot is obtained, and the values $K_m = 8.0$ mM and $I_{max} = 0.14$ μA are derived.

The layered GOx network electrodes revealed unaltered activity for 6 months when stored dry at 4 °C. The modified electrodes showed stable amperometric responses for at least 12 h at room temperature and applied potential. These stability features reflect the potential application of such modified electrodes as amperometric glucose biosensors.

The immobilization of multilayers on an electrode surface provides one approach to control the protein content associated with the electrodes. A further method to increase the enzyme content associated with a monolayer configuration involves the use of rough Au electrodes as the base substrate to assemble the multilayer enzyme network. The Au foils were amalgamated to increase their roughness.[25] By this procedure, the roughness factor of the electrodes was increased from ~1.2 to 30 (the roughness factor is defined as the ratio between the real surface area and the geometrical area). The enzyme GOx was immobilized as a layered network on the rough Au electrodes. The enzyme layers associated with the rough electrodes exhibit stability comparable to that of the layers linked to the smooth surfaces. The amperometric responses of the resulting electrodes were compared to those of the respective smooth enzyme electrodes. In these experiments, rough and smooth GOx multilayer electrodes were employed, and ferrocenecarboxylic acid was applied as diffusional electron mediator. Figure 4 shows the resulting cyclic voltammograms at different glucose concentrations

(30) (a) Sakslund, H.; Wang, J.; Hammerich, O. *J. Electroanal. Chem.* **1994**, *374*, 71. (b) Badia, A.; Carlini, R.; Fernandez, A.; Battaglini, F.; Mikkelsen, S. R.; English, A. M. *J. Am. Chem. Soc.* **1993**, *115*, 7053.

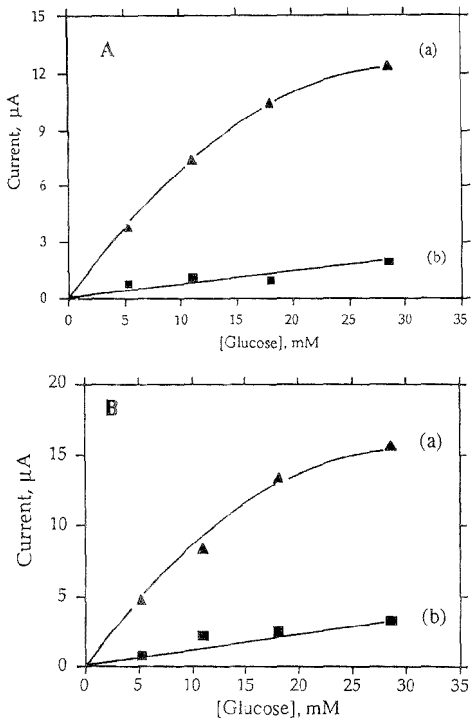

Figure 5. Calibration curves of the amperometric responses of (A) two-layer and (B) four-layer GOx electrode as a function of glucose concentrations: (a) rough Au electrode and (b) smooth Au electrode. In all experiments, 2.9×10^{-4} M ferrocenecarboxylic acid is applied as diffusional electron mediator.

of a four-layer network of GOx on the rough (A) and smooth (B) Au electrodes, respectively. Note that the cyclic voltammograms were recorded at different sensitivity scales of the current. The amperometric responses of the enzyme network associated with the rough Au electrodes are substantially higher than those observed with the smooth electrodes that have the same number of layers. Figure 5 shows the derived calibration curves corresponding to the amperometric responses of a two-layer and four-layer GOx networks immobilized onto rough and smooth electrodes, respectively. We see that the amperometric responses of the rough electrodes are 7.5- and 6-fold enhanced for the two- and four-layered network associated with the rough electrodes, respectively. The amperometric signals of the rough electrodes show saturation profiles, suggesting that the bioelectrocatalytic enzyme performance reaches a saturation value as the glucose concentration increases. The electrocatalytic anodic currents are proportional to the rate of bioelectrocatalyzed oxidation of glucose. The calibration curves, representing the anodic currents as a function of glucose concentration for the two-layer and four-layer GOx networks on rough Au electrodes (Figure 5), were analyzed according to the Michaelis–Menten model, eq 2. The Michaelis–Menten analysis was performed at a saturation concentration of the ferrocenecarboxylic acid cosubstrate (2.9×10^{-4} M). Both electrodes reveal a similar K_m value, corresponding to $K_m = 33.3$

mM. This value is very similar to that for native GOx in solution or GOx immobilized by a polymer onto electrodes.[31] The enhancement in the amperometric responses of the rough Au electrodes certainly reflects an increase in the protein content immobilized onto the electrode. For example, assuming that the GOx enzymes immobilized onto the rough and smooth electrodes exhibits similar activities, it is suggested from Figure 5A that in a two-layer network the amount of enzyme associated with the rough electrode is ~7.5-fold higher than that associated with the smooth Au electrode. Attempts to compare the content of protein associated with the rough and smooth Au electrodes using ^{3}H-labeled GOx failed, however, to yield meaningful results, and substantially lower values of protein than expected were detected on the rough electrodes. We assume that quenching of the radioactive emission by the rough surface yields the unexpectedly low counts for these electrodes. Nevertheless, assuming that the enzyme activities on the rough and smooth electrodes are similar, then by comparing the amperometric responses of the two electrodes, we conclude that the enzyme content on the two-layer network associated with the rough electrode is 7.5-fold higher than that associated with the smooth Au surface. Using the enzyme surface density value for a single monolayer on the smooth electrode, 7.5×10^{-12} mol·cm^{-2}, we estimate the surface coverage of the enzyme monolayer on the rough surface to be 5.2×10^{-11} mol·cm^{-2}.

The GOx arrays immobilized onto the rough Au electrodes were further modified by **1** to electrically communicate the protein with the electrode in a rigid assembly that eliminates the need for a diffusional electron mediator. The coulometric analysis of the charge associated with the oxidation (or reduction) of the ferrocene units linked to the enzyme arrays consisting of a different number of layers revealed an almost linear relationship between the total charge and the number of enzyme layers. This suggests that each layer is almost identically charged by the ferrocene relay units in the chemical modification step. Using the estimated value of surface coverage of GOx per monolayer, and knowing the total charge associated with the oxidation (or reduction) of ferrocene units linked to an enzyme monolayer, the average loading of an enzyme component by the ferrocene units is ~10. This value is similar to that observed for the enzyme associated with the smooth electrodes. The resulting ferrocene-modified GOx rough electrodes exhibit, similarly to the smooth Au surfaces, electrical communication between the protein and electrode (Figure 6). The electrobiocatalytic anodic current is controlled by the number of layers assembled onto the rough electrode surface. We thus conclude that organization of an enzyme network on a base SAM linked to a Au electrode and specifically, a rough surface, enables the amperometric detection of glucose. In the general perspectives, the method allows the tuning of the electrode sensitivity by the electrode roughness and number of layers associated with the electrode.

A further important feature of the enzyme electrodes originating from the method of organization of the enzyme network is the ability to construct a multienzyme network. Scheme 3 schematically outlines this advantage of the enzymes-layered electrode. Here, two enzymes are organized onto the electrode in an ordered layered array. The primary enzyme is a redox

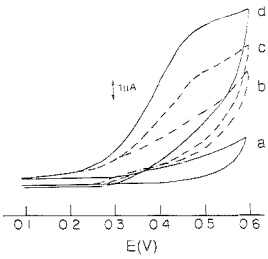

Figure 6. Cyclic voltammogram of ferrocene-modified GOx assembled onto rough Au electrodes, 0.4 cm^2. (a) One layer in the absence of glucose. (b–d) In the presence of 2×10^{-3} M glucose: (b) one layer, (c) four layers, and (d) six layers. All experiments were recorded in 0.1 M phosphate buffer, pH = 7.3, 35 ± 0.5 °C, under Ar; scan rate, 2 mV·s^{-1}.

Scheme 3. Organization of a Bifunctional Enzyme-Layered Network Where a Secondary Enzyme Is Applied for Amperometric Detection of the Product Generated from the Analyte Substrate by the Primary Enzyme

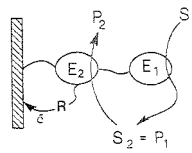

protein that electrically communicates with the electrode through the diffusional electron mediator. The second enzyme is non-redox-active, but its biocatalytic activity transforms its substrate into a product that acts as substrate for the primary redox protein. That is, amperometric detection of the product formed by the secondary enzyme, using the redox enzyme as sensing biomaterial, allows the analysis of the substrate. Thus, by the organization of coupled enzymes in a layered network, a variety of novel amperometric biosensors could be developed. This method is, however, viable only if the product formed by the secondary enzyme does not escape from the electrode interface into the bulk electrolyte solution and its amperometric detection is sufficiently rapid. Previous studies used bienzyme assemblies on electrodes by their organization in polymer matrices,[32] i.e., bienzyme electrodes composed of AChE and ChO for acetylcholine analysis.[33]

The principle of bienzyme layer electrodes was established with the development of an acetylcholine amperometric biosensor using a multilayered network consisting of the two enzymes: ChO and AChE. A network of four layers of ChO was immobilized onto a rough Au electrode, using a base cystamine monolayer and stepwise organization of the ChO network using DIDS as coupling reagent, similar to the method employed to assemble the GOx multilayer electrodes. In the presence of ferrocenecarboxylic acid, no electrical communication is established between the ChO multilayer network and the electrode. DIP acts, however, as an effective electron mediator for ChO. Figure 7A shows the

(31) (a) Shu, F. R.; Wilson, G. S. *Anal. Chem.* **1976**, *48*, 1679. (b) Swoboda, B. E. P.; Massey, V. *J. Biol. Chem.* **1965**, *240*, 2209. (c) Foulds, N. C.; Lowe, C. R. *J. Chem. Soc., Faraday Trans. 1* **1988**, *84*, 2259.

(32) (a) Kacaniklic, V.; Johansson, K.; Marko-Varga, G.; Gorton, L.; Jönsson-Pettersson, G.; Csöregi, E. *Electroanalysis* **1994**, *6*, 381. (b) Zhang, X.; Rechnitz, G. A. *Electroanalysis* **1994**, *6*, 361. (c) Yoshida, S.; Kanno, H.; Watanabe, T. *Anal. Sci.* **1995**, *11*, 251.

(33) Morelis, R. M.; Coulet, P. R. *Anal. Chim. Acta* **1990**, *231*, 27.

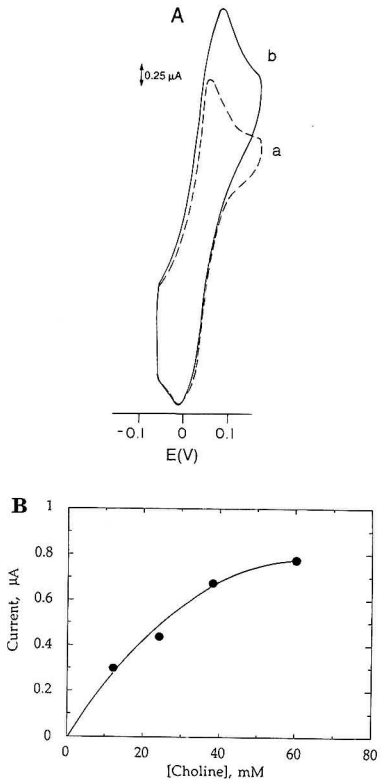

Figure 7. (A) Cyclic voltammograms of a four-layer ChO multilayer electrode using DIP, 4×10^{-5} M as diffusional electron mediator. (a) In the absence of added choline. (b) In the presence of 3.8×10^{-2} M choline. (B) Calibration curve of the amperometric responses of a four-layer ChO electrode at different choline concentrations. In all experiments, 4×10^{-5} M DIP is used as diffusional electron mediator. All experiments were recorded in 0.1 M phosphate buffer, pH = 7.8, 35 ± 0.5 °C, under Ar; scan rate, 2 mV·s^{-1}.

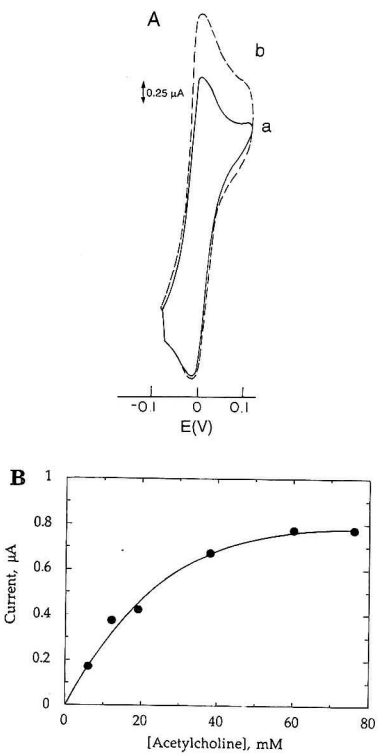

Figure 8. (A) Cyclic voltammograms of a seven-layer ChO–AChE multilayer electrode using 4×10^{-5} M DIP as diffusional electron mediator. (a) In the absence of added acetylcholine. (b) In the presence of 3.8×10^{-2} M acetylcholine. (B) Calibration curves of the amperometric responses of a seven-layer ChO–AChE electrode at different acetylcholine concentrations. In all experiments, DIP is used as diffusional electron mediator. All experiments were recorded in 0.1 M phosphate buffer, pH = 7.8, 35 ± 0.5 °C, under Ar; scan rate, 2 mV·s^{-1}.

reversible cyclic voltammogram of DIP, observed in the presence of the ChO enzyme electrode, and the electrocatalytic anodic current obtained upon addition of choline to the electrolyte cell. Control experiments revealed that no electrocatalytic anodic currents were developed in the absence of the electron mediator or upon application of a bare Au electrode in the presence of choline and the electron mediator. These results clearly indicate that the anodic current originates from the electrobiocatalyzed oxidation of choline by ChO, where DIP acts as an electron mediator that electrically communicates the enzyme with the electrode. Figure 7B shows the calibration curve of the electrocatalytic anodic currents at different choline concentrations. Michaelis–Menten analysis of the curve, according to eq 2, yields the apparent value of $K_m = 37$ mM for ChO. The Au electrode consisting of the four-layered network of ChO was further coupled to three layers of AChE using DIDS as coupling reagent, as schematically outlined in Scheme 4. Figure 8A shows the cyclic voltammograms of the two-enzyme network electrode in the absence and in the presence of acetylcholine. An electrocatalytic anodic current is developed in the presence of acetylcholine.

Scheme 4. Organization of a Bifunctional Multilayer Network of Choline Oxidase, and Acetylcholine Esterase for the Amperometric Detection of Acetylcholine

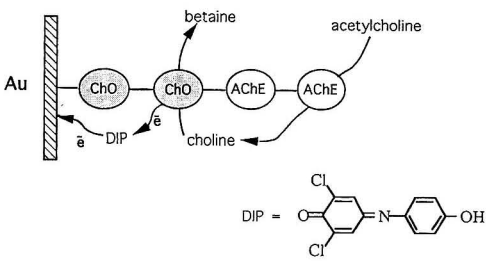

Control experiments reveal that no electrocatalytic current is developed in the absence of AChE or ChO from the multilayer enzyme network. Similarly, no direct electrooxidation of acetylcholine was detected by the bare Au electrode in the presence of DIP as electron mediator. These results indicate that the electrocatalytic anodic current originates from the electron

transfer-mediated oxidation of choline formed by the hydrolysis of acetylcholine by AChE. Scheme 4. The electrocatalytic anodic currents developed by the two-enzyme layered network at different acetylcholine concentrations are shown in Figure 8B. The calibration curve is almost identical to that observed for choline itself. That is, for a fixed acetylcholine concentration, the amperometric signal is almost of the same magnitude as that observed for choline at this concentration. These results reveal an important feature of the two-enzyme network electrode related to mass transport of the analyte within the protein network. Hydrolysis of acetylcholine to choline by AChE proceeds effectively, and the concentration of the hydrolytic product (choline) in the enzyme network is identical to that of acetylcholine in the bulk solution. The escape of the product from the enzyme network is slow, and hence the redox protein ChO senses electrochemically the hydrolysis product at a sensitivity corresponding to the similar concentration of acetylcholine (or choline) in the bulk electrolyte.

CONCLUSIONS

The advantages of organization of layered enzyme electrodes in the development of biosensor devices were discussed in the present study. It has been shown that organization of multilayers of redox proteins on a base SAM associated with a Au electrode provides a general means to design amperometric biosensors. The electrical communication between the enzyme array and the electrode interface was accomplished by diffusional electron mediators or by covalent attachment of electron relays to the protein network. Two methods to enhance the sensitivity of the enzyme electrodes were discussed: (i) application of rough Au electrodes and (ii) control of the number of layers in the network. It should be noted that the method to enhance the enzyme content on electrode surfaces by enzyme multilayers was recently elegantly further developed by Savéant and co-workers[34] using an antigen monolayer as a linking unit for antibody-modified glucose oxidase layers. This method can be viewed as complementary to the described method. The chemical method to fabricate the layered enzyme electrodes by a stepwise synthesis has important implications for future biosensor devices. We have shown that organization of two enzymes in an ordered array allows the amperometric detection of the substrate of one enzyme by electrochemical detection of the product formed by this primary enzyme. One could envisage more complex biosensor devices where several enzymes are coupled in a series and the ultimate product acts as substrate for the redox enzyme acting as the electroactive biomaterial for probing the primary non-redox-active analyte.

A further advantage of the stepwise construction of layered multienzyme electrodes could relate to the selectivity of the resulting biosensor. By the covalent attachment of appropriate enzymes, interfering reagents could be screened from the analyzing redox enzyme layers associated with the electrode.

(34) Bourdillon, C.; Demaille, C.; Moiroux, J.; Savéant, J.-M. *J. Am. Chem. Soc.* **1994**, *116*, 10328.

ACKNOWLEDGMENT

Parts of this research were supported by the Ministry of Science and Arts, Israel, and the Bundesministerium für Forschung und Technologie, Germany, and Savyon Diagnostic, Ltd., Ashdod, Israel. We thank Dr. E. Katz for his advice in the experimental work.

Received for review May 22, 1995. Accepted September 8, 1995.[⊗]

AC950480Q

[⊗] Abstract published in *Advance ACS Abstracts*, October 15, 1995.

Anal. Chem. **1995**, *67*, 4127–4132

Continuous-Flow MALDI Mass Spectrometry Using an Ion Trap/Reflectron Time-of-Flight Detector

Ling He, Li Liang, and David M. Lubman*

Department of Chemistry, The University of Michigan, Ann Arbor, Michigan 48109

A continuous-flow probe has been used to directly introduce solutions of peptides into an ion trap storage/reflectron time-of-flight mass spectrometer for MALDI/MS analysis. The advantages of the trap, including the ability to operate efficiently at the elevated pressures required for direct liquid introduction into the trap, are demonstrated. It is shown that by using low-voltage auxiliary fields applied to the endcaps of the ion trap, the unwanted solvent and matrix ions can be eliminated by resonance ejection, providing enhanced S/N for target peptide ions. Using this methodology, it is demonstrated that picomole level sensitivity can be routinely achieved with quantitation over 2 orders of magnitude for a mass range of >5000 units. The conditions required to achieve a stable continuous liquid flow and to optimize the liquid MALDI conditions are also discussed.

Continuous-flow fast atom bombardment interfaces (CF-FAB), developed by Ito et al. as "frit FAB" [1] and Caprioli et al. as a direct introduction FAB,[2] have proven to be very useful for interfacing mass spectrometry with various solution separation methods, such as liquid chromatography (LC)[3–9] and capillary zone electrophoresis (CZE).[10,11] However, the ionization efficiency of FAB decreases significantly as the molecular weight increases. Alternatively, since its introduction in 1988, matrix-assisted laser desorption/ionization (MALDI)[12,13] has been shown to be a powerful method for ion generation of large biomolecules. A continuous-flow liquid probe introduction method interfaced to MALDI with time-of-flight detection has also recently been developed by Li and co-workers.[14] This method has shown great potential as a means to combine various solution separation methods with MALDI for on-line detection of high molecular weight compounds.[15] An aerosol liquid introduction system for MALDI and other laser desorption schemes for liquid injection have also recently been developed.[16–18]

Mass analysis of ions generated by MALDI has been carried out most often with time-of-flight (TOF) mass spectrometers, primarily due to their inherent compatibility with pulsed ionization techniques and the high mass range capabilities. The main drawbacks of the MALDI-TOF arrangement have been the low resolution due to the broad energy distribution and metastable decay that results from the MALDI process[19,20] and the limited ability to perform tandem mass spectrometric (MS/MS) analysis. Therefore, there has been an effort to interface MALDI to other types of mass spectrometers to circumvent disadvantages associated with TOF. Magnetic sector instruments,[21] Fourier transform ICR devices,[22,23] and ion trap mass spectrometers[24–28] have been interfaced to MALDI.

The quadrupole ion trap in particular has many advantages for improving the results of MALDI mass spectrometry. Ion traps are optimally operated at relatively high pressure (i.e., ~1 mTorr of buffer gas[29]), so that hot ions produced in the trap via MALDI can lose kinetic energy as they undergo collisions with the buffer gas, resulting in an improved resolution. However, resonant ejection techniques must be employed to extend the mass range above the nominal limit of m/z 650 associated with the mass-selective instability mode.[27] The use of resonant ejection may result in a loss of resolution or mass accuracy as the m/z ratio increases, depending on the scan speed used. In recent work, a

(1) Ito, Y.; Takeuchi, T.; Ishii, D.; Goto, M. *J. Chromatogr.* **1985**, *346*, 161–166.
(2) Caprioli, R. M.; Fan, T.; Cottrell, J. S. *Anal. Chem.* **1986**, *58*, 2949–2954.
(3) Ito, Y.; Takeuchi, T.; Ishii, D. *J. Chromatogr.* **1986**, *358*, 201–207.
(4) Takeuchi, T.; Watanabe, S.; Kondo, N.; Ishii, D. *J. Chromatogr.* **1988**, *435*, 482–488.
(5) Boulenguer, P.; Leroy, Y.; Alonso, M. J.; Montreuil, J.; Ricart, G.; Golbert, C.; Duquet, D.; Dewaele, C.; Fournet B. *Anal. Biochem.* **1988**, *168*, 164–170.
(6) Moseley, M. A.; Deterding, L. J.; de Wit, J. S. M.; Tomer, K. B. *Anal. Chem.* **1989**, *61*, 1577–1584.
(7) Caprioli, R. M. *Anal. Chem.* **1990**, *62*, 477A–485A.
(8) Pleasance, S.; Thibault, P.; Moseley, M. A.; Deterding, L. J.; Tomer, K. B.; Jorgenson, J. W. *J. Am. Soc. Mass. Spectrom.* **1990**, *1*, 312–319.
(9) Hogge, L. R.; Balsevich, J. J.; Olson, D. J. H.; Abrams, G. D.; Jacques, S. L. *Rapid Commun. Mass. Spectrom.* **1993**, *7*, 6–11.
(10) Caprioli, R. M.; Moore, W. T.; Martin, M.; Dague, B. B. *J. Chromatogr.* **1989**, *480*, 247–257.
(11) Suter, M. J.-F.; Caprioli, R. M. *J. Am. Soc. Mass. Spectrom.* **1992**, *3*, 198–206.
(12) Karas, M.; Hillenkamp, F. *Anal. Chem.* **1988**, *60*, 2299–2301.
(13) Beavis, R. C.; Chait, B. T. *Rapid Commun. Mass Spectrom.* **1989**, *3*, 436–439.
(14) Li, L.; Wang, A. P. L.; Coulson, L. D. *Anal. Chem.* **1993**, *65*, 493–495.
(15) Nagra, D. S.; Li, L. *J. Chromatogr. A.*, submitted.
(16) Murray, K. K.; Russell, D. H. *Anal. Chem.* **1993**, *65*, 2534–2537.
(17) Lustig, D. A.; Lubman, D. M. *Rev. Sci. Instrum.* **1991**, *62*, 957–962.
(18) Koster, C.; Dey, M.; Grotemeyer, J.; Schlag, E. W. *Proceedings of the 38th ASMS Conference on Mass Spectrometry and Allied Topics*, Tucson, AZ, June 3–8, 1990; pp 1242–1243.
(19) Huth-Fehre, T.; Becker, C. H. *Rapid Commun. Mass Spectrom.* **1991**, *5*, 378–382.
(20) Beavis, R. C.; Chait, B. T. *Chem. Phys. Lett.* **1991**, *181* (5), 479–484
(21) Annan, R. S.; Kochling, H. J.; Hill, J. A.; Biemann, K. *Rapid Commun. Mass Spectrom.* **1992**, *6*, 298–302.
(22) Castro, J. A.; Koster, C.; Wilkens, C. *Rapid Commun. Mass Spectrom.* **1992**, *6*, 239–241.
(23) Hettich, R. L.; Buchanan, M. V. *J. Am. Soc. Mass Spectrom.* **1991**, *2*, 22–28.
(24) Doroshenko, V. M.; Cornish, T. J.; Cotter, R. J. *Rapid Commun. Mass Spectrom.* **1992**, *6*, 753–757.
(25) Schwartz, J. C.; Bier, M. E. *Rapid Commun. Mass Spectrom.* **1993**, *7*, 27–32
(26) Jonscher, K.; Currie, G.; McCormack, A. L.; Yates, J. R., III. *Rapid Commun. Mass Spectrom.* **1993**, *7*, 20–26.
(27) Kaiser, R. E., Jr.; Louris, J. N.; Amy, J. W.; Cooks, R. G. *Rapid Commun. Mass Spectrom.* **1989**, *3*, 225–229.
(28) Chambers, D. M.; Georinger, D. E.; McLuckey, S. A.; Glish, G. L. *Anal. Chem.* **1993**, *65*, 14–20.
(29) March, R.; Hughes, R. *Quadrupole Storage Mass Spectrometry*; Wiley: New York, 1989.

0003-2700/95/0367-4127$9.00/0

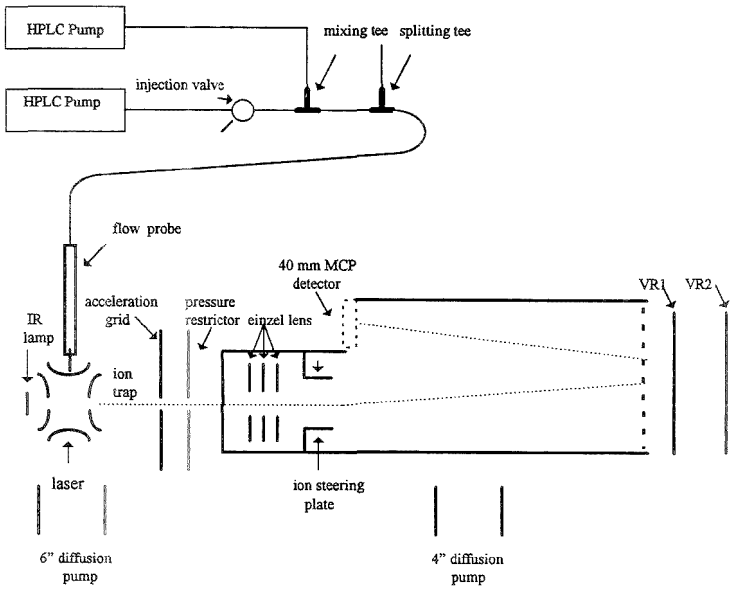

Figure 1. Experimental setup of the continuous-flow MALDI experiments.

quadrupole ion trap interfaced to a reflectron time-of-flight (reTOF) mass spectrometer was used as a detector for MALDI/MS.[30] An enhanced resolution of several thousand has been obtained for peptides up to 2100 units. The ion trap/reTOF device combines the storage capabilities of the ion trap with the speed and high mass capabilities of the TOF to produce a hybrid instrument with several potential advantages for MALDI/MS.

In this work, a continuous-flow probe is used to directly introduce solutions of peptides into an ion trap/reTOF mass spectrometer for MALDI/MS analysis. The advantages of the trap, including the ability to operate efficiently at the elevated pressures required for direct liquid introduction into the trap, are demonstrated. In addition, the advantages of the trap for improving the resolution of MALDI/TOF experiments and the ability to enhance the S/N by selective ejection of unwanted solvent and matrix ions are also shown. The capabilities and limitations of this method are evaluated herein, including the sensitivity and quantitation for several peptides. It is demonstrated that picomole level sensitivity can be routinely achieved with quantitation over 2 orders of magnitude. In addition, a mass range of >8000 units has been achieved in these experiments.

EXPERIMENTAL SECTION

Ion Trap/Reflectron Time-of-Flight Mass Spectrometer (IT/reTOF). The experimental setup used for continuous-flow MALDI is shown in Figure 1. The IT/reTOF mass spectrometer shown in Figure 1 has been described in detail elsewhere.[30] The instrument consists of a reTOF mass spectrometer (Model D850, R. M. Jordan Co., Grass Valley, CA) using a quadrupole ion trap (Model C1251, R. M. Jordan Co.) as the ion source region. The ion trap is located in a vacuum chamber pumped by a 6 in. diffusion pump and liquid N_2 cryobaffle, while the TOF flight tube is pumped by a 4 in. diffusion pump and liquid N_2 cryobaffle. The two vacuum chambers are connected by an aperture 0.12 in. in diameter so that these two regions are differentially pumped. The result is that the pressure in the flight tube is ~1–2 orders of magnitude lower than that in the ion trap chamber during the time liquid solvent is being injected into the trap region. This arrangement allows injection of liquid at ground dc potential on the trap to minimize arcing while maintaining a sufficiently low operating pressure in the reTOF to preserve resolution and detector lifetime. At the flow rates used in these experiments, 2–4 μL/min of 1:1 acetonitrile/water, the use of liquid N_2 cryopumping using the liquid N_2 cryobaffles is essential for maintaining a sufficiently low pressure for operation of the reTOF. The detector used in these experiments was a dual 40 mm microchannel plate detector with a Cu–Be postacceleration stage. The postacceleration stage operated up to ±15 kV and allowed enhanced detection of high mass ions (>2500 units) that could not otherwise be detected with the acceleration voltages used in the reTOF, and it provided enhanced sensitivity for ions below 2500 units. However, the postacceleration stage limited the resolution in static MALDI experiments to <500, as compared to a resolution of typically >1000 that can be achieved without this stage.

The continuous liquid injection flow probe is inserted into the ion trap chamber using a vacuum interlock. The flow probe is orthogonal to the reTOF flight tube axis and is inserted into a 3.1 mm hole in the ring electrode of the ion trap. The probe though does not make electrical contact with the ring electrode since the probe tip is made of Vespel, an insulating material. The fourth harmonic (266 nm) of a Nd–YAG laser (Quanta-Ray DCR3, Spectra Physics, Mountain View, CA) was collimated through a converging/diverging lens system (30:10 mm focal length) and

(30) Chien, B. M.; Michael, S. M.; Lubman, D. M. *Rapid Commun. Mass Spectrom.* **1993**, *7* (9), 837–843.

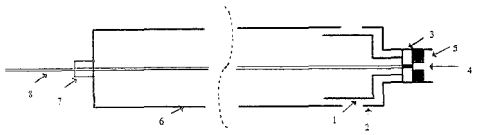

Figure 2. Schematic of the continuous MALDI flow probe: (1) the rear part of the probe tip (0.5 mm i.d.), (2) the front part of the probe tip (3.5 mm o.d.), (3) septum to prevent back flow, (4) small hole (0.4 mm diameter) to guide the capillary tube, (5) housing for the frit (1.59 mm diameter, 0.79 mm depth), (6) stainless steel tube (0.5 in. o.d., 0.375 in. i.d.), (7) LC fitting consisting of a stainless steel male nut and a PEEK ferrule (400 μm i.d.) as the vacuum seal, and (8) fused silica capillary tube (50 μm i.d., 360 μm o.d.).

passed through a 3.1 mm hole in the ring electrode and onto the probe surface. An IR lamp (F3 quartz IR lamp, Puritan Electric Co.) was placed below the ion trap to heat the trap to ~60–80 °C during the continuous-flow liquid MALDI process. The heated trap region was necessary to prevent freezing of the liquid matrix on the probe tip due to expansion of the carrier solvent. The freeze/thaw phenomenon that is otherwise observed in these experiments without the heating causes the pressure to vary unstably in the mass spectrometer.

Continuous-flow MALDI is performed from the liquid film formed on the probe tip inside the ion trap. The ions were typically stored in the trap for 311 ms and then ejected from the trap using a phase-synchronized dc pulse (−325 V, 2 μs duration) applied to the exit endcap electrode. The MALDI process was run at 10 Hz, while the IT/reTOF cycle was at 2.5 Hz, so that four laser pulses were used in each storage/ejection cycle. More pulses could be stored in each cycle, but this was generally not done to prevent saturation of the trap. Following ejection of ions from the trap into the reTOF, the ions were accelerated to the liner voltage (−2000 V) and ultimately to the MCP detector.

Probe Design. The design of the flow probe for liquid sample introduction is shown in Figure 2. It consists of a probe tip and a probe body. The probe tip is constructed of Vespel, which was chosen for its ability to maintain its mechanical strength at the operating temperature of the ion trap (60–80 °C), and it serves as an electric insulator between the ion trap ring electrode and the probe body. A small recessed area is drilled into the face of the front piece of the probe tip (2 in Figure 2), which houses the round frit disk (pore size 2 μm, $^1/_{32}$ in. diameter, $^1/_{16}$ in. thickness). A hole (0.016 in. diameter, 0.04 in. length) is drilled in the center of the recessed area to allow the capillary tubing to pass through the Vespel tip to the back of the frit. The rear part of the probe tip (1) is screwed into the front part (2) and squeezes a septum that seals tightly around the capillary tube. The dead volume for the liquid after it elutes from the capillary tubing is almost zero. A low dead volume will be important for interfacing to capillary separations and to reduce the time necessary to build an equilibrium condition on the surface of the probe. The probe tip is screwed into the probe body, which is made of stainless steel (0.5 in. o.d., 0.375 in. i.d.). An in-house-designed cap is placed on the atmospheric pressure side of the stainless steel tube, where the tube fits into one side of the cap with an O-ring seal. The other side of the cap is a standard LC fitting for capillary tubing, where a male nut and a PEEK ferrule are used to seal the capillary.

Sample Delivery. Two SM-909 isocratic HPLC pumps with microhead delivery (Anspec, Ann Arbor, MI) were used to pump the carrier solvent and the matrix solution separately. The micro pump head has a working range from 2 to 1000 μL/min. The carrier solvent was pumped into a Reodyne four-port injection valve with a 5 μL internal loop. The carrier solvent from the injection valve was then mixed with the matrix solution. The mixed solution was then split by a tee, where the splitting ratio was experimentally determined to be 1:24. A fused silica capillary tube (50 μm i.d., 360 μm o.d.) (Polymicro Technologies, Phoenix, AZ) was used to carry the split solution to the back of the frit. The composition of the matrix solution is 3-NBA/CH_3CN/H_2O/ethylene glycol/1%TFA (in H_2O) 8:40:40:2:9 (v/v). The carrier solvent is composed of acetonitrile and water in a 1:1 ratio. The optimal flow rate ratio between the matrix solution and the carrier solvent varied in the experiment for different samples.

Frequency Modulation. Two Wavetek Model 112 VCG function generators were connected in tandem to produce a modulated sweep frequency output applied to the entrance endcap electrode for resonance ejection of unwanted background from the trap. The first VCG outputs a triangular wave (600 Hz), which causes the output from the second VCG to sweep from a low frequency to a high frequency, determined by the $-V_{max}$ and the $+V_{max}$ of the first VCG, respectively. The amplitude of the modulated output can be optimized independent of the first VCG. A more detailed description of this method can be found in ref 31.

Chemicals. All peptides used in this work were purchased from Sigma Chemical Co. (St. Louis, MO). The analytes were prepared at concentrations of 0.001, 0.01, and 0.1 mg/mL in deionized water. The matrix used in this work was 3-nitrobenzyl alcohol (3-NBA) dissolved in a 1:1 (v/v) mixture of acetonitrile and water. Both the carrier solvent and the matrix solution were sonicated in order to degas the sample before use.

Data Acquisition. All the spectra were collected using a LeCroy 9350M 500 MHz digital oscilloscope. Twenty IT/reTOF (i.e., 80 laser shots) cycles were averaged for each spectrum (except the spectra in Figure 3). Each spectrum collected in the continuous mode was saved on a floppy disk by the oscilloscope and later copied into a Gateway 2000 P5-66 PC. The data were transformed into the Excel format and then pasted into MicroCal Origin (version 2.94, MicroCal Software, Inc.). Each spectrum was smoothed by three-point adjacent averaging to remove some background noise caused by the conversion dynode.

RESULTS AND DISCUSSION

In Figure 3 are shown MALDI mass spectra of gramicidin S obtained in the static and dynamic flow modes. These spectra were obtained using either static or flow probe injection in the IT/reTOF with a storage time of 311 ms. The static mode MALDI spectrum of gramicidin S in Figure 3a was taken using a liquid 3-NBA matrix at 266 nm and was averaged over 50 IT/reTOF ejection cycles using ~20 pmol of material on the probe tip. The dynamic mode MALDI spectrum in Figure 3b was taken with 3-NBA matrix solution/carrier solvent 1:5, where ethylene glycol was added to the matrix solution to prevent freezing and clogging of the capillary. The amount of gramicidin S reaching the probe tip after injection and splitting of the sample solution was also ~20 pmole. The laser was operated at a repetition rate of 10 Hz at 266 nm, and the signal of Figure 3b was also averaged over 50 IT/reTOF ejection cycles.

(31) Fountain, S. T.; Lee H.; Lubman, D. M. *Rapid Commun. Mass Spectrom.* **1994**, *8*, 487–494.

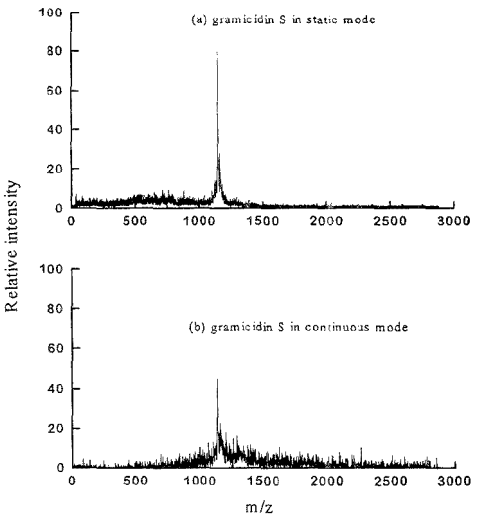

Figure 3. Comparison of the mass spectra of gramicidin S in (a) static mode and (b) dynamic mode. The same amount of sample was consumed on the probe tip in both modes.

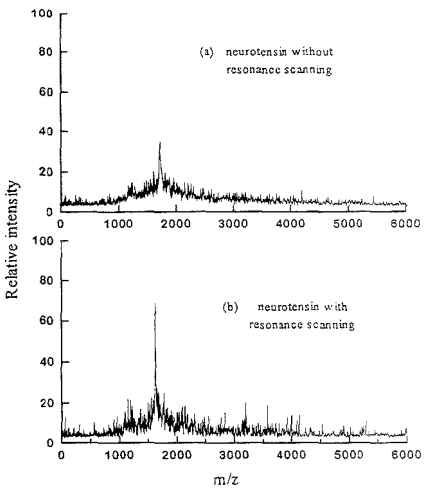

Figure 4. Comparison of the mass spectra of neurotensin in (a) dynamic mode without resonance ejection and (b) dynamic mode with resonance ejection.

The MALDI mass spectra obtained in the static mode using the IT/reTOF detector generally showed better resolution and a higher signal intensity under the same concentration conditions relative to the spectra obtained using the dynamic flow technique (shown in Figure 3b). These observations are similar to those already published by Li and co-workers.[14] The static mode MALDI/MS of gramicidin S provides a resolution of 350 with use of the IT/reTOF in these experiments under the conditions used. The main limitation to the resolution and the S/N in these experiments as compared to previous work[30] appears to be the use of a Cu–Be postacceleration stage in front of the MCP detector. In comparison, the dynamic flow mode MALDI/MS experiment results in a resolution of 280 under similar conditions. In addition, under comparable conditions of analyte concentration and laser power, the signal intensity is considerably better for the static MALDI than for the dynamic flow MALDI experiment.

The reduced resolution and signal intensity in the dynamic flow experiments might be expected due to the higher pressure and solvent background in the trap. The solvent ions in the ion trap appear to interfere with extraction of the trapped peptides ions, as compared to a lighter buffer gas such as helium. It might be expected that a lower flow rate will help to improve the resolution. However, under a lower flow rate, it becomes more difficult to maintain the "wet" surface on the probe tip due to the effect of pumping in the mass spectrometer and the elevated temperature (60–80 °C) of the ion trap. The pressure during the static MALDI experiments was estimated to be between $\sim 5 \times 10^{-4}$ and 1×10^{-3} Torr in the trap and $\sim 1 \times 10^{-6}$ Torr in the reTOF flight tube. In comparison, the pressure in the trap during the dynamic flow MALDI experiments is unknown but is estimated to be $\sim 10^{-2}$ Torr. The pressure in the flight tube during these experiments is $\sim 2 \times 10^{-6}$ Torr. The He buffer pressure in the trap and the ultimate pressure in the reTOF can be easily controlled during the static MALDI experiments to optimize resolution and signal intensity, whereas the pressure in the IT/reTOF during the dynamic flow experiments will be determined by the flow rate that is used to optimize the MALDI process from the liquid flow.

A method to improve the resolution and S/N involves eliminating the background and solvent ions in the trap using resonant ejection techniques. A unique advantage of trap technology is that this task can be accomplished by using a low radio frequency (rf) voltage on the endcaps of the trap. By properly choosing the frequencies applied to the trap, one can eject background while selectively storing the target ion. The effects of eliminating the low-mass background ions in the dynamic flow MALDI experiments are shown in Figure 4 for the peptide neurotensin at a level of 12 pmole. The auxiliary rf voltage applied to the endcaps is scanned over a frequency range of 72–1000 kHz at a repetition rate of 600 Hz and an amplitude of 9.3 V (peak-to-peak). The background noise is significantly reduced by applying the scanning frequency, and the S/N is greatly enhanced, as shown in Figure 4b compared to Figure 4a. The resolution in the nonresonance-ejection mode is not degraded significantly, which suggests that pressure in the IT/reTOF is still the limiting factor for resolution.

The detection limits of the experiment for samples introduced via the continuous-flow probe were evaluated for various peptides, as shown in Table 1. Since the detection limit can be increased markedly by ejecting background ions from the trap using resonant ejection, all measurements shown in Table 1 were taken using this methodology. The detection limits shown were determined by using the successive dilution method to generate the lowest level of sample detected. The minimum amount of sample injected was then divided by a splitting tee to a splitting ratio of 1:24, which corresponds to the actual sample sent to the probe tip. The flow rate used in these experiments was 2–3 μL/min. The detection limit was determined for peptides ranging in size from ~1000 to 8500 Da, and the limit in each case is typically in the 1–5 pmol region. The limit was determined over an average of 100 laser pulses or 10 s. Since the sample may elute

Table 1. Detection Limits of Various Peptides in Continuous-Flow MALDI

peptide	MW	detectn lim (μg/μL)	detectn lim[a] (pmol)
angiotensin III	931.1	0.0100	4.5
bradykinin	1060.2	0.0125	4.9
gramicidin S	1140.5	0.0125	4.6
angiotensin I	1296.5	0.0100	3.2
substance P	1347.6	0.0125	3.9
neurotensin	1672.9	0.0050	1.2
melittin	2847.5	0.0300	4.4
aprotinin	6511.5	0.1000	6.4
ubiquitin	8564.8	0.1000	4.9

[a] Amount of sample actually sent to probe tip.

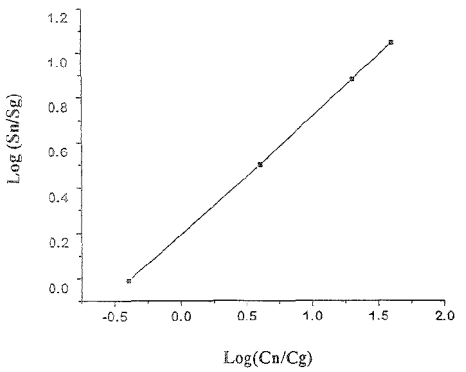

Figure 5. Quantitation plot of CF-MALDI experiment for neurotensin using gramicidin S as an internal standard. S_n/S_g represents the ratio of signal intensities of neurotensin and gramicidin S. C_n/C_g represents the ratio of concentrations of neurotensin and gramicidin S.

over 1–2 min, one might expect that if the total ion signal was collected, an additional factor of up to 10 might be feasible. Similar limits of sensitivity have been previously claimed by Li and coworkers for CF-MALDI experiments.[14]

A measure of the quantitation capabilities of the CF-MALDI IT/reTOF method was investigated for several compounds and is demonstrated for neurotensin in Figure 5. The MALDI process is very sensitive to laser fluence. Small variations in laser fluence cause large fluctuations in analyte signals. Absolute quantitative measurements of biopolymers using MALDI are difficult since the signal level is strongly dependent on laser fluence, laser beam homogeneity, sample homogeneity, and probe surface conditions. Internal calibration with molecules having similar chemical properties can be used to obtain absolute quantitative measurements.[32] In order to determine the linearity of response of the CF experiment, 5 μL sample solutions containing 0.030 nmol (0.010 μg/μL), 0.30 nmol (0.10 μg/μL), 1.5 nmol (0.50 μg/μL), 3.0 nmol (1.0 μg/μL) portions of the peptide neurotensin and 0.11 nmol (0.025 μg/μL) of gramicidin S (as internal standard) were injected into the probe. After splitting, the amount of sample that actually reaches the probe tip is 1.2, 12, 62, and 125 pmol, respectively, for neurotensin and 4.6 pmol for gramicidin S. The solvent flow rate was 3.0 μL/min in these experiments, and each

(32) Nelson, R. W.; Mclean M.; Hutchens, T. W. *Anal. Chem.* **1994**, *66*, 1408–1415.

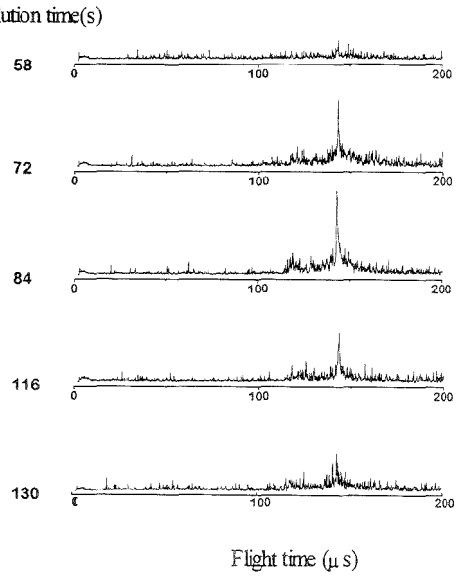

Figure 6. Mass spectra of neurotensin taken at different times after the injection of 5 μL of neurotensin (0.1 μg/μL). The flow ratio is matrix solution/carrier solvent 10:50 μL/min.

point represents the signal obtained as an average of 100 laser shots. The response was found to be linear over 2 orders of magnitude as shown in Figure 5. Above 125 pmol of sample on the probe tip, a deviation from linearity was observed that may be a result of overloading the probe surface or ion trap or possibly suppression of the gramicidin S internal standard signal.

An important factor involved in obtaining reproducible CF-MALDI results is achieving stable operation of the liquid flow from the continuous-flow probe. The stable operation of the probe can be achieved in a mass spectrometer when the rate of evaporation of the solvent from the probe surface and the pumping speed of the source of the mass spectrometer are in balance. The evaporation rate may be altered by changing either the flow rate of liquid to the probe tip, the total vapor pressure of the solution, or the amount of heat applied to the tip. Insufficient heat will lead to clogging within the capillary tip and will give rise to unsteady ion signals. When too much heat is applied to the probe tip, ion signals will disappear due to the rapid evaporation of 3-NBA. A flow rate that is excessively high may lead to arcing of the rf storage potential inside the ion trap and to space charge problems. The optimum temperature for this system was found to be 60–80 °C. The optimum flow rate was typically 2–3 μL/min.

Another important aspect of this experiment is the memory effect of the continuous-flow injection of sample. This problem will be especially important when interfacing this method to capillary HPLC. An example of the time profile of the signal for a 5 μL injection of neurotensin as a function of time is shown in Figure 6. The signal rises sharply at ~70–80 s after injection and slowly decreases for over a minute. The laser continues to desorb the neurotensin until the memory effect from neurotensin eventually is eliminated. The ability to minimize the memory

effect depends on the flow rate, the temperature of the probe tip, the desorption laser power, and the minimizing of the surface area of the probe tip. Further efforts are underway to optimize these parameters to minimize the memory effect.

It should be noted that the CF-MALDI method has certain key advantages and disadvantages as a method for generating large ions from solution as compared to electrospray ionization (ESI). For example, the CF-MALDI method generally produces molecular ions, MH^+, for identification, whereas the use of ESI may result in the production of multiply-charged ions, which can result in confusion in identification of the molecule. Although the presence of multiply-charged ions results in the ability to detect large ions at relatively low m/z, the mass range of the IT/reTOF is generally sufficient for detection of the singly-charged products of enzymatic and chemical degradation of large proteins, which would be analyzed by the CF-MALDI method.

Key advantages of CF-MALDI compared to ESI are that the molar sensitivity is relatively constant as a function of mass over a large mass range (see Table 1) and that the sensitivity is not strongly affected by the presence of salts, impurities, or organic buffers. Thus, the sample preparation is fairly simple, and the CF-MALDI process is not affected by the presence of buffers such as TFA often required in separation processes. This is in contrast to ESI, where the ionization efficiency of different compounds may vary by several orders of magnitude, depending on the peptide structure. Also, the ESI source is adversely affected by the presence of large amounts of salts, impurities, or organic buffers. Although femtomole level detection of peptides via ESI has been achieved in the IT/reTOF in the continuous-flow mode,[33] the presence of organic buffers such as TFA required in chromatographic separations often limits the sensitivity to the low picomole range.[34]

A third important advantage of the CF-MALDI technique is that it uses a relatively simple and rugged interface, where the flow probe tip is inserted directly into the ion trap for MALDI. The exact position of the probe in the trap is not critical, although the alignment of the laser beam to the probe is important. In comparison, ESI requires a rather sophisticated atmosphere-to-vacuum interface, with a high pumping speed needed to evacuate the interface region, skimmers to skim the ion beam, desolvation of ions produced under atmospheric pressure conditions, and critical alignment of the source and interface. In addition, CF-MALDI is performed directly in the ion trap, as opposed to ESI, where ion transmission through the interface and into the trap is a relatively inefficient process. It is expected that with continued improvements the CF-MALDI method will provide comparable or even improved sensitivity relative to ESI.

(33) Michael, S. M.; Chien, B. M.; Lubman, D. M. *Anal. Chem.* **1993**, *65*, 2614–2626.

(34) Qian, M.; Lubman, D. M. *Anal. Chem.* **1995**, *67*, 2870–2877.

(35) Lee, H.; Lubman, D. M. Anal. Chem. **1995**, *67*, 1400–1408.

CONCLUSIONS

In this work, a continuous-flow probe has been constructed which can deliver solutions of peptides directly into a mass spectrometer for detection by MALDI. This method generates singly-charged molecular ions from solution which can be used for identification of peptides. An ion trap storage/reTOF device has been used for detection which has distinct advantages in its ability to efficiently operate at the elevated pressures that result from direct liquid injection and to operate at ground dc potential to minimize arcing. Under the conditions of the experiment, the flow probe can operate up to a flow rate of 4 μL/min, and by optimizing the temperature of the probe, a very stable signal can be obtained. In addition, resonance ejection methods can be used with the trap to selectively eject unwanted background from the trap to enhance the S/N. Using this method, picomole level sensitivity can be obtained for peptides over a mass range of >8000 units, and the detection limit remains relatively constant as a function of mass. Also, quantitation using an internal standard was found to be linear over 2 orders of magnitude. In addition, the IT/reTOF presents the opportunity for structural analysis of these peptides in TOF using either MS/MS or MALDI activated decay in the trap.[35]

ACKNOWLEDGMENT

We gratefully acknowledge the National Science Foundation under Grant BIR-9223677 for support of this work.

Received for review June 15, 1995. Accepted August 24, 1995.[⊗]

AC950605R

[⊗] Abstract published in *Advance ACS Abstracts*, October 1, 1995.

Anal. Chem. **1995**, *67*, 4133–4138

Detection of Reaction Intermediates: Photosubstitution of (Polypyridine)ruthenium(II) Complexes Using On-Line Electrospray Mass Spectrometry

Ryuichi Arakawa,*,† Satoshi Tachiyashiki,‡ and Takekiyo Matsuo§

Department of Applied Chemistry, Faculty of Engineering, and Department of Physics, Faculty of Science, Osaka University, Machikaneyamacho 1-16, Toyonaka 560, Japan, and Laboratory of Chemistry, Kagawa Nutrition University, Sakado, Saitama 350-02, Japan

Photosubstitution of $Ru(bpy)_2BX_2$ (bpy = 2,2′-bipyridine; B = 3,3′-dimethyl-2,2′-bipyridine (dmbpy) or 2-(aminomethyl)pyridine (ampy); and $X = ClO_4^-$ or PF_6^-) has been studied in both acetonitrile and pyridine by using on-line electrospray mass spectrometry. For the complexes with B = dmbpy and ampy, intermediates with a monodentate (one-legged) B ligand, $Ru(bpy)_2BS^{2+}$ and $Ru(bpy)_2BSX^+$ (S = solvent molecule), were detected for the first time in the electrospray mass spectra, together with the photosubstitution products $Ru(bpy)_2S_2^{2+}$ and $Ru(bpy)_2S_2X^+$. For the complex with B = ampy, minor photoproducts that resulted from dissociation of bpy, $Ru(bpy)BS_2^{2+}$ and $Ru(bpy)BS_2X^+$, were detected. The solvent-released ions $Ru(bpy)_2S^{2+}$, $Ru(bpy)_2^{2+}$, and $Ru(bpy)_2SX^+$, which were secondary products from collision-induced dissociation of the photosubstitution reaction, were also seen. The effects of solvent and intensity of irradiation on the photoreactions were also studied. It was shown for the first time that the reaction intermediates with B = dmbpy can be detected after photoirradiation of electrosprayed charged droplets at the spray needle of the electrospray mass spectrometer. The electrospray technique, combined with use of a flow-through photoreaction cell or with direct photoirradiation of electrosprayed charged droplets, was demonstrated to be a powerful tool for the study of photosubstitution and for the detection of reaction intermediates.

Electrospray mass spectrometry (ES-MS) has recently been shown to be a powerful tool for measuring the molecular masses of nonvolatile, thermally unstable compounds.[1–7] The soft ionization of ES-MS yields a simple mass pattern, which allows determination of molecular masses accurately with high sensitivity. The technique has been used successfully for studies of biomolecules such as proteins and nucleic acids.[3–7] The method has also been shown to be useful for identification of inorganic metal complexes.[8–10] We have recently developed an on-line mass spectrometry system in which a photoreaction cell is attached to an electrospray interface. It was first applied to mass analysis of photoproducts of $Ru(bpy)_3^{2+}$ (bpy = 2,2′-bipyridine) and $Ru(bpz)_3^{2+}$ (bpz = 2,2′-bipyrazine).[11]

Scheme 1

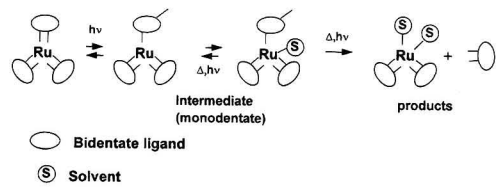

For characterization of reactions and determination of reaction pathways, it is important to trap reaction intermediates and identify them; on-line ES-MS is particularly useful for identification of unstable reaction products or short-lived intermediates. UV–vis and NMR spectroscopy, as well as separation by HPLC, have been used frequently for identification of intermediates. To test the usefulness of the on-line ES-MS method for such objectives, we examined the photosubstitution of a metal complex, one of the fundamental reactions of photoexcited metal complexes.[12]

In thermal and photo ligand substitution of a metal complex with bidentate ligands, the substitution is considered to proceed stepwise (Scheme 1), and thus an intermediate with an η^1

† Department of Applied Chemistry, Osaka University.
‡ Laboratory of Chemistry, Kagawa Nutrition University.
§ Department of Physics, Osaka University.

(1) Yamashita, M.; Fenn, J. B. *J. Phys. Chem.* **1984**, *88*, 4451–4459.
(2) Yamashita, M.; Fenn, J. B. *J. Phys. Chem.* **1984**, *88*, 4471–4475.
(3) Whitehouse, C. M.; Dreyer, R. N.; Yamashita, M.; Fenn, J. B. *Anal. Chem.* **1985**, *57*, 675–679.
(4) Fenn, J. B.; Mann, M.; Meng, C. K.; Wong, S. K.; Whitehouse, C. M. *Science* **1989**, *246*, 64–71.
(5) Fenn, J. B.; Mann, M.; Meng, C. K.; Wong, S. K. *Mass Spectrom. Rev.* **1990**, *9*, 37–70.
(6) Smith, R. D.; Loo, J. A.; Edmonds, C. G.; Barinaga, C. J.; Udseth, H. R. *Anal. Chem.* **1990**, *62*, 882–899.
(7) Mann, M. *Org. Mass Spectrom.* **1990**, *25*, 575–587.
(8) (a) Katta, V.; Chowdhury, S. K.; Chait, B. T. *J. Am. Chem. Soc.* **1990**, *112*, 5348–5349. (b) Blades, A. T.; Jayaweera, P.; Ikonomou, M. G.; Kebarle, P. *Int. J. Mass Spectrom. Ion Processes* **1990**, *101*, 325–336. (c) Blades, A. T.; Jayaweera, P.; Ikonomou, M. G.; Kebarle, P. *Int. J. Mass Spectrom. Ion Processes* **1990**, *102*, 251–267.
(9) Van Berkel, G. J.; McLuckey, S. A.; Glish, G. L. *Anal. Chem.* **1991**, *63*, 1098–1109.
(10) Arakawa, R.; Matsuo, T.; Ito, H.; Katakuse, I.; Nozaki, K.; Ohno, T.; Haga, M. *Org. Mass Spectrom.* **1994**, *29*, 289–294.
(11) Arakawa, R.; Jian, L.; Yoshimura, A.; Nozaki, K.; Ohno, T.; Doe, H.; Matsuo, T. *Inorg. Chem.* **1995**, *34*, 3874–3878.
(12) (a) Juris, A.; Balzani, V.; Barigelletti, F.; Campagna, S.; Belser, P.; Von Zelewsky, A. *Coord. Chem. Rev.* **1988**, *84*, 85–277. (b) Ford, P. C. *Coord. Chem. Rev.* **1982**, *44*, 61–82. (c) Hollebone, B. R.; Langford, C. H. *Coord. Chem. Rev.* **1981**, *39*, 181–224.

0003-2700/95/0367-4133$9.00/0

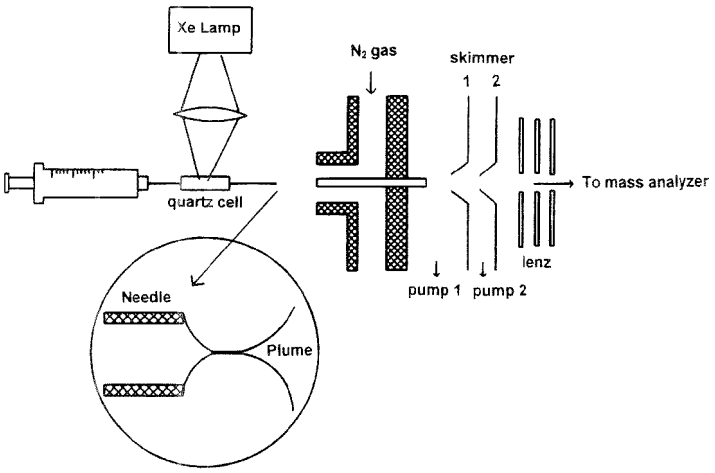

Figure 1. Schematics of electrospray mass spectrometry for on-line analysis of photochemical reactions. Two modes of photoirradiation (λ > 420 nm; a UV cutoff filter) were used: the cell mode, involving irradiation of the sample solution in a quartz cell, and the spray mode, involving irradiation of charged droplets distributed in the plume at the tip of needle.

bidentate ligand is proposed.[13] However, it has not yet been possible to demonstrate the existence of such an intermediate, at least for tris(bidentate)-type chelates. In the on-line ES-MS study of $Ru(bpy)_3^{2+}$ and $Ru(bpz)_3^{2+}$,[11] an attempt to detect an intermediate with an η^1 bidentate ligand failed after photoirradiation. However, we have recently been able to identify an intermediate with an η^1 bidentate ligand in the photosubstitution of $Ru(bpy)_2(dmbpy)^{2+}$ (dmbpy = 3,3′-dimethyl-2,2′-bipyridine) by ^1H NMR and HPLC separation.[14] We have also detected an intermediate in another complex, $Ru(bpy)_2(ampy)^{2+}$ (ampy = 2-(aminomethyl)-pyridine).[15] However, the details of the photoreaction have not yet been clarified.

In this paper, we report the use of on-line ES-MS with a flow-through photoreaction cell and direct photoirradiation of electrosprayed droplets to obtain direct evidence of intermediate formation for the two complexes mentioned above. Moreover, some mechanistic details of the photoreaction, such as the effects of solvent and intensity of irradiation, will be presented. Through this study, it is hoped that on-line electrospray mass spectrometry will be demonstrated to be a powerful tool for the study of photochemical reactions in solution.

EXPERIMENTAL SECTION

A laboratory-made ES interface was connected to a sector-type mass spectrometer (JEOL D300). As illustrated in Figure 1, a sample solution is sprayed from the tip of a needle by applying a voltage 3.5 kV higher than that of a counter electrode. The distance between the needle and the counter electrode was 1 cm. The counter electrode consists of a 12-cm-long stainless steel capillary tube (0.5 mm i.d.). A stream of heated N_2 gas (70 °C) was used to aid desolvation of sprayed charged droplets. The flow rate of the sample solution was 2 μL/min. The voltage of the second skimmer determines the translational energy of ions in the mass spectrometer. The ion translational energy was 2 keV. The voltages of the capillary electrode and the first skimmer were respectively 100 and 50 V higher than that of the second skimmer.

The sample solution was irradiated with a high-pressure Xe lamp (150 W). The light spot, focused by a lens, was ~5 mm in diameter. A light shutter was mounted at the exit of the lamp to control photoirradiation. A UV cutoff filter was used. Two different modes of irradiation (λ > 420 nm) were used for photoreaction: cell mode and spray mode irradiation. For the cell mode irradiation, a cylindrical quartz cell (1 mm i.d., 2 mm o.d.) was installed in the middle of the needle (Figure 1). It takes about 2 min for the flowing sample to pass across the irradiated area in the cell and about 40 s for it to arrive at the tip of needle for spraying; therefore, photoproducts with lifetimes of more than a few minutes can be detected by ES mass analysis using the cell mode irradiation.

Under normal circumstances, a Taylor cone and plume with charged droplets will form at the tip of the electrospray needle, as illustrated in Figure 1. The spray irradiation was carried out 3 mm from the tip; i.e., the charged droplets were irradiated in the plume state and immediately injected into the mass spectrometer. Therefore, photoproducts with lifetimes as short as several milliseconds could be detected. However, the product yield is expected to be lower for the spray mode than for the cell mode because of a much shorter irradiation time.

$Ru(bpy)_2B(ClO_4)_2$ (B = dmbpy and ampy) complexes were prepared by methods described in the literature.[14] For measurement of ES mass spectra, samples were dissolved in freshly distilled acetonitrile or pyridine, and nothing was added to promote ionization. The concentrations of samples were kept at ~0.1 mM.

(13) (a) Basolo, F.; Pearson, R. G. *Mechanisms of Inorganic Reactions*, 2nd ed.; Wiley: New York, 1967. (b) Durham, B.; Caspar, J. V.; Nagle, J. K.; Meyer, T. J. *J. Am. Chem. Soc.* **1982**, *104*, 4803–4810. (c) Kalyanasundaram, K. *J. Phys. Chem.* **1986**, *90*, 2285–2287. (d) Zhang, S.; Zang, V.; Dobson, G. R.; Van Eldik, R. *Inorg. Chem.* **1991**, *30*, 355–356.

(14) Tachiyashiki, S.; Ikezawa, H.; Mizumachi, K. *Inorg. Chem.* **1994**, *33*, 623–625.

(15) Tachiyashiki, S. 10th International Symposium on Photochemistry and Photophysics of Coordination Compounds, Sendai, Japan, 1993; Abstr. A12.

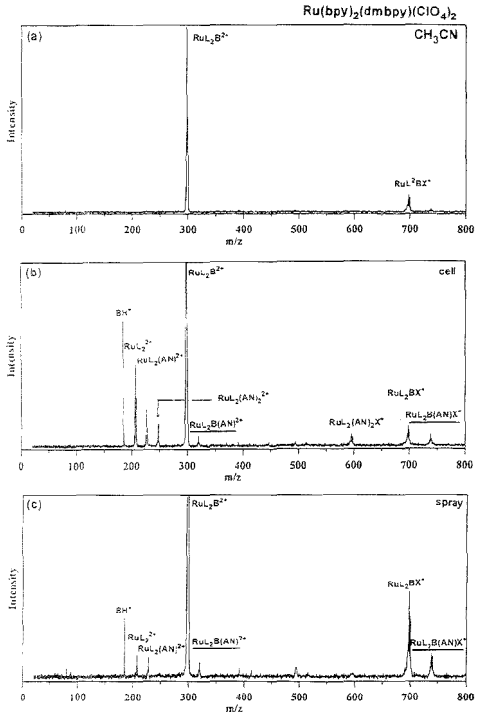

Figure 2. Positive ion ES mass spectra of $Ru(bpy)_2(dmbpy)(ClO_4)_2$ (bpy = 2,2′-bipyridine; dmbpy = 3,3′-dimethyl-2,2′-bipyridine) in acetonitrile (0.1 mM) obtained(a) without irradiation, (b) with cell irradiation, and (c) with spray irradiation ($\lambda > 420$ nm). L is bpy, B is dmbpy, AN is acetonitrile, and X is ClO_4^-. The underlined ions represent intermediates with a monodentate B ligand. The peaks given by nominal *m/z* values are unknown peaks.

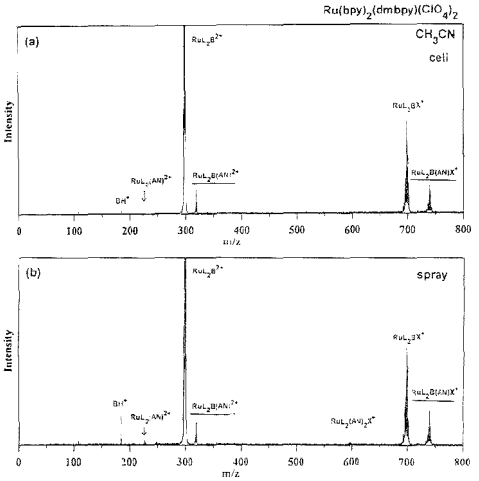

Figure 3. ES mass spectra of $Ru(bpy)_2(dmbpy)(ClO_4)_2$ in acetonitrile (0.1 mM) obtained in the dark (without room light) (a) with cell irradiation, whose effective light intensity was reduced about the same as that used for the spray irradiation, and (b) with spray irradiation.

RESULTS AND DISCUSSION

I. $[Ru(bpy)_2(dmbpy)](ClO_4)_2$. Figure 2a shows an ES mass spectrum of the complex in acetonitrile solution without photoirradiation. The spectrum is simple, showing only two peaks of RuL_2B^{2+} and RuL_2BX^+, where L, B, and X represent bpy, dmbpy, and ClO_4^-, respectively. Photoirradiation of the complex in the reaction cell (the cell mode) by visible light (>420 nm) promoted photosubstitution and resulted in the on-line ES mass spectrum shown in Figure 2b. The photoproducts were divalent $RuL_2(AN)_n^{2+}$ (AN = acetonitrile, $n = 0-2$), monovalent $RuL_2(AN)_2X^+$, and $dmbpyH^+$, the protonated dmbpy liberated from the complex. $RuL_2B(AN)^{2+}$ and $RuL_2B(AN)X^+$ were also observed; they must be reaction intermediates with a monodentate B ligand since an AN molecule is expected to coordinate to Ru in these species. Such a signal was not detected in the ES mass spectra obtained after photoreaction of $Ru(bpy)_3^{2+}$ and $Ru(bpz)_3^{2+}$.[11]

Among the signals of $RuL_2(AN)_n^{2+}$ ($n = 0-2$) in Figure 2b, the intensities of RuL_2^{2+} and $RuL_2(AN)^{2+}$ were larger than that of $RuL_2(AN)_2^{2+}$. This must be due to a facile dissociation of acetonitrile molecules from $RuL_2(AN)_2^{2+}$ by collision-induced dissociation (CID).[8,11] The relative intensity of RuL_2^{2+} increased rapidly as the collision energy was raised from 50 to 75 eV. The monovalent $RuL_2(AN)_2X^+$, a six-coordinate ion associated with a ClO_4^- anion, did not yield signals of its four- or five-coordinate species in the mass spectrum, as were detected with the divalent $RuL_2(AN)_2^{2+}$. The ClO_4^- in the monovalent ion probably protected the weakly coordinating acetonitrile molecules from CID.

The first observation of photoproducts induced by irradiation of the complex at the plume in the spray mode is shown in Figure 2c. The photoreaction products generated by the spray mode were quite similar to those seen by the cell mode, although the photoreaction environments were different—microscopic charged droplets versus ordinary solution. However, the intermediates of monodentate dmbpy, $RuL_2B(AN)^{2+}$ and $RuL_2B(AN)X^+$, were clearly observed. The effective light intensity per unit time for spray irradiation is about 10^{-5} that for cell irradiation; the flow rate of the complex ions is 10 m/s for the spray and 10^{-4} m/s for the cell irradiation. The difference between the photoreactions taking place in cell irradiation and in spray irradiation was studied in detail by an additional experiment (without room light) in which the light intensity per unit time for cell irradiation was equal to that used for spray irradiation. Under this condition, there was little secondary photolysis of the intermediates for cell irradiation (Figure 3). The spectrum for cell irradiation was quite similar to that for spray irradiation. It turned out that the intermediate with the monodentate ligand was a primary product in the photoreactions for both cell and spray irradiation. No apparent difference in the reaction environments was observed for the present system. It is shown in Figure 2c that the room light must promote the photosubstituted products. The rate of thermal rechelation of the monodentate B = dmbpy in the intermediate seems to be much slower than that of B = byp or bpz, so that the intermediate could be detected after photoirradiation. The monodentate dmbpy has steric hindrance between the 3 and 3′ methyl groups, which may hinder the rechelation.

In spray irradiation, one would expect possible complication arising from the photodissociation or photoreaction of the gas phase ions in addition to the photoreaction taking place in the

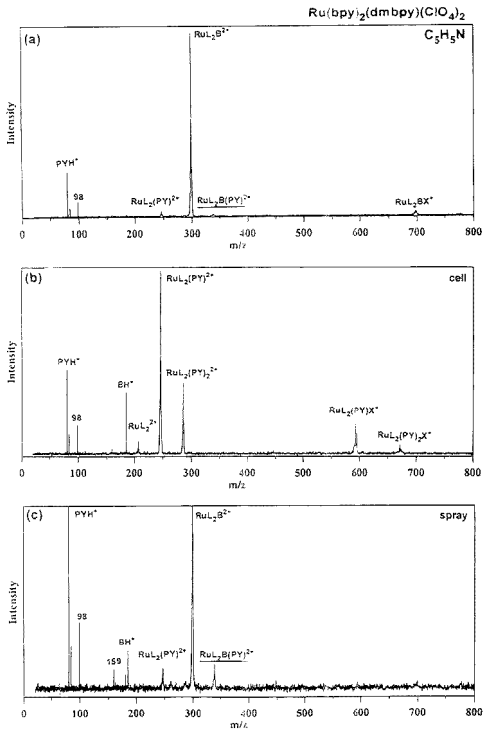

Figure 4. ES mass spectra of $Ru(bpy)_2(dmbpy)(ClO_4)_2$ in pyridine (0.1 mM) (a) without irradiation, (b) with cell irradiation, and (c) with spray irradiation.

droplet.[16] The photodissociation product of the gas phase ions, such as dmbpy-released ion $Ru(bpy)_2^{2+}$, is generated from $Ru(bpy)_2(dmbpy)^{2+}$ ion by a two-step process via the five-coordinate intermediate. On the other hand, for photoreaction in the droplet, $Ru(bpy)_2^{2+}$ is generated from CID of $Ru(bpy)_2(AN)_2^{2+}$, which is formed via six-coordinate intermediate $Ru(bpy)_2(dmbpy)(AN)^{2+}$. Since the lifetime will be far shorter for the former intermediate than for the latter, the production yield of $Ru(bpy)_2^{2+}$ in the gas phase photodissociation is much lower than that in the droplet reaction. Similarly, the production of the monodentate intermediate $Ru(bpy)_2(dmbpy)(AN)^{2+}$ is the two-step reaction involving solvent addition in both the gas and droplet phases. However, the concentration of the solvent is extremely smaller in the gas phase than in droplets. Finally, in the present system, the photoreaction of the gas phase ions is negligible compared with the photoreaction that takes place in droplets.

The mass spectra of the complex in pyridine (PY) are shown in Figure 4. Even without irradiation, weak signals of the photosubstitution product $RuL_2(PY)_2^{2+}$ and its intermediate $RuL_2B(PY)^{2+}$ were observed (Figure 4a). These must be caused by room light since they were not observed in the dark. When the cell irradiation mode, in which the light intensity is far higher than that for the room light, was used, the parent signal RuL_2B^{2+}, as well as the intermediate signal, disappeared completely (Figure 4b). Among the photoproducts, five-coordinate $RuL_2(PY)^{2+}$ ion gave the strongest signal intensity. This was probably due to the strength of the Ru–PY bond (stronger than the Ru–AN bond), which would prevent simultaneous rupture of the two Ru–PY bonds. Rather, it seems that one Ru–PY bond was broken by CID to produce the five-coordinate ion. The small amount of four-coordinate ion was probably formed from the five-coordinate ion.

A univalent ion, $RuL_2(PY)X^+$, with a coordinated solvent molecule was observed in the pyridine system. Such an ion was not observed in acetonitrile (Figure 2). Since the molecular size of PY is larger than that of AN, the ClO_4^- counterion may be able to protect one but not two PY groups from CID, resulting in a monosubstituted PY complex. The relative signal intensities of photoproduct ions with coordinated solvent molecules are different in acetonitrile and pyridine. The difference can be attributed to the sizes of the solvent molecules and their coordinating ability in relation to the protective effect of the counterions.

The photoreactivity of the complex was much greater in pyridine than in acetonitrile. This is because of the larger quantum yield of the substitution of monodentate dmbpy in the intermediate $RuL_2B(PY)^{2+}$ than in $RuL_2B(AN)^{2+}$.[17] Quantum yields for the formation of the intermediate in the two solvents were quite similar.[17] The reason that the intermediate could not be detected in the cell mode (Figure 4b) must be due to a facile photosubstitution of the intermediate of monodentate dmbpy. The weak light intensity would minimize the secondary photolysis of the intermediate. This might contribute to the detection of the intermediate by spray irradiation.

The preference for coordination of different solvent molecules was studied for $Ru(bpy)_2(dmbpy)(PF_6)_2$ in an acetonitrile/pyridine (1:1 v/v) mixture. Even without irradiation, we observed that the intermediate ions $RuL_2B(AN)^{2+}$ and $RuL_2B(PY)^{2+}$, as well as BH^+, protonated dmbpy liberated from the complex (Figure 5a). Formation of ions must be caused by room light since they were not observed in the dark (Figure 5b). A signal with m/z = 181 was assigned to $(PY)_2Na^+$; the Na^+ ion presumably came from a contamination. Using the cell irradiation mode, the parent ion RuL_2B^{2+} disappeared completely, and several divalent ions, $RuL_2(PY)_n^{2+}$ (n = 0–2), $RuL_2(AN)(PY)^{2+}$, and $RuL_2(AN)^{2+}$, and monovalent ions, $RuL_2(AN)(PY)X^+$ and $RuL_2(PY)_2X^+$, appeared (Figure 5c). Spray irradiation gave mono- and divalent intermediates with a monodentate dmbpy ligand (Figure 5d). The results showed that PY coordinates preferentially (relative to AN) to the RuL_2 moiety of the metal complex.

II. $[Ru(bpy)_2(ampy)](ClO_4)_2$. The photosubstitution intermediate RuL_2B^{2+} (B = ampy), with a monodentate ampy ligand, has been identified by using ^1H NMR in aqueous acidic solution.[15] The monodentate ampy ligand in the complex was not readily photosubstituted or thermally substituted; the intermediate could have a long lifetime in an acidic solution because protonation of ampy would prevent rechelation. In acetonitrile solution, however, no evidence has been obtained for the intermediate $RuL_2B(AN)^{2+}$ with B = ampy, despite the fact that such an intermediate has been observed for the complex with B = dmbpy (Figure 2).[14]

Figure 6a shows the ES mass spectra of the ampy complex without photoirradiation in acetonitrile solution. Figure 6b,c shows the spectra of the complex in the cell irradiation mode (λ > 420 nm) in acetonitrile and in trideuterated acetonitrile, respectively. The signals marked with a circle in Figure 6c were

(16) Suggested by the reviewers.

(17) Tachiyashiki, S.; Mizumachi, K. *Coord. Chem. Rev.* **1994**, *132*, 113–120.

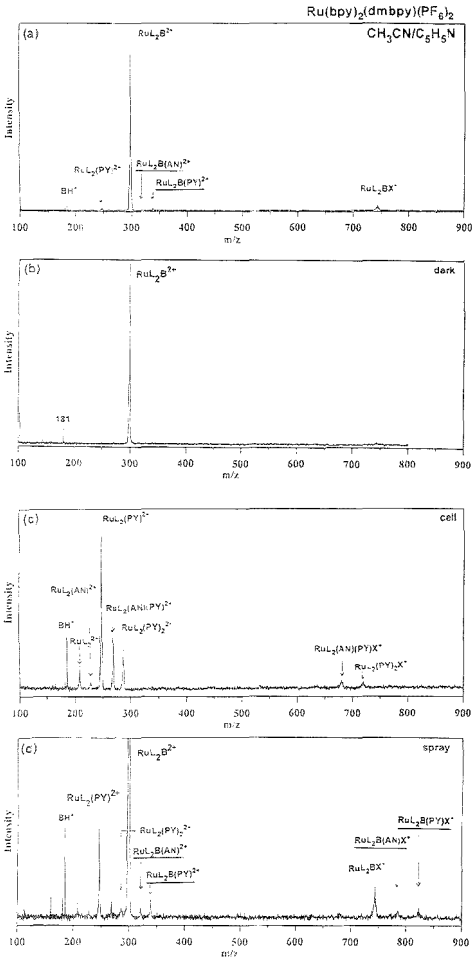

Figure 5. ES mass spectra of $Ru(bpy)_2(dmbpy)_2(PF_6)_2$ in acetonitrile/pyridine (1:1 v/v) (0.1 mM) (a) without irradiation, (b) in the dark, (c) with cell irradiation, and (d) with spray irradiation. A signal with m/z = 181 was assigned to $(PY)_2Na^+$.

identified as due to complexes with AN coordination, which all showed a 3 mass unit shifts from the respective signals in Figure 6b. The observed products were similar to those observed for $Ru(bpy)_2(dmbpy)(ClO_4)_2$. The intermediates with monodentate ampy were observed in the cell mode. In addition, new photoproducts $RuLB^{2+}$, $RuLB(AN)_2X^+$, and LH^+ were observed, which indicated that not only B but also L can be dissociated from the complex by photolysis, although the relative intensities of RuL_2^{2+} and $RuLB^{2+}$ indicated that the dissociation of L was a minor process. Such a process had not been identified in the previous UV–visible spectrophotometric study,[15] probably because the method was not sensitive enough and the intensity of the radiation may have been too weak for the reaction. Neither photoproducts nor monodentate intermediates for the ampy complex were detected in the spray irradiation.

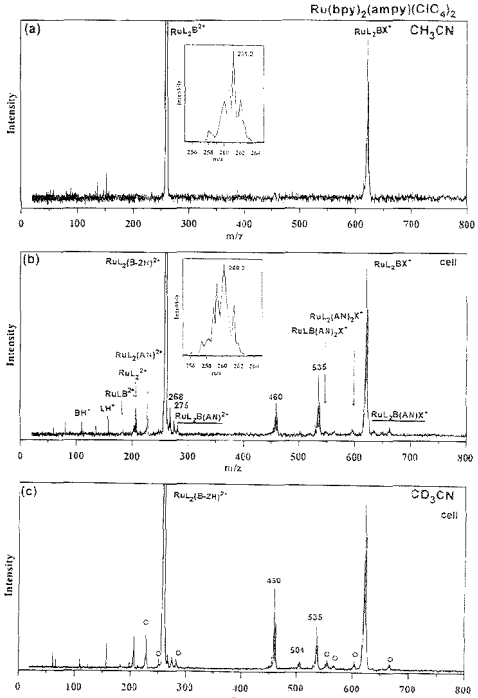

Figure 6. ES mass spectra of $Ru(bpy)_2(ampy)(ClO_4)_2$ in acetonitrile (0.1 mM) (a) without irradiation, (b) with cell irradiation in CH_3CN, and (c) in CD_3CN. The circles represent the peak shifts due to binding of acetonitrile. Unidentified peaks are shown with nominal m/z.

The results clearly indicate that ES mass spectrometry is a powerful tool for the study of photosubstitution of a mixed ligand complex.[18] It can easily tell us which ligand has been dissociated by photolysis. In Figure 6, signals with nominal m/z values are unidentified photoproducts. All of these products must contain no solvent molecules, since no m/z shifts were observed with spectra taken in deuterated acetonitrile (m/z = 460 and 535 are the most abundant isotope ratios in both spectra). Reducing the intensity of irradiation by a factor of 10 did not significantly change the spectra, but it increased the signal intensities of the intermediates. This is probably due to a decrease in secondary photolysis of the intermediates. The photolysis would connect the intermediate $RuL_2B(AN)^{2+}$ to five-coordinate RuL_2B^{2+}, which could go back to the parent complex by rechelation (Scheme 1).

Interestingly, we observed a mass shift of the base peak (the most abundant peak) near m/z = 260 in the spectra of $[Ru(bpy)_2(ampy)](ClO_4)_2$ (Figure 6). Without irradiation, the base peak had a nominal m/z = 261.2, corresponding to the parent ion RuL_2B^{2+}. The peak was shifted to m/z = 260.2 by irradiation in the cell mode. This shift must be caused by photoproduction of $RuL_2(B - 2H)^{2+}$ in the presence of oxygen in solution. There was no shift of the peak in the spectra of deaerated (N_2-purged) solutions when cell irradiation was used. The conventional

(18) Jones, W. E., Jr.; Smith, R. A.; Abramo, M. T.; Williams, M. D.; Van Houten, J. *Inorg. Chem.* **1989**, *28*, 2281–2285.

$$RuL_2(ampy)^{2+} \xrightarrow{O_2} RuL_2(ampy - 2H)^{2+} + H_2O$$

spectrophotometric study of the photolysis of the complex in acetonitrile in open air showed that the shift was due to the formation of a 2-(iminomethyl)pyridine complex, $Ru(bpy)_2(PY\text{-}CH{=}NH)^{2+}$.[19] Product analysis by column chromatography on SP-Sephadex (eluent, 0.3 M NaCl) showed the 2-(iminomethyl)-pyridine complex and an unidentified product with an absorption peak at 438 nm. The unidentified product is probably a 2-oximatopyridine complex, $Ru(bpy)_2(PY\text{-}CH{=}N{-}OH)^{2+}$, which correlates well with the unidentified mass signals of m/z = 268 ($Ru(bpy)_2(PY\text{-}CH{=}N{-}OH)^{2+}$) and 535 ($Ru(bpy)_2(PY\text{-}CH{=}N{-}O)^{+}$). These signals decreased in the spectrum obtained from the deaerated solution. The two other unidentified signals, m/z = 275 and 460, may be tentatively assigned to $Ru(bpy)_2(PY\text{-}CO{-}NO)^{2+}$ and $Ru(bpy)_2(PY\text{-}CN)(ClO_4)^{+}$, respectively. For the monovalent ion $Ru(bpy)_2(PY\text{-}CN)(ClO_4)^{+}$, which possesses a chlorine atom, the isotope mass distribution was in good agreement with the calculated ratios.

CONCLUSION

We have studied the photosubstitution of $Ru(bpy)_2B_2^{2+}$ (B = dmbpy and ampy) by on-line ES mass spectrometry in order to obtain direct evidence for intermediate formation and to have a better understanding of the photosubstitution reaction. We found that intermediates can be readily identified by this method and unequivocal evidence for the mechanism can be obtained. We also characterized the effect of solvent on the photoreaction and discovered a new reaction pathway for $Ru(bpy)_2(ampy)^{2+}$, the photoinduced oxidation of the complex.

The intermediates with monodentate dmbpy were detected by both cell and spray irradiation. However, we could not show an apparent difference in the photoproducts, although the photoreaction environment was different between solution and microscopic charged droplets. There was some difference in the extent of complete dissociation of a bidentate ligand. This is principally due to the change in the effective light intensity. On-line ES mass spectrometry was shown to be a powerful tool for the study of photochemical reactions, especially for the detection of reaction intermediates.

ACKNOWLEDGMENT

This research was financially supported by a grant-in-aid for Scientific Research (06640784) from the Ministry of Education, Science, and Culture of Japan. The authors are grateful to Prof. H. Doc for helpful discussions and to Mr. L. Jian for his assistance with ES mass spectroscopic measurements.

Received for review May 2, 1995. Accepted August 29, 1995.[⊗]

AC9504272

(19) Ridd, M. J.; Keene, F. R. *J. Am. Chem. Soc.* **1981**, *103*, 5733–5740.

[⊗] Abstract published in *Advance ACS Abstracts*, October 1, 1995.

Anal. Chem. **1995**, *67*, 4139–4144

Attomole Biomolecule Mass Analysis by Matrix-Assisted Laser Desorption/Ionization Fourier Transform Ion Cyclotron Resonance

Touradj Solouki, Jarrod A. Marto,‡ Forest M. White, Shengheng Guan,† and Alan G. Marshall*,†

Center for Interdisciplinary Magnetic Resonance, National High Magnetic Field Laboratory, 1800 East Paul Dirac Drive, Florida State University, Tallahassee, Florida 32310

Significantly improved sensitivity for analysis of biomolecules by MALDI FT-ICR mass spectrometry is achieved by (i) microscope-monitored sample deposition onto a small indentation on the probe tip and (ii) multiple remeasurement of ions from a single laser shot. A simple modification to the solids probe tip allows for microdeposition of a few amols of analyte onto small indentation spots previously aligned with the laser beam. Ion multiple remeasurement of the same ion packet enhances the signal-to-noise ratio and thus extends the achievable FT-ICR MS detection limit. We demonstrate that FT-ICR can be used to detect parent and structurally significant fragment ions of peptides and phospholipids at low amol amounts. Positive ion mass spectra for ~90 amol of a mixture of angiotensin II and bradykinin, ~40 amol of dipalmitoylglycerophosphatidylcholine, and ~8 amol of substance P constitute the lowest reported detection limits to date for FT-ICR mass analysis of MALDI-generated ions.

Matrix-assisted laser desorption/ionization (MALDI)[1] and electrospray ionization (ESI)[2] techniques have revolutionized mass analysis of biomolecules. MALDI-generated ions have been mass-analyzed by time-of-flight instruments typically at relatively low mass resolving power ($m/\Delta m$ < 1000, in which m is the ion mass and Δm is the mass spectral peak width at a specified fraction of peak maximum height), as well as with magnetic sector instruments and quadrupole ion traps.[3,4] MALDI with Fourier transform ion cyclotron resonance (FT-ICR) mass analysis[5–11] offers potentially ultrahigh mass resolving power, high mass accuracy, and multistage MS^n capabilities.[12–17] Ion axialization[18] provides for simultaneous realization of all of these advantages. Although several authors have addressed the limitations of high-mass and high-resolution MALDI FT-ICR MS,[9,16,19–22] MALDI FT-ICR sensitivity and detection limit have not been fully explored.

To date, the most successful mass analyses at low analyte concentration, e.g., $<10^{-15}$ mol, have employed other mass analyzers.[3,23,24] However, Marshall et al. determined an FT-ICR detection limit of ~177 singly-charged ions at 3.0 T in a cubic trap; the detection limit was defined for ions detected at 50% of the maximum possible ICR radius measured at a frequency of ~600 kHz and 1 s undamped single time-domain signal acquisition.[25] Recently, Bruce et al. employed a 7.0 T FT-ICR ESI mass spectrometer to detect a single bovine albumin ion; based on their results for an acquisition period of 1.28 s, the estimated minimum number of charges required for detection was 30.[26] Moreover, simultaneous detection of ions and neutrals produced by MALD near the ion formation threshold points to a neutral–ion ratio of ~10 000:1 in the laser plume.[27,28] Thus, FT-ICR detection of MALDI-generated ions from a few amols of sample should be possible.

†Also members of the Department of Chemistry, Florida State University.
‡ Department of Chemistry, The Ohio State University, Columbus, OH 43210.

(1) Karas, M.; Hillenkamp, F. *Anal. Chem.* **1988**, *60*, 2299–2301.
(2) Whitehouse, C. M.; Dreyer, R. N.; Yamashita, M.; Fenn, J. B. *Anal. Chem.* **1985**, *57*, 675–679.
(3) Strobel, F. H.; Solouki, T.; White, M. A.; Russell, D. H. *J. Am. Soc. Mass Spectrom.* **1991**, *2*, 91–94.
(4) Chambers, D. M.; Goeringer, D. E.; McLuckey, S. A.; Glish, G. L. *Anal. Chem.* **1993**, *65*, 14–20.
(5) Hettich, R.; Buchanan, M. V. *J. Am. Soc. Mass Spectrom.* **1991**, *2*, 402–412.
(6) Hettich, R. L.; Buchanan, M. V. *Int. J. Mass Spectrom. Ion Processes* **1991**, *111*, 365–380.
(7) Hettich, R. L.; Buchanan, M. V. *Int. J. Mass Spectrom. Ion Processes* **1991**, *111*, 365–380.
(8) Nuwaysir, L. M.; Wilkins, C. L. *Proc. SPIE–Appl. Spectrosc. Mater. Sci.* **1991**, *1437*, 112–123.
(9) Solouki, T.; Russell, D. H. *Proc. Natl. Acad. Sci. U.S.A.* **1992**, *89*, 5701–5704.
(10) Castoro, J. A.; Köster, C.; Wilkins, C. *Rapid Commun. Mass Spectrom.* **1992**, *6*, 239–241.
(11) Buchanan, M. V.; Hettich, R. L. *Anal. Chem.* **1993**, *65*, 245A–259A.
(12) Köster, C.; Castoro, J. A.; Wilkins, C. L. *J. Am. Chem. Soc.* **1992**, *114*, 7572–7574.
(13) McIver, R. T., Jr.; Li, Y.; Hunter, R. L. *Int. J. Mass Spectrom. Ion Processes* **1994**, *132*, L1–7.
(14) McIver, R. T., Jr.; Li, Y.; Hunter, R. L. *Proc. Natl. Acad. Sci. U.S.A.* **1994**, *91*, 4801.
(15) Solouki, T.; Gillig, K. J.; Russell, D. H. *Rapid Commun. Mass Spectrom.* **1994**, *8*, 26–31.
(16) Huang, Y.; Pasa-Tolic, L.; Guan, S.; Marshall, A. G. *Anal. Chem.* **1994**, *66*, 4385–4389.
(17) Marto, J. A.; White, F. M.; Seldomridge, S.; Marshall, A. G. *Anal. Chem.*, in press.
(18) Guan, S.; Kim, H. S.; Marshall, A. G.; Wahl, M. C.; Wood, T. D.; Xiang, X. *Chem. Rev.* **1994**, *94*, 2161–2182.
(19) Wood, T. D.; Schweikhard, L.; Marshall, A. G. *Anal. Chem.* **1992**, *64*, 1461–1469.
(20) Castoro, J. A.; Wilkins, C. L. *Anal. Chem.* **1993**, *65*, 2621–2627.
(21) Solouki, R.; Gillig, K. J.; Russell, D. H. *Anal. Chem.* **1994**, *66*, 1583–1587.
(22) Pastor, S. J.; Castoro, J. A.; Wilkins, C. L. *Anal. Chem.* **1995**, *67*, 379–384.
(23) Strupat, K.; Karas, M.; Hillenkamp, F. *Int. J. Mass Spectrom. Ion Processes* **1991**, *111*, 89–102.
(24) Jespersen, S.; Niessen, W. M. A.; Tjaden, U. R.; van der Greef, J.; Litborn, E.; Lindberg, U.; Roeraade, J. *Rapid Commun. Mass Spectrom.* **1994**, *8*, 581–584.
(25) Limbach, P. A.; Grosshans, P. B.; Marshall, A. G. *Anal. Chem.* **1993**, *65*, 135–140.
(26) Bruce, J. E.; Cheng, X.; Bakhtiar, R.; Wu, Q.; Hofstadler, S. A.; Anderson, G. A.; Smith, R. D. *J. Am. Chem. Soc.* **1994**, *116*, 7839–7847.
(27) Mowry, C. D.; Johnston, M. V. *Rapid Commun. Mass Spectrom.* **1993**, *7*, 569–575.
(28) Quist, A. P.; Huth-Fehre, T.; Sundqvist, B. U. R. *Rapid Commun. Mass Spectrom.* **1994**, *8*, 149–154.

0003-2700/95/0367-4139$9.00/0

Detectable mass spectrometric signals from low femtomole amounts of protein have been produced by Smith and co-workers by interfacing capillary electrophoresis to an FT-ICR instrument.[29] McLafferty et al. reported ESI FT-ICR results obtained from only 10^{-14} mol of sample introduced into the mass spectrometer with a commercial microvolume injector.[30]

Very recently, McIver and Li reported detection limits for a prototype external ion source MALDI FT-ICR instrument at 6.5 T for several polypeptides.[31] Typically 1–5 fmol of analyte was applied to the external sample probe, and time-domain data from several laser shots were summed to construct magnitude-mode mass spectra. Recently, Duncan and co-workers, by recovering peptides and proteins following MALDI, demonstrated that SDS–PAGE and radioimmunoassay may be performed on the recovered samples,[32] suggesting major potential improvement in MALDI detection sensitivity.

Here, we combine two methods to improve significantly the sensitivity of MALDI FT-ICR mass analysis of biomolecules: (a) sample deposition onto small indentations on the probe tip and (b) multiple remeasurement of ions from a single laser shot. First, in conventional MALDI experiments, nanomoles to picomoles of the analyte are deposited on the probe tip, whereas only amols of analyte are consumed for mass analysis. To reduce the amount of sample deposited, we constructed a probe tip with a series of small indentations, such that amols of sample could be placed on a spot <1 mm^2 in area. Second, in FT-ICR MS experiments, mass spectral peak area is proportional to the number of trapped ions,[25] thereby defining the minimum number of ions that can be detected from a single time-domain acquisition with a typical broadband detector preamplifier. However, if the initially detected ions are brought back near the ion trap central axis, either by collisional damping of the cyclotron motion alone or by combined use of azimuthal quadrupolar excitation and collisional damping, ions may be reexcited and redetected. If the ion initial population is not significantly depleted due to axial ejection and magnetron expansion, then repeating this process and summing the accumulated time-domain signals will result in an FT-ICR mass spectrum of increased signal-to-noise ratio, with a signal-to-noise ratio enhancement factor as large as $n^{1/2}$, where n is the number of summed time-domain data sets. Remeasurement of heavy ions trapped in an FT-ICR cell was first introduced by Williams et al.;[33] Speir et al. later used azimuthal quadrupolar excitation[18] to enhance remeasurement efficiency.[34] Recently, Laude and co-workers employed ion remeasurement techniques to observe real-time charge stripping of electrosprayed biomolecules.[35]

In this paper, we describe the modifications required to construct a MALDI sample probe for microsample deposition. We also discuss the experimental conditions (e.g., ion initial radius and excitation profiles) required to perform multiple FT-ICR excitation/detection events on a small number of trapped ions. Attomole detection of several MALDI-generated biomolecules by FT-ICR is demonstrated.

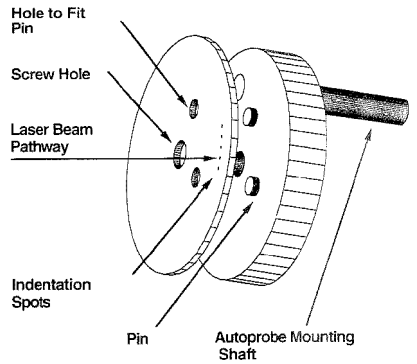

Figure 1. Modifications to a standard Extrel sample probe tip. The indentation spots are located at positions 1–5 and are 5° apart. Note the two guide pins and the corresponding holes on the indented plate, providing for alignment of the laser beam with the sample placed in the indentations (see text).

EXPERIMENTAL SECTION

Equipment. The MALDI FT-ICR mass spectra reported herein were acquired with an Extrel FTMS-2000 Fourier transform ion cyclotron resonance mass spectrometer (FTMS) equipped with a 3 T superconducting magnet, dual ion trap mass analyzer, automatic insertion probe, and Odyssey data system. Desorption/ionization was performed with a cartridge-type pulsed N_2 laser (Model VSL-33ND, Laser Science, Inc., Newton, MA) operated at a wavelength of 337.1 nm with a pulse width of 3 ns (laser power density of ~10^6 W cm^{-2}). The UV laser beam was directed through a quartz window on the analyzer side of the main vacuum chamber. The laser beam was focused to a spot size of ~ 200 μm × 200 μm on the probe tip by a 1 m focal length lens. A scanning electron microscope (environmental scanning electron microscope, Electroscan E-3) produced the sample probe surface micrographs.

Sample Probe Design. To reduce the amount of sample deposited on the stainless steel probe tip, we constructed a probe tip with a series of small indentations such that attomoles of analyte could be placed on a spot size of <1 mm^2. First, the stainless steel sample probe was mechanically polished to a mirror shine. The stainless steel surface was ground with a series of silicon carbide abrasive paper from 600–1200 grit at medium speed (300 rpm) on a Rotopol-2 Struers (Waterlake, OH) disk grinder, followed by a low-speed (150 rpm) polishing disk with a broadcloth covering. Finish polishing was performed by applying a polishing abrasive (6–1 μm diamond suspension) on a Buehler's Vibromet (Lakebluff, IL). A Vickers microhardness tester (Series 200, Wilson-Tukon, Canto, MA) confirmed that the indentations on the polished probe tip were aligned with the laser beam.

To mark the sample probe tip at the laser focal point, we applied a thin film of 4-nitroaniline to the probe tip, and several laser shots then removed the organic layer at different probe angular positions; these laser spots were identified and marked under the diamond-tipped microhardness tester with a 1000 kg load. The probe tip and indentation marks (~100 μm deep and ~5 × 10^{-3} mm^2 area) are shown schematically in Figure 1;

(29) Smith, R. D.; Wahl, J. H.; Goodlett, D. R.; Hofstadler, S. A. *Anal. Chem.* **1993**, *65*, 574A–584A.
(30) Kelleher, N. L.; Senko, M. W.; Little, D. P.; O'Connor, P. B.; McLafferty, F. W. *J. Am. Soc. Mass Spectrom.* **1995**, *6*, 220–221.
(31) Li, Y.; McIver, R. T., Jr. *Rapid Commun. Mass Spectrom.* **1994**, *8*, 743–749.
(32) Cerpa-Poljak, A.; Jenkins, A.; Duncan, M. W. *Rapid Commun. Mass Spectrom.* **1995**, *9*, 233–239.
(33) Williams, E. R.; Henry, K. D.; McLafferty, F. W. *J. Am. Chem. Soc.* **1990**, *112*, 6157–6162.
(34) Speir, J. P.; Gorman, G. S.; Pitsenberger, C. C.; Turner, C. A.; Wang, P. P.; Amster, I. J. *Anal. Chem.* **1993**, *65*, 1746–1752.
(35) Guan, Z.; Drader, J. J.; Campbell, V. L.; Laude, D. A. *Anal. Chem.* **1995**, *67*, 1453–1458.

typically, four indentation spots were required to completely mark the laser spot (laser spot size is ~200 μm × 200 μm). Two pins locked the angular position of the probe tip onto Extrel's standard solids autoprobe (Figure 1). Results were highly reproducible from one marked spot to another, confirming the accuracy of the laser alignment and spot placement (see Figure 4 and discussion of Figure 5 below).

Sample Preparation. Polypeptide (angiotensin II, bradykinin, and substance P) and phospholipid samples were purchased from Sigma Chemical Co. (St. Louis, MO) and used without further purification. A 1 M stock solution of 2,5-dihydroxybenzoic acid (DHB) matrix was prepared fresh daily in methanol acidified with 0.1% (v/v) trifluoroacetic acid (TFA). A 1 M stock solution of fructose (used for analysis of polypeptides) was prepared by dissolving fructose in distilled water. The analyte samples were weighed on a Mettler Toledo (Fisher Scientific, Pittsburgh, PA) high-resolution analytical balance to an accuracy of ~0.1 mg. Eppendorf centrifuge tubes (Fisher Scientific) prevented loss of analyte to the sample vials and reduced alkali metal contamination (e.g., sodium and potassium salts). To eliminate sample probe contamination from previous runs, we employed several acetone, alcohol, and water washes as well as sample probe sonication. Oxford BenchMate (Fisher Scientific) adjustable pipetters and Hamilton microliter (Fisher Scientific) syringes were used for sample dilution and sample delivery. Typically, <1 μL of diluted sample solution containing a few attomoles of analyte was applied onto the stainless steel sample probe tip on a previously marked spot. The sample probe was air-dried and inserted into the mass spectrometer for mass analysis. MALDI FT-ICR mass spectra were obtained at a typical matrix-to-analyte ratio of ~10^9:1.

Specifically, for the peptide mixture, ~0.8 mg samples of each polypeptide (angiotensin II and bradykinin) were dissolved in 1 mL of ethanol acidified with 0.1% TFA (solution A, 7.63×10^{-4} M solution of angiotensin II); a 5 μL aliquot from solution A was diluted to a total volume of 1 mL with ethanol (0.1% TFA, e.g., 3.81×10^{-6} M angiotensin II, solution B). Next, a 5 μL aliquot of the diluted B solution was further diluted to a total volume of 1 mL with ethanol (solution C, 1.91×10^{-8} M angiotensin II). Finally, a 5 μL aliquot from solution C was further diluted to 1 mL, to yield a 9.54×10^{-11} M solution of angiotensin II (solution D). Fifty microliters of 1 M DHB (acidified with 0.1% TFA) and 5 μL of 1 M fructose (dissolved in distilled water) were added to the final solution (solution D) to yield a final matrix-to-fructose-to-analyte ratio of 5×10^8:5×10^7:1. A 1 μL aliquot (containing ~90 amols of each polypeptide) of the final solution was applied by microsyringe onto an indentation in the probe tip in a stepwise manner; i.e., 0.1 μL of sample was added in each step, and after the sample was allowed to dry, an additional 0.1 μL was added until all of the 1 μL of solution was deposited on the probe tip.

The phospholipid sample was prepared by diluting 1 μL of 1 mM lipid solution to a total volume of 1 mL with 1 M DHB (acidified with 0.1% TFA). One microliter of this solution was again diluted to 1 mL with 1 M DHB (acidified with 0.1% TFA) to give a final matrix-to-analyte ratio of 1 × 10^9:1 and a lipid concentration of 1 fmol/μL. A 0.04 μL aliquot (containing ~40 amol of phospholipid) was applied by microsyringe onto an indentation in the probe tip. For the spectra shown in Figure 5, six sample deposits, each ~1 mm in diameter and centered on a spot of radius ~7 mm, were placed at well-spaced positions on the smooth probe tip.

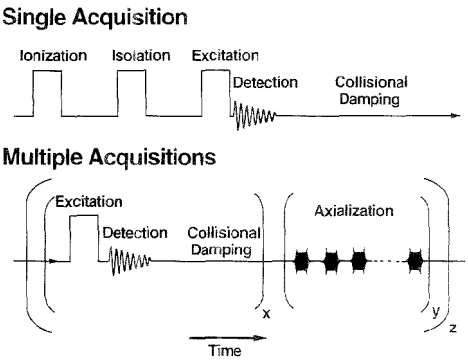

Figure 2. Experimental event sequences for single (top) and multiple (bottom) acquisitions. The number of detection events (x) and number of broadband azimuthal quadrupolar low-amplitude excitation events (y) vary from one experiment to the next (see text).

The substance P sample was prepared as for angiotensin II (Figure 3), and the solution was diluted to the desired level (8 amol/μL). A 1.0 μL aliquot (containing ~8 amol of substance P) was applied by microsyringe onto an indentation in the probe tip.

FT-ICR Experimental Event Sequence. All of the MALDI FT-ICR experiments were carried out in the source side of a dual cubic ion trap. High kinetic energy positive ions were decelerated by biasing the sample probe, source trap plate, and conductance limit plate during the laser desorption event (60–150 μs) to 0.0, 0.0, and +9 V, respectively, for the peptide samples, and −4, 0, and +8 V for the phospholipid sample. The experimental event sequence is shown in Figure 2. The single (top) and multiple acquisition (bottom) segments of the event sequence are shown separately. Restoration of the source trap and conductance limit plates to +2 V occurred 60–150 μs after ions were transferred into the trap. The trapped ions were allowed to relax, in the presence of ~4×10^{-8} Torr argon, to the central trap axis for ~5 s. A Varian leak valve (Varian Associates, Walnut Creek, CA) was used to maintain a constant argon neutral background pressure in the source side of the dual ion trap mass analyzer. When necessary, unwanted background ions (such as matrix related ions) were ejected from the ion trap by use of stored waveform inverse Fourier transform (SWIFT) dipolar excitation. For example, phospholipid ions of $150 \leq m/z \leq 690$ and $900 \leq m/z \leq 1500$ were ejected by SWIFT dipolar excitation of amplitude ~25 $V_{(p-p)}$. Coherent ICR motion was excited by frequency sweep dipolar excitation, with the sweep rate and radio frequency amplitude optimized for each experiment. Representative mass spectra from a single laser shot and single data acquisition are shown as the top spectra in Figures 3, 5, and 6.

Following the initial detection event, damping of ICR motion was achieved by collisional damping only (Figure 5) or by combining collisional damping and axialization (Figures 3 and 6). For example, after every few remeasurements (denoted by the first brackets, subscripted by x in Figure 2), azimuthal quadrupolar excitation, consisting of a series of SWIFT waveforms covering the mass range of interest in the presence of collisional cooling (second brackets, subscripted by y in Figure 2), refocused the ions close to the center of the ICR cell. A home-built relay circuit was used to switch from dipolar excitation and detection modes

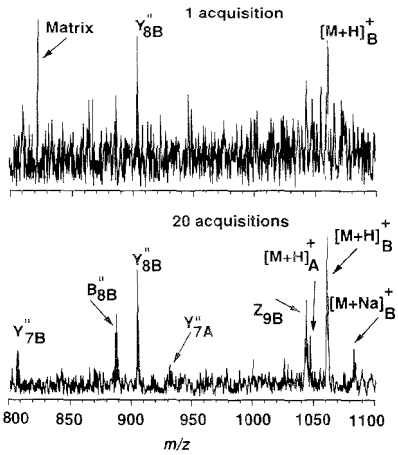

Figure 3. MALDI FT-ICR single laser shot mass spectra obtained from 90 amol of a mixture of bradykinin (FW 1060.2, RPPGFSPFR) and angiotensin II (FW 1047.6, DRVYIHPF) applied to the sample probe. Top, single time-domain data acquisition. Bottom, sum of time-domain data from 20 co-added remeasurements of the same ions. Fragment ions corresponding to angiotensin II or bradykinin are labeled "A" and "B", respectively.

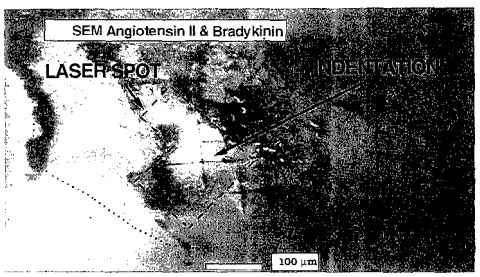

Figure 4. Scanning electron micrograph (20 keV, 130× magnification) of the stainless steel sample probe tip after 16 laser shots on the same spot. The sample applied onto the indentation consisted of 2,5-dihydroxybenzoic acid, fructose, angiotensin II, and bradykinin at mole ratio 10^9:10^8:1:1. The indentation and the laser spot are denoted by arrows. The laser spot is outlined by dashes, and the area over which sample was deposited is outlined by dotted lines.

to quadrupolar axialization mode.[34] Coherent ICR motion was excited by dipolar frequency sweep excitation (e.g., ~70 $V_{(p-p)}$, 1–500 kHz at a sweep rate of 700 Hz/μs for the peptide mixture or frequency sweep, ~55 $V_{(p-p)}$, 1–500 kHz at a sweep rate of 1000 Hz/μs for the phospholipid). Fourier transformation of the resulting time-domain signal (64*K*, 32*K*, and 128*K* time-domain data points for the peptide mixture, phospholipid, and substance P samples, respectively, at 1 MHz Nyquist bandwidth), without zero-filling or apodization, followed by magnitude calculation and frequency-to-mass conversion yielded an FT-ICR mass spectrum (Figures 3, 5, and 6).

RESULTS AND DISCUSSION

Here we report low attomole (total applied to the sample probe) detection of MALDI-generated phospholipid and polypeptide (*viz.*, angiotensin II, bradykinin, and substance P) ions. These particular

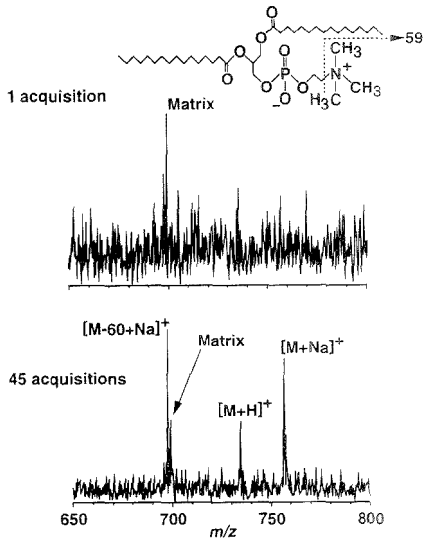

Figure 5. MALDI FT-ICR single laser shot mass spectra obtained from 40 amol of dipalmitoylglycerophosphatidylcholine applied to the sample probe (GPC = 733 Da). Top, single time-domain data acquisition. Bottom, sum of time-domain data from 45 co-added remeasurements of the same ions.

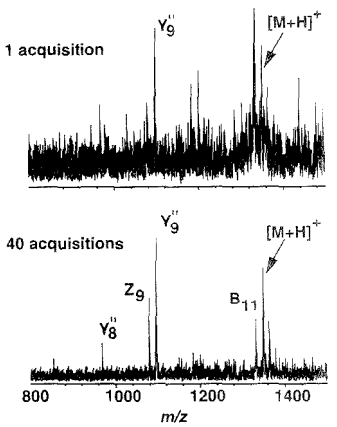

Figure 6. MALDI FT-ICR single laser shot mass spectra obtained from 8 amol of substance P (FW 1347.6, RPKPQQFFGLM) applied to the sample probe. Top, single time-domain data acquisition. Bottom, sum of time-domain data from 40 co-added remeasurements of the same ions. The sample solution contained 2,5-dihydoxybenzoic acid, fructose, and substance P at relative molar ratio 4×10^9:3×10^8:1.

polypeptides were chosen so that our results could be compared to previous mass spectral studies. For example, Russell et al. have reported detection of 100 amol of angiotensin II by MALDI tandem magnetic sector/reflectron time-of-flight mass spectrometry,[3] and a MALDI FT-ICR mass spectrum for 1 fmol of substance P was recently reported by McIver and Li.[31] Jespersen and co-workers have reported MALDI-TOF mass spectra from 2.5 amol of bradykinin through the use of "picolitre vials".[24] We also included

a phospholipid, since MALDI FT-ICR MS has recently proved capable of identifying phospholipid polar head group and fatty acid side chains.[17]

Positive Ion MALDI FT-ICR Mass Spectra for a 90 amol Mixture of Angiotensin II and Bradykinin. Figure 3 shows positive ion mass spectra for ~90 amol of a mixture of angiotensin II and bradykinin applied to the sample probe. The MALDI FT-ICR mass spectrum (Figure 3, top) obtained from a single time-domain data set exhibits a poor signal-to-noise ratio, e.g., signals from quasi-molecular ions of bradykinin (*m/z* 1060) and angiotensin II (*m/z* 1048) cannot be distinguished from background noise. To enhance remeasurement efficiency, we axialized the ions by azimuthal quadrupolar excitation in the presence of collisional cooling once ($y = 1$ in Figure 2) after 10 repeated time-domain acquisitions ($x = 10$), and then remeasured for 10 additional acquisitions ($z = 2$ in Figure 2) for a total of 20 remeasurements. Remeasurement and co-addition of the time-domain transients before Fourier transformation (again without zero-filling or apodization) improves the signal-to-noise ratio dramatically, and signals corresponding to quasi-molecular ions as well as structurally significant fragment ions are assigned (Figure 3, bottom).

It is worth noting that the fragmentation patterns observed for these species are consistent with previously reported MALDI-generated trapped ion results.[36,37] However, 90 amol for total sample consumption is orders of magnitude lower than any previously published values for MALDI FT-ICR. The present MALDI FT-ICR MS results compare favorably to those based on microchannel plate detection,[24] but with much higher mass resolving power (note ^{13}C isotopic mass resolution in Figures 3 and 6, even for relatively short data acquisition period and relatively high pressure of $\sim 4 \times 10^{-8}$ Torr).

Scanning Electron Micrograph of the Laser Spot. To ensure that the indentation marks containing the analyte samples were aligned with the laser beam, scanning electron micrograph (SEM) pictures of the laser spots were taken. Figure 4 shows an SEM image (130× magnification) of the laser spot (note 100 μm scale marker) on the sample probe containing angiotensin II, bradykinin, and matrix compounds (i.e., the same spot from which the MALDI FT-ICR mass spectra shown in Figure 3 were obtained). The indentation and the laser spot are shown with arrows. The laser spot (dashed area, showing where the organic layer has been removed by laser irradiation) is clearly well within the boundaries of the deposited sample (dotted line). Our present limitation in microsample deposition is inadequate control of the deposited droplet size. SEM images taken from several other laser spots confirmed the accuracy of the laser alignment and spot placement.

Dipalmitoylglycerophosphatidylcholine Positive Ion Mass Spectra. Figure 5 shows our current detection limit for dipalmitoylglycerophosphatidylcholine. In the single measurement spectrum shown in Figure 5 (top), the only recognizable species is a matrix cluster ion at *m/z* 699. After a 3.6 s collision period to allow for damping of the cyclotron motion, the same ion packet was again excited by frequency sweep excitation (~55 $V_{(p-p)}$ amplitude, 1−500 kHz, at a sweep rate of 1000 Hz/μs). Following dipolar detection, a 4.5 s collision period again allowed for damping of the cyclotron motion. The sequence of chirp excitation, 1 ms delay, dipolar detection, and 4.5 s relaxation period was repeated a total of 45 times (e.g., $x = 45, y = 0, z = 1$ in Figure 2, bottom); co-addition of the time-domain data yielded the bottom spectrum in Figure 5. After multiple remeasurement, several peaks of signal-to-noise ratio ≥ 3:1 are observed: protonated molecular ion (*m/z* 734), its sodium adduct (*m/z* 756), and the sodium adduct of the species corresponding to loss of trimethylamine (*m/z* 697, characteristic of the choline subclass of phospholipids). It is worth noting that the spectra are reasonably reproducible—spectra comparable to those shown in Figure 5 were obtained for four of the six sample spots applied to the probe.

Positive Ion MALDI FT-ICR Mass Spectra for 8 amol of Substance P. Figure 6 shows positive ion mass spectra for 8 amol of substance P applied to the sample probe. The trapping and excitation parameters for single acquisition were identical to those reported for Figure 3 (top). The mass spectrum from a single measurement (Figure 6, top) exhibits a poor signal-to-noise ratio. The MALDI FT-ICR mass spectrum from the sum of 40 remeasured time-domain data sets (with axialization after each acquisition, corresponding to $x = y = 1, z = 40$ in Figure 2, bottom) is shown in Figure 6 (bottom). For optimal comparison between single and multiple measurements, the excitation parameters were kept constant for all excitation events. Clearly, remeasurement improves the signal-to-noise ratio dramatically; several structurally significant fragment ions as well as the protonated molecular ion are readily observed in Figure 6 (bottom). *To date, 8 amol (total sample consumption) for MALDI FT-ICR represents the lowest reported detection limit for any FT-ICR experiment.* Moreover, for all of the spectra shown here, up to four laser shots yielded detectable signal from the same sample spot; ergo, the present detection limits could be lowered further and are limited mainly by our incomplete ability to control the size of the sample spot. The experimentally measured masses from all of the reported spectra were within 100 ppm of theoretical values, and mass resolution was in all cases adequate to distinguish carbon isotopic patterns.

LIMITATIONS, COMPARISONS, AND FUTURE DIRECTIONS

The choice of remeasurement procedure depends on the particular system under study. For phospholipids, we found that (dipolar) excitation to relatively large cyclotron radius during remeasurement resulted in significant fragmentation of the molecular ion. Thus, the observed relative abundances of these species changed during the course of many excitation/detection cycles. To avoid fragmentation, we therefore excited the phos-phospholipid ions to small cyclotron radius during each dipolar event; as a result, ion axialization was not necessary to obtain relatively high remeasurement efficiency. For bradykinin and angiotensin II, on the other hand, we found (Figure 3) that collisional cooling coupled with quadrupolar axialization was most suited to observe molecular ions (since angiotensin II easily fragments to yield Y''_7 ions). Finally, optimal remeasurement efficiency for detection of 8 amol of substance P required quadrupolar axialization after each detection event (Figure 6). At such an extremely low sample level, the relative abundance of various adduct species (e.g., $(M + Na)^+$, $(M + K)^+$) may also increase, because it is difficult to remove traces of alkali metal

(36) Lee, H.; Lubman, D. M. *Anal. Chem.* **1995**, *67*, 1400−1408.
(37) Jonscher, K.; Currie, G.; McCormack, A. L.; Yates, I. J. R. *Rapid Commun. Mass Spectrom.* **1993**, *7*, 20−26.
(38) Han, X.; Gross, R. W. *Proc. Natl. Acad. Sci. U.S.A.* **1994**, *91*, 10635−10639.

ions. In any case, the present results clearly establish the prospect of structural characterization of biomolecules at very low concentrations by MALDI FT-ICR mass spectrometry. The techniques reported here are simple, inexpensive, and reproducible.

The sensitivity of the present method compares favorably to previously reported MALDI/time-of-flight[3,24] and electrospray with other mass analyzers.[29,38-40] We are currently testing MALDI FT-ICR MS detection limit techniques on other classes of biomolecules, toward the ultimate goal of mass spectrometric analysis of intracellular components of a single biological cell.[41]

(39) Anderen, P. E.; Emmett, M. R.; Caprioli, R., M. *J. Am. Soc. Mass Spectrom.* **1994**, *5*, 605–613.
(40) Cody, R. B.; Tamura, J.; Finch, J. W.; Musselman, B. D. *J. Am. Soc. Mass Spectrom.* **1994**, *5*, 194–200.
(41) Yeung, E. S. *Acc. Chem. Res.* **1994**, *27*, 409–414.

ACKNOWLEDGMENT

We thank M. Ebrahimi for assistance in constructing the sample probe tip and for providing scanning electron micrographs. This work was supported by NSF (CHE-93-22824), NIH (GM-31683), and the National High Magnetic Field Laboratory at Florida State University.

Received for review June 19, 1995. Accepted August 28, 1995.[⊗]

AC950615S

[⊗] Abstract published in *Advance ACS Abstracts,* October 1, 1995.

Anal. Chem. 1995, *67*, 4145–4154

Comparison of Liquid Chromatography/Mass Spectrometry Interfaces for the Analysis of Polycyclic Aromatic Compounds

Joseph F. Anacleto,†,⊥ Louis Ramaley,† Frank M. Benoit,‡ Robert K. Boyd,*,§ and Michael A. Quilliam§

Department of Chemistry, Dalhousie University, Halifax, Nova Scotia, Canada B3H 4J3, Environmental Health Centre, Health Canada, Tunney's Pasture, Ottawa, Canada K1A 0L2, and Institute for Marine Biosciences, National Research Council of Canada, 1411 Oxford Street, Halifax, Nova Scotia, Canada B3H 3Z1

Three liquid chromatography/mass spectrometry interfaces were evaluated for their suitability for the analysis of complex mixtures of polycyclic aromatic compounds (PACs). Preliminary qualitative experiments, which used a carbon black extract as test material, confirmed that the moving belt interface is mechanically awkward, is limited with respect to the mobile phase composition which it can tolerate, and is not efficient in detecting the more volatile compounds. For these reasons it was not examined further, although it performed well for larger PACs and provided electron ionization (EI) mass spectra. The particle beam (PB) interface also provides EI spectra, but detection limits are poor (low nanogram range) and calibration curves are nonlinear. Only seven of the 16 PACs targeted for quantification in a complex coal tar reference material could be detected because of the difficulty the PB interface has with the analysis of compounds with very high or very low volatility. The heated pneumatic nebulizer (HPN) interface, which uses atmospheric pressure chemical ionization, produces both molecular ions ($M^{\cdot-}$) and protonated molecules (MH^+) of PACs. Detection limits were in the low picogram range, and calibration curves were linear. Using the HPN interface, 17 target PACs in the coal tar reference material could be detected and quantified within satisfactory agreement with certified values when perdeuterated internal standards were employed.

Polycyclic aromatic compounds (PACs) are potent environmental mutagens and carcinogens, formed from both natural (e.g., biosynthesis and natural combustion) and anthropogenic (e.g., high-temperature combustion) sources.[1] Complex mixtures of these ubiquitous compounds are commonly found in airborne particulates, tobacco smoke, fossil fuels, marine sediments, and food. In addition to health issues, the petroleum and synthetic crude oil industries are also concerned with the interferences that PACs produce in various upgrading processes. In particular, nitrogen-containing PACs are suspected of deactivating and poisoning catalysts during cracking and reforming processes. Plugging problems and reduced heat exchange also arise from the formation of high molecular weight polycyclic aromatic hydrocarbon (PAH) deposits in exchangers, transfer lines, and valves.[2]

The difficulties associated with the characterization of samples containing PAC fractions are due primarily to the large numbers of possible compounds and isomers (which increase with molecular weight). Even for routine qualitative analyses, therefore, methods combining good chromatographic resolving power with selective and sensitive detection are essential for meaningful results to be obtained. Although gas chromatography (GC) possesses high resolving power and can be coupled easily with mass spectrometry (GC/MS), its applicability is restricted by the limited volatility of PACs of higher molecular weights. In addition, the separation selectivity of GC for isomeric PACs is often disappointing. Quantitative analysis of complex matrices for target PACs is an even more demanding task, for which methodology is still being developed or improved. The activities of the U.S. National Institute of Standards and Technology (NIST) in this area have been summarized recently.[3]

Liquid chromatography (LC) has several advantages over GC. Less sample cleanup is required, thermally labile compounds are more easily analyzed since they are not exposed to excessive heat (though this is not a major consideration for PACs), derivatization is usually not necessary, and PACs with high molecular weights may be analyzed because volatility is not an issue for optical detection and is not such a stringent requirement for LC/MS analysis. LC is also an inherently better quantitative method because of the injection volume precision available with fixed loop injectors compared with that for syringe injections with GC. The high chromatographic efficiency available from capillary GC, however, is not currently available from conventional LC. Thus, LC chromatographic peaks are more likely to contain unresolved components, which increases the need for more selective detection methods, such as mass spectrometry. The lower chromatographic efficiency of LC is offset to some degree by the higher separation selectivity made possible through manipulation of the composition of both stationary and mobile phases, exemplified[3-5] by the LC

† Department of Chemistry, Dalhousie University.
‡ Environmental Health Centre, Health Canada.
§ Institute for Marine Biosciences, NRCC.
⊥ Present address: SCIEX, 71 Four Valley Dr., Concord, ON, Canada L4K 4V8.

(1) Lee, M. L.; Novotny, M. B.; Bartle, K. D. *Analytical Chemistry of Polycyclic Aromatic Compounds*; Academic Press: New York, 1981.
(2) Sullivan, R. F.; Boduszynski, M. M.; Fetzer, J. C. *Energy Fuels* **1989**, *3*, 603–612.
(3) Wise, S. A.; Schantz, M. M.; Benner, B. A., Jr.; Parris, R. M.; Rebbert, R. E.; Sander, L. C.; Koster, B. J.; Chesler, S. N.; May, W. E. *Fresenius J. Anal. Chem.* **1993**, *345*, 325–329.
(4) Sim, P. G.; Boyd, R. K.; Gershey, R. M.; Guevremont, R.; Jamieson, W. D.; Quilliam, M. A.; Gergely, R. J. *Biomed. Environ. Mass Spectrom.* **1987**, *14*, 375–381.

separation of some PAC isomers which are difficult or impossible to separate by GC.

The main obstacle to routine analytical applications of LC coupled directly to MS (LC/MS) has been the unavailability of rugged and reliable LC/MS interfaces, and this has also been true in the special case of PAC analysis. We have employed the moving belt (MB) interface previously for the analysis of PACs in marine sediments[4,5] and for qualitative characterization of high molecular weight PACs (MW up to 580) in a sample from a coal tar dump site.[6] Severe limitations on the mobile phase composition and flow rates were encountered. In general, solvent gradients were restricted to a low aqueous content and/or low flow rates to ensure that almost all the mobile phase was evaporated before the belt entered the ion source.

This paper describes a comparison of the MB, particle beam (PB), and heated pneumatic nebulizer (HPN) LC/MS interfaces for qualitative and quantitative analyses of PACs using reversed phase LC. Both the MB and PB interfaces were used with electron ionization (EI), while the HPN interface used atmospheric pressure chemical ionization (APCI). The capabilities of the three LC/MS interfaces to provide qualitative information on PACs with a wide range of molecular weights were tested using an extract of carbon black. In evaluations of the interfaces for quantitative analyses, detection limits and linear dynamic ranges were compared using PAC standards, and the concentrations of 17 PACs in the NIST certified coal tar reference material (SRM 1597) are reported for measurements using internal standardization with perdeuterated PAC standards. The objective of the work was to determine whether the advantages of LC/MS over GC/MS (ability to analyze larger PACs and greater separation selectivity) could be implemented in a rugged, reliable methodology with adequate sensitivity and dynamic range.

EXPERIMENTAL SECTION

Materials. HPLC grade acetonitrile and dichloromethane were obtained from BDH Chemicals (BDH Inc., Toronto, Canada) and were used without further purification. Distilled water was passed through a Milli-Q water purification system (Millipore Corp., Bedford, MA) before use. All solvent mixtures are specified as volume/volume ratios. PAC standards from Aldrich (Milwaukee, WI), Supelco (Oakville, Canada), and Anachemia (Montreal, Canada) were used without further purification.

A sample prepared by dichloromethane Soxhlet extraction of carbon black was received as a gift from Dr. J. Fetzer of Chevron Oil. This sample was redissolved in dichloromethane and filtered before use in LC experiments. A complex mixture of PACs from coal tar, standard reference material (SRM) 1597, and a standard solution of 16 priority pollutant PAHs in acetonitrile, SRM 1647, were purchased from the U.S. NIST (Gaithersburg, MD). A solution containing 21 perdeuterated PACs, DPAC-1, developed[7] by the Marine Analytical Chemistry Standards Program (MACSP) of the National Research Council (NRC) of Canada, was used as an internal standard solution for quantification experiments.

For purposes of quantification using internal standards, the DPAC-1 standard solution was spiked at four different levels into the NIST SRM 1647 PAH mixture, in ratios of 1:1, 1:5, 1:10, and 1:15 (v/v). The *exact* amounts of the two solutions mixed were determined by weighings using a 5-place digital balance. The DPAC-1 solution was designed to have *ratios* of analyte concentrations similar to those found in environmental samples,[7] but all 16 analytes in the SRM 1647 solution are at roughly the same concentration. The four spike ratios were therefore chosen to ensure that the concentration ratio of each native and perdeuterated PAH pair was approximately 1:1 in at least one of the mixed solutions. The DPAC-1 internal standard solution was also spiked into the NIST SRM 1597 coal tar mixture in a ratio of 3:1 (v/v). This spike ratio ensured that most of the analyte/internal standard concentration ratios fell within the ranges covered by the DPAC-1/SRM 1647 solutions.

Safety. Since many polycyclic aromatic compounds are mutagenic and carcinogenic, they must be handled with care. Acetonitrile and dichloromethane are toxic, volatile solvents that should be handled in a fume hood. All of these substances are harmful if swallowed, inhaled, or absorbed through the skin.

Liquid Chromatography/Mass Spectrometry. All analyses were performed using a 25 cm × 2.1 mm i.d. column packed with 5 μm Vydac 201TP octadecylsilica (Separations Group, Hesperia, CA) and an HP 1090M chromatograph (Hewlett-Packard, Palo Alto, CA) equipped with a variable volume injector/autosampler, a DR5 ternary solvent delivery system, a built-in diode array detector, and an HP7994A data system.

A mobile phase flow rate of 0.2 mL min^{-1} was used. Separations were performed with three different gradient programs: (A) Starting with 100% acetonitrile and held for 15 min, and then linearly programmed to 100% dichloromethane over 40 min and held for a further 15 min. This binary gradient was used in early work on the MB interface; it sacrificed chromatographic resolution of the early-eluting PACs but provided good resolution of the higher molecular weight components without excessive retention times and avoided the use of water, which proved troublesome for the routine use of the MB interface using gradient elution. (B) Starting with 40:60 water/acetonitrile, linearly programmed to 100% acetonitrile over 30 min, held 5 min, and then linearly programmed over 40 min to 100% dichloromethane, with a subsequent 25 min hold prior to recycling the column. This ternary gradient was used for the analysis of the carbon black extract using the PB and HNP interfaces. (C) Starting with 40:60 water/acetonitrile, linearly programmed to 100% acetonitrile over 30 min, held for an additional 30 min before being programmed back to the initial conditions over 5 min. This binary gradient was used for the coal tar SRM with the PB and HNP interfaces.

The MB interface experiments were conducted using a VG Organic 20-250 quadrupole mass spectrometer (Fisons Instruments, Altrincham, U.K.) equipped with a VG MB LC/MS interface. A VG spray deposition device was used to deposit the LC effluent on to the moving polyimide belt while simultaneously evaporating some of the mobile phase. The belt speed was maintained at 1.6 cm/s, and a post-ion source isopropyl alcohol belt wash was employed to avoid memory effects. The electron ionization source was operated at 250 °C, and the belt heater at the tip of the interface, which protrudes into the ion source, was operated with a supply voltage of 0.8 V (belt surface temperature unknown). By adjustment of the intermediate pumping stages, the instrument could be operated at an indicated pressure reading

(5) Quilliam, M. A.; Sim, P. G. *J. Chromatogr. Sci.* **1988**, *26*, 160–167.
(6) Perreault, H.; Ramaley, L.; Sim, P. G.; Benoit, F. M. *Rapid Commun. Mass Spectrom.* **1991**, *5*, 604–610.
(7) Quilliam, M. A.; Hardstaff, W. R.; Anacleto, J. F.; LeBlanc, M. D.; Stergiopoulos, V.; Dick, K. L.; Bowser, M. T.; Curtis, J. M.; Embree, D. J.; Sim, P. G.; Boyd, R. K. *Fresenius J. Anal. Chem.* **1994**, *350*, 109–118.

of 1.5×10^{-5} Torr (read from the ion gauge located on the source housing). This corresponds to pressure conditions inside the EI source such that chemical ionization occurs to only a negligible extent. The nominal electron energy was 70 eV, with a trap current of 100 μA. A VG 11-250 data system was used for instrument control and for data acquisition and processing. Mass spectra were acquired over a range m/z 150–600 with a scan cycle time of 3 s.

LC/MS analyses with a PB interface were performed using a Hewlett-Packard instrument comprising a Model 59980A particle beam interface and a Model 5988A quadrupole mass spectrometer. A detailed description of this PB interface can be found elsewhere.[8,9] Ultrahigh purity helium (Liquid Carbonic, Scarborough, Canada) was used as the nebulizing gas at a flow rate of ~1.5 L/min. The temperature of the desolvation chamber was maintained at 45 °C. EI spectra were obtained using a nominal electron energy of 70 eV, with a source temperature of 250 °C. Mass spectra were acquired over a range of m/z 100–500, with a scan cycle time of 3 s. Selected ion recording experiments on the NIST-SRM/DPAC-1 quantitation solutions monitored a total of 24 ions in three acquisition periods (8 ions/period, 1 s total cycle time): first retention time period, 0–9.8 min; second period, 9.8–33.5 min; and the last period, 33.5–60 min.

LC/MS analyses with a HPN interface and APCI were performed using an API III triple quadrupole mass spectrometer (SCIEX, Concord, Canada) equipped with an atmospheric pressure ionization (API) source. A detailed description of the HPN interface can be found elsewhere.[10] The corona discharge electrode current was maintained at 3 μA, and high-purity air was used as the nebulizing gas at a flow rate of 1.2 L/min. Full scan mass spectra were acquired over a range of m/z 100–500, with total scan cycle times between 2 and 3 s. A Macintosh IIx computer was used for instrument control, data acquisition, and processing. Selected ion recording experiments on the mixed NIST-SRM/DPAC-1 quantitation solutions monitored a total of 48 ions ($M^{+\cdot}$ and MH^+) in six acquisition periods (8 ions/period, 1 s total cycle time): first period, 0–8.8 min; second period, 8.8–10.5 min; third period, 10.5–18 min; fourth period, 18–33.4 min; fifth period, 33.4–46 min; and the last period, 46–60 min.

RESULTS AND DISCUSSION

Qualitative Analysis. The objective of this part of the work was to compare the more common LC/MS interfaces with respect to their suitability for analysis of the PACs of higher molecular weight, which are not amenable to GC/MS. Carbon black is a suitable test sample in this context, since it has been shown[11] that high molecular weight PACs can be extracted from such materials. In our hands, the thermospray interface provided no useful information on PACs and was not investigated further. The electrospray method has been shown by Van Berkel et al.[12,13] to be capable of forming molecular radical cations of PACs, using either charge-transfer complex formation with a suitable electron acceptor or electrochemical oxidation. However, success was strongly dependent on a correct choice of solvent (generally dichloromethane with 0.1% trifluoroacetic acid[12,13]), which is incompatible with gradient elution to achieve efficient LC separations. Moreover, at least in our hands, as applied to both fullerene derivatives and PACs,[14] these electrospray techniques for PACs are neither sufficiently robust nor sensitive at present to provide a useful quantitative analytical method for environmental samples. Accordingly, only the MB, PB, and HPN interfaces were investigated further in the present work.

An early demonstration of LC/MS analysis of a liquefied coal product[15] used a MB interface to confirm identities of the LC peaks. A careful study of the effects of operating parameters on both the LC and MS performance[15] used PAC standards as the test compounds. Analyte volatility was shown[17] to have an effect on both the accuracy and the precision of LC/MS determinations of PACs using the MB interface. More recent work[4–6] from this laboratory has confirmed and extended these earlier findings. In particular, use of the MB interface to provide qualitative profiles of PACs with molecular weights up to 580 was demonstrated.[6] The problem of assigning compound identities to chromatographic peaks was faced[5] in the LC/MS analysis of a marine sediment for PACs. Even when a standard compound is found to provide a good retention time match, it is often difficult to eliminate the possibility that the unknown compound is another isomer. This is, of course, a problem for all LC/MS experiments, not only those using the MB interface. The examination of UV spectra in conjunction with MS data (using the MB interface) was found[5] to help significantly with the problem of peak identification.

The performance of the MB interface in LC/MS profiling of the carbon black extract was consistent with expectations based on past experience with this interface. The total ion current chromatogram (TIC) matched reasonably well the chromatogram obtained using UV detection at 254 nm (not shown), except for the early-eluting (more volatile) components. Because EI was used, fragment ions from compounds of higher molecular weights, particularly alkylated aromatics, can be confused with molecular ions of lower mass compounds, and the complete mass spectra were essential for resolving this ambiguity. Analysis of such spectra indicated that almost all the peaks in the reconstructed ion chromatograms (RICs) represent signals from molecular ions of the PACs. Examples of such spectra and of the RICs can be found elsewhere.[18] However, the performance for relatively involatile and low-abundance compounds of molecular weights up to 424 was gratifying. Note, however, that these LC/MS experiments with the MB interface used the simpler acetonitrile/dichloromethane gradient A (see Experimental Section) since it is more difficult to operate the MB interface routinely with an aqueous gradient (isocratic elution can be handled relatively easily). Also, relatively poor sensitivity for volatile PACs of MW < 200 Da was observed and ascribed to evaporative losses in the

(8) Willoughby, R. C.; Browner, R. F. *Anal. Chem.* **1984**, *56*, 2626–2631.
(9) Winkler, P. C.; Perkins, D. P.; Williams, W. K.; Browner, R. F. *Anal. Chem.* **1988**, *60*, 489–493.
(10) Anacleto, J. F.; Boyd, R. K.; Pleasance, S.; Quilliam, M. A.; Howard, J. B.; Lafleur, A. L.; Makarovsky, Y. *Can. J. Chem.* **1992**, *70*, 2558–2568.
(11) Peaden, P. A.; Lee, M. L.; Hirata, Y.; Novotny, M. *Anal. Chem.* **1980**, *52*, 2268–2271.
(12) Van Berkel, G. J.; McLuckey, S. A.; Glish, G. L. *Anal. Chem.* **1991**, *63*, 2064–2068.
(13) Van Berkel, G. J.; McLuckey, S. A.; Glish, G. L. *Anal. Chem.* **1992**, *64*, 1586–1593.
(14) Anacleto, J. F.; Quilliam, M. A.; Boyd, R. K.; Howard, J. B.; Lafleur, A. L.; Yadav, T. *Rapid Commun. Mass Spectrom.* **1993**, *7*, 229–234.
(15) Dark, W. A.; McFadden, W. H.; Bradford, D. L. *J. Chromatogr. Sci.* **1977**, *15*, 454–460.
(16) Hayes, M. J.; Lankmayer, E. P.; Vouros, P.; Karger, B. L.; McGuire, J. M. *Anal. Chem.* **1983**, *55*, 1745–1752.
(17) Krost, K. J. *Anal. Chem.* **1985**, *57*, 763–765.
(18) Anacleto, J. F. Chromatographic–Mass Spectrometric Analysis of Polycyclic Aromatic Compounds. Ph.D. Thesis, Dalhousie University, Halifax, Canada, 1993.

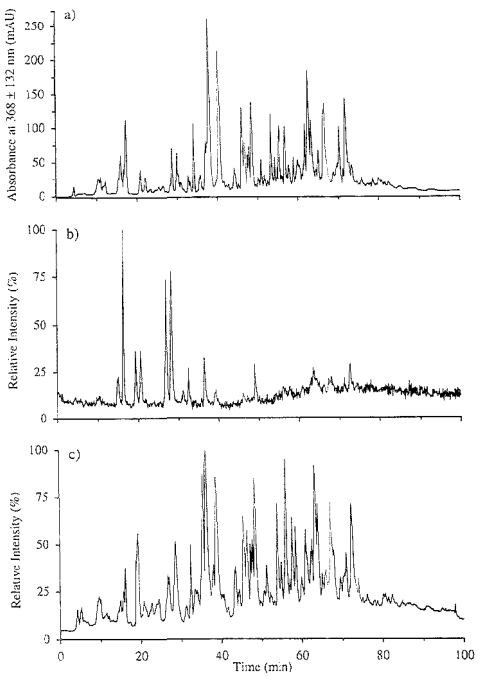

Figure 1. LC analyses of a carbon black extract, using the ternary gradient B (see Experimental Section). (a) UV detection, 236–500 nm; (b) LC/MS total ion chromatogram obtained using the PB interface with EI; (c) LC/MS total ion chromatogram obtained using the HPN interface with APCI. Mass spectrometer scanning parameters are described in the Experimental Section.

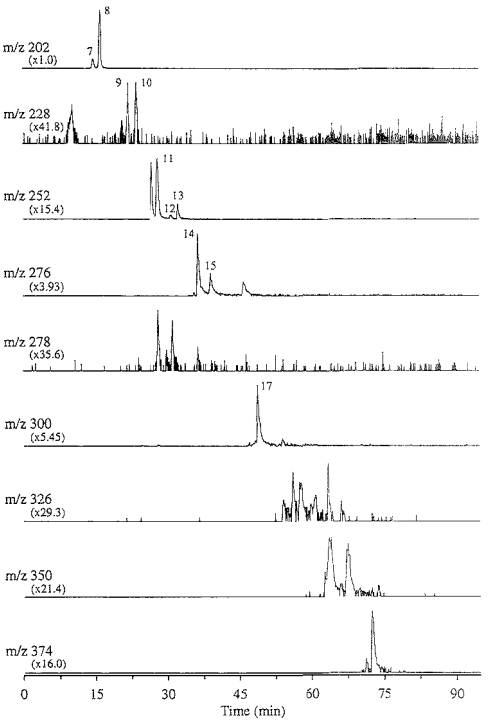

Figure 2. Reconstructed ion chromatograms for $M^{+\cdot}$ ions of PACs, from the same LC/MS analysis of the carbon black extract using the PB interface which was reported as a TIC in Figure 1b. Peak annotations correspond to numbering of analytes in Table 1.

interface. Another problem for the MB interface at lower *m/z* values is the background signal derived from the polyimide belt. The most intense peaks in this background, at *m/z* values of 113, 149, and 167, are readily removed by background subtraction and do not interfere with analyses of common PACs.

The performance of the PB and HPN interfaces in analysis of the same carbon black extract was evaluated using the aqueous acetonitrile/dichloromethane gradient B described in the Experimental Section. Figure 1a presents the LC/UV chromatogram obtained using a diode array detector with a broad bandwidth setting (368 ± 132 nm) detect all PACs. Figure 1b,c shows the TICs resulting from the LC/MS analyses using the PB and HPN interfaces, respectively. Even at this level of comparison, the HPN interface appears to provide superior performance in that the TIC obtained using this interface (Figure 1c) closely matches the LC/UV chromatogram (Figure 1a), whereas the TIC from the PB interface (Figure 1b) provides good response only for the middle-range PACs. The nature of this disappointing performance of the PB interface is made more clear in Figure 2, which shows selected RICs from this LC/MS analysis. No useful data were obtained below *m/z* 200 or above *m/z* 374. The poor performance of the PB interface for the more volatile PACs resembles that of the MB interface, while the difference in performance of these two interfaces for the larger PACs is probably due to the low volatility of these compounds. Thus, samples forming a thin layer on a moving belt are more readily volatilized as a consequence of the benefits of flash heating (by the nose heater in this case), as described by Beuhler et al.[19] and by Daves.[20] The PB interface, on the other hand, requires that small particles of analyte in the beam must strike the back surface of the ion source and be heated quickly enough to vaporize before the next-eluting analyte physically covers the first. Attempts to improve the heat transfer rate, by raising the PB ion source temperature to 300 from 250 °C, resulted in only modest gains in sensitivity.

However, in those cases for which a good response was obtained, the EI mass spectra obtained using the PB interface (e.g., Figure 3a,b) showed much less low-mass background (*m/z* < 150) than did the corresponding spectra obtained using the MB interface.[18] These relatively simple spectra can be readily matched with those contained in mass spectral libraries, although this is of questionable benefit for positive confirmations because most sets of PAC isomers produce identical EI mass spectra.[5] In addition, most alkylated PACs undergo fragmentation under EI conditions. PACs with longer alkyl chains ($> C_3$) usually produce low-intensity molecular ions. In such cases, the EI fragmentation pattern will indicate that the compound is alkylated, but the molecular weight may not be easily determined.

Positive ion APCI spectra of PACs are dominated by singly ionized molecules with no fragmentation and have a high

(19) Beuhler, R. J.; Flanigan, E.; Greene, L. J.; Friedman, L. *J. Am. Chem. Soc.* **1974**, *96*, 3990–3999.
(20) Daves, G. D., Jr. *Acc. Chem. Res.* **1979**, *12*, 359–365.

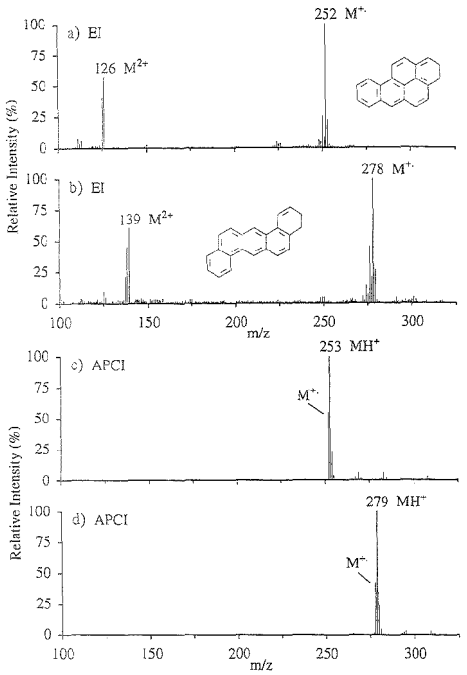

Figure 3. Background subtracted EI (a, b, PB interface) and APCI (c, d, HPN interface) mass spectra of benzo[*a*]pyrene (a, c) and dibenz[*a,h*]anthracene (b, d). Mass spectrometer conditions are described in the Experimental Section.

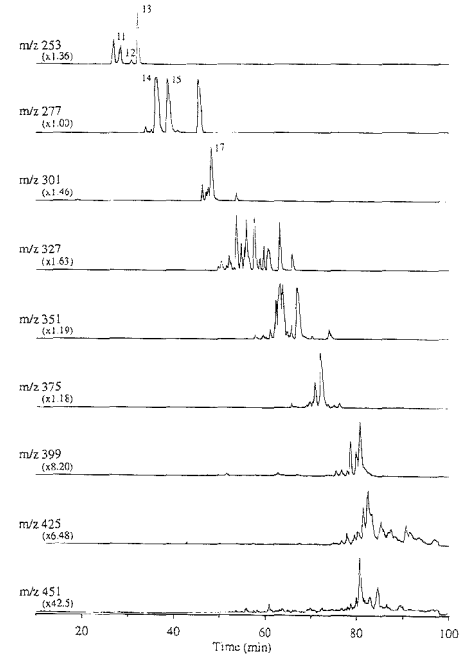

Figure 4. Reconstructed ion chromatograms, from the LC/MS analysis of the carbon black extract using the HPN interface reported as a TIC in Figure 1c. The *m/z* values labeling the RICs are those for the MH^+ ions, since these dominate the $M^{\cdot+}$ ions for these larger PACs. Peak annotations correspond to numbering of analytes in Table 1.

background at $m/z < 250$, which is, however, of constant or slowly varying intensity and can readily be accounted for by background subtraction. The details of the spectra depend upon the composition of the atmosphere in the ion source. The competing ionization mechanisms[21] are proton transfer from protonated water clusters and electron transfer to species such as $N_2^{\cdot+}$, $O_2^{\cdot+}$, and possibly NO^+, to form MH^+ and $M^{\cdot+}$ ions, respectively (e.g., Figure 3c,d). The relative importance of the two mechanisms varies with the partial pressure of water vapor within the plasma created by the corona discharge and can be controlled by doping the ion source with water or benzene vapor, as demonstrated[22] for PAC analysis by supercritical fluid chromatography using APCI mass spectrometry. In general, ionization by protonation was observed to increasingly dominate the electron transfer mechanism as the size of the PACs increased. These trends were confirmed in the LC/MS work reported here, but since ion source doping did not appear to offer any significant advantage, it was not used further in the present work. Some preliminary experiments[18] on negative ion APCI of PAC standards yielded complex mass spectra (not shown) dominated by $(M + 15)^-$ and $(M + 31)^-$ ions, with other higher mass species formed by ion–molecule reactions with the oxide and superoxide anions, which are the main negatively charged constituents of the APCI plasma.[21] These spectra were not very reproducible, in accord with general conclusions about negative ion chemical ionization in the presence of water and oxygen,[23] and this approach was not pursued further.

The performance of the HPN interface in LC/MS analysis of the higher molecular weight PACs in carbon black is illustrated in Figure 4 (the performance of this interface for the smaller PACs is described in the following section). Excellent signal-to-noise ratios are observed for all components observable in the LC/UV chromatogram out to 100 min retention time (Figure 1a). That Figure 4 does not represent an upper limit to the capabilities of the HPN interface, in analysis of large PACs, is suggested by the results of a similar analysis of carbon clusters extracted from a commercial fullerene soot.[24] Compounds up to C_{108} (MW 1296) were clearly detected,[24] and, while fullerenes are not expected to behave in a fashion entirely identical to that of PACs, this evidence suggests that the upper mass limit evident in Figure 4 reflects the composition of the carbon black extract rather than limitations of the HPN interface. This conclusion is also supported by a comparison of Figure 1 parts a and c, which suggests that all components of the carbon black extract which responded to the UV detector were also detected by the mass spectrometer when the HPN interface was used.

(21) French, J. B.; Davidson, W. R.; Reid, N. M.; Buckley, J. A. In *Tandem Mass Spectrometry*; McLafferty, F. W., Ed.; Wiley-Interscience: New York, NY, 1983; pp 353–370.

(22) Anacleto, J. F.; Ramaley, L.; Boyd, R. K.; Pleasance, S.; Quilliam, M. A.; Sim, P. G.; Benoit, F. M. *Rapid Commun. Mass Spectrom.* **1991**, *5*, 149–155.

(23) Stöckl, D.; Budzikiewicz, H. *Org. Mass Spectrom.* **1982**, *17*, 470–474.

(24) Anacleto, J. F.; Boyd, R. K.; Quilliam, M. A. *J. High Resolut. Chromatogr.* **1993**, *16*, 85–89.

It is important to understand the physicochemical origins of this remarkable performance of a device in which the gas temperature reaches no more than 120 °C or so. It seems likely that the key phenomenon is the well-known increase of vapor pressure P over the bulk value P_0 as the sample size is decreased below micrometer dimensions. The quantitative expression of this phenomenon is given by the Kelvin equation:[25-27]

$$\ln(P/P_0) = 2M\gamma/rdRT \quad (1)$$

where M is the molar mass, γ the surface energy per unit area, r the droplet radius, and d the density. For liquids, the effect is not appreciable until r falls below about 10^{-6} cm. However, if the initial nebulization of the LC eluate produces droplets of micrometer dimensions (10^{-4} cm), subsequent evaporation of solvent will leave dry particles of radius no larger than 10^{-6} cm for initial concentrations typical of LC/MS experiments. Moreover, the surface energies of solids are appreciably larger than those of liquids, so the ratio P/P_0 can be considerably greater than unity. Although the Kelvin equation deals with an equilibrium situation, while evaporation *rates* are likely important in the HPN interface, it seems likely that the same parameters controlling the thermodynamics will also control the rate. This explanation can account, at least qualitatively, for the ability of the HPN interface to facilitate acquisition of APCI mass spectra of (sometimes labile) compounds which do not vaporize from the bulk solid.[28]

The present comparison of the three LC/MS interfaces for qualitative profiling of PACs of higher molecular weights has confirmed the utility of the MB interface in this regard, although with notable restrictions on compatible LC mobile phases. The PB interface has no such mobile phase restrictions and provides a better MS background, but it provides very poor response for PACs larger than about 380 Da and less than 200 Da. The HPN interface provided the best performance with respect to both LC compatibility and mass spectrometric response to the full range of PACs present in the carbon black extract. The APCI mass spectra provided by the HPN interface contain only ions derived from intact molecules, while the EI spectra from the MB and PB interfaces contain more information and are suitable for comparisons with library spectra. However, as discussed above, this advantage is of limited practical importance for PAC analysis.

Quantitative Analysis: Standard Calibrations. In previous work from this laboratory, the MB interface was used for the quantitative analysis by LC/MS of PACs in marine sediments.[4,5] For most of the target PACs (300 Da or less), the precision obtained using the MB interface was comparable to that obtained by GC/MS for both external calibration and internal standardization techniques. However, the precision for naphthalene using the MB interface was ~50% relative standard deviation,[4] thus clearly illustrating the difficulty in analyzing volatile compounds when using this interface.

In view of both the previous documentation[4,5] of LC/MS quantification of PACs using the MB interface and also of the mobile phase compatibility limitations of this interface, which in turn limit the isomer separation selectivity (which is one of the major advantages of LC/MS for PAC analysis), only a few confirmatory experiments were conducted in the present work. For example, the performance for coronene (m/z 300) using single ion monitoring (SIM) was excellent, with respect to both instrumental limits of quantification (25 pg) and linear range (2.5 orders of magnitude demonstrated, but probably larger), and was typical of most of the larger PACs studied. The performance for carbazole (dibenzopyrrole), on the other hand, was much worse, with a SIM limit of quantification of 2 ng and a linear range up to about 300 ng with a marked fall-off from linearity above this value. The much lower sensitivity and deviation from linearity at higher sample loadings probably arise from less efficient desorption of the more polar carbazole molecules from the surface of the belt.

The use of the PB interface for quantitative analyses has been seriously hampered because of the nonlinear calibration curves it often produces. Several groups have reported quadratic responses, with slopes increasing with increasing concentration, for a number of analytes.[29-31] It has been suggested[30] that this nonlinear behavior is related to the amount of analyte in a particle and its transmission through the interface. Analyte transport efficiencies are generally less than 10% for most compounds in the particle beam interface.[32] Losses occur primarily in the momentum separator because of particle sedimentation, turbulence, and misalignment of nozzles and skimmer cones.[9] Sedimentation and turbulence losses are directly related to the size of analyte particles, which in turn is a function of analyte concentration[9] and the diameter of the nebulizer tip.[32] Thus, the nonlinear curves are a result of small particles, produced at low analyte concentrations, which are more prone to turbulent losses. More efficient mass transport occurs at higher concentrations as the particle size increases.

The calibration curves obtained for two PAC standards, shown in Figure 5a,b, can be fitted to quadratic equations. Recent reports[33,34] have claimed that, with the exception of benz[*a*]anthracene and chrysene, several PAC standards exhibited linear response behavior over the range of 20–1000 ng. The expansion of the low-mass regions of the two curves (insets, Figure 5a,b) clearly shows that the curve for benzo[*a*]pyrene is nonlinear throughout the entire concentration range, although that for dibenz[*a*,*h*]anthracene reveals acceptably linear behavior (dashed line) below 300 ng injected on-column. Above this level, the calibration curve exhibits the convex downward appearance characteristic of the PB interface. Although nonlinear response does not preclude the use of an instrumental method in quantitative analysis, it does increase the calibration requirements and necessitates interpolation from multipoint calibration curves. As an alternative in the case of the PB interface, the linearization of calibration curves through the use of the "carrier effect" (i.e., use of mobile phase additives) has been suggested.[35] Subsequent

(25) Thomson, W. *Phil. Mag.* **1871**, *42*, 448.
(26) Moore, W. J. *Physical Chemistry*, 4th Ed; Prentice Hall: Englewood Cliffs, NJ, 1972; pp 481–482.
(27) Wilemski, G. *J. Chem. Phys.* **1995**, *103*, 1119.
(28) Burlingame, A. L.; Boyd, R. K.; Gaskell, S. J. *Anal. Chem.* **1994**, *66*, 634R–683R.
(29) Brown, F. R.; Draper, W. M. *Biol. Mass Spectrom.* **1991**, *20*, 515–521.
(30) Ho, J. S.; Behymer, T. D.; Budde, W. L.; Bellar, T. A. *J. Am. Soc. Mass Spectrom.* **1992**, *3*, 662–671.
(31) Doerge, D. R.; Burger, M. W.; Bajic, S. *Anal. Chem.* **1992**, *64*, 1212–1216.
(32) Browner, R. F.; Winkler, P. C.; Perkins, D. D.; Abbey, L. E. *Microchem. J.* **1986**, *34*, 15–24.
(33) Roby, M. R.; Pace, C. M.; Betowski, L. D.; Marsden, P. J. *Proceedings of the 38th ASMS Conference on Mass Spectrometry and Allied Topics*; Tucson, AZ, June 3–8, 1990; pp 625–626.
(34) Pace, C. M.; Betowski, L. D. *J. Am. Soc. Mass Spectrom.* **1995**, *6*, 597.
(35) Bellar, T. A.; Behymer, T. D.; Budde, W. L. *J. Am. Soc. Mass Spectrom.* **1990**, *1*, 92–98.

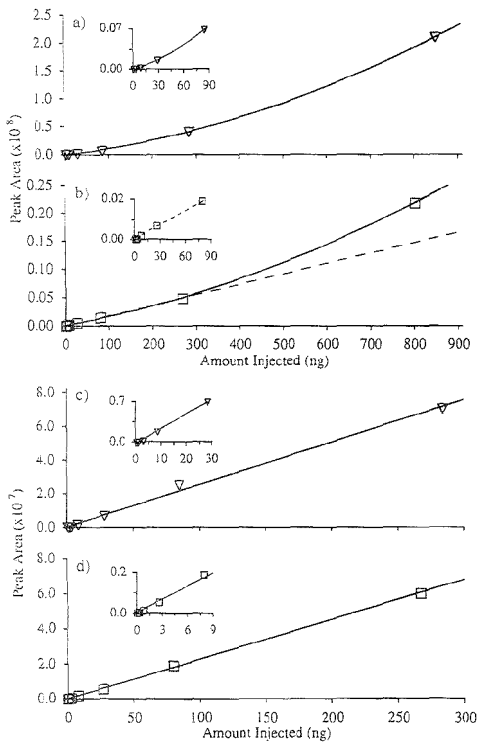

Figure 5. LC/MS calibration curves obtained for benzo[*a*]pyrene (a, c) and dibenz[*a,h*]anthracene (b, d) using the particle beam (a, b) and heated pneumatic nebulizer (c, d) interfaces.

measurements, however, indicated that this technique is limited to very few compounds and that nonlinear behavior was still prevalent.[30] The presence of unexpected coeluting substances in real-world samples can also cause calibration errors and analytical bias. The detector signal given by target analytes has been shown to increase with coeluting matrix constituents.[29] Presumably, particle size discrimination in the momentum separator, with its influence on transport efficiency, is also the basis of this phenomenon.

Instrumental detection limits for the PB interface, determined on the basis of the smallest sample size which yielded a signal-to-noise ratio of at least 3:1, were 3–4 ng injected on-column for benzo[*a*]pyrene and dibenz[*a,h*]anthracene. Previous studies[33,34] of PAC standards using a PB interface also reported detection limits in the low nanogram range. These limits are by no means universal for all PACs; however, the more volatile low molecular weight PACs are more susceptible to losses in the PB interface, thus giving rise to much higher limits of detection and of quantification. This point will be further illustrated below.

The calibration curves obtained for the same two PAH standards using the HPN interface with APCI by monitoring MH^+ ions, are shown in Figure 5c,d. The insets show that the curves are linear down to the lowest concentrations analyzed. Such curves are typical of all the PACs examined thus far using the HPN interface. The dynamic ranges found here are similar to those commonly reported in the literature,[36,37] i.e., at most three decades (10^3). There are several possible explanations for this narrow linear dynamic range. The most likely involves a depletion of APCI reagent ions when high levels of analyte are present, i.e., saturation of the APCI ionizing power. Other possible explanations involve saturation of the pulse-counting ion detection system incorporated in the instrument used for the HPN work.

Instrumental detection limits for the HPN interface, determined on the basis of the smallest amount of analyte which yielded a signal-to-noise ratio of at least 3:1, were 275 and 85 pg for benzo[*a*]pyrene and dibenz[*a,h*]anthracene, respectively. These detection limits are considerably lower than those of the particle beam interface (between 1 and 4 ng). The difference of a factor of 3 between the values obtained for these two compounds is difficult to explain in terms of gaseous ion properties, since the two ionization energies are very close[38] (7.12 ± 0.01 and 7.38 ± 0.04 eV, respectively) and, using the correlations of Meot-Ner,[39] the corresponding proton affinities are estimated to be 900 and 870 kJ mol^{-1}. These values are sufficiently close that it seems reasonable that the ratios of intensities of $M^{\bullet+}$ and MH^+ ions should be about the same for these two PAHs, as was observed in Figure 3c,d. It is also difficult to account for this difference in sensitivities in terms of information on the vapor pressures of the two solid PAHs.[40–42]

Quantitative Analysis of the NIST Certified Reference Material SRM 1597. The NIST reference material SRM 1597 is a natural complex mixture of PACs isolated from coal tar, certified for concentrations of 12 PAHs ranging from naphthalene (128 Da) to benzo[*ghi*]perylene (276 Da). The preparation and certification of this reference material have been described by Wise et al.[43] Information values for a further 18 PACs (including some PAHs) are also supplied in the NIST certification document,[44] and more recently an information value for the concentration of dibenz[*a,h*]anthracene was published.[45] This well-characterized material was chosen as a suitable test case for LC/MS analyses.

The present experiments, designed to obtain calibration curves for quantification by external standardization exemplified by Figure 5, indicated that use of internal standards would be mandatory for the PB interface. Particle beam MS has also been shown to be susceptible to tremendous fluctuations in absolute response during intra- and interday runs.[46] For example, instrument response factors for chlorinated phenoxy acid standards varied as much as 2-fold over a 24 h period.[47] This presents another significant obstacle when using an external calibration.

(36) Gilbert, J. D.; Hand, E. L.; Yuan, A. S.; Olah, T. V.; Covey, T. R. *Biol. Mass Spectrom.* **1992**, *21*, 63–68.
(37) Fouda, H.; Nocerini, M.; Schneider, R.; Gedutis, C. *J. Am. Soc. Mass Spectrom.* **1991**, *2*, 164–167.
(38) Lias, S. G.; Bartmess, J. E.; Liebman, J. F.; Holmes, J. L.; Levin, R. D.; Mallard, W. G. Gas Phase Ion and Neutral Thermochemistry. *J. Phys. Chem. Ref. Data* **1988**, *17*, Suppl. 1.
(39) Meot-Ner, M. *J. Phys. Chem.* **1980**, *84*, 2716–2723.
(40) Wakayama, N.; Inokuchi, H. *Bull. Chem. Soc. Jpn.* **1967**, *40*, 2267–2271.
(41) Murray, J. J.; Poitie, R. F.; Pupp, C. *Can. J. Chem.* **1974**, *52*, 557–563.
(42) White, C. M. *J. Chem. Eng. Data* **1986**, *31*, 198–203.
(43) Wise, S. A.; Benner, B. A.; Byrd, G. D.; Chesler, S. N.; Rebbert, R. E.; Schantz, M. M. *Anal. Chem.* **1988**, *60*, 887–894.
(44) U.S. National Institute of Standards and Technology, SRM 1597 Certificate of Analysis, 1987.
(45) Wise, S. A.; Deissler, A.; Sander, L. C. *Polycyclic Aromat. Compd.* **1993**, *3*, 169–184.
(46) Brown, M. A.; Stephens, R. D.; Kim, I. S. *Trends Anal. Chem.* **1991**, *10*, 330–336.

The obvious solution is through use of internal standards, especially isotopically labeled internal standards, which exhibit chemical behavior almost identical to that of the native substances but are readily differentiated by their mass spectra. If internal standards are chromatographically resolved from the target analytes (which is true for perdeuterated PACs), different matrix effects can still cause calibration errors through coelution of a matrix constituent with either the internal standard or the analyte.[29] The only reliable means to guarantee no selective enhancement of either the internal standard or the analyte, when using the PB interface, is through the use of coeluting isotopically labeled standards, e.g., ^{13}C-labeled standards which are, however, of limited availability and are expensive.

Experiments were conducted to determine whether perdeuterated PAC internal standards (chromatographically resolved from their native perprotonated counterparts) can be used to quantify PACs in a complex sample. A mixture of perdeuterated PAH standards (DPAC-1) was spiked at four different levels into both a certified NIST PAH standard mixture (SRM 1647) and a complex mixture of PACs from coal tar (SRM 1597). A total of 24 *m/z* values were monitored (17 PAHs including several sets of isomers, and appropriate perdeuterated PAHs) using LC/MS with the PB interface. A typical analysis of a SRM 1647/DPAC-1 mixture (10:1 volume ratio) is shown as Figure 6. Only seven of the 17 target PAHs were detected (Figure 6, second acquisition period) and subsequently quantified. The lower molecular weight PAHs (*m/z* 178 and lower), which were present in much higher concentrations than the other components (see Table 1), were among the PAHs that were not detected (Figure 6, first acquisition period). These compounds were too volatile to be efficiently transported through the PB interface. The higher molecular weight PAHs (*m/z* 276 and higher), which were present in concentrations similar to those of the PAHs that were successfully quantified (see Table 1), were also not detected (Figure 6, third acquisition period). These compounds are apparently insufficiently volatile to vaporize efficiently in the hot ion source. These discrimination effects, which were also noted in the qualitative analysis of the carbon black extract (Figure 2), represent a severe disadvantage of the PB interface.

Analysis of the same SRM 1647/DPAC-1 mixture (10:1 volume ratio), by LC/MS using the HPN interface with APCI, is shown in Figure 7. A total of 48 *m/z* values were monitored (both $M^{\bullet+}$ and MH^+ ions of 17 PAHs, including several sets of isomers, and their perdeuterated counterparts). In contrast to the results obtained using the PB interface, all 16 of the target PAHs (and also coronene) were easily detected with excellent signal-to-noise ratios and were subsequently quantified. The LC peak observed in the SIM trace for *m/z* 302 (Figure 7) probably represents interference from the ^{13}C isotopomers of the coronene ions.

Calibration curves were generated using the data from the four mixed SRM 1647/DPAC-1 solutions (raw data for only one mixture are shown in Figures 6 and 7). Plots of the protonated to deuterated PAH peak area ratios versus the known molar ratios (measured as SRM 1647/DPAC-1 weight ratios) for benzo[*b*]fluoranthene (B*b*F) are shown in Figure 8 for the PB and HPN interfaces. For all those PAHs that were detected with reasonable sensitivity using the PB interface (Figure 6), the calibration plots resembled that shown in Figure 8, in that they could be described

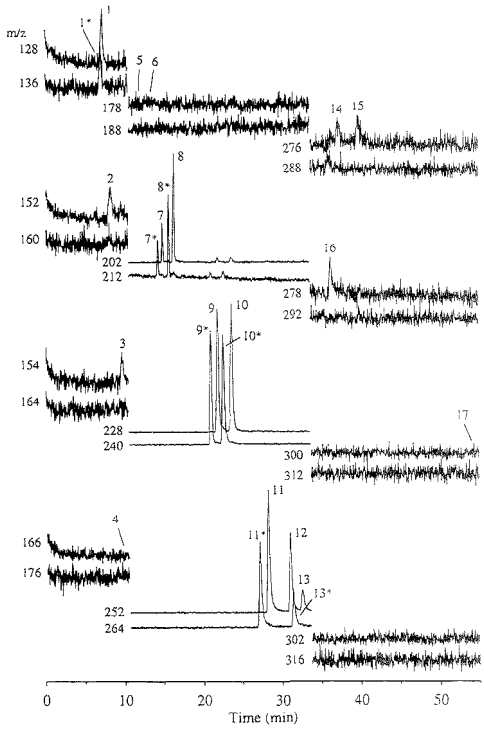

Figure 6. Analysis of a SRM 1647/DPAC-1 mixture (10:1 v/v) using particle beam LC/MS and ternary gradient C (see Experimental Section). A total of 24 *m/z* values were monitored in three acquisition periods: period 1 (0–9.8 min), *m/z* 128, 136, 152, 160, 154, 164, 166, 176; period 2 (9.8–33.5 min), *m/z* 178, 188, 202, 212, 228, 240, 252, 264; period 3 (33.5–60 min), *m/z* 276, 288, 278, 292, 300, 312, 302, 316. These *m/z* values represent $M^{\bullet+}$ ions of PAHs and their perdeuterated versions (peaks marked with an asterisk represent the perdeuterated PAH internal standards). See Table 1 for compound identities. The SIM chromatograms are labeled with their respective *m/z* values and are shown offset from one another vertically for the sake of clarity of presentation.

either as linear with non-zero intercepts or as quadratic curves including the origin. In either case, the nonideality can be interpreted in terms of lower transmission efficiencies for the native analyte than for its perdeuterated counterpart. Negative *y*-intercepts for forced linear fits, such as that observed in Figure 8 for the PB interface, are usually interpreted in terms of irreversible losses of analyte somewhere in the analytical train.[48] In this instance, analyte losses are known to occur in the PB interface, but the dependence of these losses on total sample loading makes difficult any detailed interpretation.

The calibration curve obtained for B*b*F using the HPN LC/MS interface with APCI in the analyses of the NIST 1647/DPAC-1 mixtures is also shown in Figure 8. The linear regression curves for this, and for all the other target PAHs,[7] did include the origin to within experimental error. Regression coefficients were mostly ≥0.99, although a few were not as high. For the best precision

(47) Kim, I. S.; Sasinos, F. I.; Stephens, R. D.; Wang, J.; Brown, M. A. *Anal. Chem.* **1991**, *63*, 819–823.

(48) Boyd, R. K. *Rapid Commun. Mass Spectrom.* **1993**, *7*, 257–271.

Table 1. Results of LC/MS Analyses of a Coal Tar Reference Material (NIST SRM 1597) Compared with Certified and Information Values[a]

			particle beam interface			heated pneumatic nebulizer		
no.	compound	certfd concn	LC/MS concn	RSD, % (n = 3)	reltv error, %	LC/MS concn	RSD, % (n = 3)	reltv error, %
1	naphthalene ($C_{10}H_8$)	1160 ± 50				1149	2.9	−1.0
2	acenaphthylene ($C_{12}H_8$)	250[b]				247	3.6	−1.1[b]
3	acenaphthene ($C_{12}H_{10}$)					9.2	1.0	
4	fluorene ($C_{13}H_{10}$)	140[b]				161	4.6	−15[b]
5	phenanthrene ($C_{14}H_{10}$)	462 ± 3				461	3.2	−0.1
6	anthracene ($C_{14}H_{10}$)	101 ± 2				107	5.4	6.1
7	fluoranthene ($C_{16}H_{10}$)	322 ± 4	338	13	4.9	351	11	9.0
8	pyrene ($C_{16}H_{10}$)	235 ± 2	238	11	1.2	241	5.0	2.6
9	benz[a]anthracene ($C_{18}H_{12}$)	98.6 ± 3.6	97.2	2.4	−1.4	105	4.6	6.8
10	chrysene ($C_{18}H_{12}$)	71.7 ± 1.0	59.6	1.5	−17	70.4	7.5	−1.8
11	benzo[b]fluoranthene ($C_{20}H_{12}$)	66[b]	64	2.1	−3.0[b]	63	7.9	−4.5[b]
12	benzo[k]fluoranthene[d] ($C_{20}H_{12}$)	43[b]	41	5.5	−4.7[b]	41	8.0	−4.7[b]
13	benzo[a]pyrene ($C_{20}H_{12}$)	95.8 ± 5.8	94.7	4.7	−1.2	84.8	1.1	−11
14	benzo[ghi]perylene ($C_{22}H_{12}$)	53.7 ± 7.6				57.0	3.3	6.2
15	indeno[1,2,3-cd]pyrene[e] ($C_{22}H_{12}$)	60.2 ± 4.4				60	25	−0.4
16	dibenz[a,h]anthracene ($C_{22}H_{14}$)	6.8[c]				7.4	6.6	8.8[c]
17	coronene ($C_{24}H_{12}$)	11[b]				10.7	1.2	−2.7[b]

[a] Concentrations in μg/g. Internal standards were the perdeuterated compounds (DPAC-1[7]) except where noted. [b] Values not certified by NIST; information values reported by NIST.[44] [c] Value not certified by NIST; information value obtained by HPLC by NIST.[45] [d] Perdeuteriobenzo[b]fluoranthene was used as internal standard. [e] Perdeuteriobenzo[ghi]perylene was used as internal standard.

and accuracy in quantitative analyses of this kind, multipoint calibrations and 1:1 concentration ratios (target analyte/internal standard) should be used, but the highly linear calibration curves obtained using the HPN interface reduce the stringency of this requirement.

Calibration curves such as those illustrated in Figure 8 were used to determine PAH concentrations in the NIST SRM 1597 coal tar extract, spiked with the DPAC-1 standard solution. Most of the values obtained using the HPN interface were reported previously,[7] though with less experimental detail, and are included here for comparison with the results obtained using the PB interface. Both sets of values, together with the NIST certified concentrations[44] or information values, [44,45] are listed in Table 1 for those 15 compounds whose perdeuterated analogs are included in the DPAC-1 solution or for which closely eluting perdeuterated compounds in DPAC-1 can reasonably be used as internal standards. In addition, the concentration obtained for acenaphthene (not covered by the NIST work[44,45]) is included for information.

Except for fluoranthene and chrysene, the accuracies of the concentration values obtained using the PB interface are within acceptable limits. The low concentration obtained for chrysene appears to be a result of matrix components coeluting with its perdeuterated internal standard. A full-scan analysis of the coal tar extract revealed the presence of components at m/z 216 (either a benzofluorene or a methylpyrene isomer) and 226 (probably cyclopenta[cd]pyrene) whose retention times matched those of chrysene and its perdeuterated counterpart. The chromatographic peaks of the other PAHs which were quantified were also thoroughly examined, and except for perdeuteriobenzo[b]fluoranthene, they all appeared free from coeluting components. The perdeuteriobenzo[b]fluoranthene peak was not completely resolved from another PAH of molecular mass 252 Da (probably perylene), but not to an extent sufficient to significantly affect the result listed in Table 1. In the case of fluoranthene, another PAH isomer of molecular mass 202 Da appeared to coelute, as indicated by the observation that the front baseline of the LC peak was slightly but significantly broadened. The NIST SRM 1597 certificate of analysis[44] does indicate the presence of a third isomer (acephenanthrylene) at a concentration (uncertified) of ~60 μg/g. An assumption that the present experiments measured the sum of concentrations of fluoranthene plus this isomer, together with the probable PB transmission enhancement from the matrix effect, could account for the high fluoranthene concentration reported in Table 1.

The deviations of the concentrations measured by LC/MS using the HPN interface, from the certified values, were <7.0%, with the exception of those for fluorene, fluoranthene, and benzo[a]pyrene, as discussed previously.[7] The partial coelution of another PAH isomer of molecular mass 202 Da (probably acephenanthrylene) with fluoranthene, and of an isomer of fluorene (m/z 166) in the coal tar solution, is believed to be the reason for the high values determined in the present work (Table 1). However, the LC peaks for both benzo[a]pyrene and its perdeuterated analog were completely resolved from any interferences. At this time, no explanation for this low measured concentration (Table 1) can be given.

CONCLUSIONS

The present findings concerning the relative merits of the MB, PB, and HPN interfaces for LC/MS analyses of PACs appear to reflect some of the more general impressions of these three devices. The MB interface is mechanically awkward, does not permit routine use of gradient elution with aqueous mobile phases due to related variations in pumping and heating requirements in the solvent removal stages, shows poor transmission efficiencies for the more volatile PACs, and provides a significant mass spectrometric background. On the other hand, the MB interface provides good quality EI spectra for high molecular weight PACs not amenable to GC/MS analysis and can also readily be used with chemical ionization, though this was not demonstrated here. Previous work from this laboratory[4,5] has demonstrated that, with some effort, acceptable quantification of the less volatile PACs in complex mixtures can be achieved using the MB interface.

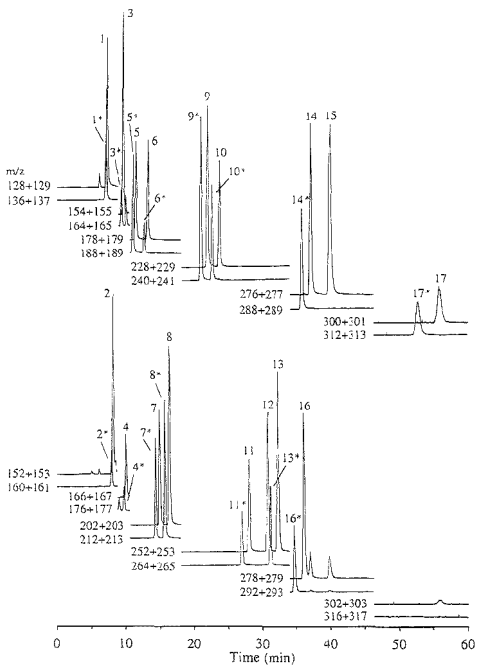

Figure 7. Analysis of a SRM 1647/DPAC-1 mixture (10:1 v/v) using the HPN LC/MS interface with APCI and ternary gradient C (see Experimental Section). A tctal of 48 ions (both $M^{\cdot+}$ and MH^+ ions of target PAHs and their perdeuterated versions) were monitored in six acquisition periods: period 1 (0–8.8 min), *m/z* 128 + 129, 136 + 137, 152 + 153, 160 + 161; period 2 (8.8–10.5 min), *m/z* 154 + 155, 164 + 165, 166 + 167, 176 + 177; period 3 (10.5–18 min), *m/z* 178 + 179, 188 + 189, 202 + 203, 212 + 213; period 4 (18–33.4 min), *m/z* 228 + 229, 240 + 241. 252 + 253, 264 + 265; period 5 (33.4–46 min), *m/z* 276 + 277, 288 + 289, 278 + 279, 292 + 293; period 6 (46–60 min), *m/z* 300 + 301, 312 + 313, 302 + 303, 316 + 317. See Table 1 for compound identities. Peaks marked with an asterisk represent the perdeuterated PAH internal standards. For the sake of clarity of presentation, the SIM chromatograms are shown offset from one another vertically.

The PB interface is compatible with aqueous mobile phases and provides EI spectra with appreciably less background than does the MB interface. However, the PB interface exhibits poor transmission efficiencies for PACs of both low (<200) and high (>380) molecular weights. The highly nonlinear calibration curves and poor detection limits obtained using the PB interface, together with the marked carrier effects due to coeluting compounds, make the PB interface difficult to use reliably in quantitative PAC analyses, even when perdeuterated PAC internal standards are employed.

The HPN interface with APCI provided the best overall performance in the present work. This LC/MS interface is compatible with a wide range of mobile phase compositions, exhibits excellent transmission efficiencies and detection limits for both low and high molecular weight PACs, and provides excellent linearity of response. The main disadvantages of the HPN interface encountered in the present work were the lack of fragment ions and thus of structural information (though this feature is of limited importance for PACs, and in general,

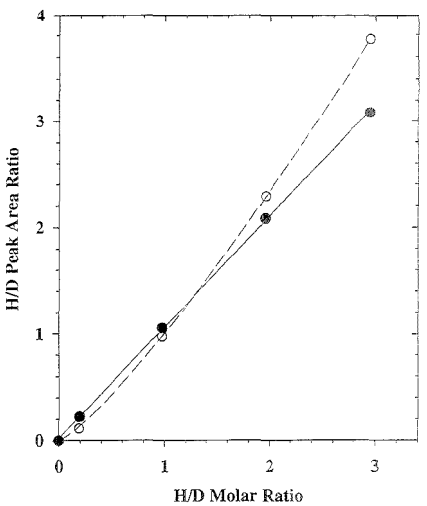

Figure 8. Calibration curves for the analysis of benzo[*b*]fluoranthene (B*b*F) using the PB (○) and HPN (●) LC/MS interfaces and using perdeuterio-B*b*F as an internal standard. Solutions were prepared by mixing varying proportions of SRM 1647 and DPAC-1 standard solutions. Each point represents the mean of triplicate measurements of the ratios of peak areas for the $M^{\cdot+}$ ions of perprotio- and perdeuterio-B*b*F. The dashed curve (PB interface) represents a least-squares fit to an assumed form ($y = ax^b$), with $a = 1.006$, $b = 1.218$, and $r^2 = 0.998$. The full curve (HPN interface) represents a fit to the linear form ($y = cx + d$), where $c = 1.042$, $d = 0.0361$, and $r^2 = 0.990$.

concentration of ion current in ionized molecular species is an advantage for SIM experiments) and the limited dynamic range (about 10^3), although it is possible that the latter may reflect the pulse-counting detection system of the APCI instrument used in the present work. The mass spectrometric background at low *m/z* values, while significant, varies slowly during the LC elution and thus provides a constant baseline for quantification by selected ion monitoring or can be corrected for by background subtraction for full mass spectral acquisition.

ACKNOWLEDGMENT

The authors are indebted to Ruth Bailey and David North of Health Protection Branch, Health Canada, for generously allowing access to their LC/MS instrument with PB interface, and to John Fetzer of Chevron Oil Corp. for the gift of the carbon black extract. J.F.A. thanks the Natural Sciences and Engineering Research Council (Canada) and Dalhousie University for graduate scholarships. Funding of this work was provided in part by the Panel on Energy Research and Development (Canada) under OERD Project No. 57217. This publication is NRCC No. 38108.

Received for review June 19, 1995. Accepted August 29, 1995.[⊗]

AC950616K

[⊗] Abstract published in *Advance ACS Abstracts,* October 1, 1995.

Anal. Chem. **1995**, *67*, 4155–4163

An Integrated Analytical Method for Determination of Polychlorinated Aryl Methyl Sulfone Metabolites and Polychlorinated Hydrocarbon Contaminants in Biological Matrices

Robert J. Letcher and Ross J. Norstrom*

Centre for Analytical and Environmental Chemistry, Department of Chemistry, Carleton University, Ottawa, Ontario, K1S 5B6 Canada, and National Wildlife Research Centre, Canadian Wildlife Service, Hull, Québec, K1A 0H3 Canada

Åke Bergman

Department of Environmental Chemistry, Wallenberg Laboratory, Stockholm University, S-10691 Stockholm, Sweden

A simple column chromatography method was developed for separation and cleanup in the determination of chlorinated hydrocarbon contaminants and their methyl sulfone ($MeSO_2$-) metabolites in biological tissues. The method was validated for determination of 11 polychlorinated biphenyls (PCBs), 15 tetra- to heptachloro 3- and 4-$MeSO_2$-PCBs, 3-$MeSO_2$-DDE, and tris(4-chlorophenyl)-methanol spiked to herring gull egg, smelt, and polar bear liver and adipose tissue using gas chromatography with electron-capture detection (GC-ECD). The overall mean recovery relative to the internal standard was 103% ± 8%, independent of analyte, substrate type, and lipid extract weights up to ~0.7 g. Precision of replicate analyses of individual congeners was good. There were no significant residual biogenic or xenobiotic interferences in the aryl methyl sulfone fraction of any substrate. Sensitivity and linearity of molar response of $MeSO_2$-PCBs and $MeSO_2$-DDE was tested for ECD and electron-capture negative ion mass spectrometry monitoring the total ion current (TIC) and the molecular ion (SIM). The mean practical quantitation limit among $MeSO_2$-PCBs and 3-$MeSO_2$-DDE was lowest for SIM (2.1 ± 0.9 pg) and similar for ECD and TIC (24.2 ± 4.6 and 44.4 ± 17.1 pg, respectively). Response factors were linear above the practical quantitation limit to at least the nanogram level for all three techniques. In spite of superior sensitivity, there was more inherent variability in the response factors for SIM (~18%–56% CV) than for ECD (~7%–12% CV) or TIC (~11%–18% CV); therefore, ECD or TIC is recommended for quantitative analysis.

Chlorinated hydrocarbon contaminants (CHCs) such as polychlorinated biphenyls (PCBs) and 1,1-dichloro-2,2-bis(4-chlorophenyl)ethene (4,4'-DDE), a metabolite of the pesticide DDT, are well-known global environmental pollutants that bioaccumulate in biota.[1] In contrast, methylsulfonyl- ($MeSO_2$-) containing metabolites of PCBs and DDE have received scant attention as environmental contaminants since their first discovery in Baltic seals in 1976.[2] Aryl methyl sulfone metabolites have escaped detection in standard analysis procedures, as they are more polar relative to other common CHCs and quantitation standards have not been readily available. Knowledge of $MeSO_2$-PCB toxicology is on the rise but remains poor relative to the parent compounds.[3,4] $MeSO_2$-DDE is a potent adrenocortical toxicant in some species.[5,6]

$MeSO_2$-PCBs are slightly less hydrophobic than the parent PCBs; however, $MeSO_2$-PCBs possess lipophilic properties similar to those of other bioaccumulating CHCs.[7] $MeSO_2$-PCBs fulfill the requirements for bioaccumulation since they have octanol/water partition coefficients (log K_{ow}) greater than 3. Furthermore, bioaccumulated $MeSO_2$-PCBs and -DDE appear to resist further metabolic degradation. At least 22 $MeSO_2$-PCB and two $MeSO_2$-DDE compounds at total levels ranging from 2% to 20% of total PCB and DDE levels have been identified in mammalian tissue, including humans.[8–13]

Aryl methyl sulfone compounds possess Lewis basicity, acid/base stability, and high polarity, which are useful properties for separation from coextracting lipids and other CHCs in biological tissues. Existing analytical methodologies for aryl methyl sulfone

* Address correspondence to this author at Environment Canada, Canadian Wildlife Service, National Wildlife Research Centre, 100 Gamelin Blvd., Bldg. #9, Hull, Québec, K1A 0H3 Canada. Telephone: (819) 997-1411. Fax: (819) 953-6612. E-mail: rnorstro@ccs.carleton.ca.

0003-2700/95/0367-4155$9.00/0

(1) Tanabe, S.; Iwata, H.; Tatsukawa, R. *Sci. Total Environ.* **1994**, *154*, 163–177.
(2) Jensen, S.; Jansson, B. *Ambio* **1976**, *5*, 257–260.
(3) Kato, Y.; Haraguchi, K.; Kawashima, M.; Yamada, S.; Masuda, Y.; Kimura, R. *Chem.-Biol. Interact.* **1994**, *95*, 257–263.
(4) Kiyohara, C.; Hirohata, T. *Toxicol. in Vitro* **1994**, *8*, 1185–1189.
(5) Jönsson, C.-J.; Lund, B.-O.; Brunström, B.; Brandt, I. *Environ. Toxicol. Chem.* **1994**, *13*, 1303–1310.
(6) Lund, B.-O. *Environ. Toxicol. Chem.* **1994**, *13*, 911–917.
(7) Bergman, Å.; Haraguchi, K. *Cambridge Isotope Laboratories Supplement*; Cambridge Isotope Laboratories: Cambridge, MA, 1994; Vol. 1, pp 1–8.
(8) Letcher, R. J.; Norstrom, R. J.; Bergman, Å. *Sci. Total Environ.* **1995**, *160*, 409–420.
(9) Bergman, Å.; Norstrom, R. J.; Haraguchi, K.; Kuroki, H.; Béland, P. *Environ. Toxicol. Chem.* **1994**, *13*, 121–128.
(10) Haraguchi, K.; Kuroki, H.; Masuda, Y.; Shigematsu, N. *Food Chem. Toxicol.* **1987**, *22*, 283–288.
(11) Haraguchi, K.; Kuroki, H.; Masuda, Y. *J. Chromatogr.* **1986**, *361*, 239–252.
(12) Bergman, Å.; Athanasiadou, M.; Bergek, S.; Haraguchi, K.; Jensen, S.; Klasson-Wehler, E. *Ambio* **1992**, *21*, 570–576.
(13) Haraguchi, K.; Athanasiadou, M.; Bergman, A.; Hovander, L.; Jensen, S. *Ambio* **1992**, *21*, 546–549.

cleanup and/or CHC separation have exploited these physicochemical characteristics by incorporation of liquid–liquid partitioning strategies.[2,9–14] Dimethyl sulfoxide, concentrated sulfuric acid, and acetonitrile partitioning have been common approaches. Lipid-destructive tissue extraction strategies, such as saponification with alcoholic potassium hydroxide at elevated temperatures, have also been used.[14] To simplify the procedures and enhance reliability of determination, we developed a simple column chromatography approach amenable to routine CHC and aryl methyl sulfone isolation from biological tissue samples. The method takes advantage of aryl methyl sulfone polarity, which is higher than that of most other biologically persistent CHCs, such as PCBs and chlorinated insecticides (e.g., DDTs and chlordanes), and the smaller molecular size of aryl methyl sulfones and CHCs than biogenic coextracting compounds, mainly triglycerides. Gas chromatography/electron-capture detection (GC-ECD) was used to determine the percent recovery of (1) standard mixtures of tetra- to heptachloro-3- and -4-$MeSO_2$-PCBs, and 3-$MeSO_2$-DDE, which are biologically significant,[8,9] and an internal standard (IS) of 3-$MeSO_2$-2-methyl-5-2′,3′,4′,5′-pentachlorobiphenyl spiked to herring gull egg, whole fish (smelt), polar bear liver, and polar bear adipose tissue homogenates and (2) the same $MeSO_2$-PCBs, 3-$MeSO_2$-DDE, IS, dichloro- to octachloro-PCBs, and tris(4-chlorophenyl)methanol (TCPMeOH) spiked to contaminant-free lipid extracts of the same samples prepared by gel-permeation chromatography (GPC). TCPMeOH has recently been shown to be a ubiquitous global environmental contaminant.[15,16] The polarity of TCPMeOH is at the high end of routinely determined CHCs, such as dieldrin, and separation from $MeSO_2$-PCBs and -DDE is a good test of the method.

The aryl methyl sulfone fractions obtained from tissue homogenates were analyzed by GC-ECD as well as by gas chromatography/electron-capture negative ion mass spectrometry (GC/ECNI-MS) to evaluate residual biogenic and xenobiotic interferences. GC/ECNI-MS has been used for $MeSO_2$-PCB chlorinated isomer group and $MeSO_2$-DDE characterization[8,9,12,13] but not as a quantitative technique. Sensitivity of $MeSO_2$-PCBs and -DDE in GC-ECD and GC/ECNI-MS in the selected ion monitoring (SIM) mode is in the low picogram range, as these compounds are electrophilic and readily capture thermally energized electrons.[11,17] In this study, the response characteristics among ECD, SIM, and TIC were compared to determine which techniques were the best for precise and accurate $MeSO_2$-PCB and -DDE quantitation. Technique sensitivity was evaluated by comparing the instrumental detection limits (IDLs) of 15 $MeSO_2$-PCBs and 3-$MeSO_2$-DDE to the corresponding method detection limits (MDLs) and practical quantitation limits (PQLs) determined from CHC-free lipid extracts of polar bear liver. The stability of ECD, SIM, and TIC molar response factors (MRFs) for the same $MeSO_2$-PCBs and 3-$MeSO_2$-DDE were determined over a mass range from ~1 to 2 ng down to PQL levels. The constancy of the relative MRFs (RMRFs) to an internal standard among congeners was evaluated to determine if isomer group RMRFs could be used for $MeSO_2$-PCB and -DDE quantitation in environmental samples.

Table 1. $MeSO_2$-PCB, $MeSO_2$-DDE, and Internal Standard Chemical Abbreviations

GC peak no. in Figure 2[a,b]	substituted biphenyl structural formula	compound abbreviation[c]
1*	3-CH_3SO_2-2,2′,4′,5-Cl_4	3-$MeSO_2$-CB49
2	4-CH_3SO_2-2,2′,5,5′-Cl_4	4-$MeSO_2$-CB52
3*	4-CH_3SO_2-2,2′,4′,5-Cl_4	4-$MeSO_2$-CB49
4	3-CH_3SO_2-2,4′,5,6-Cl_4	3-$MeSO_2$-CB64
5*	4-CH_3SO_2-2,4′,5,6-Cl_4	4-$MeSO_2$-CB64
6	3-CH_3SO_2-2,3′,4′,5-Cl_4	3-$MeSO_2$-CB70
7*	3-CH_3SO_2-2,2′,4′,5,5′-Cl_5	3-$MeSO_2$-CB101
8	4-CH_3SO_2-2,3′,4′,5-Cl_4	4-$MeSO_2$-CB70
9*	4-CH_3SO_2-2,2′,4′,5,5′-Cl_5	4-$MeSO_2$-CB101
10*	3-CH_3SO_2-DDE	3-$MeSO_2$-DDE
11*	3-CH_3SO_2-2,2′,3′,4′,5-Cl_5	3-$MeSO_2$-CB87
12*	3-CH_3SO_2-2,2′,4′,5,5′,6-Cl_6	3-$MeSO_2$-CB149
13	4-CH_3SO_2-2,2′,3′,5,5′,6′-Cl_6	4-$MeSO_2$-CB151
14*	4-CH_3SO_2-2,2′,3′,4′,5-Cl_5	4-$MeSO_2$-CB87
15*	4-CH_3SO_2-2,2′,4′,5,5′,6-Cl_6	4-$MeSO_2$-CB149
16*	3-CH_3SO_2-2,2′,3′,4′,5,6-Cl_6	3-$MeSO_2$-CB132
17*	4-CH_3SO_2-2,2′,3′,4′,5,6-Cl_6	4-$MeSO_2$-CB132
18*	3-CH_3SO_2-2,2′,3′,4′,5,5′-Cl_6	3-$MeSO_2$-CB141
19*	4-CH_3SO_2-2,2′,3′,4′,5,5′-Cl_6	4-$MeSO_2$-CB141
20*	3-CH_3SO_2-2-CH_3-2′,3′,4′,5,5′-Cl_5	IS
21*	3-CH_3SO_2-2,2′,3′,4′,5,5′,6-Cl_7	3-$MeSO_2$-CB174
22*	4-CH_3SO_2-2,2′,3′,4′,5,5′,6-Cl_7	4-$MeSO_2$-CB174
	3-CH_3SO_2-2,2′,5,5′-Cl_4	3-$MeSO_2$-CB52
	4-CH_3SO_2-2,2′,5,5′,6-Cl_5	4-$MeSO_2$-CB95
	3-CH_3SO_2-2,2′,4′,5,6-Cl_5	3-$MeSO_2$-CB91
	3-CH_3SO_2-2,3′,4′,5,6-Cl_5	3-$MeSO_2$-CB110
	4-CH_3SO_2-2,3′,4′,5,6-Cl_5	4-$MeSO_2$-CB110

[a] Standards for all compounds, except 4, 6, and 13, were used for GC-FID concentration verification. Compounds with asterisks were used for all other studies (Tables 2–4). [b] Congeners 19, 21, and 22 were not spiked to herring gull egg, and congeners 12, 14, and 16 were not spiked to polar bear liver and adipose tissue for percent recovery determinations (Table 2). $MeSO_2$-PCB congeners not numbered have not been identified in environmental samples to date. [c] Based on IUPAC numbering of precursor PCB congener.[18] CB stands for chlorobiphenyl.

EXPERIMENTAL SECTION

Chemicals and Standards. $MeSO_2$-PCBs, 3-$MeSO_2$-DDE, and the internal standard (IS), 3-$MeSO_2$-2-methyl-5-2′,3′,4′,5′-pentachlorobiphenyl, were synthesized as described previously.[17] The $MeSO_2$-PCB and -DDE metabolite chemical names were abbreviated and simplified (Table 1) on the basis of the IUPAC-derived numbering system of the parent PCBs.[18] The PCB standard mixtures, CLB-1-D and CLB-1-C, were obtained from the National Research Council (NRC) of Canada. TCPMeOH was purchased from MTM Research Chemicals (Lancaster Synthesis Inc., Windham, NH). All solvents were of analytical grade or better.

Verification of Standard Concentrations. Two standard mixtures (nominal concentration 60 ng μL^{-1} per congener), one with 15 $MeSO_2$-PCBs (Table 1), IS, and 11 dichloro- to octachloro-PCBs (NRC-CLB-1-C) and the other with seven $MeSO_2$-PCBs (Table 1), 3-$MeSO_2$-DDE, IS, and the NRC-CLB-1-C solution, were analyzed by on-column injection GC with flame ionization detection (GC-FID) to verify the concentration of the standards. GC-FID conditions are given below. FID response of halogenated hydrocarbons, even those containing heteroatoms, has been shown to be relatively constant when adjusted for the fraction of the molecular weight that is carbon.[19,20] Two standard mixtures were

(14) Haraguchi, K.; Kuroki, H.; Masuda, Y. *J. Anal. Toxicol.* **1984**, *8*, 177–181.
(15) Zook, D. R.; Buser, H.-R.; Bergqvist, P.-A.; Rappe, C.; Olsson, M. *Ambio* **1991**, *21*, 557–560.
(16) Jarman, W. M.; Simon, M.; Norstrom, R. J.; Burns, S. A.; Bacon, C. A.; Simoneit, B. R. T.; Riseborough, R. W. *Environ. Sci. Technol.* **1992**, *26*, 1770–1774.
(17) Haraguchi, K.; Bergman, Å.; Jakobsson, E.; Masuda, Y. *Fresenius J. Anal. Chem.* **1993**, *347*, 441–449.
(18) Ballschmiter, K.; Mennel, A.; Buyten, J. *Fresenius J. Anal. Chem.* **1993**, *346*, 396–402.

prepared to ensure complete GC resolution of the $MeSO_2$-PCBs, 3-$MeSO_2$-DDE, and IS, and the molar carbon response factors (MCRFs) were determined in triplicate. The mean MCRF among the 11 PCB congeners in the primary standard was 5.89 ± 1.15 peak area counts pg^{-1} injected total carbon wt^{-1} of the molecular wt. The mean MCRF of the 22 $MeSO_2$-PCB congeners, 3-$MeSO_2$-DDE, and IS (Table 1) was 5.57 ± 1.98 peak area counts pg^{-1} injected total carbon wt^{-1} of the molecular wt. MCRFs of 3-$MeSO_2$-DDE and five out of the 22 $MeSO_2$-PCB standards fell outside the mean ± SD range for PCBs. If these five $MeSO_2$-PCBs and 3-$MeSO_2$-DDE were excluded, the mean MCRF of the remaining 17 $MeSO_2$-PCB and IS standards was 5.82 ± 1.05, the same as that of the PCBs. Therefore, the nominal concentrations of the six outliers were adjusted by multiplying by the ratio of their MCRFs by the average MCRF of the PCB and other $MeSO_2$-PCB standards.

Column Chromatographic Materials and Apparatus. Florisil (magnesium silicate, BDH Chemical Inc., Toronto, Canada; pesticide analysis grade, 60–100 mesh) was activated at 600 °C overnight, cooled to 100 °C, deactivated with 1.2% (w/w) doubly distilled, *n*-hexane-washed water, and stored in a capped (Teflon-lined) glass bottle. Basic aluminum oxide (Fisher Scientific Inc., Ottawa, Canada; activity grade I, 60–325 mesh) and silica gel (Bio-Rad Laboratories, Richmond, CA; Bio-sil A, 100–200 mesh) were activated at 300 °C and 180 °C, respectively, for 3 h. The activated materials were stored at 100 °C in an open top glass bottle for no more than 1 month before reactivation. The basic alumina was deactivated with 2.3% (w/w) doubly distilled, *n*-hexane-washed water 0.5 h prior to use. Potassium hydroxide (KOH)/silica gel (33% KOH (w/w)) was prepared by combining 1 M KOH (Fisher Scientific Inc.; prepared with *n*-hexane-washed, doubly distilled water) with the appropriate amount of activated silica gel 0.5 h prior to use. Sodium sulfate (BDH Chemical Inc.; anhydrous, granular, analytical grade) was washed with 50:50 dichloromethane/*n*-hexane, air-evaporated overnight, activated at 650 °C overnight, cooled to room temperature, and stored in a Teflon-lined, capped bottle. GPC was performed using an ABC Laboratories automated system. A 2.5 cm diameter column was packed with 60 g of SX-3 Envirobeads (ABC Laboratories, Columbia, MO; 200–400 mesh) after presoaking ~1 h in 50:50 dichloromethane/*n*-hexane. Pyrex glass columns 1.0 cm in diameter were used for all liquid chromatography.

Tissue Sample Preparation, Standard Spiking, and Extraction. Samples archived at −40 °C in the specimen bank at the National Wildlife Research Centre in Hull, PQ, Canada, were used for method validation. Lake Ontario (1989) herring gull (*Larus argentatus*) egg and Lake Huron (1985) smelt (*Osmerus mordax*) samples were obtained from composites of 118 and 300 individual samples, respectively. Polar bear (*Ursus maritimus*) liver homogenate and minced adipose samples were from an adult male collected in 1993 from the Resolute Bay area of the Northwest Territories, Canada.

Homogenized or minced samples were dehydrated by grinding with sodium sulfate in a 1:5 weight ratio. Tissue substrates for method validation were spiked with one of three standard mixtures (Table 1; Figure 1, position A) consisting of 15 or 12 $MeSO_2$-PCBs, 3-$MeSO_2$-DDE, and IS (Table 1). Spiked $MeSO_2$-PCB and -DDE levels (50 μL of 52–552 pg $μL^{-1}$) approximately matched native

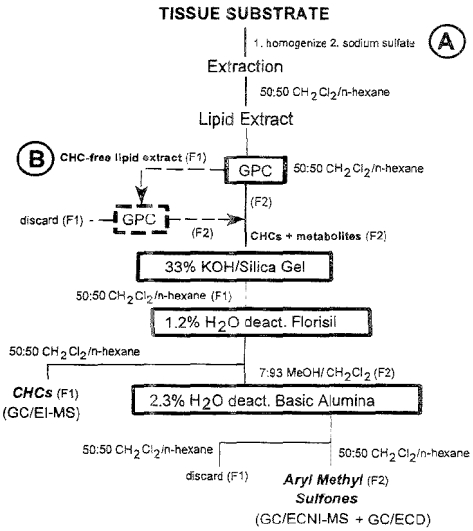

Figure 1. Schematic diagram of column chromatography methodology. $MeSO_2$-PCB, 3-$MeSO_2$-DDE, and IS standards were spiked at point A and $MeSO_2$-PCB, 3-$MeSO_2$-DDE, IS, PCB, and TCPMeOH standards at point B (Table 1) for method validation. The part of the schematic in dashed lines was for method validation with contaminant-free lipid extracts only. Extraction volumes are given in the Contaminant Enrichment and Cleanup section.

levels in 0.5 g wet wt of polar bear liver and adipose tissue to minimize error due to subtraction of GC-ECD peak areas. Native levels in herring gull egg (5.0 g) and smelt (15.0 g) were low ng g^{-1} wet wt level and nondetectable, respectively, and therefore did not require spiking concentration adjustment. Herring gull egg and smelt homogenates were spiked with the same concentrations of $MeSO_2$-PCB, 3-$MeSO_2$-DDE, and IS standards used for contaminant-free lipid extracts (see below). Lipid extracts were obtained by column extraction with 80 mL of 50:50 dichloromethane/*n*-hexane. The dump cycle of gel-permeation chromatography (GPC, see next section) was essentially free of CHCs. However, CHCs such as chlorinated paraffins are similar in molecular size to long chain lipids.[21] GPC separation is based largely on size exclusion, and therefore chlorinated paraffins, if present in the sample, coelute with the lipid extract. The lipid extract was considered "contaminant-free" since remaining chlorinated paraffins would be removed by the second GPC loop. The GPC dump cycle was spiked with 50 μL of a CLB-1-D PCB (30–295 pg $μL^{-1}$) and TCPMeOH (500 pg $μL^{-1}$) standard mixture and 50 μL of a 15 $MeSO_2$-PCB (211–604 pg $μL^{-1}$), 3-$MeSO_2$-DDE (595 pg $μL^{-1}$), and IS (436 pg $μL^{-1}$) standard mixture (Table 1) prior to a second cycle of the GPC (Figure 1, position B). Contaminant-free lipid extract weights and $MeSO_2$-PCB and $MeSO_2$-DDE spiking levels were chosen to simulate coextracted lipid loads and $MeSO_2$-metabolite levels encountered in the analysis of polar bear liver and adipose tissue.[8,9] PCBs were spiked only to contaminant-free lipid extracts because of relatively high natural PCB levels in the tissue substrates.

(19) Yiehu, H.; Qingyu, O.; Weile, Y. *Anal. Chem.* **1990**, *62*, 2063–2064.
(20) Tong, H. Y.; Karasek, F. W. *Anal. Chem.* **1984**, *56*, 2124–2128.
(21) Jansson, B.; Andersson, R.; Asplund, L.; Bergman, Å.; Litzén, K.; Nylund, K.; Reutergårdh, L.; Sellström, U.; Uvemo, U.-B.; Wahlberg, C.; Wideqvist, U. *Fresenius J. Anal. Chem.* **1991**, *340*, 439–445.

Contaminant Enrichment and Cleanup Procedure. The first step in enrichment involved removal of lipids by GPC.[22] After rotary evaporation, the lipid extract was diluted to 10 mL with 50:50 dichloromethane/*n*-hexane. An accurate 10% volumetric portion was removed to determine lipid gravimetrically.[8] The remaining volume was readjusted to 10 mL, vortexed, and loaded onto the GPC. The first 140 mL fraction, containing the lipids, was dumped or used for contaminant-free spiking. The second fraction (150 mL), containing CHCs and metabolites, was collected, reduced in volume to ~2 mL by rotary evaporation, and eluted through the 33% KOH/silica gel column (1.5 g) with 50 mL of 50:50 dichloromethane/*n*-hexane. The extract volume was reduced to ~1 mL and chromatographed on Florisil (8.0 g). The first fraction (75 mL of 50:50 dichloromethane/*n*-hexane) contained all routinely determined CHCs, including PCBs and TCPMeOH, substantially the same as the sum of the three fractions in the method outlined in Norstrom et al.[22,23] The second fraction (80 mL of 7:93 methanol/dichloromethane) contained the aryl methyl sulfones. This fraction was rotary evaporated at 30 °C under reduced pressure until just dry. The residue was redissolved in *n*-hexane and chromatographed on a 2.3% H_2O deactivated basic alumina column (3.0 g). The first 10 mL of 50:50 dichloromethane/*n*-hexane was discarded, and the second 40 mL fraction, containing aryl methyl sulfones, was collected using the same solvent mixture. The aryl methyl sulfone and CHC fractions were adjusted to 1–2 mL by rotary evaporation and quantitatively transferred to 5 mL, acid-washed borosilicate glass vials with 3 × 0.5 mL *n*-hexane washes and ~50 μL of 2,2,4-trimethylpentane. The volume was reduced to ~100 μL by a gentle stream of N_2 gas (99.99% purified) at ambient room temperature. The vial sides were washed down with ~100 μL of 2,2,4-trimethylpentane, and the volume was adjusted very slowly at ambient temperature by N_2-assisted solvent evaporation to 50 μL, followed by brief vortexing and transfer to a GC injection vial.

Instrumental Analysis. *GC-ECD.* Capillary GC-ECD was performed on a Hewlett-Packard (Palo Alto, CA) 5890 equipped with a ^{63}Ni ECD detector and HP 7673A automatic injector. The GC was fitted with a fused silica, Rtx-5 capillary column (Restek Corp., Bellefonte, PA; 30 m, 0.25 mm i.d., 0.1 μm film thickness, cross-linked 95% dimethyl–5% diphenyl polysiloxane). The carrier gas and ECD makeup gas were helium and 5% methane–95% argon, respectively. All injections were 2 μL in volume and made in the splitless mode. GC conditions and temperature ramping were optimized for $MeSO_2$-PCB and -DDE separation.[8] The injector and detector temperatures were set at 270 °C and 330 °C, respectively, and the GC oven temperature program was as follows: initial temperature held at 100 °C for 3 min, 20 °C/min to 220 °C, and 3 °C/min to 280 °C. For PCBs and TCPMeOH, the injector and detector temperatures were 250 °C and 320 °C, respectively, and the GC oven temperature program was as follows: initial temperature held at 70 °C for 2 min, 5 °C/min to 150 °C, and 3 °C/min to 250 °C.

GC-FID. The instrument and capillary column for validation of $MeSO_2$-PCB and -DDE standard concentrations were the same as for GC-ECD. The $MeSO_2$-PCB and -DDE and IS injection technique was cold on-column using the "four-segment injection" approach:[20] 0.5 μL of pure solvent (2,2,4-trimethylpentane), 0.5 μL of air, 0.6 μL of sample, and 0.8 μL of air. On-column injection was used to prevent discrimination of high molecular weight compounds. The detector temperature was 350 °C, and the GC oven temperature program was as follows: initial temperature held at 85 °C for 3 min, 20 °C/min to 200 °C, and 2.2 °C/min to 265 °C. The carrier gas was helium. The makeup gas had a total flow rate of 440 mL/min (380 mL/min compressed air, 30 mL/min helium, and 30 mL/min hydrogen).

GC/ECNI-MS. Total ion current (TIC) scanning was from 83 to 550 amu. The $(M)^-$ and $(M + 2)^-$ ions were scanned in the selected ion monitoring (SIM) mode, and the sum of their responses was determined for each congener. The ions scanned were *m/z* 368/370, 404/406, 438/440, 472/474, 418/420, and 394/396 for the tetrachloro- to heptachloro-$MeSO_2$-PCB isomer groups, IS, and 3-$MeSO_2$-DDE, respectively. GC/ECNI-MS was performed on a HP 5985 mass spectrometer upgraded with an HP 5890 series II gas chromatograph coupled with an HP 5988 GC/MS direct interface. The GC column was the same as that used for GC-ECD and operated in the splitless mode. The carrier and reagent gases were helium and methane (0.5 Torr), respectively. The instrument was tuned with perfluorotributylamine (PFTBA) at *m/z* 312, 414, and 595 for optimal conditioning. The emission current was 300 μA, and the electron voltage was 130 eV. The injection port, transfer line, and ion source temperatures were 270 °C, 260 °C, and 200 °C, respectively. The oven temperature program was the same as that used for GC-ECD. A 2 μL volume was used for all splitless injections.

Determination of Recoveries by GC-ECD. All analyses were done in triplicate. For the contaminant-free lipid extracts, herring gull egg, and smelt substrates, areas of the $MeSO_2$-PCB, 3-$MeSO_2$-DDE, PCB, and TCPMeOH peaks relative to the IS were compared to those in an external standard to determine percent recoveries. The native $MeSO_2$-PCB and 3-$MeSO_2$-DDE congener levels in polar bear liver and fat substrates were first determined by GC-ECD, and 12 of the $MeSO_2$-PCB and 3-$MeSO_2$-DDE standards were spiked to a second set of 0.5 g samples at matching levels. A spike of 100 μL of 100 pg μL^{-1} IS was also added (Figure 1, position A). The sample size was adjusted so that native $MeSO_2$-PCB and -DDE levels in the final fraction were in the 25–500 pg μL^{-1} range.[8,24] The GC-ECD peak area contributions of the analytes of the unspiked replicates ($n = 3$) were subtracted from the spiked replicates ($n = 3$) for the tissue substrates. The difference in peak areas was compared to the original $MeSO_2$-PCB and -DDE standards to determine percent recoveries for method validation.

$MeSO_2$-PCB and $MeSO_2$-DDE Response Parameters. A separate mixture of ~1 ng μL^{-1} per congener of the 15 $MeSO_2$-PCB, 3-$MeSO_2$-DDE, and IS standards used for method validation (Table 1) was prepared and serially diluted down to ~0.01 pg μL^{-1}. The IDLs for ECD, SIM ($(M)^- + (M + 2)^-$), and TIC for each congener were defined as the mass in picograms giving a signal-to-noise (S/N) ratio of 3.[25] Replicate ($n = 7$) 0.5 g wet wt equiv of polar bear liver, contaminant-free lipid extract samples were spiked with the standard mixture at concentrations near the

(22) Norstrom, R. J.; Simon, M.; Mulvihill, M. J. *Int. J. Environ. Anal. Chem.* **1986**, *23*, 267–287.
(23) Norstrom, R. J.; Simon, M.; Muir, D. C. G.; Schweinsburg, R. *Environ. Sci. Technol.* **1988**, *22*, 1063–1071.
(24) Letcher, R. J.; Norstrom, R. J.; Bergman, Å.; Muir, D. C. G. *Dioxin '92. Organohalogen Compounds*; Tampere, Finland, Aug 24–28, 1992; Finnish Institute of Occupational Health: Helsinki, Finland, 1992; Vol. 8, pp 357–360.
(25) MacDougall, D.; Lal, J.; Amore, F. J.; Langner, R. R.; Cox, G. V.; McClelland, N. I.; Crosby, D. G.; Phillips, W. F.; Freeman, D. H.; Pojasek, R. P.; Gibbs, W. E.; Sievers, R. E.; Gordon, G. E.; Keith, L. H. *Anal. Chem.* **1980**, *52*, 2242–2249.

Table 2. Mean Percent Recoveries for $MeSO_2$-PCBs, 3-$MeSO_2$-DDE, and the Internal Standard from Tissue Substrates and $MeSO_2$-PCBs, 3-$MeSO_2$-DDE, IS, PCBs, and TCPMeOH from Contaminant-Free Lipid Extracts Determined by GC-ECD

	herring gull egg	smelt	polar bear liver	polar bear adipose
	Tissue Substrates[a]			
wet wt (g)	5.0	15.0	0.5	0.5
% lipid	10.0	4.4	2.7	65.0
	Methyl Sulfones			
mean % recovery	77 ± 5	78 ± 4	83 ± 5	83 ± 3
relative mean % recovery[b]	88 ± 6	104 ± 5	108 ± 7	104 ± 4
	Contaminant-Free Lipid Extracts[a]			
lipid extract wt (g)	0.18	0.15	0.019	0.65
	Methyl Sulfones			
mean % recovery	78 ± 5	75 ± 3	76 ± 4	80 ± 3
relative mean % recovery[a]	105 ± 7	105 ± 3	102 ± 5	102 ± 4
	PCBs			
mean % recovery	75 ± 7	79 ± 1	84 ± 5	79 ± 3
relative mean % recovery[b]	101 ± 9	110 ± 3	113 ± 7	100 ± 4
	TCPMeOH			
relative mean % recovery[b]	116 ± 2	110 ± 3	114 ± 2	99 ± 3

[a] ±SD among congeners. See Table 1 for congener structures in each matrix spike. There are 14 dichloro- to octachloro-PCBs in the NRC-CLB-1-D solution. [b] Relative to the IS.

IDL for determination of the corresponding MDLs. The MDLs were defined as three times the significance of variation (SV) calculated using Student's t statistic. The SVs were calculated from the SDs (n = 7) using the appropriate Student t-values according to

$$SV = SD_{MDL} t_{(n-1, 95\%)} \quad (1)$$

where $t_{(n-1, 95\%)}$ was the t-distribution constant for $n - 1$ degrees of freedom at the 95% confidence level. The commonly accepted MDL is 3 SV, and the practical quantitation limit (PQL) is 10 SV (i.e., 3.3 MDL).[25,26]

MRFs for ECD, SIM, and TIC were determined in triplicate at several concentrations from ~1000–1700 pg down to the MDLs to determine the linear concentration range. The variance in the MRFs, IDLs, and MDLs were assessed by a one-way analysis of variance (ANOVA) using Quattro Pro 6.0 (Novell Inc., Orem, UT). The significance level of the TIC response variance was 95% for n = 3 replicates at a given concentration and n = 6 concentrations. There were n = 7 different concentrations for ECD and SIM. The MRFs relative to the IS (RMRF) were also calculated.

RESULTS

Recovery Studies. The 15 $MeSO_2$-PCB standards chosen for method validation (Table 1) represented a majority of the 22 congeners identified so far in biota.[8,9,12,13,24] The mean percent recoveries obtained for the analyte standards spiked to tissue substrates and contaminant-free lipid extracts are shown in Table 2. Percent recoveries were consistently greater than ~75% regardless of tissue matrix or variation in sample weight. The SDs of the mean recoveries indicated that there was no significant discrimination among $MeSO_2$-PCBs, 3-$MeSO_2$-DDE, IS, PCBs, and TCPMeOH, substrates or sample weights. High method precision

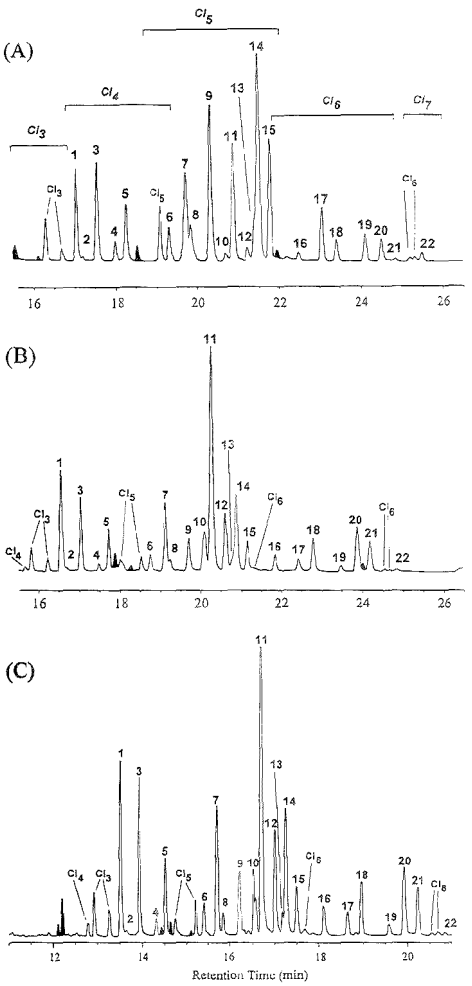

Figure 2. Chromatograms of the aryl methyl sulfone fraction obtained from the column chromatography methodology: (A) GC-ECD of polar bear fat, (B) GC-ECD of polar bear liver, and (C) GC/ECNI-MS(TIC) of polar bear liver. Peaks numbers refer to the $MeSO_2$-PCB and -DDE structures in Table 1. Peaks denoted Cl_x were identified as $MeSO_2$-PCB isomers by GC/ECNI-MS(TIC). The approximate GC elution window for $MeSO_2$-PCB isomer groups are denoted in chromatogram A. The shaded peaks were non-$MeSO_2$-PCB or -DDE compounds.

was indicated by the low SD of percent recovery of individual congeners, which ranged from 0.3% to 10% but was generally between 1% and 6% (not shown).

$MeSO_2$-PCB and -DDE Congener Identity and Method Cleanup Efficiency. GC-ECD chromatograms of the aryl methyl sulfone fraction of unspiked polar bear fat and liver samples are shown in Figure 2A,B, and the GC/ECNI-MS(TIC) mass chromatogram of unspiked polar bear liver is shown in Figure 2C. Virtually all of the peaks were identified as specific $MeSO_2$-PCB congeners by comparison to authentic standards or as isomeric

(26) Tuner, W. E.; Patterson, D. G., Jr.; Isaacs, S. G.; Alexander, L. R. *Chemosphere* 1992, *25*, 793–804.

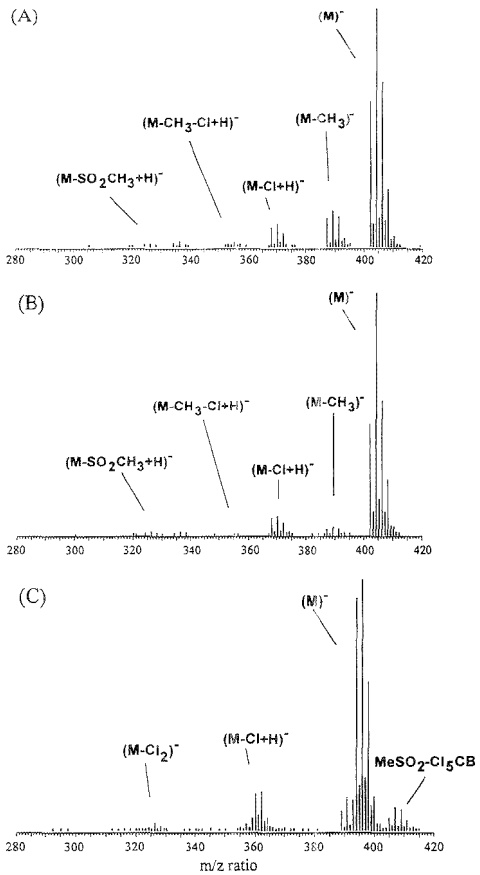

Figure 3. Representative ECNI mass spectra for (A) 3-$MeSO_2$-CB101, (B) 4-$MeSO_2$-CB101, and (C) 3-$MeSO_2$-DDE selected from the mass chromatogram of the aryl methyl sulfone fraction from polar bear liver (Figure 2). The molecular and major fragment ions are labeled. A $MeSO_2$-Cl_5CB impurity coeluted with 3-$MeSO_2$-DDE and is labeled.

$MeSO_2$-PCBs from the GC/ECNI-MS mass spectra. Native levels of total $MeSO_2$-PCBs in polar bear liver and fat samples were ~2000 and ~400 ng g^{-1} on a lipid weight basis, respectively, consistent with results found previously.[8,24]

The $MeSO_2$-PCB and -DDE congener pattern in herring gull egg (not shown) was similar to that in polar bear adipose and liver (Figure 2). Herring gull egg had relatively high native levels of total $MeSO_2$-PCBs, estimated to be ~150 ng g^{-1} on a lipid weight basis. Despite substantial levels of PCBs and other CHCs, aryl methyl sulfones were not detectable in smelt. The aryl methyl sulfone elution window for smelt and herring gull egg substrates was also essentially free of interferences for both GC-ECD and TIC (not shown).

GC/ECNI-MS mass spectra of native 3- and 4-$MeSO_2$-CB101 and 3-$MeSO_2$-DDE (peaks 7, 9, and 10, respectively, Figure 2C) in polar bear liver are shown in Figure 3A–C, respectively. All ions arose from molecular and fragment anions of $MeSO_2$-PCBs

Table 3. Mean Instrumental and Method Detection Limits for $MeSO_2$-PCBs, 3-$MeSO_2$-DDE, and the Internal Standard

		GC/ECNI-MS	
	GC-ECD	SIM	TIC
IDL (pg)[a,c]	0.23 (87) [24]	0.08 (47) [34]	0.99 (37) [4]
MDL (pg)[b,c]	6.15 (85) [19]	0.55 (34) [39]	11.25 (59) [31]
SV (pg)[d]	2.42	0.21	4.44

[a] IDLs of the sulfone standards used for method validation (Table 1), $n = 3$ replicates analysis for each congener. [b] For MDLs, the same standards used for IDL determination were spiked at concentration levels near the IDLs to n CHC-free polar bear liver lipid extracts (n = 6 for ECD and TIC, $n = 7$ for SIM). [c] The % CV contributions of among-congener variance (parentheses) and among-replicate variance [brackets] of total variance were determined by a one-way ANOVA. [d] Mean significance of variation (eq 1) of congener MDLs.

and -DDE. Similarly clean mass spectra were found in the aryl methyl sulfone fraction of all four tissue substrates.

$MeSO_2$-PCB and $MeSO_2$-DDE Response Parameters. The mean MDL was generally sub-picogram for SIM and in the low picogram range for ECD and TIC (Table 3). The mean MDL to mean SV ratios were ~2.5 for the three techniques. A ratio of ~3 is acceptable for reliable, low mass quantitation. The ratio of mean MDL to mean IDL was seven for SIM, 11 for TIC, to 27 for ECD. ANOVA of the MDL and IDL data was performed to determine the relative significance of among-congener and among-replicate variance (Table 3). The among-congener variance was larger than among-replicate variance, especially for TIC. Trends in MDL and IDL values with respect to $MeSO_2$-PCB and -DDE structure were not obvious for any technique. The mean PQLs among congeners, defined as 10 SV, were 24.2 ± 4.6 pg for ECD, 2.1 ± 0.9 pg for SIM, and 44.4 ± 17.1 pg for TIC.

Mean MRFs were relatively undeviating among $MeSO_2$-PCB congeners for all three techniques, especially SIM (Table 4). There was less than a factor of 2 difference between the highest and lowest mean MRFs for each technique. There was not a pronounced tendency for mean MRFs to increase with increasing degree of chlorination from four to seven chlorines per molecule. No consistent pattern in MRF values between 3- and 4-$MeSO_2$-PCB pairs could be discerned because differences were similar to the SDs for each congener and within the expected accuracy of the standard concentrations in most cases. By far the largest difference occurred between 3- and 4-$MeSO_2$-CB101. The mean MRF for 3-$MeSO_2$-DDE was similar to those of the $MeSO_2$-PCBs. The constancy of MRFs for all congeners using the three detection techniques, over a concentration range from low picogram levels up to 1.7 ng, was similar to that represented by the four $MeSO_2$-PCBs in Figure 4. The exact threshold congener masses at which serious deviation from linearity began were not determined, but they were less than the PQL.

ANOVA of the MRF data was performed to determine the relative significance of among-mass and among-replicate variance, which are given as % CV in Table 4. The mean F-ratios among congeners for ECD (18.68 ± 14.68) and TIC (55.67 ± 38.17) far exceeded the critical value (2.51)[27] for the null hypotheses that among-mass variance was the same as among-replicate variance. Thus, the among-mass variance was significantly larger (e.g., the

(27) Pearson, E. S.; Hartley, H. O. *Biometrika Tables for Statisticans*, 2nd ed.; Cambridge University Press: Cambridge, UK, 1958; Vol. 1.

Table 4. Mean Molar Response Factors and MRFs Relative to the IS for $MeSO_2$-PCB and 3-$MeSO_2$-DDE[a]

		GC-ECD				GC/ECNI-MS							
						SIM $(M)^- + (M+2)^-$				TIC			
Cl	congener	MRF[b]		RMRF[c]		MRF[b]		RMRF[c]		MRF[b]		RMRF[c]	
Cl_4	3-$MeSO_2$-CB49	0.46	(8.6) [2.4]	0.66	(0.45)	1.33	(21.5) [13.2]	1.12	(19.6)	0.82	(9.0) [2.2]	0.78	(8.9)
	4-$MeSO_2$-CB49	0.38	(9.2) [2.2]	0.56	(5.4)	1.62	(19.4) [13.8]	1.35	(14.8)	0.81	(9.9) [4.1]	0.77	(10.4)
	4-$MeSO_2$-CB64	0.44	(8.5) [2.2]	0.63	(4.8)	1.33	(29.7) [15.6]	1.11	(22.5)	0.75	(9.7) [3.0]	0.71	(9.8)
Cl_5	3-$MeSO_2$-CB101	0.39	(7.4) [2.0]	0.57	(1.8)	0.93	(27.2) [16.5]	0.81	(21.0)	0.65	(9.0) [2.0]	0.62	(8.1)
	4-$MeSO_2$-CB101	0.56	(8.3) [2.2]	0.81	(2.5)	0.73	(17.0) [16.2]	0.61	(18.0)	0.86	(8.1) [2.7]	0.82	(9.8)
	3-$MeSO_2$-CB87	0.62	(9.1) [2.2]	0.89	(4.5)	1.24	(28.0) [22.7]	1.04	(24.0)	0.96	(12.1) [2.3]	0.90	(10.0)
	4-$MeSO_2$-CB87	0.66	(9.5) [2.2]	0.95	(4.2)	1.29	(18.7) [5.8]	1.08	(7.4)	1.18	(9.6) [3.4]	1.12	(10.7)
Cl_6	3-$MeSO_2$-CB149	0.63	(6.2) [2.1]	0.91	(3.3)	1.34	(21.5) [13.4]	1.12	(17.8)	1.06	(11.5) [2.5]	1.01	(8.9)
	4-$MeSO_2$-CB149	0.57	(8.7) [2.6]	0.82	(4.9)	1.45	(21.5) [15.0]	1.22	(21.3)	0.99	(10.8) [3.0]	0.93	(6.4)
	3-$MeSO_2$-CB132	0.67	(6.5) [2.4]	0.96	(1.0)	1.45	(26.1) [14.3]	1.22	(22.1)	1.11	(9.6) [1.7]	1.06	(9.4)
	4-$MeSO_2$-CB132	0.58	(5.5) [2.2]	0.84	(2.4)	1.35	(29.0) [18.0]	1.13	(22.1)	0.95	(13.0) [2.0]	0.90	(12.2)
	3-$MeSO_2$-CB141	0.65	(8.6) [2.4]	0.95	(2.1)	1.39	(29.0) [27.1]	1.17	(28.2)	1.16	(12.4) [3.9]	1.10	(7.3)
	4-$MeSO_2$-CB141	0.64	(6.7) [2.3]	0.93	(1.1)	1.62	(28.4) [14.2]	1.36	(22.0)	1.15	(13.1) [2.0]	1.09	(9.2)
Cl_7	3-$MeSO_2$-CB174	0.75	(6.0) [2.4]	1.09	(2.8)	1.20	(25.6) [15.3]	1.01	(21.8)	1.14	(14.1) [3.6]	1.08	(8.3)
	4-$MeSO_2$-CB174	0.59	(4.6) [2.6]	0.85	(2.4)	1.06	(16.0) [17.4]	0.89	(19.1)	0.96	(15.0) [2.8]	0.91	(5.5)
	mean % CV		(7.6) [2.3]				(23.9) [15.9]				(11.1) [2.7]		
	mean total % CV		(9.9)		(3.2)		(39.8)		(20.1)		(13.8)		(9.0)
	3-$MeSO_2$-DDE	0.70	(9.4) [1.9]	1.02	(7.8)	1.51	(24.1) [16.5]	1.26	(20.6)	1.06	(12.6) [1.8]	1.02	(17.6)
	IS	0.69	(5.6) [2.3]			1.20	(13.0) [5.4]			1.06	(13.4) [3.3]		

[a] MRF × 10^{18} (peak area counts/mol) for analysis at i mass levels from ~20 to 1700 pg for ECD and TIC and from ~20 to 600 pg for SIM: i = 7 for GC-ECD and GC/ECNI-MS(SIM) and i = 6 for GC/ECNI-MS(TIC). At each i mass level, n = 3 replicates. [b] The % CV contributions of among-mass variance (parentheses) and among-replicate variance [brackets] of total variance were determined by a one-way ANOVA. See Results section for the F-statistics. [c] The % CV (parentheses) is for the total variance.

mean % CV for ECD was 7.6) than among-replicate variance (e.g., the mean % CV for ECD was 2.3) for these techniques (Table 4). The mean F-ratio among congeners (3.04 ± 2.24) and F-critical value (2.85)[27] were very close for SIM, indicating that among-replicate variance was closer to, but still not significantly higher than, among-mass variance for this technique. Mean MRFs for SIM also had the greatest total variance. It therefore appears that SIM is an inherently less reliable technique than ECD and TIC.

The mean MRFs relative to the IS (RMRFs) ranged from 0.6 to 1.4 for all three techniques (Table 4). The total % CV of the mean RMRFs were less than the total % CV of the corresponding mean MRFs. The deviation from linearity of MRFs for ECD and TIC at low concentrations (Figure 4A,B) was improved slightly after conversion to RMRFs. In contrast, RMRFs for SIM declined more at low concentrations than did MRFs (Figure 4C). Fluctuations in the congener MRFs for SIM over the entire concentration range were not reduced after conversion to RMRFs.

DISCUSSION

Extraction and Cleanup/Qualitative Analysis. The present column chromatography-based extraction and cleanup method (Figure 1) is simple and nondestructive and is applicable to determination of CHCs in a wide range of animal tissue substrates. Although the method was not validated for all CHC compound classes normally determined, the normal range in polarity (elution order from Florisil and alumina columns) was spanned by PCBs and TCPMeOH. The method was extended to the even more polar aryl methyl sulfones. This method is therefore suitable for multiresidue, routine determination of CHCs, including aryl methyl sulfones, in animal tissues. The method has advantages over those previously used for aryl methyl sulfones, which included liquid–liquid partitioning steps[2,9–13] or saponification.[11,14] There is a risk of analyte loss or fraction contamination using liquid–liquid partitioning. Strong acid and base conditions destroy some CHCs, rendering these methods unsuitable for multiresidue analysis. For example, higher chlorinated dibenzo-*p*-dioxins are base labile,[28] and the oxygenated organochlorines, oxychlordane and dieldrin, are strong acid labile.[29]

Most coextracting biogenic material was separated from CHCs by GPC. Under the same operating conditions, GPC has been shown to remove ~99% of long-chain lipids and about half of the carotenoid pigments from chicken egg yolk.[22] Residual acidic biogenic material remaining in the CHC fraction after GPC is also retained. In a separate experiment, we were able to retain approximately half the lipid extract weight from polar bear adipose tissue on the 33% (w/w) KOH-impregnated silica gel column.

The aryl methyl sulfones were cleanly separated from other CHCs, including TCPMeOH, by chromatography on 1.2% water-deactivated Florisil. The aryl methyl sulfones require high-polarity solvents for quantitative elution from Florisil. Neat methanol has been used for elution of $MeSO_2$-PCBs and -DDE with no further cleanup, although significant levels of residual interferences were observed in the aryl methyl sulfone fraction.[15,30] The presence of long-chain lipids was unlikely since lipid extracts had been subject to GPC prior to Florisil. However, residual interferences from polar compounds with smaller molecular diameters, such as retinols and sterols, may have coeluted in the aryl methyl sulfone fraction. These compounds are sufficiently electrophilic as a result of conjugation or oxygenation to be ECD and ECNI-MS responsive.[31] In the present study, a 7:93 methanol/dichloromethane solvent mixture eluted $MeSO_2$-PCBs and -DDE while retaining residual colored biogenic coextractants. Color retention was

(28) Lamparski, L. L.; Nestrick, T. J.; Stehl, R. H. *Anal. Chem.* **1979**, *51*, 1453–1458.
(29) Smith, L. M.; Stalling, D. L.; Johnson, J. L. *Anal. Chem.* **1984**, *56*, 1830–1842.
(30) Buser, H.-R.; Zook, D. R.; Rappe, C. *Anal. Chem.* **1992**, *64*, 1176–1183.
(31) Gurr, M. I.; James, A. T. *Lipid Biochemistry: An Introduction*, 3rd ed.; Chapman and Hall: London, 1980; Chapters 1 and 3.

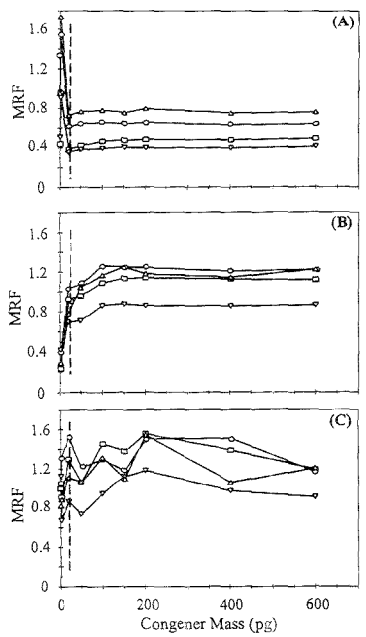

Figure 4. Mean molar response factor (MRF, peak area counts/mol of compound × 10^{18}, n = 3 per point) profile of representative $MeSO_2$-PCBs over a concentration range commonly used for determination of CHCs[8,9,12,13,33] by (A) GC-ECD, (B) GC/ECNI-MS(TIC), and (C) GC/ECNI-MS(SIM). □, 3-$MeSO_2$-CB49; ▽, 3-$MeSO_2$-CB101; ○, 3-$MeSO_2$-CB149; and △, 3-$MeSO_2$-CB174. Error bars on individual points were not shown for clarity; see Table 4 for response variation contributions of the mean MRFs. The vertical line denotes the approximate low mass limit of MRF linearity.

especially obvious for polar bear liver. Some interferences were observed in the ECD and TIC chromatograms after Florisil, but these mostly eluted prior to the aryl methyl sulfone elution window. Remaining interferences in the aryl methyl sulfone window were removed by the 2.3% H_2O-deactivated basic alumina column, giving clean chromatograms for all three techniques (Figure 2). Five or fewer minor peaks in the aryl methyl sulfone elution windows of polar bear adipose (Figure 2A) and polar bear liver (Figure 2B,C) were not $MeSO_2$-PCB or -DDE compounds. The lack of interfering ions in the ECNI mass spectra for $MeSO_2$-PCBs and -DDEs from polar bear liver (Figure 3) also emphasized the absence of non-aryl sulfone compounds. Furthermore, the $(M)^-/(M + 2)^-$ ion abundance ratios of ~50:100 and 60:100 for 3- and 4-$MeSO_2$-CB101, respectively (Figure 3A,B), resembled the ideal 61.5:100 ratio for pentachloro-$MeSO_2$-PCBs. The recently reported bis(4-chlorophenyl) sulfone (BCPS) in fish from the Baltic Sea[32] was found by ECNI-MS in the herring gull egg sample. BCPS eluted in the aryl methyl sulfone window among the hexachloro-$MeSO_2$-PCB congeners. It is therefore possible that the present method is suitable for determination of diaryl sulfones.

ECD and ECNI-MS Quantitation. Internal standard correction improved accuracy of $MeSO_2$-PCB/DDE analysis but overcompensated for PCB and TCPMeOH recovery in smelt and polar bear liver. Approximately 10% of the losses in the present study were subsequently shown to have occurred because of incomplete sample loading in the GPC step. Recoveries of all analytes from polar bear adipose and liver tissue have now been improved to ~90% by optimizing GPC operating conditions.[8,33] Good recoveries have also been obtained for standards spiked to other matrices and isolated by liquid–liquid partitioning-based methodologies. For example, ~90% recovery was achieved for five dichloro- to hexachloro-substituted $MeSO_2$-PCBs spiked to bovine fat[14] and ^{14}C-labeled $MeSO_2$-DDE spiked to rat tissues.[9] However, routine analysis using these methods has not been thoroughly demonstrated.

Precision of the whole analytical method was best demonstrated by the low variance in recoveries of $MeSO_2$-PCB and -DDE from spiked polar bear tissues. The recoveries were based on the difference between determination of native levels and spiked levels of the same compounds. The variance in the recoveries was therefore a compound variance of both spiked and unspiked determinations. In spite of this, the SD of replicate analysis of individual compounds ranged from 2% to 10%, with a mean of 6 ± 2%, well within an acceptable range for environmental analyses. The best overall precision for $MeSO_2$-PCB and -DDE determination was obtained in the analysis of smelt. The mean SD of replicate determinations was 2.0 ± 1.1%. Precision of determination of PCBs and TCPMeOH in contaminant-free lipid extracts was also excellent. Only one out of 60 triplicate recovery determinations for the PCBs and TCPMeOH had a SD >7%. The SD of the mean recovery among $MeSO_2$-PCB and PCB congeners was <9%, indicating no discrimination among CHCs, regardless of compound class or degree and position of chlorine substitution.

The electron-capturing ability of PCBs[31] is enhanced by the presence of the electronegative $MeSO_2$ functional group;[17,30] therefore, instrument detection limits were generally subpicogram for all three techniques (Table 4). These detection limits were lower by an order of magnitude relative to those previously reported for SIM and TIC, which ranged from 2 to 6 pg and 30 to 88 pg for SIM and TIC, respectively.[17] Sensitivity in the latter study may have been decreased by oxygen reactions in the ion source, since $(M - Cl + O)^-$ fragment ions were abundant.

Method detection limits for $MeSO_2$-PCB and -DDE quantitation increased in the order SIM < ECD ≤ TIC (Table 3). Therefore, if extremely high sensitivity is required, SIM is the best detection technique, capable of subpicogram detection. The low-picogram detection limits of ECD and TIC were close enough that other criteria need to be considered to choose between them. In samples analyzed to date, the separation of aryl methyl sulfones from potential interferences has been so effective that ECD could be chosen because of significantly lower cost. However, if GC/ECNI-MS instrumentation is available, determination using TIC has the added benefit that the spectra can be checked for possible interferences.

Linearity of ECD response in determination of $MeSO_2$-PCBs has been assumed in previous studies.[8,9,12,13] Knowledge of the response stability over a practical concentration range is necessary for the most precise and accurate quantitation.[25] Therefore, in the present study, linearity was tested over the low picogram to nanogram range for all three detection techniques (Figure 4). This

(32) Olsson, A.; Bergman, Å. *Ambio* **1995**, *24*, 119–123.

(33) Letcher, R. J.; Norstrom, R. J.; Bandiera, S. M.; Ramsay, M. A. *Toxicol. Appl. Pharmacol.*, in press.

(34) Stemmler, E.; Hites, A. *Biomed. Mass Spectrom.* **1988**, *17*, 311–328.

covers the range of masses usually injected for GC-ECD quantitation of $MeSO_2$-PCBs and -DDE in environmental samples.[8,9,12,13,24,33]

ECD was the most linear of the three techniques, as evidenced by minimal variation in molar response factors over the ~20–600 pg range (Figure 4A). Nonlinearity in TIC response began below 100 pg and became significantly nonlinear below 20 pg, indicating that a calibration curve would be required for accurate quantitative analysis (Figure 4B). SIM response did not fall precipitously until below 20 pg, as was the case for TIC, but response was highly variable among runs (Figure 4C). The variability of response factors among replicates was higher for SIM than ECD and TIC (Table 4). Furthermore, the total variance in response factors for SIM among congeners and over the mass range tested was very high compared to ECD and TIC. SIM response variability may have been due in part to fluctuations in fragmentation between runs. The formation of hydrogen inclusion fragment ions (e.g., $(M - Cl + H)^-$ and $(M - SO_2CH_3 + H)^-$) is known to occur by heterogeneous catalysis at the source walls and is dependent on ion source conditions like temperature and pressure.[35] Among-replicate variations in these parameters or changes in source wall condition may result in variable abundance of fragment ions and thus variable molecular ion abundance. TIC may not be as affected. Thus, in spite of superior sensitivity, the more inherent variability in the molar response factors for SIM indicates that the technique is less suitable than ECD or TIC for quantitation of $MeSO_2$-PCBs and -DDEs.

$MeSO_2$-PCB response factors relative to a single internal standard (IS) are commonly used to quantitate $MeSO_2$-PCBs and -DDEs.[8,9,12,13,24,33] The IS of choice has been a methylated $MeSO_2$-PCB, as it possesses physicochemical properties similar to those of $MeSO_2$-PCBs. The conversion of the MRFs to RMRFs made little difference to the linearity of ECD response; however, the linearity of TIC response was improved in the low picogram range. The % CV of RMRFs was lower than that of MRFs for all three methods of detection, indicating that the IS compensated for a large amount of the overall response variation (Table 4). Furthermore, the RMRFs for SIM were actually more variable (% CV ≈20%) than MRFs, indicating that a single IS is probably not satisfactory for accurate quantitative analysis by SIM.

Variation in molar response factors among $MeSO_2$-PCB congeners was significantly lower than that found for PCBs,[36] probably because the proportionate contribution of the $MeSO_2$ group to electron capturing outweighs the changes in electronegativity going from four and seven chlorines per molecule (Table 4). Variation in molar response for all three detection techniques was least among hexachloro-$MeSO_2$-PCBs, and little accuracy would be lost by using an average response factor for this group. However, the molar responses of pentachloro-$MeSO_2$-PCBs were more variable, driven largely by a low value for 3-$MeSO_2$-CB101. The RMRF of 3-$MeSO_2$-CB101 resembled those of the tetrachloro-$MeSO_2$-PCB congeners (Table 4). Most of the biologically relevant $MeSO_2$-PCB and -DDE standards are now available;[7] therefore, individual standards should be used.

(35) Stemmler, E. A.; Hites, R. A.; Arbogast, B.; Budde, W. L.; Deinzer, M. L.; Dougherty, R. C.; Eichelberger, J. W.; Foltz, R. L.; Grimm, C.; Grimsrud, E. P.; Sakashita, C.; Sears, L. J. *Anal. Chem.* **1988**, *60*, 781–787.

(36) Mullin, M. D.; Pochini, C. M.; McCrindle, S.; Romkes, M.; Safe, S. H.; Safe, L. M. *Environ. Sci. Technol.* **1984**, *18*, 468–476.

ACKNOWLEDGMENT

We thank Dr. Koichi Haraguchi (Daiichi College of Pharmaceutical Sciences, Fukuoka, Japan) for some of the $MeSO_2$-PCB standards. The assistance of Dr. Jiping Zhu (JPZtech Co., Gloucester, ON, Canada) in the GC/ECNI-MS analysis was appreciated. This study was supported by research grants from the Natural Sciences and Engineering Research Council (NSERC) of Canada (to R.J.N.). Support was also obtained from the Canadian Arctic Environmental Strategy Greenplan Program. Data were presented in part at the 14th International Symposium on Chlorinated Dioxins, PCB and Related Compounds, Kyoto, Japan, November 1994, and at the 24th International Symposium on Environmental Analytical Chemistry, Ottawa, ON, Canada, May 1994.

GLOSSARY

GC-ECD	gas chromatography with electron-capture detection
GC/ECNI-MS	gas chromatography with electron-capture, negative ion mass spectrometry
SIM	selected ion monitoring
TIC	total ion current monitoring
MDL	method detection limit
IDL	instrumental detection limit
PQL	practical quantitation limit
MRF	molar response factor
RMRF	relative molar response factor to the IS
MCRF	molar carbon response factor

Received for review May 15, 1995. Accepted August 31, 1995.[⊗]

AC950465L

[⊗] Abstract published in *Advance ACS Abstracts*, October 15, 1995.

Anal. Chem. **1995**, *67*, 4164–4169

Ion Remeasurement in the Radio Frequency Quadrupole Ion Trap

Douglas E. Goeringer,*,† Richard I. Crutcher,‡ and Scott A. McLuckey†

Chemical & Analytical Sciences Division and Instrumentation & Controls Division, Oak Ridge National Laboratory, Oak Ridge, Tennessee 37831-6365

Multiple remeasurement of the same population of stored ions in a radio frequency (rf) quadrupole ion trap is demonstrated. As the secular frequency of stored ions is swept across a fixed-frequency resonance excitation signal via amplitude modulation of the confining rf voltage, the image current generated by the resulting coherent ion motion is measured simultaneously with tuned-circuit, phase-sensitive detection. Judicious selection of the resonance excitation frequency and rf voltage ramp limits enables the excitation–detection process to be performed over a range of mass-to-charge values. Furthermore, the inherent focusing of the quadrupole field and use of helium buffer gas ($\sim 10^{-4}$ Torr) enable repeated scans to be made with negligible ion loss. For a collection of $C_3F_5^+$ ions (m/z 131) produced via a single electron ionization event, the remeasurement efficiency during 24 scans, as judged by the scan-to-scan loss in signal, was >99%.

The radio frequency (rf) quadrupole ion trap, a device having three electrodes that are complementary hyperboloids of rotation and using ac potentials to generate electrodynamic fields for charged particle confinement, has traditionally been used in the physics community for high-resolution atomic spectroscopy and high-precision frequency measurements. Recently, use of the ion trap for mass spectrometric applications has increased significantly following the development of the mass-selective instability[1,2] mode of operation for the device. In this mode of operation, the amplitude of the confining rf voltage is increased linearly with time, causing trajectories of stored ions to become unstable in the axial direction sequentially from low to high mass-to-charge. Ejected ions are subsequently detected by an external electron multiplier. Thus, any further manipulations of the original ion packet are precluded by ion ejection and subsequent collision with the detector surface.

Trapped ions can also be detected via nondestructive means. For example, resonance absorption of energy by stored ions from a supplementary excitation signal can be detected by power absorption. Alternatively, the varying differential charge on the trap electrodes induced by coherent ion motion is detectable as fluctuating image currents in an external circuit. Both of these in situ detection techniques have been used extensively in ion cyclotron resonance (ICR) mass spectrometry,[3] although image current detection is now used almost exclusively due to its compatibility with Fourier transform (FT) signal processing.[4] However, the first use of in situ ion detection in the context of a mass spectrometry experiment was made not in an ICR study but as part of the development of the rf quadrupole or Paul trap. Paul et al.,[5] Fischer,[6] and Rettinghaus[7] used such in situ detection techniques in their early rf ion trap studies, and variations of their approach are currently the method of choice in certain applications.[8,9] In addition, image current detection and FT signal processing were later applied to ion trap mass spectrometry by Syka and Fies.[10]

The nondestructive nature of in situ ion detection was recently exploited by McLafferty's group in their development of a method for multiple remeasurement of ions[11] in FT-ICR mass spectrometry. In their experiment, the same population of ions was measured repeatedly by using multiple excitation–detection–relaxation cycles. A maximum cycle-to-cycle remeasurement efficiency of 98% was observed for gramicidin D (m/z 1904), with subsequent signal averaging of spectra from 25 such remeasurement cycles yielding a 4-fold enhancement in signal-to-noise. Unfortunately, each remeasurement cycle required 180 s, most of which was ion relaxation time. This was a consequence of the low background pressures typically required for high-performance FT-ICR operation and the associated reduction in collisional damping of the ion cyclotron motion. Furthermore, the remeasurement efficiency was found to decrease with decreasing ion mass. This drawback derives from competition between the desired reduction of the cyclotron orbit and axial oscillations via ion–neutral collisional damping[12] and the undesired ion loss via concomitant cooling and expansion of the magnetron orbit.[13] Taking advantage of the reduced scattering angles and increased collision cross sections of large electrospray ions, Laude and coworkers[14] later demonstrated unit remeasurement efficiency and 100-ms time scale relaxation times in FT-ICR. More recently, Amster's group[15] has shown that quadrupolar excitation[16,17] in combination with collisional axialization can improve remeasure-

† Chemical & Analytical Sciences Division.

‡ Instrumentation & Controls Division.

(1) Stafford, G. C., Jr.; Kelley, P. E.; Syka, J. E. P.; Reynolds, W. E.; Todd, J. F. J. *Int. J. Mass Spectrom. Ion Processes* **1984**, *60*, 85.
(2) Stafford, G. C.; Kelley, P. E.; Stephens, D. R. U.S. Patent 4,540,884, 1985.
(3) Marshall, A. G. *Acc. Chem. Res.* **1985**, *18*, 316.
(4) Comisarow, M. B.; Marshall, A. G. *Chem. Phys. Lett.* **1974**, *25*, 282.
(5) Paul, W.; Reinhard, H. P.; Von Zahn, U. *Z. Phys.* **1958**, *152*, 143.
(6) Fischer, E. *Z. Phys.* **1959**, *156*, 1.
(7) Rettinghaus, G. *Z. Angew. Phys.* **1967**, *22*, 321.
(8) Schuessler, H. A.; Holder, C. H., Jr. *J. Appl. Phys.* **1979**, *50*, 5110.
(9) Parks, J. H.; Pollack, S.; Hill, W. *J. Chem. Phys.* **1994**, *101*, 6666.
(10) Syka, J. E. P.; Fies, W. J., Jr. U.S. Patent 4,755,670, 1988.
(11) Williams, E. R.; Henry, K. D.; McLafferty, F. W. *J. Am. Chem. Soc.* **1990**, *112*, 6157.
(12) Beu, S. C.; Laude, D. A., Jr. *Int. J. Mass Spectrom. Ion Processes* **1991**, *108*, 255.
(13) Francl, T. J.; Fukuda, E. K.; McIver, R. T., Jr. *Int. J. Mass Spectrom. Ion Phys.* **1983**, *50*, 151.
(14) Guan, Z.; Hofstadler, S. A.; Laude, D. A., Jr. *Anal. Chem.* **1993**, *65*, 1588.

0003-2700/95/0367-4164$9.00/0

ment efficiency by converting magnetron motion to cyclotron motion, thereby reducing ion loss.

The rf quadrupole ion trap does not require a magnetic field for ion confinement. As a result, ion losses due to collisional destabilization of the magnetron motion are eliminated, as is the associated need for quadrupolar excitation instrumentation. In contrast, typical helium bath gas pressures (10^{-4}–10^{-3} Torr) used in standard ion trap mass spectrometry generally aid ion confinement by promoting collisional damping of ion motion to the trap center. Such helium pressures are also compatible with the method used in this study for acquisition of mass spectra. The success with multiple remeasurement of ions in FT-ICR, along with the potential advantages of implementing nondestructive ion detection in the quadrupole ion trap, has led us to investigate adapting ion remeasurement to ion trap mass spectrometry. This paper describes the basis for image current detection in the quadrupole ion trap, some of the considerations involved in modifying the ion trap to function as a mass spectrometer in image current detection mode, and the results obtained in our experiments with ion remeasurement.

EXPERIMENTAL SECTION

Radio Frequency Quadrupole Ion Trap. A Teledyne-Hitachi 3DQ rf quadrupole ion trap mass spectrometer was used for these studies. The stainless steel trapping electrodes are machined in the conventional hyperboloidal shape,[18] the ring electrode having an inner radius, r_0, of 1 cm. The electrodes in the standard instrument configuration are assembled so that the trap center-to-endcap spacing, z_0, is somewhat elongated compared with the value of $r_0/2^{1/2}$ for the pure quadrupole trap, thereby intentionally introducing minor hexapole and octapole content to the trapping field.[19] Although such modifications are known to produce nonlinear resonances[20] at certain combinations of the reduced operating parameters, a_z and q_z, the multipole character can also have a beneficial effect in certain areas of instrument performance.[21]

The ring electrode is connected to the output of the standard rf generator, which operates at $\Omega/2\pi = 0.909$ MHz. A 16-bit DAC controls the output voltage (0–5000 V_{0-p}). An auxiliary signal generator normally provides the capability for resonance excitation, but it was disconnected from the endcaps to prevent interference with the image current detection electronics. The standard ion trap assembly also is fitted with an electron ionization source, the filament being housed in one of the endcaps. An ion lens, located in the other endcap, focuses ejected ions into an electron multiplier positioned along the axis (z) of rotational symmetry.

The ion trap assembly and detector are housed in a 10- × 12- × 38-cm vacuum chamber having two standard ports. For our experiments, a Bayard-Alpert ionization tube was inserted into one of the ports to provide vacuum measurements. Flanges fitted with BNC vacuum feedthroughs also were bolted to two additional ports custom-machined into the sides of the vacuum chamber. The feedthroughs were connected to the endcaps via shielded signal cables. The vacuum chamber is pumped by the standard 56 L s^{-1} turbomolecular pump, producing a base pressure of ~2 × 10^{-7} Torr.

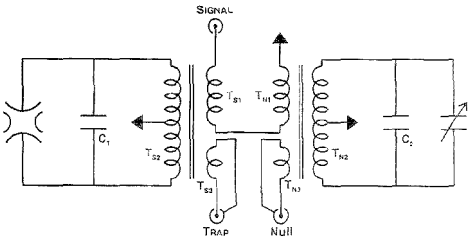

Figure 1. Tuned bridge circuit used in the quadrupole ion trap remeasurement experiments. The resonance excitation signal at 79 kHz is coupled to the ion trap endcaps via windings T_{S3} and T_{S2} of the signal transformer. The resulting ion image current signal flowing through the resonant LC impedance formed by T_{S2}, C_1, and the two endcaps produces a corresponding voltage signal in T_{S1}. Contribution of the resonance excitation signal to the voltage signal is nulled by adjusting the phase and amplitude of the signal applied to T_{N3} of the matching null transformer.

Image Current Detection Electronics. A major obstacle to image current detection in the rf quadrupole ion trap, in contrast with the FT-ICR, is the trapping rf signal. A fraction of this high-voltage signal is coupled to the endcaps via the small ring-to-endcap capacitance, producing a background signal whose amplitude is dependent on the ac impedance between each endcap and ground. Consequently, connecting the endcaps directly to the inputs of a high-impedance differential amplifier, as is the normal practice in FT-ICR, is not practicable because the high background signal (typically tens of volts) overloads the inputs. In the experiments described here, a transformer-coupled bridge circuit was used to circumvent the rf drive background while simultaneously enabling resonant excitation and image current detection. Figure 1 shows a schematic diagram of the circuit, which is similar to that used by Rettinghaus.[7] The endcaps were directly coupled to either end of the transformer secondary (T_{S2}), with the center tap providing the necessary dc ground. The transformer primary (T_{S1}) and secondary were trifilar wound on a toroidal core (Amidon Associates, FT140-77, $A_L = 2250$ nH) with 50 and 100 turns, respectively, of 26 AWG wire. T_{S2} ($L = 25$ mH) and the ion trap, wiring, and auxiliary capacitor C_1 ($C = 80$ pF) form a parallel L–C circuit having a resonant frequency $\omega_R/2\pi \approx 79$ kHz and a measured $Q = 40$, yielding a resonant impedance ($Z_R = Q\omega_R L$) of ~0.5 MΩ. Another single turn (T_{S3}) of wire around the core (producing an input impedance of ~50 Ω) enabled the resonance excitation signal ($\pm[V_E/2]_{0-p}$ at ω_E) from an external signal generator (Wavetek Model 295, San Diego, CA) to be applied across the endcaps via T_{S2}. The resulting image current flowing through the parallel L–C circuit generated a corresponding signal voltage across T_{S1}.

Because the ring-to-endcap capacitances are closely matched, the rf background signals on the endcaps were virtually in-phase and equal in amplitude. Therefore, very little of the rf drive signal appeared on T_{S1}. Furthermore, $\omega_R \approx \Omega/10$, so the tuned L–C circuit significantly reduced the background at Ω. However, the

(15) Speir, J. P.; Gorman, G. S.; Pitsenberger, C. C.; Turner, C. A.; Wang, P. P.; Amster, I. J. *Anal. Chem.* **1993**, *65*, 1746.
(16) Savard, G.; Becker, S.; Bollen, G.; Kluge, H.-J.; Moore, R. B.; Otto, T.; Schweikard, L.; Stolzenberg, H.; Wiess, U. *Phys. Lett. A* **1991**, *158*, 247.
(17) Schweikhard, L.; Guan, S.; Marshall, A. G. *Int. J. Mass Spectrom. Ion Processes* 1992, *120*, 71.
(18) Knight, R. D. *Int. J. Mass Spectrom. Ion Phys.* **1983**, *51*, 127.
(19) Wang, Y.; Franzen, J.; Wanczek, K. P. *Int. J. Mass Spectrom. Ion Processes* 1993, *124*, 125.
(20) Dawson, P. H.; Whetten, N. R. *Int. J. Mass Spectrom. Ion Phys.* **1969**, *2*, 45.
(21) Franzen, J. *Int. J. Mass Spectrom. Ion Processes* **1993**, *125*, 165.

presence of the resonance excitation voltage superimposed on the much smaller signal voltage of the same frequency made direct signal measurement difficult. Thus, a second parallel L–C circuit (T_{N2}–C_2), identical to the first except for a capacitor (C_2, C = 160 pF) substituted for the ion trap, was used to balance the excitation voltage. The out-of-phase ends of T_{S1} and T_{N1} were connected, the opposite end of T_{N1} was grounded, and the signal side of T_{S1} was sent to an FET preamplifier (SR560, Stanford Research Systems, Sunnyvale, CA). Another phase-locked output (balance signal) from the signal generator was applied to T_{N3}, and the resonance excitation signal was nulled by adjusting the phase and amplitude of the balance signal to give minimum preamplifier signal output without ions in the trap. The preamplifier output signal would normally be suitable for direct input to the digital lock-in amplifier (SR850, Stanford Research Systems). However, gating of the electron beam produced high-amplitude ringing in the high-Q, L–C network, thus overloading the preamplifier input. Gating the preamplifier alleviated this problem. The starting point and duration of the TTL gating signal, triggered by the sync pulse from the ion trap Electronics Tower, were adjusted to correspond with the image current detection sweep. In addition to being gated, the signal was also low-pass filtered (100 kHz) by the amplifier. The amplifier output was then processed by the lock-in amplifier, which was phase-locked to the excitation signal generator. Maximum operating frequency for the lock-in was 100 kHz. The dc output signals from the lock-in were digitized and displayed by a digital sampling oscilloscope (LeCroy 7200, Model 7242B plug-in, Chestnut Ridge, NY). The data were also stored on floppy disks for transfer to computer for further processing.

Control Software. Manufacturer-supplied firmware (Version 0.52) for the electronics tower and software (Version 0.52) for the computer (80486-DX2) allow near-real-time control and modification of most instrument parameters, such as ionization duration, amplitude and ramp rate of the rf voltage, resonance excitation mass-to-charge, amplitude, and duration, sync pulse triggering, mass-to-charge scan range, etc. Although instrument modifications for image current detection prevented use of the standard resonance excitation signal generator, all other instrument functions remained intact. Consequently, the standard software, providing effective and flexible instrument control, was used throughout these experiments.

Sample/Buffer Gas Introduction. Perfluorotributylamine (PFTBA) sample vapors were continuously introduced into the vacuum chamber via a solenoid valve controlled by the software. The pressure, monitored via the Bayard-Alpert ionization gauge, was adjusted with a needle valve in series with the solenoid valve. Helium buffer gas was admitted through a spare port machined into the vacuum chamber. The helium pressure was adjusted with a precision leak valve; pressure readings were corrected using the ion gauge sensitivity factor.

THEORY

Dipolar Excitation of Coherent Ion Motion. The differential equations describing ion trajectories in a three-dimensional quadrupole ion trap are often presented in the parameterized form known as the Mathieu equation,[22,23]

$$d^2u/d\xi^2 + [a_u - 2q_u \cos(2\xi)]u = 0$$

in which u refers to ion motion in the z- and r-dimensions and $\xi = \Omega t/2$. The z and r fields are uncoupled, enabling ion motion in those directions to be treated independently. The a_u and q_u parameters, defined below, contain the terms m/q, ion mass/charge, U, dc voltage, and V_{rf}, zero–peak voltage of the rf trapping signal applied between the ring and endcap electrodes. For rf-only operation (U = 0) with q_z < 0.4, the z-axis oscillations of trapped ions can be treated as simple harmonic motion at a mass-dependent secular frequency, $\omega_0 = (q_z/2^{1/2})(\Omega/2)$. If a dipolar resonance excitation signal, $(V_E/2)\cos(\omega_E t)$, is applied to the endcaps so that a uniform dipolar excitation field, $E(z) = (V_E/2z_0)\cos(\omega_E t)$, is created, then the time-dependent form of the Mathieu equation can be written,

$$a_z = -2a_r = \frac{-16qU}{m(r_0^2 + 2z_0^2)\Omega^2}$$

$$q_z = -2q_r = \frac{-8qV_{rf}}{m(r_0^2 + 2z_0^2)\Omega^2}$$

$$\frac{d^2z}{dt^2} + \alpha\frac{dz}{dt} + \omega_0^2 z = \frac{\Gamma q V_E}{2mz_0}\cos(\omega_E t) \qquad (1)$$

where $\alpha(dz/dt)$ is a damping term representing the effect of ion–neutral collisions and the factor Γ (~0.82) compensates for the hyperbolic geometry of the endcaps.[24,25] The solution[26] to eq 1, which describes a driven harmonic oscillator with damping, is given by eq 2.

$$z(t) = \frac{\Gamma q V_E}{2mz_0}\frac{\cos(\omega_E t - \theta)}{[(\omega_0^2 - \omega_E^2)^2 + 4(\alpha/2)^2\omega_E^2]^{1/2}} + \frac{1}{\beta}\left[\frac{\kappa^2 + \xi^2}{(\omega_0^2 - \omega_E^2)^2 + 4(\alpha/2)^2\omega_E^2}\right]^{1/2}\exp\left(-\frac{\alpha}{2}t\right)\cos(\beta t + \lambda) \qquad (2)$$

$$\beta = [\omega_0^2 - (\alpha/2)^2]^{1/2}$$

$$\kappa = \beta\left[\frac{\Gamma q V_E}{2mz_0} + z(0)(\omega_E^2 - \omega_0^2) - z'(0)\alpha\right]$$

$$\xi = -\frac{\Gamma q V_E}{2mz_0}\left(\frac{\alpha}{2}\right) + z(0)\left(\frac{\alpha}{2}\right)(\omega_E^2 + \omega_0^2) + z'(0)\left[\left(\frac{\alpha}{2}\right)^2 + \omega_E^2 - \beta^2\right]$$

$$\lambda = \tan^{-1}\left(\frac{-\xi}{\kappa}\right) - \tan^{-1}\left[\frac{-2(\alpha/2)\beta}{(\alpha/2)^2 + \omega_E^2 - \beta^2}\right]$$

$$\theta = \tan^{-1}\left(\frac{\alpha\omega_E}{\omega_0^2 - \omega_E^2}\right)$$

Although the initial positions ($z(0)$) and velocities ($z'(0)$) of trapped ions are random with regard to the phase space of stable

(22) Dawson, P. H. In *Quadrupole Mass Spectrometry*; Dawson, P. H., Ed.; Elsevier Scientific Publishing Co.: Amsterdam, The Netherlands, 1976; p 65.

(23) March, R. E.; Hughes, R. J. In *Quadrupole Storage Mass Spectrometry*; Winefordner, J. D., Kolthoff, I. M., Eds.; Chemical Analysis Series 102; John Wiley & Sons: New York, 1989; pp 31–110.

(24) Wineland, D. J.; Dehmelt, H. G. *J. Appl. Phys.* **1975**, *46*, 919.

(25) Gaboriaud, M. N.; Desaintfuscien, M.; Major, F. G. *Int. J. Mass Spectrom. Ion Phys.* **1981**, *41*, 109.

trajectories, eq 2 indicates that dipolar excitation at frequency ω_E imparts coherent z-oscillations at that frequency to the ion packet due to an exponential ($\tau = 2/\alpha$) decay in the state of the initial conditions with time. Thus, image current detection is possible.

Analysis of Image Current Detection. The magnitude of the image current, $I(t)$, can be obtained[27] by determining the differential charge, $\Delta Q(z)$, induced on the endcaps as a function of ion position, substituting the time-dependent expression for the center of trapped ion charge, $z_c(t)$, and differentiating the resulting expression with respect to time. The potential corresponding to the dipolar excitation field noted above is $\Phi(z) = \Gamma V_E z/2z_0$, so from reciprocity,[28] $\Delta Q(z)$ is given by

$$-\Delta Q(z)/q = z_c/z_0$$

Substituting the complex form for $z_c(t)$ at steady state, as given in eq 2, yields an expression for $\Delta Q(t)$,

$$\Delta Q(t) = -\frac{qZ_c(t)}{z_0}\exp(j\omega_E t)$$

where $Z_c(t)$ is the amplitude of the rapid z_c motion. $I(t)$ is the rate of change in $\Delta Q(t)$ (divided by 2 in this case to avoid counting both the current entering one endcap and that exiting the other). Under steady-state conditions, $Z_c \neq f(t)$, so that

$$I(t) = \frac{\mathrm{d}}{\mathrm{d}t}\frac{\Delta Q(t)}{2} = -\frac{qZ_c}{2z_0}\frac{\mathrm{d}}{\mathrm{d}t}\exp(j\omega_E t) \qquad (3)$$

The corresponding signal voltage, $V(t)$, can be found by analyzing the detection circuit. The flow of $I(t)$ between endcaps can also be written as the sum of the individual currents through C and L,

$$i(t) = C\frac{\mathrm{d}V(t)}{\mathrm{d}t} + \frac{\int_0^t V(t)\,\mathrm{d}t}{L} \qquad (4)$$

where L represents the inductance of T_{S2} and C the parallel combination of endcap-to-endcap and auxiliary (C_1) capacitances. $V(t)$ is generated by image current flow through the impedance of the parallel $L-C$ circuit. Combining eqs 3 and 4 yields

$$-\frac{qZ_c}{2z_0}\frac{\mathrm{d}}{\mathrm{d}t}\exp(j\omega_E t) = C\frac{\mathrm{d}V(t)}{\mathrm{d}t} + \frac{\int_0^t V(t)\,\mathrm{d}t}{L}$$

Differentiating each side with respect to time gives If we assume

$$-\frac{qZ_c}{2z_0}\frac{\mathrm{d}^2}{\mathrm{d}t^2}\exp(j\omega_E t) = C\frac{\mathrm{d}^2V(t)}{\mathrm{d}t^2} + \frac{V(t)}{L}$$

that $V(t)$ is of the form

$$V(t) = V_S\exp(j\omega_E t) \qquad (5)$$

where V_S is the amplitude of the voltage signal, then substitution and differentiation gives

$$\frac{qZ_c\omega_E^2}{2z_0}\exp(j\omega_E t) = -C\omega_E^2 V_S\exp(j\omega_E t) + \frac{V_S}{L}\exp(j\omega_E t)$$

Dividing through by $\exp(j\omega t)$, factoring, and rearranging produces

$$V_S = \left(\frac{Z_c}{z_0}\right)\frac{q\omega_E^2 L}{2(1-\omega_E^2 LC)}$$

Substituting the above result for V_S into eq 5 yields

$$V(t) = \left(\frac{Z_c}{z_0}\right)\frac{q\omega_E^2 L}{2(1-\omega_E^2 LC)}\exp(j\omega_E t)$$

Using the approximation $\omega_E \approx \omega_0$ near resonance and substituting $1/\omega_0^2$ for LC gives

$$V(t) = \left(\frac{Z_c}{z_0}\right)\frac{q\omega_0^4 L}{2(\omega_0^2-\omega_E^2)}\exp(j\omega_E t)$$

Finally, making the approximations $\omega_E + \omega_0 \approx 2\omega_0$ and $2(\omega_0 - \omega_E) \approx \Delta\omega$, defining $Q = \omega_0/\Delta\omega$, and taking the real part of the result yields eq 6. The in-phase and out-of-phase components of

$$V(t) = \left(\frac{Z_c}{z_0}\right)\frac{qQ}{2C}\cos(\omega_E t) \qquad (6)$$

the ion signal can be separated if phase-sensitive detection is used.

Thus, the maximum steady-state signal voltage, V_M, generated across the parallel $L-C$ circuit by coherent motion of n_{ion} ions is $n_{ion}(qQ/2C)$ since $Z_c \leq z_0$. If the electronic noise is assumed to be Johnson noise limited, then the corresponding signal-to-rms-noise ratio is

$$(S/N)_M = \frac{V_M}{\sqrt{4kTZ_R\Delta_f}} \qquad (7)$$

where the detection bandwidth, $\Delta_f = 1$ kHz, is determined by the time constant of the lock-in amplifier in these experiments. When the experimental parameters are substituted into eq 7, the minimum number of ions, n_{min}, detectable with signal-to-noise ratio, S/N, can be estimated by

$$n_{min} = 1.44(S/N)$$

However, the fraction of V_M actually attained is dependent on the nonexponential term on the right-hand side of eq 2, as well as the harmonic content of the ion motion. Furthermore, the expression for Z_c becomes more complex when ω_E (or ω_0) is scanned,[29,30] since $Z_c = f(t)$.

RESULTS AND DISCUSSION

Mass Spectral Scanning with Image Current Detection. Due to the narrow bandpass of the high-Q, parallel $L-C$ circuit,

(26) Gardner, M. F.; Barnes, J. L. *Transients in Linear Systems, Volume I: Lumped-Constant Systems*; John Wiley & Sons, Inc.: New York, 1942.
(27) Grosshans, P. B.; Shields, P. J.; Marshall, A. G. *J. Chem. Phys.* **1991**, *94*, 5341.
(28) Dunbar, R. C. *Int. J. Mass Spectrom. Ion Processes* **1984**, *56*, 1.
(29) Goeringer, D. E.; Whitten, W. B.; Ramsey, J. M.; McLuckey, S. A.; Glish, G. L. *Anal. Chem.* **1992**, *64*, 1434.
(30) Arnold, N. S.; György, H.; Meuzelaar, H. L. C. *J. Am. Soc. Mass Spectrom.* **1994**, *5*, 676.

only a narrow mass-to-charge range can be scanned by varying the resonance excitation frequency, ω_E. Thus, we have chosen instead to fix ω_E ($= \omega_R$) and scan the secular frequency, ω_0, of trapped ions through the excitation–detection frequency. Description of mass spectral scanning by this method is facilitated by use of the reduced parameters, a_z and q_z, and the expressions for β and ω_0.

$$\beta = \sqrt{a_z + q_z^2/2} \qquad \omega_0 = \beta(\Omega/2)$$

$$a_z \ll 1 \qquad q_z < 0.4$$

It is clear from the expression for q_z that m/q is directly proportional to V_{rf} for a fixed value of q_z, so that a mass/charge range can be scanned linearly through a selected q_z value by ramping V_{rf} at a constant rate. Such a procedure is the basis for the mass-selective instability mode; an increasing V_{rf} ramp produces z-axis ejection of ions from low to high mass/charge as they reach the $q_z = 0.908$ boundary of the ion trap stability diagram. Although the relationship between q_z and β becomes nonlinear above $q_z \approx 0.4$, a unique value of ω_0 still exists for each combination of m/q and V_{rf}. Consequently, the linear V_{rf} ramp also sweeps the secular frequencies for a range of m/q values through resonance with a (fixed) resonance excitation signal at $\omega_E = \omega_R$. Note that the scan remains linear with mass/charge despite the fact that ω_0 is inversely related to m/q.

However, an ion remeasurement scheme based on a V_{rf} ramp/image current detection combination differs from the mass-selective instability mode in that the targeted mass/charge range must be scanned nondestructively. Therefore, sweeping a targeted mass/charge range, $(m/q)_{lo} \rightarrow (m/q)_{hi}$, through ω_R without ion loss at the stability region boundary clearly requires $\omega_R < \Omega/2$ (i.e., $q_z < 0.908$). Here, $(m/q)_{lo}$ and $(m/q)_{hi}$ represent the low and high m/q values, respectively, of the targeted mass/charge range. Further analysis of the situation indicates that for ω_R corresponding to $q_z = 0.908/n$ or $(m/q)_{hi}/n$, $[n \geq (m/q)_{hi}/(m/q)_{lo}]$, a V_{rf} ramp from $(m/q)_{lo}/n \rightarrow (m/q)_{hi}/n$ satisfies the ion loss requirements over the targeted mass/charge range. In addition, the amplitude of ω_E must be adjusted to provide for maximum signal (see eq 6) while avoiding ion ejection. The resonant L–C frequency used in these studies, $\omega_R = 79$ kHz, corresponds to $q_z = 0.24$ and $n = 3.7$. For any specific $(m/q)_{lo} \rightarrow (m/q)_{hi}$ range, the nondestructive image current sweep is also a factor of n faster than the corresponding mass-selective instability sweep. External detection scan rates equal to those for in situ detection can be produced, however, by further increasing the amplitude of ω_E so that ion ejection occurs at resonance, a technique known as resonance ejection.[31,32]

Multiple Remeasurement. One of the potential advantages of ion remeasurement is signal-to-noise improvement via signal averaging. However, as pointed out by Williams et al.[11] in their original paper on multiple remeasurement of ions in FT-ICR, the signal-to-noise enhancement factor drops quickly with reduction in remeasurement efficiency. The ion signal, RS_i, after i remeasurement cycles of the same ion population is

(31) Fulford, J. E.; Hoa, D.-N.; Hughes, R. J.; March, R. E.; Bonner, R. F.; Wong, G. J. *J. Vac. Sci. Technol.* **1980**, *17*, 829.
(32) Kaiser, R. E.; Louris, J. N.; Amy, J. W.; Cooks, R. G. *Rapid Commun. Mass Spectrom.* **1989**, *3*, 225.

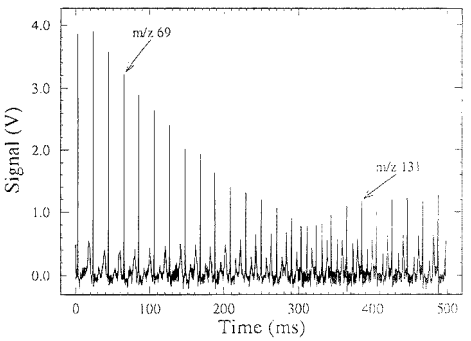

Figure 2. Signal resulting from 24 consecutive remeasurement scans of a single population of ions generated via electron ionization of perfluorotributylamine. The mass/charge range (52–163) was scanned by linearly ramping the amplitude of the rf trapping voltage, thereby sweeping the secular frequencies of trapped ions through resonance with the excitation signal at 79 kHz.

$$RS_i = RS_0 \epsilon_R^{\,i}$$

where RS_0 represents the signal from the initial measurement and ϵ_R is the remeasurement efficiency. The value of ϵ_R can be determined from a plot of $\ln(RS_i)$ vs i. Summing signals from n remeasurement cycles produces a signal-to-noise ratio, $(S/N)_n$, given by

$$(S/N)_n = \left(\frac{RS_0}{N_0}\right)\frac{\sum_{i=0}^{n} \epsilon_R^{\,i}}{\sqrt{n+1}}$$

where the noise for each cycle, N_0, is assumed to be constant and is given by the Johnson noise voltage.

Figure 2 shows the image current signal obtained from 24 remeasurement scans following 20-ms electron ionization (EI) of PFTBA. The sample pressure was 1.4×10^{-6} Torr, and the helium bath gas pressure was 8.9×10^{-5} Torr. Each scan was made at an rf ramp rate of 1500 amu s^{-1} between rf levels corresponding to m/z cutoffs 14–44 ($q_z = 0.908$). When combined with the effective scan rate increase (3.7×) resulting from the image current detection frequency of 79 kHz, the mass/charge range 52–163 was scanned in 20 ms. There was no delay period between scans other than the very short time required for the rf amplitude to return to the starting level for the next scan. Unresolved problems with the scan editor, which enables creation of the scan functions, limited the number of remeasurement scans to a maximum of 24.

The major PFTBA fragment ions in the scanned range and their (approximate) relative abundances are as follows: CF_3^+, m/z 69 (100%); $C_2F_4^+$, m/z 100 (18%); and $C_3F_5^+$, m/z 131 (48%). Although the rapid decline in the m/z 69 signal would normally imply poor remeasurement efficiency, two observations argue against it. First, the signals at m/z 100 and 131 increase and then plateau over the same time, suggesting that they are the products of an ion–molecule reaction involving CF_3^+. Second, the m/z 69 signal drops by the same amount when the ion packet is stored for the same period without intervening scans. The ion–molecule rate constant, 9×10^{-11} cm^3 $molecule^{-1}$ s^{-1}, estimated from the

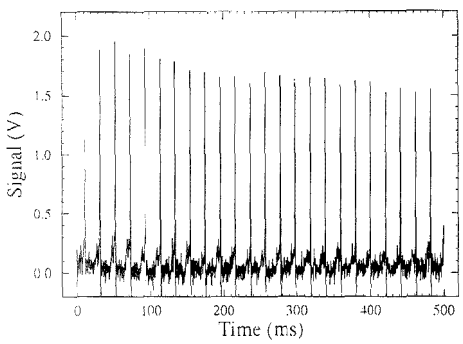

Figure 3. Signal resulting from a remeasurement experiment identical to that used to produce Figure 2, except all ions but those at mass/charge 131 were ejected prior to the sequence of remeasurement scans. Analysis of the peak intensities yields a remeasurement efficiency of >99%.

decay data, is within the range of typical values. Furthermore, an independent experiment performed in the same instrument with external ion detection rather than in situ detection confirmed the decline in the CF_3^+ ion signal and the associated increase in $C_2F_4^+$ and $C_2F_5^+$ ion signals. Despite the inability to successfully demonstrate efficient ion remeasurement using the *m/z* 69 ion, the above experiment suggests that the remeasurement technique has potential for monitoring ion–molecule reactions of a single ion population as a function of time, as shown by Laude et al.[33] in FT-ICR.

Figure 3 shows the results obtained from another remeasurement experiment identical to the previous except all ions other than those at *m/z* 131 were ejected immediately following ionization and before the remeasurement sweeps. Thus, any scan-to-scan changes in the image current signal at *m/z* 131 during the remeasurement experiment were not due to ion–molecule reactions involving any other ions. In contrast to the previous remeasurement experiment, the Figure 3 data indicate that the image current signals from each remeasurement scan (other than the first) are quite similar in amplitude when the noise is ignored. Analysis of the data as indicated in the previous section produced a remeasurement efficiency of >99%. However, summing the 24 remeasurement scans yielded a signal-to-noise enhancement factor of only ~2.4 compared to the theoretical value of 4.38 (at 99% remeasurement efficiency). Examination of the averaged spectrum revealed the noise had a large nonrandom component, suggesting the reason for the lower-than-predicted improvement in signal-to-noise ratio. EMI pickup by the long signal leads running from the ion trap to the tuned circuit and from there to the preamplifier was probably the source of the signal contamination and presumably could be reduced by more careful circuit design.

(33) Guan, Z.; Drader, J. J.; Campbell, V. L.; Laude, D. A. *Anal. Chem.* **1995**, *67*, 1453.

CONCLUSIONS

The results presented here indicate that by employing nondestructive image current detection in a radio frequency quadrupole ion trap, multiple remeasurements of a single population of stored ions can been achieved with >99% efficiency during operation with ~10^{-3} Torr helium buffer gas pressure. Despite the fact that a narrow bandpass, tuned circuit is used for image current detection, ions within a range of mass-to-charge values can be excited and detected by sweeping the secular frequencies of trapped ions through resonance via amplitude modulation of the confining radio frequency voltage. Furthermore, the relatively low mass ions studied here required no additional delay periods between remeasurement scans to allow for ion relaxation due to the inherent ion focusing of the quadrupole field and helium bath gas.

ACKNOWLEDGMENT

This work was sponsored by the United States Department of Energy Office of Research and Development. Oak Ridge National Laboratory is managed for the U.S. Department of Energy by Lockheed Martin Energy Systems, Inc., under Contract DE-AC05-84OR21400.

Received for review June 19, 1995. Accepted August 29, 1995.[⊗]

AC9506185

[⊗] Abstract published in *Advance ACS Abstracts*, October 1, 1995.

Anal. Chem. **1995**, *67*, 4170–4177

On-Line Microreactors/Capillary Electrophoresis/ Mass Spectrometry for the Analysis of Proteins and Peptides

Larry Licklider,[†] Werner G. Kuhr,*[,†] Martin P. Lacey,[‡] Thomas Keough,[‡] Michael P. Purdon,[§] and Ray Takigiku*[,⊥]

Department of Chemistry, University of California, Riverside, California 92521, and Corporate Research Division, Corporate Professional & Regulatory Division, and Procter and Gamble Pharmaceuticals, The Procter and Gamble Company, Miami Valley Labs, P.O. Box 538707, Cincinnati, Ohio 45253-8707

We report the use of trypsin and carboxypeptidase Y-modified capillary microreactors (50 μm i.d. and 20 nL volume per centimeter length) in combination with mass spectrometry for peptide molecular mass mapping of various peptides and proteins. Advantages of immobilized enzyme capillary microreactors include picoliter to nanoliter volume requirements, longer enzyme lifetimes, higher stability, and the ability to reuse enzymes conveniently. Additionally, extremely efficient sample handling modes are used, and the reaction products are easily separated from the enzyme reagents. Plasma desorption and matrix-assisted laser desorption/ionization were used for off-line analyses of digestion products. The use of MassMap for the identification of proteins is also discussed. Finally, a trypsin microreactor was integrated on-line with capillary electrophoresis/ion spray mass spectrometry for fast peptide mapping. Digestion of the oxidized insulin B-chain in an on-line trypsin microreactor and electromigration of aliquots from the capillary microreactor into the CE separation capillary allowed the entire peptide mapping procedure to be completed in <1 h. The on-line technique is especially well-suited for the characterization of minute quantities of proteins, because it transfers picoliter to nanoliter volumes of digestion products with minimum sample handling which could lead to losses or contamination.

The use of two-dimensional gel electrophoresis (2-D gel) and micropreparative high-performance liquid chromatography (HPLC) has made identification and internal sequencing of low picomole levels of proteins a routine, though time-consuming, procedure by automated Edman degradation. Unfortunately, >50% of all proteins are blocked at their N-termini. Proteolytic digestion and HPLC fractionation are required first steps in the Edman sequencing of blocked proteins. These additional steps increase both analysis times and sample consumption. To minimize these problems, considerable effort has gone into the development of mass spectrometry-based methods for protein characterization. The mass spectrometry approach often employs proteolytic enzymes to create peptide maps, which are used for the confirmation of known protein sequences and for investigation of post-translational modifications in proteins.[1,2] Because unique peptide "fingerprints" are generated by specific proteolytic digestions, search algorithms have been developed which utilize these fingerprints for protein identification from extensive databases. This procedure has been referred to as "mass fingerprinting".[3–7]

Typically, after proteins are isolated using 2-D gel electrophoresis, the excised gel slices can be placed into a solution of a protease. Alternatively, the isolated proteins can be transferred from the gel to poly(vinylidene difluoride) (PVDF) membranes and digested in situ.[8] Both approaches have been used in mass fingerprinting procedures to allow rapid identification of low picomole quantities of known proteins from a database.[4,6] Plasma desorption (PD),[9] electrospray ionization (ESI),[10] and matrix-assisted laser desorption/ionization (MALDI)[11] have been utilized for mass fingerprinting analyses of either the unfractionated digestion mixture or the fractions obtained by HPLC. Direct analysis of the in situ digestion products by MALDI-MS has reduced the total analysis time to several hours.[4] Direct analysis of the in situ digestions by MALDI-MS has also been demonstrated after insertion of the PVDF membranes into the mass spectrometer source.[12]

[†] University of California.
[‡] Corporate Research Division, Procter and Gamble.
[§] Corporate Professional & Regulatory Division, Procter and Gamble.
[⊥] Proctor and Gamble Pharmaceuticals.

(1) Morris, H. R.; Panico, M.; Taylor, G. W. *Biochem. Biophys. Res. Commun.* **1983**, *117*, 299–305.
(2) Morris, H. R.; Greer, F. M. *Trends Biotechnol.* **1988**, *6*, 140–147.
(3) James, P.; Qaudroni, M.; Carafoil, E.; Gonnet, G. *Biochem. Biophys. Res. Commun.* **1993**, *195*, 58–64.
(4) Henzel, W. J.; Billeci, T. M.; Stults, J. T.; Wong, S. C.; Grimley, C.; Watanabe, C. *Proc. Natl. Acad. Sci. U.S.A.* **1993**, *90*, 5011–5015.
(5) Mann, M.; Hojrup, P.; Roepstorff, P. *Biol. Mass Spectrom.* **1993**, *22*, 338–345.
(6) Pappin, D. J. C.; Hojrup, P.; Bleasby, A. J. *Curr. Biol.* **1993**, *3*, 327–332.
(7) Yates, J. R.; Speicher, S.; Griffin, P. R.; Hunkapiller, T. *Anal. Biochem.* **1993**, *214*, 397–408.
(8) Aebersold, R. H.; Leavitt, J.; Saavedra, R. A.; Hood, L. E.; Kent, S. B. H. *Proc. Natl. Acad. Sci. U.S.A.* **1987**, *84*, 6970–6974.
(9) Nielsen, P. F.; Klarskov, K.; Hojrup, P.; Roepstorff, P. *Biomed. Environ. Mass Spectrom.* **1988**, *17*, 355–362.
(10) Fenn, J. B.; Mann, M.; Meng, C. K.; Wong, S. F.; Whitehouse, C. M. *Mass Spectrom. Rev.* **1990**, *9*, 37–70.
(11) Beavis, R.; Chait, B. *Proc. Natl. Acad. Sci. U.S.A.* **1990**, *87*, 6873–6877.
(12) Vestling, M. M.; Fenselau, C. *Anal. Chem.* **1994**, *66*, 471–477.

0003-2700/95/0367-4170$9.00/0

Detection limits from the low picomole (PD) into the femtomole range (using either MALDI or ESI) have been demonstrated for peptide mixtures when sample discrimination and component-specific suppression are minimized.[13-15] Relatively high tolerance to salts present within the digestion mixtures has been obtained using MALDI.[4,6,12,15] The mass accuracy for MALDI applied to peptide mixtures depends on a number of factors; however, recent reports have demonstrated accuracy approaching 0.01%.[16,17] ESI has also demonstrated a mass accuracy of at least 0.01% or better for peptide mixtures, which is ~1 order of magnitude better than that obtained with PDMS.[13] Multiply charged ions formed in ESI allow the use of relatively inexpensive quadrupole mass analyzers for large peptide and protein molecular weight determinations and have generated much interest in augmenting mass spectrometry-based peptide mapping with primary sequence information gained by tandem mass spectrometry.[18] Due to the complexity of protein digests, an on-line separation greatly facilitates the interpretation of the ESI spectra.[7,18,20]

The difficulty in obtaining high specificity in trypsin digestion with low picomole quantities of protein is primarily due to the dilution of the target protein, which reduces the rate of reaction. Ideally, a minimal solution volume should be used with an adequate ratio of protein to trypsin (typically 100:1), but these conditions are often difficult to produce, since the low protein concentrations are further reduced by adsorption of either target or proteolytic enzymes onto surfaces.[21] Therefore, addition of nearly equal quantities of trypsin to target proteins has been common in the in situ digestions of proteins adsorbed to PVDF membranes,[21] resulting in a large quantity of trypsin autolytic fragments, which seriously complicate the observed mass spectra. To overcome difficulties in producing optimum digestion conditions, enzyme capillary microreactors of extremely low volume (20 nL per centimeter length) have been developed.[22-24] The large surface area to volume within the 50 μm i.d. fused-silica capillaries provided a support for a variety of enzymes possessing different specificity toward peptide bond cleavages. Immobilization of a biotinylated enzyme to the biotin-modified capillary wall via biotin–avidin interaction is accomplished under exceptionally mild conditions. This stabilization of the enzyme eliminates the need for additional enzyme during the digestions and allows convenient reuse of the enzyme with multiple protein samples. This design allows efficient migration of protein samples through the microreactor by either hydrodynamic or electroosmotic flow and also allows optimization of mass transfer within the microreactor.[24] The 20 nL/cm volume of the microreactor digestions can be sampled efficiently via an open fluid junction with a CE separation capillary, which allows independent optimization of digestion and separation conditions in an on-line peptide mapping procedure.[23-25] Sampling of aliquots from the capillary microreactor conserves the remainder of the digest sample and prevents significant losses, modification, or contamination of picomole quantities of protein digest.

The feasibility of performing microreactor digestions and analyzing the resulting products off-line with mass spectrometry is demonstrated in this work. Off-line protein digestions in carboxypeptidase Y- and trypsin-modified microreactors yielded C-terminal sequences and mass fingerprints, by either MALDI-MS or PDMS, which were compared to protein fragment databases for identification. Finally, on-line trypsin digestion followed by CE/ESI-MS is demonstrated for greatest efficiency in peptide mapping analyses.

EXPERIMENTAL SECTION

Chemicals and Reagents. The following chemicals were used: ammonium acetate, glacial acetic acid, sodium acetate, formic acid, ammonium bicarbonate, sodium periodate, calcium chloride, ethylenediaminetetraacetic acid (EDTA), dimethyl sulfoxide, acetone (Fisher Scientific, Fairlawn, NJ), benzamidine, immobilized *p*-aminobenzamidine (Sepharose), sodium azide, triethanolamine, urea, equine myoglobin, human angiotensin-1, oxidized insulin B-chain, Lys-bradykinin, bovine cytochrome *c*, and hemoglobin (Sigma, St. Louis, MO), (3-aminopropyl)triethoxysilane (APTES), triethylamine (Aldrich, Milwaukee, WI), NeutrAvidin, sulfosuccinimidyl 6-(biotinamido)hexanoate (NHS-LC-biotin), biotin-LC-hydrazide (Pierce, Rockford, IL), 6-[(6-(biotinoylamino)hexanoyl)amino]hexanoic acid succinimidyl ester (NHS-XX-biotin; Molecular Probes, Eugene, OR), trypsin (TPCK treated; Worthington Enzymes, Freehold, NJ), carboxypeptidase-Y (CPY; Calbiochem-Novabiochem, San Diego, CA). An electric engraving tool was purchased locally (Dremel, Racine, WI). Fused-silica capillaries (FSCs, 50 μm i.d., 360 μm o.d.; Polymicro Technologies, Phoenix, AZ) were used in the preparation of the microreactors and for CE. Water was distilled and deionized (Millipore, Bedford, MA).

Biotinylation of Enzymes and Preparation of Proteolytic Microreactors. The procedures for the preparation of trypsin and CPY microreactors have been described in detail previously.[22,24]

Trypsin Microreactor Digestions for Off-line Mass Spectrometry. Several 90 cm lengths of microreactor were attached to the house vacuum line to draw several capillary volumes of ammonium bicarbonate digestion buffer (0.1 M, pH 8.1) through the microreactors at 25 °C. Test protein solutions (1 mg mL^{-1}) were prepared in the digestion buffer. After the free ends of the microreactors were attached to the house vacuum to siphon several microliters of a protein solution, the microreactor ends were placed into a sterile rubber septum. The microreactors were vibrated with an electric engraving tool for a 10–11 h period at 25 °C. Afterward, a 1 mL syringe containing digestion buffer was coupled to one end of each of the microreactors to elute their contents into 0.5 mL vials, using several microreactor volumes of buffer. The vials were stored frozen.

Trypsin Digestion of Oxidized Insulin B-Chain. The oxidized insulin B-chain solution (2 mg mL^{-1} in NH_4HCO_3 buffer) was introduced into a microreactor by suction using a house

(13) Loo, J. A.; Edmonds, C. G.; Smith, R. D.; Lacey, M. P.; Keough, T. *Biomed. Environ. Mass Spectrom.* **1990**, *19*, 286–294.
(14) Nielsen, P. F.; Roepstorff, P. *Biomed. Environ. Mass Spectrom.* **1989**, *18*, 131–137.
(15) Billeci, T. M.; Stults, J. T. *Anal. Chem.* **1993**, *65*, 1709–1716.
(16) Verm, O.; Roepstorff, P.; Mann, M. *Anal. Chem.* **1994**, *66*, 3281–3287.
(17) Verm, O.; Mann, M. *J. Am. Soc. Mass Spectrom.* **1994**, *5*, 955–958.
(18) Covey, T. R.; Huang, E. C.; Henion, J. D. *Anal. Chem.* **1991**, *63*, 1193–1200.
(19) Edmonds, C. G.; Loo, J. A.; Loo, R. R.; Udseth, H. R.; Barinaga, C. J.; Smith, R. D. *Biochem. Soc. Trans.* **1991**, *19*, 943–947.
(20) Thibault, P.; Paris, C.; Pleasance, S. *Rapid Commun. Mass Spectrom.* **1991**, *5*, 484–490.
(21) Roepstorff, P. *Methods Enzymol.* **1990**, *193*, 432–441.
(22) Amankwa, L. A.; Kuhr, W. G. *Anal. Chem.* **1992**, *64*, 1610–1613.
(23) Amankwa, L. A.; Kuhr, W. G. *Anal. Chem.* **1993**, *65*, 2693–2697.
(24) Licklider, L. J.; Kuhr, W. G. *Anal. Chem.* **1994**, *66*, 4400–4407.
(25) Kuhr, W. G.; Licklider, L. J.; Amankwa, L. A. *Anal. Chem.* **1993**, *65*, 277–282.

vacuum line. After several capillary volumes had eluted, the vacuum line was removed, and the microreactor was carefully connected to an electrically insulated Teflon cell. Both ends of the microreactor were held level to prevent flow during ~30 min incubation of the protein sample in the microreactor.

CPY Digestions. One end of either a 50 or a 25 cm microreactor was attached to the house vacuum line to draw several capillary volumes of an ammonium acetate digestion buffer (0.05 M, pH 5.5, 6.5, or 7.0, with 1 mM EDTA and 0.02% sodium azide) through the microreactors at 25 °C. Angiotensin-1 solutions, 1 mg mL^{-1}, pH 6.5 and 7.0, and a Lys-bradykinin solution, 1 mg mL^{-1}, pH 5.5, were prepared in the digestion buffer. The Lys-bradykinin solution was introduced to a 50 cm length of microreactor by dipping one end of the microreactor in the protein solution and raising it ~30 cm above the free end. The protein solution continuously eluted over a ~1 h period, during which time several microliters of fluid was collected in a 0.5 mL vial and stored frozen. Angiotensin-1 solutions were introduced from a 1 mL syringe coupled to 25 cm lengths of microreactor. The microreactors were immediately attached to an electric engraving tool, which vibrated the microreactors for a 20 min period. Afterward, the microreactors were coupled to the syringe, and the microreactor products were eluted into 0.5 mL vials using several microreactor volumes of buffer. The vials were stored frozen.

Mass Spectrometry. PD mass spectra were collected on a BioIon 20 (BioIon KB, Uppsala, Sweden) time-of-flight (TOF) mass spectrometer fitted with a 10 μCi ^{252}Cf ion source as described previously.[26] Low picomole levels of microreactor eluants were typically mixed with 5 μL of EtOH, and the entire solution was then loaded onto the PD sample foil. Higher levels of digestion products were typically diluted with 10–20 μL of 0.1% TFA, and 50% of the resulting solution was loaded onto the foil after addition of 5 μL of EtOH. After 10 min, the foils were rinsed with distilled, deionized water and dried under a stream of nitrogen. Spectra were accumulated for 2×10^6 primary events at 15 kV ~20 min acquisition time). Mass calibration was achieved using H^+ and Na^+ as internal reference standards.

MALDI-TOF spectra were collected on a Vestec VT 2000 linear TOF mass spectrometer (Perseptive Biosystems Vestec Division, Houston, TX) as described previously.[27] Approximately 0.5–1 μL sample aliquots were mixed with 0.5 μL of a solution of α-cyano-4-hydroxycinnamic acid, prepared fresh daily at a concentration of 10 g/L in 0.1% aqueous TFA/acetonitirle (70:30). The resulting mixtures were loaded onto the end of a stainless steel sample probe and dried at ambient temperature. Samples were irradiated with the frequency-tripled output of a Q-switched Nd–YAG laser (Lumonics HY-400, 355 nm, pulse width 10 ns, repetition rate 10 Hz). Spectra were produced from 50 to 100 laser pulses, and they were recorded and processed as previously described.[27]

The CE capillary was interfaced via an ion spray atmospheric pressure ionization interface to a Sciex triple-quadrupole mass spectrometer (Perkin-Elmer Corp., Norwalk, CT), as described by Thibault and co-workers,[20] with the following modifications. The CE buffer was 2 M formic acid, and the APTES was applied to the fused-silica separation capillary using the procedure for APTES modification of a microreactor capillary.[22] Makeup buffer was a 0.2% formic solution of 1:1 methanol/water, which was supplied coaxially at 5 μL/min. CE separations were carried out on a home-built CE system consisting of a Hippotronics 0–50 kV high-voltage power supply (Model R50B; Brewster, NY) with platinum wire electrodes.

Microreactor/CE/MS Interface. The trypsin microreactor and CE separation capillary were aligned in an electrically insulated well with a solution gap of 100 μm.[23–25] A digestion sample was transferred after the well was filled with a 10-fold dilution of the 2 M H_2CO_2 separation buffer and then applying −12 kV across the coupled microreactor/separation capillary for a 10 s period. The well was then emptied to replace the diluted buffer with the 2 M run buffer before commencing the separation run.

Protein Identification. MassMap v. 1.0 (Finnigan MAT Ltd., Hemel Hempstead, UK) was used on a Gateway 2000 486/DX33 computer (Gateway 2000, N. Sioux City, SD). Protein databases were supplied on CD-ROM by the National Center for Biotechnology Information (Bethesda, MD). The databases used were Brookhaven Protein Database (October 1993), Swiss Prot (release 27.0), PIR International Release 38.0, Protein Research Foundation Database (November 1993), Gen Bank (release 81.0), EMBL (release 37.0), DDBJ (January 1994), dbEST (release 1.35), and the U.S. and European patent databases. The combined set of databases contains over 165 000 protein entries. Input search parameters include protease or chemical cleavage reagent (trypsin), measured peptide masses, a mass tolerance (typically 2.5 Da), and a molecular mass range for the intact protein. Enzyme cleavage rules can be input by the user. For these experiments, both complete and incomplete digestions were allowed. The products of complete tryptic digestion are indicated as T_i in the table and figures. The subscript i designates tryptic fragment number, where the N-terminal fragment is assigned as T_1. The products of incomplete tryptic digestion are indicated as $T_{i-1,i}$.

RESULTS AND DISCUSSION

Several possibilities were envisioned for coupling a microreactor with mass spectrometry and are outlined in Figure 1. In the simplest case (Figure 1a), pure protein is admitted into the microreactor, digested material is eluted, and the contents are transferred to the mass spectrometer. Although this could be accomplished with either on-line or off-line mass spectrometry, the off-line approach more easily permits independent optimization of both parts of the procedure (i.e., digestion and analysis). In the second case (Figure 1b), the contents of the microreactor could be loaded onto a separation column before mass spectrometry. The separation could be accomplished either by HPLC or CE. An intriguing possibility investigated here is the direct coupling of the microreactor and CE capillaries via a gap junction,[23–25] followed by on-line CE/ion spray mass spectrometry. Finally, in the third case shown (Figure 1c), an on-line separation step prior to the microreactor could conceivably result in the highest degree of automation for the analyses of complex mixtures. Individually purified proteins could be sequentially loaded onto a microreactor, or parallel microreactors could be employed. Digestion products could then be analyzed either directly or after a separation step.

Procedures utilized earlier for peptide mapping in a CE format[22–25] were duplicated in our investigations of the optimal

(26) Takigiku, R.; Keough, T.; Lacey, M. P.; Schneider, R. E. *Rapid Commun. Mass Spectrom.* **1990**, *4*, 24–29.
(27) Keough, T.; Takigiku, R.; Lacey, M. P.; Purdon, M. *Anal. Chem.* **1992**, *64*, 1594–1600.

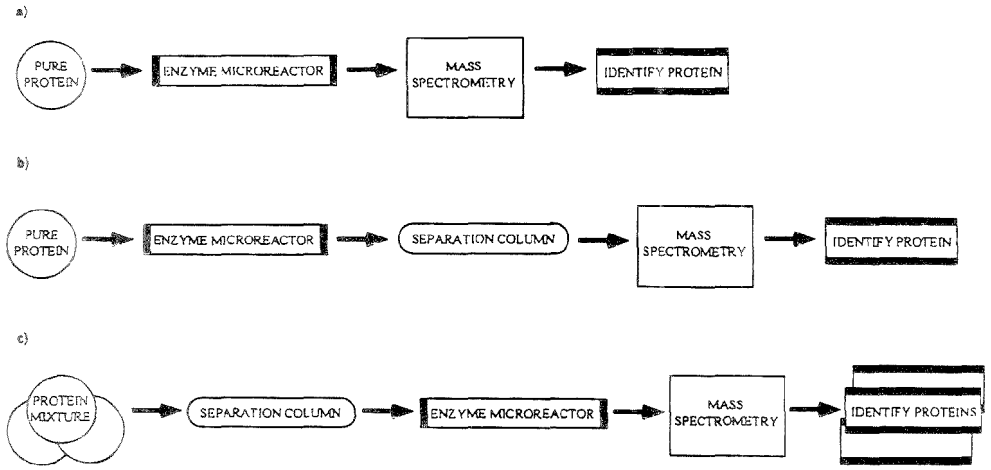

Figure 1. Modes of combining microreactors with MS. (a) Pure protein is admitted into the microreactor, digested material is eluted, and the contents are transferred to the off-line mass spectrometer. (b) Contents of the microreactor are loaded directly onto a separation column (HPLC or CE) before ion spray mass spectrometry. (c) On-line separation is used to purify proteins from complex mixtures prior to microreactor digestion, which is followed by mass spectrometry.

preparation, isolation, and transfer of the microreactor digestion products to facilitate rapid and convenient determinations of peptide molecular masses. In particular, optimization of the trypsin digestion of globular protein structures was essential.[24] Identification of proteins by mass fingerprinting is generally successful, even when only a small subset of the tryptic peptides is used for a given protein.[4-6] Since a complete set of tryptic fragments is not required for identification, the purified proteins were simply solubilized in digestion buffer and placed in the trypsin microreactor without any manipulations which could lead to losses, contamination, or undesired modification. Introduction of peptides and proteins to the microreactors was accomplished by hydrodynamic flow. For example, gravity alone sustained the flow of Lys-bradykinin and the oxidized insulin B-chain solutions through a CPY-modified microreactor. This resulted in continuous elution of the digestion products for convenient collection in 0.5 mL vials. Angiotensin-1 and proteins incubated in the microreactors prior to off-line collection were eluted using several microreactor volumes of dilute digestion buffer. The collection of relatively large digestion samples was done to facilitate off-line collection and storage without lyophilizing or modifying the samples. Shorter lengths of microreactor would be advantageous for generating digestion samples in smaller volumes.

The length of incubation in trypsin microreactors was chosen on the basis of preliminary CE analyses of the optimized microreactor digestion of representative globular proteins (α_1 acid glycoprotein, cytochrome *c*). The observed peptide maps contained only the peptide fragments after 10 h. More recently, CE analyses have indicated that only peptide fragments are recovered from the microreactor within 4 h of incubating 4 pmol of undenatured cytochrome *c* per centimeter length of microreactor (data not shown). Other rapid (<1 h) digestions of low picomole quantities of cytochrome c and other proteins have been demonstrated using trypsin immobilized on either agarose in Pyrex glass tubing (1 mm i.d.)[28] or macroporous silica supports packed into FSCs (0.32–0.50 mm i.d.).[25] A complication in utilizing these designs for protein digestion at the low picomole level has been the 100-fold or greater dilution following elution and off-line collection of the digestion products. Off-line collection of the products was followed either by an off-line lyophilization procedure after elution from the agarose support[28] or by concentration on a reverse-phase column for HPLC analysis.[29] A major concern for the use of the silica enzyme support was loss of protein sample due to adsorptive processes. Recovery of the products was observed to decrease with reductions in the initial protein concentrations loaded, being only 50–60% for the highest cytochrome *c* concentrations (10–50 pmol/μL).[29] The use of this capillary packing for digestion of several picomoles of protein complicated the peptide mapping analysis with the production of relatively large quantities of trypsin autolytic fragments.[20]

The specificity of trypsin microreactor digestions of proteins is demonstrated by the purity of the observed mass spectra obtained by off-line MALDI-MS analyses of the digestion products. Figure 2a shows a MALDI-TOF mass spectrum of the peptide products from equine myoglobin (MW 16 952). Sequence assignments are summarized in Table 1. Approximately 200 nL, representing 10% of the total microreactor volume, was mixed with the UV-absorbing matrix prior to generating the spectrum. The molecular masses determined for the microreactor digestion mixture were used in a database search to test the feasibility of protein identification using this procedure. The identification of equine myoglobin was unambiguous. The four most likely candidate proteins assigned from the databases were all horse heart myoglobin. Nine of the 10 most probable candidates were myoglobin from various sources. The assignment of partial sequences to the measured peptides was straightforward (Table

(28) Cobb, K. A.; Novotny, M. V. *Anal. Chem.* **1992**, *64*, 879–886.
(29) Davis, M. T.; Lee, T. D.; Ronk, M.; Hefta, S. A. *Anal. Biochem.* **1995**, *224*, 235–244.

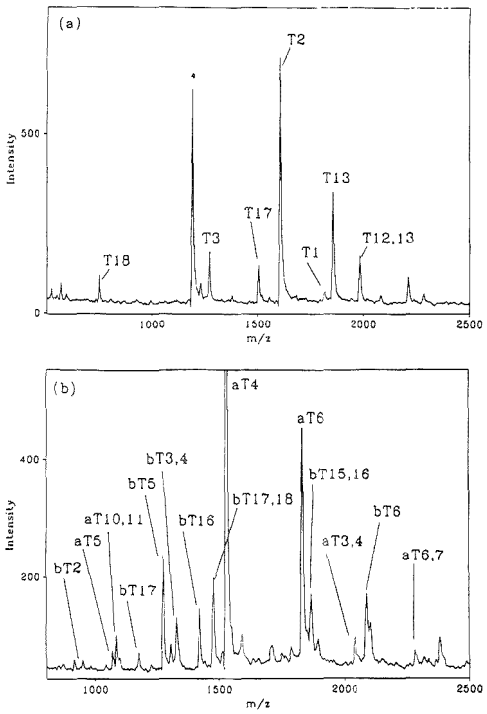

Figure 2. Positive ion MALDI-TOF mass spectrum of the trypsin microreactor digestion products from (a) equine myoglobin and (b) bovine hemoglobin.

1), particularly since no fragments associated with the autolysis of trypsin were observed. Notice that incomplete tryptic digestion products appear in Table 1. Incomplete digestion can be advantageous, since it often allows observation of small fragments that might otherwise have been lost in sample handling or analysis. For the myoglobin tryptic peptides, observation of $T_{12,13}$ in addition to T_{13} allows confirmation of residue 79, which was not seen directly as T_{12}. Roughly 54% coverage of the protein sequence, 82 out of 153 residues, was achieved in this analysis. Denaturation of the protein before microreactor digestion would presumably allow even greater coverage in the peptide map. However, observation of only 3–4 tryptic peptide masses should serve to identify a protein from databases.[4-6] Therefore, a rapid and convenient means of generating mass fingerprints with minimal sample handling was demonstrated by this experiment.

Figure 2b shows a MALDI-TOF mass spectrum of the peptide products from bovine hemoglobin. Approximately 30 pmol of protein, representing 300 fmol/cm, was incubated in the microreactor. Sequence assignments are summarized in Table 1. Twelve of the most abundant masses from Figure 2b were used as inputs for the search algorithm. In the initial search, the protein molecular mass range was limited to 60 000–70 000 Da, the mass range for intact hemoglobin. The hemoglobin tetramer was not identified in this way. Unrelated structures were identified as the most likely candidate proteins. Since the globulin subunits and not the tetrameric protein would appear in the MALDI mass spectra, the search was repeated using the same input masses

Table 1. Summary of Molecular Mass Measurements and Sequence Assignments for the Observed Tryptic Peptides Formed in Microreactor Digestions

		MH^+	
tryptic fragment	residues	measd	calcd
	Equine Myoglobin		
T_{18}	134–139	748.9	748.9
T_3	32–42	1272.4	1272.5
T_{17}	119–133	1503.6	1502.7
T_2	17–31	1607.8	1607.8
T_1	1–16	1816.3	1817.0
T_{13}	80–96	1854.6	1855.1
$T_{12,13}$	79–96	1982.6	1983.2
	Bovine Hemoglobin		
α-chain			
T_5	32–40	1072.3	1071.6
$T_{10,11}$	91–99	1088.1	1087.6
$T_{1,2}$	1–11	1101.4	1101.6
T_4	17–31	1530.4	1529.7
T_6	41–56	1834.3	1833.9
$T_{3,4}$	12–31	2043.7	2043.0
$T_{6,7}$	41–61	2284.2	2284.1
β-chain			
T_2	8–16	951.6	950.5
T_4	19–29	1100.5	1101.6
T_{17}	132–143	1178.6	1177.7
T_5	30–39	1275.7	1274.7
$T_{3,4}$	17–29	1329.6	1328.7
T_{16}	120–131	1423.0	1422.7
$T_{17,18}$	132–145	1478.7	1477.8
$T_{15,16}$	117–131	1869.1	1869.0
T_8	40–58	2090.2	2090.0
	Bovine Cytochrome *c*		
$T_{3,4}$	8–13	763.1	763.0
T_{15}	80–86	780.1	780.0
$T_{13,14}$	73–79	806.8	807.0
$T_{15,16}$	80–87	908.7	908.2
T_8	28–38	1169.6	1169.3
$T_{7,8}$	26–38	1435.9	1434.7
$T_{9,10}$	39–53	1587.5	1585.7
$T_{4,5}$	9–22	1635.1	1635.0
T_{12}	56–72	2010.6	2011.3
$T_{12,13}$	56–73	2138.9	2139.4
$T_{11,12}$	54–72	2251.2	2253.5

but restricting the protein molecular mass range to that of the A- and B-chains (15 000–20 000 Da). Under these circumstances, the top 10 candidate proteins were hemoglobin or the hemoglobin A- and B-chains. Obviously, caution is required when oligomeric proteins are encountered in the current database searching procedure. It is obvious from the data in Figure 2b and Table 1 that the intact protein must have been hemoglobin and not just the A- or B-chain. This experiment yielded 79% coverage of the entire sequence of bovine hemoglobin.

Figure 3 shows the PD mass spectrum acquired for a trypsin microreactor digestion of bovine cytochrome *c* (MW 11 572) with ~2 pmol of the protein digested per centimeter length of microreactor. Sequence assignments are summarized in Table 1. An abundant ion corresponding to the free heme is evident in the spectrum at *m/z* 619. A few components which were not identified as tryptic peptides may have been due to impurities present in the sample. The sequence coverage achieved in this experiment was ~79% (82 out of 104 residues). PDMS tryptic mass maps acquired for a variety of proteins were comparable to MALDI-MS mapping of myoglobin and hemoglobin digests, in regard to the same extent of percentage sequence coverage observed.

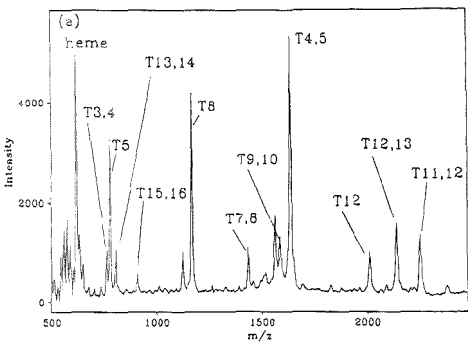

Figure 3. Positive ion PD mass spectra of trypsin microreactor digestion products from bovine cytochrome *c*.

Direct analysis of peptide mixtures by mass spectrometry has been advantageous for monitoring the CPY-mediated hydrolysis of the carboxyl (C)-termini of large peptides and proteins for identification of their C-terminal sequences.[30-33] As anticipated on the basis of the considerable variation in the rate of release for different C-terminal amino acids,[34] a complex mixture of truncated peptides was produced for human angiotensin-1 and Lys-bradykinin samples after only 20–30 min in the microreactor. PDMS analyses of these digests revealed a concatenated series of peptides, from which 3–4 residues of the C-terminal sequences can be identified. The ion abundances suggested that reaction rates in the CPY microreactor may be comparable to reaction rates obtained for the solubilized enzyme. Small changes in pH near the pH optimum for CPY greatly affect the respective rates of cleavage for acidic, neutral, and basic amino acid residues.[35] In microreactors of 500 nL volume produced from a single 50 cm length of microreactor, ~20 pmol of human angiotensin-1 (MW 1295.5) per centimeter length of microreactor was digested at pH 7.0 and 6.5. The PD mass spectra observed appear in Figure 4, parts a and b for pH 7.0 and 6.5, respectively. Although the ion intensity axes differ between the mass spectra, each contained three truncated peptides, demonstrating the release of leucine, histidine, and phenylalanine. Al_2C_3 cluster ions were responsible for most of the low-abundance ions observed in the spectra. A greater extent of the reaction was observed at pH 7 than at pH 6.5, as would be expected for a sequence containing a basic residue.

Figure 4c shows the PD mass spectrum acquired for a CPY microreactor digestion after collecting ~1 microreactor volume (1 μL) of a Lys-bradykinin solution flowing continuously through the microreactor. Efficient recovery of nanoscale volumes of digestion products could be facilitated using this approach. Elution time from the 50 cm length of microreactor was ~30 min. Using the information contained in Figure 4c, four truncated peptides were identified, which led to the conclusion that

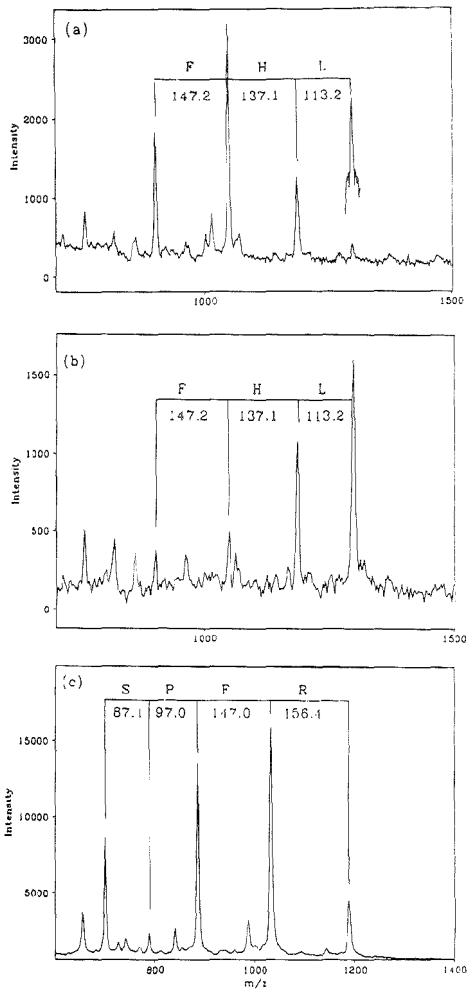

Figure 4. Positive ion PD mass spectra of the CPY microreactor digestion products from angiotensin-1 at (a) pH 7.0 and (b) pH 6.5. (c). Positive ion PD mass spectrum of the CPY microreactor digestion products of Lys-bradykinin.

sequential release of four C-terminal amino acid residues, arginine, phenylalanine, proline, and serine, had occurred. Several unidentified ions of low abundance appear in Figure 4c near a molecular ion (*m/z* 788.8) of similar abundance which had been assigned to a digestion product. Although identification of the molecular ion of interest is complicated by the nearby ions, it is the difference in reaction rates for removal of the C-termini (proline and serine) which resulted in a relatively low yield for this peptide molecular ion. Rapid removal of the digestion products from the microreactor and control of the reaction conditions are essential to allow identification of each digestion product.

The ultimate utility of nanoliter (and smaller) microreactors can be gained only by the removal of all sample handling steps.

(30) Thiede, B.; Wittmann-Liebold, B.; Bienert, M.; Krause, E. *FEBS Lett.* **1995**, *357*, 65–69.
(31) Schar, M.; Bornsen, K. O.; Gassman, E. *Rapid Commun. Mass Spectrom.* **1991**, *5*, 319–326.
(32) Self, R.; Parente, A. *Biomed. Mass Spectom.* **1983**, *10*, 78–82.
(33) Klarskov, K.; Breddam, K.; Roepstorff, P. *Anal. Biochem.* **1989**, *180*, 28–37.
(34) Hayashi, R. *Methods Enzymol.* **1977**, *47*, 84–93.
(35) Hayashi, R.; Bai, Y.; Hata, T. *J. Biochem.* **1975**, *77*, 69–79.

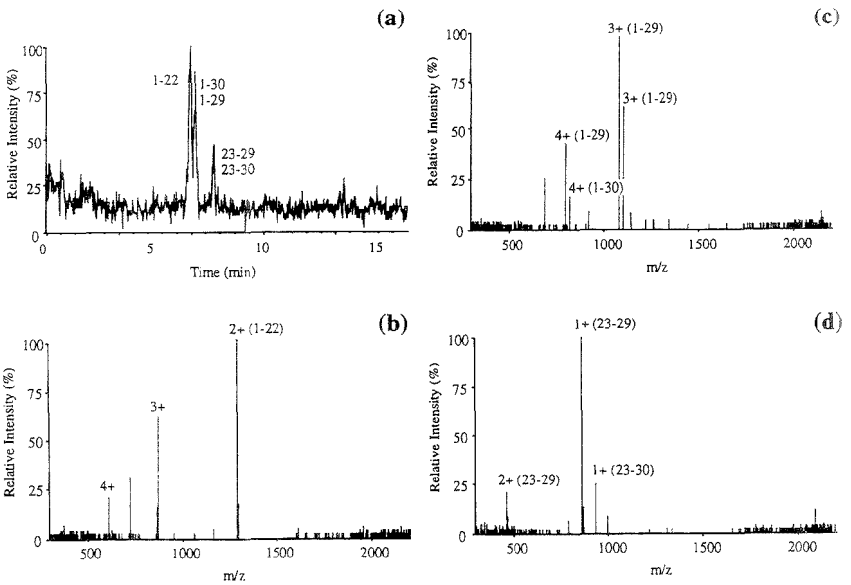

Figure 5. (a) On-line CE/MS total ion chromatogram of the products formed by tryptic digestion of the oxidized insulin B-chain. Ion spray mass spectra of (b) the early-eluting component and (c, d) the unresolved later-eluting components.

The sample must be introduced to the reactor, digested, separated, and transferred to the mass spectrometer without any intervening steps. Such an on-line procedure, which integrates a variety of enzyme microreactors with a CE separation of the digests, was reported previously.[23,24] Figure 5a shows a total ion chromatogram (TIC) obtained for a CE/ESI-MS analysis of the tryptic fragments of the oxidized B-chain of bovine insulin following a 10 s on-line injection from a trypsin microreactor. A fluid junction integrated the microreactor with CE/ESI-MS, allowing the transfer of low nanoliter aliquots of tryptic digest to the separation capillary. A high separation efficiency of $\sim 10^5$ plates and a mass accuracy of 0.03% were demonstrated. The high ion abundances indicate that electromigration of digest aliquots from a capillary microreactor into a CE separation capillary can provide the most efficient means of sampling the digestion products. Efficient digestion of a large quantity of the oxidized insulin B-chain occurred within ~40 min, and the entire peptide mapping required <1 h. Eleven picomoles of the oxidized insulin B-chain was digested per centimeter of microreactor, using a 50 cm length of microreactor. Because only nanoliter scale volumes of digestion products were transferred for the on-line CE/ESI-MS analysis, much smaller quantities of the protein sample would be sufficient for on-line peptide mapping procedure. Experiments are currently in progress utilizing short microreactor segments integrated in a CE system.

Figure 5, parts b and c contain selected mass spectra collected over time intervals associated with the peaks appearing in Figure 5a. A triply charged molecular ion originating from the (1–22) fragment and a singly charged molecular ion originating from the (23–29) fragment differed only by 1 in m/z ratio; preceding the mass analysis by CE was vital to the assignment of these ions. Although neither the (1–29) and (1–30) tryptic fragments, nor the (23–29) and (23–30) pair were resolved, an increase in the electrophoresis voltage or lowering of the electroosmotic flow rate may increase the resolution obtained by CE. Off-line microreactor digestion followed by a CE/ESI-MS analysis, providing ~50% longer separation time, did successfully resolve the (23–29) and (23–30) fragments (data not shown).

CONCLUSIONS

The picoliter to nanoliter volume requirements and the efficient modes of sample handling demonstrated with trypsin- and CPY-modified capillary microreactors of 20 nL volume per centimeter length facilitated the preparation, isolation and transfer of picomole quantities of protein digests. Complex proteolytic digests prepared in the microreactors were analyzed either off-line by PD and MALDI-MS, or by on-line CE/ESI-MS. The mass spectra contained abundant ions corresponding to highly specific enzyme cleavages. The absence of enzyme autolysis products simplified the interpretation of the mass spectra. Ions that could not be assigned to tryptic peptides were generally of very low abundance, which has not been possible for peptide mass mapping utilizing low-volume, homogeneous digestions. The sequence coverage provided by the observed tryptic fragments varied between the observed MALDI spectra of myoglobin (54%) and hemoglobin (79%). Additional sample preparation to completely unfold the polypeptide chains would, conceivably, produce additional tryptic fragment masses in the 500–2500 Dal range. The integration of PDMS and MALDI-MS data with software methods designed to search protein sequence databases allowed rapid identification of the test proteins used in these investigations. C-Terminal sequences covering 3–4 residues were obtained from the PD mass spectra obtained following CPY microreactor digestions of angiotensin-1 and Lys-bradykinin. This much information should adequately define the C-termini of peptides for many applications.

An on-line method of sample handling, involving electromigration of aliquots from a capillary microreactor into a CE separation capillary, allowed rapid peptide mapping of the oxidized insulin B-chain in an on-line trypsin microreactor/CE/ESI-MS system. The entire peptide mapping procedure required <1 h.

ACKNOWLEDGMENT

This work was supported, in part, by a National Science Foundation Presidential Investigator Award (Grant CHE-897394) and by a grant provided by Procter & Gamble Corp.

Received for review May 12, 1995. Accepted August 29, 1995.[⊗]

AC950461G

[⊗] Abstract published in *Advance ACS Abstracts*, October 15, 1995.

Anal. Chem. **1995**, *67*, 4178–4183

Identification and Quantification of Lipid Sulfate Esters by Electrospray Ionization MS/MS Techniques: Cholesterol Sulfate

Karl Metzger,[†] Petra A. Rehberger,[‡] Gerhard Erben,[†] and Wolf D. Lehmann*[,†]

Central Spectroscopy Department and Research Programme Tumor Cell Regulation, German Cancer Research Center, Im Neuenheimer Feld 280, D-69120 Heidelberg, Germany

Negative ion electrospray ionization mass spectrometry combined with collisional activation is used for specific detection of sulfate esters in the presence of phosphomonoesters and phosphodiesters. The energy dependence for the formation of the relevant collision-induced fragment ions is investigated. Sulfomonoesters give rise to a specific $[SO_3]^-$ fragment at *m/z* 80, whereas phosphomonoesters generate a specific $[PO_3]^-$ fragment at *m/z* 79 and a specific $[PO_2]^-$ fragment at *m/z* 63. In addition, both sulfo- and phosphomonoesters generate an isobaric fragment ion at *m/z* 97, with the composition $[HSO_4]^-$ or $[H_2PO_4]^-$, respectively. Phosphodiesters generate this fragment ion with 2–3 orders of magnitude lower relative abundance compared to phosphomonoesters. A clear discrimination between sulfo- and phosphoesters was achieved by product ion analysis of the M + 2 satellite ion of their corresponding $[M - H]^-$ species: in the presence of ^{34}S, the fragment ions split into doublets, whereas the fragment ions of phosphate esters remain monoisotopic signals. Cholesterol 3-sulfate is identified and quantitated from total lipid extracts of mouse skin keratinocytes without chromatographic separation and using dihydrocholesterol 3-sulfate as internal standard. During epidermal differentiation, the level of cholesterol 3-sulfate increases from about 16 ng/10^6 cells found in basal cells to about 400 ng/10^6 cells observed in the most differentiated cells.

Biochemically relevant organic sulfate esters include drug metabolite conjugates, hormone conjugates, sulfopeptides, sulfated nucleotides, and sulfolipids such as sulfatides and cholesterol sulfate.[1,2] Intact sulfoesters can be analyzed by mass spectrometry (MS) using a soft ionization technique such as fast atom bombardment,[3–6] electrospray ionization (ESI), or matrix-assisted laser desorption.[7] In the negative ion mode, these organic sulfate esters form intense $[M - H]^-$ ions due to their anionic nature. This investigation describes the low-energy collision-induced dissociation (CID) of lipid sulfate ester anions generated by negative ion ESI with emphasis on the use of MS/MS techniques for discrimination between isobaric sulfate and phosphate esters, a problem also relevant in the area of peptide and protein analysis.[8] As a biochemically relevant application of these techniques, the identification of cholesterol 3-sulfate in total lipid extracts from mouse keratinocytes is described. Further, it is shown that MS/MS methods can be used for a straightforward and highly sensitive quantification of cholesterol 3-sulfate in total lipid extracts from subfractions of mouse skin keratinocytes separated according to their state of differentiation.

EXPERIMENTAL SECTION

Materials. Hydrocortisone 21-sulfate, hydrocortisone 21-phosphate, cholesterol 3-sulfate, dihydrocholesterol 3-sulfate, and dipalmitoylphosphatidic acid were obtained from Sigma (Deisenhofen, FRG). All solvents used were of analytical grade and obtained from E. Merck (Darmstadt, FRG).

Fractionation of Mouse Keratinocytes. Keratinocytes were obtained from neonatal NMRI mice (Institut für Versuchstierkunde, Hannover, FRG) and subfractionated using a preformed discontinuous Percoll (Pharmacia, Freiburg, FRG) gradient as described.[8] Aliquots of the keratinocyte subfractions were counted in a Neubauer chamber. Between 5×10^6 and 15×10^6 cells per fraction were investigated in a single experiment.

Extraction of Membrane Lipids and Quantification of Cholesterol 3-Sulfate. Keratinocyte subfractions were pelleted by centrifugation, washed once with ice-cold PBS buffer, and resuspended in 200 μL of ice-cold PBS buffer. After addition of 10 nmol of dihydrocholesterol 3-sulfate as internal standard to the samples containing between 5×10^6 and 15×10^6 cells, lipids were extracted according to a modified Bligh and Dyer procedure.[9] Shortly, 4 mL of ice-cold chloroform/methanol (2:1) was added to the sample, and the solution was mixed vigorously. The organic phase was separated by centrifugation at 2000*g* for 10 min at 4 °C and washed with 1 mL of 0.1 M potassium chloride. The extract was evaporated under a stream of nitrogen and the residue redissolved in 500 μL of a chloroform/methanol (1:1) mixture. This solution was directly infused into the ESI ion source.

Ethanolic stock solutions of cholesterol 3-sulfate and dihydrocholesterol 3-sulfate with a concentration of 200 μg/mL each were

Central Spectroscopy Department.
‡ Research Programme Tumor Cell Regulation.

(1) Rearick, J. I.; Jetten, A. M. *J. Biol. Chem.* **1986**, *261*, 13898–13904.
(2) Uchida, Y.; Iwamori, M.; Nagai, Y. *Jpn. J. Exp. Med.* **1988**, *58*, 153–161.
(3) Gaskell, S. J.; Brownsey, B. G.; Brooks, P. W.; Green, B. N. *Biomed. Mass Spectrom.* **1983**, *10*, 215–219.
(4) Lehmann, W. D.; Kaspersen, F. M. *J. Labelled Compd. Radiopharm.* **1984**, *2*, 455–469.
(5) Gaskell, S. J. *Biomed. Environ. Mass Spectrom.* **1988**, *15*, 99–104.
(6) Carr, S. A.; Hemling, M. E.; Bean, M. F.; Roberts, G. D. *Anal. Chem.* **1991**, *63*, 2802–2824.
(7) Talbo, G.; Roepstorff, P. *Rapid Commun. Mass Spectrom.* **1993**, *7*, 201–204.
(8) Fürstenberger, G.; Gross, M.; Schweizer, J.; Vogt, I.; Marks, F. *Carcinogenesis* **1986**, *7*, 1745–1753.
(9) Bligh, E. G.; Dyer, W. J. *Can. J. Biochem. Physiol.* **1959**, *37*, 911–917.

0003-2700/95/0367-4178$9.00/0

Table 1. Parameters of Linear Regression Calibration Lines $y = a + mx$ for the Quantification of Cholesterol 3-Sulfate Using Dihydrocholesterol 3-Sulfate as Internal Standard[a]

sample	mode of measurement	a	m
pure standards	regular scan	0.020	1.201
	parent scan, m/z 97	0.011	1.244
spiked U937 cells	regular scan	0.060	1.075
	parent scan, m/z 97	0.020	1.158

[a] y, corrected ratio m/z 465 over 467; x, gravimetric molar ratio of cholesterol sulfate over dihydrocholesterol sulfate.

prepared. Eight different mixtures were prepared according to the following volume ratios of cholesterol sulfate to dihydrocholesterol sulfate stock solutions: 1:9, 2:8, 3:7, 5:5, 6:4, 7:3, 8:2, 9:1. To 100 μL of each of these mixtures was added 900 μL of methanol to obtain a set of standard mixtures with a total concentration of cholesterol sulfate plus dihydrocholesterol sulfate of 20 μg/mL.

In these standard mixtures, the intensity ratio of m/z 465 over 467 was measured by ESI-MS. The intensity of the signal at m/z 467 was corrected for the contribution of the M + 2 isotope peak of cholesterol sulfate of 10.16% relative abundance, and the corrected ratio was plotted against the molar ratio of the standard mixtures. In addition to the regular scan mode, the standard mixtures were analyzed in the more specific parent ion scan mode on the basis of the $[HSO_4]^-$ fragment ion, which represents the most intense collision-induced fragment ion of cholesterol 3-sulfate and dihydrocholesterol 3-sulfate under the conditions of low-energy collisions. Since the fragment at m/z 97 does not contain the ^{34}S isotope, the isotopic correction for the spillover from m/z 465 to 467 is reduced from 10.16% to 5.47% for evaluation of the parent ion scan mode data. To mimic the quantification of cholesterol sulfate in the presence of cellular phospholipids, aliquots of 10^6 cells were spiked with 4 μL of each standard mixture (corresponding to 80 ng of sulfate esters/10^6 cells), lipids were extracted as described above, and the intensity ratio of the signals at m/z 465 over 467 was determined in the same way as for the pure standard mixtures. For these measurements, U937 cells were selected, since this cell line does not contain detectable amounts of cholesterol 3-sulfate. For all series of calibration measurements, linear calibration plots with similar slopes and y-axis intersections were obtained. The corresponding data determined by linear regression are given in Table 1.

The calibration plots obtained by analyzing the spiked cellular extracts from U937 cells were used for quantification for cholesterol 3-sulfate in keratinocytes. These calibration plots are given below in Figure 8.

Mass Spectrometry. All mass spectrometric analyses were performed using a triple quadrupole instrument Model TSQ 7000 (Finnigan MAT, San Jose, CA) equipped with the Finnigan ESI source. The electron multiplier was operated at 1.4 kV, and the transfer capillary was maintained at 200 °C. Argon was used as collision gas at a nominal pressure of 2 mTorr. Lipid extracts were infused at a rate of 3 μL/min in chloroform/methanol (1:1).

RESULTS AND DISCUSSION

CID Fragments of Sulfate and Phosphate Esters. Upon collisional activation of $[M - H]^-$ ions, both sulfate and phosphate monoesters form a fragment ion of m/z 97, representing an

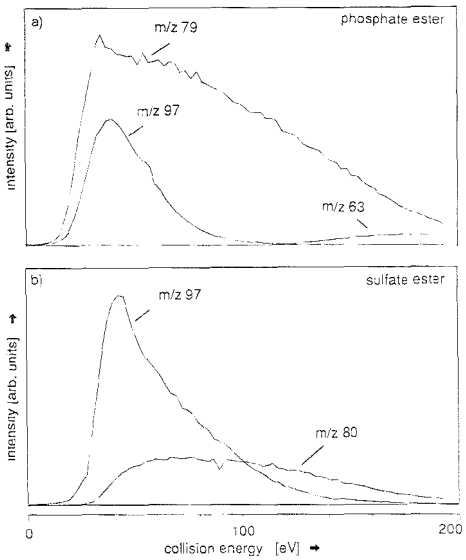

Figure 1. Fragment ion intensities as a function of the q2 collision energy. (a) CID of $[M - H]^-$ of hydrocortisone 21-phosphate at m/z 441 and detection of the fragments at m/z 97, 79, and 63. (b) CID of $[M - H]^-$ of hydrocortisone 21-sulfate at m/z 441 and detection of m/z 97 and 80.

Scheme 1. Fragmentation of Sulfate and Phosphate Monoester $[M - H]^-$ Ions upon Collisional Activation[a]

$$[R\text{-}O\text{-}S\text{-}O_3]^- \rightarrow \underset{\textbf{m/z 97}}{[HSO_4]^-} \rightarrow \underset{\text{m/z 80}}{[SO_3]^-}$$

$$[R\text{-}O\text{-}PO_3H]^- \rightarrow \underset{\text{m/z 97}}{[H_2PO_4]^-} \rightarrow \underset{\textbf{m/z 79}}{[PO_3]^-} \rightarrow \underset{\text{m/z 63}}{[PO_2]^-}$$

[a] The main fragment ions are given in bold print.

$[H_2PO_4]^-$ or $[HSO_4]^-$ ion, respectively. In addition, specific fragments are formed, namely $[SO_3]^-$ at m/z 80 for sulfate esters as well as a $[PO_3]^-$ fragment ion at m/z 79 and a $[PO_2]^-$ fragment at m/z 63. The fragmentation behavior for phosphate monoesters has been demonstrated (e.g., for phosphorylated peptides) and used as the basis for discrimination between phosphorylated and nonphosphorylated peptides by electrospray MS/MS techniques.[10,11] The fragmentation of sulfate and phosphate monoesters under CID conditions is summarized in Scheme 1.

The energy dependence of these fragment ions is shown in Figure 1 for the low-energy collisional activation of the pair of model compounds hydrocortisone 21-sulfate and hydrocortisone 21-phosphate.

For hydrocortisone sulfate, the energy plots in Figure 1b suggest a precursor/product relationship between the $[HSO_4]^-$ and the $[SO_3]^-$ fragments. At collision energies below 30 eV, only the m/z 97 fragment ion is observed. By increasing the collision energy, this fragment is converted into the m/z 80 fragment ion

(10) Huddleston, M. J.; Annan, R. S.; Bean, M. F.; Carr, S. A. *J. Am. Soc. Mass Spectrom.* **1993**, *4*, 710–717.
(11) Ding, J.; Burkhart, W.; Kassel, D. B. *Rapid Commun. Mass Spectrom.* **1994**, *8*, 94–98.

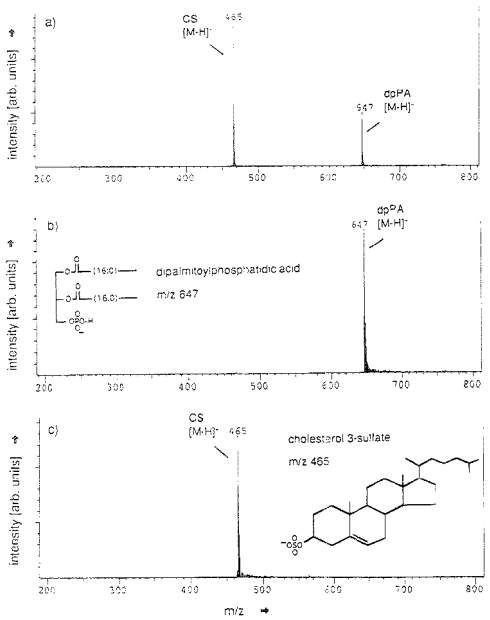

Figure 2. Negative ion ESI analysis of a roughly equimolar mixture of cholesterol sulfate (CS) and dipalmitoylphosphatidic acid (dpPA): (a) normal scan, (b) parent scan, *m/z* 79, at 120 eV collision energy, and (c) parent scan, *m/z* 80, at 120 eV collision energy.

by loss of an OH radical. A different relationship is observed for the phosphate ester fragments $[H_2PO_4]^-$ and $[PO_3]^-$, as evident from the energy plots in Figure 1a. With an onset at about 20 eV, the $[PO_3]^-$ ion is observed consistently as the most intense fragment ion, probably because the loss of water from $[H_2PO_4]^-$ is energetically favored compared to the loss of an OH radical from $[HSO_4]^-$. Compared to data from the literature concerned with optimal detection of phosphate ester-specific fragment ions from peptide phosphomonoesters with CID and negative ion ESI-MS,[11] the collision energies required for optimal fragmentation of lipid phosphomonoesters observed in this study are significantly lower. We ascribe this effect to the different model of mass spectrometer used rather than to the different class of phosphoesters investigated.

On the basis of the energy plots in Figure 1, a clear distinction between a phosphate and a sulfate ester can be made: At collision energies of 30–40 eV, a sulfate ester shows a single low-mass fragment ion at *m/z* 97, whereas for a phosphate ester, both *m/z* 97 and 79 fragment ions are observed at an intensity ratio of about 1:2. At higher collision energies of 80–120 eV, a sulfate ester shows two fragment ions (*m/z* 80 and 97) of comparable intensity, whereas under identical conditions, a phosphate ester generates predominantly the fragment at *m/z* 79. The fragments at *m/z* 80 and 79 can be used for specific detection of sulfate and phosphate esters by a corresponding parent ion scan. According to the energy plots in Figure 1, this parent ion scan can be performed at collision energies between 50 and 150 eV. Figure 2 shows this for a mixture of cholesterol 3-sulfate and dipalmitoylphosphatidic acid analyzed with a parent scan of *m/z* 79 and 80 and a collision energy of 120 eV.

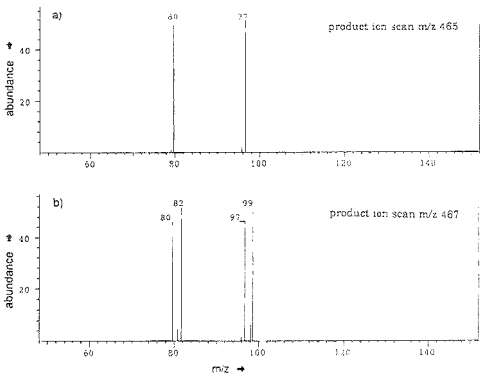

Figure 3. Collision-induced dissociation of authentic cholesterol 3-sulfate at 120 eV collision energy. (a) Product ion analysis of $[M - H]^-$ at *m/z* 465. (b) Product ion analysis of $[M - H + 2]^-$ at *m/z* 467.

The spectra in Figure 2 verify the conclusions drawn from the energy diagrams in Figure 1 and clearly identify the $[M - H]^-$ ions of cholesterol sulfate as the precursor of the $[SO_3]^-$ fragment at *m/z* 80 and the $[M - H]^-$ ions of dipalmitoylphosphatidic acid as the sole precursor of the $[PO_3]^-$ fragment ion at *m/z* 79. Thus, it is demonstrated that sulfate and phosphate monoesters can be selectively identified in mixtures by parent ion analysis of a specific fragment ion.

Another possibility for positive identification of sulfate esters makes use of the isotopic distribution of sulfur, which contains ^{34}S with a natural abundance of 4.2%. In contrast, phosphorus is naturally occuring as a monoisotopic element. There are three ways to visualize the presence of sulfur in sulfate ester ion signals: (i) via the isotopic distribution of the intact $[M - H]^-$ ion, (ii) via the isotopic distribution of the $[HSO_4]^-$ or of the $[SO_3]^-$ fragment ion produced by CID of the unselected ion beam (atmospheric pressure ionization CID, API-CID, octapole CID), and (iii) via CID of the $[M - H + 2]^-$ satellite ion. The first and second methods require that a mass spectrum with low background signals can be recorded, since an accurate determination of the isotopic distribution is needed, as will be demonstrated below. The third identification method, via product ion analysis of the $[M - H + 2]^-$ ion, is more specific and generally applicable for mixture analysis. CID of the $[M - H + 2]^-$ satellite ion of cholesterol sulfate results in a splitting of the $[HSO_4]^-$ and $[SO_3]^-$ fragment ion signals into doublets separated by 2 mass units. For cholesterol sulfate, this method results in the generation of an ion doublet consisting of two ions of about equal intensity, as shown in Figure 3.

The roughly 1:1 doublet splitting observed for cholesterol 3-sulfate is due to the fact that the ion at *m/z* 467 contains about equal amounts of ^{32}S and ^{34}S. The estimation of the isotopic composition of the ion at *m/z* 467 of cholesterol sulfate and of the corresponding fragment ions is given in Table 2. Exact calculation gives a ratio of 1.2:1 of the ^{34}S-containing ions at *m/z* 82 and 99 relative to the ^{32}S-containing ions at *m/z* 80 and 97. This calculation is in good agreement with the experimental data shown in Figure 3.

Identification of Cholesterol Sulfate in Keratinocytes. When total lipid extracts from mouse keratinocytes were investigated by ESI mass spectrometry, a signal at *m/z* 465 was

Table 2. Estimation of the Isotopic Distribution of the $[HSO_4]^-$ Fragment Ion Generated by Collision-Induced Dissociation of the $[M - H + 2]^-$ Ion of the Cholesterol Sulfate Anion at *m/z* 467

brutto formula	(M + 2) relative abundance (%)	main isotopic species
$C_{27}H_{45}$	4.63	$^{13}C_2{}^{12}C_{25}$
$C_{27}H_{45}O_4$	5.48	$^{13}C_2{}^{12}C_{25}{}^{16}O_4$ (4.63%) + $^{12}C_{27}{}^{16}O_3{}^{18}O$ (0.85%)
$C_{27}H_{45}SO_4$	10.17	$^{13}C_2{}^{12}C_{25}{}^{16}O_4{}^{32}S$ (4.63%) + $^{12}C_{27}{}^{16}O_3{}^{18}O{}^{32}S$ (0.85%) + $^{12}C_{27}{}^{16}O_4{}^{34}S$ (4.69%)

CID		
$H^{32}S^{16}O_4$	$H^{32}S^{16}O_3{}^{18}O$	$H^{34}S^{16}O_4$
absolute abundance, %	*m/z* 97, 4.63	*m/z* 99, 0.85	*m/z* 99, 4.69

Ratio *m/z* 97/*m/z* 99 for Fragmentation of *m/z* 467

calcd	1:1.197
obsd, synthetic cholesterol sulfate	1:1.3

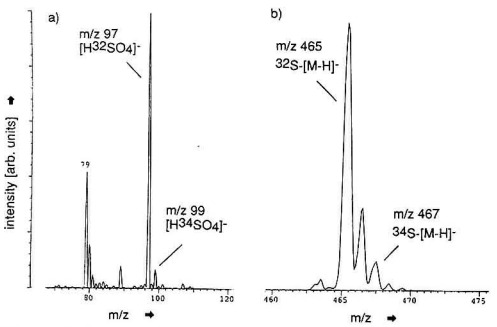

Figure 4. Isotopic patterns of cholesterol sulfate ions observed in negative-ion ESI mass spectra from a total lipid extract from stratum spinosum (fraction I) of mouse keratinocytes. (a) $[HSO_4]^-$ ion at *m/z* 97, produced by API-CID with 65 eV collision energy. (b) $[M - H]^-$ signal at *m/z* 465. The signals were acquired in the profile mode, and 10 scans of 2 s duration were averaged.

observed which did not fit to any common polar lipid constituent of a cell membrane extract. In a variety of studies concerned with epidermal cell differentiation in rabbit,[1,12] mouse,[13] and humans,[14] it has been shown that the induction of cholesterol sulfotransferase can be regarded as a differentiation marker in these cells. Therefore, it was suspected that the signal at *m/z* 465 could represent the $[M - H]^-$ ion of cholesterol sulfate with a nominal molecular weight of 466. Since the nominal mass could not distinguish between a cholesterol sulfate ester and its corresponding phosphate ester, first the isotopic distributions of the molecular ion signal at *m/z* 465 and of the fragment at *m/z* 97 produced by API-CID at 65 eV were considered. The molecular ion signal showed a $[M - H + 2]^-$ signal of about 10% relative intensity, and the fragment ion at *m/z* 97 showed a satellite ion at *m/z* 99 of about 7%, as shown in Figure 4. Both findings and the occurrence of a fragment ion signal at *m/z* 80 are in agreement with the presence of sulfur in the corresponding ion species. The

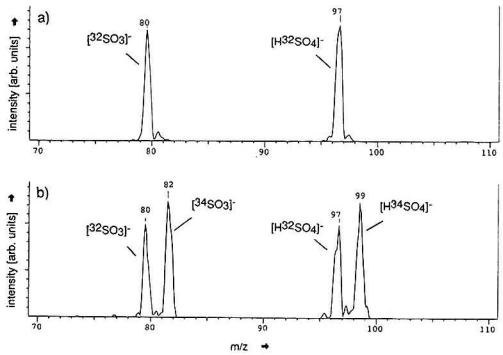

Figure 5. Collision-induced dissociation of cholesterol 3-sulfate ion signals observed in a negative ion ESI spectrum of a total lipid extract from fraction I of mouse keratinocytes. (a) Product ion analysis of *m/z* 465. (b) Product ion analysis of *m/z* 467. The collision energy used was 120 eV in both experiments, the data were acquired in the profile mode, and 10 scans of 2 s duration were averaged.

$[PO_3]^-$ fragment ion at *m/z* 79 is generated by the phospholipids present in the lipid extract in large excess over cholesterol 3-sulfate. Phosphodiesters form a $[H_2PO_4]^-$ fragment at *m/z* 97 with an efficiency which is about 2–3 orders of magnitude lower than that of phosphomonoesters (data not shown).

To specifically investigate the fragmentation behavior of the molecular ion group around *m/z* 465 shown in Figure 4, a product ion analysis of the ions at *m/z* 465 and 467 was performed. The results are shown in Figure 5 and are virtually identical to those obtained for synthetic cholesterol sulfate at the same collision energy of 120 eV. Fragment ions other than the $[HSO_4]^-$ and $[SO_3]^-$ fragment ions species were not observed upon collisional activation of the ion species at *m/z* 465 and 467, respectively.

The fragmentation of *m/z* 465 shows the sulfate ester-characteristic two fragment ions at *m/z* 80 and 97. Upon fragmentation of the M + 2 satellite ion at *m/z* 467, both fragment ions split into a doublet at *m/z* 80 and 82 and 97 and 99, with the characteristic intensity ratio observed for authentic cholesterol 3-sulfate (see Figure 3 and Table 1). Thus, it has been demonstrated that the signal at *m/z* 465 represents cholesterol sulfate.

Quantification of Cholesterol 3-Sulfate. Based on the observation of an induction of cholesterol sulfotransferase as a differentiation marker of keratinocytes, we attempted to set up a quantitative assay for cholesterol sulfate based on electrospray ionization mass spectrometry. In earlier studies, the accumulation of cholesterol sulfate in the course of epidermal cell differentiation could be demonstrated by accumulation of $[^{35}SO_4]^-$ in lipid extracts upon incubation with ^{35}S-labeled sulfate. However, the actual levels of cholesterol sulfate are difficult to estimate by this method, since a uniform labeling of the cholesterol sulfate pool and knowledge of the specific activity are required for a calculation of the cholesterol sulfate level by this method. For quantification of cholesterol sulfate by mass spectrometry, we tested the suitability of dihydrocholesterol sulfate as internal standard in the normal scan mode as well as in the parent ion scan mode for the *m/z* 97 fragment ion, which is the most intense fragment of sulfate monoesters, as evident from Scheme 1 and Figure 1.

To demonstrate the utility of the parent scan mode for the analysis of a total lipid extract from keratinocytes, Figure 6 shows

(12) Rearick, J. I.; Albro, P. W.; Jetten, A. M. *J. Biol. Chem.* **1987**, *262*, 13069–13074.

(13) Kagehara, M.; Tachi, M.; Harii, K.; Iwamori, M. *Biochim. Biophys. Acta* **1994**, *1215*, 183–189.

(14) Jetten, A. M.; George, M. A.; Nervi, C.; Boone, L. R.; Rearick, J. I. *J. Invest. Dermatol.* **1989**, *92*, 203–209.

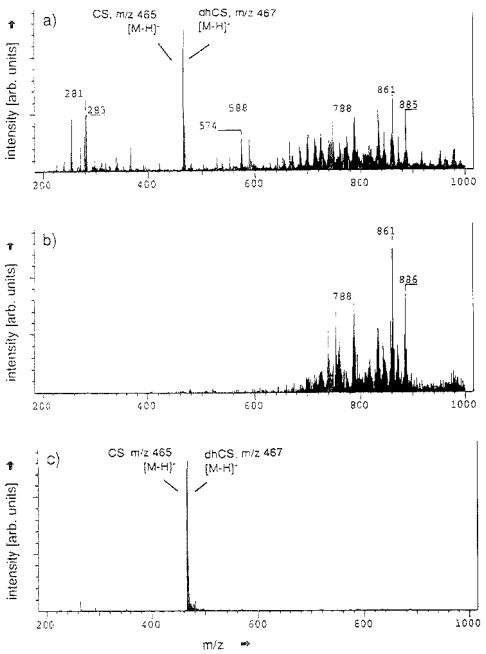

Figure 6. Negative ion ESI mass spectra of a total lipid extract of mouse keratinocytes from fraction I with dihydrocholesterol added as internal standard: (a) normal scan mode, (b) parent ion scan of the $[PO_3]^-$ fragment at *m/z* 79 at 60 eV collision energy, and (c) parent ion scan of the $[HSO_4]^-$ fragment at *m/z* 97 at 60 eV collision energy. Phosphodiesters form a *m/z* 97 fragment with a relative abundance which is between 2 and 3 orders of magnitude smaller than that of phosphomonoesters.

the corresponding negative ion ESI mass spectra obtained in the normal scan mode, the parent ion analysis of *m/z* 97, and the parent ion analysis of *m/z* 79.

The normal scan mode shows intense ion signals for cholesterol sulfate, dihydrocholesterol sulfate added as internal standard, and the variety of phospholipids, in particular of phosphatidylethanolamine, phosphatidylserine, and phosphatidylinositol. The parent ion scan for the $[PO_3]^-$ fragment ion at *m/z* 79 selectively shows only the phospholipids, whereas the parent ion scan at *m/z* 97 representing the $[HSO_4]^-$ fragment ion selects for cholesterol sulfate and its dihydro analogue. Since phosphodiesters form a *m/z* 97 fragment with about 2–3 orders of magnitude lower relative abundance than that of phosphomonoesters, this parent ion scan provides a high specificity for sulfate monoesters present in a mixture with phosphodiesters, as is the case in total lipid extracts of cellular origin.

The parent ion scan mode was evaluated for its suitability as a quantification method, since it provides a highly specific analysis mode for lipid mixtures, as shown, e.g., for the quantification of dehydroepiandrosterone sulfate in serum samples[5] by fast atom bombardment MS/MS. As the basis for a quantification based on parent ion analysis, we first investigated the energy dependence of the $[HSO_4]^-$ fragment ion formation for cholesterol sulfate (CS) and of the selected internal standard dihydrocholesterol sulfate (dhCS). An equimolar mixture of CS and dhCS was infused, and

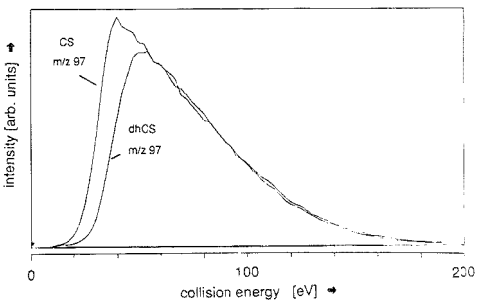

Figure 7. Fragment ion intensity of the $[HSO_4]^-$ fragment at *m/z* 97 as a function of the q2 collision energy for cholesterol 3-sulfate (CS) and dihydrocholesterol 3-sulfate (dhCS). An equimolar mixture of CS and dhCS was infused, and product ion experiments with detection at *m/z* 97 were performed for the corresponding molecular ions at *m/z* 465 and 467, respectively.

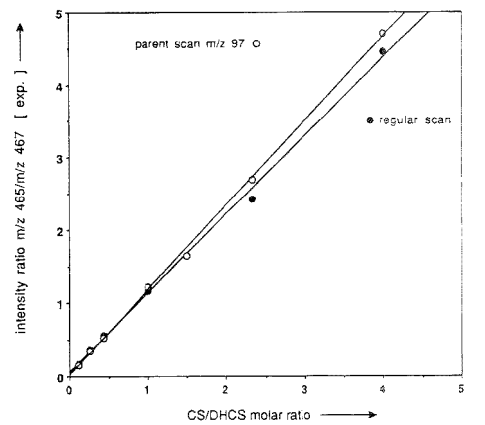

Figure 8. Calibration plots for the quantification of cholesterol 3-sulfate (CS) with dihydrocholesterol 3-sulfate (dhCS) as internal standard using the normal scan mode and the parent ion scan of *m/z* 97 at 60 eV collision energy.

product ion experiments with detection of *m/z* 97 were performed by selecting the corresponding $[M - H]^-$ ions at *m/z* 465 and 467. The results are given in Figure 7.

In spite of the small chemical difference between cholesterol sulfate and dihydrocholesterol sulfate, the former shows an onset of the *m/z* 97 fragment ion formation at a significantly lower collision energy. However, the collision energy plots in Figure 7 also show that when a collision energy in excess of about 55 eV is selected, both cholesterol sulfate and its dihydro form fragment with the same efficiency. Therefore, a collision energy of 60 eV was selected for the *m/z* 97 parent ion scans.

Investigations of standard mixtures of cholesterol 3-sulfate and dihydrocholesterol sulfate showed that dihydrocholesterol 3-sulfate can be used as internal standard for the quantification directly from total lipid extracts. Figure 8 gives a calibration plot established by addition of standard mixtures to about 10^6 cells. U937 cells were selected for this purpose, since these do not contain cholesterol sulfate. These cells were spiked with standard mixtures of cholesterol sulfate and dihydrocholesterol sulfate and analyzed as described in the Experimental Section.

Table 3. Quantitative Determination of Cholesterol Sulfate (Nanograms/10^6 Cells) in Crude Lipid Extracts from Density Gradient-Fractionated[8] Mouse Back Skin Keratinocytes by Negative Ion ESI-MS[a]

fraction	direct scan	parent scan, m/z 97
I	461 ± 172	405 ± 115
II	304 ± 54	240 ± 47
III	59 ± 16	19 ± 5
IV	59 ± 40	16 ± 2

[a] In each sample, quantification was performed both in the direct scan mode and in the parent ion scan mode for m/z 97 using dihydrocholesterol sulfate as internal standard as described. The arithmetic mean and standard deviations are shown for data obtained in three separate cell fractionation experiments.

The calibration plots in Figure 8 were used for the quantification of cholesterol 3-sulfate in keratinocyte fractions. Using density gradient centrifugation, mouse skin keratinocytes can be separated into four fractions representing the order of their vertical arrangement in native skin corresponding to different states of terminal differentiation.[8] The fractions exhibiting the highest densities, fractions III and IV, mainly contain vital basal cells from the stratum basale. The less dense cells in fraction II contain postmitotic cells from the stratum spinosum and the stratum granulosum. The uppermost fraction I consists mainly of late granular cells and aggregates of corneocytes. Quantification of cholesterol sulfate in these fractions by ESI-MS using dihydrocholesterol sulfate as internal standard and the calibration plots established above gave the data shown in Table 3.

The data in Table 3 show a significantly increased content of cholesterol sulfate in the terminally differentiated cells of fractions I and II compared to the basal cell fractions III and IV. Quantification has been performed both in the normal scan and in the parent ion scan mode based on the fragment ion at m/z 97. Using this parent ion scan of m/z 97, a factor of about 50 is lost in sensitivity. The lower concentration data observed in the parent scan mode indicate a higher specificity of this quantification mode. Obviously, the parent scan mode excludes the influence of nonspecific background ions arising from other biological components present in the crude lipid extract and of those arising from the density gradient fractionation. The data obtained by the parent scan method show an increase of the cholesterol sulfate concentration in mouse skin epidermis by a factor of about 25 between the basal and the uppermost epidermal cell layer. This observation is in agreement with a variety of investigations concerned with epidermal cell differentiation which demonstrated a strong induction of cholesterol sulfotransferase activity in the course of epidermal cell differentiation.[12-14]

CONCLUSIONS

Negative ion electrospray ionization mass spectrometry, combined with collisional activation and MS/MS scan techniques, represents a powerful technique for the specific detection of organic sulfate esters in mixtures in the presence of large amounts of phosphomonoesters, phosphodiesters, or both. Based on these features and on the outstanding basic sensitivity of negative ion ESI for sulfate ester compounds such as cholesterol sulfate, a direct quantification of those componds is possible in crude lipid extracts of cellular origin.

ACKNOWLEDGMENT

We are indebted to H. Richter and G. Fürstenberger for valuable comments and discussions. We thank U. Wittig for providing a sample of U937 cells.

Received for review February 2, 1995. Accepted August 14, 1995.[⊗]

AC950118B

[⊗] Abstract published in *Advance ACS Abstracts,* October 15, 1995.

Anal. Chem. **1995**, *67*, 4184–4189

Microchip Separations of Neutral Species via Micellar Electrokinetic Capillary Chromatography

Alvin W. Moore, Jr., Stephen C. Jacobson, and J. Michael Ramsey*

Chemical and Analytical Sciences Division, Oak Ridge National Laboratory, P.O. Box 2008, Building 4500S, MS 6142, Oak Ridge, Tennessee 37831-6142

Micellar electrokinetic capillary chromatography (MECC) of three neutral coumarin dyes was performed on glass microchips. Manifolds of channels for analyte injection and separation were machined into one surface of the glass substrates using standard photolithographic, etching, and deposition techniques. Coverplates were then directly bonded over these channels to form capillary networks, with fluid flow in these networks controlled by varying the applied high-voltage potentials at the outlets. The separation capillary was 16.5 cm long for a serpentine channel chip and 1.3 cm long for a straight channel chip. Detection of analyte zones was accomplished by laser-induced fluorescence using the UV lines (~350 nm) of an argon ion laser. At low applied electric field strengths, MECC analyses with on-chip injections gave high reproducibilities in peak areas and migration times (<1% for two of the three coumarins) and near constant separation efficiencies throughout the analysis. At high fields (>400 V/cm), analysis times were shorter, but separation efficiency decreased at later migration times. These peaks showed significant broadening, consistent with mass transfer effects.

Many of today's applications of analytical chemistry involve collection of samples from some remote site, transportation of these samples back to the laboratory, and analysis using benchtop instrumentation. These situations range from detection of pollutants in water supplies to process monitoring for quality control. In the typical analytical laboratory, a universal detection system such as a UV absorption detector and a separation technique such as liquid chromatography (LC) or capillary electrophoresis (CE) are used to quantify the analyte of interest. The separation method provides the selectivity between components and classes of components that the universal detector lacks. If the analysts' needs change, such that they must quantify other species, the selectivity can be easily modified by changing the separation conditions such as the pH of the mobile phase or buffer, the organic solvent content, or the elution gradient. The enhanced versatility of this method comes at the expense of requiring that samples be collected and transported to the lab.

An attractive means of saving time and expense would be to take the instrument to the sample. Micromachining technology may allow the ultimate miniaturization of chemical measurement instrumentation. Liquid phase separation devices are particularly amenable to miniaturization because analytical separation performance often improves with decreasing size of the components involved. CE is a relatively new separation method which has used microcolumn capillaries from its inception. Because CE gives high-efficiency separations but requires no high-pressure pump or gas supply, it is especially well suited for miniaturization. Substantial progress has already been made in this area.[1-4]

A problem with CE for general analysis is its inability to separate uncharged species. All neutral species in a particular sample will have zero electrophoretic mobility and thus the same migration time. Previously, our group has investigated open-channel electrochromatography (OCEC) on a microchip as a means of separating neutrals.[5] In this previous work, sample components were separated by their partitioning interaction with a stationary phase coated on the channel walls. The mobile phase was driven not by a conventional pump but by electroosmotic flow. Micellar electrokinetic capillary chromatography (MECC) is a operational mode of CE which was developed by Terabe et al.[6] to address the separation of neutrals by CE. A surfactant such as sodium dodecyl sulfate (SDS) is added to the CE buffer in sufficient concentration to form micelles in the buffer. In a typical experimental arrangement, the micelles move much more slowly toward the cathode than does the surrounding buffer solution. The partitioning of solutes between the micelles and the surrounding buffer solution provides a separation mechanism similar to that of LC.

In this work, MECC was performed in a capillary etched into the surface of a glass chip. All of the fluidic manipulation necessary for sample injection and analysis was done through a manifold of channels, with flow controlled by the voltage applied to the reservoir at the end of each channel. Laser-induced fluorescence detection was used to monitor the separations. Some results of this implementation of MECC will be shown, and some of its advantages and disadvantages for chip-based microinstrumentation will be discussed.

OVERVIEW

An in-depth treatment of the theory of MECC has been given by others[6-8] and is beyond the scope of this paper. Only a brief

(1) Harrison, D. J.; Manz, A.; Fan, Z.; Lüdi, H.; Widmer, H. M. *Anal. Chem.* **1992**, *64*, 1926–1932.
(2) Seiler, K.; Harrison, D. J.; Manz, A. *Anal. Chem.* **1993**, *65*, 1481–1488.
(3) Jacobson, S. C.; Hergenröder, R.; Koutny, L. B.; Warmack, R. J.; Ramsey, J. M. *Anal. Chem.* **1994**, *66*, 1107–1113.
(4) Jacobson, S. C.; Hergenröder, R.; Koutny, L. B.; Ramsey, J. M. *Anal. Chem.* **1994**, *66*, 1114–1118.
(5) Jacobson, S. C.; Hergenröder, R.; Koutny, L. B.; Ramsey, J. M. *Anal. Chem.* **1994**, *66*, 2369–2373.
(6) Terabe, S.; Otsuka, K.; Ando, T. *Anal. Chem.* **1985**, *57*, 834–841.
(7) Sepaniak, M. J.; Powell, A. C.; Swaile, D. F.; Cole, R. O. In *Capillary Electrophoresis: Theory and Practice*; Grossman, P. D., Colburn, J. C., Eds.; Academic Press, Inc.: San Diego, CA, 1992; pp 159–89.
(8) Sepaniak, M. J.; Cole, R. O. *Anal. Chem.* **1987**, *59*, 472–476.

0003-2700/95/0367-4184$9.00/0

review will be given here. For neutral solutes, the separation mechanism is essentially chromatographic and can therefore be described with modified chromatographic relationships. The capacity factor, k', for a given solute and experimental conditions is the ratio of the total moles of solute in the stationary phase (here, the pseudostationary phase of the micelles) to those in the mobile phase. For MECC, k' is modified to account for the movement of the micelles,

$$k' = \frac{t_R - t_0}{t_0(1 - t_R/t_m)} = K(V_s/V_m) \quad (1)$$

where t_R is the solute retention time, t_0 is the "void time" (retention time for a solute moving at the rate of the electroosmotic flow), t_m is the micelle retention time (i.e., retention time of a completely retained solute), K is the partition coefficient, V_s is the volume of the micellar phase, and V_m is the volume of the mobile phase. If the micelles were indeed stationary, t_m would become infinite and the equation would reduce to its conventional form for chromatography.

Because t_0 is the retention time for a solute moving with the electroosmotic flow, and t_m is that of a solute completely retained in the micelles, neutral solutes must elute between t_0 and t_m. Resolution can be improved by increasing the difference between t_0 and t_m, thus increasing the "window" of time over which sample components can elute. Resolution can also be improved by changing the k' values of the solutes, which affects both the retention and the selectivity of the separation. This can be done in many of the same ways it is done in liquid chromatography, such as by adjusting the temperature, buffer concentration, or pH, or by the addition of organic modifiers. Organic solvents such as methanol and acetonitrile can have multiple effects in that they may modify the electroosmotic flow in the system or alter the hydrophobic interactions between solute and micelle, but they also affect micelle structural interactions and so alter the partitioning kinetics. Changes in the organic solvent content of the buffer also modify the electroosmotic flow in the system.

EXPERIMENTAL SECTION

The microchips were constructed using standard photolithographic, wet chemical etching and bonding techniques described previously.[9] An ordinary soda lime glass microscope slide was used as a substrate, into which was etched a network of open channels (see Figure 1). The serpentine channel geometry (Figure 1a) allowed use of a longer separation capillary within a small area, while the straight channel geometry (Figure 1b) allowed experiments with high applied electric field strengths. These channel networks were closed with thin coverplates, directly bonded to the substrate, to form capillary networks. Cylindrical glass reservoirs were then bonded with epoxy to the capillary outlets. The lengths of the capillary channels may vary with the placement of the coverplate. Figure 1 gives the channel lengths for the two chips used in this work. Use of the wet chemical etch on a glass substrate results in an isotropic etch. That is, the glass etches at the same rate in all directions, and the resulting channel geometry is trapezoidal.[5] The channel cross section dimensions were the same for both chips used in this work. The channels were 10 μm deep, 60 μm wide at the bottom, and 80 μm wide at the top. These dimensions were measured with a profilometer (Alpha-Step 200, Tencor Instruments, Mountain View, CA) after bonding the coverplate but before attaching the reservoirs.

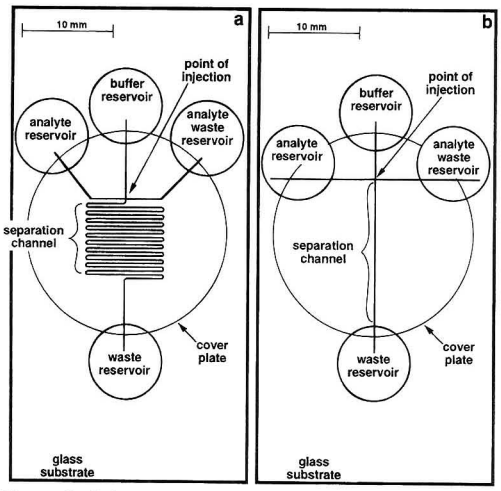

Figure 1. Schematic diagrams of microchip geometry. The large outer boxes show the outlines of the glass substrates. Individual capillary lengths are measured from the point of injection to the point where the capillary passes beyond the cover plate into the respective reservoir. (a) The serpentine channel geometry used for the majority of the work, with channel lengths as follows: analyte channel, 9.2 mm; buffer channel, 6.6 mm; analyte waste channel, 7.7 mm; waste (separation) channel, 171 mm. (b) The straight channel geometry used for the high-field experiments, with channel lengths as follows: analyte channel, 8.0 mm; buffer channel, 4.6 mm; analyte waste channel, 9.8 mm; waste (separation) channel, 17.2 mm.

Separation of the analyte zones was monitored via laser-induced fluorescence using an argon ion laser (351.1–363.8 nm, all lines; ~50 mW; Coherent Innova 90, 5 W; Palo Alto, CA) for excitation. The UV beam from the laser was prefiltered with a Corning 7-37 colored glass filter (blue, narrow bandpass; transmittance, 30% at 360 nm) to reduce plasma emissions and then focused at the desired point on the capillary with a planoconvex fused silica lens (focal length, 100 mm; Newport Corp., Irvine, CA). The laser impinged on the chip at an angle of 45° with the surface. The fluorescence signal was collected from below the chip by a 21× microscope objective (Bausch & Lomb Opt. Co., Rochester, NY), filtered with a Corning 3-73 colored glass filter (yellow, sharp cut-on at 426 nm), and detected with a photomultiplier tube (PMT; Oriel 77340, Stratford, CT). The PMT current was amplified and converted to a proportional voltage with a Keithley 617 electrometer (Keithley Instruments Inc., Cleveland, OH). The analog voltage output of the electrometer was measured with a multifunction interface board (AT-MIO-16X, National Instruments, Austin, TX) controlled by software written in-house using LabVIEW 3.0 for Windows (National Instruments, Austin, TX) on a PC compatible computer. Separation efficiencies were obtained by calculation of peak statistical moments, also in LabVIEW.

Platinum electrodes in each reservoir provided electrical contact between the buffer solutions and the CE high-voltage power supply (CZE1000R, Spellman Inc., Plainview, NY). A

(9) Jacobson, S. C.; Koutny, L. B.; Hergenröder, R.; Moore, A. W., Jr.; Ramsey, J. M. *Anal. Chem.* **1994**, *66*, 3472–3476.

voltage divider/relay apparatus described earlier[10] was used to set the relative voltages applied to each reservoir and to switch between run and inject modes under computer control. For both chip geometries, the separation voltage was applied over the entire length of the capillary channel for all analyses. However, for individual groups of analyses, the length of the separation channel used was set by the location of the point of detection.

The reservoirs at the end of each capillary channel had a volume of only 200 μL. To avoid problems with changes in buffer concentration due to evaporation, the reservoirs were sealed with thin rubber septa held in place with parafilm. The platinum electrodes could be inserted through the septa if the septa was initially pierced with a syringe needle. The reservoirs could be flushed and filled a in similar manner with a syringe of buffer or sample. In use, the seal formed around the electrodes was almost gas-tight. The resolution between peaks could be maintained from run to run for several hours before significant evaporation effects were noticed. Only the data in Figure 3, as mentioned below, were acquired with open buffer reservoirs.

The analytes used in these experiments were the neutral dyes coumarin 440 (C440), coumarin 450 (C450), and coumarin 460 (C460, Exciton Inc.). Individual stock solutions of each dye were prepared in methanol and then diluted in the analysis buffer before use. The concentration of each dye was ~50 μM unless indicated otherwise. The substrate is glass rather than quartz, so there is substantial background fluorescence where the UV laser strikes the chip. No attempt was made to measure limits of detection with the present system. The MECC buffer was composed of 10 mM sodium borate (pH 9.1), 50 mM SDS, and 10% (v/v) methanol. The methanol aids in solubilizing the coumarin dyes in the aqueous buffer system and also affects the partitioning of some of the dyes into the micelles. Due care must be used in working with coumarin dyes as the chemical, physical, and toxicological properties of these dyes have not been fully investigated.[11]

Sample Injection. The microchips were operated in a "pinched injection" mode described previously.[3] The voltages applied to the reservoirs are set to either an "inject" (sample loading) or a "run" (separation) configuration. In the inject mode, a frontal chromatogram of the solution in the analyte reservoir is pumped electroosmotically through the intersection and into the analyte waste reservoir. Voltages applied to the buffer and waste reservoirs also cause weak flows into the intersection from the sides and then into the analyte waste reservoir. These flows serve to confine the stream from the analyte reservoir to give a well-defined plug of sample in the intersection. The chip remains in this mode until the slowest moving component of the sample has passed through the intersection. At this point, the sample plug in the intersection is representative of the analyte solution, with no electrokinetic bias.

An injection is made by switching the chip to the run mode, which changes the voltages applied to the reservoirs such that buffer now flows from the buffer reservoir through the intersection, into the separation column, and eventually into the waste reservoir. The plug of sample which was previously in the intersection is swept onto the separation column. Proportionately lower voltages are applied to the analyte and analyte waste reservoirs to cause a weak flow of buffer from the buffer reservoir into these channels. These flows ensure that the sample plug is cleanly "broken off" from the analyte stream and that no excess analyte leaks into the separation channel during the analysis. This sample loading method is time-independent (after the initial time necessary to pump all components through the intersection), nonbiased, and reproducible.

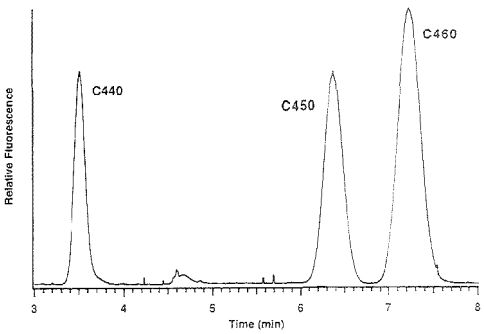

Figure 2. Microchip MECC analysis of a mixture of coumarin dyes. The small peak at 4.6 min is an unidentified impurity in one of the dyes. Concentration of each dye was ~50 μM. Other analysis conditions are given in the text.

RESULTS AND DISCUSSION

The results of an MECC analysis of a mixture of C440, C450, and C460 are shown in Figure 2. The peaks were identified by individual analyses of each dye. The migration time stability of the first peak, C440, with changing methanol concentration (see below) was a strong indicator that this dye did not partition into the micelles to a significant extent. Therefore, it was considered an electroosmotic flow marker with migration time t_0. The last peak, C460, was assumed to be a marker for the micellar migration time, t_m. Using these values of t_0 and t_m from the data in Figure 2, the calculated elution range, t_0/t_m, is 0.43. This agrees well with a literature value of $t_0/t_m = 0.4$ for a similar buffer system[8] and supports our assumption. This analysis was done in the serpentine chip with a separation length of 21.3 mm and an applied electric field strength of 47 V/cm.

Buffer Evaporation. Figure 3 shows several successive analyses of the same three component sample over a period of 30 min. These analyses were done with an applied field of 96 V/cm and a separation length of 17 mm. Notice that from parts a to c of Figure 3, the C440 peak and the C450/C460 peak pair tend to move closer together (the elution range decreases), and the resolution between the C450 and C460 peaks gradually decreases. The high voltage was switched off for 5 min between parts b and c of Figure 3, so that if gradual heating of the MECC buffer in the chip were responsible for the lost resolution, it should have been partially restored in Figure 3c. Obviously, this was not the case. Immediately before the analysis shown in Figure 3d, the buffer and sample solutions were replaced. Notice that the resolution between the last two peaks has been restored, indicating some change in the buffer solutions during the course of the analyses shown in Figure 3a–c.

For the data in Figure 3, the reservoirs at the end of each capillary channel were open to the surrounding air. When the

(10) Jacobson, S. C.; Hergenröder, R.; Moore, A. W., Jr.; Ramsey, J. M. *Anal. Chem.* **1994**, *66*, 4127–4132.
(11) Exciton, Inc., Dayton, OH, 1991.

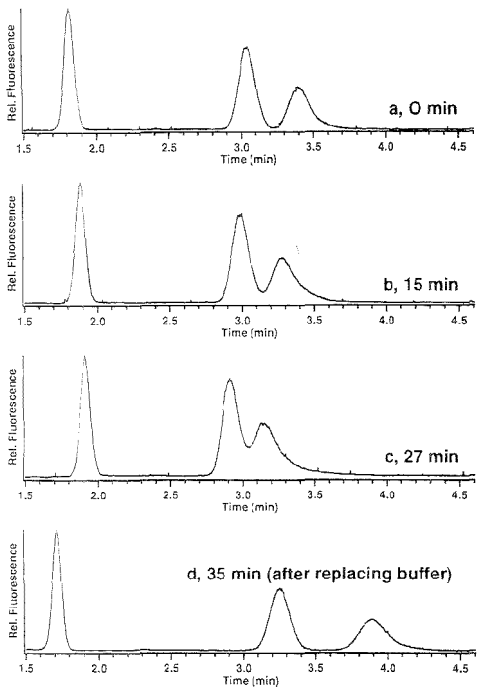

Figure 3. Effects of methanol evaporation in microchip MECC. The times indicated in the figure are times between the ends of the analyses, immediately after acquisition when the data were saved. Peaks are identified as in Figure 2.

buffers were entirely aqueous, buffer evaporation was not a significant problem. However, the MECC buffer contained 10% (v/v) methanol, so methanol evaporation might be significant. A decrease in the methanol concentration would cause the C450 to prefer the free buffer solution less and partition to a greater extent into the micelles. That is, the partition coefficient of the C450 would increase, and the selectivity between C450 and C460 would decrease, lowering the resolution between them. Also, addition of methanol is known to extend the elution range in MECC,[7] so the decrease seen in Figure 3a–c agrees well with a decrease in methanol concentration due to evaporation. Weinberger and Lurie[12] have suggested that similar evaporation problems with MECC buffers containing organic modifiers contribute to poor run-to-run reproducibility.

Reproducibility. The results for five replicate analyses of the three coumarin dyes mix as in Figure 2 are shown in Table 1. The migration times, peak areas, and peak variances were obtained from the best-fit values for Gaussian curves fitted to the experimental data. The percent relative standard deviation (%RSD) of the migration times and peak areas are slightly lower than expected for MECC. Some authors have reported %RSD of migration times of 2% or less,[7,12] with some as high as 10% over the course of a day,[13] while %RSD values for peak area are

(12) Weinberger, R.; Lurie, I. *Anal. Chem.* **1991**, *63*, 823–827.
(13) Northrop, D. M.; Matire, D. E.; MacCrehan, W. A. *Anal. Chem.* **1991**, *63*, 1038–1042.

Table 1. Peak Parameters[a]

	migration time (s)	peak area	theoretical plates (N)	HETP (μm)
		C440		
av (n = 5)	209.1	2.82	3523	6.05
SD	1.94	0.03	60	0.10
%RSD	0.93	0.91	1.71	1.71
		C450		
av (n = 5)	384.6	4.92	3855	5.53
SD	3.27	0.05	80	0.12
%RSD	0.85	0.92	2.09	2.09
		C460		
av (n = 5)	438.1	7.62	3705	5.75
SD	5.76	0.17	101	0.16
%RSD	1.31	2.21	2.73	2.78

[a] Data for five replicate analyses with applied electric field of 47 V/cm, separation length of 21.3 mm.

Table 2. Ratio Peak Parameters[a]

	migration time ratio		peak area ratio		capacity factor (k'),
	C440/ C450	C460/ C450	C440/ C450	C460/ C450	C450
av (n = 5)	0.544	1.14	0.574	1.55	6.89
SD	0.01	0.01	0.01	0.02	0.05
%RSD	1.57	0.54	1.11	1.51	0.78

[a] Ratio values and capacity factor for C450 calculated from the data used in Table 1.

generally even higher. Here, for the C440 and C450 peaks, peak area %RSD values are <1%. For C460, the %RSD values for migration times and peak areas are 1.3 and 2.2%, respectively. Such low values are presumably due to the on-chip injection scheme: all fluid handling for sample injection and analysis is done on-chip with no moving parts (other than the buffer itself). Thus, many of the sources of variance associated with benchtop instruments, such as those resulting from moving the separation capillary between vials, are minimized.

To better correct for environmental variances, peak migration time and peak area ratios may be calculated relative to an internal standard peak. These ratios help to account for differences in flow rate and injection volume from run to run. The %RSD for ratio data is usually <2%.[7] In Table 2, we have calculated ratio values for C440 and C460 considering C450 an internal standard, based on the same raw data used to construct Table 1. As expected, our %RSD values for these ratios are also <2%. Alternately, some have calculated capacity factors, k', for the analytes of interest. Because the partitioning into the micelles is similar to the partitioning found in liquid chromatography, the k' values are distinctive for a given compound under given experimental conditions.

If we consider the migration time of C440 to be that of the electroosmotic flow, and that of C460 to be that of the micelles, then a k' value for C450 can be calculated for each analysis. The %RSD for the k' value of C450 is also below 1%, which compares well to a value of 0.5% found in the literature.[13]

For a given applied electric field (47 V/cm, as above), and consequently, a constant plate height, the number of theoretical plates should increase as the length of the separation capillary (the distance from point of injection to point of detection) increases. Figure 4 is a plot of efficiency data gathered from

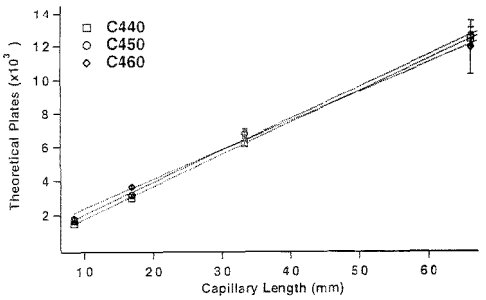

Figure 4. Plot of peak efficiency versus length of separation capillary. Each point represents the average of three analyses, with error bars above and below the average at 1 SD. See text for further description.

triplicate analyses at four different capillary lengths. The dotted lines are the best-fit lines for each of the components (C440, C450, and C460). As expected, at each capillary length, the measured peak efficiencies for each of the three compounds are similar. The linear increase in efficiency as the separation length increases demonstrates the homogeneity of the capillary walls over the length of the separation.

MECC at High Applied Field Strengths. The straight channel chip (Figure 1b) was used to study the effects of applied electric field strength on the MECC separations. Because the separation capillary in the straight chip is much shorter, significantly higher applied fields can be obtained for the same total applied voltages. In our present experimental arrangement, applied voltages of >4 kV begin to give arcing between the buffer reservoirs, so studies of higher applied field strengths are best done with shorter separation capillaries.

A single analyte, C450, was used for the range of applied fields studied. C450 was chosen because it is partially retained by the micelles, and thus its behavior should be indicative of free solution and micellar effects. In Figure 5a, average analyte velocity is plotted versus applied electric field strength, with a best-fit line through the four points at the lowest field strengths. Theoretically, the analyte velocity should increase linearly with applied field. The curve upward seen in the actual data indicates Joule heating effects at the higher applied fields. This is not unexpected, considering the high ionic strength of the MECC buffer. Analyses were also done at 1340 V/cm, but the C450 migration time continually drifted to earlier times. The precision is greatest for the points at low field. This is due both to the lack of heating effects, so that the capillary is nearer its point of thermal equilibrium, and to the longer migration times, any variations in which will be a smaller percentage of the average value.

In Figure 5b, the average plate height for these analyses is plotted against the average analyte velocity. Error bars are shown at the 1 standard deviation (SD) points for both dimensions because both are calculated from the experimental data. The data give a Van Deemter-like plot, similar to that found in LC. The plate height at 0.9 mm/s is high relative to the trend of the other points and is probably the result of a systematic error in the analyses at that point. With this point omitted, a curve fit of the Van Deemter equation to the experimental data gave an r^2 value of 0.9990.

The general form of the Van Deemter equation is

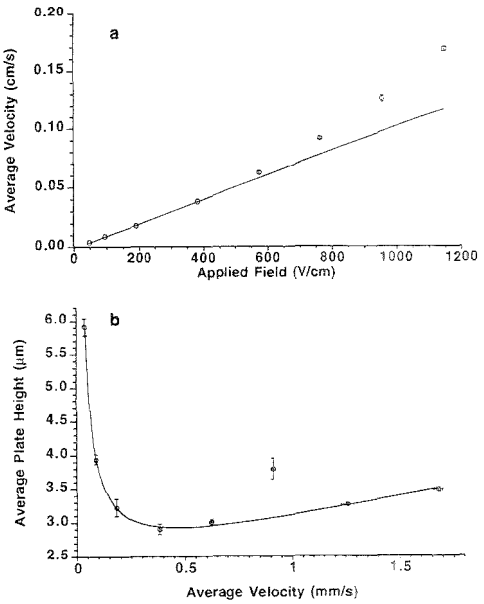

Figure 5. (a) Plot of analyte velocity versus applied electric field strength. Each point represents the average of three analyses, with error bars above and below the average at 1 SD. The fitted data are calculated from a linear regression fit of the four data points at the lowest applied fields. See text for further description. (b) Plot of plate height versus analyte velocity. Each point rspresents the average of three analyses, with error bars in both dimensions at plus and minus 1 SD. The point at 0.9 mm/s is omitted from the data fit to the Van Deemter equation. The fit equation is of the form $H = A + B/u + Cu$, where $H_{eo} = A$, $H_l = B/u$, and $(H_{mc} + H_{ep}) = Cu$, to give $H_{To} = H_{eo} + H_l + H_{mc} + H_{ep}$. From the curve fit, $A = 2.32$ μm, $B = 0.141$ (μm²)/s, and $C = 0.651$ s. For this fit, $\chi^2 = 0.0063$ and $r^2 = 0.9990$. See text for further description.

$$H = A + B/u + Cu \qquad (2)$$

where H is the theoretical plate height, u is the velocity of the mobile phase, A represents band broadening effects independent of u (such as eddy diffusion in LC), B represents band broadening effects inversely dependent on u (such as longitudinal diffusion), and C represents band broadening effects directly dependent on u (such as the mass transfer term in LC).

For MECC, the major causes of on-column band broadening have been studied by Terabe et al.[14] and Sepaniak and Cole.[8] The mobile phase velocity represented as u above is given by the electroosmotic flow velocity v_{eo} in MECC. The A term can include all constant additions to the plate height, such as extracolumn effects of the injector and detector, because with free solution CE or MECC, there is no eddy diffusion term. This is written as H_{eo} and is independent of the electroosmotic flow velocity. The B term is a longitudinal diffusion term as in LC which is inversely proportional to the electroosmotic flow velocity, written as H_l. The C term for MECC includes two terms, H_{mc} and H_{ep}. The sorption/desorption kinetics term, H_{mc}, is the plate height due to the rate at which solutes move into and out of the micelles. In most cases,

(14) Terabe, S.; Otsuka, K.; Ando, T. *Anal. Chem.* **1989**, *61*, 251–260.

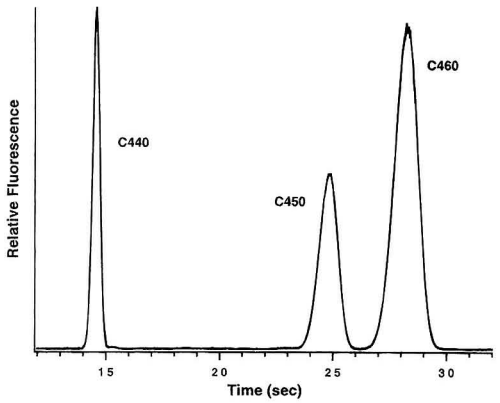

Figure 6. High-field MECC analysis of a mixture of coumarin dyes. Analysis conditions are given in the text. As described in the text, the analysis time is much shorter, but the separation efficiency is no longer constant over the course of the analysis. The number of theoretical plates calculated for each peak was as follows: C440, N = 8800; C450, N = 3900; C460, N = 3200.

H_{mc} is small, but it can be significant if the sorption/desorption kinetics are very slow, such as with ionic interactions between the solute and the micelle. The electrophoretic dispersion term, H_{ep}, is the plate height due to the variance in micelle size (micelle polydispersity). The micelle solution gives a distribution of micelle sizes with a standard deviation of as much as 20% from the average. Both H_{mc} and H_{ep} increase with increasing v_{eo}. Thus

$$H_{Tot} = H_{ec} + H_{l} + H_{mc} + H_{ep} \quad (3)$$

where H_{Tot} is the total plate height.

From the fit equation in Figure 5b, H_{ec} is the major fraction of the total plate height. This indicates a large constant contribution to the plate height, such as from extracolumn effects. A detailed examination of these effects was beyond the scope of this work. Terabe's work was done in the same range of v_{eo} as in Figure 5b. After a minimum at 0.4 mm/s, our curve shows a linear increase in H_{Tot} with increasing v_{eo}. This reveals the contribution of the two velocity-dependent terms, H_{mc} and H_{ep}. Terabe suggests that the contributions from sorption/desorption kinetics and micelle polydispersity would become more significant for solutes with larger capacity factors. Obviously, the capacity factor for C450 should be larger because its migration time is nearer to that of the C460, which is totally included in the micelles. Additionally, the Joule heating observed in Figure 5a would further contribute to the plate height.

Figure 6 shows a sample chromatogram of the three coumarins analyzed by MECC at an applied field of 500 V/cm, over a distance of 1.3 cm. Notice that the efficiency now decreases over the course of the separation. At this field strength, the C450 and C460 show the mass transfer effects described above, while the C440 remains sharp because it partitions only slightly or not at all into micelles.

CONCLUSIONS

In our previous work with open capillary electrochromatography (OCEC), three neutral coumarin dyes were separated on a microchip which employed a serpentine column geometry.[5] For comparison, the same three dyes were analyzed here on a microchip of the serpentine configuration as well as on a straight channel chip. As would be expected, the elution order was the same as that found with OCEC. In Figure 2, the three dyes are baseline resolved in 8 min. The longer analysis time results from the lower applied field strength for the long serpentine channel. In Figure 6, with the straight channel and resultant higher applied fields, the analysis time is shorter than for OCEC. The MECC resolution is better than that of the OCEC, and the peak shape is significantly improved. At low applied fields, the separation efficiency over the course of the analysis is relatively constant for MECC. As mentioned above, at high fields, peaks for later-eluting sample components show more broadening due to the higher capacity factors of those components. Even with these high-field effects, however, the efficiency of the later peaks does not decrease as rapidly as in the OCEC analysis.

The MECC has the advantage that the stationary phase (pseudostationary phase) is continuously replaced as fresh buffer is brought into the chip. In addition, the capacity factor of solutes can be varied by changing the micelle concentration.[7] This effectively changes the "stationary phase loading". In OCEC, the stationary phase is bonded to the capillary surface before use, so the stationary phase loading is fixed. Also, as with other bonded LC columns, the performance of the bonded stationary phase in the microchip degrades over time with repeated use.

As a microchip technique, MECC gives better than average reproducibility for neutral species and is relatively simple to implement. The same chip used for CE can be used for MECC with only a change in buffer. Analysis times can be decreased by using high applied fields, while further addition of organic modifiers such as methanol or acetonitrile would increase the rate of solute exchange kinetics and so sharpen later peaks. Use of higher micelle concentrations would limit the contribution of micelle polydispersity and thus would also help sharpen later peaks. Higher micelle concentrations would also give higher electrophoretic currents, and thus more problems with Joule heating of the buffer, but these could be circumvented by the use of narrower channels in the chip. Finally, evaporation problems would be eliminated in an actual portable instrument by using sealed reservoirs.

ACKNOWLEDGMENT

This research was sponsored by U.S. Department of Energy (DOE), Office of Research and Development. Oak Ridge National Laboratory is managed by Lockheed-Martin Energy Systems, Inc., for the U.S. Department of Energy under Contract DE-AC05-84OR21400. Also, this research was sponsored in part by an appointment for A.W.M. to the ORNL Postdoctoral Research Associates Program. These postdoctoral programs are administered by the Oak Ridge Institute for Science and Education and ORNL.

Received for review June 21, 1995. Accepted August 18, 1995.[⊗]

AC950629Y

[⊗] Abstract published in *Advance ACS Abstracts,* October 1, 1995.

Anal. Chem. **1995,** *67,* 4190–4196

Coaxial Capillary and Conductive Capillary Interfaces for Collection of Fractions Isolated by Capillary Electrophoresis

Rick W. Chiu, Kathleen L. Walker,† Jeffrey J. Hagen, Curtis A. Monnig,* and Charles L. Wilkins

Department of Chemistry, University of California, Riverside, California 92521-0403

An instrument is described that allows the automated collection of fractions isolated by capillary electrophoresis. This instrument allows the electrical connection to be established with the separation capillary by using a coaxial capillary flow cell or by treating the outer surface of the capillary with a gold-filled epoxy to allow electrophoresis. The coaxial interface is most useful when the electroosmotic flow in the capillary is small, and the conductive capillary interface is favored when dilution and contamination of the sample must be minimized. Both geometries permit closely spaced fractions to be acquired with minimal cross-contamination and dilution. Sample recoveries were better than 80% and virtually independent of the chemical characteristics of the sample. Fractions isolated with this instrument were successfully analyzed by high-pressure liquid chromatography and electrospray mass spectrometry.

Capillary electrophoresis (CE) is a popular method for rapid and efficient separation of complex mixtures. The small dimensions of the capillary allow the rapid dissipation of Joule heat, enabling the separations to be performed in high potential fields without significant loss of separation efficiency. The capillary format also reduces the volume of sample required for an analysis. Although these reduced sample demands are desirable, identification of unknown molecules is more difficult because of the small quantity of analyte available for detection. Since most on-column CE detectors provide limited chemical and structural information about the isolated molecules, acquisition of more detailed information usually requires that the zones isolated in the capillary be collected and subjected to additional analyses.

Fraction collection for CE shares many common characteristics with fraction collection for high-pressure liquid chromatography (HPLC), but also has its own unique set of challenges. Specifically, the volumetric flow rate through the column is low (typically 100 nL min^{-1} or less), and electrical contact must be maintained with the buffer in the capillary for the separation to occur. Determining when a fraction should be collected at the capillary outlet can also be difficult as the migration velocity of each sample constituent varies with its electrophoretic mobility.

Despite these problems, numerous attempts have been made to collect CE fractions for postseparation analysis. Rose and Jorgenson[1] described a fraction collector that sequentially positioned the outlet of a separation capillary in vials containing 25 μL of buffer and that was held at ground potential. This instrument configuration is simple, robust, and similar to the fraction collection option available with many commercial capillary electrophoresis instruments. Furthermore, this fraction collection method had little effect on the biological activity of an enzyme collected with this instrument. Unfortunately, the nanoliter CE fractions are diluted into microliter volumes of buffer, which can make subsequent analyses difficult. An additional problem is that it is almost unavoidable that the electrophoresis current be interrupted for a short period of time during the capillary transfer. This introduces a temporal uncertainty in the migration of zones as the number of fractions collected is increased.

To avoid the problems associated with dilution of the sample and interruption of the electrophoresis, several methods for grounding the separation capillary at positions other than the outlet have been proposed. These methods usually involve the formation of cracks or frits in the capillary wall to establish electrical contact with the separation buffer prior to the capillary outlet. The force of the electroosmotic flow is used to push the zone from the capillary. This type of interface has been used for continuous fraction collection onto filter paper[2,3] and to collect samples for plasma desorption and matrix-assisted laser desorption mass spectrometry.[4,5] This method of collecting fractions minimizes sample dilution and contamination with buffer salts but requires that a strong electroosmotic flow be maintained in the capillary. This requirement may not be practical if capillary coatings are required to minimize analyte interaction with the walls of the capillary or if the electroosmotic flow must be altered to optimize a separation. An additional limitation of this interface design is that it requires accurate estimates of the electroosmotic flow in the capillary and electrophoretic mobility of a substance to accurately predict when the analyte zone migrates from the capillary outlet.

An alternative method for continuously collecting the effluent from capillary electrophoresis columns is to place a rotating moist membrane maintained at ground potential in electrical contact with the outlet of the capillary.[6–8] Alternatively, Tracht and co-workers utilized a silver-coated capillary to establish electrical contact with electrophoresis buffer while the analyte was captured on a peptide-

† Current address: Department of Pharmacology, The Johns Hopkins University, School of Medicine, 725 N. Wolfe St., Baltimore MD 21205.

(1) Rose, D. J.; Jorgenson, J. W. *J. Chromatogr.* **1988,** *438,* 23–34.
(2) Huang, X.; Zare, R. N. *J. Chromatogr.* **1990,** *516,* 185–189.
(3) Huang, X.; Zare, R. N. *Anal. Chem.* **1990,** *62,* 443–446.
(4) Takigiku, R.; Keough, T.; Lacey, M. P.; Schneider, R. E. *Rapid Commun. Mass Spectrom.* **1990,** *4,* 24–29.
(5) Keough, T.; Takigiku, R.; Lacey, M. P.; Purdon, M. *Anal. Chem.* **1992,** *64,* 1594–1600.
(6) Eriksson, K. O.; Palm, A.; Hjerten, S. *Anal. Biochem.* **1992,** *201,* 211–215.
(7) Cheng, Y.; Fuchs, M.; Andrews, D.; Carson, W. *J. Chromatogr. A* **1992,** *608,* 109–116.
(8) Warren, W.; Cohen, S. *LC-GC* **1994,** *12,* 12–17.

0003-2700/95/0367-4190$9.00/0

binding membrane and radioisotope detection performed in place.[9] These membrane collection devices help maintain the efficiency of the separation by trapping the analyte before it can migrate in the membrane by diffusion or capillary action. The membranes can also act as an additional selectivity parameter, only capturing molecules with the appropriate chemical characteristics. However, the use of these membranes requires a priori knowledge of the chemical characteristics of the analyte. Further, if the molecule cannot be analyzed while attached to the membrane, it must be released by some means,[8] which can make the processing of large numbers of samples very labor intensive. Finally, the act of physically being adsorbed and released from a membrane may alter the activity of some biomolecules.

Several papers report the use auxiliary flows to maintain electrical contact with the capillary and help transfer the zones to a collection vial or surface for subsequent off-line analysis.[10-12] Although each of these instruments has been shown to be capable of collecting CE fractions, their performance has not been well characterized and the samples are diluted with the auxiliary flow of liquid.

In this report, we provide detailed descriptions of a fraction collection instrument which can be configured for use under most CE analysis conditions. This instrument is easily constructed, allows automated collection of large numbers of fractions, and maintains the efficiency provided by the electrophoretic separation. As will be demonstrated, fractions can be collected from capillaries in which the inner surface was chemically modified to minimize analyte adsorption, and the resulting fractions are suitable for analysis by many different off-line analytical techniques.

EXPERIMENTAL SECTION

Reagents and Materials. Proteins and methylparaben were purchased from Sigma Chemical Co. (St. Louis, MO). Hexadimethrine bromide (Polybrene), mesityl oxide, phthalic acid, 2,5-dihydroxybenzoic acid, dicumyl peroxide, and hexamethyldisilazane were obtained from Aldrich Chemical Co. (Milwaukee, WI). Ucon was obtained from Alltech Associates, Inc. (75-H-90,000, Deerfield, IL), and all other reagents were obtained from Fisher Scientific (Pittsburgh, PA). Solutions were prepared with deionized water from a Nanopure Ultrapure water system (Barnstead Thermoline, Dubuque, IA).

Capillary Electrophoresis. The CE instrument used in these investigations was constructed in-house from available components. A regulated high-voltage dc power supply (Model EH50R02, Glassmann High Voltage, Inc., Whitehouse Station, NJ) provided the driving potential for the electrophoretic separations through a 22-gauge platinum wire electrode immersed in the inlet buffer reservoir. All separations were performed in a field ranging from 250 to 333 V cm^{-1}. To minimize arcing and protect the operator from accidental shock, the inlet buffer reservoir and high-voltage end of the capillary were enclosed in a Plexiglas box. Separations were carried out in fused-silica capillaries (Polymicro Technologies Inc., Phoenix, AZ) which had the following dimensions: 52- or 75-μm inner diameter (i.d.), 363 μm outer diameter (o.d.), 50 cm from the inlet to detection window, and 10 cm from the detector to the outlet. Electrokinetic and hydrodyamic sample introduction procedures were used to introduce sample into the capillary, and the separation was monitored with an on-column variable-wavelength absorption detector (Model 200 with a capillary flow cell, Scientific Systems, Inc., State College, PA) at 200 or 254 nm. The detector signal was digitized at 7 Hz with a 16-bit analog-to-digital convertor (Model XL-1900 chassis with an ADC2/16 analog-to-digital convertor, Elexor Associates, Morris Plains, NJ), and the resulting data were transferred to a NeXTstation computer (NeXT Computer, Inc., Redwood City, CA) for processing and display. Current in the capillary was determined by monitoring the voltage across a 1.0-kΩ resistor used to electrically connect the outlet of the capillary and ground. The reproducibility of the separations was maintained by flushing the capillaries between runs with fresh buffer and by replacing the buffer in the inlet reservoir after a small number (i.e., 5) analyses.

Coaxial Capillary Interface. The coaxial capillary interface (Figure 1A) was constructed from a $^1/_{16}$-in. stainless steel tee (Swagelok Co., Niagra Falls, ON, Canada) and a 2-cm length of 530-μm-i.d., 700-μm o.d. fused-silica capillary (Polymicro Technologies, Inc.). The separation capillary was threaded through the tee as shown in Figure 1A so that ~1 cm of the capillary extended beyond the tee. The 530-μm-i.d. coaxial capillary was positioned over the separation capillary so that the smaller tube extended ~0.5 mm beyond the outer capillary, and the fittings on the tee secured. Fluid was continuously pumped through the tee and the outer capillary with a 100-μL syringe mounted on a syringe pump (Model 341B, Sage Instruments, Boston, MA). When the coaxial fluid is conducting and the stainless steel tee is held at ground potential, the capillary outlet is also maintained at ground potential. Under typical operating conditions, a flow of at least 100 nL min^{-1} of an aqueous solution was required to maintain electrical contact with the separation capillary.

Fractions from the separation capillary were automatically collected utilizing the same computer software used to monitor the detector output. This program uses operator-specified criteria (e.g., migration time, peak height, etc.) to identify peaks in the detector signal and, once a peak is detected, estimates the time the zone will emerge from the capillary. This estimate is obtained with the following formula:

$$T_r = T_1(L_2/L_1) \quad (1)$$

where T_r is the time required for the zone to migrate from the capillary inlet to the outlet, T_1 is the time required for the analyte to travel from the capillary inlet to the detector, and L_1 and L_2 are the distances from the capillary inlet to the detector and total capillary length, respectively. At the appropriate time (T_r), the computer sequentially (1) signals a solenoid to lower the stage on which the stepper motor and sample probe are positioned so that the probe is no longer in contact with the separation capillary, (2) rotates the probe with a high-resolution stepper motor (M83-93 motor, 2100-1 indexer, Compumotor Corp., Petaluma, CA) so the capillary is over a previously unused position, and (3) signals the solenoid to reposition the sample probe ~0.5 mm below the outlet of the separation capillary. This movement is accomplished very quickly, typically in less than 1 s. To avoid unnecessary dilution and contamination of the sample, the capillary is repositioned at a designated waste position on the probe after each fraction has been collected. Each of these movements is recorded

(9) Tracht, S.; Toma, V.; Sweedler, J. V. *Anal. Chem.* **1994,** *66,* 2382–2389.
(10) Hjerten, S.; Zhu, M. *J. Chromatogr.* **1985,** *327,* 157–164.
(11) Castoro, J. A.; Chiu, R. W.; Monnig, C. A.; Wilkins, C. L. *J. Am. Chem. Soc.* **1992,** *114,* 7571–7572.
(12) van Veelen, P. A.; Tjaden, U. R.; van der Greef, J.; Ingendoh, A.; Hillenkamp, F. *J. Chromatogr.* **1993,** *647,* 367–374.

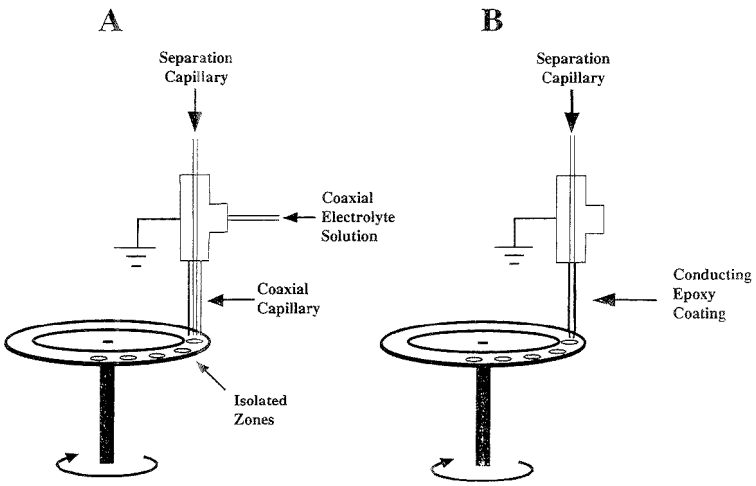

Figure 1. Expanded view of capillary interface for (A) coaxial flow interface and (B) conductive capillary interface.

by the computer so peaks in the electropherogram can be associated with specific positions on the sample probe.

Conductive Capillary Interface. The conductive capillary interface (Figure 1B) was constructed by tapering the outlet of the separation capillary by abrasion with 600-grit sandpaper, then sequentially rinsing the beveled surface with methanol and water, and allowing it to dry. A 9:1 (v/v) mixture of gold-filled epoxy and heat-curing epoxy (H81E and 353ND, respectively, Epoxy Technology, Inc., Billerica, MA) was prepared and applied as a thin layer on the final 1.5 cm of this capillary. After curing the epoxy at 120 °C for 15 min, the conductive coating was polished with 600-grit sandpaper to give a smooth surface. This capillary was mounted in a $^1/_{16}$-in. stainless steel tee (Swagelok Co.) with graphite ferrules to securely position the capillary and allow electrical contact to be established with the conductive coating. The movement of the sample probe under the capillary outlet was controlled with the same software and hardware used with the coaxial capillary interface.

Capillary Surface Coatings. The inner walls of some separation capillaries were coated with the polymer Ucon utilizing the procedure of Malik et al.[13] or Polybrene using the following procedure. The capillary was sequentially flushed with methylene chloride for 1 min, an aqueous solution of 0.5% (v/v) hydrofluoric acid for 30 s, 0.1 N NaOH for 5 min, deionized water for 5 min, and finally a solution containing 1.0% (w/w) polymer in deionized water for a period of not less than 5 min. Following exposure to the cationic polymer solution, the capillary was flushed with the analysis buffer while an electric field of several hundred volts per centimeter was applied for several minutes. Capillaries prepared this way produce stable electroosmotic flow and demonstrate excellent efficiency for several days before the coating degrades.[14]

High-Pressure Liquid Chromatography. All HPLC separations were performed with a reciprocating pump (Model L-6200A, Hitachi Ltd.,Tokyo, Japan) equipped with a 10-μL loop injector (Model 9125-080, Rheodyne, Cotati, CA). For the capillary liquid chromatography separations, the pump flow was set to 0.8 mL min^{-1} and a precolumn split was made using a 5-cm piece of 50-μm-i.d. capillary to produce a flow through the chromatography column of 4 μL min^{-1}. The separation capillary (180-μm i.d., 10.2 cm in length) was packed with Poros IIR (10-μm diameter, PerSeptive Biosystems, Cambridge, MA). Separations were also performed on a small reversed phase column (ODS-5S column, Bio-Rad, Inc., Richmond, CA). The effluent from the columns was monitored with an absorbance detector (Spectra 100, Spectra Physics Analytical, San Jose, CA) equipped with a capillary or biocompatible flow cell, as necessary.

Electrospray Ionization Mass Spectrometry. Electrospray spectra were acquired and processed with a quadrupole mass spectrometer configured with an electrospray interface (Model 201 mass filter with options ES and E2000, Vestec Corp., Houston, TX). This instrument has been described in detail elsewhere.[15] Samples were introduced into the electrospray interface through a fused-silica capillary with a tapered outlet and coated with the gold-filled epoxy. During the analysis, this capillary was held at a potential sufficient to provide an electrospray current of 0.2 μA. The resulting spectra were converted to ASCII files and transferred to a NeXTstation computer (NeXT Computer, Inc.) for processing with a multiplicative correlation algorithm.[16]

RESULTS AND DISCUSSION

The first instrument used to collect fractions from the CE capillary utilized the coaxial capillary configuration shown in Figure 1A. Although coaxial capillary geometries are popular for coupling CE with electrospray ionization mass spectrometry, three previous publications have utilized this type of interface to collect fractions.[11,12,17] In these reports, little effort was made to characterize the efficiency with which material can be transferred from

(13) Malik, A.; Zhao, A.; Lee, M. L. *J. Microcolumn Sep.* **1993**, *5*, 119–125.
(14) Chiu, R. W.; Jimenez, J. C.; Monnig, C. A. *Anal. Chem. Acta* **1995**, *307*, 193–201.
(15) Penn, S. G.; Chiu, R. W.; Monnig, C. A. *J. Chromatgr.* **1994**, *680*, 233–241.
(16) Hagen, J. J.; Monnig, C. A. *Anal. Chem.* **1994**, *66*, 1877–1883.
(17) Weinmann, W.; Parker, C. E.; Deterding, C. E.; Papac, D. I.; Hoyes, J.; Przybylski, M.; Tomer, K. B. *J. Chromatogr.* **1994**, *680*, 353–361.

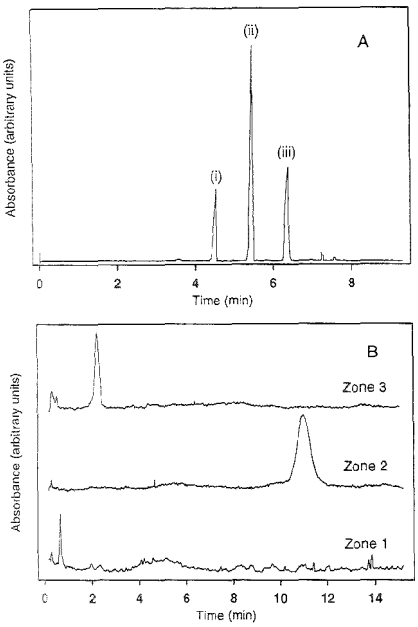

Figure 2. Fraction collection of small molecules separated by capillary electrophoresis with coaxial interface: (A) Electropherogram of (i) phthalic acid, (ii) methylparaben, and (iii) 2,5-dihydroxybenzoic acid. (B) Chromatograms of fractions collected from (A) at 4.23–4.77, (zone 1), 5.15–5.71, (zone 2), and 6.06–6.61 min (zone 3). Detection for the electropherogram and the chromatograms was at 254 nm. Experimental details are described in the text.

the separation column or to define the experimental conditions (buffer pH and concentration, electroosmotic flow velocity, etc.) that can be utilized.

One concern with the coaxial capillary interface was whether the flow over the outlet of the separation capillary would induce a flow in the column and degrade the efficiency of the separation. To measure any induced flow in the separation capillary, a capillary was coated with Ucon to suppress electroosmotic flow and the migration time of myoglobin was monitored as a function of coaxial fluid flow rate. Ucon efficiently suppresses electroosmotic flow and minimizes protein interactions with the capillary wall[13] so any change in migration time must be caused by the coaxial fluid flow. No significant change in migration time was observed as the flow was varied from 0.36 to 7.6 μL min.$^{-1}$.

To test the viability of the coaxial interface, a sample containing 76 pmol of phthalic acid, 110 pmol of methylparaben, and 116 pmol of 2,5-dihydroxybenzoic acid was separated by CE, and fractions corresponding to each of these components were collected and further analyzed by liquid chromatography. The CE separations were performed in a 75-μm-i.d, 363-μm-o.d. fused-silica capillary filled with 50 mM sodium borate buffer (pH 9.0). Figure 2A shows the electropherogram for this mixture. Each zone corresponding to a peak in Figure 2A was deposited on a stainless steel surface, allowed to dry, and then resuspended in 15 μL of deionized water; 10 μL of this mixture was analyzed by HPLC to confirm purity and identity. The HPLC separations were performed under isocratic conditions with a mobile phase of 0.1% TFA in water on a reversed phase column (ODS-5S column, Bio-Rad, Inc.). From the chromatograms in Figure 2B, it is clear that there is little, if any, cross-contamination between fractions. A comparison of the peak area for each of the fractions with standard solutions indicates that more than 90% of each analyte introduced into the electrophoresis capillary was detected by HPLC. Together, these results indicate that eq 1 is valid for the proposed application and that it is possible to quantitatively recover fractions deposited on metal surfaces.

A popular application for capillary electrophoresis is analysis of protein mixtures. Proteins can be difficult to analyze since they often interact with the walls of the capillary.[18] Any association between the analyte and the capillary wall will degrade separation efficiency and can adversely impact the stability of the electroosmotic flow in the capillary.[19,20] The ability to efficiently collect fractions from mixtures containing molecules that interact with the capillary walls is dependent on the ability to control or eliminate these adverse processes.

One method to reduce analyte–wall interactions is to chemically modify or physically block the sites of interaction.[21] To demonstrate that fractions could be collected from surface-modified capillaries with the coaxial capillary interface, a standard protein mixture was separated in a Ucon-coated capillary and fractions were collected. Initial attempts to assay these fractions by capillary HPLC indicated that the analyte often did not emerge from the capillary during the expected time intervals. Typically, the zones were delayed and broadened, but in some extreme cases no analyte was detected. One likely explanation for these observations was that the analyte was being trapped in a small stagnant region at the outlet of the capillary. The reduced electroosmotic flow in the capillary and the rapid decrease in the electric field at the outlet of the capillary are the most likely explanations for the stagnation. Consequently, transport of the analyte away from this region is primarily dependent on convective forces and molecular diffusion, both of which are slow processes.

To assist with the transport of the analyte away from the capillary outlet, the end of the capillary was tapered by abrasion with 600-grit sandpaper so that the coaxial liquid flow could more efficiently sweep the critical outlet region. Unfortunately, this change did not significantly alter the retention of the proteins. Alternatively, a supplemental flow was induced in the capillary by raising the inlet buffer reservoir relative to the capillary outlet. For our investigations, a height difference of 3 cm eliminated the delay. Raising the capillary inlet relative to the outlet will increase zone broadening because of the parabolic flow velocity profile induced in the capillary. The theory of zone broadening in an open tube developed by Golay[22] was used to estimate the maximum separation efficiency possible under these analysis conditions. For a 50-μm-i.d. capillary and molecular diffusion coefficient of 5×10^{-5} cm^2 s^{-1}, a maximum separation efficiency of 17 200 theoretical plates should result when the inlet is raised 3 cm and the inlet-to-detector distance is 47 cm. This estimate is

(18) Maa, Y. F.; Hyver, K. J.; Swedberg, S. A. *J. High Resolut. Chromatogr.* **1991**, *14*, 65–67.
(19) Bolger, C. A.; Zhu, M.; Rodriguez, R.; Wehr, T. *J. Liq. Chromatogr.* **1991**, *14*, 895–906.
(20) Nashabeh, W.; El. R. Z. *J. Chromatogr.* **1991**, *559*, 357–383.
(21) Timerbaev, A. R.; Buchberger, W.; Semenova, O. P.; Bonn, G. K. *J. Chromatogr.* **1992**, *630*, 379–389.
(22) Golay, M. J. E. In *Gas Chromatography*; Desty, D. H., Ed.; Butterworth: London, 1958; pp 36–55.

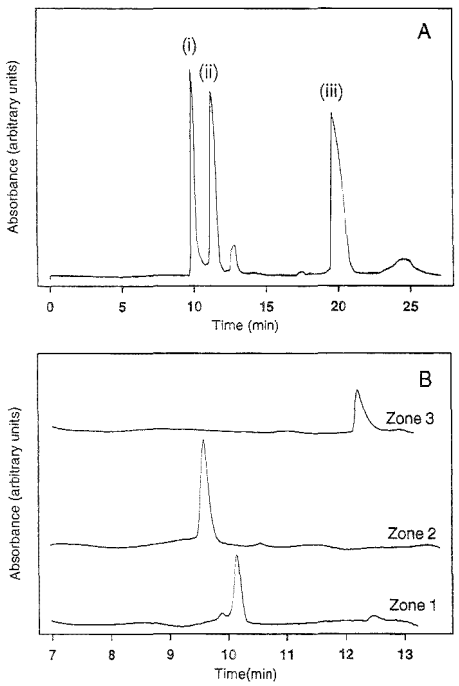

Figure 3. Fraction collection with the coaxial capillary interface and HPLC analysis of three proteins separated by capillary electrophoresis: (A) Electropherogram for a solution containing (i) myoglobin, (ii) cytochrome *c*, and (iii) lysozyme. (B) Chromatograms for the fractions corresponding to 9.5–10.5, (zone 1), 11.0–12.0, (zone 2), and 20.0–21.0 min (zone 3) in (A). See text for analysis conditions.

in reasonable agreement with the empirically determined efficiency reported here. It is interesting to note that for the analyses reported here, lowering the inlet reservoir so that it is level with the capillary outlet did not significantly enhance the separation efficiency. This is likely the result of the relatively large sample quantities that must be introduced into the capillary to allow detection by HPLC and electrospray ionization mass spectrometry (ESI-MS). If smaller analyte concentrations are employed, the reduction in efficiency produced by this pressure-induced flow would be significant.

Protein samples were prepared at concentrations of 2.5×10^{-4} M in the analysis buffer. The capillary inlet was held 5.7 cm higher than the outlet for 50 s to introduce 9.4 pmol of each protein into the capillary. The separations were performed in a fused-silica capillary with an inner diameter of 75 μm and filled with pH 5.0, 30 mM tris–acetate buffer. An electric field of 340 V cm^{-1} was used to drive the separation, and the coaxial flow was adjusted to a flow of 1.1 μL min^{-1}. Fractions deposited on the sample probe were allowed to dry and then dissolved in 15 μL of double-deionized water, and 10 μL of this solution was introduced into the capillary HPLC column. The proteins were eluted from the capillary with a solution that contained increasing amounts of acetonitrile (25–47%) in water and 0.1% trifluoroacetic acid. Figure 3A is the electropherogram showing the separation of lysozyme, cytochrome *c*, and myoglobin. Figure 3B show the corresponding chromatograms for the fractions for each of these proteins. By comparing the peak areas for these chromatograms with standards, it is estimated that approximately 70–80% of each protein introduced into the CE capillary was successfully transferred to the HPLC column. Possible mechanisms for protein loss include adsorption to the capillary and surfaces of instruments used to transfer the samples and incomplete collection of the solvent used to suspend the sample.

Conductive Capillary Interface. Another promising alternative, which eliminates the need for a coaxial flow, is the addition of a grounded conducting film near the capillary outlet. Wahl and co-workers used Tollen's reaction to provide electrical contact at the capillary outlet for a design for the coupling of CE to electrospray ionization mass spectrometry without using a sheath flow.[23] A similar design has been implemented for fraction collection onto peptide-binding membranes.[9]

A gold-coated capillary was constructed to allow the collection of CE effluents without the addition of coaxial flow. Gold was chosen as the conductive medium because it is relatively inert and has excellent electrical properties. A stable electroosmotic flow in the capillary (~2 nL s^{-1} for Polybrene-treated and bare fused-silica capillaries) efficiently sweeps the analyte from the column and establishes the necessary electrical contact between the buffer and the conductive coating. Eliminating the coaxial flow alleviates the need for a syringe pump, dramatically reduces the volume of liquid deposited with each fraction, and consequently minimizes the quantity of buffer salt collected with the analyte. The smaller liquid volume is advantageous when it is desirable to place the entire fraction in the smallest spot possible. The reduced salt minimizes any possible interference with subsequent analysis techniques.

The gold-coated capillary is very simple to manufacture and can be used continuously for several days before the gold/epoxy coating softens and degrades. In our initial attempts to construct a conductive capillary, we coated the capillary with silver-doped epoxy (Epo-Tech No. H20S). Although the resulting columns appeared very stable over an extended period of time, inspection of the metal surfaces on which the samples were collected and the coating at the outlet of the separation capillary clearly indicated that silver was being lost from the coating and deposited on the sample probe. Oxidation of the metal seems to be the result of an electrochemical process, although chemical stripping may also play a role under some analysis conditions. Despite this loss of metal, the coating remained conductive for an extended period of time (i.e., weeks) in agreement with earlier statements concerning the stability of these types of coatings.[9] Unfortunately, the release of silver from the coating could lead to adduct formation and potentially could alter the chemical properties of some analytes, as well as interfer with mass spectral analyses. In particular, many enzymes are known to be sensitive to silver "poisoning".

Although the gold-coated capillary also lost its coating over time, visual inspection of the sample probe, mass spectrometry of isolated fractions, and collection and assay of the activity of the enzyme trypsin showed no evidence of metal ions and/or adduct formation. The softening of the gold-filled epoxy is electrochemically driven, with an increasing amount of current decreasing the lifetime of the coating. Fortunately, the coating

(23) Wahl, J. H.; Goodlett, D. R.; Udseth, H. R.; Smith, R. D. *Anal. Chem.* **1992**, *64*, 3194–3196.

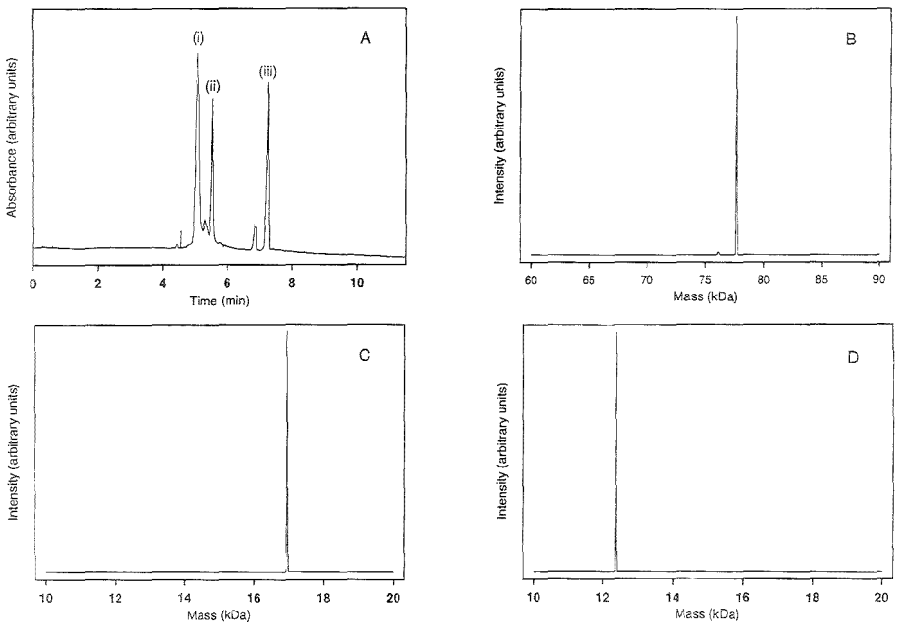

Figure 4. Analysis of capillary electrophoresis fractions by electrospray ionization mass spectrometry: (A) Electropherogram of (i) conalbumin, (ii) myoglobin, and (iii) cytochrome *c*. The reconstructed mass spectrum for the fraction corresponding to (B) 4.82–5.33, (C) 5.33–5.73, and (D) 7.03–7.45 min in (A). See text for analysis conditions.

can quickly be restored by polishing the end of the capillary to obtain a clean surface and then recoating the tip by utilizing the procedure described in the Experimental Section. This entire procedure typically requires 20 min and was performed after 3–5 days of operation.

Analysis of Fractions by ESI-MS. To characterize compounds isolated by capillary electrophoresis, protein fractions were analyzed by electrospray ionization mass spectrometry. Electrospray ionization techniques can be adversely affected by ionic species in the sample, often leading to the formation of undesirable adduct ions, increased instability in the spray current or both. Furthermore, most of the buffers employed for CE are nonvolatile and so are generally considered incompatible with ESI-MS when used as an on-line detector. Off-line fraction collection with the conductive capillary interface provides one means of reducing sample contamination with electrolytes and nonvolatile species, making these samples easier to analyze by ESI-MS.

To demonstrate the utility of CE with fraction collection for off-line analysis of isolated zones, a synthetic mixture containing 2.5 pmol of conalbumin and 5 pmol of both myoglobin and cytochrome *c* was introduced into a capillary by hydrodynamic injection and separated. The surface of the capillary was modified with Polybrene and the separation performed in a pH 5.0, 30 mM acetic acid–sodium acetate buffer. Figure 4A shows the electropherogram for this separation. Three fractions corresponding to the three major peaks were deposited with the conductive capillary interface on stainless steel pins and allowed to dry. These samples were suspended in 15 μL of a 50:47:3 methanol–water–acetic acid solution, and 8.4 μL of this mixture was introduced into the mass spectrometer over a period of 6 min. These electrospray spectra were averaged, converted to ASCII files, and processed with a multiplicative correlation program as previously described.[16] The resulting mass spectra are shown in Figure 4B–D. The mass assignments for conalbumin, myoglobin, and cytochrome *c* are 77 586, 16 952, and 12 359, respectively, in reasonable agreement with the values 77 500, 16 950, and 12 360 previously reported.[24] Previous attempts to collect fractions for ESI-MS suffered from both a loss of sensitivity due to sample dilution and contamination with buffer salts.[25] Although the procedure employed for this analysis also diluted the sample, contamination of the sample was greatly reduced, which allows both instruments to be independently optimized and greatly simplified their operation.

CONCLUSIONS

The ability to quickly and efficiently collect fractions isolated by capillary electrophoresis opens new possibilities for the characterization of microscopic samples. The combination of on-column detection and automated deposition of the sample maintains the separation resolution and simplifies operation of the instrument. Deposition of fractions on a clean surface eliminates the requirement that the analyte-binding properties be known prior to analysis and can simplify sample handling. Off-line analysis of these fractions effectively decouples the temporal demands of the separation and postcolumn analysis technique and allows each instrument to be optimized independently. Fractions isolated by this instrument have been successfully analyzed by liquid chro-

(24) Smith, R. D.; Loo, J. A.; Edmonds, C. G.; Barinaga, C. J.; Udseth, H. R. *Anal. Chem.* **1990**, *62*, 882–899.
(25) Albin, M.; Chen, S. M.; Louie, A.; Pairaud, C.; Colburn, J.; Wiktorowicz, J. *Anal. Biochem.* **1992**, *206*, 382–388.

matography and mass spectrometry, but could potentially be processed with any analytical technique that demonstrates the requisite sensitivity, and so provides a significant advance in the analyst's ability to characterize microscopic unknown samples.

ACKNOWLEDGMENT

Financial support was provided by the Arnold and Mabel Beckman Foundation (C.A.M.), Lawrence Livermore National Laboratory (C.A.M. Contract B244803), and the W. M. Keck Foundation.

Received for review March 8, 1995. Accepted September 1, 1995.[®]

AC950234E

[®] Abstract published in *Advance ACS Abstracts,* October 15, 1995.

Anal. Chem. 1995, *67*, 4197–4204

Off-Line Coupling of Capillary Electrophoresis and Matrix-Assisted Laser Desorption/Ionization Time-of-Flight Mass Spectrometry

Kathleen L. Walker,† Rick W. Chiu, Curtis A. Monnig,* and Charles L. Wilkins*

Department of Chemistry, University of California, Riverside, California 92521-0403

An automated fraction collection interface is used in conjunction with matrix-assisted laser desorption/ionization (MALDI) time-of-flight mass spectrometry to analyze material isolated by capillary electrophoresis (CE). CE fractions are deposited directly on the MALDI probes so that individual peaks from the electropherogram are associated with a single sample spot on the probe. MALDI matrices with high acid concentrations afford enhanced tolerance of electrophoresis buffers. The utility of this hybrid instrument is demonstrated by separation and mass analysis of a tryptic digest of cytochrome *c* and synthetic mixtures of four proteins. Mass assignments corresponding to the protonated molecular ions are in good agreement with those predicted from molecular structure. Miniaturization of the interface affords enhanced sensitivity, with good-quality spectra from separations of as little as 25 fmol of protein.

Capillary electrophoresis (CE) is an efficient tool for the separation of mixtures of ionized molecules. When compared with liquid chromatography, CE usually requires similar analyte concentrations (i.e., nanomolar and above) but smaller sample volumes (nanoliters). As a consequence, the quantity of analyte available for detection is extremely limited. The characterization of unknown molecules isolated by CE requires a sensitive detector that can provide detailed chemical information about the analyte. Mass spectrometry is an analytical technique capable of providing the requisite sensitivity and chemical information but does not routinely lend itself to analysis of complex mixtures. However, when mass spectrometry is coupled with CE, the resulting instrument provides a very effective means for characterizing difficult samples.

The utility of capillary electrophoresis with mass spectrometric detection has long been recognized, but relatively difficult to implement. Most often these instruments have been coupled through an on-line electrospray ionization source. Electrospray ionization is capable of monitoring a diverse range of chemical species but can be adversely effected by ionic species such as the salts used in CE buffers (e.g., NaH_2PO_4, NaH_2BO_3, etc.). Further, because the column effluent is continuously introduced into the ion source of the mass spectrometer, it is generally limited to buffers that only contain volatile species. Consequently, these hybrid instruments have not found widespread use as a routine method of analysis. A more practical instrument configuration would tolerate nonvolatile and ionic electrolytes and not require that the separation method be tailored to accommodate the shortcomings of the mass spectrometry.

Matrix-assisted laser desorption/ionization (MALDI) time-of-flight mass spectrometry (TOF-MS) is a powerful analytical technique capable of excellent sensitivity and tolerant of diverse analysis conditions. As such, it is an excellent candidate as a detector for CE. Recent attempts to couple CE and MALDI TOF-MS with an on-line interface have met with limited success.[1] An on-line interface requires differential pumping in the interface region to maintain pressures of at least 10^{-5} Torr in the MALDI source. Further, continuous introduction of buffer into the source will increase the maintenance requirements of an instrument and may ultimately degrade its performance.

Off-line coupling of CE with MALDI MS has several distinct advantages over on-line analysis. Commercially available MALDI mass spectrometers can be utilized with little if any modification of the sample probe and ion source. Contamination of the ion source with nonvolatile sample concomitants is also minimized, allowing nonvolatile electrophoresis buffers to be utilized. Finally, physically decoupling the instruments allows the analysis conditions for both the separation and the mass analysis to be independently optimized.

Peptides and proteins isolated by CE were first collected and analyzed by plasma desorption mass spectrometry[2] and MALDI TOF-MS[3] in 1990 and 1992, respectively. In 1992, CE was also coupled with MALDI Fourier transform mass spectrometry through an automated fraction collection interface.[4] Subsequently, several other reports describe the coupling of CE effluents with MALDI TOF-MS.[5,6] All of these studies utilized compromised conditions that sacrificed separation efficiency and/or mass spectral resolution to facilitate the acquisition of mass spectra. Furthermore, many of these instruments were very labor intensive, often requiring manual collection of sample fractions and extensive treatment of the isolated fractions prior to mass analysis.

In this report we describe two methods for off-line coupling of capillary electrophoresis with MALDI time-of-flight mass spec-

† Current address: Department of Pharmacology, School of Medicine, The Johns Hopkins University, 725 N. Wolfe St., Baltimore, MD 21205.

(1) Williams, E. R.; Jones, G. C., Jr.; Fang, L.; Zare, R. N. *Applied Spectroscopy in Material Science II*; Golden, W. G., Ed. *Proc. SPIE* **1992**, *1636*, 172–181.
(2) Takigiku, R.; Keough, T.; Lacey, M. P.; Schneider, R. E. *Rapid Commun. Mass Spectrom.* **1990**, *4*, 24–29.
(3) Keough, T.; Takigiku, R.; Lacey, M. P.; Purdon, M. *Anal. Chem.* **1992**, *64*, 1594–1600.
(4) Castoro, J. A.; Chiu, R. W.; Monnig, C. A.; Wilkins, C. L. *J. Am. Chem. Soc.* **1992**, *114*, 7571–7572.
(5) van Veelin, P. A.; Tjaden, U. R.; van der Greef, J.; Ingendoh, A.; Hillenkamp, F. *J. Chromatogr.* **1993**, *647*, 367–374.
(6) Weinmann, W.; Parker, C. E.; Detering, L. J.; Papac, D. I.; Hoyes, J.; Przybylski, M.; Tomer, K. B. *J. Chromatogr. A* **1994**, *680*, 353–361.

0003-2700/95/0367-4197$9.00/0

trometry that address many of the problems associated with these first-generation instruments. A coaxial capillary sheath flow interface[4] is used to collect fractions from electrophoresis capillaries in which the electroosmotic flow (EOF) has been suppressed. If strong EOF is present in the separation capillary, superior performance is provided with a fraction collection interface that utilizes a separation capillary coated with a conductive epoxy. Application of a MALDI matrix containing formic acid on dried CE fractions allows the acquisition of well-resolved, adduct-free mass spectra in the presence of salts and buffer additives.

EXPERIMENTAL SECTION

Reagents and Materials. Protein standards, trypsin, 2,5-dihydroxybenzoic acid, α-cyano-4-hydroxycinnamic acid, buffer salts, and fucose were obtained from Sigma Chemical Co. (St. Louis, MO) in the highest purity available and used without further purification. Sigma Chemical Co. also supplied the formic acid (ACS grade) and trifluoroacetic acid (protein sequencing grade). Matrix solvents and acetonitrile were obtained from Fisher Scientific (Fairlawn, NJ) in HPLC or ACS grade.

Buffers were prepared by titration of appropriate salts with acid or base to the correct pH. Matrices for the mass spectrometry were prepared as follows. α-Cyano-4-hydroxycinnamic acid was initially dissolved in a 100:100:1 mixture of 0.1% aqueous TFA, acetonitrile, and ethanol to form a 42 mM solution. For samples treated with a high concentration of acid, the matrix solution was further diluted with 10% formic acid to yield a final concentration of 15.3 mM α-cyano-4-hydroxycinnamic acid and 6.4% formic acid. 2,5-Dihydroxybenzoic acid was dissolved in a 1:1 solution of 0.1% TFA and acetonitrile diluted to yield a solution with a final concentration of 41 mM. Further dilution was with 3% TFA to yield final matrix-to-analyte molar ratios of 5000:1. Fucose was prepared by dilution to 40.6 mM with high-purity water. 2,5-Dihydroxybenzoic acid and fucose were used together, each in the ratio of 5000:1 to the analyte.

Instrumentation. A detailed description of the capillary electrophoresis instrument and fraction collection interfaces used in these studies has been published elsewhere.[7] Briefly, the CE instrument used in these investigations was constructed in-house from available components. A regulated high-voltage dc power supply (Model EH50R02, Glassmann High Voltage, Inc., Whitehouse Station, NJ) provided the driving potential for the electrophoretic separations. To minimize arcing and protect the operator from accidental shock, the inlet buffer reservoir and high-voltage end of the capillary were enclosed in a Plexiglas box. Separations were carried out in fused-silica capillaries (Polymicro Technologies Inc., Phoenix, AZ) that had the following dimensions: 52- or 75-μm inner diameter (i.d.), 363-μm outer diameter (o.d.), 50 cm from the inlet to detection window, and 10 cm from the detector to the outlet. To minimize analyte interactions with the capillary walls, the inner surface was modified with one of four reagents, (3-aminopropyl)triethyloxysilane (APTES; Sigma Chemical Co.), Ucon (75-H-90,000, Alltech Associates Inc., Deerfield, IL), polyarginine (MW 139 300, Sigma Chemical Co.), or Polybrene (Aldrich Chemical Co., Milwaukee, WI), utilizing previously published procedures.[8-10] Electrokinetic and hydrodyamic sample introduction procedures were used to introduce sample into the capillary, and the separation monitored with an on-column variable-wavelength absorption detector (Model 200 with a capillary flow cell, Scientific Systems, Inc., State College, PA) at 200 or 254 nm. The detector signal was digitized at 7 Hz with a 16-bit analog-to-digital convertor (Model XL-1900 chassis with an ADC2/16 analog-to-digital convertor, Elexor Associates, Morris Plains, NJ) and the resulting data transferred to a NeXTstation computer (NeXT Computer, Inc., Redwood City, CA) for processing and display.

The coaxial capillary interface was constructed from a $^1/_{16}$-in. stainless steel tee (Swagelok Co., Niagra Falls, ON, Canada) and a 2-cm length of 530-μm i.d., 700-μm o.d. fused-silica capillary (Polymicro Technologies, Inc.). The separation capillary was threaded through the tee so that 1 cm of the capillary emerged from the end, and the 530-μm i.d. coaxial capillary was positioned over the separation capillary so that it extended 0.5 mm beyond the inner capillary. Fluid was continuously pumped through the tee and the outer capillary with a 100-μL syringe mounted on a syringe pump (Model 341B, Sage Instruments, Boston, MA).

The conductive capillary interface was constructed by tapering the outlet of the separation capillary by abrasion with 600-grit sandpaper, then sequentially rinsing the beveled surface with methanol and water, and allowing it to dry. A 9:1 (v/v) mixture of gold-filled epoxy and heat-curing epoxy (H81E and 353ND, respectively, Epoxy Technology, Inc., Billerica, MA) was prepared and applied as a thin layer on the final 1.5 cm of this capillary. After curing the epoxy at 120 °C for 15 min, the conductive coating was polished with 600-grit sandpaper and mounted in a $^1/_{16}$-in. stainless steel tee (Swagelok Co.) with graphite ferrules to securely position the capillary and allow electrical contact to be established with the conductive coating.

Fractions from the separation capillary were automatically collected with the same computer software used to monitor the detector output. This program uses operator-specified criteria (e.g., migration time, peak height, etc.) to identify peaks in the detector signal and, once a peak is detected, estimates the time the zone will emerge from the capillary. This movement is controlled by computer software that estimates the time required for each sample zone to pass from the detector to the capillary outlet. At the appropriate time, the computer signals the solenoid and stepper motor to position a clean portion of the sample probe under the capillary outlet to collect the fraction. After the zone is deposited on the probe, it is rotated so that a waste position is positioned under the capillary outlet until the appearance of the next zone. The software can be instructed to collect specific peaks or to sequentially collect all zones. Zones not selected are deposited on the waste position of the sample probe.

MALDI time-of-flight mass spectra were measured with a LaserTec ResearcH mass spectrometer (Vestec Corp., Houston, TX) equipped with a neodymium–YAG laser (Yagmaster 200, Lumonics Ltd., Warwickeshire, England). All samples were desorbed with the frequency-tripled (355 nm) output of the laser. The sample irradiance was controlled with a variable attenuator (Model 935-5-OPT UV, Newport Research Corp., Irvine, CA). Under typical analysis conditions, a spot 50 μm in diameter was sampled with 30-μJ pulses to deliver a peak fluence of 10^7 W cm^{-2}.

(7) Chiu, R. W.; Walker, K. L.; Hagen, J. J.; Monnig, C. A.; Wilkins, C. L. **1995**, *67*, 4190–4196.

(8) Moseley, M. A.; Deterding, L. J.; Tomer, K. B.; Jorgenson, J. W. *Anal. Chem.* **1991**, *63*, 109–114.

(9) Malik, A.; Zhao, Z.; Lee, M. L. *J. Microcolumn. Sep.* **1993**, *5*, 119–125.

(10) Chiu, R. W.; Jimenez, J. C.; Monnig, C. A. *Anal. Chim. Acta* **1995**, *307*, 193–201.

All spectra were measured in the linear time-of-flight mode (1.2-m flight path). Ions were accelerated with a potential of 29 or 30 kV and detected by an ion multiplier biased at 5 kV. The resulting ion current was monitored at 2-ns intervals with a digital oscilloscope (Model TDS 520, Tektronix Inc., Beaverton, OR). Mass spectra were generated from the average of 12–75 single consecutive acquisitions from the same spot on the sample probe. Savitsky-Golay smoothing over a range of 5–10 points was applied to the spectra when necessary.

Mass assignments were made by estimating the centroid of the peaks with a commercial software package (Grams 386). Spectra were externally calibrated using the singly-charged and doubly-charged protonated ions of horse heart cytochrome *c* (*m/z* 12361.5 and 6180.75) and myoglobin (*m/z* 16951.7 and 8476.35).

The expected masses of tryptic peptides were determined for the average mass $(M + H)^+$ ions using the computer program MASS BIOSPEC 1.0 §2 (PE Sciex Instruments, Thornhill, ON, Canada).

Experimental Conditions. *Capillary Electrophoresis.* Unless otherwise indicated, the quantity of each analyte introduced in the separation capillary was 2 pmol. For protein separations in polyarginine-treated capillaries, the separation was performed in 20 mM pH 5.0 sodium acetate buffer. The sample was introduced into the capillary by raising the capillary inlet 6.5 cm relative to the outlet until the desired quantity of analyte was introduced into the capillary. Protein separations in APTES-modified capillaries utilized 30 mM pH 5.0 sodium acetate or 50 mM pH 2.5 sodium phosphate buffer, while Ucon-coated capillaries were used with 30 mM pH 5.0 Tris–acetate buffer or 40 mM pH 5.0 Tris-HCl buffer. Analyses performed with APTES and Ucon capillaries utilized electrokinetic sample introduction. Tryptic digest mixtures were separated in fused-silica capillaries treated with Polybrene or APTES and filled with 50 mM pH 2.5 sodium phosphate. In this case, the cationic polymer was present to ensure a strong electroosmotic flow at the low pH of the buffer. All separations utilized driving potentials between 200 and 408 V cm^{-1}, the exact value being determined by the conductivity of the buffer. In no case did the power dissipation in the capillary exceed 1 W m^{-1}. The voltage from the power supply was held at negative potentials for separations performed in capillaries treated with cationic modifiers (e.g., APTES, Polybrene, and polyarginine) and at positive potentials for Ucon-modified capillaries.

Tryptic Digest. The tryptic digest of bovine cytochrome *c* was prepared by procedures previously described.[11] For these studies, 7.2 mg of bovine cytochrome *c* was digested and an aliquot corresponding to 5 pmol of the protein was introduced into the separation capillary. After separation, the isolated fractions were deposited directly on the stainless steel sample pins and allowed to dry, and 1.0-μL aliquots of the 15.3 mM α-cyano-4-hydroxycinnamic acid matrix solution were deposited directly on each fraction. Assuming that 23 peptides are generated in the digest, the estimated average peptide quantity introduced into the capillary is 2.4 pmol for an average matrix-to-analyte ratio of 6375:1.

Protein Mixtures. The 15.3 mM α-cyano-4-hydroxycinnamic acid matrix solution was also used for the analysis of pmol and fmol quantities of protein. For 2.0-pmol samples, 2.0-μL droplets were deposited on the sample pins to yield matrix-to-analyte ratios of 15 300:1. For analyses of 150-fmol fractions, 0.7-μL droplets were deposited on top of the dried analyte fractions to yield matrix-to-analyte ratios of 71 400:1. For samples containing less than 150 fmol, 0.7-μL droplets of matrix were also used.

(11) Ross, G. A.; Lorkin, P.; Perrett, D. *J. Chromatogr.* **1993**, *636*, 69–79.

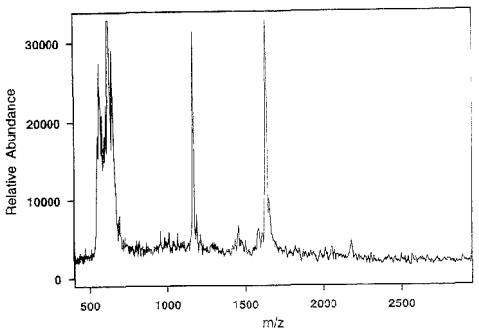

Figure 1. Linear MALDI TOF-MS spectrum of an unfractionated mixture of a tryptic digest of cytochrome *c*.

Some isolated proteins fractions were co-deposited on the sample probe with a solution containing 36.4 mM α-cyano-4-hydroxycinnamic acid in 1:1 acetonitrile–0.1% TFA or 2,5-dihydroxybenzoic acid in 50% acetonitrile solvent. These matrix solutions were introduced in the sheath liquid flow at a rate sufficient to generate a matrix-to-analyte ratio of ~5000:1. When the matrix was added to the dried fractions after the separation, 2.0-μL droplets of 5.1 mM α-cyano-4-hydroxycinnamic acid (solvent: 6.27% acetonitrile, 0.13% ethanol, and 93.6% of aqueous 3% TFA) were utilized to produce matrix-to-analyte ratios of 5000:1.

RESULTS AND DISCUSSION

Peptide and protein mixtures were analyzed using separation capillaries with several different surface coatings, sheath flow and conductive capillary interfaces, and various matrix solutions. All configurations provided good results, but the lowest detection limits were obtained with capillaries treated with cationic reagents (polyarginine and Polybrene) utilizing a sodium acetate buffer and fraction deposition with the conductive epoxy-coated capillary interface.

Analysis of Peptides and Proteins. To demonstrate the utility of CE/MALDI TOF-MS for complex mixture analysis, the tryptic digest of bovine cytochrome *c* and a synthetic mixture of proteins were analyzed. The latter mixture was analyzed under a variety of CE conditions to demonstrate the versatility of the hybrid instrument. Excellent separation efficiencies were realized under some conditions, and the fractions from these separations deposited directly on the laser target, dried, and analyzed without washing or lyphilization. To optimize MALDI performance in the presence of these buffers, multiple matrices and matrix conditions were examined to establish conditions that enhance the formation of proton attached spectra, signal-to-noise ratio, and spectral resolving power.

A tryptic digest of bovine cytochrome *c* was separated and characterized with the CE/MALDI TOF-MS combination, and these results were compared with the spectra obtained by MALDI TOF-MS without prior separation. The mass spectrum for the unfractionated digest is shown in Figure 1. Spectral resolution is poor, with a large cluster of peaks present in the mass range of the heme group (*m/z* 600) and two other large peaks in the *m/z*

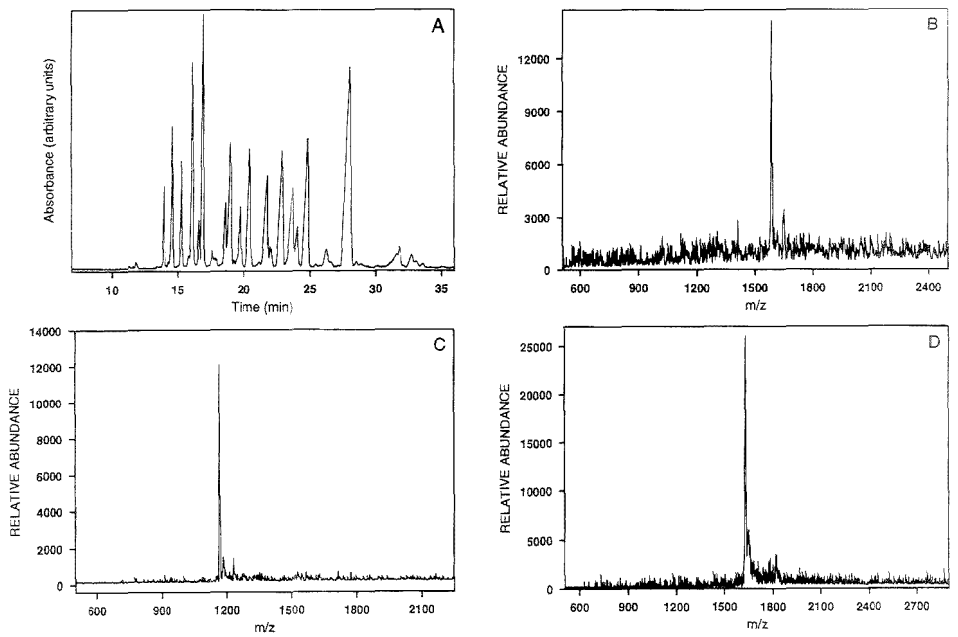

Figure 2. (A) Electropherogram of a tryptic digest of bovine cytochrome *c*. Panels B–D are the MALDI TOF-MS spectra of the sixth (18.72–19.24 min), eleventh (24.50–25.09 min), and twelfth (27.49–28.32 min) fractions of a tryptic digest of cytochrome *c* isolated by CE [shown in (A).

1200 and 1600 range. The peptides from a digest of bovine cytochrome *c* lie throughout the mass range 600 to 2200,[11] but few of the expected peptides are observed in this spectrum. Two possible explanations for the lack of peaks in this region are detector saturation by the *apparently* larger quantities of the predominant peaks and peak suppression due to competitive ionization effects. Regardless of the source of this suppression, Figure 1 demonstrates that MALDI TOF-MS alone is not suitable for the analysis of complex mixtures.

When the peptide mixture was separated by CE (Figure 2A), 20 separate fractions were obtained, 11 of which were analyzed by MALDI TOF-MS. The representative spectra shown in Figure 2B–D demonstrate the excellent performance of the hybrid instrument for complex mixture analysis. As is evident from the data in Figure 2 and Table 1, excellent mass accuracy, resolution, and signal intensity were obtained. Although some CE fractions contained more than one component, MALDI analysis is much more amenable to mixtures containing 2–4 components than to those containing 20 or 30. If desired, these fractions could be further purified by a second separation method prior to mass analysis.

It is important to note that the separation shown in Figure 2A was carried out in a concentrated sodium phosphate buffer (50 mM), but there is little indication of the formation of sodium adducts in Figure 2B and C, and only minor peaks corresponding to sodium and potassium adducts in Figure 2D. In all spectra, the dominate peaks are the protonated species. These results were obtained by the addition of relatively high concentrations (6.4%) of formic acid to the matrix solution.

Table 1. Mass Data for Peptides from a Tryptic Digest of Bovine Cytochrome *c* Separated by CE and Analyzed by MALDI

	mass			
peptide sequence[a]	expected (*m/z*)[b]	measd (*m/z*)	accuracy (ppm)	resolutn
KTGQAPGFSYTDANK	1584.77	1584.6	107	380
TGPNLHGLFGR	1168.62	1168.6	17	283
IFVQKCAQCHTVEK	1633.82	1633.4	257	200

[a] Peptide sequences and expected masses obtained from the program MASS BIOSPEC 1.0 §2 (PE Sciex Instruments, Thornhill, ON, Canada). [b] Average masses, $(M + H)^+$ ion.

Synthetic protein mixtures prepared with basic proteins (horse skeletal myoglobin, ribonuclease A, horse heart or bovine cytochrome *c*, and hen egg lysozyme) were also separated by CE, collected, and subjected to MALDI analysis to demonstrate the versatility of the instrument. These proteins have a strong affinity for many surfaces and so are difficult to separate with good efficiency by CE. Furthermore, the high mass of these molecules increases the difficulty of detecting subpicomole quantities by MALDI TOF-MS. As such, they are an excellent test of instrument performance. To compare the behavior of the protein standards in MALDI MS independently of the CE, individual protein standards were suspended in high-purity water and mixed with α-cyano-4-hydroxycinnamic acid matrix; aliquots containing 1.0 pmol of protein were deposited directly on the sample probe. These standards varied slightly in their relative sensitivity in MALDI, but none were particularly difficult to detect under these

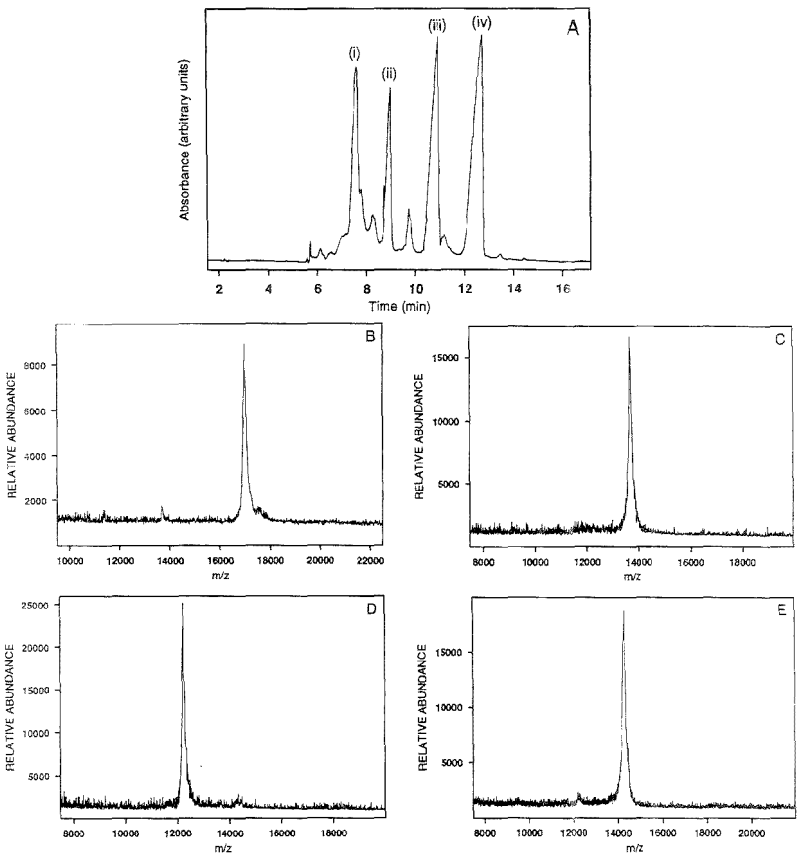

Figure 3. (A) Electropherogram of 2 pmol each of a synthetic protein mixture containing (i) horse skeletal myoglobin, (ii) bovine pancreas ribonuclease A, (iii) bovine cytochrome *c*, and (iv) hen egg lysozyme. Panels B–E are the MALDI TOF-MS spectra of the fractions isolated in the time interval (B) 6.28–6.74, (C) 7.07–7.51, (D) 8.69–9.19, and (E) 9.19–9.59 min.

conditions. When diluted to 50 nM with 30 mM buffers, the proteins did not respond as well to MALDI and the signal-to-noise ratio and/or mass spectral resolution were degraded. Matrix solutions were modified to compensate for the presence of the buffers. The MALDI behavior in the presence of various buffers and matrix modifications is summarized below.

Figure 3A is the electropherogram for a sample containing 2 pmol of each of the four protein analytes. The largest peaks are the four protein standards, while the smaller peaks are impurities in the proteins as delivered from the supplier. The CE capillary was treated with polyarginine and then filled with a 20 mM sodium acetate buffer solution. Fractions were collected using the coaxial flow interface. The peaks in the electropherogram are broad, indicating a significant loss of separation efficiency. Large quantities of analyte can alter the electric field in the capillary and increase zone broadening. The MALDI spectra (Figure 3B–E) of the four collected fractions illustrate that the separations are successful, with single peaks corresponding to $(M + H)^+$ ions. Mass accuracy and resolution data are summarized in Table 2. Initial attempts to analyze these fractions with matrix solutions containing 0.1% trifluoroacetic acid yielded spectra with substantially poorer signal-to-noise ratios and resolution than those shown in Figure 3. Increasing the formic acid in the matrix solution to 6.4% improved resolution and the signal-to-noise characteristics of the signal (see Figure 3).

Table 2. Mass Data from Synthetic Protein Mixture Separated by CE and Analyzed by MALDI[a]

	mass			
protein	expected[b] (*m/z*)	measd (*m/z*)	accuracy (ppm)	resolutn
myoglobin	16 951.7	16 950.36	79	120
ribonuclease A	13 683	13 684.2	90	285
cytochrome *c*	12 231.88	12 233.4	124	157
lysozyme	14 307	14 306.3	49	104

[a] Each analyte, 2 pmol. [b] Average masses, $(M+H)^+$ ion.

To facilitate the analysis of smaller analyte quantities by CE/MS, the MALDI sample probes were modified to deposit the CE fraction in a smaller area. The sample pins are 1.5 mm in

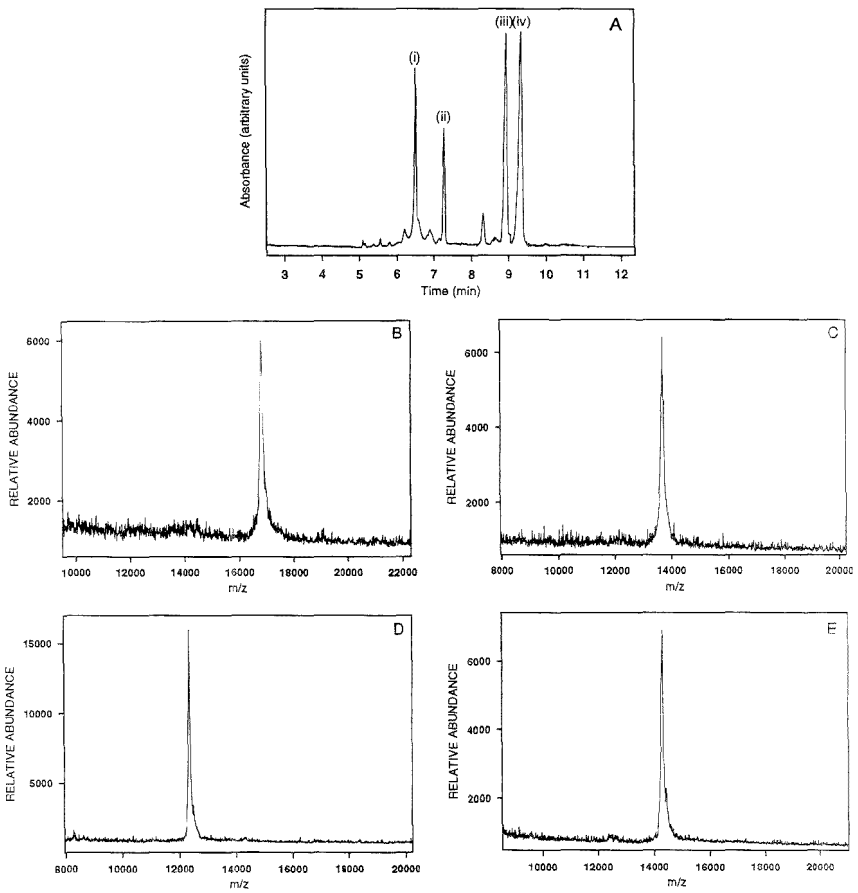

Figure 4. (A) Electropherogram of 150 fmol each of a synthetic protein mixture containing (i) horse skeletal myoglobin, (ii) bovine pancreas ribonuclease A, (iii) horse heart cytochrome *c*, and (iv) hen egg lysozyme. Panels B–E are the MALDI TOF-MS spectra of the fractions isolated in the time interval (B) 7.15–7.97, (C) 8.58 9.27, (D) 10.31–11.23, and (E) 12.01–13.03 min.

diameter, while the focused laser beam has a diameter of ~50 μm. Thus, for a sample distributed across the pin, only a small fraction of the sample is desorbed by a single laser shot and detection sensitivity suffers. The buffer flow from the coaxial capillary interface dilutes and distributes the sample over the surface of the pins and prevented routine detection of the signal from less than 500 fmol of protein.

When wells measuring 100 μm in diameter (total volume of ~100 nL) were drilled in the center of the MALDI sample probes, samples were confined to this reduced area and detection sensitivity was enhanced. In the experiments previously described, electrical contact was established with the capillary via the coaxial flow of buffer over the capillary outlet. When larger (500 fmol) analyte quantities are collected, the buffer volume from the coaxial flow (~1 μL) dilutes the sample, but a reasonable ion signal is still obtained. When less protein is collected, the coaxial buffer volume distributes the sample over a larger area and the ion signal is reduced. This problem was overcome by coating the last 1.5 cm of the electrophoresis capillary with a thin layer of a gold-doped epoxy. With this arrangement, electrical contact was maintained with the capillary without the addition of liquids, and nanoliter volumes of analyte could be deposited in very small spots on the probe surface.[7] To further assist with the transfer of liquid from the capillary to the probe surface, the outlet of the capillary was sharpened to a fine point to reduce the area of the capillary in contact with the sample liquid. Surface tension allowed volumes as small as several tens of nanoliters to be efficiently deposited on the surface of a stainless steel probe. Silver- and silver-doped epoxies were also tested with the conducting capillary interface, but the metal coating rapidly degraded under the separation conditions employed. Electroplating gold on top of these silver coatings improved the stability of the layers, but did not completely eliminate these problems.

Figure 4 presents the electropherogram and MALDI MS spectra produced when a sample containing 150 fmol of each of several proteins was analyzed. The separation conditions are the same as those used with the pmol analyte quantities; i.e., the separations were performed in polyarginine-treated capillaries with

Table 3. Mass Data from Synthetic Protein Mixture Separated by CE and Analyzed by MALDI[a]

protein	mass: expected[b] (m/z)	mass: measd (m/z)	mass: accuracy (ppm)	resolutn
myoglobin	16 951.7	16 949.7	118	142
ribonuclease A	13 683	13 683.5	37	131
cytochrome *c*	12 361.5	12 363.1	129	180
lysozyme	14 307	14 306.7	21	157

[a] Each analyte, 150 fmol. [b] Average masses, $(M + H)^+$ ion.

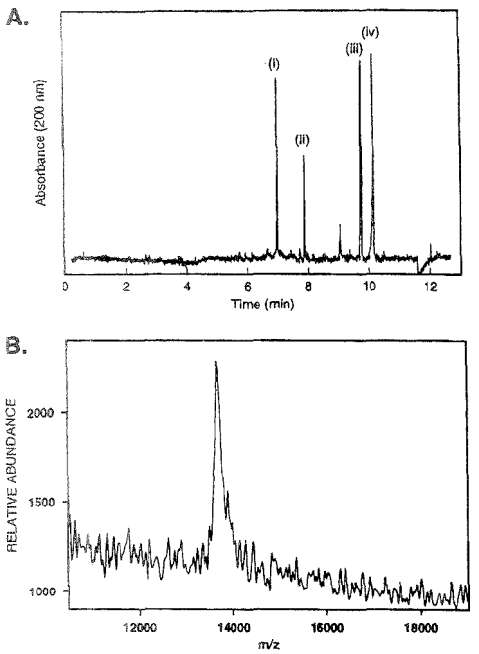

Figure 5. (A) Electropherogram of 25 fmol each of a synthetic protein mixture containing (i) horse skeletal myoglobin, (ii) bovine pancreas ribonuclease A, (iii) horse heart cytochrome *c*, and (iv) hen egg lysozyme. (B) MALDI TOF-MS spectrum of a 25 fmol ribonuclease fraction isolated by CE from a synthetic protein mixture containing horse skeletal myoglobin, ribonuclease A, horse heart cytochrome *c* and hen egg lysozyme.

20 mM pH 5.0 sodium acetate buffer. Separation efficiency was increased to 130 000 theoretical plates with the lower analyte concentration. The MALDI TOF-MS spectra still show very good signal-to-noise ratios with an average resolution of 150 and provided an accurate estimate of molecular mass (Table 3). Figure 5 shows the electropherogram and a mass spectrum obtained from a sample that contains 25 fmol of the four proteins also used in Figures 3 and 4. It is clear from the data in Figure 5A that the reduced quantity of sample allows higher separation efficiency to be achieved (593 000, 1 169 000, 463 000, and 829 000 theoretical plates, respectively). The ribonuclease fraction from this separation was collected, mixed with the high acid matrix, and mass analyzed. The resulting mass spectrum is shown in Figure 5B. These data suggest that the detection limit for the CE MALDI instrument is below 25 fmol with this instrumentation. Continued optimization of the fraction collection interface and improved methods for preparing the sample for mass spectrometry should further reduce these detection limits.

Matrix Deposition. If the electroosmotic flow in the capillary is high, or if electromigration of the matrix is away from the capillary inlet, it is possible to co-deposit the matrix with the analyte using the coaxial capillary sheath flow interface. If these conditions are not established, the matrix can migrate back into the separation capillary. The resulting change in analysis conditions and interference with detection would greatly complicate these analyses. Initial experiments closely mimicked the standard MALDI sample preparation procedure, with the matrix and analyte being mixed as they are deposited on the probe surface. Although high-quality spectra were obtained for these analyses, several problems were encountered. The analysis of large biopolymers often necessitates the use of capillary coatings that suppress the EOF (e.g., acrylamide, Ucon, etc.).[12] To prevent the interference of the matrix with the electrophoresis and detection, columns that generate strong EOF, or matrix molecules that would not electromigrate into the capillary, could be used.

α-Cyano-4-hydroxycinnamic acid and 2,5-dihydroxybenzoic acid were co-deposited with several proteins determine the relative performance of the matrices. The MALDI performance was found to be substantially better in the presence of the α-cyano-4-hydroxycinnamic acid matrix but no better than the results obtained when the matrix was added to the sample after deposition. Excellent results were obtained when the CE fractions were deposited directly on the stainless steel pins and allowed to dry, and the matrix solution was deposited directly on these spots. This method was routinely used through these investigations because it is compatible with all of the instrument configurations and consistently provided high-quality MALDI spectra. Conversely, when CE fractions were deposited on preformed matrix layers as described by Vorm et al.,[13] detection limits and resolution suffered.

MALDI Matrix Selection. Several common matrices were used with the CE protein standards in the presence of buffers. When the α-cyano-4-hydroxycinnamic acid matrix was used, the spectra showed the most abundant and best resolved ion signals. A mixture of 2,5-dihydroxybenzoic acid (DHB) with fucose was also investigated but did not provide sensitivity and resolution comparable to the α-cyano-4-hydroxycinnamic acid matrix.

Six buffers commonly used in CE were tested with the α-cyano-4-hydroxycinnamic acid matrix. For these tests, protein standards were diluted to 500 nM with the analysis buffer. In each case, an aliquot corresponding to 1.0 pmol of the analyte was deposited on the stainless steel sample probe and allowed to dry. Subsequently, 2.0 μL of α-cyano-4-hydroxycinnamic acid (the matrix mixture) was deposited on the dried CE fractions. The results of this investigation are summarized in Table 4. MALDI ion signals were evaluated on the basis of signal-to-noise ratio and resolution. Samples diluted with Tris–acetate were found to give the best response, sodium phosphate and sodium citrate buffers responded well, sodium borate and sodium acetate provided intermediate responses, and sodium carbonate performed poorly.

As previously discussed, the formation of adducts with buffer salts was suppressed by the addition of formic or trifluoroacetic

(12) Monnig, C. A.; Kennedy, R. T. *Anal. Chem.* **1994**, 66, 280R–314R.
(13) Vorm, O.; Roepstorff, P; Mann, M. *Anal. Chem.* **1994**, *66*, 3281–287.

Table 4. Relative Performance of Protein MALDI in the Presence of 30 mM Buffers for CE

buffer	pH	rel perform.
Tris–acetate	5.0	best
sodium phosphate	2.5	good
sodium citrate	4.0	good
sodium borate	9.0	fair
sodium acetate	5.0	fair
potassium carbonate	6.0	poor

acid to the matrix in concentrations above the standard 0.1%. The amount of acid required to give optimal results was dependent on the form of the buffer. Buffers that interfered most with MALDI generally required the use of higher quantities of acid. The relative MALDI MS signal response for proteins in the α-cyano-4-hydroxycinnamic acid matrix (0.1% TFA) are summarized. When the α-cyano-4-hydroxycinnamic acid matrix was diluted with a solution of 10% formic acid, MALDI ion signals were enhanced and the overall sensitivity improved in the presence of the interfering buffers. Solutions that contained 2.6% TFA worked well when the buffer was 30 mM Tris–acetate. However, when the buffer was sodium acetate, performance was most enhanced by matrix solutions containing 6.4% formic acid. Increasing the acid concentration above 6.4% suppressed the signal for some proteins. This matrix mixture was the most buffer tolerant so was subsequently used for all protein analyses.

Successful applications of the CE MALDI interface were realized with several separation conditions other than the polyarginine-coated capillary with sodium acetate buffers. Two-picomole quantities of the proteins were separated and analyzed in Ucon-coated capillaries with Tris–acetate and Tris-HCl buffers and an APTES-coated capillary with a sodium acetate buffer and co-deposition of matrix. The resulting electropherograms and MALDI MS spectra are similar to those shown in Figure 3.

Quantitation. Direct quantitation of analytes by MALDI is not routinely possible and tedious when attempted. Internal standards can be utilized to determine relative concentrations of analytes[14] but are sometimes problematic. Use of an internal standard for quantitation assumes that the relative signal response of each mixture component is equivalent from each crystal on the probe. Because use of an internal standard requires that a mixture be analyzed, the shot-to-shot signal response of the different mixture components is likely to vary, as analytes tend to concentrate themselves in specific crystals in varying amounts. This phenomenon gives rise to the "good spots" often described in the MALDI MS literature. However, when MALDI MS is used with CE, it is possible to determine absolute analyte quantities with the UV detector, assuming complete separations, as confirmed with the MALDI MS results. A calibration plot of analyte concentration versus absorbance can be generated with standards of known concentration. For any subsequent analysis, UV response can be compared to the calibration curve to estimate the quantity of analyte.

(14) Nelson, R. W.; McLean, M. A.; Hutchens, T. W. *Anal. Chem.* **1994**, *66*, 1408–1415.

CONCLUSIONS

An off-line interface has been successfully applied to couple CE and MALDI TOF-MS under a variety of separation conditions that are realistic for separations of biological macromolecules. Bonded (Ucon, APTES) and chemisorbed (polyarginine, Polybrene) capillary coatings were used with a variety of buffers, ranging from 30 mM Tris–acetate to 100 mM sodium phosphate, and separated fractions collected directly on the laser target pins with an automated interface. Decreasing the pH of the MALDI matrix solutions enhanced spectral resolution and the signal-to-noise ratio by preferential formation of protonated molecular ions in the presence of the buffer salts.

Sample quantities as large as a few picomoles can be separated and analyzed; however, the separation quality is not optimal under these conditions. Miniaturization of the interface and use of a capillary coated with a conducting polymer allows acquisition of high-quality MALDI spectra from sample quantities as small as 25 fmol. Under these conditions, the efficiency of capillary electrophoresis is optimal and the analysis of complex mixtures realistic.

ACKNOWLEDGMENT

The financial support of the Keck Foundation, the Arnold and Mabel Beckman Foundation (C.A.M.), and the National Science Foundation under Grant CHE-92-01277 (C.L.W.) are gratefully acknowledged.

Received for review March 8, 1995. Accepted September 1, 1995.[⊗]

AC9502357

[⊗] Abstract published in *Advance ACS Abstracts*, October 15, 1995.

Anal. Chem. **1995**, *67*, 4205–4209

End-Label, Free-Solution Capillary Electrophoresis of Highly Charged Oligosaccharides

Jan Sudor and Milos V. Novotny*

Department of Chemistry, Indiana University, Bloomington, Indiana 47405

The effect of fluorescent tags on the separation of negatively charged oligosaccharides, derived from a partially hydrolyzed κ-carrageenan, was studied. When the charge-to-friction ratio of oligosaccharides is increased by the end-label, the migration order is from smaller to larger oligomers, and the resolution of larger oligomers could be improved by using a sieving medium. The migration order can be entirely reversed when the charge-to-friction ratio of the solute is decreased by the end-label. The experimental electrophoretic mobilities obtained in this work are in excellent agreement with the recently reported theoretical model (Mayer, P.; Slater, G. W.; Drouin, G. *Anal. Chem.* 1994, *66*, 1777–1780). The maximum number of separated oligomers (M_{max}) as a function of applied voltage and injection time was also studied, but no strong dependencies were found. Resolution between small oligomers could be significantly improved by following this separation principle.

The electrophoretic mobility of any solute is proportional to its charge-to-friction ratio, and it is well known that this ratio is constant and independent of the solute size for uniformly charged polyelectrolytes[1] such as DNA. To separate such polyelectrolytes by means of electrophoresis, the common remedy has been to use a sieving medium (a permanent gel or a polymer solution): in high-performance capillary electrophoresis (HPCE), this strategy has worked well for the separation of polynucleotides,[2-4] amino acid homopolymers,[5,6] and negatively charged oligosaccharides.[7] Yet another strategy for separation may involve imparting additional charge or friction to the solute to alter its charge-to-friction ratio. In fact, Mayer et al.[8] recently proposed a physical model and derived theoretically a set of conditions for high-performance DNA sequencing in gel-free medium, in which uniformly charged biopolymers are end-labeled with a molecular moiety (e.g., a homogeneous protein). They have called this approach "end-labeled free-solution electrophoresis" (ELFSE).

The fundamental strategy for analyzing oligosaccharides and other glycoconjugates by HPCE (for a review, see refs 9 and 10) happens to involve end-labeling with a fluorescent moiety. For the sake of sensitive detection by laser-induced fluorescence (LIF), various oligosaccharides were labeled with CBQCA[7] or ANTS and other fluorescent labels.[11-13] Separation of their derivatives was accomplished electrophoretically in either concentrated gels[7] or free buffer media.[11-13] The end-labeled oligosaccharides with a uniform charge thus seemed appropriate for testing the model by Mayer et al.,[8] albeit in a very different molecular weight range than the proposed DNA sequence. Of the available oligosaccharides, we have chosen here the mixtures of partially hydrolyzed κ-carrageenan [a highly charged polyelectrolyte with a linear galactan backbone which is known to contain approximately one sulfate group per disaccharide unit[14] (Figure 1)]. Of the fluorescence tags, we have selected one which increases the charge-to-friction ratio of the solute (ANTS) and another which decreases this ratio (6-aminoquinoline). It should also be noted that the hydrodynamic and electrostatic interactions between the solute and reagents as well as conformational heterogeneity of the end-labels (which seems to be a problem when working with large end-labels, such as streptavidin, avidin, etc.) were neglected in this study.

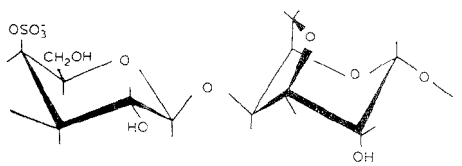

Figure 1. Structure of a κ-carrageenan disaccharide unit.

First, we investigated the effect of the fluorescent tag's nature on the electromigration behavior of carrageenan oligomers. By changing the charge and friction at the end-labeling site, we could reverse the electromigration order. The measured electrophoretic mobilities have been further correlated with the ELFSE theory,[8] and the effects of applied voltage and injection time were also studied.

(1) Hermans, J. J. *J. Polym. Sci.* **1955**, *18*, 529–534.
(2) Cohen, A. S.; Najarian, D. R.; Paulus, A.; Guttman, A.; Smith, J. A.; Karger, B. L. *Proc. Natl. Acad. Sci. U.S.A.* **1988**, *85*, 9660–9663.
(3) Swerdlow, H.; Wu, S.; Harke, H.; Dovichi, N. J. *J. Chromatogr.* **1990**, *516*, 61–67.
(4) Grossman, P. D.; Soane, D. S. *Biopolymers* **1991**, *31*, 1221–1228.
(5) Dolnik, V.; Novotny, M. V.; Chmelik, J. *Biopolymers* **1993**, *33*, 1299–1306.
(6) Dolnik, V.; Novotny, M. V. *Anal. Chem.* **1993**, *65*, 563–567.
(7) Liu, J.; Shirota, O.; Novotny, M. V. *Anal. Chem.* **1992**, *64*, 973–975.
(8) Mayer, P.; Slater, G. W.; Drouin, G. *Anal. Chem.* **1994**, *66*, 1777–1780.
(9) Novotny, M. V.; Sudor, J. *Electrophoresis* **1993**, *14*, 373–389.
(10) El Rassi, Z.; Nashabeh, W. High performance capillary electrophoresis of carbohydrates and glycoconjugates. In *Carbohydrate Analysis: High Performance Liquid Chromatography and Capillary Electrophoresis*; El Rassi, Z., Ed.; Elsevier Science: Amsterdam, 1994; pp 447–514.
(11) Chiesa, C.; Horvath, C. *J. Chromatogr.* **1993**, *645*, 337–352.
(12) Stefansson, M.; Novotny, M. V. *Anal. Chem.* **1994**, *66*, 1134–1140.
(13) Nashabeh, W.; El Rassi, Z. *J. Chromatogr.* **1992**, *600*, 279–287.
(14) Yalpani, M. *Polysaccharides: Synthesis, Modifications and Structure/Property Relations*; Elsevier: Amsterdam, 1988.

0003-2700/95/0367-4205$9.00/0

EXPERIMENTAL SECTION

Apparatus. A home-built capillary zone electrophoretic (CZE) system, described previously,[15] was used in all experiments. A high-voltage power supply (Spellman High Voltage Electronics, Plainview, NY) capable of delivering 0–40 kV was employed. The separation capillaries, 30–60-cm effective length (40–70-cm total length; 50-μm i.d.; 363-μm o.d.), were purchased from Polymicro Technologies (Phoenix, AZ). The inner surface of the separation capillary was modified by the attachment of a linear polyacrylamide.[16] The capillary was enclosed in a Plexiglas box with an interlock safety system. On-column fluorescence measurements were carried out with a helium–cadmium laser (Model 56X, Omnichrome, Chino, CA) used as a light source (5-mW output power at 325 nm). The incident laser beam was aligned to its optimum by adjusting the position of the collecting optics between the optical cell and the detector. Fluorescence emission (>495 nm) was collected through a 600-μm fiber optic placed at a right angle to the incident laser beam. Signals isolated by a long-pass, low-fluorescence filter with the cutoff wavelength at 495 nm (Oriel, Stradford, CT) were monitored with a R928 photomultiplier tube (Hamamatsu Photonics K.K., Toyooka Vill., Iwata-Gun, Shizuoka Prefecture, Japan) and amplified with a Model 128A lock-in amplifier (EG&G Princeton Applied Research, Princeton, NJ).

The electrophoretic mobilities were calculated from 3–5 replicate measurements. The relative standard deviation of all collected data was better than ±2%.

Chemicals. Citric acid was purchased from EM Science (Cherry Hill, NJ), sodium hydroxide and hydrochloric acid were from Fisher Scientific (Fair Lawn, NJ), and acetic acid (glacial) was from Mallinckrodt (Paris, KY). Acrylamide, ammonium persulfate, and Tris buffer [tris(hydroxymethyl)aminomethane] were received from Bio-Rad Laboratories (Hercules, CA). κ-Carrageenan and D-glucose-6-sulfate were received from Sigma (St. Louis, MO), and sodium cyanoborohydride was from Aldrich (Milwaukee, WI). 8-Aminonaphthalene-1,3,6-trisulfonic acid (ANTS) and 6-aminoquinoline were the products of Molecular Probes, Inc. (Eugene, OR). The linear polyacrylamide ($M_w \approx (5–6) \times 10^6$) was purchased from Polysciences, Inc. (Warington, PA).

Sample Preparation. Partially hydrolyzed κ-carrageenan and D-glucose-6-sulfate were derivatized through the Schiff base formation between the aromatic amine of a reagent and the aldehyde form of a sugar, followed by reduction of the Schiff base to a stable product. The concentrations of the reagents were 30–70 mM in 3% (w/w) acetic acid.[17] A 10-mg amount of the sugar was dissolved in 1 mL of 0.1 M HCl and mixed with 100 μL of reagent. The mixture was heated to 95 °C for 2 min before addition of 50 μL of 2 M sodium cyanoborohydride and then derivatized at 95 °C for 3 h. The samples were stable when stored at −20 °C before analysis. The hydrodynamic and electrokinetic techniques of sample introduction were employed.

RESULTS AND DISCUSSION

Figure 2 compares the separation of the oligomers, derivatized with ANTS, from the partially hydrolyzed κ-carrageenan in (A) a gel-free medium and (B) 1% linear polyacrylamide ($M_w \approx (5–6) \times 10^6$), both recorded at pH = 3. It is clear that the migration proceeds from smaller to larger oligomers and that the separation of larger oligosaccharides is improved in the polymer solution in comparison to the free-buffer condition. This is a well-known phenomenon, as the separation mechanisms in a polymer solution could be accounted for by the Ogston sieving model (for the large oligomers on which the label has little effect). In the case of oligosaccharides, the end-labeling happens to be a sensible remedy to detection problems.[9,10] In most cases, the fluorescence tag is likely to have a different charge-to-friction ratio than the monomeric unit in an oligosaccharide structure and can, therefore, change the electrophoretic mobility of small oligomers significantly. This is actually seen in Figure 3A, where the same mixture of sulfated oligosaccharides, now derivatized with a slightly positive (at pH = 3) reagent, 6-aminoquinoline,[13] is displayed (for better clarity of presentation, only a zoom of the entire run is shown in this figure). The migration order now starts with large oligomers (the unresolved "hump" at the beginning) and proceeds to smaller ones. This occurs because the reagent has decreased

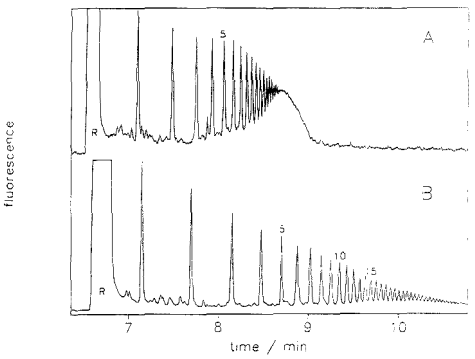

Figure 2. Separation of the ANTS-derivatized oligosaccharides derived from a partially hydrolyzed κ-carrageenan. Numbers 5 and 10 above the peaks correspond to deca- and eicosasaccharide, respectively. Capillary: 60-cm effective length (70-cm total); 50-μm i.d. (363-μm o.d.); coated with a linear polyacrylamide. Buffer: (A) 25 mM sodium citrate, pH = 3.0; hydrodynamic injection, Δh = 10 cm, injection time, 10 s. (B) 25 mM sodium citrate, pH = 3.0; 1% linear polyacrylamide ($M_w \approx (5–6) \times 10^6$); electrokinetic injection, 10 s at 100 V/cm. Applied voltage: 350 V/cm (24 kV).

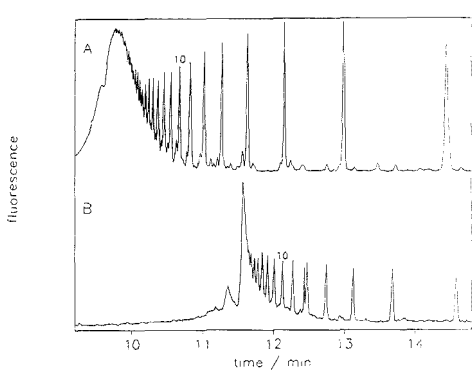

Figure 3. Separation of 6-aminoquinoline-derivatized oligosaccharides derived from a partially hydrolyzed κ-carrageenan. Conditions were the same as in Figure 2.

(15) Liu, J.; Hsieh, Y.-A.; Wiesler, D.; Novotny, M. V. *Anal. Chem.* **1991**, *63*, 408–412.
(16) Hjerten, S. *J. Chromatogr.* **1985**, *347*, 191–198.
(17) Jackson, P. *Biochem. J.* **1990**, *270*, 705–713.

the charge-to-friction ratio of the small oligomers significantly more than for the larger mixture components. We further demonstrate (Figure 3B) that the resolution of larger oligosaccharides deteriorates upon the presence of a sieving medium in the capillary. This is because the faster (larger) oligomers are now being retarded by the polyacrylamide medium more than the slower (smaller) oligomers.

Using the end-labeling strategy for a gel-free medium, the following equation becomes applicable:[8]

$$\mu_{(M)} \approx \varrho(M + \beta)/\xi(M + \alpha) = \mu_0(M + \beta)/(M - \alpha) \quad (1)$$

where ρ and ξ are the charge and friction of one monomer unit, and β and α are the charge and friction of the end-label (normalized to the charge and/or friction of the monomer), respectively. M is the number of monomers, and $\mu_0 = \rho/\xi$ is the electrophoretic mobility of the polyelectrolyte without an end-label.

The limiting cases of eq 1 can be expressed as follows:

$$\mu_{(M)} \approx \begin{cases} \mu_0(\beta/\alpha) = \beta_R/\alpha_R, & M = 0 \quad (2) \\ \mu_0, & M \gg \beta \text{ and } M \gg \alpha \quad (3) \end{cases}$$

where β_R and α_R are the charge and friction of the end-structure (not normalized to the charge and friction of the solute).

For the case of $M = 0$ (eq 2), one obtains an electrophoretic mobility of the end-label which is proportional to its charge-to-friction ratio. In the second case, when $M \gg \beta$ and $M \gg \alpha$ (eq 3) (the charge as well as the friction of an oligomer are much larger than that of the end-label), one obtains the electrophoretic mobility of a polyelectrolyte not influenced by the end-label (which is constant and size-independent).

We have further used the ELFSE model of Mayer et al.[8] to describe the above experiments. First, the migration times of oligosaccharides (derivatized with ANTS and/or 6-aminoquinoline) were measured and recalculated into the electrophoretic mobilities (in Figure 4, the electrophoretic mobilities are plotted as their absolute values). These experiments were done in 25 mM Tris–acetate buffer (pH = 8.1) to simplify the system. It is reasonable to assume that the reduced Schiff base is not protonated at such a high pH; therefore, the charges on the end-labels are given solely by their functional groups (i.e., −3 for ANTS and 0 for 6-aminoquinoline). To identify the separated peaks, the sample was spiked with D-glucose-6-sulfate. As seen in Figure 4, D-glucose-6-sulfate migrated before the first peak (for ANTS label) and between the first and the second peaks (for 6-aminoquinoline). This proves that the first peak of the sample has a smaller charge-to-friction ratio than the monosaccharide with one negative charge. Moreover, it is known from the literature[14] that the κ-carrageenan contains approximately one sulfate group per disaccharide unit (Figure 1), and the charge increases linearly with the number of disaccharide units. Consequently, it seems plausible that the first peak in the sample is a disaccharide, and that disaccharide (with one sulfate group) behaves as a monomeric unit. It is also important to mention that M_{max} for ANTS-derivatized oligosaccharides increased through elevated pH, and consequently, M_{max} for 6-aminoquinoline-derivatized oligosaccharides decreased. This seems to be a logical consequence of the charge-to-friction ratio changes of end-labels at increasing pH, while the charge-to-friction ratio of the solute remained constant (see also eqs 4 and 5 of ref 8).

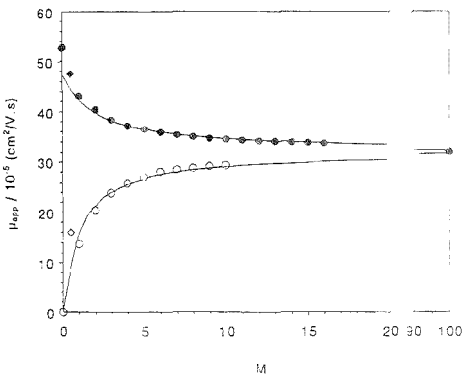

Figure 4. Dependence of the electrophoretic mobility on the monomeric number (M) of oligosaccharides derived from a partially hydrolyzed κ-carrageenan. Capillary: 30-cm effective length (40-cm total). Buffer: 25 mM Tris–acetate (pH = 8.1). Applied voltage: 400 V/cm (16 kV). ●, ANTS-derivatized oligosaccharides; ○, 6-aminoquinoline-derivatized oligosaccharides. The lines are the values calculated using eq 1: $\alpha = 2.02$, $\beta = 3$ (ANTS); $\alpha = 1.023$, $\beta = 0$ (6-aminoquinoline); and $\mu_0 = 31.93 \times 10^{-5}$ cm^2/V·s. ◆, D-Glucose-6-sulfate derivatized with ANTS; ◇, D-glucose-6-sulfate derivatized with 6-aminoquinoline.

Another important parameter that can be obtained experimentally is the μ_0-value. We have estimated μ_0 from the migration time of the unseparated hump (Figures 2A and 3A: $\mu_0 = 31.93 \times 10^{-5}$ cm^2/V·s ± 3.06%, which is the average value for both reagents). To calculate $\mu_{(M)}$, we must also know the β- and α-values. In the case of 6-aminoquinoline, $\beta = 0$ (pH = 8.1), and α can be easily obtained from a linear form of eq 1:

$$\mu_0/\mu_{(M)} = \alpha/M + 1 \quad (4)$$

From the dependence of $\mu_0/\mu_{(M)}$ on the reciprocal of M, we obtained the intercept, which was very close to unity (0.984), and the slope was 1.023 ($\alpha = 1.023$, $R^2 = 0.997$). In the case of ANTS-derivatized oligosaccharides, we rearranged eq 1 into the following form:

$$\beta(\mu_0/\mu_{(M)}) = M(1 - \mu_0/\mu_{(M)}) + \alpha \quad (5)$$

and from the intercept (extrapolating M to zero) of the dependence $\beta(\mu_0/\mu_{(M)})$ vs M, we further obtained α ($\alpha = 2.02$, knowing that $\beta = 3$).

By using the values for α, β, and μ_0, we calculated next the electrophoretic mobilities from eq 1 and compared them with our experimental data (Figure 4); the points are experimental data, and the lines are the corresponding calculated mobilities. The values of μ_0 are indicated for a large M (~100). We observe excellent agreement between the experimental data and the mobilities calculated from the ELFSE model (Figure 4).

Going back to Figures 1 and 2 (at pH = 3.0) and using the α-values obtained from eqs 4 and 5, the experimental electrophoretic mobilities were made to fit with the calculated values using once again eq 1. The values of β found for the best fit were

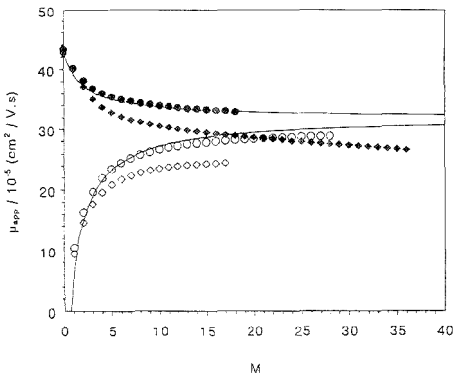

Figure 5. Dependence of the electrophoretic mobilities on the monomeric number (M) of the oligosaccharides derived from a partially hydrolyzed κ-carrageenan. ●, ANTS-derivatized oligosaccharides; ○, 6-aminoquinoline-derivatized oligosaccharides. Conditions were the same as in Figure 2A. Corresponding lines are the calculated values using eq 1: $\alpha = 2.02$, $\beta = 2.7$ (ANTS); $\alpha = 1.023$, $\beta = -0.6$ (6-aminoquinoline); $\mu_o = 31.93 \times 10^{-5}$ cm^2/V·s. ◆, ANTS-derivatized oligosaccharides; ◇, 6-aminoquinoline-derivatized oligosaccharides. Conditions were the same as in Figure 2B.

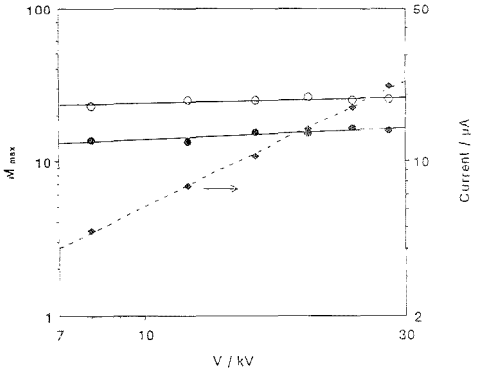

Figure 6. Dependence of M_{max} on the applied voltage (kV). ●, ANTS-derivatized oligosaccharides; ○, 6-aminoquinoline-derivatized oligosaccharides. Capillary: 30-cm effective length (40-cm total). The slopes are 0.15 (ANTS) and 0.07 (6-aminoquinoline). ◆, Measured current (μA) (slope = 1.2). Other conditions were the same as in Figure 2A.

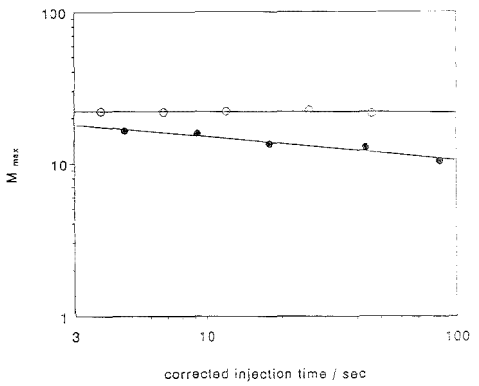

Figure 7. Dependence of M_{max} on injection time. Applied voltage: 400 V/cm (16 kV). The slopes are −0.15 (ANTS) and −0.005 (6-aminoquinoline). $\Delta h = 10$ cm. Other conditions were the same as in Figure 6.

2.7 for ANTS and −0.6 for 6-aminoquinoline (Figure 5), indicating the charge of ANTS to be approximately −2.7, and that for 6-aminoquinoline, +0.6 (at pH = 3.0). The electrophoretic mobilities of oligosaccharides obtained in 1% linear polyacrylamide did not agree with the calculated values because, besides the ELFSE principle, the Ogston sieving model is also involved in the separation mechanism (Figure 5).

Next, we tested the limiting behavior of the ELFSE model as described by Mayer et al.[8] This model predicts for $M \gg \alpha$ and a small initial width of the bands, w_0, that $M_{max} \approx V^{1/3}$ ($V = EL$, where E is the applied electric field strength and L is the effective length of the separation capillary [see eq 4, ref 8]). M_{max} was measured as a function of applied voltage (in kV) (Figure 6), and the exponents were obtained from a log−log plot (the slope is 0.15 for ANTS-derivatized and 0.07 for 6-aminoquinoline-derivatized oligosaccharides, while the theoretical value is $^1/_3$). We assume that there is only a slight dependence of M_{max} on the applied voltage in this case, concluding that M is not much larger than α. This dependence should be more important when larger end-labels are used, but this does not seem to be particularly pertinent to a typical oligosaccharide analysis.

In the second limiting case (for small molecules and large w_0), $M_{max} \approx w_0^{1/2}$ (see eq 5 of ref 8), we measured M_{max} as a function of injection time (in s). Because the amount of injected sample was not a linear function of injection time, we measured the area of a selected peak (the second peak in the sample, corresponding to tetrasaccharide) and plotted it logarithmically as a function of injection time [the slope was 0.96 ($R^2 = 0.998$) for ANTS and 0.84 ($R^2 = 0.996$) for 6-aminoquinoline]. Consequently, the injection times were recalculated according to the slopes (corrected injection time = injection time^{slope}). Interestingly, the slope for 6-aminoquinoline-derivatized oligosaccharides was smaller than that for ANTS-derivatized oligosaccharides. This is most probably due to the different viscosities of these two samples. The molar concentration of 6-aminoquinoline in the sample during derivatization was approximately twice that of ANTS. Because both reagents are weak bases, the hydrogen ions were more easily neutralized by 6-aminoquinoline, and the corresponding carrageenan sample was less hydrolyzed than the sample using ANTS. Once again, we obtained the slopes from the log−log plot of M_{max} vs corrected injection time (Figure 7). No strong dependence was visible [slope was −0.15 (for ANTS, the less viscous solution) and −0.005 (for 6-aminoquinoline)]. The measurements were done on the capillary with a total length of 40 cm. We noticed that M_{max} was more dependent on injection time in shorter capillaries (e.g., 20-cm total length), but the absolute values of exponent were still much smaller than $^1/_2$ (results not shown). It should be noted that, due to the high sensitivity of the LIF technique and a higher viscosity of sample compared to the buffer used, the injection time should not significantly influence M_{max}.

We experienced a strong dependence of M_{max} on the migration distance (the effective length of a separation capillary, L). Nevertheless, as the experimental results obtained here were slightly influenced by different values of w_0 for varying capillary

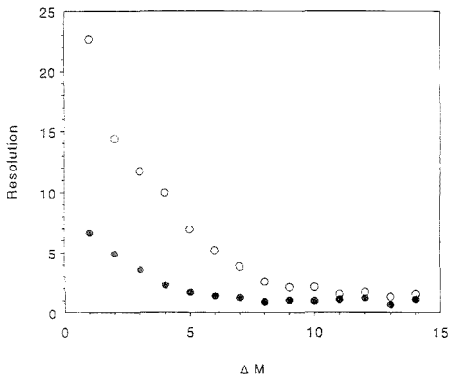

Figure 8. Resolution between the neighboring oligosaccharides. (Resolution is defined as $R_{i,j} = 2(t_{m,j} - t_{m,i})/(Y_j + Y_i)$, where t_m is the migration time and Y is the peak width at the baseline). Note that resolution between the first and second peaks is shown at $\Delta M = 1$, between the second and the third peaks at $\Delta M = 2$, etc. ●, ANTS-derivatized oligosaccharides; ○, 6-aminoquinoline derivatized oligosaccharides. Other conditions were the same as in Figure 2A.

lengths, we find that the values of M_{max} are typically proportional to $L^{1/3}$–$L^{1/2}$.

Finally, we were interested in the effect of reagents on resolution between neighboring oligosaccharide molecules. This dependence is shown in Figure 8. Note that resolution between the first and the second peaks is shown at position one (on the x-axis), resolution between the second and third peaks at position 2, etc. As seen in Figure 8, resolution between small oligosaccharides derivatized with 6-aminoquinoline is significantly better than that for the oligosaccharides labeled by ANTS. This could be explained by a greater difference in the charge-to-friction ratio between 6-aminoquinoline and a disaccharide unit than the corresponding relation for ANTS and a disaccharide unit. However, resolution between the adjacent oligosaccharides decreases relatively fast in both cases and vanishes for larger oligomers.

CONCLUSIONS

We have shown that the charge-to-friction ratio due to an end-label has a significant effect on the electrophoretic mobility of fluorescently labeled, charged oligosaccharides. By changing a charge and/or friction of the end-label, the migration order can be reversed. This principle was hypothetically described elsewhere,[8] and a theoretical model was derived for the sake of improved DNA sequencing in gel-free media. We have shown here experimentally that the same model is applicable to additional cases of the oligomers with a constant charge-to-friction ratio (independent of their size) which are labeled with an end-label whose charge-to-friction ratio is different from that of the oligomers. In all likelihood, the range of resolved components and their resolution can be adjusted by molecular design of appropriate end-labels.

Since the fluorescence tags in oligosaccharide analysis are rather small, M_{max} does not depend on the applied voltage. In addition, we have not experienced a strong dependence of M_{max} on injection time, which supports the idea that, through using LIF detection and a higher sample viscosity, the values of w_0 are small, and M_{max} is not limited by injection time. However, we experienced some dependence of M_{max} on the effective length of a separation capillary.

ACKNOWLEDGMENT

This research was supported by Grant No. CHE-9321431 from the National Science Foundation and a grant-in-aid from Astra/Hässle, Mölndal, Sweden. The authors thank Anastasia Crowell for her information on derivatization of κ-carrageenan, which proved very useful in this work.

Received for review July 14, 1995. Accepted September 8, 1995.[⊗]

AC950701S

[⊗] Abstract published in *Advance ACS Abstracts*, October 15, 1995.

Anal. Chem. **1995**, *67*, 4210–4216

Individual and Simultaneous Class Separations of Cationic and Anionic Surfactants Using Capillary Electrophoresis with Indirect Photometric Detection

Shahab A. Shamsi and Neil D. Danielson*

Department of Chemistry, Miami University, Oxford, Ohio 45056

Various chromophoric cationic and anionic reagents and combinations thereof are evaluated for individual and simultaneous class separations of nonchromophoric cationic and anionic surfactants using capillary electrophoresis (CE) with indirect photometric detection (IPD). Optimization results indicated a pH of 6–7 with at least 50% methanol is necessary for separations of long-chain cationic (tetrahexylammonium, didodecyl dimethylammonium) or anionic (C_{14}–$C_{18}SO_3^-$ or C_{14}–$C_{18}SO_4^-$) compounds along with medium- to short-chain ionic surfactants of each class. For individual class separations, benzylamine (BA) or l-ephedrine (EP) are recommended electrolytes for cationic surfactants, and naphthalenemonosulfonate (NMS) provided better detectability than *p*-toluenesulfonate (PTS) for anionic surfactants. Using an electroosmotic flow driven approach, a combined separation of a five-component tetraalkylammonium cationic and 10-component anionic (C_4–$C_{18}SO_3^-$) surfactant mixture is possible in about 45 min using either BA-NMS or BA-PTS electrolytes. The BA-NMS mixture will provide better detectability of anionic surfactants with some loss of sensitivity for cationic surfactants, whereas the reverse is true with the BA-PTS combination. The commercially available pyridinium (PY)-PTS reagent in the absence of methanol could separate a three-component tetralkylammonium cationic and a 10-component anionic (C_1–C_{14}-SO_3^-) surfactant mixture in less than 7 min.

Surfactants or surface-active substances are important additives in a variety of chemical processes and have found widespread application as cleaning agents, emulsifiers, solubilizers, and stabilizers. Anionic alkyl sulfates and alkanesulfonates as well as cationic quaternary ammonium surfactants exist in many commercial formulations as homologues and isomers. Structurally, these compounds consist of an aliphatic hydrocarbon tail with a polar head group and nonchromophoric substituent. Mixed-mode reversed-phase ion chromatography (RP/IC) with indirect photometric, fluorometric, nonsuppressed, or suppressed conductivity detection has been successfully used for the separation and detection of anionic surfactants.[1–5] Less work using RP/IC with indirect detection has been directed toward cationic surfactants.[6] The reports on the development of capillary electrophoresis (CE) for the separate determination of nonchromophoric anionic surfactants[7–10] show that CE is a complementary technique to RP/IC with respect to retention order. Minimal organic solvent consumption and inexpensive column replacement are practical benefits of CE beside its inherent good peak capacity. A literature survey revealed that the separation of non-UV active cationic surfactants by CE is rare. There is one report of the separation of C_{12}–C_{16} trimethylammonium compounds by CE using benzyldimethyldodecylammonium as the indirect photometric detection (IPD) electrolyte in a phosphate running buffer with a tetrahydrofuran (THF) organic modifier.[11]

One area of CE with indirect detection that holds particular promise for ion analysis is the advent of combined anion and cation determinations in a single run. Two different approaches can be considered to produce this analytical method. One of these procedures utilizes Ce^{3+} and *p*-hydroxybenzoate counterions for indirect fluorescence of some cations and anions, respectively.[12] However, dual detectors, one at each end of the capillary, are required since the anions and cations migrate in opposite directions. A second approach not reported in the literature to the best of our knowledge is envisoned as follows. If the velocity of the electroosmotic flow (EOF) is high enough, then both nonchromophoric cations and anions can be determined in one run provided that they have a suitable mobility match with their respective indirect photometric counterions.

In this paper, we concentrated on the comparison of five one-component and three two-component detection counterions for the respective individual and combined class separation of cationic and anionic surfactants with IPD. Separation and detection factors such as the electrolyte/analyte mobility match, pH, and the use of organic solvents are first optimized for the individual electrolytes. Simultaneous separations of cationic and anionic surfactants using a pair of selected electrolytes having a good absorbance match are demonstrated.

(1) Shamsi, S. A.; Danielson, N. D. *Chromatographia* **1995**, *40*, 237–246.
(2) Shamsi, S. A.; Danielson, N. D. *J. Chromatogr. Sci.* **1995**, *33*, 505–513.
(3) Hoeft, C. E.; Zollars, R. L. *J. Liq. Chromatogr.* **1994**, *17*, 619–641.
(4) Zhou, D.; Pietrzyk, D. J. *Anal. Chem.* **1992**, *64*, 1003–1008.
(5) Maki, S. A.; Wangsa, J.; Danielson, N. D. *Anal. Chem.* **1991**, *63*, 699–703.
(6) Walker, T. A.; Akbari, N.; Ho, T. *J. Liq. Chromatogr.* **1991**, *14*, 619–641.
(7) Nielen, W. F. *J. Chromatogr.* **1991**, *588*, 321–326.
(8) Goebel, L. K.; McNair, H. M.; Rasmussen, H. T.; McPherson, B. P. *J. Microcolumn Sep.* **1993**, *5*, 47–50.
(9) Chen, S.; Pietrzyk, D. J. *Anal. Chem.* **1993**, *65*, 2770–2775.
(10) Shamsi, S. A.; Danielson, N. D. *Anal. Chem.* **1994**, *66*, 3757–3764.
(11) Weiss, C. A.; Hazlett, J. S.; Datta, M. H. *J. Chromatogr.* **1992**, *608*, 325–334.
(12) Backmann, K.; Haumann, I.; Groch, T. *Fresenius J. Anal. Chem.* **1992**, *343*, 901–2.

0003-2700/95/0367-4210$9.00/0

EXPERIMENTAL SECTION

CE Instrumentation and Data Collection. The CE instrument employed was an Applied Biosystems (Foster City, CA) Model 270 A. Data acquisition was carried out with MacIntegrator I software with a Rainin Instruments (Woburn, MA) interface connecting the CE system to the software. The leads of the signal cable connecting the interface and the CE instrument were reversed to obtain positive peaks for IPD. The CE detector time constant was set at 0.5 s, and the data acquisition rate was 20 points s^{-1}. All data were collected and stored on a MacIntosh SE computer. The fused-silica capillary (Applied Biosystems) dimensions were 75 cm × 50 μm i.d. with a 50-cm effective distance from the point of injection to the center of the detector cell. Because organic solvents were used in the running buffer, the acrylic cathode reservoir was replaced with a glass one and the acrylic manifold was covered with Teflon tape. Both ends of the capillary were burned to remove the polyimide coating, which can swell in the presence of organic solvents and effect injection reproducibility.

Reagents. Benzylamine (BA), naphthalenemonosulfonic acid (NMS), and pyridinium-*p*-toluenesulfonate (PY-PTS) with a purity range of 99–99.5% were purchased from Eastman Kodak (Rochester, NY). *p*-Toluenesulfonate (PTS) in the acid form and l-ephedrine (EP), also known as α-(1-methylaminoethyl)benzyl alcohol, were bought from the Aldrich Chemical Co. (Milwaukee, WI). Boric acid (99.5%) and pyridine were purchased from the Fisher Scientific Co. (Fair Lawn, NJ). The sodium salts of alkyl sulfates and alkanesulfonates of various carbon chain length were obtained from Lancaster Synthesis (Windham, NH). The chloride salts having tetramethylammonium (TMA^+), chloroethyltrimethylammonium ($ClETMA^+$), and tetrabutylammonium (TBA^+) cations as well as the perchlorate salts having tetraethylammonium (TEA^+) or tetrahexylammonium (THA^+) cations were delivered from Aldrich. The didodecyldimethylammonium ($DDMA^+$) bromide salt was purchased from Eastman Kodak.

Preparation of Electrolyte and Analyte Solutions. A 50 mM stock solution of each basic (BA, EP) and acidic (NMS, PTS) electrolyte was prepared in triply distilled water; however, in some cases a few milliliters of methanol was added to promote complete dissolution. One-component electrolytes were used after subsequent dilution. Two-component electrolytes such as BA-NMS and BA-PTS were prepared by mixing an equimolar concentration of BA with NMS or PTS whereas PY-PTS was used as received. All one- and two-component electrolytes were dissolved in 100 mM boric acid and adjusted to the desired pH using either 1 mM NaOH or H_2SO_4, and then the appropriate volume of methanol was added. All the final operating electrolytes were filtered using 0.2-μm syringe filters from Gelman Science (Ann Arbor, MI) by creating a vacuum inside the syringe. Stock solutions of anionic analytes up to C_{12} in chain length were prepared in water, but the longer chain compounds were dissolved in acetonitrile. The cationic surfactant stock solutions were prepared in methanol. Aliquots of the 1000 mg/L stock solutions were diluted to the appropriate volume in water, and these working solutions were filtered before use.

CE Procedures. Prior to first use, a new capillary was subjected to a standard wash cycle for 6 h using 1 M NaOH at 60 °C. As a daily routine procedure, the capillary was flushed with 1 M H_3PO_4 and NaOH for 10 min each and then with triply deionized water (2 min), and finally it was equilibrated with the operating buffer for 10 min before any sample injections. The separation was initiated by applying a voltage (+30 kV) between the two capillary ends, which were immersed in reservoirs containing the operating buffer. Replenishment of the inlet buffer solution was made after every run. Between injections, the capillary was flushed for 2 min with each of the following solutions: 1 M NaOH, water, 1.0 M H_3PO_4, water again, and then the operating buffer. This procedure resulted in improved peak shapes, and the migration time reproducibility was ≤2.0% relative standard deviation (RSD) for the cationic and anionic surfactants.

Electrophoretic Mobility Determination. Salicylanilide added to the standard mixture of cationic and anionic carrier electrolytes acted as the neutral marker for the electroosmotic flow (EOF) determination. The observed mobility (μ_{obs}) for each of the various cationic and anionic IPD reagents was determined in 100 mM H_3BO_3, pH 6.0, and 50% methanol buffer. The parameters EOF or μ_{obs} were calculated by the following equation: EOF or $\mu_{obs} = L_d L_t/(t_m V)$ ($cm^2\ V^{-1}\ s^{-1}$), where L_d and L_t are the length of the capillary to the detector and the total length of the capillary, respectively; V is the separation voltage; and t_m is the migration time of the salicylanilide or IPD compound. The reproducibility of migration time for three replicate injections of IPD reagent ranged from 0.9 to 1.5% RSD. The electrophoretic mobility (μ_{ep}) for each IPD compound was obtained by subtracting EOF from the μ_{obs}.

RESULTS AND DISCUSSION

Selection of Suitable Anionic and Cationic Electrolytes. Because aliphatic surfactants such as anionic alkyl sulfates, alkanesulfonates, and tetraalkylammonium cations do not show any appreciable UV absorbance even at 200 nm, IPD represents an excellent detection strategy for such analytes. When selecting electrolytes for the CE separation of ionic compounds with IPD, reagents prepared at a low concentration with high molar absorptivity (ε) and dynamic reserve (DR) are preferred.[13] In addition, highest sensitivity can be achieved for those analytes having an effective mobility close to the IPD compound;[14] those of low electrophoretic mobility (μ_{ep}) are best for the detection of surfactants.[10] The μ_{ep}, ε, and DR values measured experimentally inside the capillary for some anionic and cationic chromophoric reagents are summarized in Table 1. Mobilities of the cationic and anionic electrolytes are in the range of +2.71 to -1.89×10^{-4} $cm^2\ V^{-1}\ s^{-1}$ and follow the expected order of migration, which is dependent on the charge to mass ratio, pH, and the degree of ionization. For instance PY ($pK_a = 5.23$) at pH 4.0 under aqueous conditions is reported to have a higher mobility than EP or BA (pK_a values of 9.33 and 10.14).[15] However, in a pH 6.0, borate buffer with 50% methanol (conditions found appropriate for our study), PY is the least mobile among the cationic electrolytes. The PY reagent should provide a better mobility match to analytes retained in the 4-min range. For both BA and EP, quite short analyte retention in the 2–3-min range would be the best mobility match. Although BA and EP have respectable ε and DR values, the lower ε and DR values for PY may pose a detectability problem. For the anionic electrolytes tested, the DR and ε of NMS are greater than those for PTS. PTS and NMS have similar μ_{ep} values with the best mobility match to analytes retained in the

(13) Wang, T.; Hartwick, R. A. *J. Chromatogr.* **1992**, *607*, 116–125.
(14) Foret, F.; Fanali, S.; Ossicini, L.; Bocek, P. *J. Chromatogr.* **1989**, *470*, 299–308.
(15) Lee, Y. H.; Lin, T. I. *J. Chromatogr.* **1994**, *675*, 227–36.

Table 1. Characteristics of Cationic and Anionic Detection Reagents for CE/IPD

electrolyte	electrophoretic mobility (μ_{ep})[a] ($cm^2 V^{-1} s^{-1}$) × 10^5	molar absorptivity[b] (λ_{max})	dynamic reserve[c]
	Cationic		
benzylamine (BA)	+2.71	5 440 (204)	618
ephedrine (EP)	+2.19	5 560 (204)	626
pyridine (PY)	+0.19	2 000 (254)	390
	Anionic		
naphthalenemonosulfonate (NMS)	−1.74	11 520 (206)	596
p-toluenesulfonate (PTS)	−1.89	7 520 (221)	554

[a] $\mu_{ep} = \mu_{obs}$ − EOF where EOF = 3.45 × 10^{-4} $cm^2 V^{-1} s^{-1}$, (average RSD for μ_{ep} = 1.2%, n = 3). [b] Obtained from the slope of the calibration curve/5.0 × 10^{-3} cm. [c] Calculated as ratio of background absorbance/background noise.

8–9-min range. At this point, it is still difficult to decide which cationic and anionic reagents would be the best for the cationic and anionic surfactant separations without analyte mobility data. The concentration and type of organic modifiers as well as pH, which all influence both analyte migration time and detection, need to be determined.

It should be emphasized that the use of organic modifiers is essential for both solubility and to obtain selectivity between the homologues of long-chain ionic surfactants. Selection of methanol over acetonitrile is preferred because the EOF can be reduced by a factor of 2 by increasing the percent of methanol from 0 to 40%; acetonitrile showed very little change in EOF with percent composition.[16] Our experience with THF was also not very encouraging as reported before.[17,18] Even though the THF-containing buffers were thoroughly degassed, bubble formation during the CE run (generated as spikes) was a problem. More extensive mixing of the THF–buffer solutions may be important; one of the reviewers of this paper indicated that 60% THF could be used. However, we found a 50% methanol composition in the run buffer to be a reasonable compromise between analysis time and resolution of the cationic and anionic homologues (optimization data not shown).

Both separation and detection can be optimized by a judicious selection of electrolyte pH. Each of the aromatic bases and acids listed in Table 1 is studied over a pH range of 4.0–8.0 at a fixed IPD reagent concentration of 5 mM in 100 mM H_3BO_3/50% methanol. Since both cationic (tetraalkylammonium) and anionic (alkanesulfonate) analytes are strong enough bases and acids to be fully ionized over a wide pH range, an increase in pH decreases the migration time solely because of the increase in EOF (Figure 1). The migration time for PY decreased by about a factor of 2 as the pH increased from 4 to 6.5. A retention time reversal is noted for THA^+ and $DDMA^+$ from pH 4 to pH 6. From pH 6.5 to pH 8, the change in migration time is more gradual. Although the pK_a value for PY is 5.3, it remained an effective counterion for the detection of cationic surfactants throughout a wide pH range. At pH 8, the PY concentration is about 1 × 10^{-5} M. Mobilities, μ_{ep}, calculated at pH 6 to be about 2 × 10^{-4} for

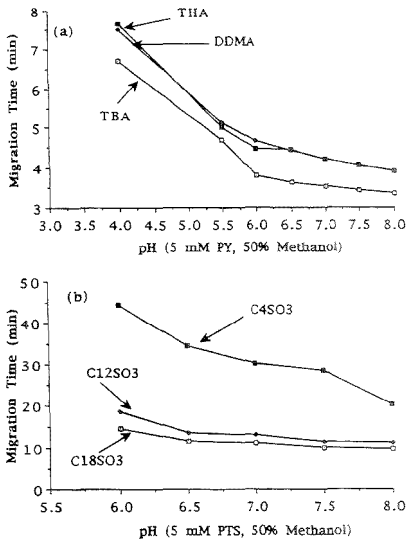

Figure 1. Migration times of cationic (a) and anionic (b) surfactants as a function of electrolyte pH. Electrolyte composed of 5 mM PY-PTS, 100 mM H_3BO_3, and 50% methanol. Vacuum injection for 1.0 and 3.0 s for 50–100 mg/L cationic and anionic surfactants. Separation voltage was +30 kV, and current was 3–7 μA. IPD at 220 nm.

TBA^+ and −4 × 10^{-5} for THA^+ and $DDMA^+$ match μ_{ep} for PY quite well. Electrolytes BA and EP show similar migration behavior with pH except that the THA^+/$DDMA^+$ peak pair was baseline resolved at all pH values. Using PTS, the migration time change with pH was particularly pronounced for short-chain anionic surfactants. Similar migration time profiles were seen for NMS. Mobilities, μ_{ep}, calculated to be −3.1 × 10^{-4} for $C_4SO_3^-$ and −2.5 × 10^{-4} for C_{12} or $C_{18}SO_3^-$ closely match the μ_{ep} values for PTS or NMS.

The peak area response of the same surfactants with the same IPD reagents as in Figure 1 is plotted as a function of pH in Figure 2. Similar peak height versus pH profiles were also seen. For cationic surfactants, response first improves with the increase in pH from 4.0 to 7.5 mainly due to a decreasing contribution of H^+ ions and reduced background. However, at a pH >7.5, a drop in peak area for the cationic surfactants can be explained by the increased fraction of the neutral form of PY. Checking pH 6 and pH 8, a similar drop in peak areas of cationic surfactants for BA and EP is not observed due to their higher pK_a values (9.3 and 10.0, respectively). For anionic surfactants using PTS (a fully ionized anionic eluent), there is an increase in peak area for all anionic surfactants (C_4–$C_{18}SO_3^-$) when the pH of the PTS electrolyte is raised from 6.0 to 6.5. This enhancement in detection continues for slowly migrating ions such as $C_1SO_3^-$ as the pH increases to 7.0. These observations confirm that the sensitivity of IPD can also be influenced to some extent by the ion migration time.[19] A further increase in pH from 7.0 to 8.0 decreases the IPD response for all anionic surfactants due to the competition of borate and hydroxide with the PTS ion. The system peak also increases in the pH 7–8 range, which can cause

(16) Janini, G. M.; Chan, K. C.; Barnes, J. A.; Muschik, G. M.; Issaq, H. J. *Chromatographia* **1993**, *35*, 497–502.
(17) Liu, Y.; Chan, K. F. *Electrophoresis* **1991**, *12*, 402–8.
(18) Landers, J. P., Ed. *Handbook of Capillary Electrophoresis*; CRC Press, Inc: Boca Raton, FL, 1993; p 276.
(19) Damm, J. B. L.; Overklift, G. T. *J. Chromatogr.* **1994**, *678*, 151–165.

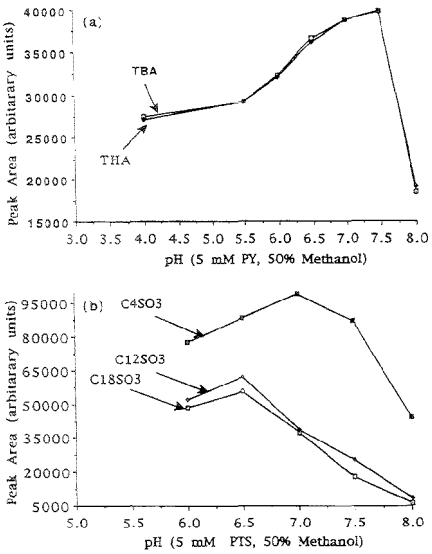

Figure 2. Peak areas of cationic (a) and anionic (b) surfactants as a function of electrolyte pH. Conditions are the same as in Figure 1.

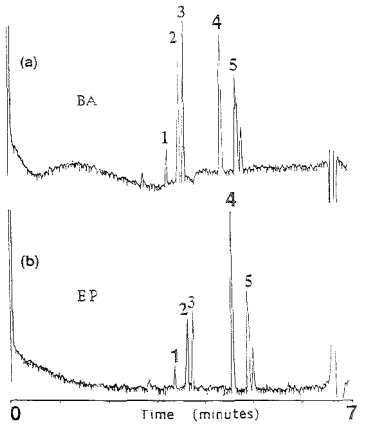

Figure 3. Comparison of BA (a) and EP (b) for the separation of a standard mixture of cationic surfactants. Electrolyte composed of 5 mM BA or EP with 100 mM H_3BO_3, pH 6.0, and 50% methanol. Peak identification: 35 mg/L each of 1, TEA^+; 2, $ClETMA^+$; 3, TBA^+; 4, THA^+; 5, $DDMA^+$. Vacuum injection for 1 s, +30 kV, 2 μA. IPD at 204 nm.

the complete loss of certain peaks. The appearance of system peaks in CE caused by a pH mismatch of sample and electrolyte has been reported previously.[20] Similar migration and sensitivity trends were also observed with the NMS electrolyte (data not shown). The pH optimization study clearly indicates that a trade-off exists between analysis time and response; this can be achieved by using electrolytes of pH around 6–7.

Separation of Nonchromophoric Cationic Surfactants. For some reason, PY alone without PTS using the same borate buffer/50% methanol solution was an ineffective IPD reagent for cations; no peaks were seen regardless of the chosen pH. Using a 95% methanol/5% pH 6.9 borate buffer with PY-PTS, negative TEA^+ and $ClETEA^-$ peaks but positive $TBA^+$and THA^+ peaks were observed. A similar phenomenon for short chain cationic surfactants has been reported previously.[21] Figure 3 shows 7-min electropherograms for a five-component cationic surfactant mixture using the two best cationic (BA and EP) electrolytes. As expected, the cationic surfactants are detected in order of increasing number of carbon atoms and hydrophobicity. Even though BA and EP have similar values of ϵ and DR (Table 1), the electropherograms clearly show that the sensitivity depended on the mobility match of the analyte with the IPD reagent. When the mobilities of the IPD compound and analyte are equal, a one-to-one displacement can occur enhancing sensitivity.[22] For BA, the peak heights for the first three peaks ($ClETMA^+$, TEA^+, and TBA^+) are better due to a close mobility match. Literature detection limit data for cationic surfactants by CE-IPD is lacking in specifics. The limit of detections (LOD) for $ClETMA^+$, TEA^+, and TBA^+ are found to be 1.0, 0.5, and 0.25 mg/L, respectively, with BA, based on an injection volume of 24 nL (8-s vacuum). The IPD reagent EP, which has a lower mobility than BA provided a sharp and symmetrical peak for THA^+. Therefore, the LOD is lowest for THA^+(0.25 mg/L, 8-s vacuum injection) with the EP electrolyte. On the other hand, the peak shape for $DDMA^+$ is similar using either BA and EP, as neither reagent has a very close mobility value to this analyte.

Separation of Nonchromophoric Anionic Surfactants. Figure 4, panels a and b, compares electropherograms of a standard mixture of C_4–$C_{18}SO_3^-$ with PTS and NMS electrolytes. Similar retention patterns can be seen with both anionic electrolytes in which the migration time is inversely related to the number of methylene groups (the least mobile $C_{18}SO_3^-$ being detected first and the mobile $C_1SO_3^-$ detected last). However, NMS because of its large ϵ and DR compared to PTS provides for a better analyte response. An electropherogram of an alkyl sulfate mixture containing C_4–$C_{18}SO_4^-$ with NMS (not shown) was very similar with respect to both peak shape and separation time to that shown in Figure 4. A similar C_4–$C_{18}SO_4^-$ electropherogram but with smaller peaks was found using PTS. All the C_4–$C_{18}SO_3^-$ or C_4–$C_{18}SO_4^-$ peaks are baseline resolved within their homologous series, except peak $C_8SO_3^-$ (Figure 4) and peak $C_{10}SO_4^-$, which partially overlap with a system peak. At pH values 7 or higher, the system peak overlap increases, causing peak 5 to be obscured. The system peak overlap can be omitted if the percent of methanol is increased above 50%, however, only at the expense of longer migration times for $C_3SO_3^-$ or $C_3SO_4^-$.

The separation of complex mixtures of alkyl sulfates and alkanesulfonates of identical chain length is a challenging problem in CE because of their very similar electrophoretic mobilities. Chen and Pietrzyk[3] were able to resolve C_6–$C_{10}SO_3^-/SO_4^-$ pairs by incorporating Mg^{2+} in a salicylate buffer. However, the CE resolution of longer alkyl surfactant pairs was not considered. We found that a combination of the best anionic electrolyte system such as NMS with 50% methanol can enable the baseline separation of $C_{18}SO_3^-/SO_4^-$ and $C_{14}SO_3^-/SO_4^-$ pairs along with

(20) Becker, J. L. *J. Chromatogr.* **1994**, *662*, 153–166.
(21) Williams, S. J., Bergström, E. T., Goodall, D. M., Kawazumi, J., Evans, K. P. *J. Chromatogr.* **1993**, *636*, 39–45.
(22) Bruin, G. J. van Asten, A. C., Xu, X., Poppe, H. *J. Chromatogr.* **1992**, *608*, 97–102.

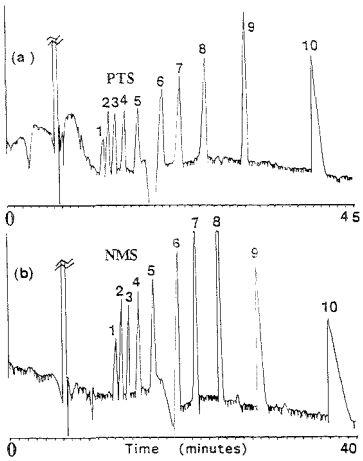

Figure 4. Comparison of PTS (a) and NMS (b) for the separation of a standard mixture of anionic sulfonated surfactants. Electrolyte composed of 5 mM PTS or NMS with 100 mM H_3BO_3, pH 6.0, and 50% methanol. Peak identification: 100 mg/L each of 1, $C_{18}SO_3^-$; 2, $C_{16}SO_3^-$; 3, $C_{14}SO_3^-$; 4, $C_{12}SO_3^-$; 5, $C_{10}SO_3^-$; and 70 mg/L each of 6, $C_9SO_3^-$; 7, $C_7SO_3^-$; 8, $C_6SO_3^-$; 9, $C_5SO_3^-$; 10, $C_4SO_3^-$. Vacuum injection for 3 s, +30 kV applied for separation, current 2–3 μA. IPD at 221 nm with PTS and 206 nm with NMS.

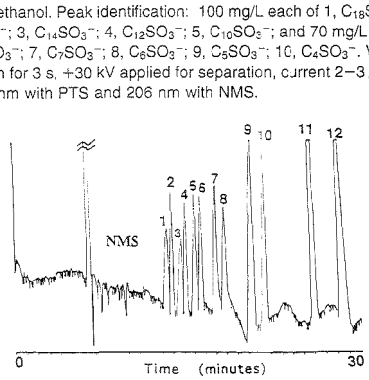

Figure 5. Separation of standard mixture of anionic sulfonated and sulfated surfactants. Electrolyte composed of 5 mM NMS with 100 mM H_3BO_3, pH 6.0, and 50% methanol. Peak identification: 100 mg/L each of 1, $C_{18}SO_3^-$; 2, $C_{18}SO_4^-$; 3, $C_{14}SO_3^-$; 4, $C_{14}SO_4^-$; 5, $C_{12}SO_3^-$; 6, $C_{12}SO_4^-$; 7, $C_{10}SO_3^-$; 8, $C_{10}SO_4^-$; and 70 mg/L each of 9, $C_8SO_3^-$; 10, $C_8SO_4^-$; 11, $C_6SO_3^-$; 12, $C_8SO_4^-$. Vacuum injection for 3.5 s, +30 kV applied for separation, current 2–3 μA. IPD at 206 nm.

the C_6–$C_{12}SO_3^-$/-SO_4^- pairs in 30 min (Figure 5). A similar electropherogram but with smaller peaks could be generated with PTS. Resolution with NMS can be further improved by decreasing the injection size without any significant loss in analyte signal. Using a NMS electrolyte, the LOD values at S/N = 3 for C_{18}–$C_{14}SO_3^-$ or C_{18}–$C_{14}SO_4^-$ are in the 0.5–1.0 mg/L range. This range corresponds to a LOD of about 0.1 pmol, similar to previously reported detection limits.[9]

Combined Separations of Nonchromophoric Cationic and Anionic Surfactants. In the past, IPD has proven to be a useful approach for the detection of inorganic anions and cations separated simultaneously by ion exchange columns.[23–27] Nevertheless, this strategy for CE has not been reported to the best of our knowledge. To obtain a favorable simultaneous separation of cationic and anionic surfactants using CE with IPD, the countercation and counteranion electrolytes must fulfill the following criteria: (1) A two-component IPD solution must be chromophoric with high ϵ and DR. (2) They must provide a suitable mobility match, i.e., small ΔT value (ΔT = migration time of IPD reagent − migration time of analyte ion). (3) IPD reagents should preferably be strong organic bases or acids to ensure that a high fraction of both are ionized for enhanced analyte displacement and good sensitivity; however, they must have reasonable solubility in an organic solvent. (4) Contribution from the non-UV-absorbing counterion must be minimized. For this reason, mixing of free aromatic bases and acids (instead of the salts) to generate a two-component IPD reagent system is important. This procedure minimizes the dilution of the UV-absorbing component by nonabsorbing extraneous spectator ions. A pH range of 6–7 minimizes the contribution of H^+ and OH^- ions (generated from the buffer), which in turn improves the detectability of IPD. (5) Absorbance match of the IPD reagents should be as close as possible (i.e.−ΔA should be minimum) so that neither the cation nor the anion is masking the absorbance of the other ion. (6) The total background absorbance (A_t) should be additive and be within the linear range of the UV absorbance detector. The A_t value for this particular instrument was found to be definitely linear up to 0.2 AU and fairly linear to 0.5 AU.[28] Although the normal linear range found for most instruments is about 0.1 AU, the selection of an electrolyte that suppresses analyte electromigration dispersion can extend the calibration range in IPD.[14]

Taking into consideration all the above-mentioned factors, BA or PY bases were mixed with NMS or PTS acids to generate various combinations of two-component IPD reagents. For the selection of a suitable wavelength for simultaneous detection of both IPD reagents (criterion 5), the background absorbance of 5 mM each of BA, PTS, or NMS was measured from the readout of the CE detector by flushing the capillary with the solutions. The cation − anion background absorbance (ΔA) values for BA-PTS and BA-NMS electrolytes as a function of wavelength were determined in 1–2-nm increments throughout the region of 200–220 nm. With BA-PTS, ΔA values (+3 mAU) are found to be smallest at 201 and 208 nm, whereas a value of −61 mAU is found with the BA-NMS electrolyte at its minimum interference wavelength of 200 nm.

Table 2 list the total background absorbance (A_t) and total dynamic reserve (DR_t) values of the three binary IPD reagents at the optimum wavelengths. The A_t values (within an average relative error of ±1.1%) are found to be additive of the individual absorbances and fall within the linear range of 0.5 AU of the UV detector used. The DR_t of BA-PTS is lower than BA-NMS as the background absorbance/noise ratio of NMS is greater than that for the PTS counteranion (see Table 1). The reason for PY-PTS having the lowest DR_t value is due to the difficulty in finding a suitable wavelength where both counterions possess high absorbance. A wavelength of 220 nm was deemed to be best for PY-PTS; however, the absorbance of PTS is quite a bit stronger than PY.

(23) Pietrzyk, D. J.; Senne, S. M.; Brown, D. M. *J. Chromatogr.* **1991**, *546*, 101–10.
(24) Hayakawa, K.; Sawada, T.; Shimbo, K.; Miyazaki, M. *Anal. Chem.* **1987**, *59*, 2241–45.
(25) Small, H. *Ion Chromatography*; Plenum Press: New York, 1989; pp 202–5.
(26) Iskandarani, Z.; Miller, T. E. *Anal. Chem.* **1985**, *57*, 1591–94.
(27) Small, H.; Miller, T. E. *Anal. Chem.* **1982**, *54*, 463–69.
(28) Shamsi, S. A.; Danielson, N. D. *Anal. Chem.* **1995**, *67*, 1345–52.

Author Index

Table 1. Recovery of Calcium from Water, Serum, and Urine Using Ion Exchange Membrane Filters and Oxalate Precipitation

extraction method	water	serum	urine
cation exchange[a]			
Ca loaded, mg	1.0	0.09	0.6
recovery, %[b]	85.5 ± 0.9	74.0 ± 3.4	65.9 ± 2.5
Chelex exchange[a]			
Ca loaded, mg	1.0	0.09	0.6
recovery, %[b]	64.6 ± 9.5	97.8 ± 3.2	19.6 ± 0.8
precipitation[c]			
Ca loaded, mg	0.2	0.2	0.1
recovery, %	93.0	100.0	96.3

[a] $n = 3$ filters; a total of 3 mL of eluent was collected for each filter. [b] Data reported as mean ± SD. [c] $n = 1$.

Table 2. Linear Regression Analysis of the Enrichment of the $^{44}Ca/^{48}Ca$ Ratio of Ion Exchange Treated Standard Curves (Ordinate) versus Oxalate-Precipitated Standard Curves (Abscissa)[a]

matrix	treatment	regression line	RS_{yx}[b]
water	cation	$y = -0.367 + 1.016x$	0.020
	Chelex	$y = -0.118 + 1.000x$	0.026
serum	cation	$y = 0.041 + 0.976x$	0.025
	Chelex	$y = 0.573 + 0.952x$	0.014
urine	cation	$y = -0.628 + 1.017x$	0.026
	Chelex	$y = -0.813 + 0.990x$	0.031

[a] Range of enrichment was 10%–30%. Duplicate standard curves were prepared for each matrix. [b] RS_{yx} is relative standard error of the estimate of the regression line.

to those observed from the oxalate precipitation curves. The linear regression analyses are shown in Table 2. All curves were linear with slopes not different from 1 ($p < 0.001$)[11] and standard errors of the estimate less than 1. No isotopic fractionation was observed for the three matrices investigated.

Automated Data Analysis Efficiency. Table 3 shows the results of the effect of extraction method on automatic data analysis for the three matrices investigated. Interruption of automated data analysis of oxalate-precipitated calcium is a problem observed principally with urine samples in this laboratory. In this experiment, urine samples yielded the lowest number of

Table 3. Effect of Extraction Method on Automatic Data Analysis Efficiency, Expressed as a Percentage of Total Number of Filaments Analyzed[a]

extraction method	water	serum	urine
oxalate precipitation	75% (12)	94% (18)	58% (12)
cation exchange	92% (12)	83% (18)	79% (14)
Chelex exchange	100% (12)	90% (20)	62% (16)

[a] The number in parentheses indicates the total number of filaments analyzed.

filaments analyzed automatically. A 39% improvement in automatic filament analysis was observed for urine samples extracted with cation exchange filters. Water-extracted samples also showed improvements in automated data analysis when extracted with cation (21%) or Chelex (33%) ion exchange filters. No improvement was observed for the already very effective automated analysis of serum calcium samples.

CONCLUSIONS

We report a method that allows for easy and rapid extraction and purification of calcium from biological fluids prior to isotopic enrichment analysis. The use of ion exchange filters resulted in an improvement in automated sample analysis for water and urine samples. Sample preparation for thermal ionization mass spectrometric analysis using ion exchange filters requires 1 day, as opposed to a 2 day procedure for oxalate precipitation.

Received for review May 22, 1995. Accepted August 21, 1995.[⊗]

AC950484V

[⊗] Abstract published in *Advance ACS Abstracts*, October 1, 1995.

multiple 1 mL volumes of 6 M and 1 M HCl from the cation and Chelex filters, respectively.[9] Three 1 mL eluent fractions were collected into acid-washed glass centrifuge tubes and were analyzed individually for total Ca using flame atomic absorption spectrophotometry (Perkin-Elmer Model 5000, Perkin-Elmer Corp., Norwalk, CT).

The procedure for the oxalate precipitation has been described previously.[5]

Isotope Dilution Mass Spectrometry. Duplicate standard curves were prepared for mass spectrometric analysis by the addition of highly enriched (98.95%) ^{44}Ca tracer to aliquots of water (0.1 mg of Ca/mL), serum (0.091 mg of Ca/mL), and urine (0.045 mg of Ca/mL). Enrichments approximated 10%, 20%, and 30% of the naturally occurring ^{44}Ca. Following a 24 h equilibration period, calcium was extracted from each prepared standard by precipitation and cation and Chelex ion exchange using one-third of the total volume for each extraction approach. The serum (but not the water or urine) ion exchange filters were washed with 10 mL of deionized water prior to elution of the calcium. Calcium was extracted with 2 mL of eluent for all standards. The elutions were heated and dried in an argon stream. Concentrated HNO_3 was added to the dried precipitates, and these solutions were dried again. All precipitates (oxalate, cation, Chelex) were then dissolved in 3% HNO_3 for mass spectrometric analysis. Isotope ratios were measured using the Finnigan MAT THQ Thermoquad mass spectrometer with electron multiplier detection in the dual filament mode. All ratios were measured relative to ^{48}Ca, and fractionation correction was made using the $^{43}Ca/^{48}Ca$ ratio.

Automated Data Analysis Efficiency. Thermal ionization filaments were loaded with a 5 μL droplet of extracted calcium (cation exchange, Chelex, oxalate precipitated) from water, serum, and urine samples. The filaments were loaded onto the sample magazine (13 filaments/magazine), which was then mounted in the THQ mass spectrometer. Eleven magazines were analyzed using the THQ automatic data analysis program. The total number of filaments automatically analyzed was expressed as a percentage of the total number of filaments loaded in the instrument for each matrix.

RESULTS AND DISCUSSION

Total Recovery of Calcium. Figure 1 shows the cumulative percentage recovery of calcium extracted with each successive eluent fraction collected. It is evident that more than 3 mL of eluent will extract only minimal additional calcium. An additional 2 mL of eluent added to the serum cation filter only resulted in the recovery of an additional 3.6% of Ca loaded (total recovery of 77.6 ± 2.1%). A more detailed comparison of recovery efficiencies between the three extraction methods is shown in Table 1. These results demonstrate that the cation filter is more efficient for extracting Ca from water and urine matrices, while Chelex is more efficient for serum samples. The different extraction efficiencies between the cation and Chelex filters observed for the three matrices can be explained on the basis of extraction equilibria and residence time (i.e., amount of time the sample remains in contact with the resin).[10] Chelex has a longer equilibration time than the cation resin. Therefore, the more viscous serum would remain in contact with the resin-embedded filter longer than the water or urine matrices, thereby resulting in the observations

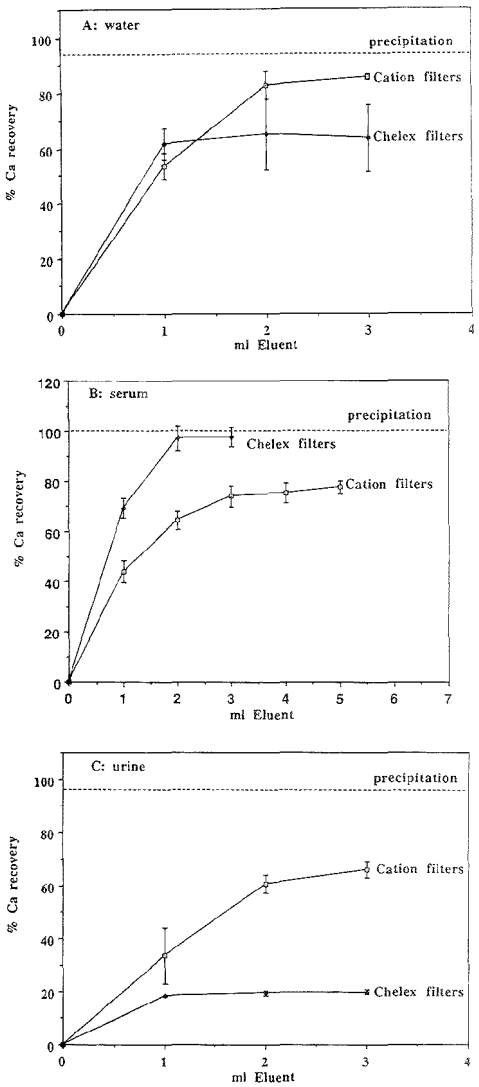

Figure 1. Total calcium recovery. Comparison of oxalate precipitation (dotted line), cation exchange ($n = 3$) and Chelex ion exchange ($n = 3$) calcium extraction from (A) water standard, 1 mg of Ca, (B) human serum, 0.091 mg of Ca, and (C) human urine, 0.585 mg of Ca. Data points are mean ± standard deviation.

reported here. In addition to increased residence time, the binding constant of Chelex is higher than that of most proteins.[10] This property would augment the already efficient Chelex extraction of calcium from serum.

Isotope Dilution Mass Spectrometry. The $^{44}Ca/^{48}Ca$ enrichments for the ion exchange standard curves were compared

(9) Strelow, F. W. E. *Anal. Chem.* **1960**, *32*, 1185–1188.
(10) Wood, R. Bio-Rad Laboratories, Richmond, CA, unpublished data.
(11) Zar, J. H. *Biostatistical Analysis*. 2nd ed.; Prentice-Hall Inc.: Englewood Cliffs, NJ, 1984; Chapter 17.

Anal. Chem. **1995**, *67*, 4217–4219

Extraction of Serum and Urine Calcium with Ion Exchange Membrane Filters for Isotope Enrichment Determination Using Thermal Ionization Mass Spectrometry

Nancy E. Vieira* and Alfred L. Yergey

Laboratory of Theoretical and Physical Biology, National Institute of Child Health and Human Development, National Institutes of Health, Bethesda, Maryland 20892

The extraction of calcium from water, serum, and urine using Bio-Rex 25 mm ion exchange membrane filters was compared with the oxalate precipitation procedure currently used in our laboratory. Total recoveries of a known quantity of calcium loaded onto the membrane filters for water, serum and urine were as follows: (a) cation exchange filter, 85%, 74%, and 66%; (b) Chelex, 65%, 98%, and 20%; and (c) oxalate precipitation, 93%, 100%, and 96%, respectively. Regression analysis for precipitation versus ion exchange isotope ratio measurements of standards prepared using highly enriched calcium-44 showed slopes of unity. An improvement of automated sample analysis was observed for water and urine calcium samples extracted with ion exchange filters.

We have used calcium stable isotopes extensively to study the absorption and kinetics of calcium in a variety of populations, including premature infants, pregnant and lactating women, and patients with disorders of calcium metabolism.[1-5] Calcium had been extracted from serum and urine samples by oxalate precipitation,[6] a procedure that may also coprecipitate other cations that could interfere with the thermal ionization process of the extracted calcium.[7] Such interference may cause irreproducible sample volatilization from the ionization filament, resulting in the interruption of automated data acquisition. This is observed principally in work with urine samples. We recently published a method using ion exchange membrane filters for the extraction and separation of magnesium from biological fluids.[8] In this work, we found that the chromatographic separation/extraction of Mg using membrane filters exactly mimics column chromaography and that it was a more convenient and less time consuming procedure. The objective in this study was to evaluate calcium extraction using membrane filters for the possibility of yielding a calcium sample containing fewer potentially confounding cations, thereby improving automated data acquisition.

EXPERIMENTAL SECTION

Materials and Reagents. $^{44}CaCO_3$ (98.95 atom % enriched) was obtained from Oak Ridge National Laboratory (Oak Ridge, TN) and was used to enrich water and the biological matrices under investigation. Water standards were prepared using a Ca atomic spectral standard, 1 mg/mL (Fisher Scientific, Fair Lawn, NJ).

All storage vessels, glassware, and disposable pipet tips were soaked overnight in a 10% HNO_3 bath (Baker-Analyzed, J. T. Baker, Phillipsburg, NJ), rinsed four times with deionized water (Hydro Service and Supplies, Durham, NC), and air-dried under cover.

Bio-Rex (Bio-Rad Laboratories, Richmond, CA) 25 mm syringe filters (AG 50W-X8, H^+ and Chelex ion exchange resin filters) were used for ion exchange chromatography. Ultrex II HCl and HNO_3 (J. T. Baker), high-purity HPLC grade methanol (Baxter Healthcare Corp., Burdick & Jackson Division, Muskegon, MI), and deionized water were used for all filter preconditioning and eluent solution preparation. All reagents used for the oxalate precipitation procedure have been previously described.[6]

Total Calcium Recovery. Three cation exchange and three Chelex filters were evaluated for calcium recovery efficiency for each matrix. Filters were conditioned prior to sample loading by the addition of 10 mL of methanol and then rinsed with 10 mL of deionized water. Filters were loaded with 1 mL of water standard (1 mg/mL, pH > 5), 1 mL of serum (0.091 mg/mL, pH 7), or 3 mL of urine (0.195 mg/mL, pH 5). Calcium was eluted with

* Address correspondence to this author at LTPB, NICHD, NIH, 10 Center Dr., MSC 1580, Building 10, Room 6C208, Bethesda, MD 20892-1580.

(1) Abrams S. A.; Yergey A. L.; Schanler R. J.; Vieira N. E.; Welch T. R. *J. Pediatr. Gastroenterol. Nutr.* **1994**, *18*, 20–24.
(2) Cross, N. A.; Hillman, L. S.; Allen, S. H.; Krause, G. F.; Vieira, N. E. *Am. J. Clin. Nutr.* **1995**, *61*, 514–523.
(3) Specker B. L.; Vieira N. E.; O'Brien K. O.; Ho, M. L.; Heubi J. E.; Abrams S. A.; Yergey A. L. *Am. J. Clin. Nutr.* **1994**, *59*, 593–599.
(4) Shoemaker L.; Welch T. R.; Bergstrom W.; Abrams S. A.; Yergey A. L.; Vieira N. *Pediatr. Res.* **1993**, *33*, 92–96.
(5) Abrams, S. A.; Lipnick, R. N.; Vieira, N. E.; Stuff J. E.; Yergey, A. L. *J. Rheumatol.* **1993**, *20*, 1196–1200.
(6) Yergey, A. L.; Vieira, N. E.; Hansen, J. W. *Anal. Chem.* **1980**, *52*, 1811–1814.
(7) Kolthoff, I. M.; Sandell, E. B. *Textbook of Quantitative Inorganic Analysis*, 3rd ed.; Macmillan Co.: New York, 1952; Chapter 8.
(8) Vieira, N. E.; Yergey, A. L.; Abrams, S. A. *Anal. Biochem.* 1994, *218*, 92–97.

same, improved detectability of cationic surfactants was observed with BA-PTS. These observations can be explained by the higher background absorbance of NMS, which is good for anionic surfactants, but can have some loss of sensitivity for cationic surfactants due to its masking effect on the BA background absorbance.

CONCLUSION

For the combined separation of cationic and anionic surfactants, peak capacity is higher for the latter class of compounds. Mixtures containing short-chain cationic and anionic surfactants can be separated in less than 7 min because methanol is not needed for solubility reasons in the run electrolyte. Peak resolution is improved with the addition of methanol in the running buffer but at the sacrifice of short separation times. The BA-NMS electrolyte will improve detectability of anionic surfactants because of the negative ΔA value but BA-PTS will detect cationic surfactants better as predicted by the positive ΔA value.

ACKNOWLEDGMENT

Purchase of the ABI CE instrument was possible through funds granted by the Miami University Committee for Faculty Research and the Academic Challenge Program.

Received for review May 26, 1995. Accepted September 8, 1995.[®]

AC9505132

[®] Abstract published in *Advance ACS Abstracts*, October 15, 1995.

Table 2. Characteristics of Two-Component IPD Reagents

cationic + anionic electrolyte	total background absorbance (A_t)[a]	total dynamic reserve (DR_t)[b]
benzylamine–naphthalene monosulfonate (BA-NMS)	0.313 (200 nm)	735
benzylamine–*p*-toluene sulfonate (BA-PTS)	0.224 (208 nm)	614
pyridinium–*p*-toluene sulfonate (PY-PTS)	0.193 (220 nm)	494

[a] The average relative error = ≤1.1% was calculated using the equation $A_{t\ exp} - A_{t\ theor}/A_{t\ theor} \times 100\%$. $A_{t\ theor}$ was sum of the individual background absorbances of cationic and anionic electrolytes. [b] Calculated as ratio of total background absorbance/total background noise.

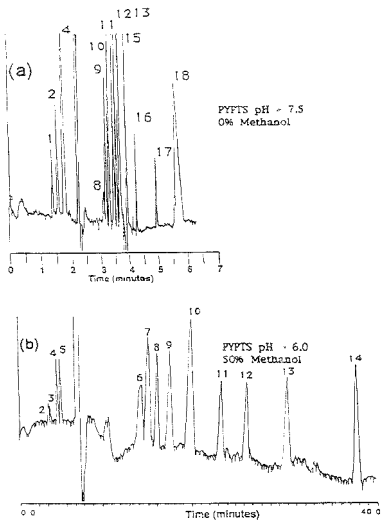

Figure 6. Comparison of electropherograms of a mixture of cationic and anionic surfactants in the absence (a) and presence (b) of 50% methanol. Electrolyte composed of 5 mM PY-PTS with 100 mM H_3BO_3, at pH 7.5 (a) and at pH 6.0 (b). Peak identification: 50 mg/L each of 1, TMA^+; 2, TEA^+ 3, ClETMA$^+$; 4, TBA^+; 5. THA^+; 100 mg/L each of 6, $C_{18}SO_3^-$; 7, $C_{16}SO_3^-$; 8, $C_{14}SO_3^-$; 9, $C_{12}SO_3^-$; 75 mg/L of 10, $C_{10}SO_3^-$; and 50 mg/L each of 11, $C_8SO_3^-$; 12, $C_7SO_3^-$; 13, $C_6SO_3^-$; 14, $C_5SO_3^-$; 15, $C_4SO_3^-$; 16, $C_3SO_3^-$; 17, $C_2SO_3^-$; 18, $C_1SO_3^-$; vacuum injection for 3.0 s, +30 kV applied for separation, current 8–10 μA in (a) and 4–5 μA in (b). IPD at 220 nm with PY-PTS.

Figure 6 compares the simultaneous separation of anionic and cationic surfactants in the absence (a) and the presence (b) of methanol using the PY-PTS electrolyte. An electropherogram taken using 50% methanol with an electrolyte pH value of 7.5 when compared to Figure 6a indicated the sensitivity (average peak area) for tetraalkylammonium cations increased only by a factor of 1.2, whereas the sensitivity for alkane sulfonates (C_8–$C_{18}SO_3^-$) showed a significant drop by at least 3-fold. Analysis time is longer with the use of methanol; however, no separation of longer chain anionic (C_{16} or $C_{18}SO_3^-$) or cationic surfactants (THA^+, $DDMA^+$) is possible without methanol. Note the weaker signal obtained for $C_{14}SO_3^-$ (peak 8) at 0% methanol as compared to 50%. This is despite the fact that pyridine is more ionized at pH 6.0 compared

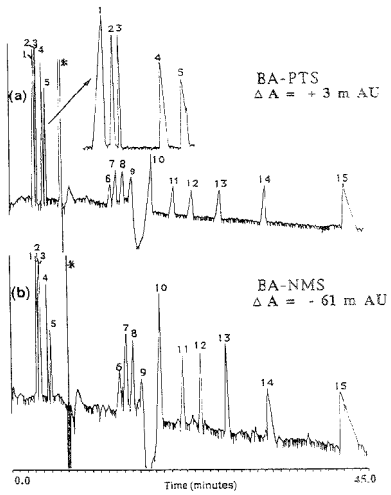

Figure 7. Comparison of BA-PTS (a) and BA-NMS (b) for the simultaneous separation of a standard mixture of cationic and anionic surfactants. Electrolyte composed of 5 mM BA-PTS or BA-NMS with 100 mM H_3BO_3, pH 6.0, and 50% methanol. Peak identification: 50 mg/L of 1, TEA^+; 25 mg/L each of 2, ClETMA$^+$; 3, TBA^+; 4, THA^+; 5, $DDMA^+$; 50 mg/L each of 6, $C_{18}SO_3^-$; 7, $C_{16}SO_3^-$; 8, $C_{14}SO_3^-$; 9, $C_{12}SO_3^-$; 75 mg/L of 10, $C_{10}SO_3^-$; and 35 mg/L each of 11, $C_8SO_3^-$; 12, $C_7SO_3^-$; 13, $C_6SO_3^-$; 14, $C_5SO_3^-$; 15, $C_4SO_3^-$; vacuum injection for 3.0 s, +30 kV applied for separation, current 4–5 μA. IPD at 208 nm with BA-PTS and at 200 nm with BA-NMS.

to a pH value of 7.5. However, for cationic surfactants such as TBA^-, TEA^+, and TMA^+, better detectability and shorter migration times are observed with 0% methanol. The shorter chain anionic surfactants, (C_1–$C_4SO_3^-$) are only shown in Figure 6a because their migration times are reasonable in the absence of methanol; however, the system peak eluting at about 4 min obscuring peak $C_5SO_3^-$ in Figure 6a is pronounced since both a higher pH and lower percent of methanol seem to be related to system peak intensity and position. This may not be a significant disadvantage as most of the commercial formulations of anionic surfactants usually contains RSO_3^- or RSO_4^- with R in the range of C_8–C_{18}.

Figure 7 compares electropherograms for the simultaneous separation of a 15-component mixture of anionic and cationic surfactants using BA-PTS and BA-NMS IPD electrolytes. Similar combined separations can also be obtained with ephederine–naphthalenemonosulfonate (EP-NMS), or ephederine–*p*-toulene–sulfonate (EP-PTS) electrolytes. As expected with the normal or positive polarity CE configuration, all cationic surfactants of increasing chain length are eluted before, and all anionic surfactants of decreasing chain length are eluted after the large rectangular water peak (*). This water peak increases in size with an increase in injection volume and has been used previously as an EOF marker in IPD.[14,21] The percentage of methanol in the BA-PTS or BA-NMS electrolyte can be raised to increase the peak capacity, lengthen the system peak retention, and promote detection of ≥C_{14} chain length cationic surfactants as in the PY-PTS case. However, the migration times of ≤$C_{10}SO_3^-$ or $C_{10}SO_4^-$ chain length compounds will become excessive. The detectability of anionic surfactants is better using the BA-PTS electrolyte than with BA-NMS. Even though the aromatic countercation is the

ANALYTICAL CHEMISTRY Information Express

Get the product data you need fast...

By Phone: Use the reference list below, and contact the companies to fill an immediate need, or...
By Fax: Use the fax form on the opposite page to send a direct written request.

Company	Page	Issue	RSN	Data+	Phone	Fax	Contact
AC Analytical Controls	623 A	10/1/95	415		215-638-7078	215-638-7096	Jim McCormack
Aldrich Chemical	IFC	10/15/95	none	●	414-273-3850	414-273-2095	Rich Gross
Burdick & Jackson	IFC	11/1/95	13	●	616-726-3171	616-728-8226	Kenneth L. Clark
Beckman Instruments	622 A	10/1/95	410	●	800-742-2345	714-773-8186	Amy Bratcher
Bioanalytical Systems	564 A	9/1/95	408	●	317-403-4572	317-497-1102	Craig Bruntlett
Brinkmann Instruments	657 A	11/1/95	2	●	800-645-3050	516-334-7506	C. Shevchenko
Bruker Instruments	560 A	9/1/95	401	●	508-667-9580	508-66-3954	Mark Chaykovsky
Bruker Instruments	668 B*	11/1/95	16		0721/9528-0	0721/9528-712	
Carl Zeiss	565 A	9/1/95	415	●	800-356-1090	914-681-7443	Irv Toplin
Carl Zeiss Jena GmbH	623 A	10/1/95	417		49-3641-64-2500	49-3641-64-3311	Zeiss Gruppe
Chem Service	538 A	9/1/95	1	●	800-452-9994	610-692-8729	Ron Gray
Chem Service	638 A	11/1/95	1	●	800-452-9994	610-692-8729	Ron Gray
Chromocol	681 A	11/1/95	412	●	203-261-7582	203-261-7319	Donna Anthony
Comstock	681 A	11/1/95	413	●	615-483-7690	615-481-3884	Susan Zell
Distek	680 A	11/1/95	409	●	908-422-7585	908-422-7310	Gerald Brinker
EG&G Instruments (Princeton)	610 A	10/1/95	10, 11	●	609-530-1000	609-883-7259	Ruth Rearick
Finnigan MAT	529 A	9/1/95	9	●	408-433-4800	408-433-4823	Gary Spear
Finnigan MAT	574 A	10/1/95	9	●	408-433-4800	408-433-4823	Gary Spear
Finnigan MAT	662 A	11/1/95	14	●	408-433-4800	408-433-4823	Gary Spear
Finnegan/Tremetrics	565 A	9/1/95	411	●	512-251-1555	512-251-1597	Elaine Moody
Fisons Instruments	622 A	10/1/95	413	●	508-524-1000	508-524-1100	Cathy Schaub
Fisons Instruments	618 A	10/1/95	401	●	508-524-1000	508-524-1100	Cathy Schaub
Fisons Instruments	676 A	11/1/95	401	●	508-524-1000	508-524-1100	Cathy Schaub
Fluka Chemie	509 A	9/1/95	5		41-81-7552511	41-81-7565449	
Fluka Chemie	571 A	10/1/95	1	●	41-81-7552511	41-81-7565449	
Hamilton	OBC	9/1/95	8	●	800-648-5950	702-856-7259	B. Milne/R. Beavers
Hamilton	OBC	11/1/95	7	●	800-648-5950	702-856-7259	B. Milne/R. Beavers
Hewlett-Packard	618 A	10/1/95	402	●	415-857-5603	415-857-8228	Doug Forsyth
Hiden Analytical	623 A	10/1/95	416		44-1925-445225	44-1925-416518	Ian D. Neale
Hiden Analytical	681 A	11/1/95	415		44-1925-445225	44-1925-416518	Ian D. Neale
Hinds Instruments	564 A	9/1/95	410	●	503-690-2000	503-690-3000	Ted Oakberg
Hi-Tech Scientific	564 A	9/1/95	409	●	44-722-323643	44-722-412153	David Mitchell
IN/US Systems	622 A	10/1/95	407	●	800-875-4687	813-620-3708	John Hnizdil
Isco	639 A	11/1/95	9-12	●	402-464-0231	402-464-0318	John R. Allington
Jeol USA	561 A	9/1/95	402	●	508-535-5900	508-536-2205	Robert DiPasquale
Jeol USA Inc.	OBC	10/1/95	7	●	508-535-5900	508-536-2205	Brian Musselman
John Wiley & Sons	581 A	10/1/95	5	●	212-850-6137	212-850-6264	S. Nelson
Kratos Analytical	676 A	11/1/95	402	●	201-825-7500	201-825-8659	David Surman
Labsphere	622 A	10/1/95	412	●	603-927-4266	603-927-4694	Joan A. Beaulieu
LPA	629 A	11/1/95	6		703-836-1360	703-836-6644	
Macherey-Nagel	580 A	10/1/95	2		(02421) 969-0	(02421) 969-199	
Mallinckrodt Baker	647 A	11/1/95	8	●	800-582-2537	908-859-9318	William Broad
Melles Griot	622 A	10/1/95	409		800-835-2626	714-261-7589	Lynn Strickland
Metrohm	512 A	9/1/95	2	●	41-071-538-585	41-071-538-9041	R. Steiner
Metrohm	584 A	10/1/95	3	●	41-071-538-5	41-071538-90	R. Steiner
Metrohm	6 C	10/15/95	none	●	41-071-538-5	41-071538-90	R. Steiner
Mettler-Toledo	565 A	9/1/95	412	●	800-638-8537	609-426-0121	Al Beronio
Molecular Devices	680 A	11/1/95	405		415-322-4700	415-322-2069	Kim Mulcahey
Oxford Instruments	681 A	11/1/95	416	●	508-371-9009	508-371-0204	Caroline Frankovich
Molecular Dynamics	564 A	9/1/95	407		800-333-5703	408-773-1493	Jim Bull
PE Nelson	618 A	10/1/95	403	●	408-577-2200	408-894-9307	Alycia Cortez-Frank
Perkin-Elmer	OBC	9/15/95	none	●	203-761-2574	203-762-6000	Mary Cooke-Kager
Perkin-Elmer	IBC	9/15/95	none	●	415-570-6667	415-638-6199	Valerie Tucker
Perkin-Elmer	589 A	10/1/95	6	●	415-570-6667	415-638-6199	Valerie Tucker
Perkin-Elmer	OBC	10/15/95	none	●	203-761-2574	203-762-6000	Mary Cooke-Kager
Perkin-Elmer	IBC	10/15/95	none	●	415-570-6667	415-638-6199	Valerie Tucker
Perkin-Elmer	642 A	11/1/95	5	●	415-570-6667	415-638-6199	Valerie Tucker
Perkin-Elmer	OBC	11/15/95	none	●	203-761-2574	203-762-6000	Mary Cooke-Kager
PerSeptive Biosystems	680 A	11/1/95	408	●	800-899-5858	508-383-7885	Charles Cuneo
Photometrics	564 A	9/1/95	405	●	602-889-9933	602-573-1944	Michelle Downs
Photometrics	680 A	11/1/95	410	●	602-889-9933	602-573-1944	Michelle Downs
Physical Electronics	676 A	11/1/95	403		612-828-6100	612-828-6109	John Hammond
Pickering Laboratories	681 A	11/1/95	414	●	415-694-6700	415-968-0749	John Deutschlander
Polymer Laboratories	680 A	11/1/95	407	●	413-253-9554	413-253-2476	Sheri Fettig
Princeton Gamma-Tech	680 A	11/1/95	406	●	609-924-7310	609-924-1729	Peter Quigley
Sapidyne Instruments	622 A	10/1/95	408		208-345-7677	208-392-4985	Steve Lackie
Scott Specialty Gases	IFC	9/1/95	7	●	215-766-8861	215-766-0320	Donna M. Vito
Scott Specialty Gases	599 A	10/1/95	8	●	215-766-8861	215-766-0320	Donna M. Vito
Scott Specialty Gases	670 A	11/1/95	15	●	215-766-8861	215-766-0320	Donna M. Vito
Shandon Lipshaw	565 A	9/1/95	413		800-547-7429	412-788-1138	Beverly Miller
Shimadzu Scientific Instruments	IFC	9/15/95	none	●	800-477-1227	410-381-1222	Colleen Bixler
Shimadzu Scientific Instruments	IFC	10/1/95	4	●	800-477-1227	410-381-1222	Colleen Bixler
Shimadzu Scientific Instruments	5 C	10/15/95	none	●	800-477-1227	410-381-1222	Colleen Bixler
Shimadzu Scientific Instruments	632 A	11/1/95	3	●	800-477-1227	410-381-1222	Colleen Bixler
Shimadzu Scientific Instruments	IFC	11/15/95	none	●	800-477-1227	410-381-1222	Colleen Bixler
Siemens Industrial Automation	622 A	10/1/95	411	●	404-740-3931	404-740-3998	Herbert Stuhler
Spectra-Tech	680 A	11/1/95	411		203-926-8998	203-926-8909	Debbie Esposito
Supelco	623 A	10/1/95	414	●	800-247-6628	800-447-3044	Michael Gray
Teledyne Electronic Technologies	521 A	9/1/95	3	●	415-962-6526	415-967-4353	Sharon Gomez
Thermo Separation Products	619 A	10/1/95	404	●	800-532-4752	408-526-9810	Brent Davis
Topac Scientific Instruments	565 A	9/1/95	414		617-740-8778	617-740-8779	Antoni Drybanski
Varian Associates	561 A	9/1/95	403, 404	●	415-424-6786	415-858-0480	Carl Hadjis
Varian Associates	619 A	10/1/95	405	●	415-242-6880	510-945-2335	Deborah Kohnstamm
Varlen Instruments	564 A	9/1/95	406		800-729-4447	815-729-3700	Steve Klinger
Waters	619 A	10/1/95	406	●	800-252-4752	508-482-2674	Tony Lewtas
Xelon	677 A	11/1/95	404		201-564-8833	201-564-8657	Jerry Rosenthal

Data+ Column: A bullet indicates that additional product and company information is available in the 1996 *Analytical Chemistry* LabGuide Edition.
RSN: Reader Service Number; *International Edition Only

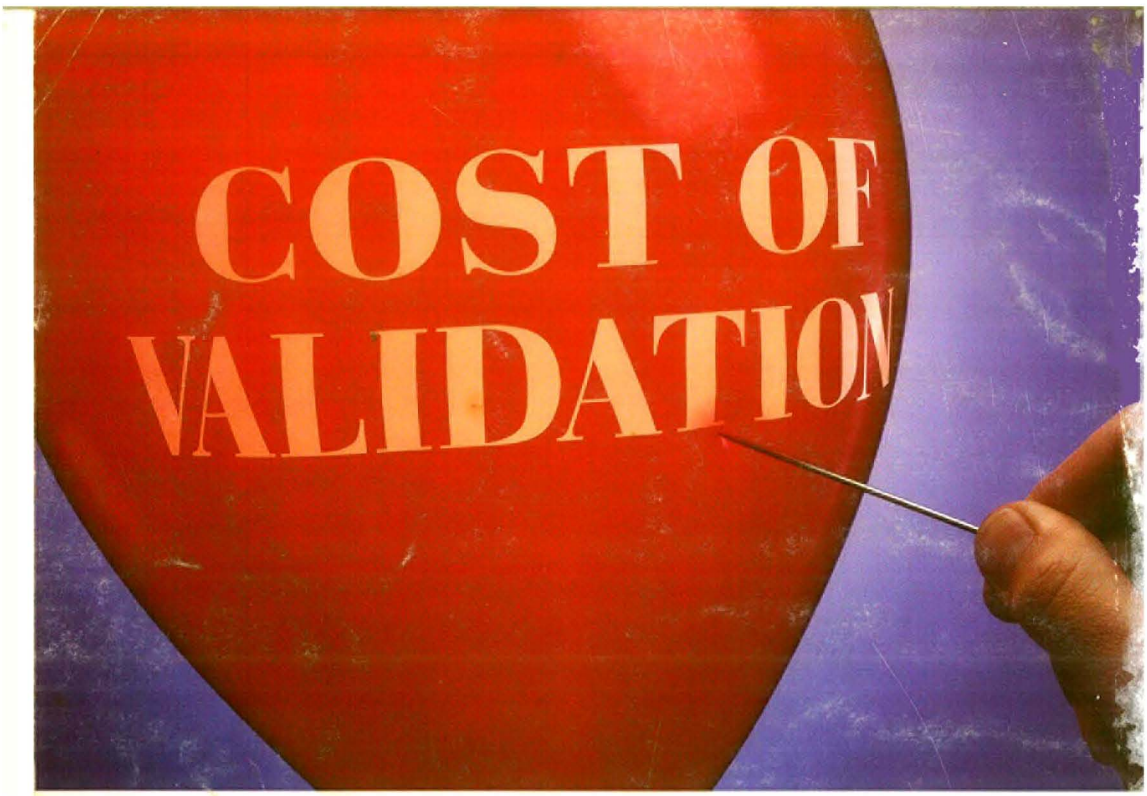

Spectrum FT-IR systems get right to the point.

Whether your goal is GLP for regulatory compliance or you simply want to get the right answers, Spectrum™ FT-IR keeps the cost of validation from rising.

To verify the integrity of instrument data, Spectrum FT-IR systems are available with Automatic Precision Validation (APV™) using built-in certified reference materials.

Spectrum systems also ensure that your processed data are reliable with Spectrum for Windows™—the world's first validated FT-IR software.

So get right to the point. Reduce your validation costs with Spectrum FT-IR systems. And make sure you are getting the right answers. For sales information or literature, in the U.S. call 1-800-762-4000. Outside the U.S., contact your Perkin-Elmer representative. On the Internet: http://www.perkin-elmer.com.

ISO 9001 CERTIFIED

New Spectrum FT-IR Systems

PERKIN ELMER

The Perkin-Elmer Corporation, 761 Main Avenue, Norwalk, CT 06859-0012, USA
Perkin-Elmer Ltd., Post Office Lane, Beaconsfield, Bucks HP9 1QA, UK. Bodenseewerk Perkin-Elmer GmbH, Postfach 10 17 61, D-88647 Ueberlingen, Germany

Order No. 95-331